AERO RESEARCH AVENUE

DISCOVERING THE WORLD

JUNE 2024

STUDENT CO-ORDINATOR'S
SHAIK MAHABOOB YESDAN ADAM

FACULTY CO-ORDINATOR
MR A SAI KUMAR

MLR INSTITUTE OF TECHNLOGY

DEPARTMENT OF AERONAUTICAL ENGINEERING

"AERO RESEARCH AVENUE"

2024

MARRI LAXMAN REDDY
GROUP OF INSTITUTIONS
MLR
Institute of Technology

Institute Vision:

Promote academic excellence, research, Innovation, and entrepreneurial skills to produce graduates with human values and leadership qualities to serve the nation

Institute Mission:

Provide student-centric education and training on cutting-edge technologies to make the students globally competitive and socially responsible citizens.

Create an environment to strengthen the research, innovation and entrepreneurship to solve societal problems.

Vision of the Department:

To be a centre of excellence in Aeronautical engineering with emphasis on Research & Innovation to serve the needs of industry with human values to build strong nation. The department's vision is derived from the institute vision and it vouches to help the institute in fulfilling its vision by becoming a center of excellence in Aeronautical Engineering.

Mission of the Department:

The mission statements are the action statements; the department intends to implement in fulfilling its vision. The key components are quality oriented technical education, multidisciplinary skills and Research & Innovation activities with human values.

M1. Provide quality oriented education, well-grounded in the fundamental principles of Aeronautical Engineering.

M2. Consistently produce top quality Aeronautical engineers with core and multidisciplinary skills, who can become ace leaders and successful entrepreneurs with human values.

M3. Continuously strive for knowledge; undertake Research and Innovation that will contribute to the industrial development of the nation.

Results in Engineering 23 (2024) 102607

Contents lists available at ScienceDirect

Results in Engineering

journal homepage: www.sciencedirect.com/journal/results-in-engineering

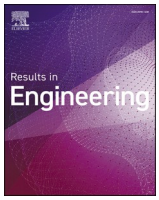

Split injection timing optimization in ammonia/biodiesel powered by RCCI engine

Elumalai Pv [a,b,c,*], Krishnaiah Ravi [d,**], Ramachandran Elumalai [d], Chan Choon Kit [e], Suresh Kumar K [f,***], Krishnasamy Karthik [g,****], M. Satyanarayana Gupta [h], Mohammad Asif [i]

[a] Department of Mechanical Engineering, Aditya University, Surampalem, India
[b] Research Fellow, Faculty of Engineering. Shinawatra University, Thailand
[c] Department of Mechanical Engineering, Saveetha School of Engineering, Saveetha Institute of Medical and Technical Sciences (SIMATS), Chennai, Tamil Nadu, 602105, India
[d] School of Mechanical Engineering, VIT University, Vellore, India
[e] Faculty of Engineering and Quantity Survey INTI International University, Persiaran Perdana BBN, Putra Nilai, 71800, Nilai, Negeri Sembilan, Malaysia
[f] Department of Mechanical Engineering, Faculty of Engineering and Technology, SRM Institute of Science and Technology, Kattankulathur, Chennai, 603203, Tamilnadu, India
[g] Vel Tech Rangarajan Dr Sagunthala R&D Institute of Science and Technology, Avadi, Chennai, 600 062, India
[h] Department of Aeronautical Engineering, MLR Institute of Technology, Hyderabad, Telangana, India
[i] Department of Chemical Engineering, King Saud University, P.O. Box 800, Riyadh, 11421, Saudi Arabia

ARTICLE INFO

Keywords:
Reactivity controlled compression ignition
Carbon free ammonia as IC engine fuel
Low carbon foot print algal biodiesel
Split injection strategy
Pollution

ABSTRACT

Employing carbon-neutral (NH_3) and low carbon footprint (biodiesel) fuels in Reactivity Controlled Compression Ignition (RCCI) engine mode is one possible method for minimizing carbon emissions in diesel engines. In this study, a Compression Ignition (CI) engine was customized to run in RCCI mode, employing High Reactive Fuel (HRF) as biodiesel and Low Reactive Fuel (LRF) as ammonia (NH3). Based on our earlier findings, the proportion of ammonia in premixing is fixed at 40 %. In the first phase, the primary injection timing of the algal biodiesel varied between 12 and 21°CA bTDC at a preset pre-injection timing of 46°CA bTDC. In the next phase, the pre-injection time varied between 46 and 54°CA bTDC, with the optimal main injection time being 18°CA. The result suggested that the optimal main and pre-injection at 18 and 58°CA bTDC increased the Cylinder Pressure (CP) by 30.1 %, and peak HRR and combustion phase angle were advanced. Brake Thermal Efficiency exhibited an 11 % enhancement, with Brake Specific Energy Consumption decreasing by 24.1 %. Nitrogen Oxide levels saw an increase of around 39.5 %. In contrast, reductions of 19.2 %, 23.5 %, 39.7 %, and 21.7 % were observed in Hydrocarbons, Carbon Monoxide, smoke emissions, and Exhaust Gas Temperature, respectively, compared to the single injection under full load conditions.

1. Introduction

1.1. Low temperature combustion (LTC)

According to research, greenhouse gases (GHG) released by human activities are intimately associated with global climate change, natural environment degradation, and energy resource scarcity [1]. Reduced usage of fossil fuels, aggressive development of renewable energy, mitigation of climate change, and the development of a low-carbon economy have established worldwide consensus [2–4]. Transportation-related carbon emissions totaled 896 million tons in 2020 [5]. Essentially, the use of fossil fuels in internal combustion engines (ICEs) is the primary source of CO_2 emissions in the transport sector. ICEs are not only the most thermally efficient technology, but

* Corresponding author.
** Corresponding author.
*** Corresponding author.
**** Corresponding author.
E-mail addresses: elumalaimech89@gmail.com (E. Pv), ravi.krishnaiah@vit.ac.in, ravikrish97@gmail.com (K. Ravi), sureshkk@srmist.edu.in (S.K. K), karthikmeed@gmail.com (K. Karthik), masif@ksu.edu.sa (M. Asif).

https://doi.org/10.1016/j.rineng.2024.102607
Received 9 March 2024; Received in revised form 20 July 2024; Accepted 22 July 2024
Available online 23 July 2024
2590-1230/© 2024 The Authors. Published by Elsevier B.V. This is an open access article under the CC BY-NC license (http://creativecommons.org/licenses/by-nc/4.0/).

also an important base industry that supports the rapid expansion of new industries in the world and continues to lead the way [6]. As a result, low-carbon and zero-carbonization of ICEs justifies continuous effort. Among these ICEs, CI engines are extensively used as sources of power in transportation and energy supply owing to their great fuel economy and sturdiness, but their usage has been limited due to rigorous pollution restrictions [7]. Therefore, significant improvements have been achieved in reducing NOx and smoke emissions, mainly from CI engines [8]. To fulfill rigorous emissions rules, certain combustion techniques like RCCI, PCCI and HCCI have been developed in recent years. These techniques are known as LTC [9]. Decreasing the combustion temperature and minimizing the fuel rich regions may significantly decrease NOx emissions in LTC [10]. Chemical kinetics entirely govern the LTC combustion process [11].

1.2. RCCI combustion

The RCCI engine is superior to other combustion concepts in terms of operating range, thermal efficiency, and emission value improvements without the need for aftertreatment [12]. RCCI permits the injection of two different reactivity fuels using various injection techniques to develop a reactivity gradient inside the cylinder. Premixed LRF is fed into the cylinder via the intake port. The HRF is delivered straight into the cylinder. When the cylinder temperature is high enough during the end of compression stroke, the combustion process begins where there are higher concentrations of HRF and disseminates throughout the remainder of the combustion chamber [13,14]. The type and proportion of LRF in RCCI mode have a notable effect on flame development [15]. Research compares RCCI combustion to Conventional Diesel Combustion (CDC). The findings demonstrate that enhancing the fraction of low-reactivity fuel energy from 10 % to 60 % enhanced CP owing to accelerated combustion timing and volumetric energy discharge. In the cumulative heat release analysis, RCCI mode exhibited higher energy release compared to CDC mode [16]. For instance Okcu et al. [12] used octanol and heptanol as LRF and diesel as HRE. According to the research, modifying the type and proportion of LRF might result in better controlled combustion. They were able to observe that, the increase in CO and HC emissions remains a concern at lower loads. As a result, substantial research into LRF for use in RCCI operations is required to minimize unburned emissions. The effects of diesel main injection timings on the RCCI engine were meticulously explored in a study by Liu J et al. The results reveal that by advancing the main injection from 15 to 27°CA bTDC, the peak CP rises, the knock propensity lowers greatly, and CO, HC and soot emissions are decreased by 55.6 %, 43.1 %, and 28.8 %, respectively [17]. In an experimental investigation, natural gas was advocated for usage in RCCI engines due to its greater octane number and reduced carbon to hydrogen ratio. According to reports, these qualities reduced the peak CP and produced incomplete combustion emissions [18]. In an investigation, it was studied that the petrol/biodiesel RCCI mode may achieve efficient combustion by delaying direct injection time in conjunction with later intake valve closing timing. Moreover, the Brake Thermal Efficiency (BTE) of the RCCI mode rose by 15 % following the addition of exhaust gas recirculation technology [19]. Research was conducted to compare the engine combustion, performance, and emission analysis of LTC modes, namely RCCI and PCCI, with the CI combustion mode. The results reveal that at greater engine loads, RCCI mode combustion achieved significantly enhanced BTE than CI and PCCI combustion modes. Another significant conclusion of this research was that RCCI combustion had a much lower EGT than PCCI and CI combustion modes [20]. A study was conducted to explore the influences of the RCCI engine with biodiesel blends as the HRF and ethanol as the LRF. Results revealed that HC and CO emissions rose while significant NOx emissions decreased [21]. Research investigated the combustion, performance, and emission characteristics of PCCI and RCCI. According to the study's findings, RCCI has a 3.9 % greater thermal efficiency than PCCI. Furthermore, RCCI outperforms PCCI in terms of HC, CO, NOx, and soot emissions [22]. Rangasamy et al. [23] examined the emissions characteristics of the methanol/biodiesel and the methanol/diesel RCCI operations. The methanol/biodiesel RCCI mode was more stable than the methanol/diesel RCCI mode because the ignition delay (ID) was shorter, and the reactivity gradient was wider when the cetane of the LRF was higher. Also, the HC, CO, and smoke emissions of the methanol/biodiesel operation improved, whereas the NOx decreased. Additionally, a number of studies have been done employing fossil fuels with high octane numbers as LRFs in RCCI operations. These fuels are observed to cause significantly greater CO and HC emissions [24].

1.3. Split injection technique

The split injection technique involves dividing the main injection pulse into two or more injections, enhancing the reaction zone between the combustion chamber air and the flame boundary while reducing the fuel-rich zone [25]. High-viscosity biodiesel with a mechanical injection system reduces thermal efficiency while increasing smoke and hydrocarbon emissions. Adapting the fuel injection system can address the challenges posed by increased viscosity. Common-Rail Direct Injection (CRDI) systems, in contrast to mechanical injection, enhance thermal efficiency and diminish emissions of Hydrocarbons (HC) and smoke [26]. The effect of the most important factors on RCCI engine combustion, including injection timing and injection duration, was numerically analyzed in a methane/natural gas-powered RCCI engine. The results show that delaying the commencement of single-stage injection increases HC, CO, and NOx emissions. The findings for different double injection schedules show that the cylinder temperature and rate of heat release decrease. Moreover, increasing the injection duration (from 55° to 70°CA) also decreases CO, NOx, and HC emissions [9]. In light of this, CRDI stands as a proven method for boosting engine performance while lowering exhaust pollutants. It also enables the implementation of split injection strategies and adjustments to split injection ratios to achieve further emission reductions. Split injection is proposed as a viable approach to enhancing in-cylinder combustion and emission traits without the need for extensive engine modifications [27]. Kakaee et al. [28] examined the utilization of CH_4 in RCCI engines. According to reports, natural gas was used as LRF and diesel as HRF in the RCCI operation using the split injection technique. Another research investigated the influence of injection timing on mixture reactivity and stratification by using various diesel injection techniques. The research found that advancing diesel injection enhances reactivity within the cylinder mixture, whereas delaying injection enhances mixture stratification. Moreover, the dual injection method proves more effective in scenarios with lower premixed energy ratios, while the single injection strategy performs better in cases with higher energy premixing levels [29]. According to the research, engine load and fuel premix ratio had an impact on engine characteristics. The effects of pilot mass, split diesel fuel injection timings, and the amount of pre-mixed natural gas on RCCI operation were investigated. The results showed that engine thermal efficiency could be increased, and smoke and NOx could be decreased by altering the experiment settings. Additionally, there are fewer emissions of HC and CO [30]. Yousefi et al. [31] investigated the use of the split injection technique to enhance BTE and lower emissions in an ammonia diesel powered dual-fuel CI engine. The results indicates that split injection increases indicated thermal efficiency by 39.72 % while simultaneously reducing engine exhaust emissions.

1.4. Ammonia as ICE fuel

The significant growth in GHG concentrations over the last millennia has raised the world average temperature, which may create climatic difficulties and have an influence on our humanity [32]. Because of the challenges and hazards associated with conventional carbon-based fossil energy, carbon offsets in transportation are increasingly necessary. The

increase in CO_2 emissions from the transportation sectors contributes significantly to the rise in GHG concentrations [33]. Controlling the CO_2 emissions of ICEs may therefore aid in GHG reduction [34]. Widening the usage of carbon-free fuels is one strategy to lower the ICE's carbon emissions. Carbon-free sources like hydrogen and ammonia help to mitigate environmental problems caused by GHG emissions [35]. The use of H_2 in ICEs has been extensively studied and has performed well [36,37]. But, because of its strong reactivity, hydrogen easily explodes when combined with air. Hydrogen is an excellent source of energy and a cleaner fuel with a better heating value than fossil fuel. However, improved storage methods are necessary, and the complexity of liquidation raises storage and transportation costs. As a result, hydrogen as a carbon-neutral alternative fuel in ICEs has limits [38]. Apart from hydrogen, ammonia, which is a hydrogen carrier, is an excellent energy source for transportation vehicles owing to its availability and storage capabilities [39,40]. As a result, ammonia usage in ICEs has been a major topic of study recently in an effort to reduce carbon emissions. Using carbon-free fuels like ammonia may aid in the decarburization of ICEs [41]. A study demonstrated the effects of substituting diesel fuel with ammonia in an ammonia-diesel blend dual-fuel engine. The results demonstrate that ammonia can deliver 84.2 % of the input energy, while increasing the diesel replacement increases thermal efficiency. Moreover, augmenting the ammonia energy content transitioned the combustion phase in dual fuel mode from diffusion to premixed combustion. This adjustment resulted in a 6.8°CA reduction in combustion duration and a shift of 32°CA in combustion phasing. While ammonia effectively decreased CO_2 and CO emissions, it also led to an increase in NO_X emissions [42]. Forby N et al. [43] investigated the ammonia energy in the dual fuel engine as LRF and n-heptane as HRF. Exhaust emissions are decreased due to increased ammonia combustion efficiency with split injection of direction injection fuel. Therefore, the investigation suggested that multi-injection and advance injection of HRF were two conceivable possibilities for ammonia combustion. Moreover, the work's innovation is highlighted by the split injection parameters calibration of the CRDI engine employing RCCI impact among the operating parameters.

1.5. Biodiesel as ICE fuels

The reason for an alternate source of energy is the energy security problem with traditional crude-based fuels as well as increased exhaust gas emissions from the CI engine, which operates on diesel fuels. Biofuels, which are produced from diverse biomass feedstocks, are the ideal replacement for renewable and ecologically beneficial fuels [44]. Renewable sources of energy like biofuels have great potential to displace fossil fuels. They provide plenty of benefits, including reusability, sustainability, a decrease in GHG emissions, and regional development [45]. The most popular biofuel is biodiesel because it has qualities that are extremely comparable to diesel fuel and can be used with only minor engine modifications [46,47]. When compared to petroleum-based diesel, biodiesel has several advantages, including being oxygenated, environmentally friendly, having an elevated flash point (storage), being biodegradable, emitting fewer emissions, and being produced from an abundance of resources, such as vegetable, algal, and waste oils [48,49]. There are also disadvantages to using biodiesel in addition to these specific benefits [50–52]. Their poor cold flow and spray qualities, greater viscosity, lower heating value, higher NOx emission levels, engine power losses, and increase in BSEC may all be listed as severe drawbacks [53,54]. Therefore, reducing biofuel and increasing the use of carbon-free fuels will sustain the CI engine.

2. Aims and aspirations in the current research

The investigation is based on a four-stroke, electronically regulated common-rail CI engine altered to use NH_3 as fuel. Ammonia usage in CI engines significantly affects exhaust characteristics. However, ammonia has certain shortcomings in terms of combustion characteristics and compatibility. Hence, recommending its adoption as a substitute for fossil fuels, relying solely on engine performance metrics, requires further scrutiny. It is necessary to evaluate the pre- and main-injection strategies to address the deficiencies of NH_3 combustion, resulting in an improved early Start of Combustion (SoC) of algal biodiesel. Consequently, a substantial study has been conducted into the effects of NH_3 on CI engines. The investigation's goal is to decrease engine emissions by minimizing biodiesel and improving carbon-free fuels for CI engine combustion. As a result, low-carbonization and zero-carbonization of ICE require continuous effort. On the contrary, ammonia demonstrates the lowest adiabatic flame temperature, superior latent heat of vaporization, and diminished combustion efficiency. Therefore, partitioning the primary injection of biodiesel into pre- and main injections with ammonia would augment combustion efficiency. The initial injection of biodiesel plays a pivotal role in this process by effectively delaying the ignition, a critical aspect of the combustion process.

To achieve optimal combustion efficiency for ammonia/biodiesel mixtures in CI engines, an in-depth analysis of RCCI dynamics using adjustable split injection is imperative. This study concentrates on performance metrics, combustion processes, and emission profiles across diverse load scenarios at a steady engine speed of 1500 rpm. Contemporary research examines the combustion traits of ammonia when amalgamated with other fuels, underscoring the prospective advantages and difficulties inherent in these blends. Also, the utilization of NH_3/biodiesel mixtures in RCCI mode-operated engines using biodiesel split injection has yet to be extensively examined. According to our previous investigations, maintaining an NH_3 premixing ratio of 40 % in RCCI mode is ideal; any deviation from this ratio tends to diminish the engine's thermal efficiency. By analyzing the combustion dynamics, performance metrics, and emission characteristics associated with pre-and main-injection timings in RCCI engines, our research suggests that fine-tuning these parameters can significantly improve the combustion efficiency of NH_3 when used as a fuel in RCCI engines. The current research focuses on how various biodiesel pre- and main-injection angles burn 40 % premixed ammonia with the 45 % biodiesel split ratio (45 % pre-injection and 55 % main-injection) by measuring combustion, performance, and emissions factors. Initially, the engine test rig was configured to operate in a dual-fuel mode with 40 % NH_3 and biodiesel, utilizing a single biodiesel injection approach across different load conditions. Subsequently, the engine continued to run in the 40 % NH_3/biodiesel dual-fuel mode and scrutinized the impacts of pre- and main injection of biodiesel under varying load scenarios.

3. Experimental methodology

3.1. Ammonia supply system

A 150-pound NH_3 cylinder was utilized to store the liquid NH_3, with its temperature maintained at 38 °C via a heating blanket affixed to the cylinder. Gaseous ammonia from the cylinder is routed through a pressure regulator and a mass flow meter to quantify the ammonia flow rate before reaching a solenoid injector within the intake manifold. A gas reservoir was installed upstream of the ammonia injectors to dampen flow fluctuations caused by pressure swings. Vaporized NH_3 is dispensed into the intake manifold using an electronically regulated port fuel injection system. An electronic control unit (ECU) governed the pulse width, injection pressure, and timing of the injections. The NH_3 energy premixing percentage was obtained by adjusting the injector's input voltage. The pressure regulator moderates high inlet pressures to suitable output levels and controls the flow of NH_3 gases. Additionally, it strives to uphold consistent exit pressure despite fluctuations in input pressure. The mass flow rate of gaseous NH_3 is meticulously regulated by passing it through a precision flow control valve before reaching the NH_3 mass flow meter. 40 % of the ammonia's energy contribution was introduced via the port injection method, while the remaining biodiesel

fuel was delivered using an ordinary fuel injection method.

3.2. Energy fraction methodology

According to equation (1), the energy share of NH_3 is calculated as the ratio of the energy from ammonia to the total energy provided for combustion:

$$\%NH_3 = \frac{(m_{NH3} \times CV_{NH3})}{(m_{BD} \times CV_{BD}) + (m_{NH3} \times CV_{NH3})} \times 100 \quad (1)$$

Where m_{NH3} and m_{BD} are the ammonia and biodiesel mass flow rates, respectively. The calorific values of NH_3 and biodiesel fuels are represented as CV_{NH3} and CV_{BD}, respectively. The tests incorporated into the scope of the research were performed under varying loads and at 1500 rpm. The test engine was thermally stabilized to 80 °C to ensure consistent operating conditions. Experimental trials were conducted in triplicate to mitigate data acquisition discrepancies, and the outcomes were averaged for precision. Tables 1 and 2 outline NH_3 and algae biodiesel fuels' properties and flow metrics.

3.3. Experimental setup

For this investigation, a 4-stroke mono-cylinder constant-speed common-rail injection system was designated from the Kirloskar research engine. Table 3 delineates the comprehensive engine parameters and specifications. The adaptable engine setup is rigidly placed on the test bench, with mechanical linkage to an eddy current dynamometer. A strain gauge load cell is employed to measure the applied load. A water-cooling arrangement is utilized to maintain optimal temperatures for both the dynamometer and engine. To examine the temperature of the exhaust emission, a K-type thermocouple sensor is correctly positioned at the appropriate junction. The CP with respect to crank angle (CA) data is necessary for the investigation of fuel combustion behavior. Moreover, a piezoelectric transducer and a charge amplifier are installed to collect pressure data. The airflow sensor, calorimetric fuel sensor, and thermal model FT1 flowmeter are used to detect the rate of consumption of intake air, directly injected fuel, and port-injected ammonia by the engine at each cycle for performance analysis. Fig. 1 illustrates a schematic representation of the experimental engine configuration. Furthermore, the engine control system is adjusted to manual mode for experimentation, incorporating a customizable control feature for injection timing. The MCAR software package's ECU, which is controlled by NIRA, was launched to allow this to happen. The data acquisition system makes use of the observed data. Further, it is utilized to determine the different combustion and performance parameters by applying thermodynamic principles. The AVL gas analyzer assesses exhaust emissions like HC, CO, and NOx, while the AVL 444 smoke meter model evaluates smoke opacity. A moisture trap and filtration system safeguard the gas analyzer from moisture and particulates.

Table 1
Properties of test fuels.

Properties	Unit	Algae biodiesel	NH_3
Viscosity @ 40 °C	cSt	5.07	–
Density @ 20 °C	g/ml	0.88	0.73
Flame velocity	m/s	0.3	0.32
Calorific value	MJ/kg	41.08	18.5
Cetane number	–	42	–
Octane number	–	–	130
Mass diffusivity in air	cm^2/s	–	0.22
Latent heat of vaporization	kJ/kg	306	1371
Minimum ignition energy	mJ	–	8
Auto ignition	K	523	651
Flash point	°C	91	132
Fire point	°C	121	148
Flammability limit	% vol	0.6–7.5	14–33.8
Stoichiometric A/F ratio	–	–	6.06

3.4. Uncertainty

To compute the uncertainties of measured parameters with $+2\sigma$ confidence levels, the Gaussian-distribution method was utilized. To evaluate variability, measurements were done under similar operating conditions. The uncertainties of the experiment are shown in Table 4.

Thus, any measured parameter uncertainty is computed as $(\Delta Xi) = 2\sigma_i / \overline{X_i} * 100$

To give accurate error limitations for the estimated parameters, the root-mean-square approach is utilized, and the degree of inaccuracy is expressed in equation (2).

$$\Delta R = \sqrt{\{(\partial R/\partial X_1) * \Delta X1)^2 + ((\partial R/\partial X_2) * \Delta X2)^2 + \ldots\ldots + ((\partial R/\partial Xn) * \Delta Xn)^2\}} \quad (2)$$

The experimentation overall uncertainty is calculated as follows:

$$= \sqrt{0.7^2 + 1.67^2 + 0.79^2 + 0.8^2 + 0.1^2 + 0.5^2 + 0.58^2 + 0.58^2}$$
$$= 2.33\%$$

4. Results and discussion

4.1. Combustion characteristics

4.1.1. In-cylinder pressure

4.1.1.1. Main-injection strategy. The peak CP for the single injection of dual fuel combustion along with the different main-injection timings of the biodiesel split injection are shown in Fig. 2. The rate of combustion of premixed fuel affects in-cylinder pressure. We observe that the CP rises when the pre-injection time is held constant at 46 °CA bTDC and the main injection is simply advanced from 12 to 18 °CA bTDC. The significant peak CP for a single injection of 40 % ammonia in dual fuel operation was 57.86 bar. Similarly, the various crucial main injection timings at 12, 15, 18, and 21°CA bTDC for 40 % ammonia-fueled operation with the 45 % split ratio peak pressures were 60.3 bar, 63 bar, 66.9 bar, and 65.6 bar, respectively. The maximum CP obtained among various main-injection timings is 18°CA bTDC, which is 15.6 % higher peak pressure than the 40 % ammonia-biodiesel dual fuel single injection operation at 26°CA bTDC injection timing.

It can be attributed to the port induction of ammonia and the pre-injection of biodiesel, which lengthens the mixing period with air and help the mixture become homogenous. The main biodiesel injection acts as the source of ignition for the homogeneous mixture. The homogeneous charge makes it easy to initiate the phenomenon of prompt multipoint auto ignition, which leads to intensified combustion pressure [17]. The dual-fuel combustion process continues to advance with the advancement of the main injection angle; peak CP increases progressively; their corresponding phases shift towards TDC; and the combustion period tends to reduce [55]. As a result, the peak CP increases. But with further advancement of the main injection to 21°CA bTDC, the peak CP was reduced. As the main injection angle advances, the cylinder air and biodiesel mixture gets more homogeneous and reduces the local equivalency ratio when cylinder temperature and pressure reach auto ignition condition [56].

4.1.1.2. Pre-injection strategy. The CP for the optimized main injection along with the different pre-injection timings of the biodiesel split injection are shown in Fig. 3. We observe that the CP rises when the main-injection time is held constant at 18 °CA bTDC and the pre-injection timing is simply advanced from 46 to 54°CA bTDC. The peak CP of various pre-injection timings at 46°CA, 50°CA, 54°CA, and 58°CA bTDC for 40 % ammonia-fueled operation with the 45 % split ratio were 66.9 bar, 69.6 bar, 75.3 bar, and 72.4 bar, respectively. The highest CP

Table 2
Experimental matrix and mass flow rates of fuels of dual fuel operation.

Test No	Operating mode	PortNH_3 (%)	Split angle (°CA bTDC) pre/main	Split ratio (%) pre/main	Mass flow rate (kg/h) for 40 % NH_3 and 60 % biodiesel										Acronym
					20 %		40 %		60 %		80 %		100 %		
					NH_3	BD	NH_3	BD	NH_3	BD	NH_3	BD	NH_3	BD	
1	Single injection	40	–	0/100	0.278	0.184	0.475	0.315	0.595	0.395	0.681	0.452	0.779	0.517	IT = 26 bTDC
2	Split injection	40	46/12	45/55	0.275	0.182	0.466	0.309	0.577	0.383	0.653	0.433	0.815	0.541	SIT = 46:12 bTDC
			46/15		0.272	0.181	0.456	0.303	0.560	0.372	0.626	0.416	0.780	0.518	SIT = 46:15 bTDC
			46/18		0.267	0.177	0.438	0.291	0.527	0.350	0.577	0.383	0.728	0.483	SIT = 46:18 bTDC
			46/21		0.269	0.179	0.447	0.297	0.543	0.360	0.601	0.399	0.749	0.497	SIT = 46:21 bTDC
			50/18		0.263	0.175	0.429	0.285	0.511	0.339	0.554	0.368	0.700	0.464	SIT = 50:18 bTDC
			54/18		0.256	0.170	0.412	0.274	0.481	0.319	0.511	0.339	0.646	0.429	SIT = 54:18 bTDC
			58/18		0.261	0.173	0.421	0.279	0.496	0.329	0.532	0.353	0.676	0.449	SIT = 58:18 bTDC

Table 3
Experimental engine setup.

Parameters	Details
Make	Kirloskar
Engine	CI
Cooling type	Water cooling
Power output	3.5 kW @ 1500 rpm
Compression Ratio (CR)	17.5
SoI (direct injection)	24 °CA bTDC
Bore × stroke	87.5 mm × 110 mm
Fuel Injection	Common rail direct injection
Torque	23.5 N-m

obtained from the various pre-injection timings is 54°CA bTDC, which is 12.5 % higher peak pressure than optimal main-injection operation at 18°CA bTDC for the 45 % biodiesel split ratio and 30.05 % higher than 40 % ammonia-biodiesel single injection operation at 26°CA bTDC injection timing. The peak CP apparently increased, and the corresponding phase shifted towards TDC. With the advance of the biodiesel pre-injection angle, when the main injection angle is optimum, the HR of ammonia-biodiesel combustion continues to increase, and the phases of combustion are further advanced. The peak values of CP further advanced to TDC and reached their maximum. Since the advancement of the pre-injection angle allows the pre-injected biodiesel sufficient time for physical delay and diffusion, thus progressively increasing the combustion auto-ignition point, when the main injection starts and the premixed combustion phase is constantly enhanced, more intense combustion occurs with improved peak CP [57]. But further advancement of the pre-injection angle to 58°CA bTDC, the maximum CP was further advanced closer to constant volume combustion [58]. The peak CP decreases as the pre-injection angle further advances. When the pre-injection angle is earlier than 54 °CA bTDC, there will be noticeable compression negative work, which causes the BSEC to fluctuate.

4.1.2. Heat release rate

4.1.2.1. Main injection strategy. The heat release (HR) for the single injection of dual fuel operation along with the different main-injection timings of the biodiesel split injection are shown in Fig. 2. We observe that the peak HRR rises when the pre-injection angle is held constant at 46 °CA bTDC and the main injection is simply advanced from 12 to 18 °CA bTDC. Double-peak HRR amplified noticeably, and the corresponding CA shifted towards TDC. The HRR of split injection shifts to a single peak HRR; this effect is attributed to pre-injected biodiesel, which enhances the premixed combustion. Earlier main biodiesel injection advances the start of combustion (SoC) and enhances the peak HRR in comparison to the 40 % ammonia-biodiesel single injection at 26°CAbTDC. With the advance of the early main injection of biodiesel from 12 to 18°CA, BTDC causes a higher quantity of biodiesel mixed with air, which develops combustion earlier. Advancing main injection also enhances the peak of HRR because more premixed charge is formed, resulting in a higher rate of combustion at premixed combustion phase [59]. But further advancement of the main injection to 21°CA bTDC, the phase of HRR was retarded. It can be attributed to the in-cylinder air temperature and pressure being lower, so ID increased and peak HRR was somewhat reduced and delayed [60]. When the injection timing is away from TDC, as the main injection angle advances, the cylinder air and biodiesel mixture gets more homogeneous and reduces the local equivalency ratio when cylinder temperature and pressure reach auto ignition conditions. Poor combustion might occur if the injection angle is increased or decreased beyond a specific limit [56,61].

4.1.2.2. Pre injection strategy. A dual-fuel operation pre-injection angle is a crucial variable, and useful technique for enhancing the enhancement of the combustion kernel throughout the in-cylinder. The HRR for the optimized main injection along with the different pre-injection timings of the biodiesel split injection are illustrated in Fig. 3. As the pre-injection advanced, the premixed combustion phase of HRR was noticeably enhanced noticeably, and the corresponding CA further moved towards TDC. However, by increasing the pre-injection angle to 58°CA bTDC, the HRR phase was delayed. It is evident that the pre-injection angle also has an important influence on how well the main biodiesel injection burns. The combustion process of the pre-injected biodiesel in the elevated temperature zone improved the SoC and flame development of the main-injected biodiesel in a suitable range, which ranges from 46°CA bTDC to 54°CA bTDC, and the cylinder charge approaches ignition conditions sooner, the combustion phases advance, and HRR becomes closer to constant-volume combustion [62]. The primary peak of HRR is dependent on the pre-biodiesel injection angle; by advancing the pre-biodiesel injection, the pre-injected biodiesel has ample time to create a homogeneous combination with ammonia and air. The SoC was further advanced, and the pre-injected biodiesel almost began to burn with the biodiesel main injection. According to this finding, the premixed combustion phase is improved, whereas the diffusion combustion phase is decreased. Moreover, as the pre-injection angle progressively advanced to 58°CA bTDC, the primary peak of the HRR curve increased and the corresponding CA further advanced, which is attributed to the negative compression work [63].

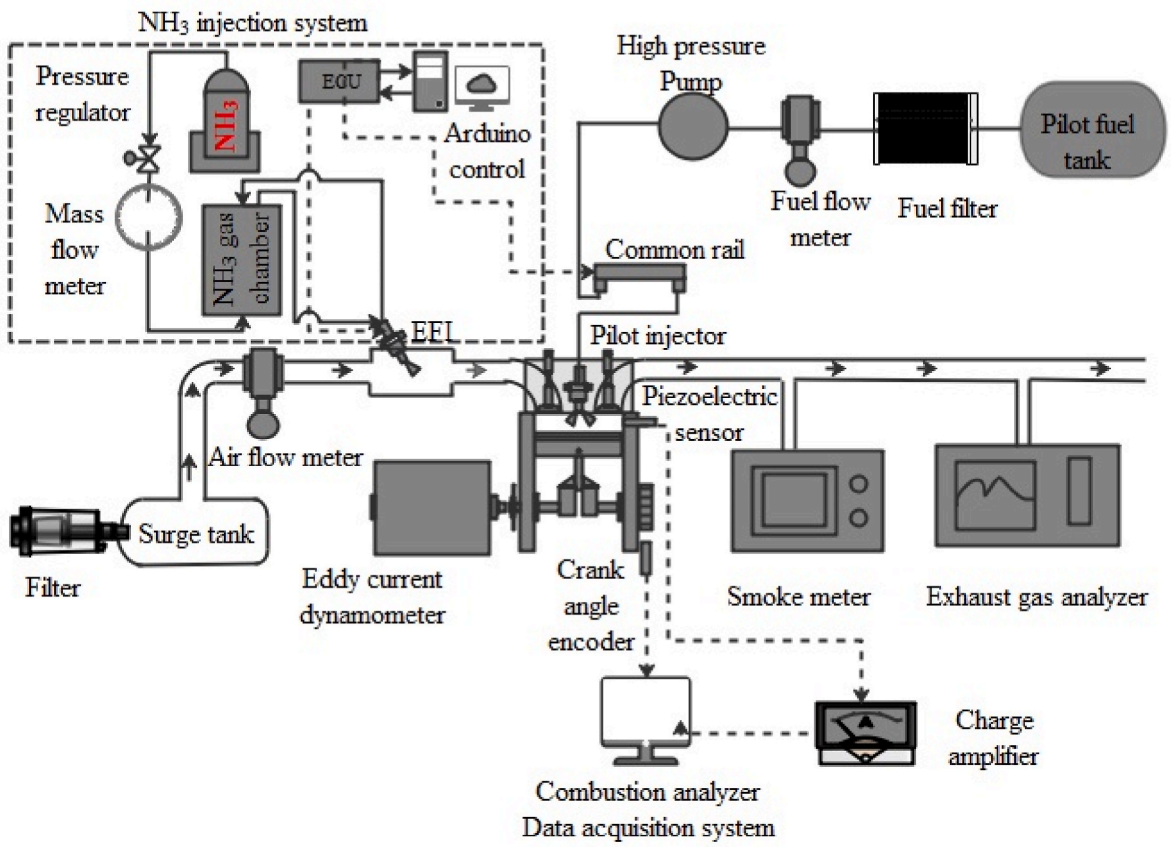

Fig. 1. Schematic of an experimental setup.

Table 4
Uncertainty particulars.

Parameters	Accuracy	% Uncertainty
Brake power (BP) (kW)	±0.5	±0.7
Pressure (bar)	±0.1	±1.67
Fuel consumption (kg/h)	±0.001	±0.79
Hydrocarbon (HC) (ppm)	±1.25	±0.8
Carbon monoxide (CO) (% vol.)	±0.08	±0.1
Nitrogen oxides (NOx) (ppm)	±1	±0.5
Smoke opacity (%)	±1.33	±0.58
Exhaust gas temperature (°C)	±1.1	±0.52

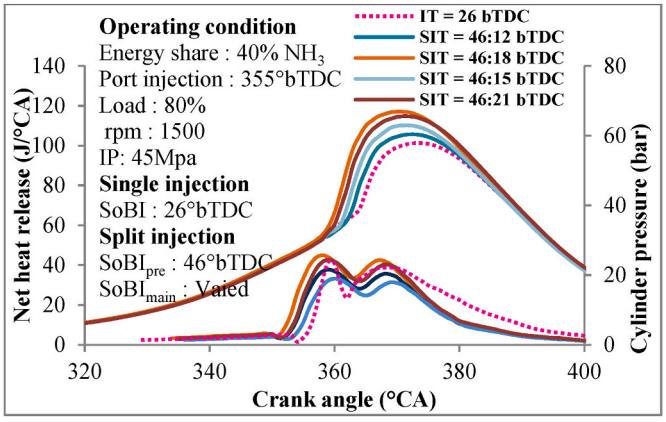

Fig. 2. Effects of main-injection angle on CP and HRR.

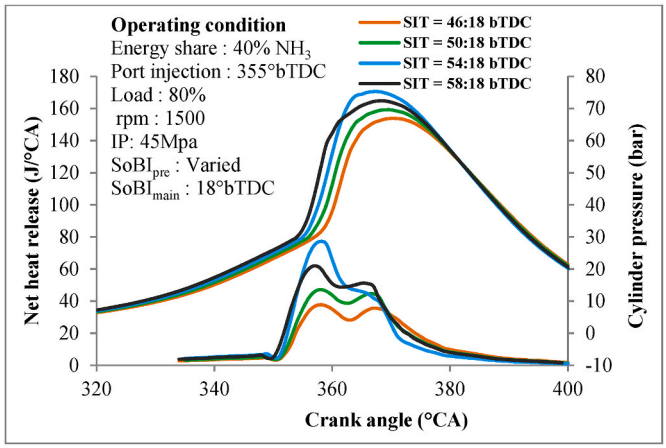

Fig. 3. Effects of pre-injection angle on CP and HRR.

4.2. Performance characteristics

4.2.1. Brake Thermal Efficiency and brake specific energy consumption

4.2.1.1. Main-injection strategy. Brake thermal efficiency and brake specific energy consumption are always one the inverse of the other. The performance of the IC engine that indicates a successful conversion of the fuel's chemical energy into useable power output is described as BTE. Fig. 4 demonstrates the difference in BTE and BSEC with regard to load for various main injection angles with the single injection of 40 % ammonia biodiesel in dual fuel operation mode for comparison. It increases with the gradual rise in load. It was noted that the BTE for a

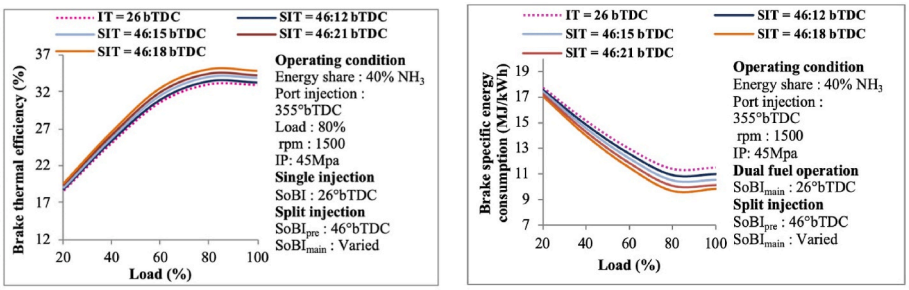

Fig. 4. Effects of main-injection angle on BTE and BSEC.

single-injected dual-fuel operation was 32.82 % at peak load conditions. Similarly, the BTE of different main injection timings at 12, 15, 18, and 21°CA bTDC operation for 40 % ammonia-fueled operation with the 45 % split ratio were 33.2 %, 33.8 %, 34.7 %, and 34.2 %, respectively. The maximum BTE obtained is 18°CA bTDC, which is 5.8 % higher than 40 % ammonia-biodiesel dual fuel single injection operation at 26°CAbTDC injection timing. Similarly, at peak load conditions, the average BSEC for a single injection of 40 % ammonia energy share in dual fuel operation was 11.5 MJ/kWh. Similarly, the BSEC of various main injection timings at 12, 15, 18, and 21 bTDC for the 40 % ammonia premixed split injection operation with the 45 % split ratio were 11, 10.5, 9.8, and 10.1 MJ/kWh, respectively. As related to single injection operations, the BSEC of 12, 15, 18, and 21°CA bTDC operations dropped by 4.3 %, 8.5 %, 14.5 % and 12.0 %, respectively. As main injection further advances to 21°CA bTDC, due to the reduced global temperature, the diffusion combustion phase increases, reducing the thermal efficiency. The main injection of 18°CA bTDC was chosen as the optimal main injection and may be utilized for further research based on acceptable performance and fuel attributes. Advancing of main injection angle from 12 to 18°CA bTDC, premixing is enhanced, which reduces the ID and thereby reduces fuel consumption. Further advancing the main injection to 21°CA bTDC, it was observed that the CP and temperature remained low at that time, the portion of the fuel could not be mixed with air, and an over-rich zone was created, resulting in inefficient combustion and higher energy consumption [64,65].

4.2.1.2. Pre-injection strategy. Fig. 5 exhibits the variation of BTE with regard to load for various pre-injection angles with optimum main injection of 40 % ammonia biodiesel dual fuel operation mode for the comparison. At peak load conditions, the maximum BTE for different pre-injection timings at 46°CA, 50°CA, 54°CA, and 58°CA bTDC for the 40 % ammonia premixed split injection operation with the 45 % split ratio were 34.7 %, 35.3 %, 36.4 %, and 35.8 %, respectively. As advancing the pre-injection to 54°CA bTDC rises the thermal efficiency remarkably by 4.9 % compared to optimum main injection operation at 18°CA bTDC and 11 % higher than 40 % ammonia-biodiesel dual fuel single injection operation at 26°CA bTDC injection timing. This might be due to the earlier SoC. Advancing both the pre- and main-injection timings further does not offer significant benefits and instead results in a decrease in Brake Thermal Efficiency (BTE) [56,64]. Similarly, at peak load conditions, the BSEC for different pre-injection timings at 46°CA, 50°CA, 54°CA, and 58°CA bTDC for the 40 % ammonia premixed split injection operation with the 45 % biodiesel split ratio were 9.9, 9.5, 8.7, and 9.1 MJ/kWh, respectively. As advancing the pre-injection angle to 54°CA bTDC, the highest reduction of BSEC is remarkably by 11.2 % than optimum main injection operation at 18°CA bTDC and 24.1 % higher than the 40 % ammonia-biodiesel dual fuel single injection operation at 26°CA bTDC injection timing. At an advanced pre-injection timing of 58°CA bTDC, the Peak Rate of Pressure Rise (PRR) at the end of the compression stroke increases, leading to higher negative compression work. This results in decreased thermal efficiency due to reduced net work output and increased fuel consumption. While advancing the injection timing initially enhances Brake Thermal Efficiency (BTE) and reduces energy consumption, there is a threshold beyond which these benefits diminish. Ultimately, the optimal injection timing for maximizing engine efficiency depends on the combustion characteristics of the specific fuel being used [55]. On further advancement, pre-injection leads to pre-auto ignition, which causes more fuel to get burned before TDC and significant heat loss, indicating that more fuel is needed to produce the same amount of power [66].

4.3. Emission characteristics

4.3.1. Unburned hydrocarbon emission

4.3.1.1. Main-injection strategy. The operating parameters of the engine, the fuel chemical composition, the fuel injection timing, and the air-fuel interaction inside the cylinder all affect the quantity of unburned hydrocarbon (UBHC) in the exhaust. Fig. 6 exhibits the difference in HC emissions with regard to load for the dual fuel single injection and various main-injection angles of split injection operations. The reduction in UBHC emission for main injection operation as compared to single main injection operation was found to be 3.8 % for 12°CA bTDC, 7.3 % for 15°CA bTDC, 13.4 % for 18°CA bTDC, and 10.2 % for 21°CA bTDC. The source of hydrocarbon emission is only from biodiesel combustion because ammonia doesn't contain carbon structure. The

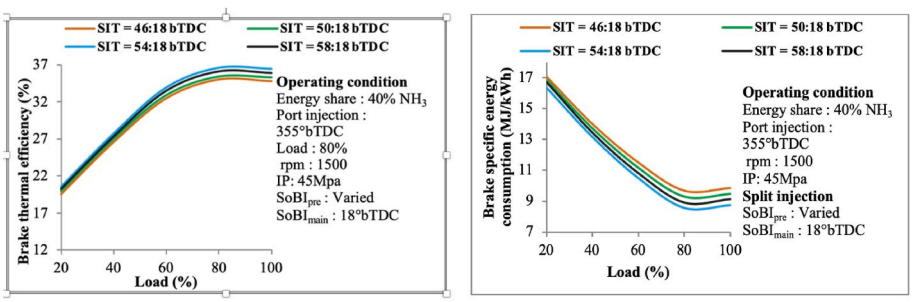

Fig. 5. Effects of pre-injection angle on BTE and BSEC.

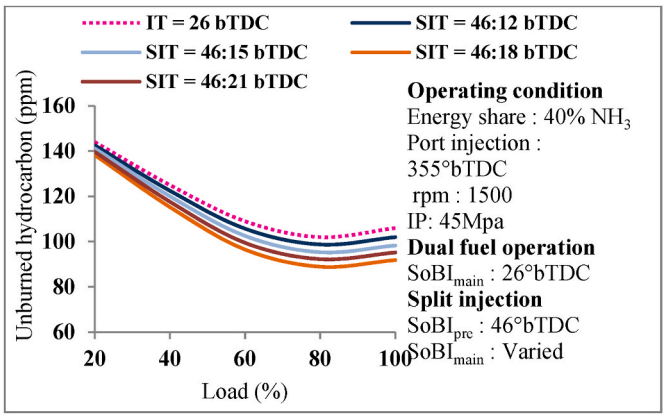

Fig. 6. Effects of main-injection angle on HC.

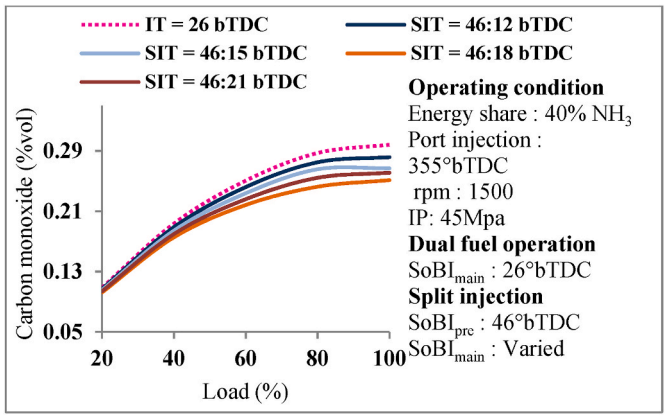

Fig. 8. Effects of main-injection angle on CO.

amount of UBHC emissions is decreased by improved biodiesel combustion efficiency. Furthermore, at peak loads, the HC emissions are reduced regardless of the injection angle due to combustion temperature, which enhances the oxidation of UBHC emission [67]. Improved atomization ratio is the primary factor in lower HC emissions at peak engine load. Simultaneously, high engine loads also contribute to turbulence or accelerated intake air flow. This promotes fuel atomization, homogenizes the mixture, and decreases HC emissions [68].

4.3.1.2. Pre-injection strategy. Fig. 7 shows the variation of HC emissions with respect to load for the optimum main injection and various pre-injection angles. The UBHC emissions noted for pre-injection timings of 46°CA bTDC, 50°CA bTDC, 54°CA bTDC, and 58°CA bTDC are 92 ppm, 89 ppm, 86 ppm, and 83 ppm. In contrast to the optimal main injection strategy, the UBHC of pre-injection is 3.2 %, 6.8 %, and 9.8 % reduced, respectively. Advancing pre-injection from 46 to 54 °CA bTDC results in reduced UBHC emissions. This is because of the advancement of the pre-injection effect; there was a longer dwell time, greater atomization, evaporation, and an enhanced air-fuel combination, which resulted in effective combustion [69]. Further advancement to 58 °CA bTDC elicited a shorter ID, due to which early SoC, which promotes constant-volume combustion and increases the cylinder temperature, results in a higher reduction of UBHC emissions.

4.3.2. Carbon monoxide emission

4.3.2.1. Main-injection strategy. The CI engine's CO emissions demonstrate poor fuel combustion. The CO release is another sign of improper fuel combustion. Fig. 8 indicates the difference in CO emissions with regard to load for various main injection angles with the single injection of 40 % ammonia biodiesel in dual fuel operation mode. The CO emission with the no pre-injection case (injection timing 26°CA bTDC) is much higher because the ID is extremely high in this situation. At peak load conditions, the observed highest CO emission for the single injection operation is 0.298 % vol. Similarly, for the main injection operationat12°CA bTDC was 0.282 % vol., 15°CA bTDC was 0.267 % vol., 18°CA bTDC was 0.251 % vol., and21°CA bTDC was 0.261 % vol. The drop in CO emissions as compared to dual fuel single injection was found to be 5.5 %, 10.5 %, 15.7 %, and 12.4 %, respectively.

The main causes of CO emissions include a heterogeneous charge mixture, insufficient oxygen, shorter resident time, and inefficient CO_2 promotion. Among them, the air-fuel ratio has a significant impact on CO emissions. At maximum load, CO emissions were high. This might be attributable to a rich air-fuel combination that hindered CO oxidation [70]. As explained earlier main injection advances the SoC and combustion phase, but further advanced the combustion efficiency is reduced because of cylinder temperature and pressure, which are not conducive for the auto ignition of main injected biodiesel. As a consequence of the delayed combustion, injected fuel may not have sufficient time to burn entirely, resulting in higher CO emissions [57,71].

4.3.2.2. Pre-injection strategy. Fig. 9 illustrates the difference in CO emissions with regard to load for different pre-injection angles with optimum main injection of 40 % ammonia biodiesel in dual fuel operation mode. The CO emissions found for the advanced pre-injection angle at 46, 50, 54, and 58°CA bTDC are 0.251, 0.239, 0.228, and 0.218 % vol. It was discovered that the 58°CA bTDC emits minimal CO, around 0.218 % vol., under the same working conditions. Compared with optimal main injection and the dual fuel single injection operation, the CO emissions for the 58°CA bTDC were reduced by 13.3 % and 26.9

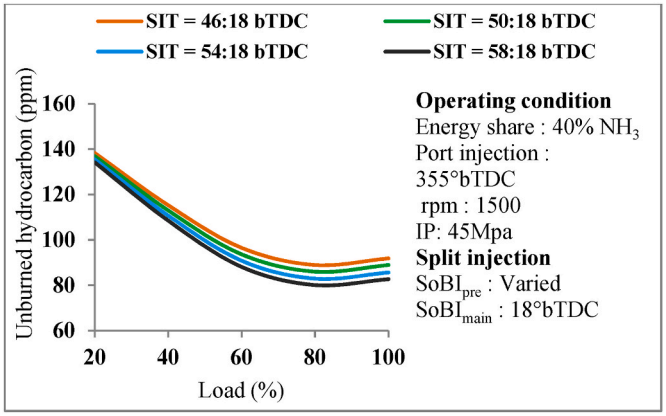

Fig. 7. Effects of pre-injection angle on HC.

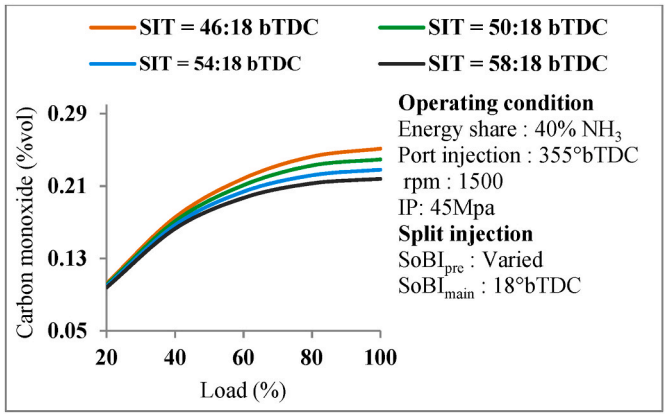

Fig. 9. Effects of pre-injection angle on CO.

%, respectively. Due to prolonged and sluggish combustion and the accompanying lower average in-cylinder temperature, CO emissions are considerable with single injection. With an increase in pre-injection time from 46 to 54°CA bTDC, resulting in greater oxidation levels and lower CO emissions. Because of the lower cylinder temperatures, pre-injection extends its ID time and forms a stoichiometric mixture, resulting in a greater combustion rate when main injection begins [63]. Further advancing to 58°CA bTDC, the CO oxidation is reduced. This can be attributed to higher fuel consumption due to negative compression work and insufficient time for complete combustion, which leads to increased CO emission [72].

4.3.3. Nitrogen oxides emission

4.3.3.1. Main-injection strategy. Nitrogen and oxygen actively interact together, resulting in nitrogen oxide (NOx) emission under high cylinder temperature regimes. Combusting the air-fuel mixture under stoichiometric conditions significantly contributes to NO_X formation. Similarly, NOx emissions were found to be greater around the maximum load state. Fig. 10 shows the difference in NOx emissions with regard to load for the dual fuel single injection and various main injection angle operations. The NOx emission for the dual fuel single injection operation was 456 ppm. Similarly, for the main injection operation at 12°CA bTDC was 482 ppm, 15°CA bTDC was 509 ppm, 18°CA bTDC was 538 ppm, and 21°CA bTDC was 509 ppm. As related to the dual fuel single injection operation, the NOx emissions for the 12, 15, 18, and 21°CA bTDC operations were increased by 5.6 %, 11.5 %, 25.2 %, and 17.9 %, respectively. It demonstrates a general law that NOx always grows as the main injection time advances. The fundamental reason is that it raises the combustion temperature as well as the residence time of high-temperature-burned gas, where NOx is aggressively formed [73]. As earlier explained, by further increasing main injection to 21°CA bTDC, NOx was reduced.

4.3.3.2. Pre-injection strategy. Fig. 11 illustrates the trend of NOx emissions with regard to load for various pre-injection timings with optimum main injection timing. The NOx emissions found for the pre-injection strategies such as46°CA, 50°CA, 54°CA, and 58°CA bTDC with 40 % ammonia-fueled operationsare572 ppm, 602 ppm, 637 ppm, and 671 ppm, respectively, compared with the optimum main injection, which has 5.2 %, 11.5 %, and 17.3 % higher NOx emissions. NOx emissions grow consistently as pre-injection timing advances. Because the advanced fuel injection timing results in an extended ID phase, the biodiesel may be properly mixed at the SoC, resulting in a more concentrated HR process and enhanced combustion perfection [74].

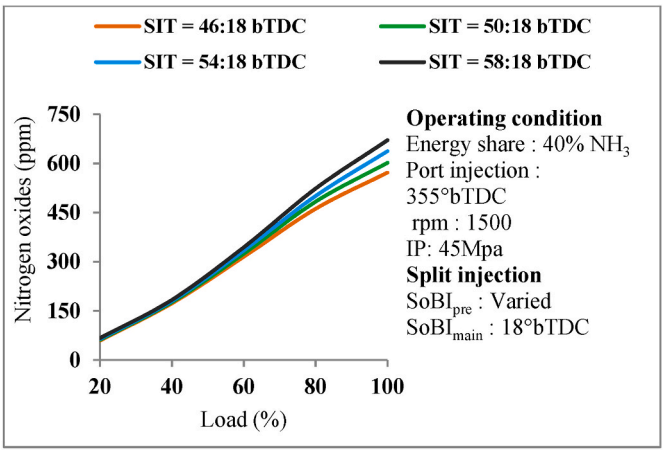

Fig. 11. Effects of pre-injection angle on NOx.

4.3.4. Smoke emission

4.3.4.1. Main-injection strategy. Smoke emission results from incomplete combustion, influenced by an improper air-fuel mixture, ineffective fuel burning, limited oxygen supply, and low combustion temperatures. Fig. 12 shows the variation of smoke opacity with respect to load for the dual fuel single injection and various main injection angle operations. The highest smoke emissions is for dual fuel single injection operation, which is 21.6 %. Similarly, the smoke emission of various main injection timings of 12, 15, 18, and 21°CA bTDC operation were 19.9 %, 17.1 %, and 18.5 %, respectively. The decrease in smoke emission for the dual fuel different main injection operation as compared to dual fuel single injection was found to be 8 % for 12°CA bTDC, 14.2 % for 15°CA bTDC, 27.1 % for 18°CA bTDC, and 21 % for 21°CA bTDC. Biodiesel has a beneficial effect on reducing smoke emissions due to its incomplete evaporation properties. However, as the engine load increases, there is a marked rise in smoke opacity emissions for the test fuel. The higher engine load increases fuel consumption, and the incomplete combustion of the injected fuel leads to elevated smoke emissions [75].

At the same time, the exhaust smoke emissions were reduced when the main injection angle advanced from 12 to 18°CA bTDC at high load conditions, because when the main injection is advanced, the cylinder temperature raises, which improves fuel and oxygen reactions. Another probable cause is the existence of ample time for the fuel vaporization and form a homogeneous charge, which reduced the intensity of the exhaust smoke [76]. Further advancement of the main injection increases smoke emissions because the combustion efficiency decreases.

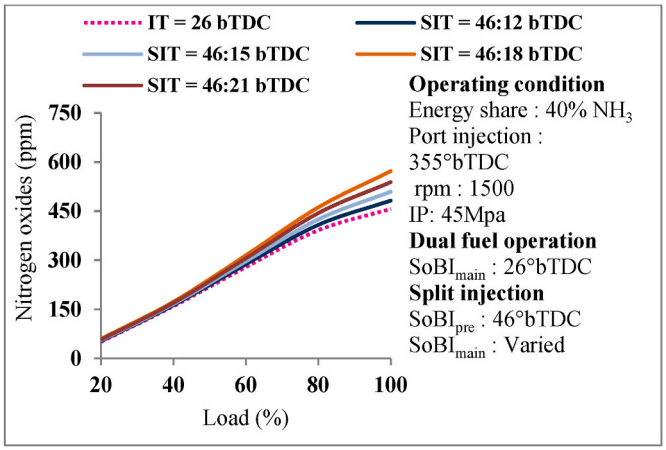

Fig. 10. Effects of main-injection angle on NOx.

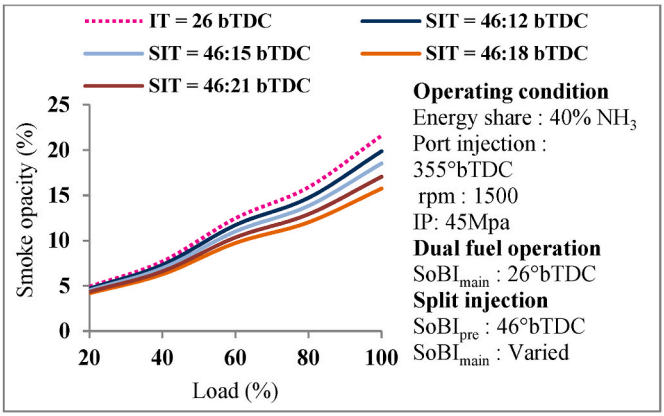

Fig. 12. Effects of main-injection angle on smoke.

4.3.4.2. Pre-injection strategy. Fig. 13 shows the difference in smoke opacity with regard to load for various pre-injections with optimum main injection timing. At peak load conditions, the smoke opacity for different pre-injection angles of 46, 50, 54, and 58°CA bTDC split injection operations was 15.8 %, 14.5 %, 13 %, and 13.5 %, respectively. The study showed a reduction in smoke intensity as advancing the pre-injection up to 54°CA bTDC, highest decrease of smoke opacity by 17.36%compared to optimum main injection operation and 39.73 % than dual fuel single injection operation. With the advancement of biodiesel pre-injection, the ID of the primarily injected biodiesel increased, and a more combustible charge formed, which resulted in higher ignition points and greater ignition energy inside the cylinder, resulting in an increase in CP. Simultaneously, the pre injection causes combustion to begin sooner, and the smoke produced by combustion has a longer duration for oxidation processes, resulting in lower smoke emissions [77]. Further advancing pre-injection to 54°CA bTDC, greater fuel consumption reduced the cylinder temperature, and fuel was not completely combusted, resulting in more smoke emissions. As a consequence, both injection techniques will result in decreased levels of smoke emissions within the region.

4.3.5. Exhaust gas temperature

4.3.5.1. Main-injection strategy. The exhaust gas temperature (EGT) demonstrates how well a fuel's thermal energy is utilized. Heat loss or a rise in exhaust gas temperature indicate that the thermal energy in the fuel has been converted to work [78]. The effects of main-injection timing on EGT with respect to load are shown in Fig. 14. The noticed EGT for the dual fuel single injection operation was 458 °C. Similarly, for the main injection operation at 12°CA bTDC, it was 436 °C, 15°CA bTDC was 420 °C, 18°CA bTDC was 389 °C, and 21°CA bTDC was 407 °C. As related to the dual fuel single injection operation, the EGT for the 12, 15, 18 and 21°CA bTDC operations were reduced by 4.8 %, 8.2 %, 11.2 %, and 11.2 %, respectively. The decreased level of exhaust temperature might be explained by the fact that ammonia has a lower calorific value and a greater cetane number than biodiesel. Because of the greater cetane number, which resulted in a lower exhaust temperature, ID occurred for shorter periods. Simultaneously, since biodiesel has a greater density and viscosity, spray penetration in dual fuel single injection produces a poor atomization rate [79,80]. Therefore, some fuel tends to combust later in the expansion stroke, subsequently, after burning happens, these factors increase the EGT [81]. Regardless of injection timing, the EGT increases at full loads; this might be because of greater amounts of fuel being consumed at greater loads to fulfil the power requirements and better combustion, which would raise the EGT [82]. EGT is greater in single-injection dual-fuel operation; this may be owing to a longer physical delay time, which results in combustion at a later expansion stroke.

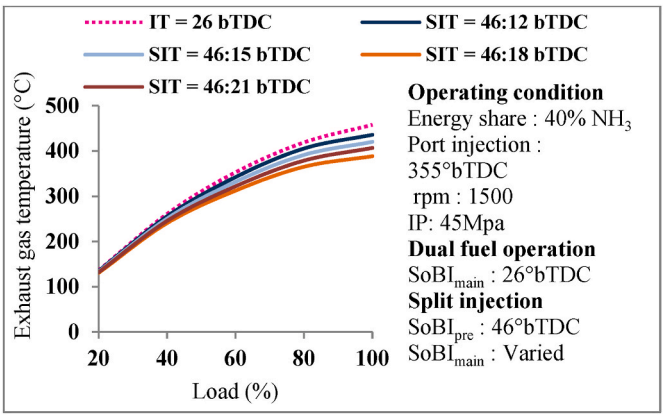

Fig. 14. Effects of main-injection angle on EGT.

4.3.5.2. Pre-injection strategy. The effects of pre-injection on EGT with respect to load are shown in Fig. 15. At peak load conditions, the EGT found for the pre-injection strategies such as 46°CA, 50°CA, 54°CA, and 58°CA bTDC split injection operations is389, 371, 358, and 350, respectively, compared with the optimum main injection timing, which is 18.9 %, 21.7 %, and 23.6 % lower EGT. As the advancement of pre-injection angle from 46 to 54°CA bTDC indicates the low EGT indicates that the pre-injection of biodiesel burned successfully and converted into a beneficial work. Further advancing the pre injection 58°CA bTDC, it was noted that the wall heat loss is higher due to prior combustion in the cycle, and it also makes negative compression work. For this condition, the heat energy is converted into negative work, thereby reducing the exhaust gas temperature [83]. When compared to dual fuel single injection, the reduced engine EGT shows that the biodiesel split injection efficiently burns in the cylinders [84,85].

5. Conclusion

In this research, initially the main injection angle of biodiesel was adjusted from 12 to 21°CA bTDC, and the pre-injection angle was fixed at 46°CA bTDC. From the initial investigation, the optimal main injection time was found to be 18°CA. In the next step, the pre-injection angle was adjusted from 46 to 58°CA bTDC, with the optimal main injection angle at 18°CA. and results were compared with 40 % ammonia-biodiesel dual fuel RCCI mode with a single injection at 26° bTDC. The optimal pre-injection timing is established as 54°CA. The results are as follows.

- From the initial investigation, the optimal main injection time of 18°CA bTDC increased the CP by 15.6 %, and the peak HRR and

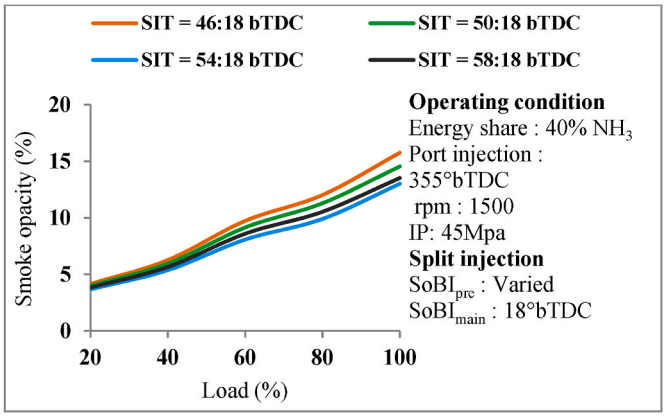

Fig. 13. Effects of pre-injection angle on smoke.

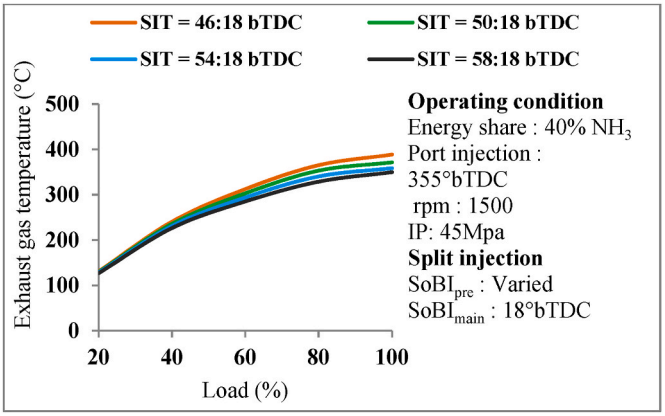

Fig. 15. Effects of pre-injection angle on EGT.

corresponding phasing angle were advanced. BTE was improved by 5.8 %, BSEC was reduced by 14.5 %, the NOx level was significantly increased by about 25.2 %, and HC, CO, smoke, and exhaust temperature were reduced by 13.4 %, 15.7 %, 27.1 %, and 15.2 % in comparison to the 40 % ammonia-biodiesel single injection mode at full load condition.

- In the next stage, the optimal pre-injection time of 54°CA bTDC increased the CP by 12.59 %, and the peak HRR and corresponding phasing angle were further advanced. BTE was improved by 4.9 %, BSEC was reduced by 11.3 %, the NOx level was significantly increased by about 11.4 %, and HC, CO, smoke, and exhaust temperature were reduced by 6.8 %, 9.25 %, 17.4 %, and 7.7 % in comparison to the optimal main injection mode at full load conditions.
- Overall, in contrast to dual fuel single injection operation, the optimal main and pre-injection angle of 18 and 54°CA bTDC increased the CP by 30.1 %, and the peak HRR and combustion phase angle were advanced. BTE was improved by 11 %, BSEC was reduced by 24.1 %, the NOx level was significantly increased by about 39.5 %, and HC, CO, smoke, and exhaust temperature were reduced by 19.2 %, 23.5 %, 39.7 % and 21.7 % at full load conditions.

CRediT authorship contribution statement

Elumalai Pv: Data curation. **Krishnaiah Ravi:** Writing – original draft, Supervision. **Ramachandran Elumalai:** Writing – original draft, Conceptualization. **Chan Choon Kit:** Formal analysis. **Suresh Kumar K:** Funding acquisition. **Krishnasamy Karthik:** Formal analysis. **M. Satyanarayana Gupta:** Data curation. **Mohammad Asif:** Funding acquisition.

Declaration of competing interest

The authors declare that they have no known competing financial interests or personal relationships that could have appeared to influence the work reported in this paper.

Data availability

Data will be made available on request.

Acknowledgments

We appreciate the financial support from the Researchers Supporting Project (RSP2024R42) at King Saud University in Riyadh, Saudi Arabia.

References

[1] M. Mehrpooya, B. Ghorbani, F.K. Bahnamiri, M. Marefati, Solar fuel production by developing an integrated biodiesel production process and solar thermal energy system, Appl. Therm. Eng. 167 (2020) 114701, https://doi.org/10.1016/j.applthermaleng.2019.114701.

[2] S. Muntasir Shovon, F. Ahamed Akash, M. Abdur Rahman, W. Rahman, P. Chakraborty, M.U. Monir, S.M. Sarkar, A. Abd Aziz, S. Chowdhury, Advancements in hydrogen generation, storage, and utilizations: a comprehensive review of current trends in Bangladesh, Energy 292 (2024) 130477, https://doi.org/10.1016/j.energy.2024.130477. Elsevier BV.

[3] X. Lu, Application of artificial intelligence algorithms in precision marketing with flow data analysis models, in: 2024 5th International Conference on Mobile Computing and Sustainable Informatics (ICMCSI), IEEE, 2024, https://doi.org/10.1007/s10973-023-12750-9.

[4] S.A. Jourabchi, S. Gan, H.K. Ng, Comparison of conventional and fast pyrolysis for the production of Jatropha curcas bio-oil, Appl. Therm. Eng. 99 (2016) 160–168, https://doi.org/10.1016/j.applthermaleng.2016.01.045. Elsevier BV.

[5] M. Zhao, T. Sun, Dynamic spatial spillover effect of new energy vehicle industry policies on carbon emission of transportation sector in China, Energy Pol. 165 (2022) 112991, https://doi.org/10.1016/j.enpol.2022.112991.

[6] J. Liu, H. Ma, L. Wang, W. Liang, Q. Ji, P. Sun, et al., Effects of EGR on combustion and emission characteristics of PODE/methanol RCCI mode at high load, Appl. Therm. Eng. 223 (2023) 120036, https://doi.org/10.1016/j.applthermaleng.2023.120036.

[7] Y. Yamineva, S. Romppanen, Is law failing to address air pollution? Reflections on international and <scp>EU</scp> developments, Review of European, Comparative & International Environmental Law 26 (3) (2017) 189–200, https://doi.org/10.1111/reel.12223. Wiley.

[8] V. Soloiu, A. Rivero-Castillo, M. Muinos, M. Duggan, S. Harp, W. Peavy, et al., Simultaneous reduction of NOX and Soot in a diesel engine through rcci operation with PFI of n-butanol and di of cottonseed biodiesel, SAE Tech Pap 1 (2014), https://doi.org/10.4271/2014-01-1322.

[9] M. Armin, M. Gholinia, Comparative evaluation of energy, performance, and emission characteristics in dual-fuel (CH4/Diesel) heavy-duty engine with RCCI combustion mode, Results Eng 16 (2022) 100766, https://doi.org/10.1016/j.rineng.2022.100766.

[10] V. Soloiu, J.D. Moncada, R. Gaubert, M. Muiños, S. Harp, M. Ilie, et al., LTC (low-temperature combustion) analysis of PCCI (premixed charge compression ignition) with n-butanol and cotton seed biodiesel versus combustion and emissions characteristics of their binary mixtures, Renew. Energy 123 (2018) 323–333, https://doi.org/10.1016/j.renene.2018.02.061.

[11] P. Berwal, S. Kumar, B. Khandelwal, A comprehensive review on synthesis, chemical kinetics, and practical application of ammonia as future fuel for combustion, J. Energy Inst. 99 (2021) 273–298, https://doi.org/10.1016/j.joei.2021.10.001.

[12] M. Okcu, M. Fırat, Y. Varol, Ş. Altun, F. Kamışlı, O. Atila, Combustion of high carbon (C7-C8) alcohol fuels in a reactivity controlled compression ignition (RCCI) engine as low reactivity fuels and ANN approach to predict RCCI emissions, Fuel 319 (2022), https://doi.org/10.1016/j.fuel.2022.123735.

[13] J.J. Thomas, G. Nagarajan, V.R. Sabu, C.V. Manojkumar, V. Sharma, Performance and emissions of hexanol-biodiesel fuelled RCCI engine with double injection strategies, Energy 253 (2022) 124069, https://doi.org/10.1016/j.energy.2022.124069.

[14] X. Liu, W. Zhong, P. Jiang, L. Dai, Z. He, Q. Wang, Optimizing RCCI combustion for improved engine performance under low load conditions: impact of low-reactivity fuel and direct injection timing, Fuel 351 (2023) 128871, https://doi.org/10.1016/j.fuel.2023.128871.

[15] S.P. Wategave, N.R. Banapurmath, M.S. Sawant, M.E.M. Soudagar, M.A. Mujtaba, A. Afzal, et al., Clean combustion and emissions strategy using reactivity controlled compression ignition (RCCI) mode engine powered with CNG-Karanja biodiesel, J. Taiwan Inst. Chem. Eng. 124 (2021) 116–131, https://doi.org/10.1016/j.jtice.2021.04.055.

[16] A.K. Subramani, G. Duraisamy, N. Govindan, A. Krishnasamy, Understanding the combustion mode transition from CDC to RCCI and RCCI to CDC – an experimental approach, Energy Convers. Manag. 270 (2022), https://doi.org/10.1016/j.enconman.2022.116233.

[17] J. Liu, Y. Liu, Q. Ji, P. Sun, X. Zhang, X. Wang, et al., Effects of split injection strategy on combustion stability and GHG emissions characteristics of natural gas/diesel RCCI engine under high load, Energy 266 (2023) 126542, https://doi.org/10.1016/j.energy.2022.126542.

[18] E. Arslan, N. Kahraman, The effects of hydrogen enriched natural gas under different engine loads in a diesel engine, Int. J. Hydrogen Energy 47 (2021) 12410–12420, https://doi.org/10.1016/j.ijhydene.2021.09.016.

[19] H. Wang, D. Liu, T. Ma, L. Tong, Z. Zheng, M. Yao, Thermal efficiency improvement of PODE/Gasoline dual-fuel RCCI high load operation with EGR and air dilution, Appl. Therm. Eng. 159 (2019) 113763, https://doi.org/10.1016/j.applthermaleng.2019.113763.

[20] A.P. Singh, V. Kumar, A.K. Agarwal, Evaluation of comparative engine combustion, performance and emission characteristics of low temperature combustion (PCCI and RCCI) modes, Appl. Energy 278 (2020) 115644, https://doi.org/10.1016/j.apenergy.2020.115644.

[21] M.Z. Is, Analysis of Ethanol RCCI Application with Safflower Biodiesel Blends in a High Load Diesel Power Generator Mehmet Zerrakki Is, vol. 184, 2016, pp. 248–260, https://doi.org/10.1016/j.fuel.2016.07.017.

[22] G. Xu, H. Duan, Y. Cai, Y. Li, M. Jia, Potential of the Reverse-Reactivity Controlled Compression Ignition (R-RCCI) Combustion for Maintaining Ultra-low Emissions and Enhanced Thermal Efficiency, vol. 280, 2023.

[23] G. Duraisamy, M. Rangasamy, N. Govindan, A comparative study on methanol/diesel and methanol/PODE dual fuel RCCI combustion in an automotive diesel engine Conventional Mode of Operation, Renew. Energy 145 (2020) 542–556, https://doi.org/10.1016/j.renene.2019.06.044.

[24] M.R. Saxena, R.K. Maurya, Effect of premixing ratio, injection timing and compression ratio on nano particle emissions from dual fuel non-road compression ignition engine fueled with gasoline/methanol (port injection) and diesel (direct injection), Fuel 203 (2017) 894–914, https://doi.org/10.1016/j.fuel.2017.05.015.

[25] N. Ganesan, K. Viswanathan, S.V. Karthic, P. Ekambaram, W. Wu, D.V.N. Vo, Split injection strategies based RCCI combustion analysis with waste cooking oil biofuel and methanol in an open ECU assisted CRDI engine, Fuel 319 (2022) 123710, https://doi.org/10.1016/j.fuel.2022.123710.

[26] A. Ramanathan, A. Santhoshkumar, Feasibility analysis of pyrolysis waste engine oil in CRDI diesel engine, Energy Proc. 158 (2019) 755–760, https://doi.org/10.1016/j.egypro.2019.01.201.

[27] S. Ramalingam, D. Babu, A. Santhoshkumar, R. Deepakkumar, D. Ravikanth, Impact of exhaust gas recirculation and split injection strategy combustion behavior on premixed charge compression ignition engine fuelled with moringa oleifera methyl ester, Fuel 319 (2022) 123702, https://doi.org/10.1016/j.fuel.2022.123702.

[28] A. Kakaee, P. Rahnama, A. Paykani, Journal of Natural Gas Science and Engineering in fl uence of fuel composition on combustion and emissions

characteristics of natural gas/diesel RCCI engine, J. Nat. Gas Sci. Eng. 25 (2015) 58–65, https://doi.org/10.1016/j.jngse.2015.04.020.
[29] A. Kumar, G. Duraisamy, N. Govindan, An innovative method of ammonia use in a light- duty automotive diesel engine to enhance diesel combustion , performance , and emissions, Int. J. Hydrogen Energy (2023), https://doi.org/10.1016/j.ijhydene.2023.06.183.
[30] A. Paykani, A. Kakaee, P. Rahnama, R.D. Reitz, Effects of diesel injection strategy on natural gas/diesel reactivity controlled compression ignition combustion, Energy 90 (2015) 814–826, https://doi.org/10.1016/j.energy.2015.07.112.
[31] A. Yousefi, H. Guo, S. Dev, S. Lafrance, B. Liko, A study on split diesel injection on thermal efficiency and emissions of an ammonia/diesel dual-fuel engine, Fuel 316 (2022) 123412, https://doi.org/10.1016/j.fuel.2022.123412.
[32] A. Sánchez, E. Castellano, M. Martín, P. Vega, Evaluating ammonia as green fuel for power generation: a thermo-chemical perspective, Appl. Energy 293 (2021) 116956, https://doi.org/10.1016/j.apenergy.2021.116956.
[33] E. Perumal Venkatesan, A. Kandhasamy, A. Sivalingam, A.S. Kumar, K. M. Ramalingam, P james thadhani Joshua, et al., Performance and emission reduction characteristics of cerium oxide nanoparticle-water emulsion biofuel in diesel engine with modified coated piston, Environ. Sci. Pollut. Res. 26 (2019) 27362–27371, https://doi.org/10.1007/s11356-019-05773-z.
[34] H. Kobayashi, A. Hayakawa, K.D.K.A. Somarathne, E.C. Okafor, Science and technology of ammonia combustion, Proc. Combust. Inst. 37 (2019) 109–133, https://doi.org/10.1016/j.proci.2018.09.029.
[35] Y. Feng, J. Zhu, Y. Mao, M. Raza, Y. Qian, L. Yu, et al., Low-temperature auto-ignition characteristics of NH3/diesel binary fuel: ignition delay time measurement and kinetic analysis, Fuel 281 (2020) 118761, https://doi.org/10.1016/j.fuel.2020.118761.
[36] H. Derikvand, M. Shafiey Dehaj, H. Taghavifar, The effect of different sampling method integrated in NSGA II optimization on performance and emission of diesel/hydrogen dual-fuel CI engine, Appl. Soft Comput. 128 (2022) 109434, https://doi.org/10.1016/j.asoc.2022.109434.
[37] C. Kurien, M. Mittal, Review on the production and utilization of green ammonia as an alternate fuel in dual-fuel compression ignition engines, Energy Convers. Manag. 251 (2022) 114990, https://doi.org/10.1016/j.enconman.2021.114990.
[38] Ø. Skreiberg, T. Li, E. Vantaggiato, L. Wang, M. Bugge, T. Løvås, An evaluation of effects of operational parameters on NOx emissions through detailed chemical kinetics simulations, Energy Proc. 158 (2019) 103–110, https://doi.org/10.1016/j.egypro.2019.01.053.
[39] P. Dimitriou, R. Javaid, A review of ammonia as a compression ignition engine fuel, Int. J. Hydrogen Energy 45 (2020) 7098–7118, https://doi.org/10.1016/j.ijhydene.2019.12.209.
[40] E.C. Blanco, A. Sánchez, M. Martín, P. Vega, Methanol and ammonia as emerging green fuels: evaluation of a new power generation paradigm, Renew. Sustain. Energy Rev. 175 (2023) 113195, https://doi.org/10.1016/j.rser.2023.113195.
[41] S. Mi, H. Wu, X. Pei, C. Liu, L. Zheng, W. Zhao, et al., Potential of ammonia energy fraction and diesel pilot-injection strategy on improving combustion and emission performance in an ammonia-diesel dual fuel engine, Fuel 343 (2023) 127889, https://doi.org/10.1016/j.fuel.2023.127889.
[42] E. Nadimi, G. Przybyła, M.T. Lewandowski, W. Adamczyk, Effects of ammonia on combustion, emissions, and performance of the ammonia/diesel dual-fuel compression ignition engine, J. Energy Inst. 107 (2023), https://doi.org/10.1016/j.joei.2022.101158.
[43] N. Førby, T.B. Thomsen, R.F. Cordtz, F. Bræstrup, J. Schramm, Ignition and combustion study of premixed ammonia using GDI pilot injection in CI engine, Fuel 331 (2023) 125768, https://doi.org/10.1016/j.fuel.2022.125768.
[44] A.S. Mohammed, S.M. Atnaw, A.V. Ramaya, G. Alemayehu, A comprehensive review on the effect of ethers, antioxidants, and cetane improver additives on biodiesel-diesel blend in CI engine performance and emission characteristics, J. Energy Inst. 108 (2023) 101227, https://doi.org/10.1016/j.joei.2023.101227.
[45] M. Elkelawy, H.A.E. Bastawissi, E.A. El Shenawy, M.M. Shams, H. Panchal, K. K. Sadasivuni, et al., Influence of lean premixed ratio of PCCI-DI engine fueled by diesel/biodiesel blends on combustion, performance, and emission attributes; a comparison study, Energy Convers. Manag. X 10 (2021) 100066, https://doi.org/10.1016/j.ecmx.2020.100066.
[46] B. Ashok, K. Nanthagopal, Eco Friendly Biofuels for CI Engine Applications, Elsevier Ltd., 2019, https://doi.org/10.1016/b978-0-08-102728-8.00015-2.
[47] K. Simhadri, P. Srinivasa Rao, M.K. Paswan, Effect of changing injection pressure on Mahua oil and biodiesel combustion with Ceo2 nanoparticle blend on Ci engine performance and emission characteristics, SSRN Electron. J. (2022), https://doi.org/10.2139/ssrn.4181180.
[48] N. Ganesan, T.H. Le, P. Ekambaram, D. Balasubramanian, V.V. Le, A.T. Hoang, Experimental assessment on performance and combustion behaviors of reactivity-controlled compression ignition engine operated by n-pentanol and cottonseed biodiesel, J. Clean. Prod. 330 (2022) 129781, https://doi.org/10.1016/j.jclepro.2021.129781.
[49] B. Maleki, Y. Kalanakoppal Venkatesh, Ashraf Talesh S. Siamak, H. Esmaeili, S. Mohan, G.R. Balakrishna, A novel biomass derived activated carbon mediated AC@ZnO/NiO bifunctional nanocatalyst to produce high-quality biodiesel from dairy industry waste oil: CI engine performance and emission, Chem Eng J 467 (2023) 143399, https://doi.org/10.1016/j.cej.2023.143399.
[50] S.P. Wategave, N.R. Banapurmath, M.S. Sawant, M. Elahi, M. Soudagar, M. Reza, A. Elfasakhany, A.M. Sajjan, Clean combustion and emissions strategy using reactivity controlled compression ignition (RCCI) mode engine powered with CNG-karanja biodiesel, J. Taiwan Inst. Chem. Eng. 000 (2021) 1–16, https://doi.org/10.1016/j.jtice.2021.04.055.
[51] S.S. Kumar, K. Rajan, V. Mohanavel, M. Ravichandran, P. Rajendran, A. Rashedi, A. Sharma, S.A. Khan, A. Afzal, Combustion , performance , and emission behaviors of biodiesel fueled diesel engine with the impact of alumina nanoparticle as an additive, Sustainability 13 (2021) 12103, https://doi.org/10.3390/su132112103.
[52] A. Afzal, R.G. Roy, C.P. Koshy, A. Y, M. Abbas, E. Cuce, A. Razak Rk, S. Shaik, C. A. Saleel, Characterization of biodiesel based on plastic pyrolysis oil (PPO) and coconut oil: performance and emission analysis using RSM-ANN approach, Sustain. Energy Technol. Assessments 56 (2023) 103046, https://doi.org/10.1016/j.seta.2023.103046.
[53] A. Devaraj, M. Nagappan, D. Yogaraj, O. Prakash, Y.A. Rao, A. Sharma, Influence of nano-additives on engine behaviour using diesel-biodiesel blend, Mater Today Proc 62 (2022) 2266–2270, https://doi.org/10.1016/j.matpr.2022.03.598.
[54] A. Sharma, Y. Singh, N. Kumar Singh, A. Singla, H. Chyuan Ong, W.H. Chen, Effective utilization of tobacco (Nicotiana Tabaccum) for biodiesel production and its application on diesel engine using response surface methodology approach, Fuel 273 (2020) 117793, https://doi.org/10.1016/j.fuel.2020.117793.
[55] B. Yang, K. Zeng, Effects of natural gas injection timing and split pilot fuel injection strategy on the combustion performance and emissions in a dual-fuel engine fueled with diesel and natural gas, Energy Convers. Manag. 168 (2018) 162–169, https://doi.org/10.1016/j.enconman.2018.04.091.
[56] R. Sindhu, G. Amba Prasad Rao, K. Madhu Murthy, Effective reduction of NOx emissions from diesel engine using split injections, Alexandria Eng J 57 (2018) 1379–1392, https://doi.org/10.1016/j.aej.2017.06.009.
[57] Y. Shekar Kuppili, P. Kumar, S. Singh Sandhu, A critical review of the impacts of split injection strategies on the performance, combustion and emissions characteristics of a diesel engine fueled with low carbon alcohol fuels, Mater Today Proc 72 (2023) 2928–2932, https://doi.org/10.1016/j.matpr.2022.08.020.
[58] K.P. Shrestha, C. Lhuillier, A.A. Barbosa, P. Brequigny, F. Contino, C. Mounaïm-Rousselle, et al., An experimental and modeling study of ammonia with enriched oxygen content and ammonia/hydrogen laminar flame speed at elevated pressure and temperature, Proc. Combust. Inst. 38 (2021) 2163–2174, https://doi.org/10.1016/j.proci.2020.06.197.
[59] P.S. Shelke, N.M. Sakhare, S. Lahane, Investigation of combustion characteristics of a cottonseed biodiesel fuelled diesel engine, Procedia Technol 25 (2016) 1049–1055, https://doi.org/10.1016/j.protcy.2016.08.205.
[60] A.M. Elzahaby, M. Elkelawy, H.A.E. Bastawissi, S.M. El Malla, A.M.M. Naceb, Kinetic modeling and experimental study on the combustion, performance and emission characteristics of a PCCI engine fueled with ethanol-diesel blends, Egypt J Pet 27 (2018) 927–937, https://doi.org/10.1016/j.ejpe.2018.02.003.
[61] K. Panda, A. Ramesh, Parametric investigations to establish the potential of methanol based RCCI engine and comparison with the conventional dual fuel mode, Fuel 308 (2022) 122025, https://doi.org/10.1016/j.fuel.2021.122025.
[62] Y. Zhang, W. De Ojeda, D. Wickman, Computational study of combustion optimization in a heavy-duty diesel engine using in-cylinder blending of gasoline and diesel fuels, SAE Tech Pap 8 (2012), https://doi.org/10.4271/2012-01-1977.
[63] J. Liu, P. Wu, Q. Ji, P. Sun, P. Wang, Z. Meng, et al., Experimental study on effects of pilot injection strategy on combustion and emission characteristics of diesel/methanol dual-fuel engine under low load, Energy 247 (2022) 123464, https://doi.org/10.1016/j.energy.2022.123464.
[64] S. Park, H.J. Kim, D.H. Shin, J.T. Lee, Effects of various split injection strategies on combustion and emissions characteristics in a single-cylinder diesel engine, Appl. Therm. Eng. 140 (2018) 422–431, https://doi.org/10.1016/j.applthermaleng.2018.05.025.
[65] S. Kokjohn, R.D. Reitz, D. Splitter, M. Musculus, Investigation of fuel reactivity stratification for controlling PCI heat-release rates using high-speed chemiluminescence imaging and fuel tracer fluorescence, SAE Int J Engines 5 (2012) 248–269, https://doi.org/10.4271/2012-01-0375.
[66] B. Yang, K. Zeng, Effects of natural gas injection timing and split pilot fuel injection strategy on the combustion performance and emissions in a dual-fuel engine fueled with diesel and natural gas, Energy Convers. Manag. 168 (2018) 162–169, https://doi.org/10.1016/j.enconman.2018.04.091.
[67] P. Saiteja, B. Ashok, Study on interactive effects of CRDi engine operating parameters through RSM based multi-objective optimization technique for biofuel application, Energy 255 (2022) 124499, https://doi.org/10.1016/j.energy.2022.124499.
[68] M. Canakci, A.N. Ozsezen, E. Arcaklioglu, A. Erdil, Prediction of performance and exhaust emissions of a diesel engine fueled with biodiesel produced from waste frying palm oil, Expert Syst. Appl. 36 (2009) 9268–9280, https://doi.org/10.1016/j.eswa.2008.12.005.
[69] D. Babu, R. Karvembu, R. Anand, Impact of split injection strategy on combustion, performance and emissions characteristics of biodiesel fuelled common rail direct injection assisted diesel engine, Energy 165 (2018) 577–592, https://doi.org/10.1016/j.energy.2018.09.193.
[70] T. Ravichandran, M. Nagappan, A novel technique and detailed study of concepts of low-cost hybrid vehicle design, Int. J. Ambient Energy 42 (2021) 1252–1257, https://doi.org/10.1080/01430750.2019.1592777.
[71] J. Liu, X. Zhang, Y. Liu, P. Sun, Q. Ji, X. Wang, et al., Experimental study on in-cylinder combustion and exhaust emissions characteristics of natural gas/diesel dual-fuel engine with single injection and split injection strategies, Process Saf Environ Prot 172 (2023) 225–240, https://doi.org/10.1016/j.psep.2023.02.013.
[72] M. Xu, W. Cheng, H. Zhang, T. An, S. Zhang, Effect of diesel pre-injection timing on combustion and emission characteristics of compression ignited natural gas engine, Energy Convers. Manag. 117 (2016) 86–94, https://doi.org/10.1016/j.enconman.2016.02.054.

[73] V. Bykov, M. Stein, U. Maas, Study of mechanism of ammonia decomposition and oxidation: from NOx reduction to ammonia auto-ignition problem, Proc. Combust. Inst. 0 (2022) 1–9, https://doi.org/10.1016/j.proci.2022.07.048.
[74] M. Nibin, J.B. Raj, V.E. Geo, Experimental studies to improve the performance, emission and combustion characteristics of wheat germ oil fuelled CI engine using bioethanol injection in PCCI mode, Fuel 285 (2021) 119196, https://doi.org/10.1016/j.fuel.2020.119196.
[75] N. Murugan, H. Venu, J. Jayaraman, P. Appavu, Emission and performance characteristics study on nanographene oxide additives doped palm oil methyl ester blend in a diesel engine, Int. J. Ambient Energy (2019) 1–7, https://doi.org/10.1080/01430750.2019.1697361, 0.
[76] H.G. How, H.H. Masjuki, M.A. Kalam, Y.H. Teoh, Influence of injection timing and split injection strategies on performance, emissions, and combustion characteristics of diesel engine fueled with biodiesel blended fuels, Fuel 213 (2018) 106–114, https://doi.org/10.1016/j.fuel.2017.10.102.
[77] H.G. How, H.H. Masjuki, M.A. Kalam, Y.H. Teoh, Influence of injection timing and split injection strategies on performance, emissions, and combustion characteristics of diesel engine fueled with biodiesel blended fuels, Fuel 213 (2018) 106–114, https://doi.org/10.1016/j.fuel.2017.10.102.
[78] C.C. Enweremadu, H.L. Rutto, Combustion, emission and engine performance characteristics of used cooking oil biodiesel - a review, Renew. Sustain. Energy Rev. 14 (2010) 2863–2873, https://doi.org/10.1016/j.rser.2010.07.036.
[79] K. Kalaimurugan, S. Karthikeyan, M. Periyasamy, G. Mahendran, T. Dharmaprabhakaran, Experimental studies on the influence of copper oxide nanoparticle on biodiesel-diesel fuel blend in CI engine, Energy Sources, Part A Recover Util Environ Eff 0 (2019) 1–16, https://doi.org/10.1080/15567036.2019.1679290.
[80] A. Atmanli, Comparative analyses of diesel-waste oil biodiesel and propanol, n-butanol or 1-pentanol blends in a diesel engine, Fuel 176 (2016) 209–215, https://doi.org/10.1016/j.fuel.2016.02.076.
[81] E. Ansari, M. Shahbakhti, J. Naber, Optimization of performance and operational cost for a dual mode diesel-natural gas RCCI and diesel combustion engine, Appl. Energy 231 (2018) 549–561, https://doi.org/10.1016/j.apenergy.2018.09.040.
[82] G. Sakthivel, Prediction of CI engine performance, emission and combustion characteristics using fish oil as a biodiesel at different injection timing using fuzzy logic, Fuel 183 (2016) 214–229, https://doi.org/10.1016/j.fuel.2016.06.063.
[83] S. Jindal, Effect of injection timing on combustion and performance of a direct injection diesel engine running on Jatropha methyl ester, Int. J. Energy Environ. 2 (2011) 113–122.
[84] P. Murugesan, P.V. Elumalai, D. Balasubramanian, S. Padmanabhan, N. Murugunachippan, A. Afzal, P. Sharma, K. Kiran, J.S. Femilda Josephin, E. G. Varuvel, et al., Exploration of low heat rejection engine characteristics powered with carbon nanotubes-added waste plastic pyrolysis oil, Process Saf. Environ. Prot. 176 (2023) 1101–1119, https://doi.org/10.1016/j.psep.2023.06.051.
[85] S.V. Khandal, Ü. Ağbulut, A. Afzal, M. Sharifpur, K. Abdul Razak, N. Khalilpoor, Influences of hydrogen addition from different dual-fuel modes on engine behaviors, Energy Sci. Eng. 10 (2022) 881–891, https://doi.org/10.1002/ese3.1065.

Comparative Analysis for Titanium alloy and Silicon Nitride (Si3N4) of Thermal Analysis for Deep Groove Ball Bearing

Revathi V[1*], *Dhanesh* Khalotia[2], *Tanya* Buddi[3], *Ali* K. Alhussainy [4], *Manish* Gupta[5], *A. L.* N. Rao[6], *Vivek Anand* A[7]

[1]Department of Applied Sciences, New Horizon College of Engineering, Bangalore, Karnataka, India.
[2]Department of Civil Engineering, IES College of Technology, Bhopal, Madhya Pradesh, India.
[3]Department of Mechanical, GRIET, Bachupally, Hyderabad, Telangana, India.
[4]Hilla University College, Babylon, Iraq
[5]Lovely Professional University, Phagwara, India.
[6]Lloyd Institute of Engineering & Technology, Knowledge Park II, Greater Noida, Uttar Pradesh, India.
[7]Department of Aeronautical Engineering, MLR Institute of Technology, Hyderabad, Telangana, India-500063

Abstract. In this paper, the analysis of the directional heat flux and total heat flux for the bearing balls of Titanium alloy and Silicon Nitride has been demonstrated across a temperature range between 150 to 250 degree celcius. The obtained data allowed comparing the values of total heat flux and various directional heat flux. By comparing directional and total flux of heat in materials it enables the choice of the best-suited material creating bearings with regard to the performance needed. The use of the findings of the current comparison is to ensure efficiency and durability in particular operations. The data presented in the paper helped to analyze the patterns of heat distribution and see the differences between the materials and results a better material for ball bearing. Titanium alloy has excellent mechanical properties like mechanical strength and corrosion resistance. Silicon Nitride is characterized by thermal stability and high thermal resistance and also has excellent wear properties. Thus, using the results of the analysis allows choosing the material for bearing production for high-velocity and high-load operation based on a profound comparison to select the right material. The choice of right material will allow for a more efficient and durable bearing in an industrial setting.

Keyword-: Ball bearing, Titanium alloy, Silicon Nitride, Robust, Mechanical Strength Thermal Analysis, Heat Flux, Materials.

[*] Corresponding Author: revshank153@gmail.com

© The Authors, published by EDP Sciences. This is an open access article distributed under the terms of the Creative Commons Attribution License 4.0 (https://creativecommons.org/licenses/by/4.0/).

1 Introduction

The Mechanical deep groove bearings are fundamental elements of machines that allow smooth rotatory motion and reduced friction during rotation. Basically, In ball bearings thermal properties play a big role in influencing the bearings' workability and durability, especially under very challenging and harsh conditions [1, 2]. Bearing condition monitoring is a big part of the maintenance of any machine that rotates regularly. They ensure that any potential fault with the bearings are detected earlier and repaired in good time to prevent economic loss [3-5]. Diverse analysis schedules are generally communicated for the components that are used during industrial tasks such as structural loads [6]. Furthermore, material selection for ball bearing construction also significantly influences the thermal performance, Titanium alloy and Silicon Nitride have been prominently considered due to their unique characteristics [7-9]. Suitable due to its high mechanical strength, physical properties, material properties, and lower density in thermal engineering Titanium alloy shows excellent performance [10]. On other hand, Silicon Nitride also stand out as the best materials to withstand high temperatures physically due to having excellent load-wearing properties [11-13]. Therefore, this paper aims to compare findings and thermal analysis between Titanium alloy and Silicon Nitride in the ball bearing with deep groove [14]. This paper reports the thermal behavior of the materials such as heat flux and directional heat flux measurement produced via experimenting and active analysis methods [15-17]. Temperature insights and heat flux patterns of the materials present in the paper to reveal the differences between the materials for visual support and interpretation of the materials to understand their thermal properties [18]. This study and these findings can be used to select materials adequately and improve design efficiency to obtain enhanced deep groove ball bearings' thermal performance and reliability for industrial applications [19]. Discuss on the friction, early ball bearing friction is two times more slide friction, and it should cause lesser consideration when bearing with original contact pressure of a plain bearings [20]. Friction qualities of a bearing are contingent on operational load, velocity, and lubrication viscosity age, with a small proportionate on the ratio of cleaning of the support bearin [21-24]. As mentioned in a bearing journal, it is hardly to regulate a bearing here but still using into industry under bearing bearing [25-26]. The bearings learning also varied from the fact-finding about all topics with many others observations to the perspective of the technical engineer, because the bearing allocated by genetic engineering as the case requires [27-29]. The load-carrying developer, therefore, is faced by the problem of designing a system of components which constitute the direct effect: which will fit in a given envelope, support a load of stated characteristics, and, eventually, have a life satisfactory when operated under a stated condition [30-34]. Through analyzing this paper, the selection of suitable materials based on the understanding of the thermal behavior and heat flux of Titanium alloy and Silicon Nitride becomes easier to improve the bearing efficiency and durability at high speed and high load for various purposes in the industry segment [35-36].

2 CAD Modelling and Meshing

The deep groove ball bearing is the most often used type of bearing in the industry and its market share is about 80 % of all industrial rolling element bearings sell in this sector. The computational method is used to create the model. For the 3D CAD model the parameters are diameter of the bearing from inside is 70 mm, diameter of the bearing from outside is 110 mm, diameter of rolling balls 9.525 mm and there are 12 number of balls as shown in figure.

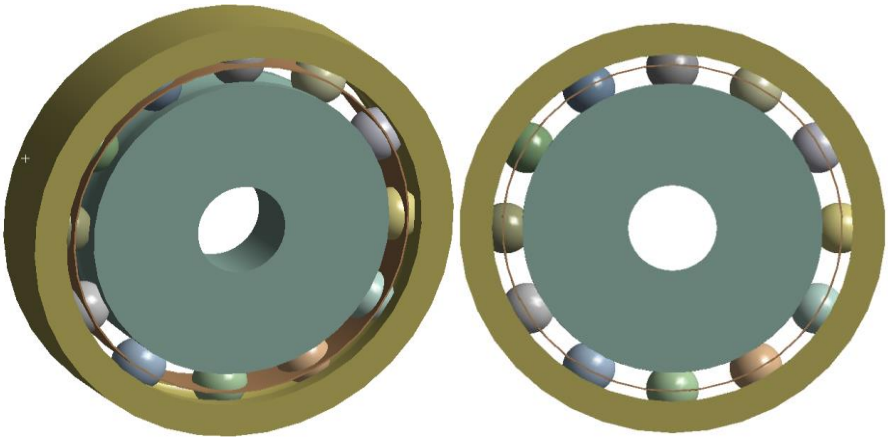

Fig. 1: CAD model representation in three dimensions of a deep groove ball bearing

Meshing is the after process, when we done with CAD modelling. This procedure involves importing the CAD model into the ANSYS workbench for further analysis then it is divided into small pieces and these small pieces are called mesh. The quality of the mesh is assessed to fulfill the criteria and after quality check it is exported to to analysis. The mesh is created for this paper shown in figure 2.

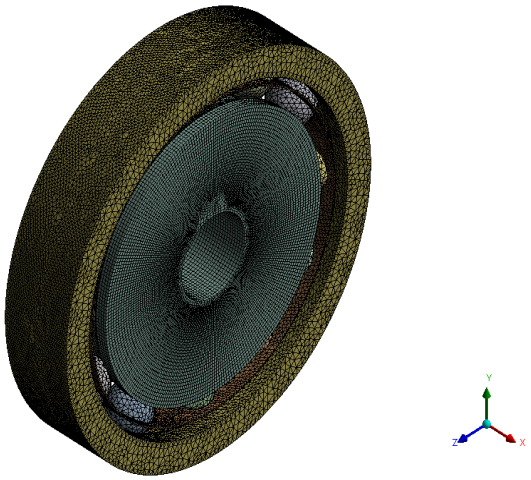

Fig. 2: CAD model representation in three dimensions of a deep groove ball bearing

3 Methodology

This paper provides a holistic process to find the thermal response of silicon Nitride and the Titanium alloy high-performance deep groove ball bearings and compare them. This process involves mathematical calculations for the frictional torque and heat generation in the presence of viscous effects. The equations are developed based on the loading and material properties of the bearing. It also includes finite analysis element which necessitates developing a detailed 3D CAD model of the high-performance deep groove ball bearing, defining precise material properties, meshing for accuracy, applying professional boundary conditions and solving the system using ANSYS Workbench. The results, i.e., temperature distribution and thermal stresses, are then processed to compare the performance of the two

materials and identify the most effective bearing material for high performance based on efficiency and longevity.

3.1 Mathematical analysis of deep groove bearing:

3.1.1 Frictional torque measured by using following relation:

$T_v = 0.8 \times f_v.(\mu_v.n)^{2/3} \times (r_i + r_b)^3$
$T_l = \mu_l \times f_l \times (F_n + F_t)(r_i + r_b)$
Where:
T_v= Frictional torque viscous effect of the lubricants
T_l = torques generated by friction when a weight is applied
f_v = Rolling coefficient of friction
n = Speed in rpm
r_i = Inside ring radius (m)
r_b = Ball or roller radius (m)
μ_l = Friction coefficient due to loading
f_l = Coefficient related to loading direction
F_n = Contact force as a result of outside loading (N)
F_t = Preload caused by heat (N)
$F_t = k_t.\varepsilon_t^{1.5}$
k_t = Value for the ball bearing's radial elastic contact coefficient
ε_t= Total radial interference change
μ_v = Lubricant viscosity (Pas)
$\mu_v = \mu_{vi}.e^{-\beta.(T_{oil}-T_i)}$
μ_{vi} = initial viscosity
β = Temperature- viscosity coefficient
e = Eccentricity of the rolling support
T_{oil} = Oil temperature
T_i = Initial temperature

3.1.2 The total frictional heat generation:

$Q_f = \frac{2\pi n T_v \ or \ T_l}{60}$
Q_f = Total frictional heat generation

3.2 Algorithm used for Analysis of finite element

The finite element analysis tool is the mathematical idealization of a real system. It is a computational method that decomposes geometry into elements and associates each one with a series of equations, which are then solved simultaneously to evaluate the behavior of the entire system. It is useful for complicated geometry, loading, and material property problems where an exact analytical solution is difficult to obtain.

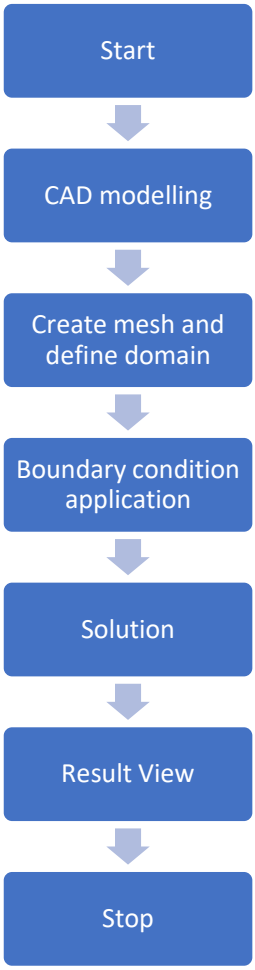

Fig. 3: Flow chart for Finite element analysis

The algorithm used for analysis of finite elements contain three steps:

1. Prior to Processing
2. Processor Solution
3. After Processing

In first step prior to processing, the design or 3D model is created in CAD by direct generation and import it to Ansys workbench to further assessments. After this process material is defined by its constants. For accurate result the material constant should be correct. At last stage of preprocessing it is broken in small parts called the mesh. Mesh is designed to generate results with high precision.

In the second step of the algorithm solution processor, this step is to solve the problem by collection of information provided by the problems. In this phase of processing the computation is used to soles the instantaneous equations created from finite element. Point to remember is that the outcome will only get when all the problem is defined in the proper method.

The third step of the algorithm is pre-processing or after processing, in this step the analysis of the yielded outcomes is occurred across the entire design of the model and the outcome is saved for further case. This After processor has the abilities to range the graphical views and tabular lists to more to more intricate data processing like combine load case and others.

3.3 Material properties

The standard ball bearings materials taken for outside and inside of balls are silicon nitride and titanium alloy. Here the paper discuss about the materials characteristics such as materials structural and thermal behaviour in the form of fundamentals like Young's modulus, Poission ration, density, conductivity specific heat with their particular units to ease the assessment of the paper. Here the materials characteristics below in the tabular form.

Table 1: Silicon Nitride Characteristics with their values

S. No.	Fundamentals	Values
1	YM (E)	3.1e+11Pa
2	PR (nu)	0.26
3	Density	3200 Kg/m^3
4	TC (V)	320 w/m.^{o}C
5	Specific heat	481 J/kg.^{o}C

In this table, paper discuss about the material's characteristics such as structural and thermal behaviour of the material in the form of fundamentals to ease the assessment of the paper. The characteristics for Silicon Nitride are Young's modulus = 3.1e+11 Pa, Poission ratio = 0.26, density = 3200 Kg/m^3, conductivity = 320 w/m. ^{o}C, and specific heat = 481 J/kg ^{o}C .

Table 2: Titanium alloy Characteristics with their values

S. No.	fundamentals	Values
1	YM (E)	1.19e+11 Pa
2	PR (nu)	0.312
3	Density	4429 Kg/m^3
4	TC (V)	7100 w/m.^{o}C
5	Specific heat	553 J/kg.^{o}C

In this table, paper discuss about the material's characteristics such as structural and thermal behaviour of the material in the form of fundamentals to ease the assessment of the paper. The characteristics for Titanium alloy are Young's modulus = 1.19e+11 Pa, Poission ratio = 0.312, density = 4429 Kg/m^3, conductivity = 7100 w/m.^{o}C, and specific heat = 553 J/kg.^{o}C .

Note: In both the above tables following terms are used YM = Young's modulus, PR = Poisson's Ratio, TC = Thermal Conductivity

4 Simulation Outcomes and Findings

From the analysis of this paper, primary aim of this work is to conduct thermal assessment on the ball bearing for the distinct steels used in this paper to increase the strength and thermal efficiency, so the 3D CAD design of the ball bearing with an outside diameter of 110mm, inside diameter of 70 mm, with 12 balls and rolling balls of 9.525 mm diameter created by ansys layout has to perform the thermal assessment for the Titanium alloy and Silicon nitride (Si3N4). After performing of thermal analysis on all above-mentioned materials some results have been obtained in the shape of diagram and graphical representation are discussed in this chapter.

In this paper the temperature distribution while thermal assessment, the temperature that is applied to the inside part of the bearing is varies between 150 to 250 degrees. In this range 150 mark shows the minimum and 250 shows the maximal amount of temperature applied

on the bearing. To improve the thermal conductivity of the materials this thermal assessment is occurred on materials. Following the completion of the thermal assessment of the bearings of distinct materials outcomes such as flux of heat and temperature distribution have been compared and represent in below table.

After performing thermal analysis on ball bearing with deep groove for Titanium alloy and Silicon Nitride (Si3N4) the heat distribution contour has been obtained, the maximum temperature of 250 ºC has been observed at inner portion of the bearing as shown in table. Following the completion of thermal analysis on ball bearing with deep groove for Titanium alloy and Silicon Nitride (Si3N4) the total thermal flux contour has been obtained, for Titanium alloy the maximum thermal flux is 3.69E+05 watt per meter square, and for Silicon Nitride the maximum thermal flux is 1.99E+06 watt per meter square has been observed. For the similar materials Titanium alloy and Silicon Nitride the directional thermal flux contour has been obtained, the maximal directional thermal flux for Titanium alloy is 1.93E+05 watt per meter square, and for Silicon Nitride the maximal directional thermal flux is 9.30E+05 watt per meter square as shown in table.

Table 3: Comparative results of thermal analysis for different materials

Materials	Temperature distribution [ºC]	Total thermal flux [watt per meter square]	Directional thermal flux [watt per meter square]
Silicon Nitride	250	1.99E+06	9.30E+05
Titanium alloy	250	3.69E+05	1.93E+05

Basically this table provides the comparative data of the deep groove ball bearing's directional and total heat flux for Titanium alloy and Silicon Nitride at max. temp. of 250 degree C. For Silicon Nitride the maximum thermal flux is 1.99E+06 watt per meter square, and for Titanium alloy the maximum thermal flux is 3.68E+05 watt per meter square has been observed. For the similar materials Titanium alloy and Silicon Nitride the directional thermal flux contour has been obtained, the maximal directional thermal flux for Silicon Nitride is 9.30E+05 watt per meter square, and for Titanium alloy the maximal directional thermal flux is 1.92E+05 watt per meter square.

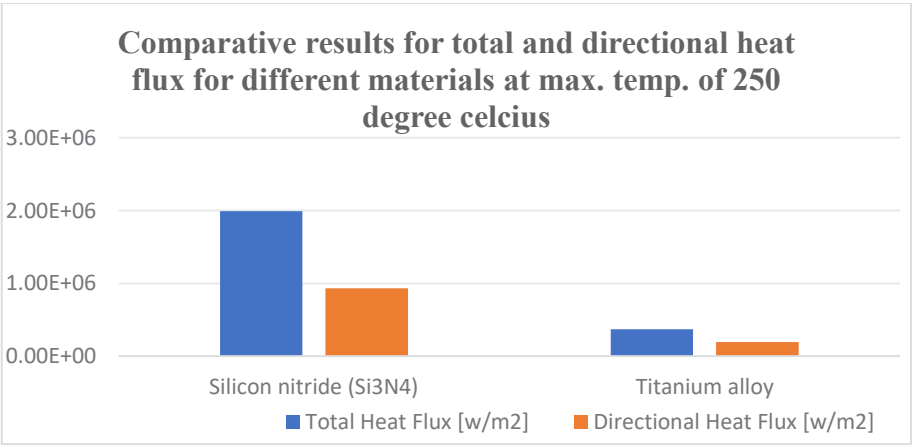

Fig. 4: Comparison of the ball bearing's directional and total heat flux for various materials at max. temp. of 250 ºC.

From the result analysis of ball bearing's different materials, it has been observed that the overall thermal flux in deep groove for Silicon Nitride (Si3N4) produces greater outcomes as compared with Titanium alloy shown in figure 4 with the bar graph representation. When the assessment is based on individuals flux performances here also Silicon Nitride performs well. It has been observed that the total thermal flux in Silicon Nitride (Si3N4) is 440.37% more than Titanium alloy and after observing the directional thermal flux in Silicon Nitride and Titanium alloy, the directional thermal flux of Silicon Nitride is 383.75% more than Titanium alloy.

5 Conclusion

This analysis on two different material assist the selection of suitable materials based on the understanding of the thermal behavior and heat flux of Titanium alloy and Silicon Nitride and this improves the bearings efficiency and durability for various purposes. There are following conclusion having been observed from the above analysis.

- After performing thermal analysis on thermal assessment for temperature range of 150 ^{o}C to 250 ^{o}C on ball bearing with deep groove for Silicon Nitride (Si3N4) , the total and directional flux of heat is 1.99E+06 w/m^2 and 9.30E+05 w/m^2 respectively.
- Following the completion of thermal assessment for temperature range of 150 ^{o}C to 250 ^{o}C on ball bearing with deep groove for Titanium alloy, the total and directional flux of heat is 3.68E+05 w/m^2 and 1.92E+05 w/m^2 respectively.
- Following the completion of thermal assessment for temperature range of 150 ^{o}C to 250 ^{o}C on ball bearing with deep groove for Silicon Nitride (Si3N4) , the total and directional flux of heat is 1.99E+06 w/m^2 and 9.30E+05 w/m^2 that is 440.37% and 383.75% respectively more than Titanium alloy.

From the result analysis it has been observed that ball bearing with deep groove has the thermal assessment in for Silicon Nitride (Si3N4) produces greater outcomes as compared with Titanium alloy.

References

1. Wang, Xingfu, Xiuhong Li, Xiaolong Ma, Wenhui Li, and Shengqiang Yang. "Advance on surface finishing technology of precision bearing cylindrical rollers." The International Journal of Advanced Manufacturing Technology 131, no. 5 (2024): 2341-2363.
2. Gloeckner, Peter, and Charles Rodway. "The evolution of reliability and efficiency of aerospace bearing systems." Engineering 9, no. 11 (2017): 962.
3. D. S. Shah and V. N. Patel, “A dynamic model for vibration studies of dry and lubricated deep groove ball bearings considering local defects on races,” Measurement, Vol. 137, pp. 535–555, Apr. 2019, DOI: 10.1016/j.measurement.2019.01.097.
4. S. S. Pachpore, M. K. Botre, A. S. Patil, and P. V. Jadhav, “Development and validation of transportation methodology by predicting dynamic behavior of container for safe transportation,” in Techno-Societal 2018, pp. 943–953, 2020, DOI: 10.1007/978-3-030-16848-3_86.
5. Heimann, Robert B. "Silicon nitride, a close to ideal ceramic material for medical application." Ceramics 4, no. 2 (2021): 208-223.
6. Trevisan, Francesco, Flaviana Calignano, Alberta Aversa, Giulio Marchese, Mariangela Lombardi, Sara Biamino, Daniele Ugues, and Diego Manfredi. "Additive manufacturing of titanium alloys in the biomedical field: processes, properties and

applications." Journal of applied biomaterials & functional materials 16, no. 2 (2018): 57-67.
7. Du, Xiaoyu, Seunghun S. Lee, Gurdial Blugan, and Stephen J. Ferguson. "Silicon nitride as a biomedical material: an overview." International Journal of Molecular Sciences 23, no. 12 (2022): 6551.
8. Li, Feizhou, and Bian Guo. "Effect of different lubricants on microstructural and tribological properties of TC21 titanium alloy against Si3N4 under fretting–reciprocating sliding." Journal of Alloys and Compounds 743 (2018): 576-585.
9. Nosewicz, Szymon, Grzegorz Jurczak, Tomasz Wejrzanowski, Samih Haj Ibrahim, Agnieszka Grabias, Witold Węglewski, Kamil Kaszyca, Jerzy Rojek, and Marcin Chmielewski. "Thermal conductivity analysis of porous NiAl materials manufactured by spark plasma sintering: Experimental studies and modelling." International Journal of Heat and Mass Transfer 194 (2022): 123070.
10. Fowell, Mark, Stathis Ioannides, and Amir Kadiric. "An experimental investigation into the onset of smearing damage in nonconformal contacts with application to roller bearings." Tribology Transactions 57, no. 3 (2014): 472-488.
11. Li, Tao, Huaitao Shi, Xiaotian Bai, Ke Zhang, and Guangfu Bin. "Early performance degradation of ceramic bearings by a twin-driven model." Mechanical Systems and Signal Processing 204 (2023): 110826.
12. Bhaskar, Sourabh, Mukesh Kumar, and Amar Patnaik. "Effect of Si3N4 ceramic particulates on mechanical, thermal, thermo-mechanical and sliding wear performance of AA2024 alloy composites." Silicon 14, no. 1 (2022): 239-262.
13. Hou, Yu, and Xi Wang. "Development of an experimental system to measure the cage slip of cylindrical roller bearing." Structural Health Monitoring 19, no. 2 (2020): 510-519.
14. Li, Naipeng, Yaguo Lei, Jing Lin, and Steven X. Ding. "An improved exponential model for predicting remaining useful life of rolling element bearings." IEEE Transactions on Industrial Electronics 62, no. 12 (2015): 7762-7773.
15. Singh, Rabindra, and Deepak Pandey. "Enhancing The Thermal Performance By Conducting Thermal Studies On The Deep Grove Ball Bearing For Various Materials."
16. Gao, Shuai, Steven Chatterton, Lorenzo Naldi, and Paolo Pennacchi. "Ball bearing skidding and over-skidding in large-scale angular contact ball bearings: Nonlinear dynamic model with thermal effects and experimental results." Mechanical Systems and Signal Processing 147 (2021): 107120.
17. Singh, Dhananjay Kr, Pankaj Kr Baitha, and J. Manam. "Enhancement of luminescence intensity and spectroscopic analysis of Eu 3+-activated and Li+ charge-compensated CaTiO 3 color tunable phosphors for solid-state lighting." Applied Physics A 122 (2016): 1-15.
18. Kumar, K. Yogesh, Himani Saini, D. Pandiarajan, M. K. Prashanth, L. Parashuram, and M. S. Raghu. "Controllable synthesis of TiO2 chemically bonded graphene for photocatalytic hydrogen evolution and dye degradation." Catalysis Today 340 (2020): 170-177.
19. Raghu, M. S., CB Pradeep Kumar, M. K. Prashanth, K. Yogesh Kumar, B. S. Prathibha, G. Kanthimathi, Siham Abdulrahman Alissa, Hanan Abdulrahman Alghulikah, and Sameh M. Osman. "Novel 1, 3, 5-triazine-based pyrazole derivatives as potential antitumor agents and EFGR kinase inhibitors: Synthesis, cytotoxicity, DNA binding, molecular docking and DFT studies." New Journal of Chemistry 45, 31 (2021): 13909-13924.
20. Suganthi, S. T., Arangarajan Vinayagam, Veerapandiyan Veerasamy, A. Deepa, Mohamed Abouhawwash, and Mariammal Thirumeni. "Detection and classification of multiple power quality disturbances in Microgrid network using probabilistic based

intelligent classifier." Sustainable Energy Technologies and Assessments 47 (2021): 101470.

21. Bale, Ajay Sudhir, Naveen Ghorpade, Muhammed Furqaan Hashim, Jatin Vaishnav, and Zahra Almaspoor. "A comprehensive study on metaverse and its impacts on humans." Advances in Human-Computer Interaction 2022 (2022).
22. Naik, Ramachandra, S. C. Prashantha, and H. Nagabhushana. "Effect of Li+ codoping on structural and luminescent properties of Mg2SiO4: RE3+ (RE= Eu, Tb) nanophosphors for displays and eccrine latent fingerprint detection." Optical Materials 72 (2017): 295-304.
23. Naik, Ramachandra, S. C. Prashantha, H. Nagabhushana, S. C. Sharma, H. P. Nagaswarupa, K. S. Anantharaju, B. M. Nagabhushana, H. B. Premkumar, and K. M. Girish. "A single phase, red emissive Mg2SiO4: Sm3+ nanophosphor prepared via rapid propellant combustion route." Spectrochimica Acta Part A: Molecular and Biomolecular Spectroscopy 140 (2015): 516-523.
24. Karuppusamy, Loheswaran, Jayavadivel Ravi, Murali Dabbu, and Srinivasan Lakshmanan. "Chronological salp swarm algorithm based deep belief network for intrusion detection in cloud using fuzzy entropy." International Journal of Numerical Modelling: Electronic Networks, Devices and Fields 35, 1 (2022): e2948.
25. Ramakrishna, G., Ramachandra Naik, H. Nagabhushana, R. B. Basavaraj, S. C. Prashantha, S. C. Sharma, and K. S. Anantharaju. "White light emission and energy transfer (Dy3+→ Eu3+) in combustion synthesized YSO: Dy3+, Eu3+ nanophosphors." Optik 127, 5 (2016): 2939-2945.
26. Jisha, P. K., Ramachandra Naik, S. C. Prashantha, H. Nagabhushana, S. C. Sharma, H. P. Nagaswarupa, K. S. Anantharaju, B. Daruka Prasad, and H. B. Premkumar. "Facile combustion synthesized orthorhombic GdAlO3: Eu3+ nanophosphors: Structural and photoluminescence properties for WLEDs." Journal of Luminescence 163 (2015): 47-54.
27. Vijay, Vallabhuni, CV Sai Kumar Reddy, Chandra Shaker Pittala, Rajeev Ratna Vallabhuni, M. Saritha, M. Lavanya, S. China Venkateswarlu, and M. Sreevani. "ECG performance validation using operational transconductance amplifier with bias current." International Journal of System Assurance Engineering and Management 12 (2021): 1173-1179.
28. Reddy, P. Venkateshwar, B. Veerabhadra Reddy, and P. Srinivasa Rao. "A numerical study on tube hydroforming process to optimize the process parameters by Taguchi method." Materials Today: Proceedings 5, 11 (2018): 25376-25381.
29. Botlagunta, Mahendran, Madhavi Devi Botlagunta, Madhu Bala Myneni, D. Lakshmi, Anand Nayyar, Jaithra Sai Gullapalli, and Mohd Asif Shah. "Classification and diagnostic prediction of breast cancer metastasis on clinical data using machine learning algorithms." Scientific Reports 13, 1 (2023): 485.
30. SushovanChaudhury, Alla Naveen Krishna, Suneet Gupta, K. SakthidasanSankaran, Samiullah Khan, AbhishekRaghuvanshi KartikSau, and F. Sammy. "Effective Image Processing and Segmentation-Based Machine Learning Techniques for Diagnosis of Breast Cancer." Computational and Mathematical Methods in Medicine 2022.
31. Devi, M. Dharani, A. Vimala Juliet, K. Hariprasad, V. Ganesh, H. Elhosiny Ali, H. Algarni, and I. S. Yahia. "Improved UV Photodetection of Terbium-doped NiO thin films prepared by cost-effective nebulizer spray technique." Materials Science in Semiconductor Processing 127 (2021): 105673.
32. Padmaja, B., VV Rama Prasad, and K. V. N. Sunitha. "A machine learning approach for stress detection using a wireless physical activity tracker." International Journal of Machine Learning and Computing 8, no. 1 (2018): 33-38.

33. Bhukya, Laxman, Narender Reddy Kedika, and Surender Reddy Salkuti. "Enhanced maximum power point techniques for solar photovoltaic system under uniform insolation and partial shading conditions: a review." Algorithms 15, 10 (2022): 365.
34. Subramanian, Malliga, Narasimha Prasad Lv, and Sathishkumar VE. "Hyperparameter optimization for transfer learning of VGG16 for disease identification in corn leaves using Bayesian optimization." Big Data 10, 3 (2022): 215-229.
35. Vijaykumar, G., Anil Gantala, Mary Swarna Latha Gade, P. Anjaneyulu, and Sk Hasane Ahammad. "Microcontroller based heartbeat monitoring and display on PC." Journal of Advanced Research in Dynamical and Control Systems 9, 4 (2017): 250-260.
36. Pittala, Chandra Shaker, Vallabhuni Vijay, and B. Naresh Kumar Reddy. "1-Bit FinFET carry cells for low voltage high-speed digital signal processing applications." Silicon 15, 2 (2023): 713-724.

Journal of Physics: Conference Series

PURPOSE-LED PUBLISHING™

PAPER • **OPEN ACCESS**

Performance Evaluation of Ternary Blended Cement Concrete with Manufactured Sand using Alccofine and Zeolite in different replacement levels

To cite this article: C Vivek Kumar *et al* 2024 *J. Phys.: Conf. Ser.* **2837** 012015

View the article online for updates and enhancements.

You may also like

- A comprehensive study on physico-mechanical properties of non-metallic fibre reinforced SCC blended with metakaolin and alcofine
S S Vivek, B Karthikeyan, Senthil Kumaran Selvaraj et al.
- Comparison of Mechanical properties of flyash-GGBS based GPC and flyash-alccofine based GPC with different concentrations of alkaline activators
Vemundla Ramesh and Koniki Srikanth
- Study On Alccofine Based High Performance Concrete
G. Srinivasan

This content was downloaded from IP address 106.0.37.90 on 21/10/2024 at 11:17

Journal of Physics: Conference Series **2837** (2024) 012015 doi:10.1088/1742-6596/2837/1/012015

Performance Evaluation of Ternary Blended Cement Concrete with Manufactured Sand using Alccofine and Zeolite in different replacement levels

Vivek Kumar C[1, a *], J S S K Vasa[2,b], M Rishabalaxmi[3,c] S J Shivraj[4,d], M Ganesh[5,e]

[1]Civil Engineering Department, Gokaraju Rangaraju Institute of Engineering and Technology, Hyderabad, India
[2]Civil Engineering Department, Malla Reddy Engineering College, Hyderabad, India.
[3]Civil Engineering Department, Akshaya College of Engineering and Technology, Coimbatore, India.
[4]Civil Engineering Department, B V Raju Institute of Technology, Narsapur, India.
[5]Department of Aeronautical Engineering, MLR Institute of Technology, Hyderabad, Telangana.

*vivekkumarcr@gmail.com

Abstract. Concrete is the most adaptable, extensively researched, and reliable building material available worldwide. minimizing the adverse impacts of the construction sector on the ecosystem as it exists today. Manufactured sand (MS) or manufactured fine aggregate (MFA) is made by crushing larger aggregate pieces into aggregate particles the size of sand. Manufactured sand is widely employed in the construction industry as a substitute for river sand, mostly for making concrete mixtures and mortar. By utilizing less cement in the concrete in the current study, Alccofine 1203 and Zeolite were partially substituted for cement, making the concrete a more sustainable material. Zeolite (ZL) is produced when ash and rock layers that simultaneously form following a volcanic eruption are used in concrete as a substitute for Portland cement, making up 4% of the total mass. The utilization of manufactured sand has recently started, with several construction projects taking place in various countries. In this experiment, alccofine (AF) 1203 is being used in M40-grade concrete in amounts ranging from 2% to 20% as a cement substitute. To create Ternary Blended Cement Concrete (TBCC), cement, 4% zeolite, and 50% MS are used in place of natural sand.

1. Introduction

In today's scenario, it is imperative to make the building industry sustainable to reduce its detrimental effects on the environment. When choosing raw materials for construction, it's critical to make environmentally friendly choices. The emissions of carbon dioxide into the environment during the production of cement are the cause of the phenomenon of global warming. This implies that examining the sustainability of the earth's resources over the long term is necessary. The growing demand is constantly depleting natural resources, which are vital to the cement-producing industry. Conversely, improper handling of landfills has been linked to damage to the environment from industrial waste materials. Several industrial waste products are utilized as partial cement substitutes since they contain cementitious properties. Supplementary cementitious materials (SCMs) with high

Content from this work may be used under the terms of the Creative Commons Attribution 4.0 licence. Any further distribution of this work must maintain attribution to the author(s) and the title of the work, journal citation and DOI.
Published under licence by IOP Publishing Ltd

silica and alumina content are necessary for the development of concrete's strength. Examples of these SCMs include fly ash (FA), silica fume (SF), metakaolin (MK), alccofine (AL), rice husk ash (RHA), ground granulated blast furnace slag (GGBFS), zeolite (ZL), etc. Once the replacement level of the SCMs went up to around 15–20%, the value of the CO2 concentration reduced abruptly; after that, the rate of decline slowed down gradually. All things considered, the CO2 and binder intensities might be determined by the specific replacement level for each SCM.

Ramya et al. [3] investigated sustainable ternary blended concrete using industrial waste materials like GGBFS and Alccofine 1203, which effectively replaced cement. To keep the optimum proportion of GGBS fixed, additional substitution of cement with alccofine was carried out, with replacement percentages ranging from 8% to 14%. Narender et al. [1] calculated the CS of these mixtures for 7, 14, and 28 days. However, it was discovered that its CS values were lower than those of the traditional concrete mixtures. The inclusion of highly reactive alccofine (AF) is responsible for the surge in early strength development observed in all ternary blended mixtures, according to studies conducted by Shankar et al. [2]. Higher replacement of alccofine [AF] above 10% resulted in a moderate dilution effect that led to a constant fall in strength; in contrast, the dilution of strength for silica fume (SF) was gradual after 15% replacement. Swetha et al. [4]. explored Zeolite and nano silica were added to the concrete to make it denser and cover the spaces left by the micron-sized cement particles. By substituting some of the PPC with mixtures of SCM, Ahmadi et al. [5] found that the mobility qualities of concrete were significantly improved. The improved paste-fine aggregate transition zone is responsible for the increase in strength, according to Donza et al.'s [6] analysis of the hydration and mortar phases of concrete. In addition to zeolite and silica fume combination, the long-term strength as well as early ages of SCC improved, according to Madandoust et al. [7] investigation.

It is crucial to make the construction sector sustainable in current circumstances to mitigate its adverse impacts on the environment. It is important to choose environmentally friendly materials while selecting raw materials for building. Global warming is caused by CO2 emissions into the atmosphere that occur during cement manufacturing. This necessitates that researchers focus on the long-term sustainability of earth's resources. Natural resources which are essential for the cement manufacturing sector are continuously being depleted because of the rising demand. On the other hand, inappropriate landfill management has been implicated in environmental harm caused by industrial waste products. Several industrial waste products are utilized as partial cement substitutes since they contain cementitious properties. Supplementary cementitious materials (SCMs) with high silica and alumina content are necessary for the development of concrete's strength. Example of these SCMs comprise fly ash (FA), silica fume (SF), metakaolin (MK), Alccofine (AL), rice husk ash (RHA), and ground granulated blast-furnace slag (GGBFS), Zeolite (ZL), etc.

Ramya et al. [3] investigated sustainable ternary blended concrete using industrial waste materials like GGBFS and Alccofine 1203, which effectively replaced cement. Keeping the optimum proportion of GGBS fixed, additional substitution of cement having Alccofine was carried out, with replacement percentages ranging from 8% to 14%. Narender er.al [1] calculated the CS of these mixtures for 7, 14, and 28 days. However, it was discovered that its CS values were lower than those of the traditional concrete mixtures. The inclusion of highly reactive Alccofine (AF) is responsible for the surge in early development of strength observed in all ternary blended mixtures, according to studies conducted by Shankar et al. [2]. Higher replacement of Alccofine [AF] above 10% resulted in a moderate dilution effect that led to a constant fall in strength; in contrast, the dilution of strength for silica fume (SF) was gradual after 15% replacement. Swetha et al [4]. explored Zeolite and nano silica were added to the concrete to make it denser and cover the spaces left by the micron-sized cement particles. By substituting some of the PPC with mixtures of SCM, Ahmadi et al. [5] found that the mobility qualities of concrete were significantly improved. The improved paste-fine aggregate transition zone is responsible for the increase in strength, according to Donza et.al [6] analysis of the hydration and mortar phases of concrete. In addition of zeolite, silica fume combination the long-term strength as well as early ages improved of SCC, according to Madandoust et al. [7] investigation. To achieve the best possible mechanical characteristics for the concrete mix, Syed Afzal Basha [8] experimented with using M-sand in place of

natural river sand, adding zeolite up to 15%. Durability qualities were established by resistivity, the cyclic wet and dry test, and the rapid chloride penetration test (RCPT) by Peruri Rahul et al. [10].

Foong Kah Yen et al. [23] study examined the inclusion of MS and rice husk ash (RHA) in lightweight oil palm shell concrete (OPSC) with the addition of cement and RS. The use of recycled MS in place of NS in mortar was investigated by Zhiming Ma et al. [9]. To enhance the qualities of cemented sands, Mola-Abasi et al. [11] examined the potential of using additional material with a zeolite stabilizer. Using alccofine, a mineral additive, Sanjeev Kumar et al. [12] replaced 30% of the coarse aggregate with coconut shell. Prasanth et al. [18] investigate the usage of M sand for microstructure investigation of HSC. Repati Mohan Babu et al. substituted cement with alccofine (AF) and GGBFS [24]. In place of natural aggregate (NA) in the concrete blend, Vivek Kumar et al. [25] used recycled coarse aggregate (Rca) and recycled fine aggregate (Rfa). Weiguo Shen et al. studied the particle shape, surface texture, and behaviour of MS concrete. Supplementary Cementitious Materials (SCMs)

2. Supplementary Cementitious Materials (SCMs)

2.1. Microstructure and Significance

Alcofine-1203, a material with a low calcium silicate percentage, is used as SCM in place of silica fume to create high-strength concrete (HSC) and high-performance concrete (HPC). Comparable to that, another material with a low calcium silicate proportion examined to build distinct types of concrete is Alccofine-1206. Alccofine-1203 constitutes a microfine substance with a high glass content and high reactivity which is also low in calcium silicate and harmless to the environment. A highly processed material called Alcofine-1203 may be generated from GGBS, the leftovers from India's iron ore manufacturing units. Crushing the huge parent mass of rock produces Manufactured Sand (MS). Zeolites have exceptionally stable solids that can withstand circumstances in the environment that would be challenging for other types of materials. They are additionally resistant to temperatures over 1000°C and have high melting points. They are also resistant to high pressure, do not dissolve in water or inorganic solvents, and because they are inert, they have no adverse impacts on the environment. In the building sector, zeolites have been employed as an additional cementitious material.

Numerous aggregate characteristics, including as chemical and mineralogical structure, petrographic categorization, relative density, hardness, strength, physical as well as chemical stability, porous structure, and colour, are thus dependent on the characteristics of the parent rock. Some characteristics of crushed sands, such as particle size, shape, and surface texture, are not present in the parent rock, whereas other characteristics, such as absorption, can alter because of crushing. The size reduction ratio, crushing plant, and degree of stratification of the rock deposit all affect the shape. These characteristics have a significant impact on the quality of newly poured and cured concrete. The scanning electron microscope (SEM) images of zeolite demonstrate that the material generally consists of small laminar crystals with rosettes attached, and the cement has become observed to have an irregular particle size. Additionally, the spherical form of ultrafine fly ash helps to the development of higher interaction.

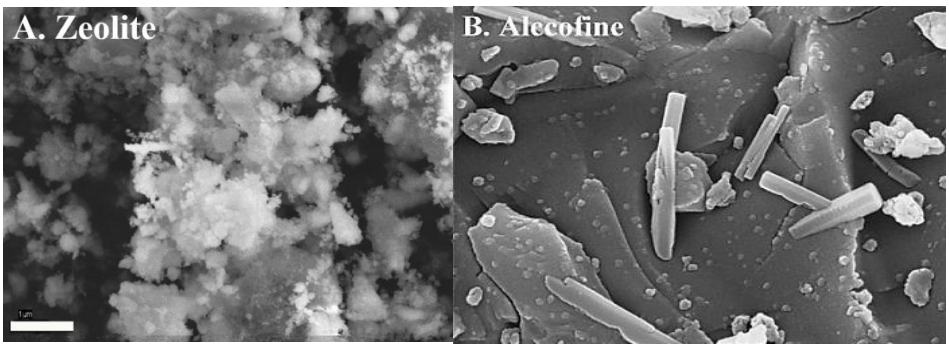

Fig.1.SEM images for (a) Zeolite (b) Alccofine

SEM pictures of concrete specimens are presented in Figure 1(a). The SEM analysis clearly identifies the hydrated and un-hydrated particles, with white portions denoting the hydrated particles while black spots denoting the un-hydrated particles. The pores found in the concrete have been delineated by the black patches. The typical mix has a high ethylene phase generation rate, that significantly decreases hydration. On the other hand, because zeolite and Alccofine are both silicate admixtures, they improve the production of C-S-H gels. Additionally, traditional concrete can form cracks, but these typically show up significantly. The binding factor that lime provides to the paste is its function in cement. According to the findings as per Figure 1(b), Alccofine also includes high amounts of Si, Al, and Ca. The binder paste gains greater strength due to the inclusion of silica and alumina. When examining the cement SEM pictures at a 100k magnification scale, it was found to include white areas, which may be signs of significant free lime in the physical form of calcium oxide. Under the identical 100k magnification scale, the rounded white patch free lime concentration was discovered to be negligible and was substituted by needle-like angular particles, that may be a mixture of silica and lime that were observed in excessive amount. Concrete strength and durability may constitute impacted by the packing density within the concrete. A denser matrix may be obtained by using mineral additives with various particle sizes. On the other hand, increasing particle packing densities decreases void gaps and pulls out the surplus water that remains in the pores for the lubricating the binder particles, which is extremely important for HPC in which lower water to binder ratio needs to be achieved. Alccofine 1203 and Zeolite have been used as a cement substitute in this investigation, with amounts ranging from 2% to 20% in M40 grade concrete. Ternary Blended Cement Concrete (TBCC) is made by mixing cement with 4% zeolite and 50% MS to replace the use of natural sand. Loss in weight and CS were subjected to durability tests that included chloride and sulfate resistance.

2.2. Material Properties and Methodology

All the mixtures are cemented with ordinary Portland cement (OPC) of 53-grade, which conforms to IS 12269-2013 [21] and has a 28-day compressive strength of 54.5 MPa. Alccofine-1203 is a highly reactive version of GGBS that has been treated through controlled granulation. The particles are irregularly shaped, with most of their diameters falling between 4 and 10 μm. Conplast SP430 evenly distributes the tiny particles in the concrete mix, which improves the performance of the concrete's water content. Conplast SP430 allows for the enhancement of additive dose and mix design and provides a full examination of the concrete mix. The average dosing range for high-strength, water-reduced concrete is 0.70 to 2.00 litres/100 kg of cementitious material, which includes PFA, GGBFS, and microsilica. High workability concrete typically uses 0.70 to 1.30 litres/100 kg of cementitious material. For concrete with high workability, the average dosage range is 0.70 to 1.30 liters/100 kg of cementitious material.

The quality of the materials used, the design of the mix, and quality control procedures during the concrete production process constitute some of the factors that affect compressive strength as a feature of concrete. The test sample with cube 10 cm x 10 cm x 10 cm is the most frequent according to the code that is implemented. The characteristics that follow of cement concrete can be determined by tests covered in IS 516:1959, Methods of Test for Concrete Strength. Knowing that it takes 28 days for concrete to set is one limiting parameter when evaluating the compressive strength of the material.

Table 1 : Properties of Cement, FA and CA.

Cement			**Fine Aggregate**	**Coarse Aggregate**
Property	**Value**	**Property**	**Value**	
Specific Gravity	3.12	Type	Crushed	Crushed
Normal Consistency	33%	Specific gravity	2.61	2.6
Initial Setting Time	34 mins	Fineness modulus	2.75	6.52
Final Setting Time	320 mins	Bulk Density	1685 kg/m^3	1754 kg/m^3

Table 2 : Chemical and Physical Properties of ZL,AF and MS

Chemical Composition (%)			**Physical Properties**			
Property	**ZL**	**AF**	**ZL**	**AF**	**Manufactured Sand (MS)**	
SiO_2	65.88	33.4	White	Whitish Grey	Finess Modulus	2.88
Al_2O_3	13.47	21.25	2 – 3.35	4 – 6	Specific Gravity	2.70
Mgo	1.07	8.45	920 kg/m^3	700 kg/m^3	Bulk Density	1850 kg/m^3
TiO_2	0.15	-	2.3	2.82	Moisture Content	1.60 %
CaO	2.52	32.1	25.73	12.02	Water Absorption	2.65 %
K_2O	2.72	-	D10	1.8		
C	2.51	-	D50	4.4		
Loss of Ignition	11.5	-	D90	9.2		

In contrast to NS, the texture along with the shape of MS lower workability at the exact same water content level while increasing concrete strength because of improved particle interlocking. Further, a significant amount of micro fines (5%–20%) will be added during the construction of MS concrete, which will affect the CS, FS and Freeze-Thaw Resistance. Fine aggregates density has been influenced by the order of distribution of their particle sizes. Compared to RS and OS, MS has a significantly greater overall density due to its presence of higher microfine. It is simple to observe that, in the case of the mixed sands, the packing density increased proportionally as the replacement levels were reduced. MS comprises an extensive particle distribution curve and is quite angular. During the MS production process, fine and ultrafine particles are removed by screening out.

During the sand selection process, the following aspects are required to be considered as colour, size of particles, form, crushing potential, chemical reactions, the degree of hardness, infiltration rates, and so on. Comparing MS particles to RS and OS particles, more angular or cubical forms were found in MS particles. With MS, which exhibits more angularity, one can see sharp tips as well as straight edges. All the mixes include manufactured sand for the fine aggregate, which confirms to the IS: 383- 1970 [15] zone II sieve passing percent. The specific gravity of MS is 2.70, its fineness modulus is 2.88, and the water absorption rate is 0.96% over a 24-hour period.MS have been taken in bulk mass from the locally available crusher around Hyderabad locality, it was evaluated for identifying the physical properties as shown in Table 3. According to ASTM C143, a slump test was conducted to determine the workability of freshly mixed concrete [17]. Cube specimens are tested using a compression testing machine with a maximum load-carrying capacity for load of 2000 kN.

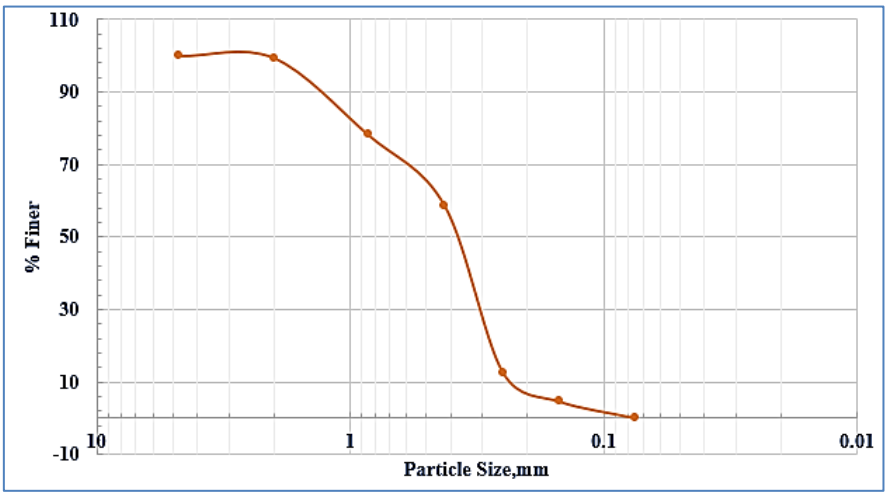

Fig 2: Particle Size distribution for MS

Plotting the resulting gradation curves against the percentage finer (%) of the size proportion under consideration, which ranges from 4.75 mm to 0.001 mm, is shown in Figure 8. When comparing the gradation curves of river sand fines, MS fines exhibit a larger percentage finer for each size fraction considered. Among the various types of sand, MS fines show the lowest percentage passing for each size fraction. It is apparent that M Sand is made by going through multiple crushing steps, which allows for a higher fine content than river sand that occurs naturally. It is possible that particles smaller than 0.001 mm of MS could have greater passing percentages; however, this is not taken into consideration in this test. According to Fig. 2, it is observed that MS exhibits lower passing percentages than RS.

3. Mix Proportioning and Testing of TBC Specimens

Employing the standards and requirements suggested by IS: 456 2000 [13] and ACI 211.4R-93 [26], a total of 14 mixtures were proportioned. In this study, Alccofine (AF) 1203 is being utilized in amounts that vary between 2% to 20% in the grade M40 concrete to serve as cement substitute. By substituting cement for natural sand and adding 4% zeolite and 50% MS, ternary blended cement concrete (TBCC) can be produced. With the addition of SCMs, the fine aggregate content is decreased in all mixes in proportion to the volume variation.

Table 3. Mix proportions of Ternary Blended Concrete for M40 Grade

Mix	Cement	AF	ZL	NS	MS	CA	S.P	Water	Slump
	Quantities in kg/m^3								mm
M1	350	0	0	660	0	1141	3.5	140	75
M2	336	14	0	330	330	1141	3.5	140	110
M3	322	14	14						105
M4	308	14	28						116
M5	294	14	42						121
M6	280	14	56						136
M7	266	14	70						139
M8	336	0	14						108
M9	322	14	14						112
M10	308	28	14						118
M11	294	42	14						124
M12	280	56	14						127
M13	266	70	14						132

To achieve the desired level of workability having a slump of at least 75 mm, superplasticizer amount was adjusted based on cementitious material weight. Table 4 lists the mixing proportions that were applied in this experimental programme. In 100 mm x 100 mm x 100 mm cubical concrete were precisely mixed in a tilting type of mixer machine. Three different samples of each number were created for each mix. After de-moulding, specimens were given time to cure in a controlled environment in the lab. The mater cement ratio is taken as 0.40, with the mix proportioning of 1: 1.88: 3.26 as per IS 10262-2009[14].

4. Results and Discussions

However, when concrete is dried without bleed water, water evaporates from the surface and causes plastic shrinkage. Although overlaying or curing concrete is typically done, avoiding plastic shrinkage cracking is an important difficulty on numerous building sites. The need for more a superplasticizer to attain the necessary flow or workability may rise in with the inclusion of SCMs. The way that the different rheological qualities change over time might be affected by them.

With the same water-binder ratio (w/b), the combined binder system's flowing response thus become very different from an ordinary Portland cement (OPC) system, primarily due to the SCMs' particle size distribution and shape. The environmental effects haven't been prioritized in the optimization of SCM contents for employing SCMs most efficiently, and when they have, the main emphasis

has been on emissions of greenhouse gases. Material performance indicators play a major role in conventional SCM optimization. The impact of the SCM to cement ratio can be quantified to help choose mixes that will least negatively affect the environment. Combining impact categories makes these computations simpler, but it may also mask some impact categories' effects, that have been confined to communities located near industrial regions.

Before starting to mix concrete, the mixer's chamber was prewetted. The pre-weighed components CA, FA, and MS were put into the mixer one at a time, together with the cementitious materials, water, and each. The combination was included once the SP had been dissolved in the water. The whole mixture was blended for three to five minutes. After adding the CA, the concrete mixture was agitated for between 10 and 15 seconds. Finally, a slump test was performed to evaluate the mechanical properties of fresh concrete. The samples were subsequently demolded and moved to the standard curing chamber for 28 days until test after being cured for 48 hours at 20 °C and 60 % relative humidity.

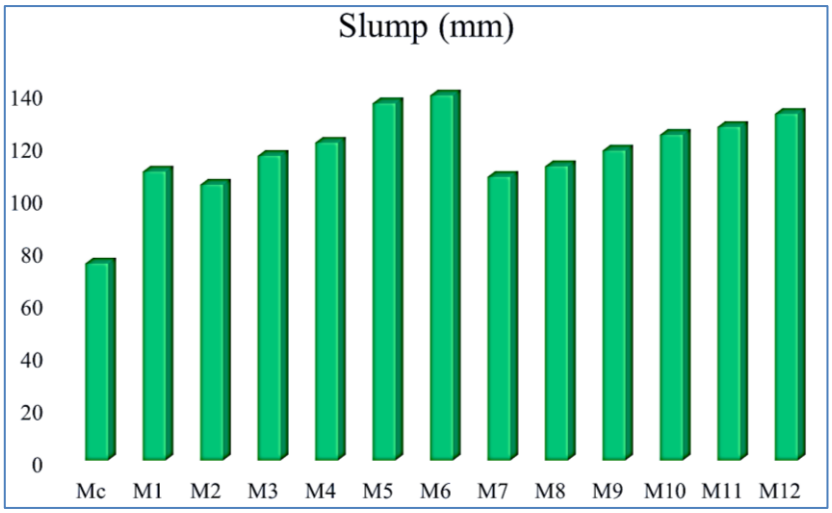

Fig: 3. Graph for Slump value of all mixes

Fig: 4. Cracking Pattern of TBCC specimens under compression

The CS of concrete specimens gives details regarding the cementing procedure, the standard of the matrix of concrete, and its connection to the MS and natural materials. The results of this test can be significantly changed by changing the specimen, sample size, mould form, and subsequent processing conditions, which is crucial for the design of the structure. The CS was conducted as per IS 1199: 1959 On TBC, CS tests are conducted in a compression testing machine (CTM), with ZL and AL percentages

increasing by every 5% from 5% to 20% and ZL and AL as 4%. Appropriate strength parameters have been determined and are shown in Table 4.

Table 4. CS results of M40 grade mixes at different ages AF/ZL concrete mixes

Mix	% replacement			CS in MPa		
	MS	AF	ZL	7 days	14 days	28 days
Mc	--	0	0	21.98	34.87	42.31
M1	50	4	0	24.52	33.53	42.26
M2	50	4	4	24.97	33.59	43.31
M3	50	4	8	25.16	34.84	45.35
M4	50	4	12	25.45	34.92	46.44
M5	50	4	16	25.92	35.71	43.72
M6	50	4	20	26.24	35.82	41.97
M7	50	0	4	19.22	31.45	39.47
M8	50	4	4	21.23	32.29	41.22
M9	50	8	4	21.98	33.74	42.24
M10	50	12	4	22.49	34.15	42.61
M11	50	16	4	23.11	33.29	41.39
M12	50	20	4	21.45	31.99	39.96

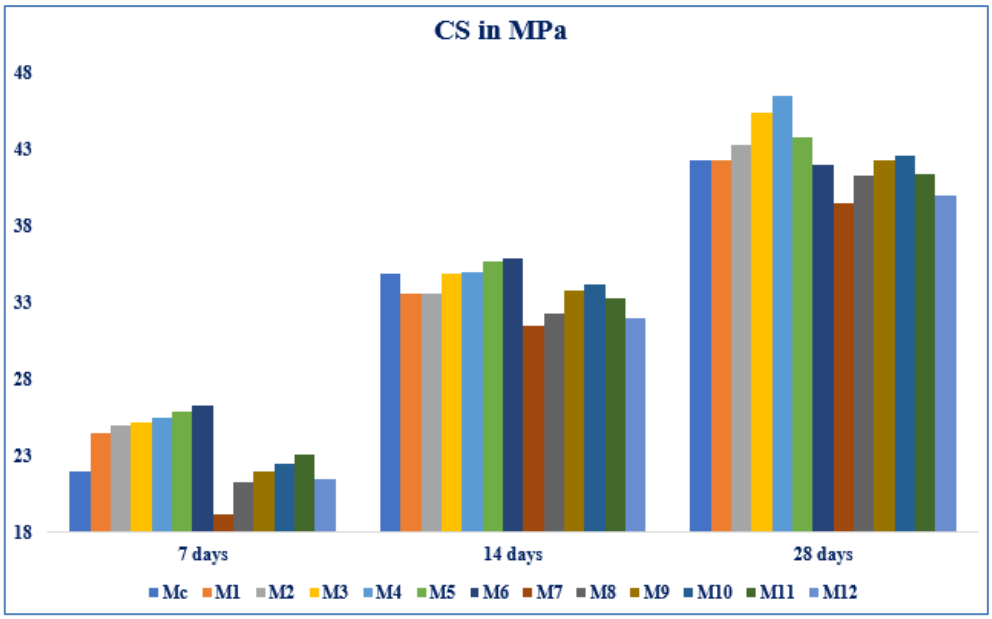

Fig.5. Graph showing Compressive Strength results for 7, 14 and 28 days

In accordance with IS 516-1959, an experiment was performed to determine the CS of concrete at 28 days age of curing. The results are shown in Table 9. Utilizing CTM, the cubes were tested. According to Figure 5, the proportion of 50% MS + 4 % AF +12% ZL, CS reaches up to 25.45 N/mm^2 for 7 days, 34.92 N/mm^2 and 46.44 N/mm^2 after 14 and 28 days gives higher CS from all other mixes, whereas CS is slightly declined to while increasing the Zeolite %. The Optimum mix proportion is taken as 50% MS + 4 % AF +12% ZL, when MS and AF is kept constant and ZL is varying. In comparison with other mixes, the percentage of 50% MS + 12% AF + 4 % ZL has a higher CS that reached up to 22.49 N/mm^2 for 7 days, 34.15 N/mm^2 and 42.61 N/mm^2 after 14 and 28 days, respectively. However, as the zeolite% is increased, the CS slightly decreases. When ZL is variable while MS and AF are constant, the optimal mix fraction is calculated as 50% MS + 4% AF +12% ZL. When compared to both

AF and ZL variables, the CS is moreover similar and effective usage or optimum mix proportion is taken as 50% MS + 4 % AF +12% ZL.

Because of the strong pozzolanic nature of the AF and its capacity to fill gaps, the CS of concrete has significantly increased. The optimal dosage of RAC is 30% according to tests on mechanical properties and workability using MS, AF and ZL. When compared to standard concrete, TBC's workability declined slightly. If the fine aggregate is smaller than 5 mm, it is challenging to distinguish finer particles on an aggregate surface. The implementation of current technologies to increase density, as well as the rate of absorption results in a limit as a result, making it difficult enough to separate from the structure of concrete and necessitating technologies to facilitate FA and CA separation in the original material.

Compared to a controlled concrete blend, adding SCMs to ternary blended concrete (TBC) can increase compressive strength by 16%, while dispersing SCMs in a water-superplasticizer solution can increase compressive strength by 12%. Therefore, by introducing SCM addition, further research can be done regarding improving the characteristics for durability and strength. About particle size distribution (PSD) and grading, MS can be utilized to create blended concrete. Standard testing procedures are also feasible to determine the dependable of AF and ZL.

5. Conclusions

In the present investigation, Zeolite (ZL) and Alccofine (AF) 1203 have been employed as cement substitutes in amounts that range from 2% to 20% in M40 grade concrete. In substitute of river sand 50% of MS have been used in all samples, Ternary Blended Cement Concrete (TBCC) is created by combining cement containing 4% zeolite and 50% MS as a constant for all mixes.

The CS is additionally identical to both the AF and ZL variables, and the effective usage or optimum mix percentage is taken as 50% MS + 12% AF + 4 % ZL having higher CS as N/mm^2. Concrete's compressive strength (CS) has greatly increased due to the AF's strong pozzolanic makeup and ability to fill voids. When compared to other AF replacements, the 12% AF substitution concrete exhibits a greater value. Higher strengths in M40 concrete grade levels have been demonstrated with a 12% replacement of AF. More specifically, the M40 grade's 7-day compressive strength for 12% substitution of AF met the 28-day strength requirement.

The ideal dosage of AF replacements for the process of hydration as well as increase in strength in compliance with the codal regulations was 12 - 16 % replacement. The partial replacements of varying between 10% and 20%, however, serve as filler during the concrete's bonding process. While 10–20% of the concrete was substituted with calcined zeolite (ZL), the autogenous shrinkage was significantly reduced, but the 28-day CS remained mostly unchanged. Another study found that stronger concrete was generated than conventional concrete when ZL powder was used in place of 10% of the concrete and 30% to 50% of the MS.

References

[1] A. Narender Reddy, T. Meena, A Study on Compressive Behavior of Ternary Blended Concrete Incorporating Alccofine, Materials Today: Proceedings, 2018, ISSN 2214-7853, https://doi.org/10.1016/j.matpr.2018.02.102.

[2] Sankar, B., & Ramadoss, P. (2022). Experimental and Statistical Investigations on Alccofine Based Ternary Blended High-performance Concrete. International Journal of Engineering, 35(8), 1629-1640. https://doi: 10.5829/ije.2022.35.08b.19

[3] Ramya, D., Lalitha, G. (2021). Optimum Utilization of Alccofine in Sustainable Ternary Blended Concrete. In: Biswas, S., Metya, S., Kumar, S., Samui, P. (eds) Advances in Sustainable Construction Materials. Lecture Notes in Civil Engineering, vol 124. Springer, Singapore. https://doi.org/10.1007/978-981-33-4590-4_47.

[4] Swetha, Suguna K. , Raghunath P. N. (2022). Strength and Durability Studies on Steel Fiber Reinforced Ternary Blended Concrete Containing Nano Silica and Zeolite. Civil Engineering and Architecture, 10(6), 2306 - 2321. DOI: 10.13189/cea.2022.100606.

[5] Ahmadi, Babak & Sobhani, Jafar & Shekarchi, Mohammad & Najimi, Meysam. (2014). Transport properties of ternary concrete mixtures containing natural zeolite with silica fume or fly ash. Magazine of Concrete Research. 66. 150-158. 10.1680/macr.13.00224.
[6] H Donza, O Cabrera, EF Irassar, High-strength concrete with different fine aggregate, Cement and Concrete Research, 2002, https://doi.org/10.1016/S0008-8846(02)00860-8.
[7] Madandoust, R., Ranjbar, M. M., & Mousavi, S. Combined Effect of Silica Fume and Zeolite on The Fresh and Hardened Properties of Self-Compacted Concrete. Concrete Research, 6(1), 53-71, (2013).
[8] Syed Afzal Basha, A. Vinod Kumar, S. Akhil Tej, C.G. Mohan Babu, Evaluation of zeolite as supplementary cementing material, Materials Today: Proceedings, 2023, https://doi.org/10.1016/j.matpr.2023.02.318.
[9] Zhiming Ma, Jiaxin Shen, Changqing Wang, Huixia Wu, Characterization of sustainable mortar containing high-quality recycled manufactured sand crushed from recycled coarse aggregate, Cement and Concrete Composites, 132, 2022, https://doi.org/10.1016/j.cemconcomp.2022.104629.
[10] Peruri Rahul, Durga Prasad Ravella, P.V. Chandra Sekhara Rao, Durability assessment of Self-Curing high performance concretes containing zeolite admixture, Materials Today: Proceedings, 60(1), 2022, https://doi.org/10.1016/j.matpr.2022.01.352.
[11] Mola-Abasi, H., Kordtabar, B. & Kordnaeij, A. Effect of Natural Zeolite and Cement Additive on the Strength of Sand. Geotech Geol Eng 34, 1539–1551 (2016). https://doi.org/10.1007/s10706-016-0060-4.
[12] Pandit, R., Duggal, P., Tomar, R.K. (2022). Study of Variation in Alccofine on Concrete Strength. In: Guo, H., Ren, H., Wang, V., Chekole, E.G., Lakshmanan, U. (eds) IRC-SET 2021. Springer, Singapore. https://doi.org/10.1007/978-981-16-9869-9_23.
[13] IS 456-2000, Bur. of Indian Stand., New Delhi, Plain and Reinforced Concrete-Code of Practice.
[14] IS 10262-2009, Bur. of Indian Stand., New Delhi, Recommended Guidelines for Concrete Mix Design.
[15] S 383-1970, Specification for Coarse and Fine Aggregates from Natural Sources for Concrete. Methods of Test for Aggregates for Concrete.
[16] IS 2386-1963, Bureau of Indian standards, New Delhi.
[17] ASTM C143/C143M-12, Standard Test Method for Slump of Hydraulic-Cement Concrete.
[18] S. Prasanth, S. Prakash Chandar; A critical review on the effects of m-sand as a fine aggregate in high strength concrete. AIP Conf. Proc. 30 September 2022; 2515 (1): 020007. https://doi.org/10.1063/5.0103028.
[19] C.V. Kumar, M.A. Parvez, T. Srinivas, Strength Behaviour of Blended Self Cured Concrete made with Cement by partial replacement of Supplementary Cementitious Materials (SCM's), E3S Web Conf. 184 (2020) 01100. https://doi.org/10.1051/e3sconf/202018401100.
[20] C.V. Kumar, P. Manisha, P. Sadula, Behavior of Monotonic Loading for Glass Fibre based High Performance Concrete in External Beam-Column Joint using ANSYS. Analysis, E3S Web Conf. 184 (2020) 01088. https://doi.org/10.1051/e3sconf/202018401088.
[21] IS 4031 - 3 (1988) (Reaffirmed 2005), Methods of Physical Tests for Hydraulic Cement, Part 3, Bur. Indian Stand. New Delhi. (2005) 1–10.
[22] IS 12269, IS (Indian Standard). 2013. Ordinary Portland Cement, 53 Grade — Specification. IS 12269-13, Bur. Indian Stand. 6 (1992)
[23] Foong, K.Y. and Alengaram, Ubagaram Johnson and Jumaat, Mohd Zamin and Mo, K.H. (2015) Enhancement of the mechanical properties of lightweight oil palm shell concrete using rice husk ash and manufactured sand. Journal of Zhejiang University Science A, 16 (1). pp. 59-69. ISSN 1673-565X, DOI https://doi.org/10.1631/jzus.A1400175.
[24] Repati Mohan Babu, G.V.V. Satyanarayana, Vivek Kumar C, Structural behaviour of triple blended high-performance concrete, E3S Web Conf. 391 01193 (2023), DOI: 10.1051/e3sconf/202339101193.

[25] C. Vivek Kumar, M. Palanisamy, C. Balakrishna, S. Pooja Sri Reddy, S. Robert Ravi, Evaluation of strength characteristics and identifying the optimum dosage with the impact of partial replacement of recycled fine and coarse aggregate from construction and demolition waste, Materials Today: Proceedings, 66(4), https://doi.org/10.1016/j.matpr.2022.05.265.

[26] Weiguo Shen, Zhenguo Yang, Lianghong Cao, Liu Cao, Yi Liu, Hui Yang, Zili Lu, Jian Bai, Characterization of manufactured sand: Particle shape, surface texture and behavior in concrete, Construction and Building Materials, 114, 2016, https://doi.org/10.1016/j.conbuildmat.2016.03.201.

[27] Kumar, C.V., Sargunan, K., Vasa, J.S.S.K. et al. Applying ANN – PSO algorithm to maximize the compressive strength and split tensile strength of blended self curing concrete on the impact of supplementary cementitious materials. Int J Interact Des Manuf (2022). https://doi.org/10.1007/s12008-022-00907-z.

Journal of Physics: Conference Series

PURPOSE-LED PUBLISHING™

PAPER • **OPEN ACCESS**

Finite element analysis on buckling behaviour of integrated wing spar

To cite this article: E. S. Elumalai *et al* 2024 *J. Phys.: Conf. Ser.* **2837** 012078

View the article online for updates and enhancements.

You may also like

- A dynamic spar numerical model for passive shape change
J P Calogero, M I Frecker, Z Hasnain et al.
- Damage evaluation by a guided wave-hidden Markov model based method
Hanfei Mei, Shenfang Yuan, Lei Qiu et al.
- Finite element analysis of aircraft wing using carbon fiber reinforced polymer and glass fiber reinforced polymer.
Salu Kumar Das and Sandipan Roy

This content was downloaded from IP address 106.0.37.90 on 21/10/2024 at 11:20

Journal of Physics: Conference Series **2837** (2024) 012078 doi:10.1088/1742-6596/2837/1/012078

Finite element analysis on buckling behaviour of integrated wing spar

E. S. Elumalai[1], R. Asokan[1], Adduru Veda Sai Vasanth Naidu[1], K. Arunkumar[2], S. Seralathan[1] *

[1]Department of Aeronautical Engineering, Hindustan Institute of Technology and Science, Chennai 603 103, Tamil Nadu, India.
[2]Department of Aeronautical Engineering, MLR Institute of Technology, Hyderabad, Telangana, India.

*Corresponding Author: siva.seralathan@gmail.com

Abstract. With advancement in manufacturing processes like 3D printing, it is easy to manufacture the components. This study focuses on the numerical simulation of an aircraft wing and spar as an integral component. The study examines the buckling behaviour of the integrated wing spar, a critical load carrying member in the wing. The spar is connected to the wing so that the buckling analysis can be performed on the wing as well. CATIA software is used to design the integrated wing spar model as well as the conventional wing spar model, and ANSYS software is used to perform FEA analysis for both the wing spars. Under different loading circumstances, the structural performance of both the wing spars is compared. Buckling occurs in both the spars. But the stress acting on the conventional spar is 280MPa whereas, the stress acting the integrated wing spar is 348MPa which is comparatively higher by 13.5%. Based on the buckling stress, strain, weight savings and cost, the results reveal that the integrated wing spar design is better than the conventional wing spar design.

1. Introduction

The design of aircraft must consider buckling analysis of a wing spar. Being a crucial part of the aircraft's structural design, the wing spar supports the wings' full weight and transmits aerodynamic forces. Therefore, a detailed buckling analysis of the wing spar is required to ensure the aircraft's safety and structural integrity. Finite element analysis (FEA) or analytical methods can be employed to perform buckling analysis. Analytical techniques offer a quick and simple way to assess the buckling capability of the wing spar, whereas FEA enables more precise, accurate and thorough details with simulations. Engineers may choose the best design parameters, such as thickness of the spar, the type of materials, etc. and use the outcomes of these analysis to get critical insights into the buckling performance of the wing spar. By this approach, the aircraft's safety and dependability can be improved further. Moreover, for an aircraft, weight is always a critical problem. Integrated wing spar is effective as it is light in weight with high strength in construction. With the advancements in manufacturing processes such as additive manufacturing, renewed interest has been created among researchers as well as manufacturers in integrating metallic structures for aircraft applications [1]. Various additive manufacturing techniques such as stereolithography, fused deposition modelling, laminated object manufacturing, selective laser melting, electron beam melting, laser engineered net shaping and binder jetting are available at present and the proposed integrated wing spar can be used

Content from this work may be used under the terms of the Creative Commons Attribution 4.0 licence. Any further distribution of this work must maintain attribution to the author(s) and the title of the work, journal citation and DOI.
Published under licence by IOP Publishing Ltd

to manufacture them. Using digital twin technologies, the computer aided design and drawings of the integrated wing spar created using CATIA software can be sliced and converted into a layer-by-layer code (G Code). Then, the 3D printing machine produces the integrated wing spar with the chosen materials using the appropriate additive manufacturing technology.

Mutturaj Girennavar *et al.* [2] performed experimental investigations on the optimum weight of wing spar and analyzed its characteristics. As stated by them, an aircraft was a complex mechanical structure with the ability to fly. It was surprisingly designed with a straightforward "strength-of-material" approach, with two major components, the fuselage, and the wing. For design optimization, stress analysis iterations were performed using a finite element approach and linear static analysis, with lightening cut-outs to optimize weight. To validate the design and stress analysis results, static testing was performed on a scaled-down model of the spar. The analysis concluded that as the load on the spar increased, the deflection in the spar increased. Buckling is an instability phenomenon that affects slender structures, and the wing box structure was made of several composite materials. Advanced wings were made of thin-walled structures with buckling top skins due to compressive stress. The finite element analysis of the buckling strength of Al 2024T3, GFRP, and sandwich panels were carried out by Karthikeyan *et al.* [3]. The sandwich panel had a higher critical load compared to other panels. The FEA results matched the theoretical outcomes, with the magnitude of strain increasing with a small increase in load. The sandwich material was observed to be harder than the other materials.

Jiayao Zhang and Chiara Bisagni [4] performed analysis on controlling the buckling behavior in composite wing structures in order to enable future morphing applications. Three buckling-driven mechanisms were investigated, involving the use of point, area, and maximum displacement constraints to limit out-of-plane buckling deformation. These mechanisms were studied numerically using a composite plate as well as a simplified thin-walled wing box. The proposed mechanisms showed the potential for the morphing of composite wings by controlled buckling of structural components. Aston and Williams [5] investigated the buckling analysis of multi-spar wing boxes made of composite materials using two different methodologies. When created, the lower bound approach offered a guaranteed lower limit and a high level of accuracy, whereas the repetitive analysis approach was quick, and required little data preparation, but cannot be relied upon to yield a lower bound result. Six variations of laboratory test specimen were used to demonstrate both the procedures, and the findings showed that the lower bound method had an accuracy of 10%. Elangovan *et al.* [6] gave insights about the materials used for the structures of the aircraft. An aircraft was a complex mechanical invention with the ability to fly. Its airframe structures were designed with the strength of materials approach in mind to achieve the lightest possible weight. The aircraft structure was made up of a fuselage and wing, with the wing being primarily responsible for carrying loads when bent. Using CATIA and ANSYS software, the study compared four different wing spar materials namely, aluminum, cobalt, steel, and high alloy steel. The findings revealed that each material behaves differently when subjected to an applied load on its free end.

The effect of random geometric imperfections on the buckling response of I-profile steel beam-column members and portal frame structures was investigated by Vissarion Papadopoulus *et al.* [7]. Monte Carlo simulation and finite element analysis were used to generate and evaluate samples of random imperfect geometries. The results demonstrated the variability of buckling loads under various loading and boundary conditions and provided useful insights into the buckling response of such structures. Luke Lapira *et al.* [8] performed experimental investigations on elastic local buckling formula for thin walled I-section. This study offered formulae for predicting the elastic local buckling stresses with high accuracy of the doubly symmetric thin-walled I-section girders subjected to combined shear and direct stresses. To quantify the relative level of fixity between the lower and upper bounds, an interaction coefficient was introduced. The coefficient was calibrated using FEA. The proposed formulae generated results that were within 5% deviation of the corresponding FEA outcomes. This was a significant improvement over the current methods, which underestimate the full cross-section buckling stress by up to 40%.

Quinn *et al.* stated [9] that plate sub-stiffening was used to improve the structural efficiency of integrally machined aluminum alloy stiffened panels. The experimental investigation along with computational validation of the idea of sub-stiffening was presented. The experimental results revealed that plate sub-stiffening can effectively regulate plate buckling modes and improved the static strength performance of the panel. When compared to an equivalent mass design, the evaluated sub-stiffening design demonstrated a considerable improvement in plate buckling performance of +89%. Numerical simulations showed similar performance improvement (+66%) in larger structures made up of repeated panels. Wang *et al*. [10] investigated the large-section extruded aluminum alloy columns of I-section and rectangular hollow section (RHS). All specimens failed in flexural buckling, indicating that the design stability resistance recommended by Euro code 9 and Chinese code GB 50429 was conservative. To improve design accuracy, a parametric analysis was performed, and a new design method was proposed. Schadt *et al.* performed [11] experimentally studied the nonlinear bending compliance of thin ply composite beams by local compression flange bending. Passive span wise bending shape adjustment had the potential to improve vehicle efficiency and maneuverability with wing-like structures. The in-plane stiffness can be adjusted using compression flange buckling to produce beams with varying pre-buckling and post-buckling bending stiffness. This concept was experimentally validated using a thin-ply laminated composite four-point bending beam, which showed a bending stiffness reduction of more than 41% after the buckling began. This demonstrated the utility of compression flange buckling for non-linear bending compliance.

Based on the review of the literature, it is evident that the conventional wing spars serve only one purpose of providing structural support to the wing. Conventional wing spar manufacturing can be complex and expensive, requiring specialized machinery and processes. The conventional wing spar consists of a lot of pieces fastened or riveted together. But the integrated wing spar can save weight by combining multiple functions into a single component. With the advancements in manufacturing processes like additive manufacturing, it is possible to produce the integrated wing spar. An integrated wing spar can provide better structural performance. Overall, the use of integrated wing spars can lead to a lighter, and more efficient aircraft with increased functionality as well as structural performance with a simpler manufacturing process.

Hence, the purpose of this study is to examine the buckling stress and deformation acting on the integrated wing spar. Since the leading spar takes most of the load acting on the wing, rear spar is not considered here. This study deals with the integration of spar and wing as a single structure and buckling analysis is performed on the proposed integrated wing spar design using ANSYS Software. Simulations are carried out and the buckling strength of conventional wing spar as well as the proposed integrated wing spar is examined.

2. Methodology

The model is created based on the dimensions of a typical commercial aircraft wing and spar [2] and the model is designed using CATIA software. The design involved the integration of several functions into a single structural support. The wingspan of the airfoil is 1067mm and the chosen airfoil is NACA 0014. To make a comparative evaluation, the conventional wing spar design is also made using the CATIA software with same dimensions. The dimensional details for the wing design are given in Table 1.

Table 1. Wing configuration

Content	Value
Wingspan (mm)	1067
Wing thickness (mm)	2.6
Width of wing spars (mm)	175.471
I-section thickness (mm)	2.6
Spar position from leading edge (mm)	245.776

Table 2. Meshing details

Content	Conventional wing spar	Integrated wing spar
Element size	17mm	12mm
Elements	10836	21360
Nodes	11176	21480

Table 3. Material properties specified for the wing spars

Description	Value
Young's modulus (MPa)	73700
Density (kg/m)	2780
Yield strength (MPa)	324
Ultimate strength (MPa)	471
Poisons ratio	0.33

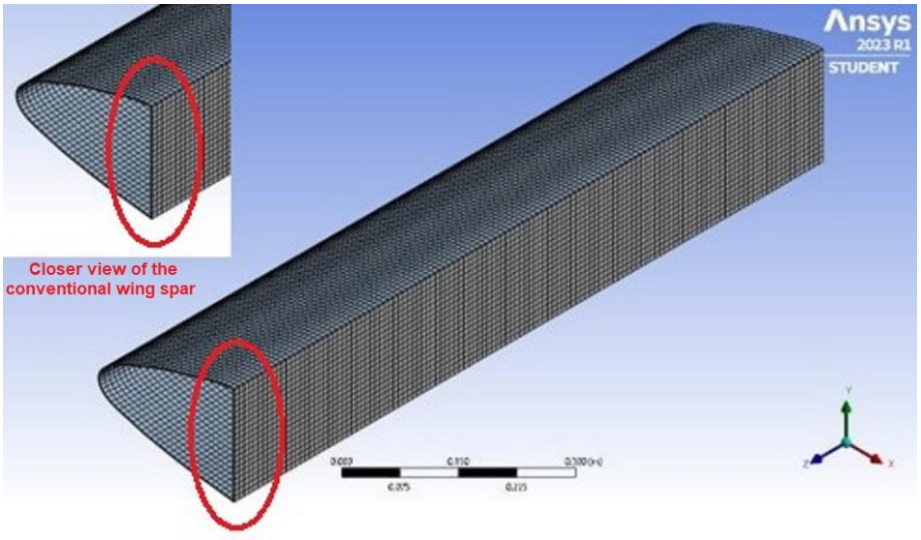

Fig. 1. Meshed model of conventional wing spar

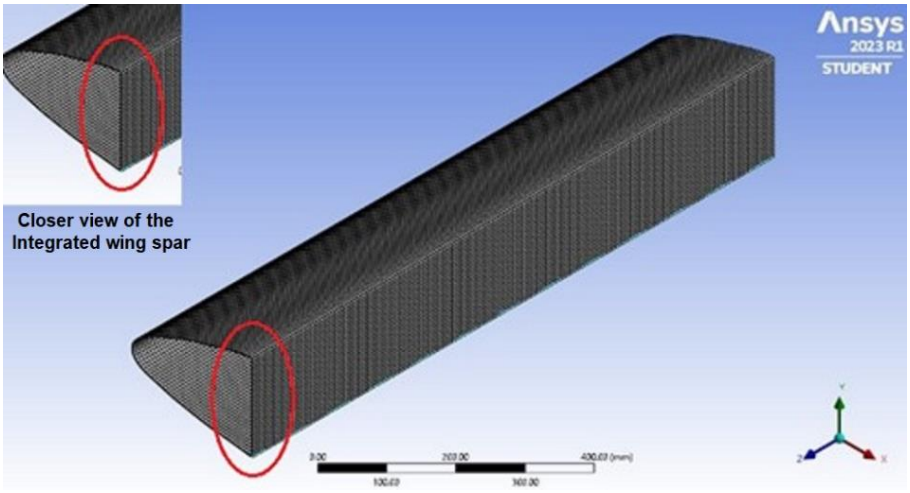

Fig. 2. Meshed model of integrated wing spar

ANSYS software is used to perform structural analysis. The two wing spar designs are evaluated using the finite element modelling (FEM) approach. The material properties used in the analysis are defined based on the findings of Quinn *et al.* [9]. Aluminum alloy is used to model both the proposed integrated wing spar, and the conventional wing spar. For both wing spar designs, the critical buckling load is determined using FEA. The meshing data for the computational domain is given in Table 2. The meshed domains of both conventional as well as integrated wing spars are shown in Figures 1 and 2. The materials properties defined in the analysis for the conventional and integrated wing spars are listed in Table 3.

The analysis is performed by fixing one end of the wing to prevent the translation and rotational motions of the joint and the other end is kept free. The loads are applied as line force at different positions along the chord. Eigen-Buckling analysis is carried out to find out the deformation that occurs in both the wing spars. The results are compared to see which spar design had the best buckling resistance. The results are reliable and accurate due to the use of finite element modelling and accurate material properties. Figure 3 shows the buckling co-efficient with respect to aspect ratio. The governing equation for buckling of panel is given as mentioned in equation (1),

$$\sigma_{cr} = \frac{k\pi^2 E}{12(1-\mu^2)}\left(\frac{t}{w}\right)^2 \qquad \text{--- (1)}$$

where σ_{cr} is the buckling stress of panel, E is the young's modulus in MPa, μ is the Poisson's ratio, t is the thickness of the panel, w is the effective width of the panel and 'k' is the buckling co-efficient which depends on the degree edge support. For the integrated wing spar, it is assumed that both the edges are simply supported. Assuming all the edges are simply supported for the conventional wing spar design, from Figure 3, for a/b = 1067/175.471 = 6.08, the value of 'k' is 4. Similarly, assuming two edges fixed, and two edges as simply supported for integrated wing spar, from Figure 3, for a/b = 1067/175.47 = 6.08, the value of 'k' is 7. Here 'a' is the wingspan in mm and 'b' is the spar width in mm.

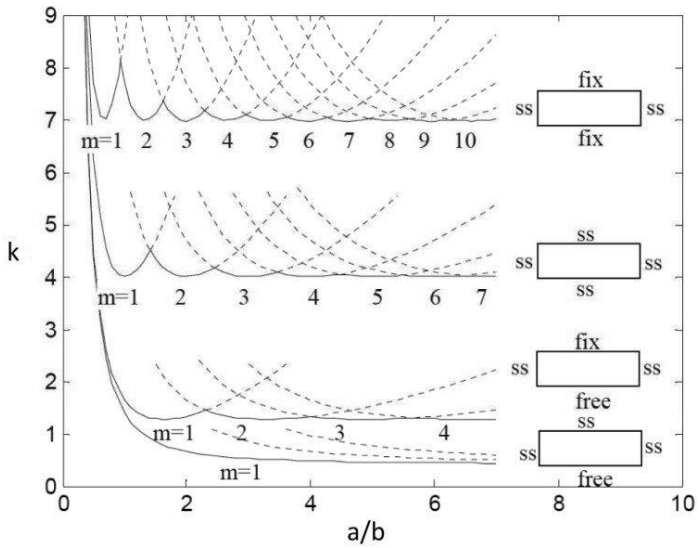

Fig. 3. Buckling co-efficient versus aspect ratio [12]

The effective width is calculated using the equation as given here as,

$$w = \pi t\sqrt{\frac{kE}{12(1-\mu^2)\sigma_{cy}}} \qquad \text{--- (2)}$$

The effective width is found to be 74.54mm for conventional wing spar whereas the effective width for the integrated wing spar is 98.56mm. Using equation (1), the buckling stress for the conventional and integrated wing spars is found to be $(\sigma_{cr})_{con} = 324.01\,MPa$ and $(\sigma_{cr})_{int} = 324.15\,MPa$

respectively. The theoretical results of the buckling stress for conventional as well as integrated wing spars are almost same, and this justifies that the proposed design is good enough to be investigated further by simulations.

3. Results and discussion

Eigen-Buckling analysis is performed for the conventional as well as integrated wing spars and comparative representation of deformation, stress and strain are represented and discussed here. The deformation contours of the conventional as well as integrated wing spars are shown in Figures 4 and 5 respectively. The deformation that occurred in the integral wing spar is almost equal to that of deformation that occurred in the conventional wing spar. As the deformation that occurred in both the wing spars are nearly same, the integrated wing spar can be considered as a better alternative for the conventional wing spar as it can withstand the same load with less stress which leads to better durability and reliability.

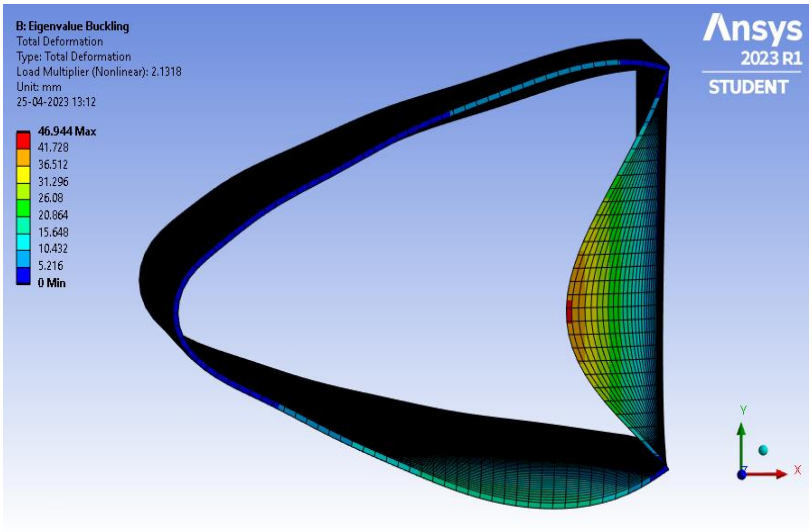

Fig. 4. Deformation contour for conventional wing spar

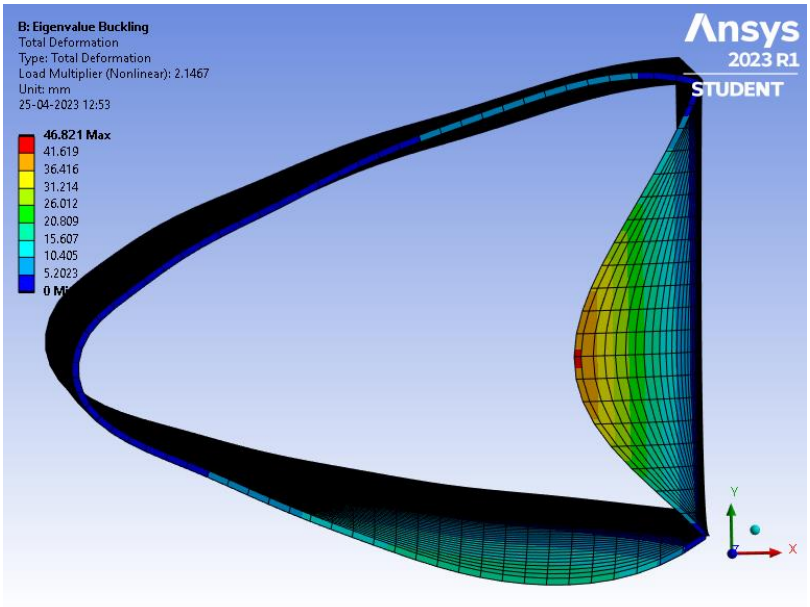

Fig. 5. Deformation contour for integral wing spar

Figure 6 shows the deformation plot for both conventional and integrated wing spars. The maximum deformation for conventional wing spar is 46.944mm and for integrated wing spar, it is 46.821mm, which almost similar same.

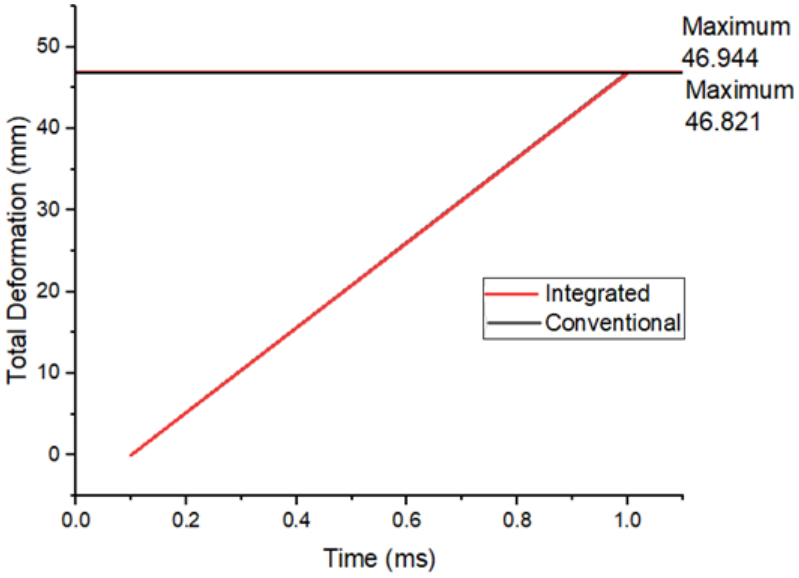

Fig. 6. Total deformation versus time

Figures 7 and 8 show the stress contours for the conventional wing spar and the integrated wing spar which clearly depicts the maximum stress values as 280.24MPa and 384.87MPa respectively. This shows 19% improvement in the integrated structure for bending strength. Figure 9 shows the stress acting on the integrated and conventional wing spars with respect to time. It is evident that the maximum stress acting on the conventional spar is 280MPa whereas the maximum stress acting on the integrated spar is 348MPa which is comparatively higher by 19%. As the stress acting on the integrated wing spar is more, the structural strength of the integrated wing spar is found to be better which helps it to withstand higher loads in comparison with conventional wing spar.

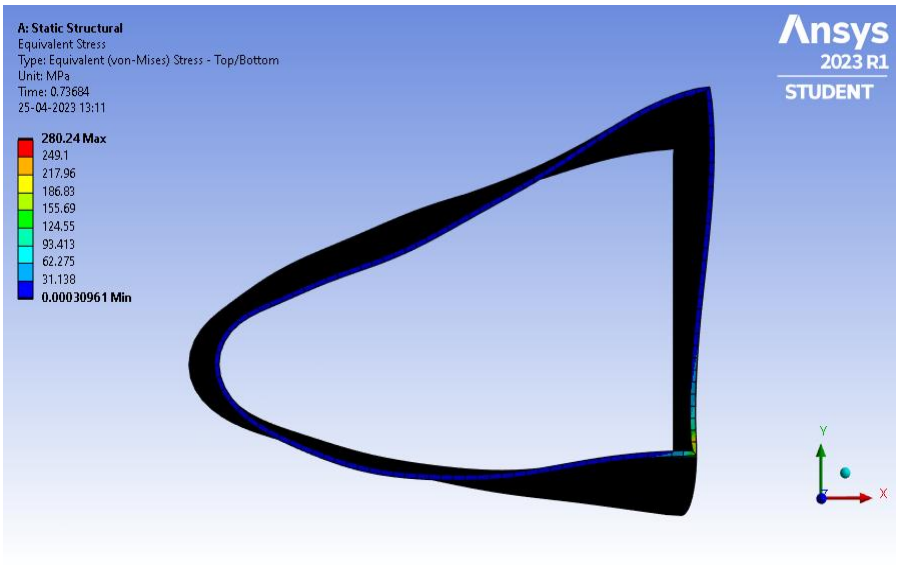

Fig. 7. Stress contour for the conventional wing spar

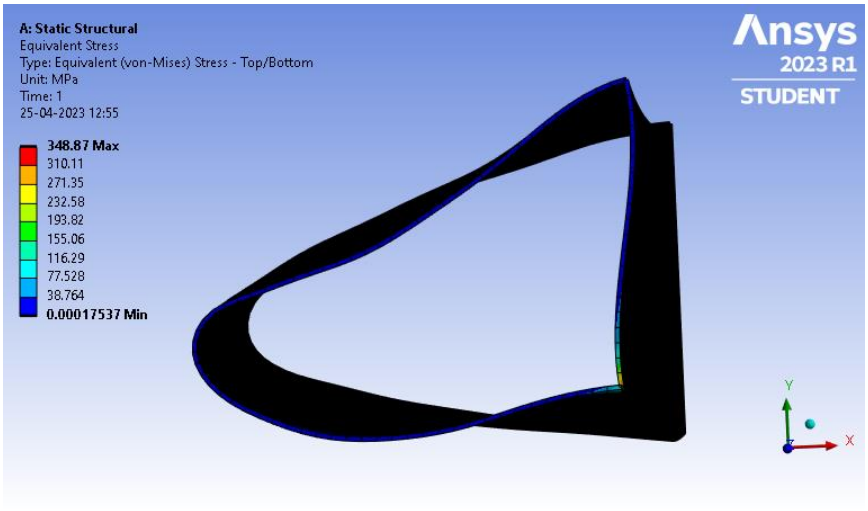

Fig. 8. Stress contour for the integral wing spar

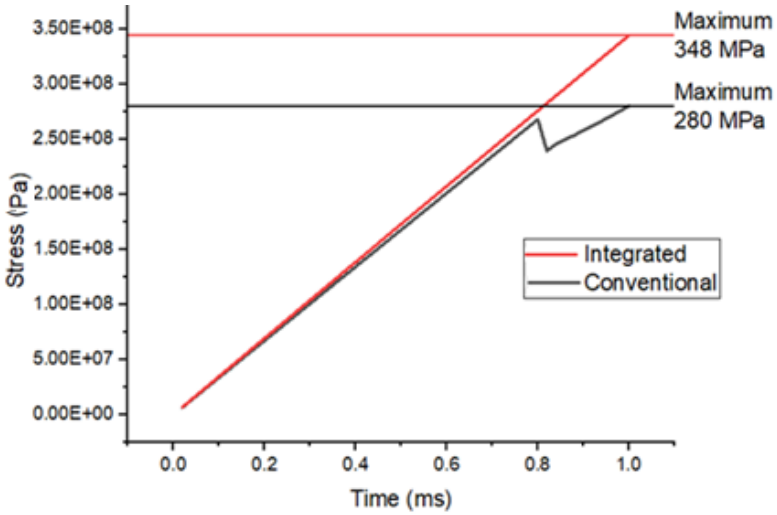

Fig. 9. Stress versus time

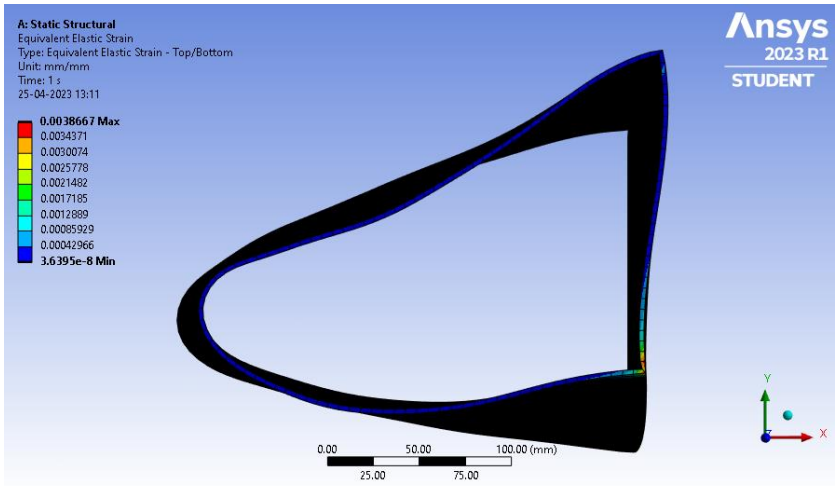

Fig. 10. Strain contour for conventional wing spar

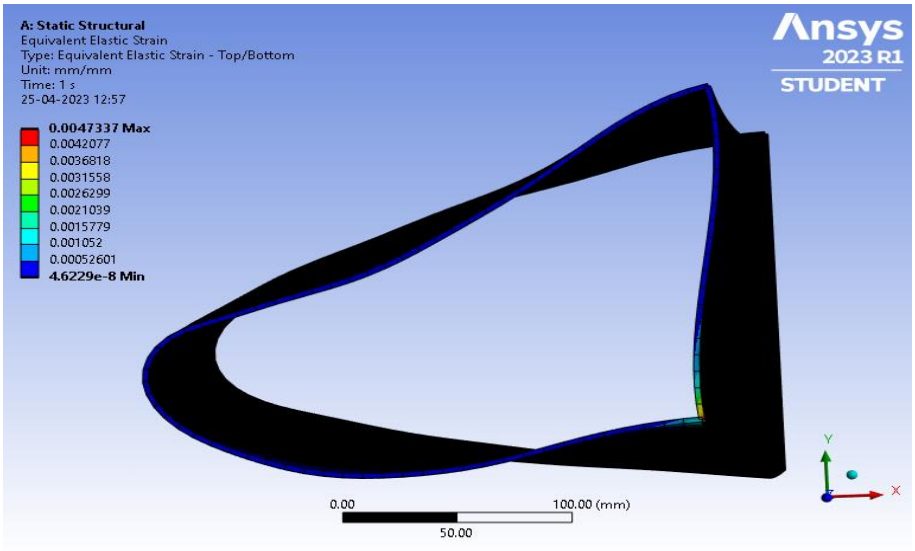

Fig. 11. Strain contour for integrated wing spar

Figures 10 and 11 show the strain contours for both the conventional and integrated wing spars. The contour explains that deformation in conventional spar components at joints is more critical compared to integrated structure.

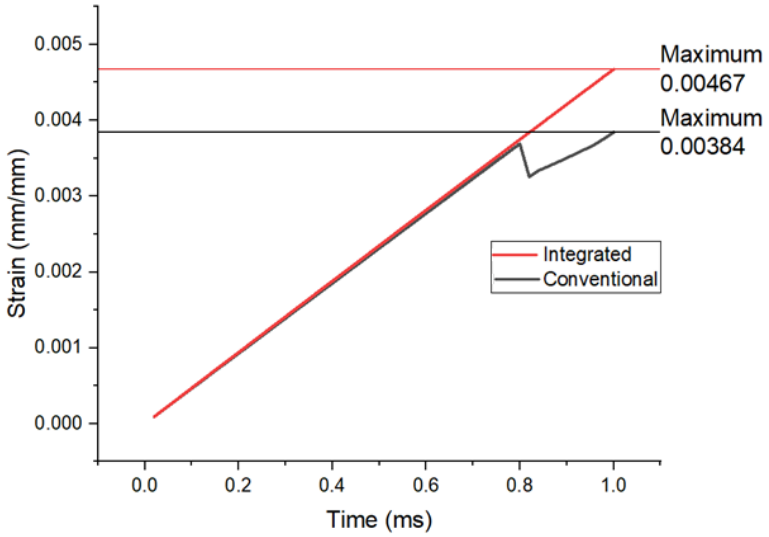

Fig. 12. Strain versus time

Figure 12 gives the information about the strain acting on both the wing spars and depicts the information for variation of equivalent strain with respect to time. As can be seen in Figure 12, the strain acting on the integrated wing spar is 4.7μm/mm whereas, the strain acting on the conventional wing spar is 3.8μm/mm. This clearly shows that the strain acting on the integrated wing spar is less compared to the conventional wing spar which clearly indicates that the proposed integrated wing spar is better suited for aircraft structures.

4. Validation

The data from FEA studies obtained through simulations are compared with the results of the theoretical analysis. Table 4 lists the data from theoretical analysis and FEA analysis. Upon

comparison, a discrepancy of around 13.5% in the buckling strength values is found for the conventional wing spar. The proposed integrated wing spar design has a variation of about 6%. As standard deviation of the values for integrated stiffened panels is less than 7%, it reinforces the outcomes of the simulations carried out in this study.

Table 4. Comparison of numerical and theoretical outcomes

Wing spar type	Buckling strength		Standard deviation
	Theoretical values (MPa)	Numerical values (MPa)	
Conventional	324.01	280	13.5%
Integrated	324.15	348	6%

5. Conclusion

Finite element analysis on the bucking behaviour of integrated wing spar is investigated and the results from this study showed that the integrated wing spar design showed significant improvement over the conventional wing spar design. Based on the investigations, the following points are listed here.

- The deformation of the integrated wing spar is quite like the deformation that occurs in the conventional wing spar. The analysis results showed an increased stress bearing ability of the integrated wing spar.
- The integrated spar design has a 0.2% higher resistance to deformation than the traditional spar design, with a maximum deformation of 46.821mm compared to the conventional spar design's maximum deformation of 46.944mm.
- The stress carrying capacity of the integrated wing spar is more. The buckling strength of the integrated wing spar is 348MPa, which is nearly 19.5% more than the conventional wing spar (buckling strength value of 280MPa).
- The strain on the integrated wing spar is 23.68% less than the strain of the conventional wing spar.

Thus, the integrated wing spar design is found to have better structural strength in terms of stress withstanding ability, improved buckling resistance and can withstand higher loads than the conventional wing spar. The proposed integrated wing spar will reduce the weight, cost, and improve ease in manufacturing the wing spar for an aircraft.

References

[1] Naing Lin Aung, Oleg Tatarnikov and Phyo Wai Aung, Optimization of composite wing spars for an unmanned aerial vehicle, IOP Conf. Series: Materials Science and Engineering, 971, 052076, 2020, 7 pages. DOI:10.1088/1757-899X/971/5/052076

[2] Mutturaj Girennavar, Soumya H V, Subodh H M. (2017), “Design, Analysis and Testing of Wing Spar for Optimum Weight”, International Journal of Research and Scientific Innovation-IJRSI, vol.4 issue 7, pp.104-112.

[3] R. Karthikeyan, R. Sridhar, P. Raja Sekaran and S. Ganesh Kumar, Hardness and buckling strength of different material panels for a wing box structure with FE analysis, Materials Today: Proceedings, Volume 33, Part 7, 2020, pp. 4509-4514. DOI: https://doi.org/10.1016/j.matpr.2020.08.003.

[4] Jiayao Zhang and Chiara Bisagni, Buckling-driven mechanisms for twisting control in adaptive composite wings, Aerospace Science and Technology, Volume 118, 107006, 2021. DOI: https://doi.org/10.1016/j.ast.2021.107006.

[5] G. Aston and F. W Williams, Simplified methods for the buckling analysis of composite multi-spar wing boxes, Composite Structures, Volume 28, Issue 2, 1994, pp. 215-223. DOI: https://doi.org/10.1016/0263-8223(94)90050-7.

[6] S. Elangovan, C. Sureshkumar and P. Divyabarathi, Design and analysis of aircraft wing spar with different materials using ANSYS, International Journal of Mechanical and Production Engineering Research and Development, Vol. 9, Issue 3, 2019, pp. 613-618.

[7] Vissarion Papadopoulus, George Soimiris and Manolis Papadrakakis, Buckling analysis of I-section portal frames with stochastic imperfections, Engineering Structures, Volume 47, 2013, pp. 54-66. DOI: https://doi.org/10.1016/j.engstruct.2012.09.009.
[8] Luke Lapira, Leroy Gardner and M. Ahmer Wadee, elastic local buckling formulae for thin-walled I-sections subjected to shear and direct stresses, Thin Walled Structures, Volume 182, Part A, 110150, 2023. DOI: https://doi.org/10.1016/j.tws.2022.110150.
[9] D. Quinn, A. Murphy, W. McEwan and F. Lemaitre, Stiffened panel stability behavior and performance gains with plate prismatic sub-stiffening, Thin-Walled Structures, Volume 47, Issue 12, 2009, pp. 1457-1468, DOI: https://doi.org/10.1016/j.tws.2009.07.004.
[10] Z.X. Wang, Y.Q. Wang, Jeong Sojeong and Y.W. Ouyang, Experimental investigation and parametric analysis on overall buckling behavior of large-section aluminum alloy columns under axial compression, Thin Walled Structures, Volume 122, 2018, pp. 585-596, DOI: https://doi.org/10.1016/j.tws.2017.11.003.
[11] F. Schadt, M. Reuppel, C. Brauner, Y. Courvoisier, K. Masania and C. Dransfeld, Non-linear bending compliance of thin ply composite beams by local compression flange buckling", Composite Structures, Volume 239, 111995, 2020. DOI: https://doi.org/10.1016/j.compstruct.2020.111995.
[12] Structural stability research council, 2009, Chapter 4: Plates, USA.

Green Energy Storage Solutions: A Research

Kambhampati Saritha[1], *Sanjeev* Sharma[2*], *Amit* Dutt[3], *Anurag* Shrivastava[4], *A*. Kakoli Rao[5], *Ameer* Haider Jawad[6], *A* Saikumar[7]

[1]Department of AI&ML, GRIET, Bachupally, Hyderabad, Telangana, India.
[2]Department of Electronics and Communication Engineering, New Horizon College of Engineering, Bangalore, Karnataka, India.
[3]Lovely Professional University, Phagwara, Punjab, India.
[4]Saveetha School of Engineering, Saveetha Institute of Medical and Technical Sciences, Chennai, Tamilnadu, India.
[5]Lloyd Institute of Engineering & Technology, Knowledge Park II, Greater Noida, Uttar Pradesh, India.
[6]Department of Anesthesia Techniques College of Medical Technology, The Islamic University, Najaf, Iraq
[7]Department of Aeronautical Engineering, MLR Institute of Technology, Hyderabad, Telangana, India-500083

Abstract. One of the key elements of decarbonizing global energy networks and integrating renewable energy sources is green energy storage technology. Energy Storage Systems (ESS), which store surplus produced electricity and make it available on demand, are essential for reducing fluctuations. Electromechanical, electromagnetic, thermodynamic, chemical and hybrid approaches have all been used in the development of energy storage technologies. A comprehensive list of current papers in the literature section is compiled to illustrate the range of advancements in this field. This paper reviews green energy storage systems, focusing on their primary uses. Power utilities will benefit from this thorough analysis of energy storage systems; the researchers choose the finest and newest energy storage technology based on its practicality and affordability. These days, several nations use energy storage systems to plan for future energy needs. Variations in solar radiation cause a solar photovoltaic generator to overproduce electricity. The implementation of a hybrid energy storage system would help to increase the reliability of solar-powered power generation. The microgrid is a crucial component of the smart grid network for solar installations. This study looks at the microgrid's energy storage system for photovoltaic systems. The topologies and storage system configurations of the microgrid are analyzed together with power electronic interference, control systems, and optimization of the energy storage system and renewable sources. a general technique for sizing the HESS of PV systems using design space as well as pinch analysis. HESS scales that link generator ratings to storage capacity are developed in the proper sizes by using pinch analysis to load and resources data.

* Corresponding author: Sharma_sanjeev22@gmail.com

© The Authors, published by EDP Sciences. This is an open access article distributed under the terms of the Creative Commons Attribution License 4.0 (https://creativecommons.org/licenses/by/4.0/).

Keyword-: Renewable Energy Sources; Power fluctuation; Energy Storage Systems; Selection Criteria.

1 Introduction

Energy may be moved between a source (a generator) and a device made specifically for its usage using electricity, which is the flow of electrons in conductive materials [1]. Light, heat, cold, and driving forces may all be produced with ease using electricity, which is unique in that it can provide a wide range of services through a variety of technological instruments [2]. Electricity is a so-called "Secondary" kind of energy, meaning that it results from the transformation of primary points and is not present in a useful form in its natural condition. The latter can come from nuclear, renewable energy sources (such as solar radiation, wind, the water cycle, biomass, etc.) or fossil fuels (oil, gas and coal) [3].

An alternative to the majority of the present energy plans is to generate power using renewable energies. Contrary to fossil fuels, electricity is a finite resource that must be transformed into another energy source in order to be utilized again. Despite the fact that there are many different ways to store energy, there are just not enough of them to supply the world's expanding need for power. This presents a major obstacle for industrial expansion, research, and innovation. Numerous, diverse, and productive investigations have been conducted in this area [4]. The majority of fundamental energies—coal, oil, and gas—are readily stored. On the other hand, storing a lot of electricity means first converting it into another type of storable energy (such thermal, chemical, kinetic, or potential energy) and then restoring it to use.

It is worth mentioning that the evolution of the world's energy situation is described by the following important discoveries: The ability of this energy vector to reduce the general use of fossil fuels, i.e. coal and oil, as well as its user-friendliness and flexibility. Will lead to a strong increase in the use of electricity in the following decades. The share of renewable energy forms in electricity production is rapidly increasing in order to achieve the goals of reducing emissions of greenhouse gases, especially water vapor (H2O), carbon dioxide (CO2), methane (CH4), nitrous oxide (or N2O) and ozone (O3), whose increased concentration in the planet's atmosphere is the main cause of global warming.

These batteries have several advantages over other mobility solutions, which explains part of their popularity. The development of efficient electrochemical generators is therefore particularly important for portable applications (computers, mobile phones, tools, etc.) due to the growing popularity of hybrid and all-electric vehicles and the electrification of vehicle functions. Airplanes This is especially true for the transport sector. But recyclability – the ability of these energy storage devices to store and release energy reversibly over several hundred cycles – means that mobility is not the main advantage. Due to threadability and more than 97% energy efficiency, the batteries are particularly attractive for stationary applications such as storing electricity produced from renewable main sources to balance supply and demand in local electricity networks (depending on the size of the building or area).

To ensure the reliability and efficiency of power grids for large-scale electric vehicle (EV) fleets, a coordinated and efficient charging mechanism must be introduced [5]. In addition, the use of electric vehicles (EV) and renewable energy sources is a practical way to reduce the use of fossil fuels and their environmental damage. It is easy to imagine the day when all cars will be electric, as more and more car manufacturers create and sell electric car models [6]. But the range of electric cars, based largely on the size of their batteries, determines their feasibility. Compact and light, fast and often chargeable, and efficient enough to transport a person to the intended destination are all the requirements of electric car batteries [7].

Lithium-ion batteries are widely used in modern smart vehicles. Lithium cobalt oxide (LCO), the most energy-dense type of lithium chemistry, is commonly used in electric vehicles.
This work, investigated several aspects related to energy storage. The first section outlines the main issues and objectives related to energy storage. In the second section of this paper, will go over the several approaches that are currently being used to store electrical energy as well as the standards that have been used to determine which approaches are best.

2 Solar Energy

One of the sustainable sources of energy available everywhere is solar energy. Solar energy applications have been introduced in the past, including drying, humidification, housing, desalination, transportation and solar energy. Many studies have been conducted in the field addressing some of these advances and applications.CSP (Concentrating solar-thermal power) is a promising method for producing heat and electricity. Large sums of money have been invested in the development of these technologies all around the world.
Numerous commercial systems have been implemented since 2005. But we don't have the experience needed to turn CSP into a stable, affordable power source. Figure 1 demonstrates two types of solar collectors: linear focusing, which depends on the focal length of their object (parabolic bottom collector and linear Fresnel reflectors), and point concentrating to the point (solar heating towers and parabolic troughs).

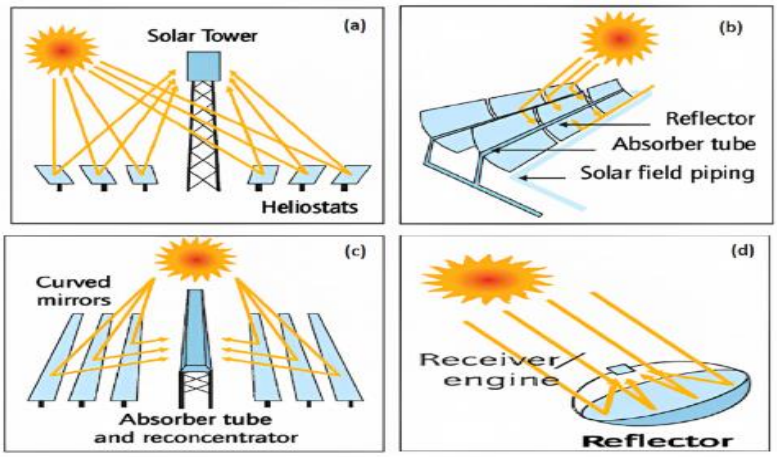

Fig. 1: CSP Technologies

Numerous investigations and analyses of extensive CSP have been carried out. Ahmadiet al.'s study [1] estimated the cost of installing CSP power systems. CSP power facilities required a larger initial investment than photovoltaic (PV) installations.Nevertheless, CSP plants' financial advantages surpassed those of PV power plants. Desideri et al.'s study [2] looked at how different technologies affected the environment. Investigations were also conducted on the environmental impacts of building, commissioning, running, and decommissioning PV and CSP plants. Compared to CSP installations, the PV system assembly had a larger environmental effect. This motivates people to study more about the CSP's historical benefits and present conditions.
Gamarra et al. [3] evaluated the implications of potential CSP project deployments on sustainability while accounting for different CSP systems and circumstances pertaining to component origin. The results showed that the central receivers had less adverse environmental effects in terms of carbon dioxide emissions and water consumption and more favorable economic effects in terms of increased added value and employment.

3 Wind Energy

Mechanical energy can be converted directly into electrical energy or indirectly into electrical energy by converting kinetic energy into electrical energy. As an integral part of all wind energy systems, wind turbines serve as a means of converting the potential energy of the wind into mechanical energy that can be used in a variety of applications by converting the wind's potential energy into mechanical energy. A wind turbine was built at the beginning of the twentieth century as a method of generating electricity by using wind power. While wind turbine technology has been slow to develop, there have been significant advancements in the design of wind turbines in the past few years. Thanks to modern technological development and the improvement of the turbine and its components, the production and efficiency of the produced electricity has improved significantly. In addition, the design of senile turbines allowed the development of certain generators and the use of power electronics. The tower, blades and hood of a wind turbine, which contain the generator, gearbox and control system, are its central components. The wind pushes the wing forward, just as an airplane wing lifts an airplane.The turbine is harnessed to power a generator located inside the hood through an opening in the drive shaft. After being converted into electrical energy by the generator, the kinetic energy is fed back to the transformer. Figure 2 illustrates the two primary wind turbine types currently employed, specifically the horizontal axis (HAWT) and vertical axes ("VAWTS").
HAWTs are the most efficient and effective wind turbines due to their greater efficiency and effectiveness. The close proximity of VAWTs to the ground reduces their exposure to wind, which decreases their power. A VAWT also needs more materials to produce the same amount of power as a HAWT and therefore, is more expensive than a HAWT since VAWTs are larger in size and require more material to produce the same amount of power.

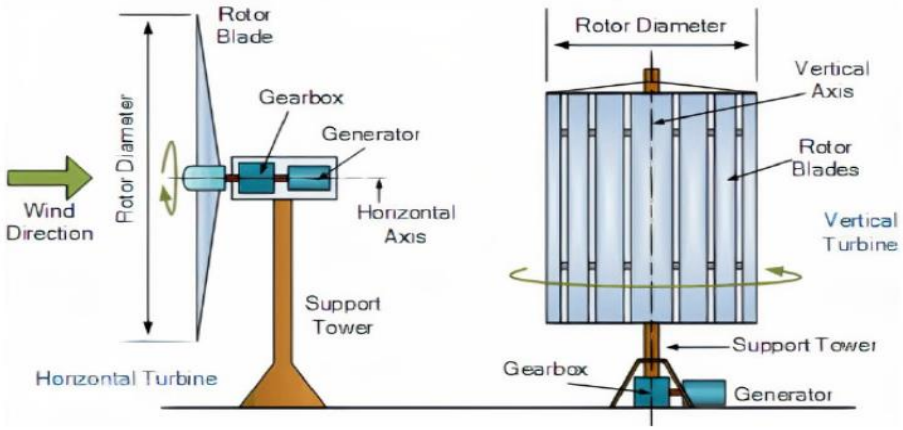

Fig. 2: Two types of wind turbine: VAWT and HAWT.

Wind turbines work on a basic rule: the wind turns the edges, which causes the shaft joined to the generator to turn. There is a gearbox that connects the turbine shaft to the generator shaft with a rotational speed of 1200-1500 revolutions per minute, which significantly increases the turbine shaft's rotational speed by 30-60 revolutions per minute. This causes the copper coil of the magnet containing the generator to rotate. Power is generated when the electrons inside the wire are energized by the relevant magnet. The regulation performance is proportional to the number of copper windings and the rotation speed of the shaft in the attractive field. Bladeless wind turbines (Vortex) are another cutting-edge specialized advancement that points to illuminate the issues of turning wind turbines such as

coordinations, aesthetics, support, damping, clamor and impacts on fowls and the environment.

4 Biomass

Among the most readily available energy sources, biomass may be utilized for a variety of purposes, from direct fuel cell use to traditional burning to generating electricity. Fuel burning is a typical approach, however it is not the most effective way to extract the energy value found in different biomass resources. Biofuel production from biomass, such as biodiesel and biochar, is a promising technique with potential uses. The biomass energy resources are displayed in Figure 3. From this vantage point, Han et al.'s study [17] employed a hydrothermal treatment to examine the impact of acid pretreatment of maize straw on the production of biochar.

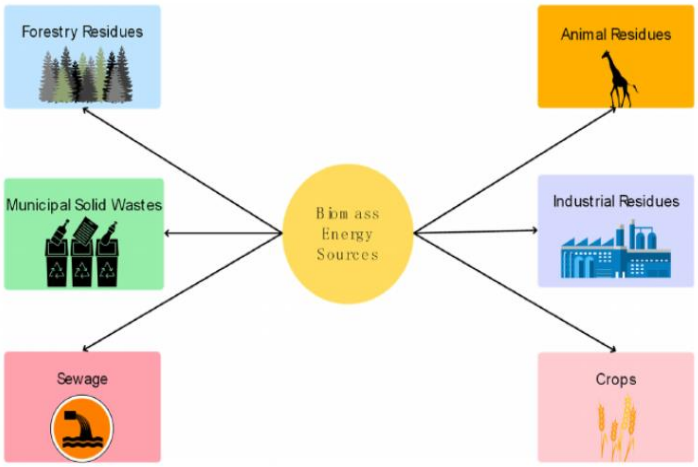

Fig. 3: Different sources of Biomass energy.

The high viscosity of bio-oil obtained through rapid pyrolysis makes it difficult to use. Therefore, Choi et al. [18] created a 35 kW pilot burner and equipped it with an air cleaning jet nozzle. The downward fuel injection system is designed to improve fuel injector performance and maintain a more consistent flame. There was a ratio of 9:1 for the quantity of bio-crude oil and ethanol. This improved the stability of combustion by giving an eddy current to that air. The increased swirl of combustion air reduced gas emissions and improved flame stability.

5 Renewable Energy Sources - A Hybrid Approach

It is generally accepted that renewable energy sources, like wind and solar power, only sometimes produce electricity, while being sustainable and having little to no adverse effects on the environment. Therefore, it is necessary to integrate energy storage systems with renewable sources of energy. Several renewable energy sources such as wind, solar, and biogas can sometimes be coupled with one or more additional energy storage devices, as seen in Figure 4. There is a primary goal of these integrations to provide a constant supply of energy throughout the day at a low cost to the user. In recent years, researchers have been

studying the fusion of different types of renewable energy systems so as to be able to produce more energy at lower costs and without emitting any carbon dioxide.

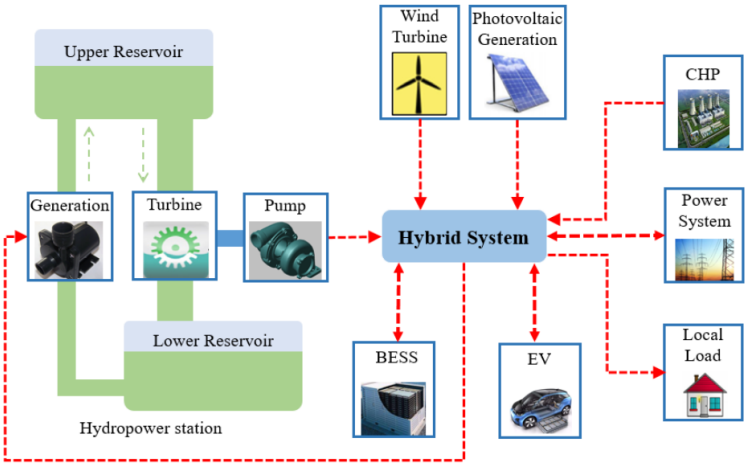

Figure 4: Power plant schematic with a combination of wind, PV, and thermal energy.

Using a computational design technique, Kim et al. [19] calculated the ratios of national electric, solar, and fuel cell systems. According to the study, the optimal energy ratio for fuel cells compared to solar cells falls between 0.46 and 0.54. Another optimization technique proposed is called DEAS, which stands for "Univariated Dynamic Search Encoding Algorithm".

5 Methods and Results

Micro-grids with renewable energy systems are connected by DC buses and Power Electronic Converters (PECs). The load and power flow are controlled by the ESS [16]. HESS is a combination of an ultracapacitor and a battery. The PV panel and microgrid are connected by the voltage controller. Figure 1 depicts the microgrid system's layout.
The PV system's output power:

$$P_{pv} = V_{pv} \times I_{pv}{}', \\ P_b = V_b \times I_b{}': \quad (1)$$

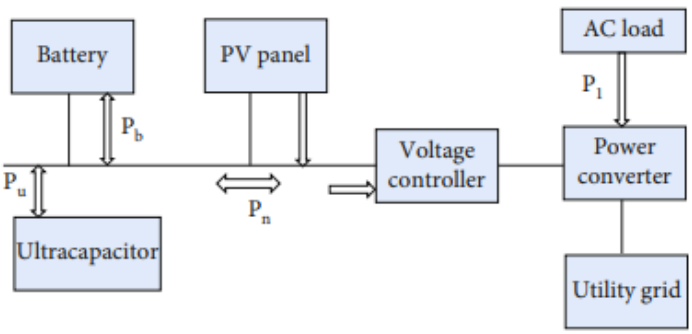

Fig. 5. Ultracapacitor's output power.

This shows the output power and current of the battery which can be seen in Equation (2):

$$P_c = V_c \times I_c\text{':} \quad (2)$$

This Fig. 5 shows the ultracapacitor's output power. Pl is for the power coming from the load, while Pu stands for the power that is transferred via the utility grid. In the energy storage system, the battery and ultracapacitor are used since one part is insufficient to conduct the changing power. The microgrid takes up minimal room and reduces the line's resistance.

6.1 Hybrid Energy Storage Topologies

It is possible to connect HESS and MG using several topologies. There are several topologies that may be utilized to combine HPS and HES. Power converter topologies come in three varieties: semiactive, active, and passive. A passive topology, which is an effective, straightforward, and reasonably priced design, makes it simple to join two storages with the same voltage. Since the ultimate voltage of the capacity gadgets is unregulated, the inner resistances and voltage-current characteristics primarily control the control dispersion between the HPS and HES gadgets. Hence, HPS acts as a moo pass channel for HESS and has exceptionally small vitality [18]. In a semi-active topology, the control converter of one capacity framework is found at its terminal and the other capacity framework is associated specifically to the DC transport. The plan offers way better maneuverability and transmission capability, in spite of the fact that the expansion of a transformer increments the establishment range and costs. The scope of HESS is amplified by extra transformers in this engineering. Two or more vitality capacity gadgets freely associated to the capacity framework through control converters include dynamic HESS topologies. While the system's expenses, complexity, and losses increase, there are certain advantages to this kind of topology. This configuration has the advantage of allowing for active management of all storage capacities [19].

6.2 Energy Storage System Configuration.

An ESS is necessary for the effective operation of an MG. Dispersed sources like as wind turbines and solar panels can be dispatched by the consumer. It makes up the majority of the contribution to balancing power demand, together with generation sources. It is possible to use the power that has been gathered to supply electricity when demand is high. The cost and complexity of producing and operating the energy storage system (ESS) increase with increased energy storage capacity. Thus, flexible and effective power regulation may be achieved by utilizing distributed and small-scale energy storage.

In the distributed ESS arrangement, a DER with several interfaces is connected to the ESS unit. For solar PV, the DC interface is necessary. Generally speaking, a DC chopper is less costly and simpler to operate than a DC converter. The cost of electrical interference is increased, and efficiency is increased, when the grid is connected to DER and ESS. These systems are often simple since they deal with only one type of source. Power lines are designed to receive electricity from renewable natural resources before storage, which helps balance energy flows that are concentrated on the line and delays line construction. This is advantageous. Losses occur during the recording process, although the DER and ESS connections of the power electronics can be connected independently of each other, and both the connections and line resistances are connected to both devices. The future holds the possibility of MG - a combination of decentralized and centralized ESS.

6.3 Power Electronic Interface of Energy Storage System

Figure 2 depicts the energy storage system's power interface. The ESS interface works continuously to keep the MG running for long periods of time, unlike traditional converters that only work when the main source is available. Therefore reliability and efficiency should be prioritized when choosing converter topologies. The three most common MG types are high-frequency, line-frequency, and DC MG, and each requires a different strategy for implementing ESS. Since ESSs can be converted to DC or have a DC interface, they are all considered DC sources for simplicity. DERs and ESS can be connected to the same DC bus using different DC converters. Using a combined multi-port converter ensures low cost, high efficiency and reliability compared to the original single converter system. One multi-port transformer topology that can be used in a high-voltage ESS is the buck-boost transformer; on the other hand, a boost converter can be used in a low voltage ESS. However, expanding the system is difficult because it is built on a unique combination of common components, and adding new sources would require rebuilding the system.

6.4 Hybrid Energy Storage System

In HESS applications, choosing the appropriate storage capacity is one of the biggest obstacles. Numerous methods for calculating storage capacity have been offered. While some methods are designed to evaluate a technology's HESS capacity, others may be used to size various storage systems regardless of technology. Examined are battery size techniques and how they are used in different RESs. Throughout the HESS sizing process, consideration should be given to the system's total cost and dependability. The inability of renewable energy sources to be stored for later use, in contrast to conventional energy sources, is their biggest disadvantage.

Therefore, it's imperative to use them for as much energy as possible while they're still available. Furthermore, it is not possible to ensure that they will always be consistent and focused because they rely on the local climate. They are hence unpredictable and erratic. Because solar behavior is so unpredictable, solar-powered energy is especially vulnerable to harmonic distortions and related errors, which might negatively impact system performance. At two power levels of 3500 kW and 10000 kW, a system's efficiency across two states of charge (SOC), measured in percentage. The SOC percentages vary from 26% all the way up to 96%. A three kilowatt system will have an efficiency of around 0.42 to 0.45 at 3500 kW if the SOC increases by 10%. When the load is 10000 kW, the efficiency starts at 0.27 at a SOC of 26%, and as the load rises to 96%, the efficiency increases to 0.55. As a result, the system performs more efficiently at higher states of charge and is especially effective at 10000 kW power levels when the system has been charged at a higher level.

HESS is necessary in these situations to reduce deviations and improve power quality. Other main tasks of the ESS are capacity regulation and provision of support services when necessary. Therefore, they are an important source of energy for the significant spread of renewable energy systems. Acting as a buffer or backup, the HESS can compensate for power imbalances that may occur between generator units and the load. If certain main sections fail, the island microgrid relies on the HESS to maintain a balance of real and reactive power as shown in Fig. 6.

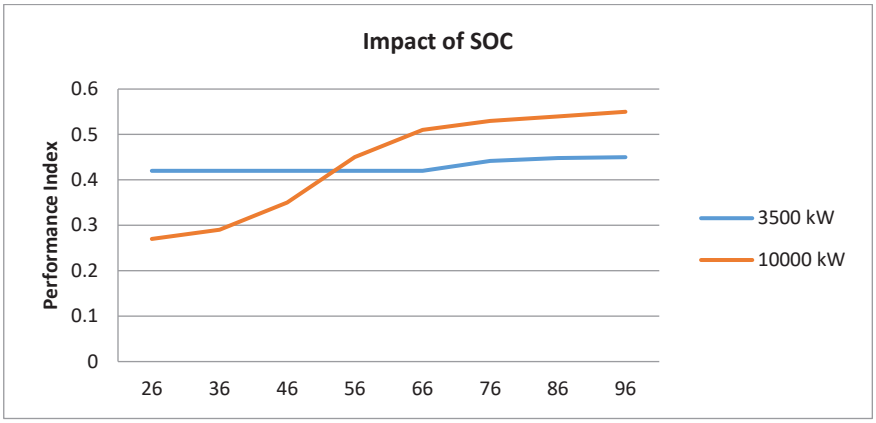

Fig. 6: Compared SOC impact on 3500kW and 10000kW.

Despite the fact that load shedding or additional generating units might be able to help solve the problem, HESS is crucial to quickly overcome the capacity shortage. The MG operates in grid-connected mode when it is connected to the grid in order to maintain the quality of the power and reactive power. Depending on the purpose of the HESS application, several HESS scaling strategies can be used. The compression analysis method is used to determine the capacity size as shown in Fig. 7.

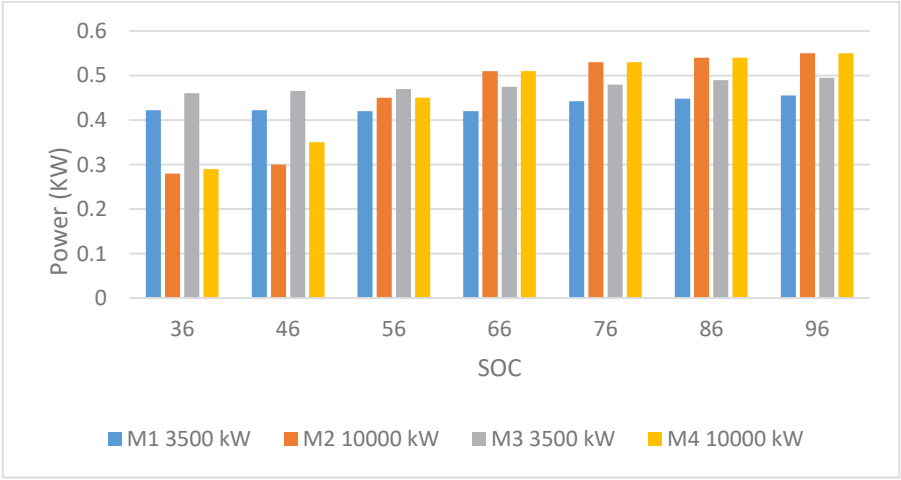

Fig. 7: Comparison of ESS with power interface.

Fig. 7 shows, Figure 7: M1 is characterized with ESS and power interface of 3500 kW, M2 with ESS of 10000 kW, M3 with ESS and power interface of 3500 kW, and M4 with ESS and power interface of 10000 kW.

6.5 Analysing pinch points.

An easy and flexible method for determining which part of a utility heat exchanger network uses the least energy is pinch analysis. This method may be used in a microgrid that is powered by renewable energy sources because it is relatively light. Pinch analysis is employed in HESS implementations. The basis of this technology is the production, loading and unloading times of the energy storage. PAM is used to generate size curves for different

ranges based on resource and load data. The data storage configuration that is practical for a particular timeline is displayed on the generated graph. Pinch analysis works well to save various resources. Separate energy systems are developed using peak analysis methods. Pinch analysis emphasizes the need to set goals before creation.
As a result, it allows analyzing multiple process goals before designing a detailed process in detail. Moreover, pitch analysis gives system architects the ability to manage and visualize decision-making processes in a more organized and systematic manner through the use of schematic tools. To solve common resource conservation problems, different pinch analysis tools can be used to divide streams from different sources into different needs and meet common quality criteria combining streams from different sources.

6.6 A system for controlling the power

The hybrid ESS control strategy is considerably more complex. For self-charging and transmission, the redistribution of the power system and the characteristics of the ESS should be investigated as shown in Fig. 8. For example, where supercapacitors and batteries are used to meet charging demands, ultracapacitors respond faster and provide higher power than batteries, but have a shorter lifetime. As a result, the supercapacitor can handle very high battery currents and decide to gradually discharge or charge the battery. In this case, the battery and supercapacitor must be arranged in pairs.independent circuit.

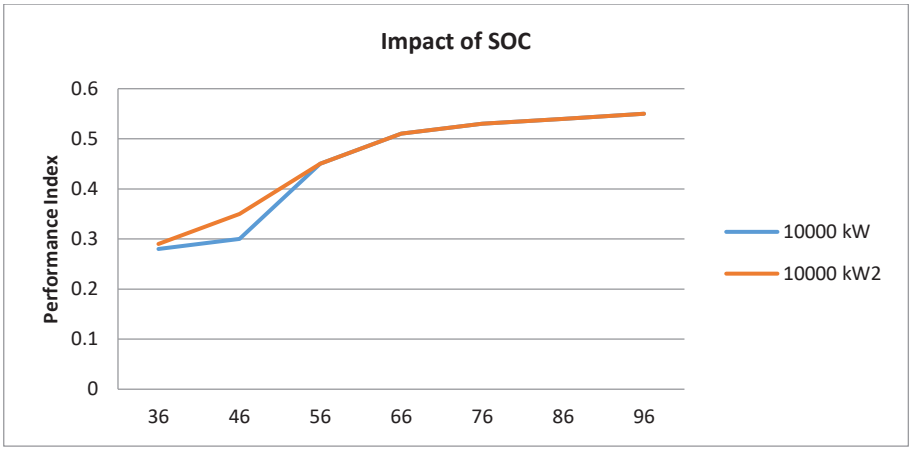

Fig. 8: performance comparison of M4

It is important to charge or discharge batteries and supercapacitors according to the instructions provided by the manufacturer if they are to have a long life, high performance and high efficiency. In order to remove sulfates from the lead plates of traditional lead-acid batteries, the batteries are charged slowly and at low intensity. There is an option to charge the ESS regularly, as well as to charge the ESS at a rate that is adjusted to the MG's power (SOC) variability.
It appears that the device is not fully charged and fully charged before charging again, which is called low SOC mode. Problems with charging and discharging are addressed by developing battery/supercapacitor management systems. There are two methods of charging an energy storage device, the current voltage method and the constant voltage method. A constant current load makes use of a steady-state feedback control strategy, whereas a direct current load makes use of a two-loop voltage control or current control strategy. It is also necessary to make use of voltage or dual circuit technology in order to control the emission of ESS. There are a variety of advanced control methods available to implement the load

integration process in a cost-effective, nonlinear manner, such as neural networks, fuzzy logic, and self-adaptive logic. Changes in cell parameters, uneven charging, discharge connections, ESS aging problems and other problems should be carefully studied.

6 Conclusion and Recommendation

This study investigates the microgrid energy storage system of a photovoltaic system. Microgrid topologies and storage system configurations are explored, along with power electronics interference, control systems and renewables, and energy storage system optimization. In a HESS PV system, sizing is usually done using the design space and density analysis method. Compression analysis is used to create HESS scale sizes that combine generator estimates of storage capacity based on load and resource data. The operation of the microgrid energy storage system is introduced and the load demand analysis is performed in relation to the load condition and power management systems. In comparison with the disturbance-free energy storage system, the microgrid energy storage system with disturbance system works better. Changes in payment status affect HESS operations. HESS supports the strong performance of a microgrid with a larger battery.

References

1. Ahmadi, M.H.; Ghazvini, M.; Sadeghzadeh, M.; Nazari, M.A.; Kumar, R.; Naeimi, A.; Ming, T. “Solar power technology forelectricity generation: A critical review”. Energy Sci. Eng. 6, (2018): 340–361.
2. Gamarra, A.R.; Banacloche, S.; Lechon, Y.; del Río, P. “Assessing the sustainability impacts of concentrated solar power deploymentin Europe in the context of global value chains”. Renew. Sustain. Energy Rev. 2023,171, 113004.
3. Hansen, K.; Vad Mathiesen, B. “Comprehensive assessment of the role and potential for solar thermal in future energy systems”. Sol. Energy 169, (2018): 144–152.
4. Lambrecht, M.; de Miguel, M.T.; Lasanta, M.I.; Pérez, F.J. “Past research and future strategies for molten chlorides application inconcentrated solar power technology”. Sol. Energy Mater. Sol. Cells 237, (2022): 111557.
5. Montenon, A.C.; Meligy, R. “Control Strategies Applied to a Heat Transfer Loop of a Linear Fresnel Collector”. Energies 15, (2022): 3338.
6. Leonardi, M.; Corso, R.; Milazzo, R.G.; Connelli, C.; Foti, M.; Gerardi, C.; Bizzarri, F.; Privitera, S.M.S.; Lombardo, S.A. “The Effectsof Module Temperature on the Energy Yield of Bifacial Photovoltaics: Data and Model”. Energies 15, (2021): 22.
7. Vance, D.; Razban, A.; Schubert, P.; Weissbach, R. “Investigation into Sizing Photovoltaic with Energy Storage for Off-GridTransactive Scenarios”. Energies 14, (2021): 1062.
8. Anani, N.; Ibrahim, H. “Performance Evaluation of Analytical Methods for Parameters Extraction of Photovoltaic Generators”. Energies 13, (2020): 4825.
9. Mohamed, A.S.A.; Maghrabie, H.M. “Techno-economic feasibility analysis of Benban solar Park”. Alex. Eng. J. 61, (2022): 12593–12607.
10. Hansen, L.H.; Madsen, P.H.; Blaabjerg, F.; Christensen, H.C.; Lindhard, U.; Eskildsen, K. “Generators and power electronicstechnology for wind turbines. In Proceedings of the IECON’01”. 27th Annual Conference of the IEEE Industrial Electronics Society, Denver, CO, USA, 29 November–2 December 2000–2005.
11. Kumar, Y.; Ringenberg, J.; Depuru, S.S.; Devabhaktuni, V.K.; Lee, J.W.; Nikolaidis, E.; Andersen, B.; Afjeh, “Wind energy: Trendsand enabling technologies” . Renew. Sustain. Energy Rev. 53, (2016): 209–224.

12. “Wind Solar Hybrid Project—Case Study|CleanMax”.
13. International Renewable Energy Agency. About IRENA. “In Renewable Energy Statistics Statistiques D’énergie Renouvelable2022”. Estadísticas de Energía Renovable 2022; IRENA: Masdar, United Arab Emirates, 2022. (26 December 2022).
14. Akinyele, D.O.; Rayudu, R.K. “Review of energy storage technologies for sustainable power networks. Sustain”. Energy Technol.Assess. 8, (2014): 74–91.
15. Hossain, S. “Comparative Study on Horizontal Axis Wind Turbines and Vertical Axis Wind Turbines. Bachelor Thesis, World University of Bangladesh, Dhaka, Bangladesh, 2019”. (7 January 2023).
16. Han, S.; Bai, L.; Chi, M.; Xu, X.; Chen, Z.; Yu, K. “Conversion of Waste Corn Straw to Value-Added Fuel via HydrothermalCarbonization after Acid Washing”. Energies 15, (2022): 1828.
17. Choi, S.K.; Choi, Y.S.; Jeong, Y.W.; Han, S.Y.; Nguyen, Q. “Characteristics of Flame Stability and Gaseous Emission of Bio-CrudeOil from Coffee Ground in a Pilot-Scale Spray Burner”. Energies 13, (2020): 2882.
18. Kim, J.-W.; Ahn, H.; Seo, H.C.; Lee, S.C. “Optimization of Solar/Fuel Cell Hybrid Energy System Using the Combinatorial DynamicEncoding” Algorithm for Searches (cDEAS). Energies 15, (2022): 2779.

Comparative Study Dynamics Analysis of a Multi-story Building with and without a Floating Column

Hemanth Raju T[1*], *Mandapati* Venkata Rama Sundari[2], *Abhishek* Saxena[3], *Manish* Gupta[4], Praveen[5], *Rahman* S. Zabibah[6], *B* Manideep[7]

[1]Department of Mechanical Engineering, New Horizon College of Engineering, Bangalore, India.
[2]Department of CSBS, GRIET, Bachupally, Hyderabad, Telangana, India.
[3]Department of Mechanical Engineering, ABES Engineering College, Ghaziabad - 201009, UP, India.
[4]Lovely Professional University, Phagwara, India.
[5]Lloyd Institute of Engineering & Technology, Knowledge Park II, Greater Noida, Uttar Pradesh, India.
[6]Medical Laboratory Technology Department, College of Medical Technology, The Islamic University, Najaf, Iraq.
[7]Department of Aeronautical Engineering, MLR Institute of Technology, Hyderabad, Telangana, India-500087

Abstract. Parking spaces, lobby areas, terrace gardens, and other amenities are highly sought-after in densely populated urban regions. Although floating columns can be useful and an achievable choice, it is important to research their structural performance and cost-effectiveness in the event of substantial ground motion imposed on by an earthquake. A building's overall dimensions, geometry, and shape all impact how it acts and acts when subjected to seismic loads. For this reason, it is necessary to assess how well floating column buildings perform in seismically vulnerable places in comparison to conventional buildings. In this work, the performance of structures with floating columns for seismic loading is observed using dynamic analytic techniques in accordance with IS 1893 (2005). This study analyses both the floating columns and the conventional building without floating columns. When compared to a regular building, the research reveals that the floating column buildings exhibit a very quick increase in base shear and story displacement. The horizontal displacements experienced by floating column buildings are proportionally larger due to an increase in the fundamental time period. If the lateral displacement exceeds the code-specified maximum limit, damage to structural and non-structural parts may result. Because of the discontinuity in the load distribution path, seismic base shear and overturning moment are also increasing in the case of buildings with floating columns. Additionally, while asymmetrically introducing floating columns, torsional irregularity has been produced but the modal mass participation ratio has decreased. While it is true that the use of floating

* Corresponding author: hemanthrt21@gmail.com

© The Authors, published by EDP Sciences. This is an open access article distributed under the terms of the Creative Commons Attribution License 4.0 (https://creativecommons.org/licenses/by/4.0/).

columns in high-rise structures allows for continuous open floor plans, they are also dangerous and susceptible in seismically active locations

1 Introduction

A column is often a vertical element designed to move weights from the foundation to the ground. Both of its lower level, or termination level, resting on a beam that is a horizontal member (either of the architectural design or the limits of the site), this is also known as a floating column. After then, the columns below the beams receive the load. A column that floats above the ground level [1-2]. Floating columns are frequently utilised in construction projects, particularly those that use transfer girders above floor, to enhance the amount of open space on the bottom level. Modern urban multi-story buildings unavoidably feature open first stories [3]. These are frequently used at reception centres and parking lots. The structure's natural period, stiffness, and mass distribution along its height can all affect the overall seismic base shear during an earthquake [4-5]. The shape, size, geometric configuration, and distribution of seismic pressures within a building all have a significant impact on how the building behaves during an earthquake [6]. The quickest route to the ground must be taken when seismic forces are produced in a building at multiple levels. This load transmission path must be straight; any deviation or discontinuity will adversely impair the building's performance [7]. Structures with vertical setbacks, such as hotel buildings that are a few stories broader than the others, have much higher earthquake forces at the discontinuity level. Damage or collapse in a given storey is more likely to occur to columns or walls that are overly tall or improperly supported. Following the 2001 Gujarat earthquake in Bhuj, numerous open-air parking structure structures collapsed and suffered significant damage [8]. The weight transmission path is disrupted by hanging or floating columns, and several studies have been conducted to compare the seismic performance of buildings with and without floating columns [9]. Possibly the most economical option is the framed construction with no floating columns due to the small nodal displacements and the uniform distribution of stresses at all beams and columns. Researchers used software to investigate how multi-story irregular buildings with floating columns responded to earthquakes [10]. They discovered that while the introduction of floating columns in building models increased story drift and displacement, story shear decreased as a result of the columns' decreased mass in the structure [11]. Additionally, they recommended against using floating columns in high-rise buildings located in areas that are very susceptible to earthquakes due to their poor performance [12]. The seismic behaviour of multistory buildings with and without floating columns using STAAD Pro V8i software and comparable static analysis techniques. They concluded that although a floating column raises the building's floor space index, it also makes the structure more vulnerable and dangerous [13-14]. Using STAAD Pro software, the seismic performance and cost-effectiveness of floating column buildings were assessed. It was found that these structures are both dangerous and not cost-effective in seismically active areas [15]. By using bracings, the seismic performance of the multi-story building with floating columns has been increased by 10% to 30% while taking into account various parameters including story drift, story shear, time period, and displacement [16-18]. Studying the seismic response of an RC frame structure with a floating column in different soil conditions, it was discovered that as building height raised the difference in maximum moments for different soil conditions decreased [19]. The floating column's presence in a two-dimensional, multi-story building using Finite Element Methods under various earthquake excitation scenarios with varying frequency content. They also proposed that decreasing the maximum displacement and inter-story drift values during earthquakes [20]. In regions with strong seismic activity, the design of these structures is mostly governed by

earthquake forces when the tank is operating at maximum capacity [21-24]. Making ensuring that necessities like the water supply are not harmed during earthquakes is crucial. Tanks should not completely collapse in extreme circumstances [25]. The primary goal of this research is to better understand how various bracing systems behave in order to reinforce traditional staging and improve its performance during earthquakes. Equivalent static analysis done to the elevated circular water tank staging in the seismic zone using various bracing system types [26]. could be achieved by increasing the column. Floating column structures have been built in metropolitan locations recently for a variety of reasons, including practicality, beauty, the assertion of city planning governance, etc . These structures are available in seismically vulnerable places to satisfy customer demands and create unique architectural designs, although they may entail greater shear and torsion than a typical building [27] . Therefore, it makes sense to look into how the floating column buildings perform seismically . With the goal to evaluate the seismic performance and compare various characteristics, such as base shear and story displacements between a conventional building and a floating column (G+7) residential multi-story building, a response spectrum method analysis (using Staad Pro) is carried out in this study [28-31] .

2 Methodology

A column is often a vertical element designed to move weights from the foundation to the earth. both of its lower level, or termination level, resting on a beam that is a horizontal member (either of the architectural design or the limits of the site), this is also known as a floating column [32]. The columns that support the beams below it then receive the loads. a column floating above the surface of the earth. Floating columns are frequently utilised in construction projects, particularly those that use transfer girders above floor, to enhance the amount of open space on the bottom level.

Table 1: Model detailed

Model detailed	
Item of model	**Properties of model**
Number of storey	G+7
Total height of structure	24m
Typical Storey height	3m
Bottom Storey height	3m
Floor diaphragm	Rigid
Bays number along length	5
Number of bays along width	5
Spacing of bays along length	3m
Spacing of bays along width	3m
Beam shape	Rectangular
Beam size	300x450mm
Column shape	Rectangular
Column size	600x600mm
Slab depth	150mm
Slab type	Thin Shell
Concrete grade	M25
Distribution bar (fysec)	Fe415
Main bar (fymain)	Fe415

These open spaces might serve as parking lots or assembly halls [33-36]. This study aims to create awareness about challenges in the design of multi-story facilities to be earthquake-resistant and to give an overview of how multi-story buildings with floating columns behave under seismic excitations [37]. In this study, a response spectrum method analysis (using Staad Pro) is conducted to examine the seismic performance and assess several comparative parameters, including base shear and story displacements between a normal building and a floating column (G+7) residential multi-story building

The table showing that the model specifications outline the detailed characteristics of the structure under consideration. The building comprises a G+7 storeys, with a complete top of 24 meters [38-40]. every storey has a typical height of 3 meters, including the bottom storey. The floor diaphragm is specified to be rigid. The building is divided into 5 bays along both the length and width, with each bay spaced 3 meters apart. Rectangular beams with dimensions of 300x450mm are applied, while the columns are also rectangular with dimensions of 600x600mm. The slab has a depth of 150mm and is classified as a thin shell. The concrete grade used is M25, and the steel reinforcement consists of Fe415 bars for both distribution and main reinforcement. These specifications provide essential details necessary for structural analysis and design considerations [41].

Table 2: Combinations of Load

S.no	Load Combination
1	1.5(DL + LL)
2	1.2(DL + LL + EQ-X DIR.)
3	1.2(DL + LL – EQ-X DIR.)
4	1.2(DL + LL + EQ-Z DIR.)
5	1.2(DL + LL – EQ-Z DIR.)
6	1.5(DL + EQ-X DIR.)
7	1.5(DL – EQ-X DIR.)
8	1.5(DL + EQ-Z DIR.)
9	1.5(DL – EQ-Z DIR.)
10	0.9DL + 1.5EQ-X DIR.
11	0.9DL – 1.5EQ-X DIR
12	0.9DL + 1.5EQ-Z DIR
13	0.9DL – 1.5EQ-Z DIR.

- DL= Dead Load
- LL= Live Load
- EQ-X DIR = Earthquake load in X- Direction
- EQ-Z DIR = Earthquake load in Z- Direction

3 Results and Discussion

Floating columns are frequently utilised in construction projects, particularly those that use transfer girders above floor, to enhance the amount of open space on the bottom level. These

open spaces might serve as parking lots or assembly halls [42]. A building's overall dimensions, geometry, and shape all impact how it acts and acts when subjected to seismic loads. For this reason, it is necessary to assess how well floating column buildings perform in seismically vulnerable places in comparison to conventional buildings [43-44]. In this work, the performance of structures with floating columns for seismic loading is observed using dynamic analytic techniques in accordance IS 1893 -2005. Building models' behaviour is examined, and the way floating column structures react to seismic loads is contrasted with that of conventional Structures. A comparison study of a structure with and without a floating column is constructed based on base shear and story displacement.

Table 3: Base Shear Evaluation for floating column

Storey	Height In Meter	Base Shear in KN
8	24.00	105
7	21.00	210
6	18.00	305
5	15.00	386
4	12.00	452
3	9.00	503
2	6.00	536
1	3.00	550
BASE	0.00	550

The table data provided presents in floating column, the storey heights of a building in meters alongside their corresponding base shear values in kilonewtons (KN). as the storey level progresses from the base (BASE) to the 8th storey, the heights decrease at the same time as the base shear tends to increase. For instance, the bottom shear starts at 105 KN on the 8th storey and gradually rises to 550 KN at the first storey. This sample illustrates the distribution of lateral forces in the building, with higher storeys experiencing greater lateral forces as compared to lower storeys. These base shear values are essential in structural engineering as they inform the design of structural factors to withstand lateral loads, such as those resulting from seismic activity.

Table 4: Storey displacement evaluation for floating column

Storey	Height in Meter	Storey displacement in MM
8	24.00	21.9
7	21.00	20.3
6	18.00	18.8
5	15.00	16.4
4	12.00	13.1
3	9.00	9.8
2	6.00	5.7
1	3.00	2.0
BASE	0.00	0.0

The table data provided offers in floating column, the storey heights of a building, measured in meters, along with the corresponding storey displacement values in millimeters (MM). The heights drop as one ascends from the base to the eighth storey, and the corresponding storey displacements likewise decrease. For instance, the displacement starts at 22.9 MM at the 8th storey and gradually decreases to 2.0 MM at the first storey. This trend indicates that higher

storeys generally experience less lateral displacement as compared to lower storeys. These displacement values are large in structural engineering as they help evaluate the constructing's response to external forces including seismic activity.

.

Table 5: Base Shear Evaluation for without floating column

Storey	Height In Meter	Base Shear in KN
8	24.00	128
7	21.00	271
6	18.00	394
5	15.00	498
4	12.00	585
3	9.00	649
2	6.00	692
1	3.00	708
BASE	0.00	708

The table provided data presents in without floating column, the storey heights of a building in meters alongside their corresponding base shear values in kilonewtons (KN). As the storey level progresses from the base (BASE) to the 8th storey, the heights decrease at the same time as the base shear tends to increase. For instance, the base shear starts at 128 KN at the 8th storey and gradually rises to 708 KN at the first storey. The distribution of lateral forces throughout the building is shown in this pattern, with higher storeys experiencing more lateral forces than lower floors. Engineers utilize this information to ensure the stability and safety of the constructing under various loading conditions.

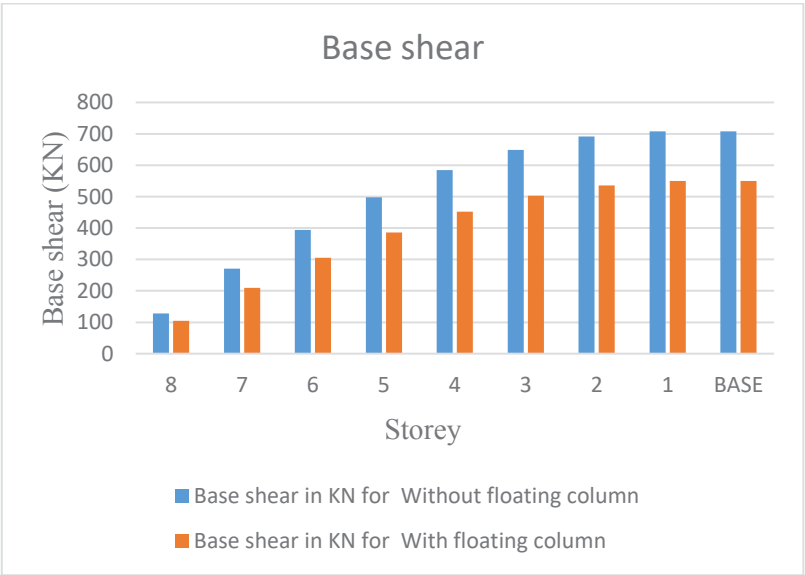

Fig. 1: Comparatively results of base shear with and without floating column

The fig presents a comparison of base shear values, measured in kilonewtons (KN), with and without floating columns for each storey of a building. as the storey level progresses from the base to the 8th storey, the bottom shear values for both eventualities are listed. Notably, the presence of floating columns appears to influence the base shear values across the storeys. For instance, at the base, the base shear with floating columns is 550 KN, even as without floating columns, it increases to 708 KN. This sample continues up the storeys, showing that base shear values are lower when floating columns are present than when they are not. Those versions are critical in structural engineering, as they impact the constructing's overall stability and its capacity to face up to external forces inclusive of seismic activity

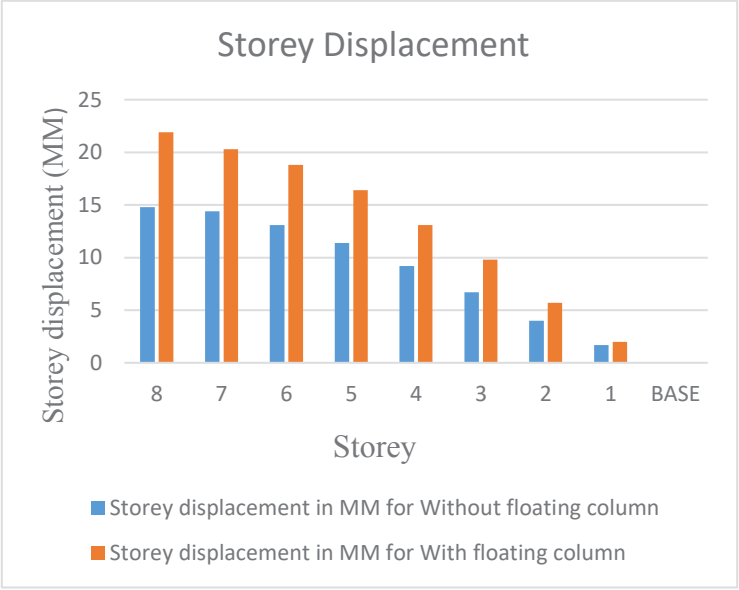

Fig. 2: Comparatively results of storey displacement with and without floating column

The fig showing compares the storey displacements of a building, measured in millimeters (MM), with and without floating columns. as the storey level progresses from the base to the 8th storey, the displacements for both scenarios are listed. Notably, the presence of floating columns tends to have an effect on the storey displacement values. for instance, on the eighth storey, the displacement without floating columns is 14.8 MM, while with floating columns, it will increase to 21.9 MM. This trend continues throughout the storeys, indicating that the inclusion of floating columns results in higher displacement values in comparison to their absence.

4 Conclusion

Floating columns can be useful and an achievable choice, it is important to research their structural performance and cost-effectiveness in the event of substantial ground motion imposed on by an earthquake. This study aims to create awareness about challenges in the design of multi-story facilities to be earthquake-resistant and to give an overview of how multi-story buildings with floating columns behave under seismic excitations. In this study, a response spectrum method analysis (using Staad Pro) is conducted to examine the seismic performance and assess several comparative parameters, including base shear and story displacements between a normal building and a floating column (G+7) residential multi-story building. Analyze behavior of elevated circular water tanks under seismic conditions. Focuses on understanding bracing patterns to enhance conventional staging.

- Examines base shear and storey displacements in a building both with and without floating columns.
- Storey level progression from base to 8th storey. Floating columns significantly affect displacement values. Without floating columns, displacement on 8th storey is 14. 8MM.With floating columns, displacement increases to 21.9 MM.
- Floating columns result in higher displacement values. Base shear values measured in KN, with and without floating columns, for each storey of a building.
- Floating columns significantly influence base shear values across storeys. Base shear with floating columns is 550 KN, without floating it increases to 708 KN. Floating columns decrease base shear values across storeys.
- Floating columns impact the building's stability and resistance to external forces, including seismic activity.

References

1. Yogananda, H. S., Basavaraj, R. B., Darshan, G. P., Prasad, B. D., Naik, R., Sharma, S. C., & Nagabhushana, H. (2018). New design of highly sensitive and selective MoO3: Eu3+ micro-rods: Probing of latent fingerprints visualization and anti-counterfeiting applications. Journal of colloid and interface science, 528, 443-456.
2. Wang, Daowei, Dong Wang, Kaipeng Wang, and Qi Liu. "Effects of agitation intensity and foam stability on the Floc-flotation of ultrafine minerals using a laboratory flotation column." Minerals Engineering 204 (2023): 108443.
3. Vijayakumar, Y., Nagaraju, P., Yaragani, V., Parne, S. R., Awwad, N. S., & Reddy, M. R. (2020). Nanostructured Al and Fe co-doped ZnO thin films for enhanced ammonia detection. Physica B: Condensed Matter, 581, 411976.
4. Azhin, M., K. Popli, A. Afacan, Q. Liu, and V. Prasad. "A dynamic framework for a threephase hybrid flotation column." Minerals Engineering 170 (2021): 107028.
5. Al-Ani, Wisam, and Dariusz Wanatowski. "Settlement analysis of floating stone columns." In Numerical modeling of construction processes in geotechnical engineering for urban environment: proceedings of the 19th international conference on soil mechanics and geotechnical engineering, Seoul. 2017.
6. Agawane, Prajakta, and Girish Joshi. "Study of Behaviour of Multistorey Building with Floating Column: A Review." International Journal of Research in Engineering, Science and Management 4, no. 4 (2021): 85-88.
7. Awasthi, A., Saxena, K. K., & Arun, V. (2021). Sustainable and smart metal forming manufacturing process. Materials Today: Proceedings, 44, 2069-2079.
8. Vandana, C. P., & Chikkamannur, A. A. (2021). Feature selection: An empirical study. International Journal of Engineering Trends and Technology, 69(2), 165-170.
9. Thote, Anil, and Ishant Dahat. "Comparative Study Of Floating Column & Non-Floating Column Without Seismic Behaviour."
10. Thakur, Arvind, and Amreen Khatun. "Comparative Seismic Analysis of Multi-storied Building with and Without Floating Columns." In Advances in Construction Materials and Sustainable Environment: Select Proceedings of ICCME 2020, pp. 863-872. Springer Singapore, 2022.
11. Telagam, N., Kandasamy, N., & Nanjundan, M. (2017). Smart sensor network based high quality air pollution monitoring system using labview. International Journal of Online Engineering (iJOE), 13(08), 79-87.
12. Suganthi, S. T., Vinayagam, A., Veerasamy, V., Deepa, A., Abouhawwash, M., & Thirumeni, M. (2021). Detection and classification of multiple power quality

disturbances in Microgrid network using probabilistic based intelligent classifier. Sustainable Energy Technologies and Assessments, 47, 101470.

13. Awasthi, A., Gupta, A., Saxena, K. K., Dwivedi, R. K., Kundalkar, D., Abdul-Zahra, D. S., ... & Saggu, H. S. (2022). Design and analysis of equal-channel angular pressing of Al6061: a comparative study. Advances in Materials and Processing Technologies, 1-10.
14. Su, Wenbing, Xiaokang Yan, Lijun Wang, Haijun Zhang, and Yijun Cao. "Effect of height of flotation column on flow field." Asia-Pacific Journal of Chemical Engineering 14, no. 3 (2019): e2311.
15. Sridhara, V., Gowrishankar, B. S., Snehalatha, & Satapathy, L. N. (2009). Nanofluids—a new promising fluid for cooling. Transactions of the Indian Ceramic Society, 68(1), 1-17.
16. Ravi, Mr Abhay Kumar, and Mr Dharmendra Singh. "Analysis Of Rcc Structures With And Without Floating Column."
17. Rao, D. S., S. Subba Rao, T. V. Vijaya Kumar, P. S. R. Reddy, G. Bhaskar Raju, S. Prabhakar, and P. More. "Beneficiation of iron ore fines by conventional flotation, flotation column and dual extraction column–A pilot scale study." Powder Handling & Processing 17, no. 2 (2005): 88-93.
18. Ramu, G. (2018). A secure cloud framework to share EHRs using modified CP-ABE and the attribute bloom filter. Education and Information Technologies, 23(5), 2213-2233.
19. Ram, J. P., Pillai, D. S., Ghias, A. M., & Rajasekar, N. (2020). Performance enhancement of solar PV systems applying P&O assisted Flower Pollination Algorithm (FPA). Solar Energy, 199, 214-229.
20. Raghu, M. S., Kumar, C. P., Prashanth, M. K., Kumar, K. Y., Prathibha, B. S., Kanthimathi, G., ... & Osman, S. M. (2021). Novel 1, 3, 5-triazine-based pyrazole derivatives as potential antitumor agents and EFGR kinase inhibitors: Synthesis, cytotoxicity, DNA binding, molecular docking and DFT studies. New Journal of Chemistry, 45(31), 13909-13924.
21. Awasthi, A., Saxena, K. K., & Arun, V. (2020). Sustainability and survivability in manufacturing sector. In Modern Manufacturing Processes (pp. 205-219). Woodhead Publishing.
22. Bouassida, Mounir, and Lassaad Hazzar. "Performance of soft clays reinforced by floating columns." Ground Improvement Cases Histories, Embankments with Special Reference to Consolidation and Other Physical Methods. In: Indraratna et al.(eds) Chap 16 (2015): 433-449.
23. Bosh, Prantik, Md Robiul Awall, and Mahmud Hasan. "Comparative study on seismic analysis of a multi-storied building with and without floating column." In AIP Conference Proceedings, vol. 2713, no. 1. AIP Publishing, 2023
24. Bhukya, L., Kedika, N. R., & Salkuti, S. R. (2022). Enhanced maximum power point techniques for solar photovoltaic system under uniform insolation and partial shading conditions: a review. Algorithms, 15(10), 365.
25. Awasthi, A., Rao, U. S., Saxena, K. K., & Dwivedi, R. K. (2022). Impact of equal channel angular pressing on aluminium alloys: An overview. Materials Today: Proceedings, 57, 908-912.
26. Prakash, S., Somiya, G., Elavarasan, N., Subashini, K., Kanaga, S., Dhandapani, R., ... & Sujatha, V. (2021). Synthesis and characterization of novel bioactive azo compounds fused with benzothiazole and their versatile biological applications. Journal of Molecular Structure, 1224, 129016.

27. Pawar, Neha, Kuldeep Dabhekar, P. B. Patil, and Isha Khedikar. "Review on “Effect of Floating Columns on Building subjected to seismic Forces”." In IOP Conference Series: Earth and Environmental Science, vol. 822, no. 1, p. 012045. IOP Publishing, 2021.
28. Parashuram, L., Sreenivasa, S., Akshatha, S., & Udayakumar, V. (2019). A non-enzymatic electrochemical sensor based on ZrO2: Cu (I) nanosphere modified carbon paste electrode for electro-catalytic oxidative detection of glucose in raw Citrus aurantium var. sinensis. Food chemistry, 300, 125178.
29. Padmaja, B., Prasad, V. R., & Sunitha, K. V. N. (2018). A machine learning approach for stress detection using a wireless physical activity tracker. International Journal of Machine Learning and Computing, 8(1), 33-38.
30. Nisar, Mr Shaikh Aasef Shaikh, P. B. Ullagaddi, and G. D. Awchat. "Seismic Analysis of a Multi-storeyed Building with Configuration of Floating Columns." International Research Journal of Engineering and Technology 8, no. 12 (2021).
31. Nisar, Mr Shaikh Aasef Shaikh, P. B. Ullagaddi, and G. D. Awchat. "Seismic Analysis of a Multi-storeyed Building with Configuration of Floating Columns." International Research Journal of Engineering and Technology 8, no. 12 (2021).
32. Naseer, S., M. Sarfraz Faiz, S. Iqbal, and S. M. Jamil. "Laboratory and numerical based analysis of floating sand columns in clayey soil." International Journal of Geo-Engineering 10 (2019): 1-16.
33. Malagavelli, V., Angadi, S., Prasad, J. S. R., & Joshi, S. (2018). Influence of metakaolin in concrete as partial replacement of cement. Int J Civil Eng Technol, 9(7), 105-111.
34. Liu, Shechuan, Dingwen Zhang, Tao Song, Guolong Zhang, and Libin Fan. "A method of settlement calculation of ground improved by floating deep mixed columns based on laboratory model tests and finite element analysis." International Journal of Civil Engineering 20, no. 2 (2022): 207-222.
35. Lingeshwaran, N., Surya KranthiNadimpalli, Shaik Sameeruddin, Y. Himath Kumar, and Sateesh Babu Madavarapu. "A study on seismic analysis of high-rise building with and without floating columns and shear wall." Materials Today: Proceedings 47 (2021): 5451-5456.
36. Kumar, K. Y., Saini, H., Pandiarajan, D., Prashanth, M. K., Parashuram, L., & Raghu, M. S. (2020). Controllable synthesis of TiO2 chemically bonded graphene for photocatalytic hydrogen evolution and dye degradation. Catalysis Today, 340, 170-177.
37. Kumar, K. U., Babu, P., Basavapoornima, C., Praveena, R., Rani, D. S., & Jayasankar, C. K. (2022). Spectroscopic properties of Nd3+-doped boro-bismuth glasses for laser applications. Physica B: Condensed Matter, 646, 414327.
38. Kalyani, G., Janakiramaiah, B., Karuna, A., & Prasad, L. N. (2023). Diabetic retinopathy detection and classification using capsule networks. Complex & Intelligent Systems, 9(3), 2651-2664.
39. Kahyaoğlu, Mehmet Rifat, and Martin Vaníček. "A numerical study of reinforced embankment-supported by encased floating columns." Acta Geotechnica Slovenica 16, no. 2 (2019): 25-38.
40. Jayabal, R., Subramani, S., Dillikannan, D., Devarajan, Y., Thangavelu, L., Nedunchezhiyan, M., ... & De Poures, M. V. (2022). Multi-objective optimization of performance and emission characteristics of a CRDI diesel engine fueled with sapota methyl ester/diesel blends. Energy, 250, 123709.
41. Deshmukh, Y. R., S. Jadhav, S. M. Shirsat, A. S. Bankar, and D. G. Rupanawar. "A study on seismic analysis of multistorey building with floating column using staad. prov8i." International Journal of Engineering Research and Technology 5 (2018).
42. Cheruvu, A., Radhakrishna, V., & Rajasekhar, N. (2017, May). Using normal distribution to retrieve temporal associations by Euclidean distance. In 2017 International Conference on Engineering & MIS (ICEMIS) (pp. 1-3). IEEE.

43. Han, Jikang, Yanfeng Li, and Peng Chen. "A study of bubble size/shape evolution in microbubble countercurrent contacting flotation column." Asia-Pacific Journal of Chemical Engineering 18, no. 2 (2023): e2865.
44. Chaudhury, S., Krishna, A. N., Gupta, S., Sankaran, K. S., Khan, S., Sau, K., ... & Sammy, F. (2022). Effective image processing and segmentation-based machine learning techniques for diagnosis of breast cancer. Computational and Mathematical Methods in Medicine, 2022.

Experimental Investigation into the Impact of Substituting Natural Sand with Manufactured Sand in Landfill Construction

Rajasekhar Boddu[1], *Ginni* Nijhawan[2], *Prashanth* K S[3*], *Abhishek* Saxena[4], *Pramod* Kumar[5], *Fouad* A. Al-Saady[6], *K* Veeranjaneyulu[7]

[1]Department of CSBS, GRIET, Bachupally, Hyderabad, Telangana, India.
[2]Lovely Professional University, Phagwara, India
[3]Department of Applied Science, New Horizon College of Engineering, Bangalore, India.
[4]Department Department of Mechanical Engineering, ABES Engineering College, Ghaziabad - 201009, UP, India.
[5]Lloyd Institute of Engineering & Technology, Knowledge Park II, Greater Noida, Uttar Pradesh 201306
[6]Medical Laboratory Technology Department, College of Medical Technology, The Islamic University, Najaf, Iraq.
[7]Department of Aeronautical Engineering, MLR Institute of Technology, Hyderabad, Telangana, India-500084

Abstract. There is a lower requirement for river sand in construction because of a number of logistical and environmental problems. In response to these issues, alternative materials are being increasingly recognized by the construction field progressively M. Sand, derived from the mining and processing of rocks that is a low-particle-size substitute to natural sand which demonstrates potential. Amongst its numerous applications are surface polishing, prefabricated cement components, hollow block development, and lightweight component production. Practitioners and researchers both have been giving special attention on the usage of M. sand in the last few years. This has led to further study into its suitability for replacing river sand in concrete production. The formulation of concrete blends using M. Sand has been made possible through various mix designs developed according to relevant design codes such as IS codes. An assessment of the mechanical properties and structural performance -of concrete containing M. Sand has been conducted using cubes, cylinders, and beams compared to traditional natural sand concrete. As a result of these tests, the compressive, flexural, and tensile strength properties of M. Sand and M. Sand can be compared, suggesting M. Sand has similar properties. Concrete construction applications can utilize sand as an environmentally sustainable and viable alternative to natural-river sand, thereby addressing sustainability concerns and resource scarcity concerns.

* Corresponding author: *prashanth.sadashivappa@gmail.com*

© The Authors, published by EDP Sciences. This is an open access article distributed under the terms of the Creative Commons Attribution License 4.0 (https://creativecommons.org/licenses/by/4.0/).

Keyword-: Logistical and environmental problems, alternative materials, mining and processing of rocks, low-particle-size substitute, potential applications.

1 Introduction

In order to meet the needs of a world that is rapidly globalizing, there may be a concentrated effort made in India to create vital infrastructure, such as power initiatives, express highways, and industrial structures. The strength and economic feasibility of concrete structures have significantly improved as a result of significant advancements in concrete technology in recent years. However, a significant portion of the natural sand used in the traditional construction of concrete comes from riverbeds; this resource is not only becoming more and more expensive, but it is also becoming scarcer. The rapid depletion of river sand stocks is a result of the increased demand for concrete across a range of construction projects, which has also led to a commensurate increase in the consumption of natural sand. Because of such an alarming depletion of natural sand resources has prompted an important need to explore alternative solutions. Manufactured sand can be produced from crushed natural stones of specific sizes and grades, which is one of the most promising options. Despite the growing demand for sand from natural sources from a wide range of sectors and concerns over its conventional nature, this technology offers a feasible and affordable replacement for manufacturing. As the manufacturing of synthetic sand through stone crushing operations is proving to be a viable and sustainable response to India's construction industry's ongoing growth and sustainability, which will lessen the country's reliance over river sand for concrete manufacturing. Sand founded near river areas has become a very significant raw material for the production of concrete in recent years, particularly in the infrastructure, building and construction sectors. In order to avoid resource depletion and compromise the needs of generations to come, sustainable construction practices are important. River weathering affects the shape and size of natural sand, which is derived from weathered rock particles. In spite of the fact that natural sand with the desired properties may be easier to obtain regionally, securing it with the desired properties from remote locations has proved to be difficult, resulting in higher construction costs. In addition, as river sand resources deplete, the problem of sand shortages becomes even more acute. Therefore, alternative substances that possess comparable properties to natural river sand may be urgently needed in order to substitute it partially or completely. Produced from crushed hard granite, manufactured sand, or M-sand, has become an effective replacement. M-sand has been graded and structured like the shape of a cube with grounded edges, often with sizes of particles from 150 microns and 4.75 mm. It is used in construction. Its higher percentage of finer particles reduces voids, thereby reducing the required cement amount and making construction more economical. The increasing demand for M-sand arises from the lack of ability of river sand to satisfy the escalating construction sector demands. Natural river sand formation is a slow process, resulting in limited supply and high costs, making M-sand essential. additionally, M-sand exhibits lower silt content and natural material in comparison to river sand, improving the durability and lifespan of concrete structures'-sand, derived from the crushing of granite stones, is obtained in controlled grading appropriate for construction purposes, serving as a feasible alternative to river sand. Its production involves processing quarry fines of specific rock types through screening and further processing to fulfill preferred specifications. The properties of M-sand must involve a more smooth texture, more powerful crushing power, and a lack of natural pollutants. Previous studies used M-sand to substitute the sand from

rivers in laboratory investigations, finding that a 50% substitution enhanced power and sturdiness. Natural river sand can be replaced with quarry fines that are abundant inside Tamil Nadu's quarries for stone. Making use of heaps of quarry fines produced by crushers could increase the amount of M-sand that is available for building. The parent rock affects M-sand's composition, texture, chemical makeup, and mineral qualities, all of which affect how suitable it is for building. This paper presents experimental results on the properties of M-sand generated from various sources to ease mix design for various concrete grades using M-sand as a natural sand substitute. Additionally, by analyzing the characteristics of clean, hardened concrete created using the suggested mix proportions, the study sheds light on the use of M-sand in the construction industry.

2 Methodology

The availability and use of river sand for construction are progressively less favoured due to various environmental and logistical limitations. The principal objective of this experimental investigation is to elucidate the ramifications of substituting natural sand with manufactured sand across various proportions (25%, 50%, 75%, and 100%) in M30 grade concrete. This comprehensive study encompasses the entire experimental process, including the casting, meticulous curing, and subsequent rigorous testing of specimens. We meticulously execute four separate trials for every water-cement ratio and mortar mix proportion, developing a systematic progression from a reference mix that replaces natural sand by 25% with manufactured sand to a scenario where manufactured sand is completely replaced. By using such a methodical approach, it will be possible to assess the performance of concrete in a variety of replacement scenarios to determine whether manufactured sand is an effective alternative for concrete. This will provide valuable insights into the effectiveness of manufactured sand. In order to ensure uniformity and accuracy of results, all experimental procedures are cautiously conducted under controlled ambient conditions to ensure they are conducted under controlled conditions. In order to ensure homogeneity and consistency of the mortar mixture, each of the mortar components, namely cement and fine combination, is meticulously blended in a dry nation prior to use. Manufactured sand is carefully supplied to partially replace natural sand, and then the exact amount of water needed to produce the appropriate workability and flow characteristics is added. To achieve the intended results, the different components are then completely mixed to guarantee a uniform dispersion and complete integration. The concrete's mechanical properties have been assessed with a 150 x 150 x 150 mm cube. Following an extensive 28-day period of curing in water, these specimens undergo by an in-depth evaluation procedure using standard equipment in order to ensure the most effective feasible development of strength. Through methodical experimentation and assessment, this research aims to provide an in-depth knowledge of the distinct advantages of manufactured compared to naturally occurring sand in cement applications, explaining any possible implications.

2.1 Investigation of Materials and Their Properties

The experiment, that was important to the research, made utilization of a variety of resources, including water from the tap, naturally occurring sand from rivers, coarse crumbled dioxide of silicon stone particles, and regular Portland cement. Conventional Portland cement was used to formulate the concrete mixtures in accordance with IS: 279-2015 standards as shown

in Table 1. The Zone II rating of a concrete mix depends upon an array of variables, such as the makeup of the smaller particles. For added strength and volume, coarse aggregate—crushed silicon dioxide stones no larger than 10 mm—was used into the cement mixtures.

Table 1. A description of the properties of OPC (ordinary Portland cement)

Attribute	Description	Attribute
Grade of Cement grade	43	Grade of Cement grade
Specific Gravity	3.15	Specific Gravity
Normal Consistency	25-30%	Normal Consistency
Initial Setting time	30 minutes	Initial Setting time
Final Setting time	600 minutes	Final Setting time
3 days compressive strength	22 N/mm²	3 days compressive strength
7 days compressive strength	33 N/mm²	7 days compressive strength
28 days compressive strength	43 N/mm²	28 days compressive strength

Grade 43 cement is commonly used in construction projects, as shown in the table below. Compressive strength is an important feature of Grade 43, which is essential to the structural integrity of the material. Its specific gravity is 3.15, which indicates its density in relationship to water, and its consistency is typically 25-30%, making it a very workable cement. Application and curing can be completed during the initial 30 minute setting period and the final 600 minute setting period. During 3 days (22 N/mm2), 7 days (33 N/mm2), and 28 days (43 N/mm2), the compressive strength values show a progressive increase, which is vital to ensuring that concrete structures remain stable and durable.

Table 2: Natural and manufactured sand have different properties

S. No	Characteristic	Natural-Sand	Manufactured-Sand
1	Density (Specific Gravity)	2.59	2.67
2	Absorption of Water	6.5%	5.6%
3	Modulus of Fineness	2.88	2.82

The Present Table 2 compares the characteristics of artificial and natural sand. The specific gravity of manufactured sand is 2.67, somewhat higher than that of natural sand, which is 2.59. The percentage with which artificially created sand absorbs water is 5.6%, in comparison to 6.5% for natural sand. Moreover, an average modulus of fineness of produced sand is 2.82, compared to 2.88 for natural sand. Using these values, construction material selection and performance evaluation can be improved by gaining insight into how natural sands differ from manufactured sands in terms of their physical characteristics.

Table 3: Coarse Aggregate's characteristics

S. No	Property	Value
1	Particular Gravity	2.85
3	Absorption of Water	0.90%
4	Index of Flakiness	20%
5	Index of Elongation	20%
6	Fineness Crushing	21.33%
7	Impact Value	15.40%
8	Value The modulus	6.65

The Table 3 outlines several key properties of a specific material, likely an aggregate used in construction. Firstly, the specific gravity is noted at 2.85, indicating its density relative to water. Additionally, its water absorption rate stands at 0.90%, highlighting its propensity to absorb water when submerged. Moreover, both the flakiness index and elongation index are recorded at 20%, illustrating the percentage of particles in the material that are flat or elongated. The crushing value of 21.33% indicates the fines produced upon crushing, while the impact value of 15.40% reflects the material's resistance to impact loads. Lastly, the fineness modulus of 6.65 suggests the overall fineness or coarseness of the aggregate particles. These properties collectively influence the material's suitability and performance in various construction applications.

3 Results and Discussion

The primary focus of this experimental study is to investigate the impact of substituting natural sand with manufactured sand at different percentages (25%, 50%, 75%, and 100%) on the hardened properties of concrete, particularly the compressive strength. The experimental procedure encompasses the casting, curing, and subsequent testing of concrete specimens. These specimens are subjected to various proportions of manufactured sand in M30 grade concrete mixes, namely M30 with 25% M-sand, M30 with 50% M-sand, M30 with 75% M-sand, and M30 with 100% M-sand. By using extensive testing, like the evaluation of split tensile, flexibility, and compressible strengths, the comparative research aims to find any significant variations in the outcomes of concrete mixes including various amounts of manufactured sand. We analyze and present the results of these tests in order to shed light on the effect that manufactured sand has on concrete's mechanical properties.

Table 4: M30 Grade after 14, 28 and 60 days in compression strength (N/mm^2)

S. No.	Ratio of Manufactured Sand to Natural Sand	Compressive Strength (N/mm^2)
S1	25% Manufactured, 75% Natural Sand	34
S2	50% Manufactured, 50% Natural Sand	36
S3	75% Manufactured, 25% Natural Sand	38

The percentage of manufactured sand that are substituted for natural sand, along with the associated compressive strengths expressed in N/mm², are shown in Table 4. After starting with a 25% substitution rate for synthetic sand and a 75% substitution rate for natural sand, 34 N/mm² was the resultant compressive strength. The compressive strength improved to 36 N/mm² when the amount of manufactured sand was increased to 50% and the percentage of natural sand was decreased to the same extent. The compressive strength then rose to 38 N/mm² at a substitution rate of 75% for synthetic sand and 25% for natural sand. The greatest compressive strength of 40 N/mm² was finally achieved by completely replacing natural sand with manufactured sand, or 100% manufactured sand and 0% natural sand.

Table 5: M30 grade split tensile strength versus 14 and 28 day tests

S. No.	Ratio of Manufactured Sand to Natural Sand	Spilt Tensile Strength (N/mm^2)
S1	25% Manufactured, 75% Natural Sand	3.25
S2	50% Manufactured, 50% Natural Sand	3.5
S3	75% Manufactured, 25% Natural Sand	3.6
S4	0% Natural Sand,	3.7

Table 5 shown in Based on their split tensile strengths measured in N/mm2, the table below shows what percentage of natural sand is replaced by manufactured sand. After substituting 25% of the natural sand for manufactured sand, the resulting split tensile strength measured 3.25 N/mm2. A split tensile strength of 3.5 N/mm2 was achieved by increasing the proportion of manufactured sand to 50% and reducing the natural sand to 25%. In addition, the split tensile strength increased further to 3.6 N/mm2 when manufactured sand was substituted for 75% of natural sand. Finally, when natural sand was totally substituted with manufactured sand, a formulation containing 100% synthetic sand and 0% natural sand produced a split tensile strength of 3.7 N/mm2.

Table 6: M30 grade flexural tensile strength versus 14 and 28 day tests

S. No.	Ratio of Manufactured Sand to Natural Sand	Flexural Strength (N/mm2)
S1	25% Manufactured, 75% Natural Sand	3.6
S2	50% Manufactured, 50% Natural Sand	3.8
S3	75% Manufactured, 25% Natural Sand	3.9
S4	0% Natural Sand	4.2

Natural sand replacement percentages are provided in the Table 6, along with the flexural strengths of products corresponding to those replacement percentages, measured in N/mm2. The flexural strength was recorded at 3.6 N/mm2 when manufactured sand was substituted at a rate of 25% and natural sand at a rate of 75%. A flexural strength of 3.8 N/mm2 was reached when the proportion of manufactured sand increased to 50% while the proportion of natural sand decreased. Subsequently, at a substitution rate of 75% for manufactured sand and 25% for natural sand, the flexural strength further increased to 3.9 N/mm². Finally, complete replacement of natural sand with manufactured sand, constituting 100% manufactured sand and 0% natural sand, yielded the highest flexural strength of 4.2 N/mm².

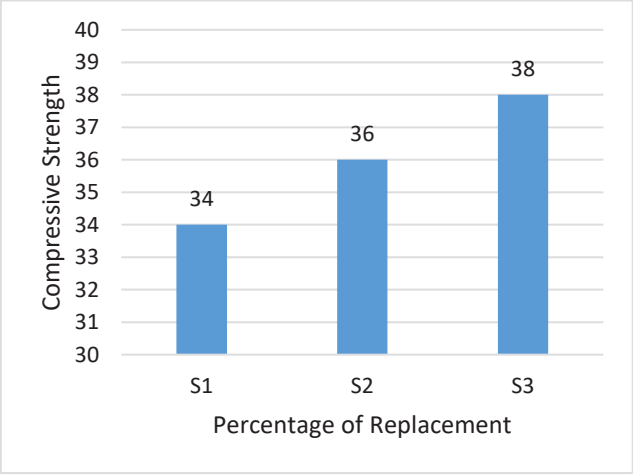

Fig. 1: Comparatively results of compressive strength for M30 grade of concrete

The compressive strengths of concrete samples that were exposed to different ratios of manufactured sand to natural sand replacement are compared in this Fig. 1. This diagram illustrates the impact of replacing all natural sand in concrete mixes with manufactured sand. Interestingly, at 40 N/mm², this substitution produced the most compressive strength yet measured. These results highlight the possible advantages of using synthetic sand in place of natural sand for producing concrete, implying improved strength characteristics in the

finished concrete samples. This comparative approach helps with concrete mixture optimization for better performance and sustainability in construction processes.

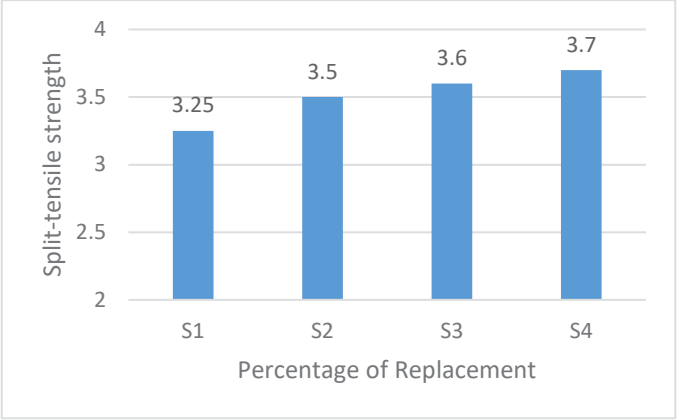

Fig. 2: Comparatively results of spilt tensile strength for M30 grade of concrete

Data on the split tensile strength of concrete samples exposed to various percentages of artificial sand substituted for natural sand are shown in Fig. 2. Higher percentages of produced sand are invariably linked with better spilt tensile strength. There is no doubt that specimens of concrete with 100% manufactured sand (0% natural sand) exhibited the highest spilt tensile strength, measured at 3.7 N/mm2. Comparing manufactured sand to other replacement ratios, this outcome suggests that manufactured sand improves tensile strength in concrete.

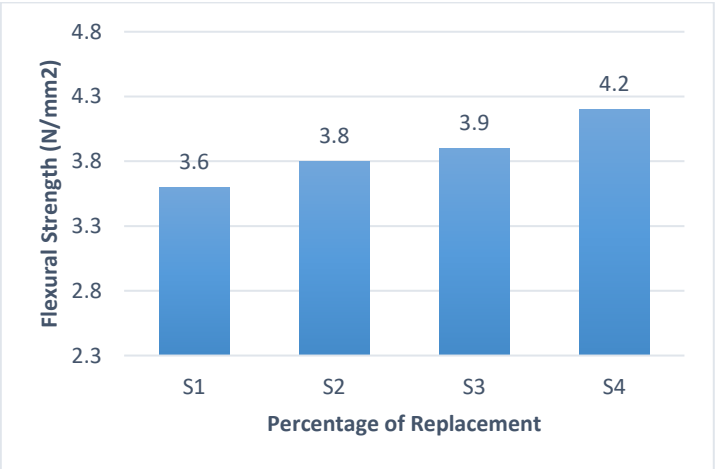

Fig. 3: Comparatively results of flexural strength for M30 grade of concrete

In the Fig. 3, different replacement percentages of natural sand by manufactured sand are shown as a comparative analysis of the flexural strength of concrete samples. With increasing proportions of manufactured sand, flexural strength shows a consistent improvement. As a result, concrete specimens with 100% manufactured sand (0% natural sand) acquired the greatest flexural strength, measuring 4.2 N/mm2, demonstrating manufactured sand's favourable influence on concrete's flexural strength. Combining these results, we can say that

artificial sand can increase concrete compositions' flexural strength without lowering the strength of natural sand.

6 Conclusion

These samples are made from M30 grade concrete mixes that have different amounts of synthetic sand in them. There are four different amounts of M-sand in these mixes: 25%, 50%, 75%, and 100%. This study uses extensive testing methodologies, such as flexural strength, split tensile strength, and compressive strength, to assess the effectiveness of substituting manufactured sand for natural sand in concrete compositions. The research work revealed a lot about the behavior of concrete when different percentages of manufactured sand were used as a substitution for natural sand.

- In an academic work of concrete samples with varying parts of manufactured sand and natural sand replacement ratios, 40 N/mm2 was the highest compressive strength measured when natural sand was completely replaced with manufactured sand in a complete replacement process, where the manufactured sand completely got replaced by natural sand in a replacement procedure.
- With the rise in manufactured sand percentage, and in combination of tensile, strength of concrete split increased consistently. It was found that concrete specimens containing 100% manufactured sand exhibited the strongest strength with 3.7 N/mm2 as their maximum strength in this process.
- This analysis exhibits the flexural strength of concrete specimens increased as the proportion manufactured sand was increased. Manufactured sand has a greater flexural strength exhibiting its maximum strength.
- It has been seen that sand substituted with manufactured sand enhanced the strength properties of concrete specimens, this will lead in future concrete production.

The conclusion drawn from this study have demonstrated that manufactured sand is a highly effective alternative to natural sand as an increase in the flexural strength of the concrete composition in building and infrastructure sectors.This contributes to ongoing endeavors aimed at optimizing concrete mixtures for improved performance and sustainability.

References

1. Nadimalla, Altamashuddinkhan, Siti Aliyyah Masjuki, Siti Asmahani Saad, Ean Lee Woen, Siti Maisarah Ali, and Naseer Ulla. "The impact of manufactured sand (m-sand) as partially and fully replacement of fine aggregate in concrete." micron 27 (2020): 8-30.
2. Pilegis, Martins, Diane Gardner, and Robert Lark. "An investigation into the use of manufactured sand as a 100% replacement for fine aggregate in concrete." Materials 9, no. 6 (2016): 440.
3. Arulmoly, Branavan, Chaminda Konthesingha, and Anura Nanayakkara. "Performance evaluation of cement mortar produced with manufactured sand and offshore sand as alternatives for river sand." Construction and Building Materials 297 (2021): 123784.
4. Kumar, K. Praveen. "Characteristics of cement mortar with M-sand as replacement of fine aggregates." Materials Today: Proceedings 5, no. 11 (2018): 25412-25419.
5. Lokeswaran, M. R., and C. Natarajan. "Study on the properties of cement concrete using manufactured sand." In Advances in Structural Engineering: Materials, Volume Three, pp. 1803-1809. Springer India, 2015.

6. Suresh, S., and J. Revathi. "Effect of M-sand on setting time of high-performance concrete." Asian Journal of Research in Social Sciences and Humanities 6, no. 10 (2016): 1648-1654.
7. Ali, Maisarah, Muhammad Hariz Nordin, and Siti Asmahani Saad. "Physical and mechanical properties of concrete incorporating manufactured sand." Advanced Materials Research 1115 (2015): 160-165.
8. Sudha, C., K. Divya Krishnan, P. T. Ravichandran, and PR Kannan Rajkumar. "Strength Characteristics of high strength concrete using M-sand." Indian Journal of Science and Technology (2016).
9. Premanand, R., K. Thirupura Sundari, N. Aishwarya, and B. Karthikeyan. "An experimental analysis on the replacement of fine aggregate by manufacture sand." Materials Today: Proceedings (2023).
10. Suresh, S., and J. Revathi. "An Experimental investigation on effect of high strength concrete using manufacturing sand." International Journal of Innovative Research in Science, Engineering and Technology 5, no. 2 (2016): 2135-2140.
11. Zhao, Minglei, Manman Dai, Jie Li, and Changyong Li. "Case study on performance of pumping concrete with super-fine river-sand and manufactured-sand." Case Studies in Construction Materials 18 (2023): e01850.
12. Mounika, T., and Ghanta Latha Bhuvaneswari. "Strength characteristics of concrete by replacing natural sand by M-sand for M20 and M30 grade concrete." International Journal of Advance Scientific Research And Engineering Trends 6, no. 2 (2021).
13. Mahakavi, P., and R. Chithra. "Effect of recycled coarse aggregate and manufactured sand in self-compacting concrete." Australian Journal of Structural Engineering 21, no. 1 (2020): 33-43.
14. Mahakavi, P., and R. Chithra. "Effect of recycled coarse aggregate and manufactured sand in self-compacting concrete." Australian Journal of Structural Engineering 21, no. 1 (2020): 33-43.
15. Nadimalla, Altamashuddinkhan, Siti Aliyyah Binti Masjuki, Sher Afghan Khan, and B. A. Akshatha. "The effect of replacement of natural sand by manufactured sand on the properties of the concrete." In 2018 IEEE 5th International Conference on Engineering Technologies and Applied Sciences (ICETAS), pp. 1-7. IEEE, 2018.
16. Nanthagopalan, Prakash, and Manu Santhanam. "Fresh and hardened properties of self-compacting concrete produced with manufactured sand." Cement and concrete composites 33, no. 3 (2011): 353-358.
17. Kavya, Ayinampudi, and A. Venkateshwara Rao. "Experimental investigation on mechanical properties of concrete with M-sand." Materials Today: Proceedings 33 (2020): 663-667.
18. Mane, K. M., P. A. Nadgouda, and A. M. Joshi. "An experimental study on properties of concrete produced with M-sand and E-sand." Materials Today: Proceedings 38 (2021): 2590-2595.
19. Sankh, Akshay C., Praveen M. Biradar, S. J. Naghathan, and Manjunath B. Ishwargol. "Recent trends in replacement of natural sand with different alternatives." In Proceedings of the international conference on advances in engineering and technology, pp. 59-66. 2014.
20. Kazmi, Danish, Mehdi Serati, David J. Williams, Sadaf Qasim, and Yi Pik Cheng. "The potential use of crushed waste glass as a sustainable alternative to natural and manufactured sand in geotechnical applications." Journal of Cleaner Production 284 (2021): 124762.

Comparative analysis of RCC and PT Slabs underneath Lateral Loading: A Structural study using ETABS

Koushal Dhamija[1], *Vegiraju* Naresh Kumar Varma[2], *Manish* Gupta[3], *Hemanth* Raju T[4*], Praveen[5], *Rahman* S. Zabibah[6], *Nayani Uday Ranjan* Goud[7]

[1]Lloyd Institute of Management and Technology, Greater Noida, Uttar Pradesh, India-201306
[2]Department of Civil, GRIET, Bachupally, Hyderabad, Telangana, India.
[3]Lovely Professional University, Phagwara, India
[4]Department of Mechanical Engineering, New Horizon College of Engineering, Bangalore, India
[5]Lloyd Institute of Engineering & Technology, Greater Noida, Uttar Pradesh, India
[6]Medical Laboratory Technology Department, College of Medical Technology, The Islamic University, Najaf, Iraq
[7]Department of Aeronautical Engineering, MLR Institute of Technology, Hyderabad, Telangana, India-500093

Abstract-. ETABS software is used to analyze the structural response of reinforced concrete (RCC) and post-tensioned (PT) slabs under lateral loading. This study investigates RCC and PT slabs' behavior by using finite element analysis to determine bending moments, shear forces, and storey drift. Prestrassed slabs display lower bending moments and shear forces than RCC slabs, demonstrating the effectiveness of prestressing in reducing structural requirements. A reduction in storey drift also indicates improved resistance to lateral deformations in PT slabs. In terms of structural performance and cost-effectiveness, PT slabs offer potential benefits for constructing layouts and construction, making them an attractive choice.

Keyword-: Concrete, flat slab structures, ETABS, Fibber reinforced concrete.

1 Introduction

Existing gradual collapse architecture building regulations include risk-based subjective scales and quantitative requirements. In order to evaluate the structural resilience of cement flat slab buildings, mathematical theories like Crucial Stress Crack Theories (CSCT) are employed. This research evaluates column punching under abrupt pillar removal situations employing the Ductility-Centered Robustness Evaluation created at Imperial College London. It also applies to devices using flat floors, showing that tying pressures necessitate connection punching beforehand. It is also demonstrated that integrity reinforcement benefits greatly from numerical modeling of post-punching [1]. In all of India's seismic zones, the dissertation examines the behavior and performance of a G+5 industrial multi-storey

* Corresponding Author: hemanthrt21@gmail.com

© The Authors, published by EDP Sciences. This is an open access article distributed under the terms of the Creative Commons Attribution License 4.0 (https://creativecommons.org/licenses/by/4.0/).

framework using smooth and standard slabs, concentrating on variables such as base shear, story drift, axial force, and displacement. A four millimeters variance in story movement and 5% higher shear and radial pressures per story for slab-like buildings than for traditional buildings are shown by the study, suggesting that these structures are suitable for different seismic zones [2].

In order to reduce bending moment and shear stresses, flat slabs are slabs without beams resting directly on supports. They transmit weight to the base and columns immediately. Column heads are extended and slab thickness is raised to sustain big loads. A plain ceiling, improved architectural look, less fire risk, improved light dispersion, simpler construction, and less expensive form work are all benefits of this design. Flat slab design is done uniquely across the country, with regulations like example IS 456-2000 and ACI 318-08 offering recommendations. With moments distributed as column strip and centered strip instances, finite element analysis and the Comparable Frame Technique are employed. An inner panel measuring 6.6 by 5.6 meters was created [3]. Significant corrosion-related degradation was the reason for the costly fix of the forty-year-old La Chandeliered parking structure in Québec, Canada. The city made the decision to install new, GFRP-barred slabs in place of the ones that were flat. A consulting agency created two designs; however, after doing a cost research, the municipality decided on the GFRP bars. The design, construction, and performance of GFRP-reinforced concrete flat slabs under actual service loads and circumstances during a 3.5-year period are examined in this study. It confirms that an initial higher GFRP cost does not always translate into a higher overall cost by providing a comparative cost comparison of steel-RC and GFRP-RC systems [4].

In multi-story structures subjected to structural loads and ISO 834 fire conditions, the study examines the resistance to fire of concrete flat slabs. It will need more trials to assess the effectiveness of the updated boundary conditions, which mirror real-world circumstances and reflect the impact of membrane movement on punching shear behavior. Given that heat transmission and distortion recovery were recorded, the test showed a much longer fireproofing endurance under limited support environments, suggesting that these parameters improve punch shear resistance [5]. Column-supported flat slabs (CSS), one type of high-strength architectural component, are using more and more fibber reinforced concrete (FR). With this technique, building times may be shortened and resources can be optimized without sacrificing structural integrity. Its usage in CSS is constrained, nevertheless. A research with an industrial focus compares the operation methods and expenses of CSS using Frs. and typical RC techniques [6]. This research examines the necessity of flex reinforcing and the time-saving benefits of using fibbers in place of steel bars for reinforcement. To determine productivity rates and specifics, databases and conversations with in site building professionals are used [7-9]. The findings indicate that while construction time and time-dependent costs have decreased, direct costs for fibber and hybrid systems have increased. The use of FR for CSS by architects and building managers is aided by this research [10]. Recommendations for the partial or complete replacement of steel reinforcing bars have arisen from the growing usage of fibber concrete reinforced (FRC) for structural applications. The impact of the fib MC-2010 FRC post-cracking strength categorization on physical reaction, for example, is a contributing factor why adoption is still not unified. Real-scale experiments were used to validate the implementation of a non-linear finite element model. For the purpose of improving construction methods with fiber-reinforced concretes; the fib investigation used the model in a real-scale test [11]. The best flexure solution was found using the structural reliability index, taking into account different post-cracking strength class &fibber types [12]. In a study in [13] the punching behavior of reinforced high strength concrete (SCH) flat slabs, this work draws attention to the paucity of experimental studies

conducted on SCH slabs [14-17]. Under monotonic vertical stress, the study examines the reasonable usage of HSC by testing four samples with SCH along with one with Osgood striking power was achieved by using just a small amount of HSC in the slabs-column connecting zone; this punching strength was almost identical to that of a slab which had been fully cast in HSC. Australia produces 30 million tons of completed building products yearly, with 56% of that amount coming from concrete and 6% from steel. This indicates that the country is consuming more construction materials. In order to maximize the amount of embodied energy, this study looks at the environmental impact of concrete foundation systems with a particular emphasis upon Low Emission Building (ZEB).An analysis of Australian regulations and standards comparing several slab systems—such as beam & slab, flat slab, and flat plates—for constructions reveals worse energy efficiency [18].

The research in [19] examines contemporary reliability analysis methods for assessing flat slab security requirements. Using three methods—the Mean-Value First Order Second Moment Technique (MVFOSM), the First Order Second Period Technique (FOSM), and Monte-Carlo simulations using Importance Samples (MC-IS)—it examines punched shear barrier design options with shear strengthening. To gauge safety standards, reliability indices are employed. The punched shear strength with reinforcement from shear reliability indices for slab with shear reinforcement are assessed in this work and compared to a target safety level of 3.8. The necessary security standard is achieved by the EN 1992-1-1 regulations, according to the results. For design equation probability, the study recommends utilizing MC-IS and FOSM; nevertheless, MVFOSM might not be appropriate for complete safety [20-22]. The punching strength of foundations and rectangular slabs with and without shear reinforcement has been thoroughly investigated by researchers in [23]. They propose that the ideas of concrete and steel may be used to characterize strength. Nevertheless, the quantity of reinforcement for shear affects how these contributions are systematically evaluated. The evolution of the concrete and steel contributions in shear-reinforced flat slabs is examined in this article, which also offers a technique for calculating and assessing both and contrasts it with guidelines for design in the Euro code [24-27].

Software is a rapid and effective tool which may be utilized to analyze and design structures in the context of earthquakes. By utilizing ETABS software to assess the impacts of wind and earthquake pressures on these structures and guaranteeing that at least 50% of the floor area is utilized for commercial activities, the study in [28] focuses on assessing and constructing business structures with various slab arrangements. Based on IS 456-2000 code book, IS 875-part 5 (2015) code book, wind speed of 55 m/s, and seismic zone 5, the evaluation and design of a structure utilizing M30 grade concrete along with Fe-500 steel is conducted. Comparing the findings to various slab arrangements, they show that a structure with a grid-like slab remains stable and cost-effective. In tall building design, lateral stiffness plays a critical role in preventing collapse caused by gravity loads and second-order P-Delta effects. Compared to traditional slab structures, flat slab buildings are less stiff; nevertheless, maximal rigidity happens when drop is supplied [29]. One-way slabs, two-way slabs, and two-way flat plate reinforcing slabs are examples of transference of load devices with their greatest shear and negative moment capacities, mutual rectangular plates are an especially cost-effective option for formwork and reinforcing thickness. Drop-supported slabs have a higher shear and positive momentary strength than waffle flat slabs, which call for specialized labor and form work. Research takes sandy soil region into consideration [30-32]. Slender, support-free slabs were vital for contemporary structural structures. There has been years of effective use of post-tensioned slabs with unbounded tendons around the world. Recently, prepossessed slabs were developed and built in Poland with span and thinness above prescribed limits. These slabs deflect far from the limit value, even though they are bigger

and thinner than is advised. In this study, a huge span slab is described [33]. Though current research focuses on BIM for point cloud assignment, which may be incorrect in situations of as-built structural changes or lack of information, the usage of terrain laser scanning devices (TLSs) on construction areas is growing. With the goal of minimizing outliers, a unique approach to robust flat and nonlinear features segmentation as well as classification is put forward computationally stage-free approach for extracting flat-slab floor and ceiling points is given, and it works well with polluted datasets. The applicability of the strategy is evaluated on a construction site with 150 million lines and a laboratory with thirty million points [34-35].

2 Methodology

This study shows a comparison between two structures with same loading and properties condition with the effect of slab stiffness considering general RCC slab structure and PT slab Structure to check variations in both in a Tall G+15 RCC building considering seismic zone V with hard soil type Under the seismic effect as per IS 1893(part I) -2016 non-linear analysis.
This study is structured into ten sequential steps. First, a comprehensive literature survey is conducted to gather insights from past research on post-tensioning (PT) techniques, structural analysis methods, and the impact of diaphragms on structures. Next, the selected geometry is modelled, with a plan area of 300 m^2 and a symmetrical frame, utilizing ETABS for structural modelling and SAFE software for modelling the PT slab. Following this, PT slabs are assigned using the analysis tool SAFE, and anchors are allocated to secure the post-tensioning tendons. Subsequently, the PT slab with tendons is generated in a flat slab configuration. Support conditions are then assigned, followed by the allocation of load conditions. The structure is analyzed using ETABS to assess its response to applied loads. Stress diagrams and contours of the loading conditions are generated to visualize the structural behaviour. Finally, the structure is thoroughly analyzed to evaluate its performance under various loading scenarios.

3 Analysis Using Etabs

Csi ETABS & SAFE is a multipurpose program for analyzing the different forms of structures. The following three activities was performed to achieve that goal

1. Modelling of the structure using ETABS
2. Assigning PT slab using SAFE.
3. Analyzing Structure for lateral loads.

Cases considered in this comparative analysis are as follows:

3.1 Case I: RCC conventional Frame with slab

For modeling an RCC traditional frame with a slab in ETABS, define beams and columns for the frame factors, assign segment properties to them, and create shell elements for the slab. Appropriately applying material properties, loadings, and boundary situations ensures correct structural analysis and design of the incorporated system.

Modelling RCC slab structures in ETABS includes developing a finite element model, defining material characteristics, assigning segment properties to slab elements, and making use of appropriate loads and boundary conditions to simulate real-world behavior and observe structural overall performance as shown in Fig .1.

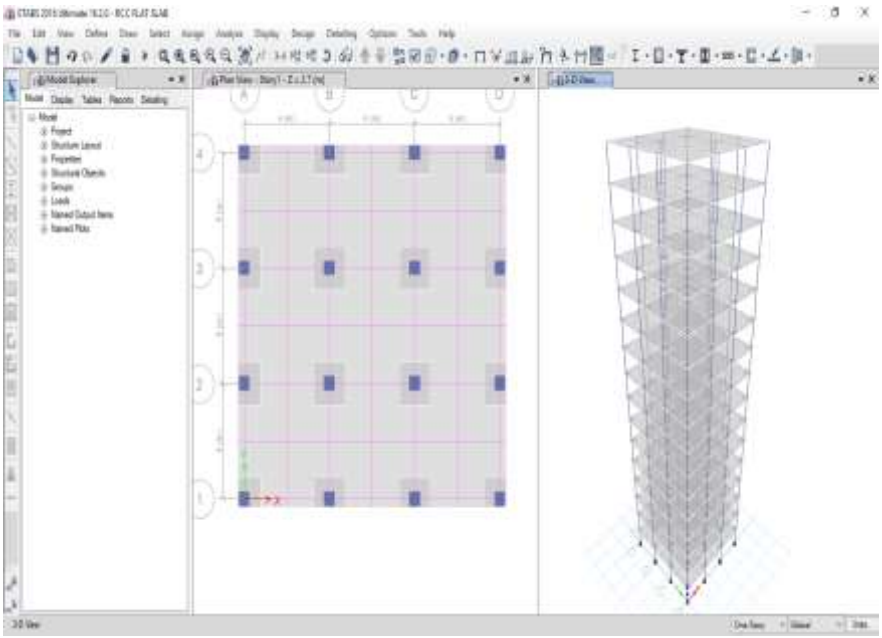

Fig. 1: RCC Slab Structure

3.2 Case II: PT Flat Slab Structure with drop panels

Modeling a post-tensioned (PT) flat slab structure with drop panels in ETABS involves incorporating the post-tensioning tendons inside the slab elements, defining the properties of the post-tensioning substances, appropriately representing the geometry and properties of the drop panels, and observing the structural behavior beneath diverse loading conditions to make certain efficient layout and performance.

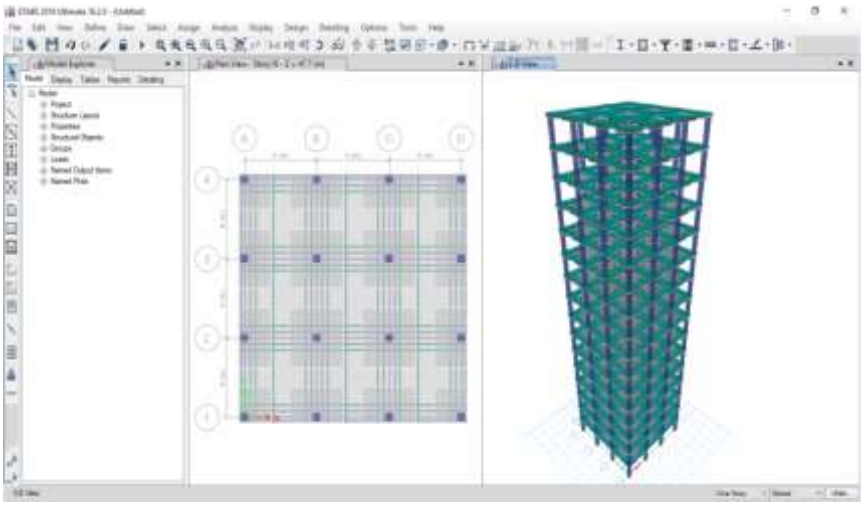

Fig. 2: PT slab structure

Fig. 2 illustrates a post-tensioned (PT) slab structure modeled in ETABS, presenting incorporated post-tensioning tendons within slab factors, correctly representing the geometry and properties of the slab to investigate structural behavior considering prestressing outcomes.

4 Results and Discussion

This is a computer-based evaluation tool used for simulating and observing engineering products and structures. FEA is an effective engineering design application however requires cautious utilization. as an example, integrating it with computer-aided design software program can result in simplistic push-button analysis in the design process, probably resulting in substantial errors, as this warning highlights.

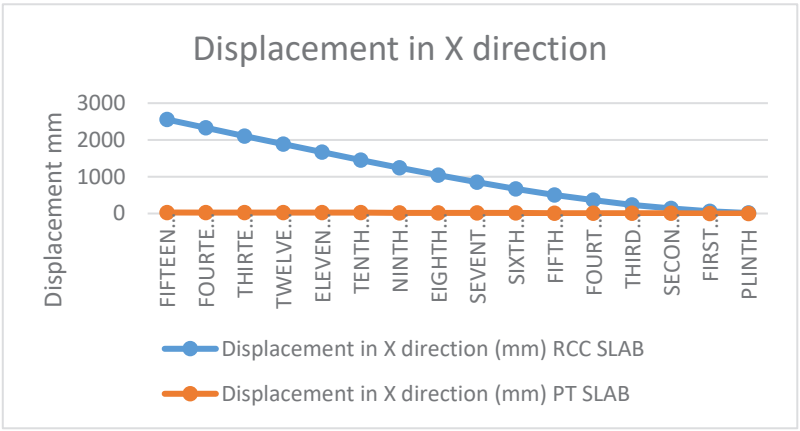

Fig. 3: Displacement in X direction

Fig. 3 depicts the displacement within the X direction, showcasing how much the structure's factors have moved horizontally under the implemented loads or boundary situations. This visualization facilitates engineers recognize how the structure responds to outside forces and become aware of ability areas of concern or immoderate deformation.

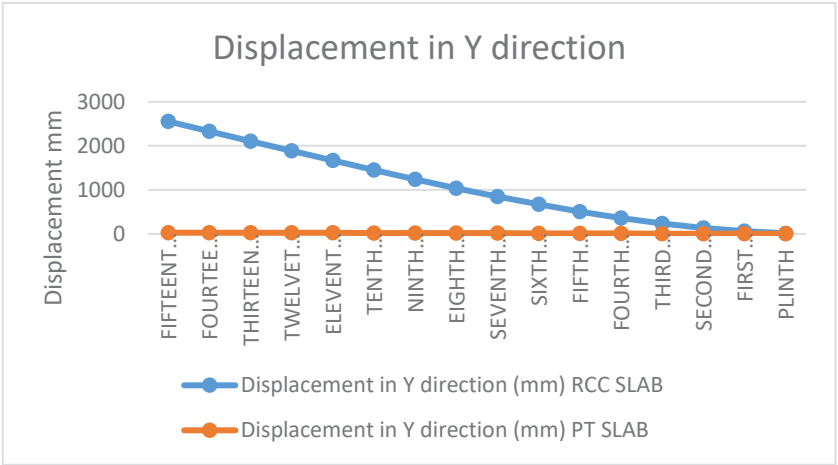

Fig. 4: Displacement in Y direction

Fig. 4 illustrates the displacement in the Y direction, indicating the vertical movement of structural factors because of implemented loads or boundary conditions. This visualization aids in assessing the structural response to vertical forces and identifying areas of huge deformation or stress.

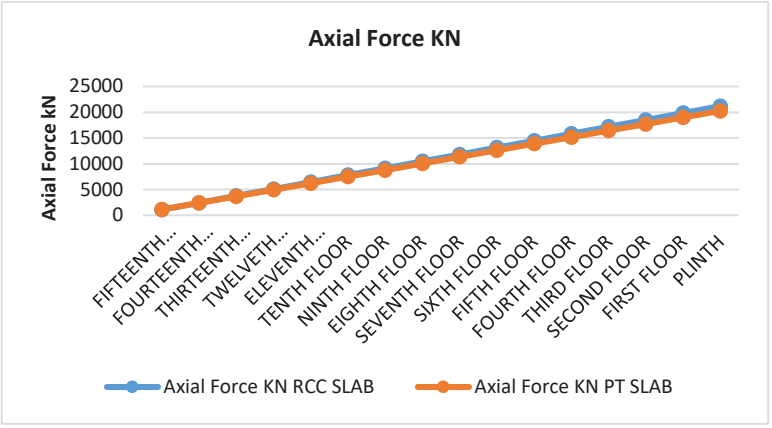

Fig. 5: Axial Force in KN

Fig. 5 provides the distribution of axial forces in kilonewtons (KN) throughout the structural components, offering insights into the magnitude and direction of inner forces alongside each member's length. This visualization serves to evaluate the load-bearing capacity and structural integrity of the factors within diverse loading scenarios.

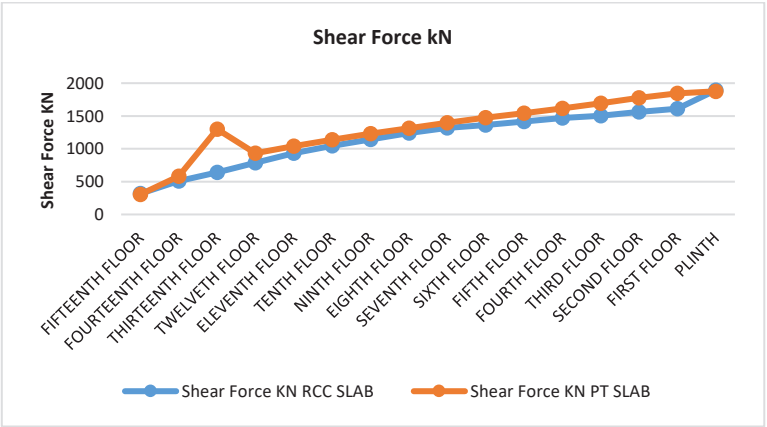

Fig. 6: Shear Force in KN

In Fig. 6, the shear force distribution in kilonewtons (KN) throughout the structural factors is depicted, imparting a detailed illustration of the magnitude and direction of internal forces appearing perpendicular to the length of each member. This visualization aids in comparing the structural balance and capability to withstand lateral loads.

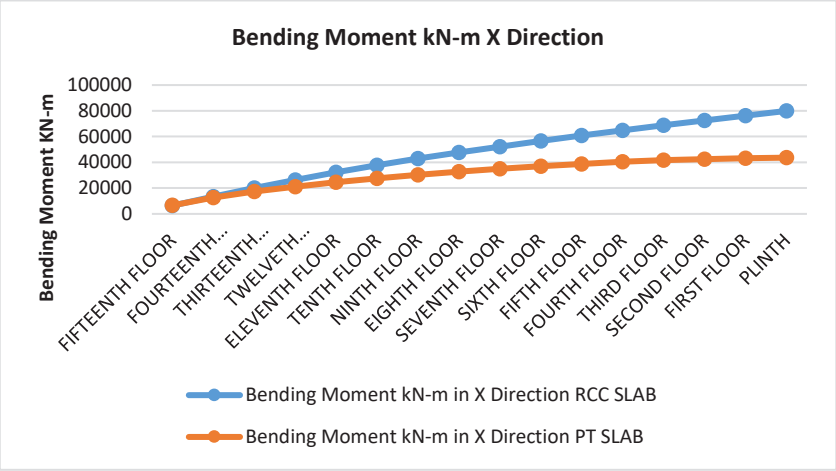

Fig. 7: Bending Moment in X Direction

For an RCC slab, Fig. 7 could imply the bending moments experienced by means of the slab elements within the X direction, supporting engineers recognize how the slab responds to implemented loads including gravity loads or lateral forces. For a PT-slab, Fig. 7 could additionally display the bending moments inside the X direction but would moreover recall the consequences of prestressing tendons on the slab's behavior.

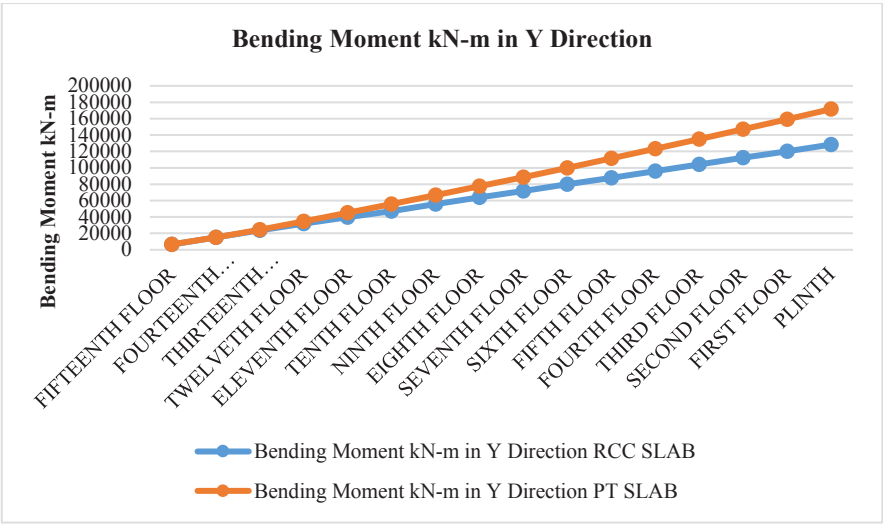

Fig.8: Bending Moment in Y Direction

Fig. 8 represents the bending moments inside the Y direction, providing perception into how structural elements experience bending forces perpendicular to their length. This visualization is critical for expertise the flexural behavior of each RCC and PT slabs, assisting within the evaluation of structural stability and the potential for bending failure.

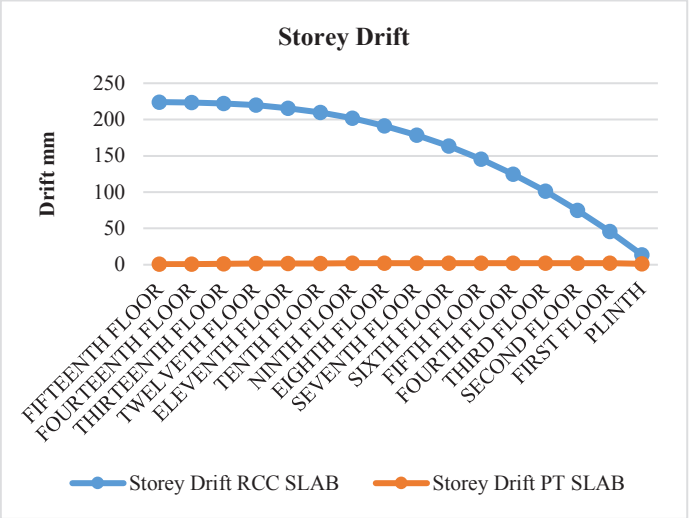

Fig. 9: Storey Drift

Fig. 9 presents the storey drift, showcasing the relative displacement among storeys of buildings subjected to lateral loads. This visualization is vital for assessing structural balance and deformation below seismic or wind forces for each RCC and PT slabs. Engineers can use information storey drift to ensure that buildings are structurally sound and protected, and to guide layout selections to meet overall performance and compliance criteria.

5 Conclusion

Under lateral loading conditions, post-tensioned slabs outperform reinforced concrete slabs (RCC) due to their superior overall performance. In terms of structural performance and stability, PT slabs exhibit reduced bending moments, shear forces, and storey drift. PT slabs seem to offer huge advantages in terms of material optimization and construction financial system, while ensuring adequate structural stability. In addition to highlighting the benefits of incorporating post-tensioning technique into structural designs, the results of this study provide valuable insight for engineers and architects in selecting slab structures for construction projects.

References

1. Sagaseta, Juan, Nsikak Ulaeto, and Justin Russell. "Structural robustness of concrete flat slab structures." American Concrete Institute Special Publication (2016): 273-298.
2. Mohana, H. S., and M. R. Kavan. "Comparative Study of Flat Slab and Conventional Slab Structure Using ETABS for Different Earthquake Zones of India." International Research Journal of Engineering and Technology 2, no. 3 (2015): 1931-1936.
3. Anjaneyulu, B., and K. Jaya Prakash. "Analysis and design of flat slab by using Etabs software." International Journal of Science Engineering and Advance Technology 4, no. 2 (2016): 105-112.
4. Ahmed, Ehab A., Brahim Benmokrane, and Maxime Sansfaçon. "Case study: Design, construction, and performance of the La Chancelière parking garage's concrete flat slabs reinforced with GFRP bars." Journal of Composites for Construction 21, no. 1 (2017): 05016001.

5. Weerasinghe, Pasindu, Kate Nguyen, Priyan Mendis, and Maurice Guerrieri. "Large-scale experiment on the behaviour of concrete flat slabs subjected to standard fire." Journal of Building Engineering 30 (2020): 101255.
6. Aidarov, Stanislav, Ana Nadaždi, Evgeniy Pugach, Nikola Tošić, and Albert de la Fuente. "Cost-oriented analysis of fibre reinforced concrete column-supported flat slabs construction." Journal of Building Engineering 51 (2022): 104205.
7. Vankadara K., Daram S.B., "A novel optimization algorithm for UC, ELD and scheduling of hybrid energy storage system," Multimedia Tools and Applications, , 2024, doi: 10.1007/s11042-024-18207-x.
8. Nayana G.H., Vimala P., "Mathematical Modeling of TFET and Its Future Applications: Ultra Low-Power SRAM Circuit and III-IV TFET," Advanced Ultra Low-Power Semiconductor Devices: Design and Applications, , pp. 77-89, 2023, doi: 10.1002/9781394167647.ch4.
9. Arul S.J., Adhikary P., Jani S.P., Haiter Lenin A., "Moisture diffusion analysis and their effects on the mechanical properties of organic particle filled natural fiber reinforced hybrid polymer composites," International Journal of Polymer Analysis and Characterization, vol. 29, no. 1, pp. 42-55, 2024, doi: 10.1080/1023666X.2023.2301271.
10. Shylaja K.R., Vijayakumar M.V., Davis D.N., Prasad E.V., "Computational test beds for synthetic and robotic agents," IMECS 2011 - International MultiConference of Engineers and Computer Scientists 2011, vol. 2, pp. 1545-1552, 2011.
11. Geluvaraj B., Santhosh Krishna B.V., Umesh M., Vishnu Girish G., Yaqoob Y., "DDoS Attack Detection and Analytics," 2023 International Conference for Advancement in Technology, ICONAT 2023, , 2023, doi: 10.1109/ICONAT57137.2023.10080075.
12. Banoth R., Bhanu G., Shishia N., Vaishnavi M., Saeed H.Y., Asha V., Nijhawan G., Khan I., "Prediction of stock with on-go billing cart using iot and advanced interdisciplinary approaches," E3S Web of Conferences, vol. 507, 2024, doi: 10.1051/e3sconf/202450701013.
13. Sujitha S., Vinod Kumar S., Dechamma V.S., Likitha J., Prajwal R.M., Jayanth R., "Study of Interfacing PLC With HMI for Industrial Applications," Proceedings of the 2023 2nd International Conference on Electronics and Renewable Systems, ICEARS 2023, , pp. 343-346, 2023, doi: 10.1109/ICEARS56392.2023.10084927.
14. Rath S., Senthil Kumar R., Nishanth S.B., Arabale A., Charanraj K.R., "A novel approach for monitoring agricultural production process using wireless sensor networks and Machine Learning," 2023 International Conference on Computer Communication and Informatics, ICCCI 2023, , 2023, doi: 10.1109/ICCCI56745.2023.10128373.
15. Zekrifa D.M.S., prakash R.D., Dhanalakshmi M., Puviarasi R., Ganesh C.S.S., Isaac J.S., Duraipandy P., Rajaram A., "Optimized Controller Design for Renewable Energy Systems by Using Deep Reinforcement Learning Technique," International Journal of Renewable Energy Research, vol. 14, no. 1, pp. 101-110, 2024, doi: 10.20508/ijrer.v14i1.14273.g8866.
16. Reddy V.V., Rajalakshmi B., Boddu B., Verma M.K., Thethi H.P., Sabah H.A., "Hybrid Swarm Intelligence Algorithms for Enhanced Optimal Power Flow in Renewable Energy Networks," 2023 International Conference on Power Energy, Environment and Intelligent Control, PEEIC 2023, , pp. 762-767, 2023, doi: 10.1109/PEEIC59336.2023.10451904.
17. Vinoth, S., Hari Prasad, K., Kanimozhi, G., Satyanarayana, N., "Electrospun nanocomposite polymer fibrous membrane electrolyte for DSSC application," AIP Conference Proceedings, vol. 2005.0, 2018, doi: 10.1063/1.5050765.
18. Rebinth A., Kumar S.M., "Channel separation with CNN model for glaucoma color spectral detection," AIP Conference Proceedings, vol. 2519, 2022, doi: 10.1063/5.0109768.

19. Guna P., "Enhancing Image Super-Resolution with Convolutional Neural Network Ensembles," 2023 International Conference on Communication, Security and Artificial Intelligence, ICCSAI 2023, , pp. 881-885, 2023, doi: 10.1109/ICCSAI59793.2023.10420967.
20. Sivaiah G., Raghu M.S., Prasad S.B.B., Anusuya A.M., Kumar K.Y., Alharethy F., Prashanth M.K., Jeon B.-H., "Synthesis, biological evaluation and molecular docking studies of new pyrimidine derivatives as potent dual EGFR/HDAC inhibitors," Journal of Molecular Structure, vol. 1309, 2024, doi: 10.1016/j.molstruc.2024.138223.
21. Srivastava A., Navaneetha C., Abed N.K., Singh N., Chandrashekar R., Singh H., "Rapid Solidification Techniques for Metal Processing: Microstructure and Properties," E3S Web of Conferences, vol. 505, 2024, doi: 10.1051/e3sconf/202450501020.
22. Prasad A., Asha V., Nirmala A.P., Madhushree S., Kumar M., Sreeja S.P., "Addictive Disorder Susceptibility Prediction Using Machine Learning Approaches," Proceedings of the 3rd International Conference on Artificial Intelligence and Smart Energy, ICAIS 2023, , pp. 627-635, 2023, doi: 10.1109/ICAIS56108.2023.10073701.
23. Mathew J.C., Ilango V., Asha V., "Early-stage Glaucoma Disease Prediction Using Ensemble Optimized Deep Learning Classifier Model," International Journal of Intelligent Engineering and Systems, vol. 16, no. 6, pp. 620-637, 2023, doi: 10.22266/ijies2023.1231.52.
24. Kumar G.M., Chaturvedi P., Rao A.K., Vyas M., Sethi V.A., Swathi B., Jabbar K.A., "Flowing Futures: Innovations in WASH for Sustainable Water, Sanitation, and Hygiene," E3S Web of Conferences, vol. 453, 2023, doi: 10.1051/e3sconf/202345301040.
25. Manjunatha D.V., Sainarayanan G., "Low-power sum of absolute difference architecture for video coding," Lecture Notes in Electrical Engineering, vol. 248 LNEE, pp. 335-341, 2014, doi: 10.1007/978-81-322-1157-0_34.
26. Dongre D., Dongre E., "Mobile multi disease management platform," 2012 International Conference on Green Technologies, ICGT 2012, , pp. 20-24, 2012, doi: 10.1109/ICGT.2012.6477941.
27. Nogales, Alejandro, and Albert de la Fuente. "Numerical-aided flexural-based design of fibre reinforced concrete column-supported flat slabs." Engineering Structures 232 (2021): 111745.
28. Inácio, Micael MG, Massimo Lapi, and Antonio Pinho Ramos. "Punching of reinforced concrete flat slabs–Rational use of high strength concrete." Engineering Structures 206 (2020): 110194.
29. Miller, Dane, Jeung-Hwan Doh, and Mitchell Mulvey. "Concrete slab comparison and embodied energy optimisation for alternate design and construction techniques." Construction and Building Materials 80 (2015): 329-338.
30. Ricker, Marcus, Tania Feiri, Konstantin Nille-Hauf, Viviane Adam, and Josef Hegger. "Enhanced reliability assessment of punching shear resistance models for flat slabs without shear reinforcement." Engineering Structures 226 (2021): 111319.
31. Schmidt, Philipp, Dominik Kueres, and Josef Hegger. "Contribution of concrete and shear reinforcement to the punching shear resistance of flat slabs." Engineering Structures 203 (2020): 109872.
32. Nishanth, CH Lokesh, Y. Sai Swaroop, Durga Chaitanya Kumar Jagarapu, and Pavan Kumar Jogi. "Analysis and design of commercial building with different slab arrangements using ETABS." Materials Today: Proceedings 33 (2020): 700-704.
33. Gupta, K. A. N. C. H. A. N., and M. D. Tasleem. "Non Linear Time History Analysis Of Asymmetrical Flat Slab Buildings." Science and Engineering 24, no. 8 (2020).

34. Szydlowski, Rafal, and Barbara Labuzek. "Post-tensioned concrete long-span slabs in projects of modern building construction." In IOP Conference Series: Materials Science and Engineering, vol. 245, no. 2, p. 022065. IOP Publishing, 2017.
35. Maalek, R., D. D. Lichti, and J. Ruwanpura. "Robust classification and segmentation of planar and linear features for construction site progress monitoring and structural dimension compliance control." ISPRS Annals of the Photogrammetry, Remote Sensing and Spatial Information Sciences 2 (2015): 129-136.

Water and Hydrology: Challenges, Sustainable Strategies and Future Trends

Aravinda K[1*], *Jajimoggala* Sravanthi[2], *Sorabh* Lakhanpal[3], *Anurag* Shrivastava[4], *Ravi* Kalra[5], *Q*. Mohammad[6], *Nirmith* Kumar Mishra[7]

[1]Department of Electronics and Communication Engineering, New Horizon College of Engineering, Bangalore, India.
[2]Department of CSE, GRIET, Bachupally, Hyderabad, Telangana, India.
[3]Lovely Professional University, Phagwara, India.
[4]Saveetha School of Engineering, Saveetha Institute of Medical and Technical Sciences, Chennai, Tamilnadu, India.
[5]Lloyd Institute of Engineering & Technology, Knowledge Park II, Greater Noida, Uttar Pradesh, India.
[6]Hilla University College, Babylon, Iraq.
[7]Department of Aeronautical Engineering, MLR Institute of Technology, Hyderabad, Telangana, India-500088

Abstract. The paper gives a comprehensive review of how human activities influence normal hydrological forms by clarifying the diverse impacts on the accessibility, quality, and conveyance of water. The paper revealed the complex exchange between data and natural morals that are reconfiguring the worldwide water scene through conflicting facts of major causes like urbanization, deforestation, industrialization, and climate change. The natural areas are all disturbed by human activities and pollution and by these changes the impact is on run-off patterns, infiltration rates, and groundwater recharge processes. In metropolitan cities, there are more impermeable spaces which leads to more runoffs. In these areas, the water filtration rate and groundwater recharge are very low. Dams and other hydropower and water system processes that disturb the natural stream of waterways in addition to their aquatic habitat division have too changed stream morphology. Urban stormwater, industrial and farming runoff, are among numerous other sources contaminate freshwater systems with pathogens heavy metals, chemicals supplements, etc hence risking both human life and natural maintainability. Changes in precipitation and temperature impact the timing of snow melt, patterns of river flow, and restoration of groundwater; changes in disaster patterns together with sea level rise worsen coastal flooding and fresh-water salinization. These adjustments to common hydrologic processes have significant suggestions for biological systems, communities, and economies consisting of water accessibility for farming, industry, and domestic purposes, energy generation, and human well being. Among procedures aimed at reacting to these challenges is the Integrated Water Resource Management (IWRM) which contends for comprehensive approaches that accommodate competing requests over water resources while guaranteeing their supportability as well as adaptability to

* Corresponding author: aravinda_K@gmail.com

© The Authors, published by EDP Sciences. This is an open access article distributed under the terms of the Creative Commons Attribution License 4.0 (https://creativecommons.org/licenses/by/4.0/).

hydrological unpredictability of availability. Feasible water administration requires an extend of activities such as water preservation and proficiency measures, contamination control, watershed management, and climate alteration adjustment. As it may, social orders can explore these exceedingly complicated interconnected issues on their water assets by adopting administrative systems, innovative advancements, and shifts in social conduct that will be pointed at economical water utilization for the eras to come.

Keyword-: Industrialization, hydrological process, climate change, sustainability, water management, pollution, groundwater, urbanization, hydropower, infiltration.

1 Introduction

Water plays a central portion in most common forms. The high particularly warm capacity of water contains an awesome impact on the worldwide vitality adjustment. Hydrology, which is actually “water science,” incorporates the examination of water's events and development over and underneath the Earth's surface, properties of water, and its interaction with biotic and non-living perspectives of the environment. Common resources' talks are inadequate without hydrological sciences. In dry locales, accomplishing reasonable allotment and sustainable use of freshwater supplies is one of the biggest challenges that governments confront, affecting both worldwide connections between nations as well as states, cities, and indeed personal clients [1]. In any case, the twentieth century has seen a colossal increment in water utilization coupled with developing dangers to its contamination, whereas these patterns have proceeded into the past thousand years. Urban hydrological teaching is generally youthful but is progressively imperative in a world that experienced a dangerous world population development in the final few decades and with distinctive urban elements around the globe. Urban highlights such as buildings, streets, stopping parcels, and asphalts modify neighbourhood meteorological conditions and in this manner influence precipitation sums and escalate [2]. The counterfeit warming properties of larger than average cities may alter the characteristics of precipitation, the way by which it falls from over cloud base to the ground surface and how it comes to the earth's surface counting escalated [3]. An extending city poses challenges in terms of water quality that can as it were be tended to through strategies aimed at decreasing weights on surface waters and their environmentally touchy riparian zones [3]. Be that as it may, the two communities of hydrology and water quality sciences are both inquisitive about understanding more approximately the spatial scale common to all three endpoints of the framework (surface, subsurface, and channels) through distinctive points [4]. Challenges posed by advancing water administration practices have required an expansion of catchment-scale-based models to mainland and worldwide scales. In this respect, hydrological data at continental and worldwide levels is exceptionally valuable for water allotment choices in worldwide bowls such as large waterways or countries [5], to realize worldwide water security objectives, as a premise for national water evaluations, to assess water assets all around, back improvement of universal surge approach and operational surge determining administrations, give advice on things relating to water quality/ecological concerns, as well as distinguish impacts of climate extremes on water assets [6].

2 Impacts of Human Activity on Natural Processes in Hydrology

The hydrological exercises of individuals have changed common methods with regard to water and the result has been a alter in its accessibility, quality and dissemination. Arrive utilize is one of the major ways through which man influences hydrologic forms [7-12]. Urbanization, deforestation, and agrarian extension adjust the arrive surface so that changes happen within the design of runoff, rates of invasion and Evapotranspiration (ET). In urban ranges for occurrence when normal vegetation is supplanted by impenetrable surfaces, it increments surface run-off in this manner driving to higher crest streams and diminished groundwater revive [13]. Once more human exercises modify the morphology or stream administration of streams, streams or wetlands. Dams and supplies are developments made for era of hydropower as well as water system direct stream streams, disturb silt transport and break up oceanic living spaces [14]. Toxins from mechanical sources, farming sources as well as urban sources are exceptionally perilous to water quality since they can effortlessly annihilate sea-going biological systems [15]. Supplement runoff from rural lands contributes to eutrophication in water bodies coming about into algal sprouts and oxygen exhaustion. Additionally overwhelming metals come into freshwater frameworks through mechanical effluents and urban runoff whereas chemicals too enter causing them to be contaminated with pathogens in this way making them destructive to both human creatures who depend on such waters for their day-to-day needs [16]. Human made climate alter compounds stresses that are as of now being experienced by hydrological frameworks, and this changes the design of introductions, heighten temperature as well as extraordinary climate occasions [17]. When snowfall softens at a diverse time than it ordinarily does, there's effect on stream designs in expansion to groundwater revive rates related with temperature and precipitation changes. There are too rising sea levels; these together with changing storm designs make coastal flooding and salinization of freshwater assets more regrettable [18]. All these adjustments that happen in common hydrological forms have far-reaching suggestions for environments, social orders and economies which influence water accessibility for horticulture, industry and household utilize in this manner affecting nourishment security, vitality generation as well as human well-being [19-22].

Besides, modifications in both water quality and supply put earthly biodiversity at chance nearby environment administrations such as water decontamination or surge direction counting living space. Integrated Water Resource Management (IWRM) approaches which advance all-encompassing administration of water assets to adjust clashing requests and guarantee maintainability are progressively being proposed as the implies towards tending to these issues [23-26]. IWRM includes different partners extending from government divisions through NGOs to nearby communities to the private segment so that they can take part in choices pointed at improving reasonable and viable utilization of water [27]. Unexpectedly, there are endless issues and issues which take after from human exercises that influence water bodies and this is often why the Integrated Water Resource Management standards are required for overseeing these challenges. Going forward we can see that ideal administration of water assets includes a blend of lawful, organization, financial and approach devices [28]. For case, advancement control directions empower maintainable hones such as green foundation and moo affect improvement to moderate impacts of urbanization on hydrologic forms. In expansion, incentive-based preservation programs may be utilized to decrease agrarian runoff by empowering ranchers to receive such hones as cover editing and supplement administration [29].With the addition, mechanical contamination impacts new water bodies hence activities such as speculation in wastewater treatment offices and authorization of contamination control measures can offer assistance in moderation whereas

at the same time driving selection of water sparing advances like dribble water system or reusing [30-33]. The issues and impacts are shown below in Table 1.

Table 1: Impacts of Human activity on Hydrology

Issues	Impact	Reference
Alteration of the land surface brought about by agricultural growth, deforestation, and urbanization	Variations in the rates of evapotranspiration, infiltration, and runoff result in higher peak flows, less groundwater recharge, and increased surface runoff.	[34]
Human activity-induced changes to the morphology and flow management of streams	Aquatic habitats, sediment transport, and natural stream flow are all hampered by the construction of dams and reservoirs.	[35]
Industrial, agricultural, and urban sources of pollution ecosystems, and health risks	Toxins, heavy metals, and chemicals contaminating water bodies, which cause eutrophication, the collapse of aquatic ecosystems, and health risks	[36]
Climate change brought on by humans	The timing of snowmelt, stream patterns, groundwater recharge rates, coastal flooding, and salinization of freshwater resources are all impacted by temperature changes, altered precipitation patterns, and extreme weather events.	[37]
Consequences for economies, societies, and ecosystems	Effects on domestic, industrial, and agricultural water availability, which have an impact on human health, energy production, and food security	[38]
Risk to terrestrial biodiversity and ecosystem services	Threat to biodiversity and ecosystem services such as water purification and flood regulation	[39]
Integrated Water Resource Management (IWRM) approaches	Advocates for holistic management of water resources involving various stakeholders to address conflicting demands and ensure sustainability	[40]
For the best management of water resources, a mix of legislative, administrative, economic, and policy instruments is required.	Development control laws that encourage environmentally friendly behaviour are a few examples, as are incentive-based conservation initiatives, the purchase of wastewater treatment plants, and the implementation of pollution control policies.	[41], [42]

3 Strategies for Managing Sustainable Use of Water

It is vital to say that this approach comprises of multidimensional procedures for overseeing the utilization of water within the long run whereas at the same time keeping up natural

judgment, guaranteeing impartial get to to water resources and assembly the wants of both current and future eras [43]. One key viewpoint of feasible water administration includes advancing water preservation and effectiveness measures over different segments, counting farming, industry, and urban regions [44]. Technology-based arrangements such as dribble water system frameworks, low-flow installations or proficient water system hones can decrease water utilization levels by colossal edges and minimize wastage [45-49]. Reusing wastewater through treatment into non-potable employments like water system, mechanical forms and groundwater revive can check on freshwater sources' exhaustion weight. Campaigns focused on at common open mindfulness, instruction activities as well as motivating forces for pro-environmental behaviours are a few of the approaches that advance person activities towards feasible water utilize [50]. Another imperative range in connection to feasible water administration incorporates tending to defilement and contamination. The endeavour coordinated towards lessening contamination from industrialization, farming also urbanization incorporate creating administrative systems, contamination control measures, contributing in squander water treatment framework [51]. Mechanical companies may be compelled to handle the squander they create some time recently discharging it into water bodies, though agrarian hones can minimize contamination of streams and lakes due to supplement runoff and soil disintegration through compelling supplement administration and disintegration control [52]. So also, speculations in wastewater treatment plants and advancement of sanitation foundation are basic for checking the release of untreated sewage into conduits consequently shielding water quality as well as human well being [53].

The coordinates watershed administration is fundamental for assurance and rebuilding of common hydrological forms at the watershed scale. It incorporates preservation and rebuilding of riparian buffers, wetlands, and other characteristic living spaces that can move forward water quality, improve surge control capacity, bolster biodiversity. Subsequently, Riparian buffer zones normally evacuate dregs and other poisons from entering into waterways; whereas wetlands act like wipes taking up abundance waters amid surges at that point discharge it gradually amid dry seasons [54]. Decentralization as well as community-based approaches towards water administration are crucial for feasible water assets. This implies that engaging nearby communities in making choices approximately their claim domains or overseeing their possess assets guarantees possession as well as responsibility, leading to more effective and equitable water management outcomes [55]. Community-based water administration activities such as water client affiliations, watershed chambers, and participatory arranging forms can upgrade neighbourhood capacity, advance social cohesion, and encourage the usage of economical water administration practices overall this incorporates creating the capacity of individuals to oversee water in an unexpected way, make strides social cohesion and advance feasible hones [56].

In arrange to adjust to the changes in precipitation patterns, rise in worldwide temperatures, expanded recurrence and concentrated of extraordinary climate occasions like dry spell and surges among others, there's require for climate alter adjustment methodologies. To be specific, setting up climate-resilient water administration strategies such as development of supplies and artificial recharge frameworks encompasses a potential to gather with overflow rainwater during stormy season that can be utilized amid consequent dry periods making it conceivable to manage with dry spell circumstances as well as inadequate in water supplies [57]. The same way, biodiversity can be improved through characteristic environments reclamation such as the coral reefs and mangroves; these are able of giving coastlines assurance against rising ocean level storm surges whereas at the same time rendering environment administrations [58]. Cultivating universal participation and collaboration is significant for tending to global water issues, advancing equitable sharing of water assets,

and overseeing water-related clashes. Fig 1 shows a process for managing sustainable use of water. Table 2 contains Six parameter about Hydrological model [59].

Table 2: Summary of the six parameters in the modified hydrological model

Parameter	Definition (Units)	Lower Bound	Upper Bound
Cmax	Maximum storage capacity (mm)	50	600
B	Shape parameter of the soil moisture capacity probability distribution	0.05	1.95
α	Ratio of the distribution of flow between quick and slow reservoirs	0.01	1
n	Number of quick flow reservoirs	1	4
Kslow	Conductivity of slow flow reservoir (1/day)	0.001	0.1
Kquick	Conductivity of quick flow reservoir (1/day)	0.1	0.95

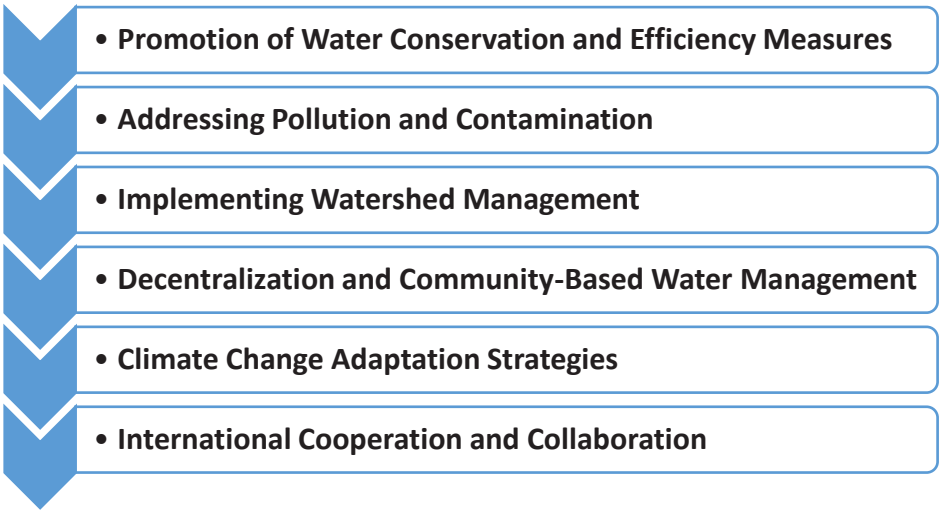

Fig. 1: Process for Managing Sustainable Use of Water

4 Future and Emerging Trends in Hydrology

Hydrology's future and developing patterns are moulded by different components counting innovation progression, climate alter and societal needs. Inaccessible detecting and geographical information examination strategies for checking hydrological forms at diverse spatial scales are progressively getting to be vital [60]. They give data on precipitation, soil dampness, ET, and arrival cover flow that empower researchers to get water-related wonders like surges, dry spells, and water accessibility way better [61]. Besides, propels in computational demonstrating, machine learning, and information digestion strategies have expanded the exactness as well as the unwavering quality of hydrological models coming about in superior water assets administration and choice making. Moreover, there's a developing mindfulness of the ties that exist between hydrological frameworks with those of other components of the Earth's framework such as the climate, biosphere, and hydrosphere. Complex feedback driving changes within the hydrological cycle in Coordinates Soil

framework models which replicate intuition between the seas, climate; arrival surface; and ice sheets.

Climate change also causes major alterations within the hydrological designs and forms and this has colossal suggestions on water assets administration and biological system well being. Temperature increment, changing precipitation designs, softening ice sheets, and ice caps shift runoff timing and size that influence water accessibility, quality, and dissemination. These changes will require inventive ways of arranging for water assets, planning foundations, and adjusting to them in this manner relieving the dangers that are related to those approaches as well as strong choice supporting apparatuses. The recurrence of extraordinary climate occasions such as typhoons, storms, and heatwaves is increasing whereas concentration is additionally rising causing hydrological dangers like surges, avalanches, and waterborne infections in this manner debilitating human lives, property, and framework. Economical water administration standards are being grasped where social orders start to realize that competing requests for rare freshwater must be adjusted against guaranteeing natural judgment as well as societal value.

For their capacity to improve water quality, control the stream, and give a few co-benefits for biodiversity preservation, climate alter adjustment, and community flexibility, nature-based arrangements such as green foundation, normal surge administration, and biological system reclamation are picking up conspicuousness. Water administration hones are being revolutionized by the rise of shrewd water innovations and computerized developments that empower optimization of operation in real-time and robotization for water frameworks. Hydrological information collection and examination utilizing web of things gadgets, shrewd sensors, and huge information analytics stages is making a difference choice producers come up with significant bits of knowledge. In expansion to empowering secure and effective exchanges and trades of water rights and allotments, this innovation is being investigated on how it can improve straightforwardness, and traceability as well as responsibility in water administration and asset administration [35-36]. In outline; quick mechanical progressions, advancing climate designs coupled with changes in societal needs characterize future patterns in hydrology. Fig 2 contains some emerging trends in hydrology field.

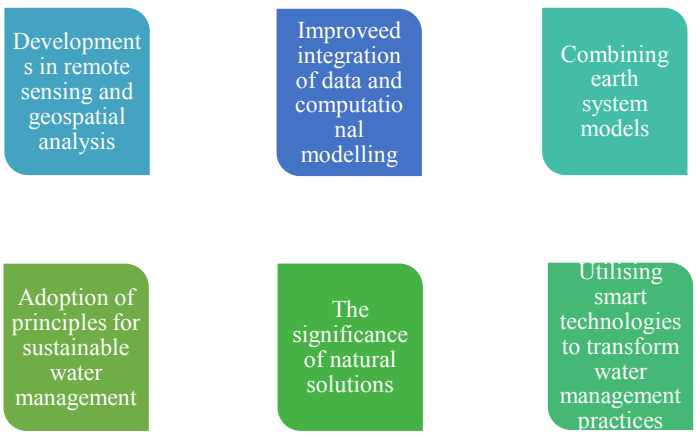

Fig. 2: Emerging trends

5 Conclusion

Eventually, this paper has given a careful examination of the complex relationship between human conduct and commonplace hydrological shapes. In this paper, we already saw that it gives a rundown of how human exercises have influenced the accessibility, immaculateness, and dispersion of water. So, the basis on that we have some key areas covered in points.

- Going forward land surfaces will be altogether changed by human exercises like urbanization, deforestation, farming, and industrialization, which also risk groundwater revive components and disturb runoff designs. On the other, these changes are advanced and exacerbated by contamination from an assortment of sources, which poses genuine threats to biological systems and human well-being.
- Contributing to growing precipitation plans and powers already-occurring exceptional climate events, climate alter increases precariousness in hydrological systems. Situations, social orders, and economies are affected when water gets to be uncommon for manufacturing, agrarian water frameworks, and other purposes outside of family utilization, such as food security, imperativeness era, and well-being headway.
- To understand all these bunch issues, IWRM has gotten to be a critical approach to water assets administration. Concerning feasible water administration, this approach offers a total framework that empowers differing procedures to cater to the distinctive needs of water, keep up maintainability, and stand up to hydrological vulnerabilities.
- In the hydrology sector, there will be future trends affected by the fast progression of innovation, moving social values, and changing climatic designs. The technological improvements and headways just like the developing reliance on remote detection or sensing, the acknowledgment of nature-based arrangements, and the improvement of keen water innovations that advance and can move forward in water asset administration and increment its flexibility, and versatility to moving hydrological situations.

All these findings underscore the requirement for facilitated nearby, national, and worldwide endeavours to moderate rising anthropogenic weights and climate potential, with an accentuation on cost-effective water administration for the display and future. By putting high esteem on agreeable strategies, inventive arrangements, and versatile forms, social orders can successfully investigate the complex web of water-related challenges and get ready to guarantee water assets and develop adaptability within the confront of a questionable future and that will be one of the great moves my mankind.

References

1. Hornberger, George M., Patricia L. Wiberg, Jeffrey P. Raffensperger, and Paolo D'Odorico. Elements of physical hydrology. JHU Press, 2014.
2. Hutchins, Michael G., Scott J. McGrane, James D. Miller, Alex Hagen-Zanker, Thomas R. Kjeldsen, Simon J. Dadson, and Clare S. Rowland. "Integrated modeling in urban hydrology: reviewing the role of monitoring technology in overcoming the issue of 'big data'requirements." Wiley Interdisciplinary Reviews: Water 4, no. 1 (2017): e1177.
3. McGrane, Scott J. "Impacts of urbanisation on hydrological and water quality dynamics, and urban water management: a review." Hydrological Sciences Journal 61, no. 13 (2016): 2295-2311.
4. Hrachowitz, Markus, Paolo Benettin, Boris M. Van Breukelen, Ophelie Fovet, Nicholas JK Howden, Laurent Ruiz, Ype Van Der Velde, and Andrew J. Wade. "Transit times—The link between hydrology and water quality at the catchment scale." Wiley Interdisciplinary Reviews: Water 3, no. 5 (2016): 629-657.

5. United Nations Economic Commission for Europe, Convention on the Protection and Use of Transboundary Watercourses and International Lakes, GE.13-26823—February 2014—3,129—ECE/MP.WAT/41, U. N. Off. at Geneva, 2014.
6. Archfield, Stacey A., Martyn Clark, Berit Arheimer, Lauren E. Hay, Hilary McMillan, Julie E. Kiang, Jan Seibert et al. "Accelerating advances in continental domain hydrologic modeling." Water Resources Research 51, no. 12 (2015): 10078-10091.
7. Wada, Yoshihide, Marc FP Bierkens, Ad De Roo, Paul A. Dirmeyer, James S. Famiglietti, Naota Hanasaki, Megan Konar et al. "Human–water interface in hydrological modelling: current status and future directions." Hydrology and Earth System Sciences 21, no. 8 (2017): 4169-4193.
8. Ferreira, Carla Sofia Santos, Rory Peter Dominic Walsh, João Pedro Carvalho Nunes, Tammo S. Steenhuis, Manuel Nunes, João Luís Mendes Pedroso de Lima, Celeste Oliveira Alves Coelho, and António José Dinis Ferreira. "Impact of urban development on streamflow regime of a Portuguese peri-urban Mediterranean catchment." Journal of soils and sediments 16 (2016): 2580-2593.
9. Zhang, Xuan, Changling Fang, Yuan Wang, Xiaoyi Lou, Ying Su, and Dongmei Huang. "Review of effects of dam construction on the ecosystems of river estuary and nearby marine areas." Sustainability 14, no. 10 (2022): 5974.
10. Wurtsbaugh, Wayne A., Hans W. Paerl, and Walter K. Dodds. "Nutrients, eutrophication and harmful algal blooms along the freshwater to marine continuum." Wiley Interdisciplinary Reviews: Water 6, no. 5 (2019): e1373.
11. Awasthi, A., Saxena, K. K., & Arun, V. (2021). Sustainable and smart metal forming manufacturing process. Materials Today: Proceedings, 44, 2069-2079.
12. Dierauer, Jennifer R., D. M. Allen, and P. H. Whitfield. "Climate change impacts on snow and streamflow drought regimes in four ecoregions of British Columbia." Canadian Water Resources Journal/Revue canadienne des ressources hydriques 46, no. 4 (2021): 168-193.
13. Upadhyay, Ravi Kant. "Markers for global climate change and its impact on social, biological and ecological systems: A review." American Journal of Climate Change 9, no. 03 (2020): 159.
14. Katusiime, Juliet, and Brigitta Schütt. "Integrated water resources management approaches to improve water resources governance." Water 12, no. 12 (2020): 3424.
15. Ibisch, Ralf B., Janos J. Bogardi, and Dietrich Borchardt. Integrated water resources management: concept, research and implementation. Springer International Publishing, 2016.
16. Batalini de Macedo, Marina, Marcus Nobrega Gomes Junior, Thalita Raquel Pereira de Oliveira, Marcio H. Giacomoni, Maryam Imani, Kefeng Zhang, Cesar Ambrogi Ferreira do Lago, and Eduardo Mario Mendiondo. "Low Impact Development practices in the context of United Nations Sustainable Development Goals: A new concept, lessons learned and challenges." Critical Reviews in Environmental Science and Technology 52, no. 14 (2022): 2538-2581.
17. Pandey, A., Awasthi, A., & Saxena, K. K. (2020). Metallic implants with properties and latest production techniques: a review. Advances in Materials and Processing Technologies, 6(2), 405-440.
18. Kattel, Giri, Jessica Reeves, Andrew Western, Wenjing Zhang, Wei Jing, Suzanne McGowan, Lan Cuo et al. "Healthy waterways and ecologically sustainable cities in Beijing-Tianjin-Hebei urban agglomeration (northern China): Challenges and future directions." Wiley Interdisciplinary Reviews: Water 8, no. 2 (2021): e1500.
19. Julio, Natalia, Ricardo Figueroa, and Roberto D. Ponce Oliva. "Water resources and governance approaches: Insights for achieving water security." Water 13, no. 21 (2021): 3063.

20. Hoekstra, Jorrit Feike. "Water-saving at the household level using gamification features: A design-oriented study in the Netherlands." Master's thesis, University of Twente, 2022.
21. Sahoo, S., and S. Goswami. "Theoretical framework for assessing the economic and environmental impact of water pollution: A detailed study on sustainable development of India." Journal of Future Sustainability 4, no. 1 (2024): 23-34.
22. Onu, Matthew Adah, Olusola Olaitan Ayeleru, Helen Uchenna Modekwe, Bilainu Oboirien, and Peter Apata Olubambi. "Water and wastewater safety plan in sub-Saharan Africa." In Water, the Environment and the Sustainable Development Goals, pp. 223-240. Elsevier, 2024.
23. Muhar, Susanne, Jan Sendzimir, Mathias Jungwirth, and Severin Hohensinner. "Restoration in integrated river basin management." Riverine ecosystem management: Science for governing towards a sustainable future (2018): 273-299.
24. Mugoro, Amare, Lakew Desta, Tariku Alemu, and Alex Schumacher. "Community Based Participatory Watershed Guideline CBPWSG Part-1." (2020).
25. Dhyani, Shalini, Anil Kumar Gupta, and Madhav Karki, eds. Nature-based solutions for resilient ecosystems and societies. New Delhi: Springer, 2020.
26. Yazar, Attila, and Akhtar Ali. "Water harvesting in dry environments." Innovations in dryland agriculture (2016): 49-98.
27. Awasthi, A., Saxena, K. K., & Arun, V. (2020). Sustainability and survivability in manufacturing sector. In Modern Manufacturing Processes (pp. 205-219). Woodhead Publishing.
28. Pettorelli, N., Safi, K., & Turner, W. Satellite remote sensing for applied ecologists: opportunities and challenges. Journal of Applied Ecology, 51(4), (2014), 839-848.
29. Pandey, Ashish, Gagandeep Singh, V. M. Chowdary, Mukunda Dev Behera, A. Jaya Prakash, and V. P. Singh. "Overview of geospatial technologies for land and water resources management." Geospatial Technologies for Land and Water Resources Management (2022): 1-16.
30. Kumar, Vijendra, Naresh Kedam, Kul Vaibhav Sharma, Darshan J. Mehta, and Tommaso Caloiero. "Advanced machine learning techniques to improve hydrological prediction: A comparative analysis of streamflow prediction models." Water 15, no. 14 (2023): 2572.
31. Stocker, T. F., & Schmittner, A. Influence of CO2 emission rates on the stability of the thermohaline circulation. Nature, 388(6641), (2016), 862-865
32. Yildiz, Veysel, Murat Ali Hatipoglu, and S. Yurdagül Kumcu. "Climate change impacts on water resources." In Water and Wastewater Management: Global Problems and Measures, pp. 17-25. Cham: Springer International Publishing, 2022.
33. Parashuram, L., Sreenivasa, S., Akshatha, S., & Udayakumar, V. (2019). A non-enzymatic electrochemical sensor based on ZrO2: Cu (I) nanosphere modified carbon paste electrode for electro-catalytic oxidative detection of glucose in raw Citrus aurantium var. sinensis. Food chemistry, 300, 125178.
34. Kumar, K. Y., Saini, H., Pandiarajan, D., Prashanth, M. K., Parashuram, L., & Raghu, M. S. (2020). Controllable synthesis of TiO2 chemically bonded graphene for photocatalytic hydrogen evolution and dye degradation. Catalysis Today, 340, 170-177.
35. Jayabal, R., Subramani, S., Dillikannan, D., Devarajan, Y., Thangavelu, L., Nedunchezhiyan, M., ... & De Poures, M. V. (2022). Multi-objective optimization of performance and emission characteristics of a CRDI diesel engine fueled with sapota methyl ester/diesel blends. Energy, 250, 123709.
36. Masum, J. H. "Climatic Hazards in Bangladesh: A Literature Review." Coastal Development Partnership (CDP), Bangladesh, Coastal Development Partnership (CDP), Bangladesh (2019).

37. Padmaja, B., Prasad, V. R., & Sunitha, K. V. N. (2018). A machine learning approach for stress detection using a wireless physical activity tracker. International Journal of Machine Learning and Computing, 8(1), 33-38.
38. Malagavelli, V., Angadi, S., Prasad, J. S. R., & Joshi, S. (2018). Influence of metakaolin in concrete as partial replacement of cement. Int J Civil Eng Technol, 9(7), 105-111.
39. Awasthi, A., Saxena, K. K., & Dwivedi, R. K. (2021). An investigation on classification and characterization of bio materials and additive manufacturing techniques for bioimplants. Materials Today: Proceedings, 44, 2061-2068.
40. Bhukya, L., Kedika, N. R., & Salkuti, S. R. (2022). Enhanced maximum power point techniques for solar photovoltaic system under uniform insolation and partial shading conditions: a review. Algorithms, 15(10), 365.
41. Vijayakumar, Y., Nagaraju, P., Yaragani, V., Parne, S. R., Awwad, N. S., & Reddy, M. R. (2020). Nanostructured Al and Fe co-doped ZnO thin films for enhanced ammonia detection. Physica B: Condensed Matter, 581, 411976.
42. Cheruvu, A., Radhakrishna, V., & Rajasekhar, N. (2017, May). Using normal distribution to retrieve temporal associations by Euclidean distance. In 2017 International Conference on Engineering & MIS (ICEMIS) (pp. 1-3). IEEE.
43. Kumar, K. U., Babu, P., Basavapoornima, C., Praveena, R., Rani, D. S., & Jayasankar, C. K. (2022). Spectroscopic properties of Nd3+-doped boro-bismuth glasses for laser applications. Physica B: Condensed Matter, 646, 414327.
44. Kalyani, G., Janakiramaiah, B., Karuna, A., & Prasad, L. N. (2023). Diabetic retinopathy detection and classification using capsule networks. Complex & Intelligent Systems, 9(3), 2651-2664.
45. Telagam, N., Kandasamy, N., & Nanjundan, M. (2017). Smart sensor network based high quality air pollution monitoring system using labview. International Journal of Online Engineering (iJOE), 13(08), 79-87.
46. Chaudhury, S., Krishna, A. N., Gupta, S., Sankaran, K. S., Khan, S., Sau, K., ... & Sammy, F. (2022). Effective image processing and segmentation-based machine learning techniques for diagnosis of breast cancer. Computational and Mathematical Methods in Medicine, 2022.
47. Ramu, G. (2018). A secure cloud framework to share EHRs using modified CP-ABE and the attribute bloom filter. Education and Information Technologies, 23(5), 2213-2233.
48.
49. Abdelfattah, I., and A. M. El-Shamy. "Review on the escalating imperative of zero liquid discharge (ZLD) technology for sustainable water management and environmental resilience." Journal of Environmental Management 351 (2024): 119614.
50. Wendling, Laura A., and Erika E. Holt. "Integrating engineered and nature-based solutions for urban stormwater management." Women in Water Quality: Investigations by Prominent Female Engineers (2020): 23-46.
51. Padhy, P. K., et al. Urban water demand forecasting—a review of methods and models. Water Resources Management, 30(5) (2016), 1831-1854.
52. Trigoso, F. F., Sankaran, S., & Jeppesen, E. Big data in water research: a systematic review. Science of the Total Environment, 649 (2018), 1281-1294.
53. Satilmisoglu, Talat Kemal, Yusuf Sermet, Musa Kurt, and Ibrahim Demir. "Blockchain Opportunities for Water Resources Management: A Comprehensive Review." Sustainability 16, no. 6 (2024): 2403.
54. Jung, Donghwi, Young Hwan Choi, and Joong Hoon Kim. "Multiobjective automatic parameter calibration of a hydrological model." Water 9, no. 3 (2017): 187.
55. Yogananda, H. S., Basavaraj, R. B., Darshan, G. P., Prasad, B. D., Naik, R., Sharma, S. C., & Nagabhushana, H. (2018). New design of highly sensitive and selective MoO3:

Eu3+ micro-rods: Probing of latent fingerprints visualization and anti-counterfeiting applications. Journal of colloid and interface science, 528, 443-456.

56. Vandana, C. P., & Chikkamannur, A. A. (2021). Feature selection: An empirical study. International Journal of Engineering Trends and Technology, 69(2), 165-170.
57. Suganthi, S. T., Vinayagam, A., Veerasamy, V., Deepa, A., Abouhawwash, M., & Thirumeni, M. (2021). Detection and classification of multiple power quality disturbances in Microgrid network using probabilistic based intelligent classifier. Sustainable Energy Technologies and Assessments, 47, 101470.
58. Sridhara, V., Gowrishankar, B. S., Snehalatha, & Satapathy, L. N. (2009). Nanofluids—a new promising fluid for cooling. Transactions of the Indian Ceramic Society, 68(1), 1-17.
59. Ram, J. P., Pillai, D. S., Ghias, A. M., & Rajasekar, N. (2020). Performance enhancement of solar PV systems applying P&O assisted Flower Pollination Algorithm (FPA). Solar Energy, 199, 214-229.
60. Raghu, M. S., Kumar, C. P., Prashanth, M. K., Kumar, K. Y., Prathibha, B. S., Kanthimathi, G., ... & Osman, S. M. (2021). Novel 1, 3, 5-triazine-based pyrazole derivatives as potential antitumor agents and EFGR kinase inhibitors: Synthesis, cytotoxicity, DNA binding, molecular docking and DFT studies. New Journal of Chemistry, 45(31), 13909-13924.
61. Prakash, S., Somiya, G., Elavarasan, N., Subashini, K., Kanaga, S., Dhandapani, R., ... & Sujatha, V. (2021). Synthesis and characterization of novel bioactive azo compounds fused with benzothiazole and their versatile biological applications. Journal of Molecular Structure, 1224, 129016.

Construction and Seismic Performance Evaluation of Concrete Water Tanks

Koushal Dhamija[1], *OSD* Hima Bindu[2], *N V* Uma Reddy[3*], *Rajeev* Sobti[4], *Q*. Mohammad[5], *Ravi* Kalra[6], *B Nagaraj* Goud[7]

[1]Lloyd Institute of Management and Technology, Greater Noida, Uttar Pradesh, India.
[2]Department of Civil, GRIET, Bachupally, Hyderabad, Telangana, India.
[3]Department of Artificial Intelligence and Machine Learning, New Horizon College of Engineering, Bangalore, India
[4]Lovely Professional University, Phagwara, India
[5]Hilla University College, Babylon, Iraq
[6]Lloyd Institute of Engineering & Technology, Greater Noida, Uttar Pradesh, India.
[7]Department of Aeronautical Engineering, MLR Institute of Technology, Hyderabad, Telangana, India-500094

Abstract- The construction of concrete water tanks is a crucial aspect of water distribution structures, ensuring dependable water supply at predetermined elevations for numerous purposes. Municipalities and corporations closely depend upon these tanks to store water, combustible fluids, and synthetic compounds. However, the safety of these tanks, especially during seismic events, is paramount. To address this, robust support structures inclusive of reinforced concrete (RC) propped outlines, metallic frameworks, RC shafts, and masonry platforms are employed. The RC casing approach could be the most common support system due to its effectiveness and durability. This paper gives a FEM based technique the use of Staad.pro employed inside the construction and evaluation of concrete water tanks.

Keyword-: Water tank, FEM, Stad.pro, concrete, support systems

1 Introduction

A raised water tank serves as a vital factor in water distribution systems, presenting a reliable supply of water at a predetermined elevation. Those tanks are important for ensuring adequate water stress and availability for numerous purposes. Municipalities and companies depend on fluid garage tanks not only for water but additionally for storing flamable fluids and synthetic compounds. But, it is critical to note that tanks containing unsafe or flammable substances pose widespread protection concerns, particularly for the duration of seismic events. To mitigate risks, these tanks are prepared with strong help structures, together with bolstered concrete (RC) propped outlines, metal frameworks, RC shafts, and masonry structures [1]. Every assist machine is designed to resist the load of the tank and its contents

* Corresponding Author: nvumareddy@gmail.com

© The Authors, published by EDP Sciences. This is an open access article distributed under the terms of the Creative Commons Attribution License 4.0 (https://creativecommons.org/licenses/by/4.0/).

at the same time as maintaining structural integrity, even under seismic pressure. Amongst these help systems, the RC casing approach is the maximum commonly followed due to its validated effectiveness and sturdiness, as shown in Fig.1. In the course of seismic events, making sure the integrity of fluid garage tanks is paramount to prevent leakage or spillage of risky materials. Proper layout and production techniques, along with everyday preservation and inspection, are essential for boosting the resilience of those tanks in opposition to seismic forces. By way of enforcing suitable aid systems and adhering to protection protocols, the risk of loss or damage to tank contents may be minimized, safeguarding each human life and the environment [2].

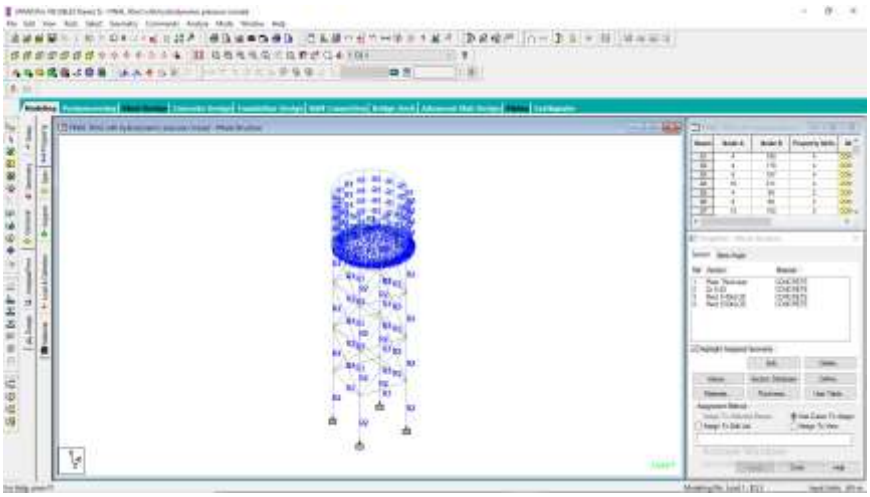

Fig. 1: Elevated Water Tank Supported by Inclined Columns

Component of factories, fireplace structures, and civic water structures is the raised water tank. Damage from earthquakes can threaten the provision of easy drinking water, positioned out fires, and result in financial loss. It is vital to investigate the seismic behavior of these buildings so one can fulfil safety requirements and shop constructing and maintenance charges. Using ANSYS software program, the study examined the response behavior of a raised RCC rectangular water reservoir under numerous water fill situations. The reactions of the tanks expanded with water height, according to the consequences [3]. Although concrete water tanks need to meet stringent requirements for serviceability, severe fractures can compromise their integrity and result in leaks. A 30 x 20 x 3.6 m water tank near the Arabian Gulf has cracks, according to a discipline exam [4-7]. To decide the problem and placed a restore plan into conduct, diagnostics research, outdoor inspections, lab testing, and 3-d modeling have been carried out. The study examined the properties of the concrete mix's heat of hydration using a semi-adiabatic calorimeter. It turned into discovered that tank walls cracked because of tensile loads which have been too amazing due to shrinkage lines and temperature. To get functionality backwards, a repair plan was counseled [8]. The use of non-corrosive reinforcing in reinforced concrete tanks of water and wastewater treatment centers is investigated in this study. It compares four substances—glass-fiber strengthened polymer (GFRP), stainless steel, epoxy-covered steel, and black iron—using existence-cycle cost evaluation [9]. The findings display that, despite its high preliminary cost, GFRP begins getting inexpensive following 35 years, suggesting that it is able to be a viable alternative for lengthy-time period concrete durability. In step with the have a look at, the internet cutting-edge cost of GFRP-strengthened concrete become 43% much less than that of black metal-bolstered concrete. Stainless steel was much less economical but had a twenty-five percent

decrease NPC. Epoxy coated metal confirmed a 15-12 months' growth in lifespan and an 11% discount in NPC [10-13]. The study discusses the design processes, building specifics, leakage testing, and monitoring outcomes for the world's first reinforced-concrete water chlorination tank. The purpose of the tank is to solve corrosion issues in RC tanks triggered by particular substances or treatment techniques' tank for a new water treatment facility is being built in Thetford Mines, Quebec, Canada. With a capacity of more than 2,500 m3, the tank satisfies the serviceability and durability specifications of ACI 350/350R-06, CAN/CSA S806-12, and ACI 440.1R-06. It is reinforced with GFRP bars [14]. Using non-destructive testing, this research assesses the state of brought up cement water tanks, including the development of cracks. Requirements for environmental quality influence tank design and construction. Water line cracks can pollute groundwater and harm storage tanks [15]. The research looks at leaks' causes and consequences. In addition to visual evaluations, hammer checks, design checks, cement compression tests, and Ultrasonic Pulse Velocity testing on tank construction parts was also part of the inquiry. Results included higher bending that planned, over time drying shrinkage cracks on the diagonally of the floor foundation, and flex type fractures in the centered span and diagonally beams of the main beam [16]. The behaviour of an elevated concrete water tank under seismic stress is investigated in this work by means of artificial seismic stimulation. It contrasts seven instances using models from the finite element strategy, mechanical designs, and actual dynamic analysis. Findings indicate that the axial power, overturning moment, or shear force at the tank's base are significantly impacted [17-20]. For big water tanks used in water treatment plants, in specific, the study revisits the application of iron cement in the construction of civil engineering. It is an appealing substitute that is particularly appropriate for poor nations, despite its low cost and plastic potential. Improving design methods and material comprehension is the goal of current study [21]. At order to compare different finite element models with experimental data, this study looks at numerical and experimental tests on big fibrocement tanks at Indianapolis, Brazil. The focus is on modeling accuracy and homogeneity procedures [22].
One world is becoming more aware of the problems associated with construction and civil engineering systems, especially as they relate to building water tanks. For the sake of economy, sustainability, as well as quality control, hybrid fiber concrete is the main focus of concrete manufacturing. Using this method will improve the quality of the finished product whereas building water reservoirs in Malaysian [23]. This study examines the nonlinear seismic response of raised water tanks made of reinforced concrete (RC), with an emphasis on a variety of tank sizes and RC pedestal measurements. Then takes a methodical approach, choosing and creating 48 model configurations, and then does linear static analysis utilizing a finite element technique. Research is being done to establish seismic reaction parameters for raised water tanks and to produce pushover curves for models [24]. The characteristics that are evaluated include the seismic design category, tank size, height to diameter ratio, and basic frequency. It shows that two cracking patterns are seen and that the size of the tank is important in seismic reaction [25]. The study investigates the application of water tanks as passively adjusted liquid dampers to reduce seismic activity in reinforced concrete structures. Tests were conducted on three 4-story models using a shaking table with different water levels. According to the study, for Models 1 and 2, water masses of 3.5 and two percent, respectively, provided the least reaction velocity and deflection [26-30]. In this essay, precast concrete water tanks and the R.C. water tanks are contrasted. It creates R.C.C. water tanks with an average size and uses MS Excel programming to compare the outcomes. RCC water tanks are more affordable for smaller-diameter tanks, but not for bigger ones, according to the results. The study highlights how crucial it is to choose the appropriate construction method for certain situations and building types [31]. Utilizing a probabilistic approach grounded on FAME P695, a research verifies the response modification factor of reinforced concrete pedestals in raised water tanks. Using incremental dynamic analysis, the likelihood

of collapse under various seismic loading situations is calculated for ten models that have different tank abilities and pedestal elevations. The nature of linear earthquakes is shown to be greatly influenced by tank size, with larger, heavier tanks being more susceptible [32-34]. Following sixty years of functioning, the highest possible and serviceability limit states for a reinforced concrete water towers tank are examined in this research. It consists of experimental research, site surveys, and computations to evaluate the load-bearing capacity, crack widths, and technical state of the tank and suggest structural repairs [35].

2 Problem Identification and Loading condition

This study aimed to evaluate the seismic performance of RCC elevated water tanks with columns positioned at various slant degrees. Loading conditions, including dead weight, seismic load, and hydrodynamic load under full water conditions, were considered. Altering the placement of columns can mitigate tensional modal analysis in circular tanks. Despite circular tanks being more cost-effective, rectangular tanks require a larger number of nodes for structural modelling. Structural modelling and analysis were conducted using the analytical software STAAD.Pro.

Concrete utilized in construction is of M30 grade, while reinforcement bars are of FE500 quality. The modulus of elasticity is measured at 1.95 x 10^5 Mega Pascals (MPa), with an ultimate tensile strength of 1860 MPa. The soil type is categorized as medium, while wind pressure is recorded at 39 meters per second. Hydraulic pressure considerations encompass tension and stress factors. Finally, seismic loads are accounted for within Zone II parameters. Those material residences serve as foundational facts crucial for design and construction levels, ensuring structural integrity and protection requirements are met.

The geometrical facts for the tank consists of a peak of 3.5 meters and a staging top of 8 meters. The tank's base diameter measures 4.4 meters, matching the diameter of the field. Supported by four columns, the tank is constructed the use of M30 grade concrete and reinforced with FE415 grade steel. Each column has a length of 500 square millimetres, even as beams degree 350 through 250 millimetres. Plate thickness is about at 800 millimetres, with wall thickness at 450 millimetres. For added support, bracing is furnished through I.S.M.B. 100 individuals. These specs offer important facts for the layout and construction stages, ensuring structural integrity and adherence to safety standards throughout the challenge.

3 Proposed Methodology

Study results were evaluated in many steps in order to ensure comprehensiveness and accuracy. A literature review was conducted as the first step to gather pertinent data and insight from previous studies regarding the underlying case. To comprehend the context and background of the study, existing literature, studies, and reviews were reviewed. Based on the results of this investigation, upcoming research and investigation are needed to address limitations or gaps in current studies. Analytical software STAAD.pro was used to prepare a geometrical shape for the study. The word STAAD refers to Structural Analysis and Design. One well-known program for assessing and developing structures, including buildings, towers, highways, industrial use, modes of transport, and functionality structures, is called STAAD Pro. These models were used to create digital versions of the water tank, columns, beams, and other structural elements. The superior features and competencies of STAAD.pro were leveraged to ensure realistic and reliable results. In the third step, the model's structural

sections were given material properties. There were specifics that were provided in regard to the concrete, metals, and any other materials that were to be used in the construction, as well as their properties. STAAD.pro will be able to simulate and analyze the structural behavior of the model appropriately after accurately defining the material properties, such as power and elasticity.

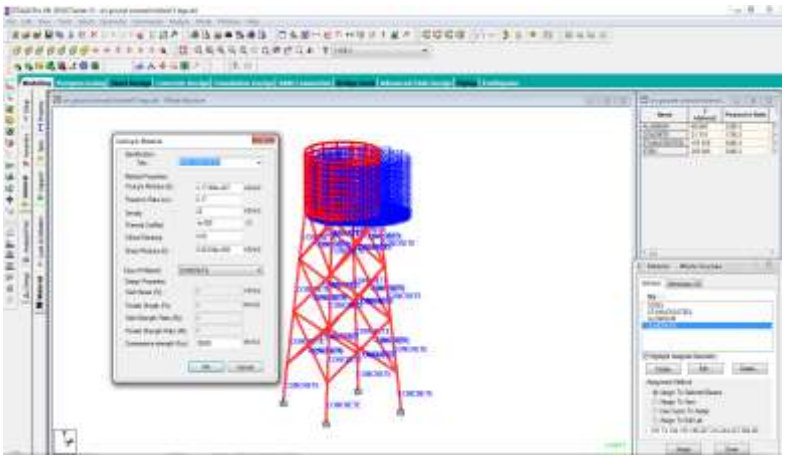

Fig. 2: Assigning Material Properties

As part of step 4, section properties were defined for the structural factors in the model, including geometric characteristics and mechanical characteristics. This step covered specifying the cross-sectional dimensions, including width, intensity, and thickness, of beams, columns, and other structural participants. Moreover, material properties such as modulus of elasticity, yield electricity, and remaining strength had been assigned to appropriately represent the behaviour of the materials underneath load. Through meticulously defining these phase homes, the structural response of the model to diverse loading situations will be accurately expected. This step performed a vital position in making sure the constancy and accuracy of the structural evaluation carried out the use of analytical software program like STAAD.pro.

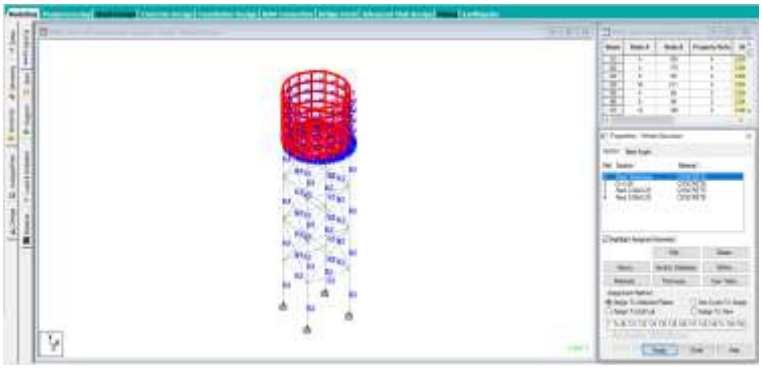

Fig. 3: Sectional Data

Step 5: in this step, weak springs were assigned at the base beams and cylindrical surface of the shape. Susceptible springs, additionally referred to as boundary springs, are virtual elements used to represent the relationship between the shape and its basis or assist machine. By means of assigning weak springs at strategic locations, which includes the bottom beams and cylindrical surface, the interaction between the structure and its surroundings could be

appropriately modeled. Those vulnerable springs mimic the flexibility and resilience of the foundation, allowing for a extra realistic simulation of the structural reaction to external loads, which include seismic forces. This step is crucial for capturing the dynamic behavior of the shape and ensuring that the analysis consequences replicate real-world situations appropriately**.**

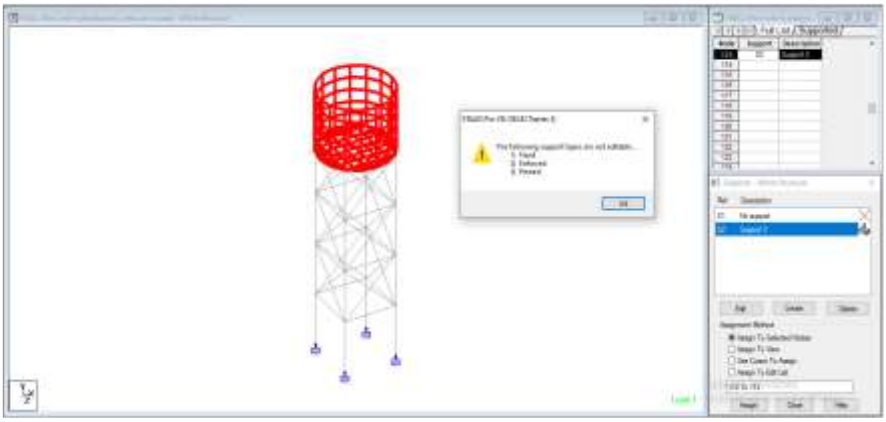

Fig. 4: Assigning Surface

Step 6: Assigning hydrostatic pressure in complete circumstance includes accounting for the strain exerted by way of water when the tank is at full capability. This step is important for as it should be simulating the structural reaction of the tank underneath hydrostatic loading conditions. By way of assigning hydrostatic pressure to the model, the distribution of forces appearing at the tank's walls and base may be appropriately represented. This consists of considering the weight of the water as well as any extra strain exerted because of the intensity of the water column.

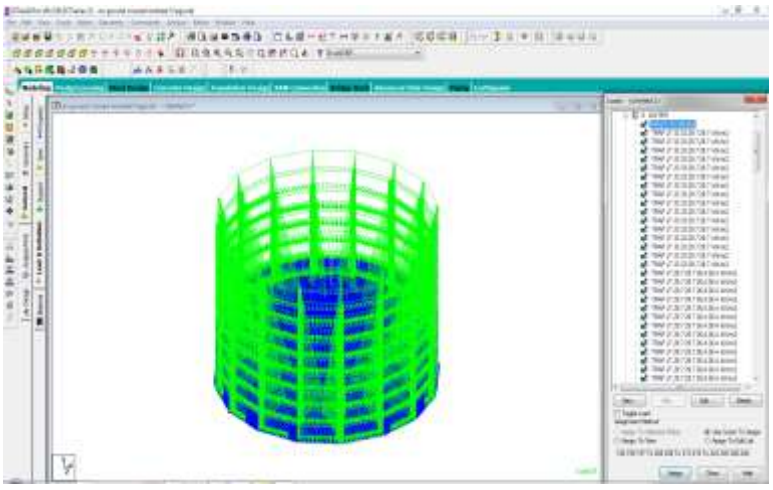

Fig. 5: Assigning Hydrostatic Load

Step 7: Assigning wind pressure as consistent with IS 875-III: 2015, with a wind velocity of 39 m/s, and seismic load as according to IS 1893-I: 2016, involves incorporating external environmental elements into the structural analysis. Wind pressure, according with the relevant code, is applied to the model to simulate the results of wind loading on the shape.

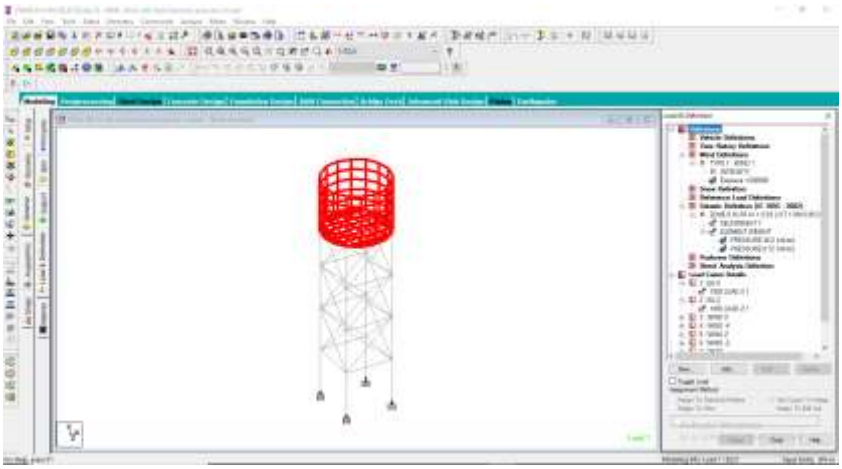

Fig. 6: Assigning Lateral Loads namely wind load and seismic load

Step 8: The Finite element method (FEM) analysis of the structure the use of the analytical application STAAD.pro includes accomplishing a comprehensive computational evaluation to assess the structural conduct and response below numerous loading situations. STAAD.pro utilizes superior numerical techniques to discredited the structure into finite elements, taking into consideration the accurate representation of complex geometries and material behaviours.

4 Results and Discussion

After conducting the FEM analysis the usage of STAAD.pro, the effects were evaluated and post-processed the usage of MS Excel. In this phase, the output records from STAAD.pro, consisting of stresses, displacements, and different structural responses, have been imported into Excel for similarly analysis and visualization.

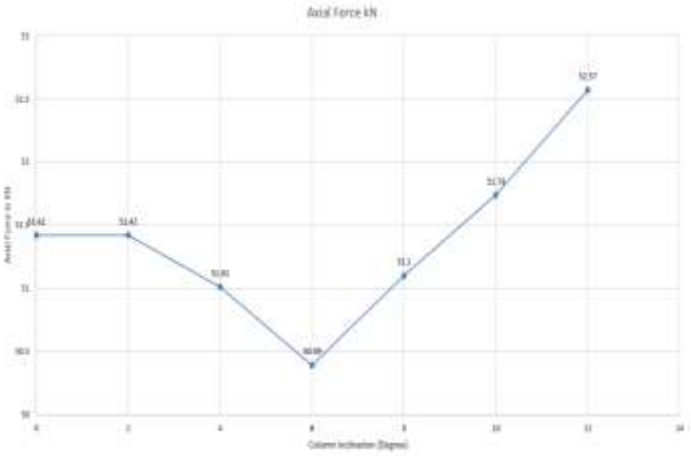

Fig. 7: Axial Force at Top Beam

Fig. 7 indicates the inner force exerted alongside the longitudinal axis of the beam at its uppermost segment. This force can be either compressive (pushing together) or tensile (pulling aside), relying on the loading and structural configuration. Evaluating the axial force

facilitates verify the beam's capability to resist vertical loads and contributes to determining its overall structural integrity and stability.

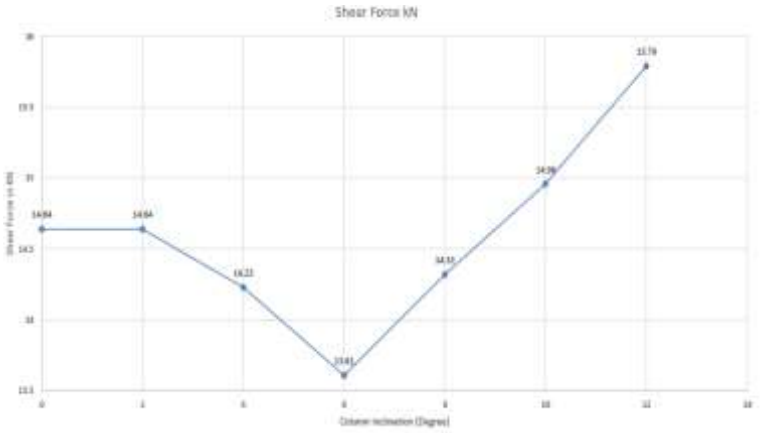

Fig. 8: Shear Force at Top Beam

Fig. 8 suggests the inner force performing parallel to the cross-sectional region of the beam at its uppermost part. This force represents the tendency of one part of the beam to slip or shear beyond another element. Evaluating the shear pressure facilitates determine the beam's resistance to lateral forces and contributes to determining its ordinary structural stability and performance.

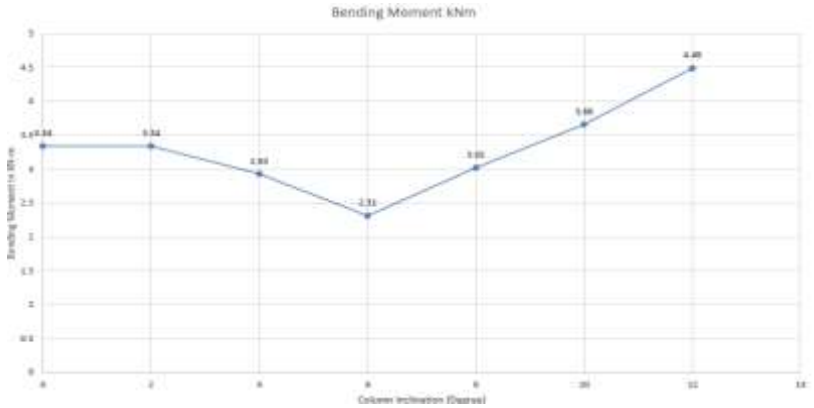

Fig. 9: Bending Moment at Top Beam

Fig. 9 shows the internal second or torque exerted at the beam at its uppermost section because of external loads. This moment induces curvature or bending inside the beam, inflicting it to deflect. Evaluating the bending moment facilitates assess the beam's capacity to resist bending and contributes to determining its usual structural energy and balance.

Fig. 10 shows the force exerted by means of a structural assist, such as a column or foundation, in response to the burden applied to the structure. This reaction pressure acts perpendicular to the help surface and is equal in value and opposite in path to the carried out load. Evaluating help reactions is crucial for studying the structural stability and ensuring that the aid machine can efficaciously bring and distribute the hundreds to the foundation or ground below.

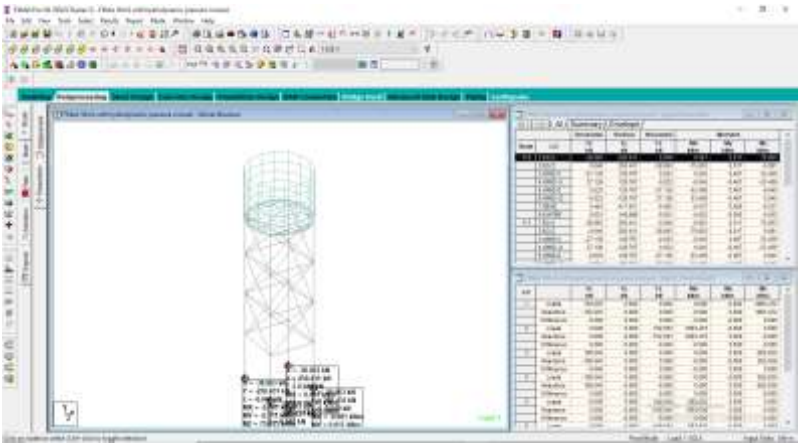

Fig. 10: Support Reaction

5 Conclusion

Concrete water tanks play a essential role in ensuring reliable water supply and storage. By using appropriate support structures and adhering to safety protocols, the risk of harm or leakage all through seismic occasions may be minimized. Numerous studies have explored unique elements of concrete water tank production, along with layout, fabric selection, and seismic overall performance evaluation. These research make contributions treasured insights to the continued efforts to beautify the safety, sturdiness, and efficiency of concrete water tanks. Further studies in this vicinity is important to address emerging challenges and improve the resilience of water garage infrastructure against natural dangers.

References

1. Mohammed, Hasan Jasim. "Economical design of water concrete tanks." European journal of scientific research 49, no. 4 (2011): 510-520.
2. MorVyankatesh, K., and T. More Varsha. "Comparative study on dynamic analysis of elevated water tank frame staging and concrete shaft supported." IOSR Journal of Mechanical and Civil Engineering (IOSR-JMCE) 14, no. 1 (2017): 38-46.
3. George, Raji Ruth, and Asha Joseph. "Dynamic analysis of elevated cement concrete water tank." Int J Innov Res SciTechnol 3 (2016).
4. Saeed, Muneer K., Muhammad K. Rahman, Mohammed H. Baluch, and Lutf A. Tooti. "Cracking in concrete water tank due to restrained shrinkage and heat of hydration: field investigations and 3D finite element simulation." Journal of Performance of Constructed Facilities 34, no. 1 (2020): 04019100.
5. Younis, Adel, Usama Ebead, PrannoySuraneni, and Antonio Nanni. "Cost effectiveness of reinforcement alternatives for a concrete water chlorination tank." Journal of Building Engineering 27 (2020): 100992.
6. Mohamed, Hamdy M., and BrahimBenmokrane. "Design and performance of reinforced concrete water chlorination tank totally reinforced with GFRP bars: Case study." Journal of Composites for Construction 18, no. 1 (2014): 05013001.
7. Kumar A., Sharma H., Gaur N., Nanthaamornphong A., "PAPR analysis in OTFS using the centre phase sequence matrix based PTS method," Results in Optics, vol. 15, 2024, doi: 10.1016/j.rio.2024.100664.

8. Ramaprabha J., Prema P., Gunasekar S., "HealthApex: Complete Healthcare Assistance With Consent Based Analytics," 2023 International Conference on System, Computation, Automation and Networking, ICSCAN 2023, , 2023, doi: 10.1109/ICSCAN58655.2023.10395884.
9. Roja Ramani D., Rachna P., Pavan G., Reddy R., Huzaifa M., "Agrobot: Agricultural Robot using IoT and Machine Learning (ML)," Proceedings - 2023 3rd International Conference on Smart Data Intelligence, ICSMDI 2023, , pp. 497-500, 2023, doi: 10.1109/ICSMDI57622.2023.00094.
10. Navya R., Bv S.K., Rawat A., Satheeshkumar S., "Cardiac Arrhythmia - Prediction and Classification using Support Vector Machine," 2023 International Conference on System, Computation, Automation and Networking, ICSCAN 2023, , 2023, doi: 10.1109/ICSCAN58655.2023.10394774.
11. Govindaraj M., Asha V., Saju B., Sagar M., Rahul, "Machine Learning Algorithms for Disease Prediction Analysis," Proceedings - 5th International Conference on Smart Systems and Inventive Technology, ICSSIT 2023, , pp. 879-888, 2023, doi: 10.1109/ICSSIT55814.2023.10060987.
12. Ramesh Babu, M., Mohana Roopa, Y., "Component-based self-adaptive middleware architecture for networked embedded systems," International Journal of Applied Engineering Research, vol. 12.0, no. 12, pp. 3029.0-3034.0, 2017.
13. De Poures M.V., Sudhir Chakravarthy K., Jabihulla Shariff M.D., Srinivasa Reddy Y., Siva Prasad V., Sreenivasa Rao K., Kaliyaperumal G., Venkatesh R., Kishore Kumar V., "Excellence of Nano SiC on Mechanical Behaviour of Low Density Polyethylene Hybrid Nanocomposite," Journal of The Institution of Engineers (India): Series D, , 2024, doi: 10.1007/s40033-024-00713-9.
14. Shivangi, Sah R.K., Shreeyam, Florance G., Nirmala M., "CNNCalc - An Implementation of a Handwritten Mathematical Equation Solver," Proceedings of the 7th International Conference on Intelligent Computing and Control Systems, ICICCS 2023, , pp. 638-645, 2023, doi: 10.1109/ICICCS56967.2023.10142278.
15. Yogitha, Rachana P., Milina M., Sabhahit N.G., Ainain M., "Breast Histopathology Image Classification: A Comparative Evaluation of SVM, Random Forest and CNN," 2023 3rd International Conference on Intelligent Technologies, CONIT 2023, , 2023, doi: 10.1109/CONIT59222.2023.10205567.
16. Bandi, G.N.S., Rao, T.S., Ali, S.S., "Data Analytics Applications for Human Resource Management," 2021 International Conference on Computer Communication and Informatics, ICCCI 2021, , 2021, doi: 10.1109/ICCCI50826.2021.9402300.
17. Rajendra Prasad, K., Mohammed, M., Narasimha Prasad, L.V., Anguraj, D.K., "An efficient sampling-based visualization technique for big data clustering with crisp partitions," Distributed and Parallel Databases, vol. 39.0, no. 3, pp. 813.0-832.0, 2021, doi: 10.1007/s10619-021-07324-3.
18. Deepak, D., Cornelio, J.A.Q., Midhun Abraham, M., Shiva Prasad, U., "Numerical analysis of the effect of nozzle geometry on flow parameters in abrasive water jet machines," Pertanika Journal of Science and Technology, vol. 25.0, no. 2, pp. 497.0-506.0, 2017.
19. Anitha A., Vinoth Kumar K., Bedant A., Madhav Reddy C., Abhisek K., "Non-Invasive Method of Detecting Anemia using AI & IoT," International Conference on Innovative Data Communication Technologies and Application, ICIDCA 2023 - Proceedings, , pp. 805-808, 2023, doi: 10.1109/ICIDCA56705.2023.10099915.
20. Srikrishnan, S., Dash, P.K., "2d cfd analysis of deflagration to detonation transition in closed pipe using different blockage," International Journal of Mechanical Engineering and Technology, vol. 8.0, no. 6, pp. 447.0-454.0, 2017.

21. Chaturvedi R., Darokar H., Patil P.P., Kumar M., Sangeeta K., Aravinda K., Kadhim A.A., "Maximizing towards the Sustainability: Integrating Materials, Energy, and Resource Efficiency in revolutionizing Manufacturing Industry," E3S Web of Conferences, vol. 453, 2023, doi: 10.1051/e3sconf/202345301036.
22. Manjunatha B., Kumar K.D., Goundar S., Kavin B.P., Seng G.H., "Sustainable waste management OOA-Enhanced MobileNetV2-TC model for trash image classification," Computational Intelligence for Green Cloud Computing and Digital Waste Management, , pp. 227-247, 2024, doi: 10.4018/979-8-3693-1552-1.ch012.
23. Sonia P., Srinivas R., Kansal L., Abdul-Zahra D.S., Reddy U., Kumari V., "Bioinspired Composites a Review: Lessons from Nature for Materials Design and Performance," E3S Web of Conferences, vol. 505, 2024, doi: 10.1051/e3sconf/202450501024.
24. Reddy, V.A., Solanki, C.H., Kumar, S., Reddy, K.R., Du, Y.-J., "Comparison of limestone calcined clay cement and ordinary Portland cement for stabilization/solidification of Pb-Zn smelter residue," Environmental Science and Pollution Research, vol. 29.0, no. 8, pp. 11393.0-11404.0, 2022, doi: 10.1007/s11356-021-16421-w.
25. Gantala, A., Vijaykumar, G., Telagam, N., Anjaneyulu, P., Phaniram, B., "Design of smart sensor using Linux-2.6.29 kernel," International Journal of Applied Engineering Research, vol. 12.0, no. 18, pp. 7891.0-7896.0, 2017.
26. Ganesan S., Dhanalakshmi, Asuti M., Kapadnis A.V., Saloni Belliappa B., "Augmented Reality as a Visual Aid for Classrooms: Supplemented by a Case Study," 14th International Conference on Advances in Computing, Control, and Telecommunication Technologies, ACT 2023, vol. 2023-June, pp. 1625-1635, 2023.
27. TaufiqRochman, Suhariyanto. "State of the art of tank structural evaluation review: A case study of an elevated concrete water tank concerning crack initiation." Journal of Southwest Jiaotong University 56, no. 5 (2021).
28. Algreane, G. A., SitiAminah Osman, O. Karim, and AnuarKasa. "Behavior of elevated concrete water tank subjected to artificial ground motion." EJGE 16 (2011): 387-406.
29. Moita, Gray F., Estevam B. de Las Casas, Edgar V. Mantilla Carrasco, and Sávio N. Bonifácio. "Experimental and numerical analysis of large ferrocement water tanks." Cement and Concrete Composites 25, no. 2 (2003): 243-251.
30. Azizan, M. A., N. Z. Noriman, N. Ishak, and H. Desa. "Application of Hybrid Fibre Concrete As Advanced Material For Concrete Water Tank Construction." In IOP Conference Series: Earth and Environmental Science, vol. 920, no. 1, p. 012012. IOP Publishing, 2021.
31. Ghateh, R., M. R. Kianoush, and W. Pogorzelski. "Seismic response factors of reinforced concrete pedestal in elevated water tanks." Engineering Structures 87 (2015): 32-46.
32. Ahmad, Muhammad Jamil, Qaiseruz Zaman Khan, and Syed Muhammad Ali. "Use of water tank as tuned liquid damper (TLD) for reinforced concrete (RC) structures." Arabian Journal for Science and Engineering 41 (2016): 4953-4965.
33. Sameer, Riyaz, A. R. Mundhada, and SnehalMetkar. "Comparison of RCC and prestressed concrete circular water tanks." Int. J. Emerging Technol. Advan. Eng 2, no. 12 (2012): 394-397.
34. Ghateh, Razmyar, Reza Kianoush, and Wes Pogorzelski. "Response modification factor of elevated water tanks with reinforced concrete pedestal." Structure and Infrastructure Engineering 12, no. 8 (2016): 936-948.
35. Dyba, Marcin, and Lukasz Slaga. "Technical Condition Assessment, Ultimate and Serviceability Limit States of the Water Tower Reinforced Concrete Tank after its Operation Lifetime." In IOP Conference Series: Materials Science and Engineering, vol. 471, no. 5, p. 052084. IOP Publishing, 2019.

Comparative Study of RCC Rectangular Underground Water Tanks Considering earth quake and without earth quake condition

Karuna Gudapalli[1], *N V* Uma Reddy[2*], *Sorabh* Lakhanpal[3], *Anurag* Srivastava[4], *Ravi* Kalra[5], *Zainab* Falah Hasan[6], Sravanthi[7]

[1]Department of CSBS, GRIET, Bachupally, Hyderabad, Telangana, India.
[2]Department of Artificial Intelligence and Machine Learning, New Horizon College of Engineering, Bangalore, India.
[3]Lovely Professional University, Phagwara, India
[4]Department of Mechanical Engineering, ABES Engineering College, Ghaziabad-201009, UP, India.
[5]Lloyd Institute of Engineering & Technology, Knowledge Park II, Greater Noida, Uttar Pradesh, India.
[6]Department of Anesthesia Techniques College of Medical Technology, The Islamic University, Najaf, Iraq
[7]Department of Aeronautical Engineering, MLR Institute of Technology, Hyderabad, Telangana, India-500086

Abstract. There are various kinds of water tanks and reservoirs that are used for storing different liquids such as water, petroleum, and chemicals. Residential and commercial use of water tanks is essential in order to meet the needs of those living in these places on a daily basis. During their lifetime, these tanks are subjected to the pressure of the water inside and the pressure of the earth outside. The tank bases are subjected to soil reaction from the bottom and internal water pressure from the inside. In order to protect them from top to bottom, they are always covered from top to bottom. Providing optimum height for easy pumping of water to the overhead tank is the purpose of this rectangular underground tank. Due to the underground nature of the water tank, lateral earth pressure and water pressure also need to be considered during design calculations, so the design must comply with IS code standards. An underground rectangular tank is designed in this project. Our project involves the design and research of an underground water tank capable of holding 3 lakh litters under earthquake conditions. The design in this project comprises of side walls, base slab and roof slab. STAD.PRO is used for the analysis and design of underground water tanks. For this design project limit state method is used. Researchers investigate parameters related to water tanks, including shear force and bending moment, to better understand how they respond to seismic forces, and to aid in more effective design and construction.

Keyword-: Water pressure, Earth pressure, Soil reaction, Tank bases, Covered tanks, Underground tanks.

* Corresponding author: *nvumareddy@gmail.com*

© The Authors, published by EDP Sciences. This is an open access article distributed under the terms of the Creative Commons Attribution License 4.0 (https://creativecommons.org/licenses/by/4.0/).

1 Introduction

Water tanks are one of the essential infrastructural components that are used for the storage and supply of potable water for drinking, domestic, commercial, industrial, as well as other purposes. Scarcity, erratic supply, and security of water are the factors that make tanks installation in urban, rural, and industrial settlements inevitable [1]. The size of water tanks can vary from small, medium to big and made-up of any material. The underground water tanks are designed to be installed at a position below the ground level and therefore offer a discreet and space-saving option for storing water[2]. They protect the weathering elements, hence are found to be of great use at places where extreme weather conditions exist, or the scenic beauty of the ambiance needs to be maintained [3]. In the case of highly crowded urban metropolitans where the ground at the surface is available in very restricted quantities, the underground water tanks are quite useful indeed. Also, they are used in storing water in making full utilization of space processes in businesses, homes, and industries [4]. Underground water tanks are used to store fluids, such as gas, oil and water. Both internal and external water and earth pressure are applied to these tanks [5]. Tank bases are subjected to internal water pressure and soil reaction from below. These are always completely covered. These tanks should to be specially built for loading, since that produces the least useful results [6]. Underground tank's function and are designed in the same way as above-ground tanks. Both external soil pressure and internal water pressure can affect the walls of underground tanks. The wall segment is designed to operate under water pressure and subsurface pressure simultaneously and independently [7]. The unpredictable and strong movements of the Earth's crust cause seismic loads, which present a significant obstacle for structural engineers. The fact that they have the ability to exert powerful forces and significantly distort subterranean water tanks highlights how crucial it is to be prepared and knowledgeable [8]. These loads can inflict havoc on structures that are not designed to withstand their impact because of their very characteristics, which are often characterized by their suddenness and quantity [9]. Seismic pressure creates special obstacles for underground water tanks. These underground, hidden facilities are in charge of protecting this important resource: water [10]. But just the force of an earthquake can turn the peaceful surroundings into a conflagration of potential destruction. These tanks have to be able to bear the weight of the water as well as the fury of the elements due to the fact they are protector of an essential resource [11]. It is crucial to make sure they'll be robust and resilient enough to continue to exist a seismic attack like this. Past the bodily international, form disintegrate can have an extended manner-achieving consequences that endanger lifestyles itself, worsen emergency conditions, and disrupt supply lines [12]. For this reason, it is evident that an in-depth study into know underground water tanks behave under seismic loading situation is essential. This calls for a thorough examination of the seismic forces causing these tanks move, shake, and shake in the face of such a powerful opponent [13]. Under addition, the evaluation in their performance under those harsh circumstances acts as a safety beacon, supporting engineers and designers in growing structures that can withstand unanticipated occurrences. The main goal of this study is to ensure that these tanks keep to characteristic as effective defenses during seismic interest, in preference to best comprehending the nuances of seismic behaviour, as compared to simply understanding the subtleties of seismic behaviour [14]. It entails transforming engineering expertise into public mental peace. It involves using knowledge to defend oneself against the force of nature. And it's about reinforcing the concept that safety and functionality are not just ideals—they are the very foundations upon which structures and societies stand. The research and design of an underground water tank with a 3-lakh trash capacity, both with and without earthquake conditions in both full and empty tank condition, are the focus of this project [15]. The design of this project consists of base and roof slabs as well as side walls. Subterranean water tank analysis and design are

done with Staad.pro. This design task is approached using the limit state method. Shear force and bending moment are two of the factors included in the study, which is centered on the tanks. It offers crucial information on how earthquakes affect water tanks, information that might improve construction and design techniques [16].

2 Methodology

Underground water tanks are used to store fluids, such as gas, oil and water. Both internal and external water and earth pressures are applied to these tanks. Soil reaction from below and internal water pressure are factors that affect tank bases. These are always well taken care of. These tanks should to be built for loading, since that produces the least useful results. This study is targeted towards presenting the comparative evaluation of rectangular water tank considering with earthquake and without earthquake in zones of iv and soil type -soft to recognize the behaviours of the structure while dead load, live load and seismic load are carried out at the structure. Use of the staad. Pro software completes the modelling and analysis. Rectangular underground water tanks in two distinct states—full and empty—are taken into consideration for study in order to determine the realistic behaviour with and without an earthquake in relation to the overall plan and elevation. The water tank is modelled for soil type -soft and zone IV. Staad Pro is used to provide fixed support for the models that use the Response Spectrum seismic analysis approach. Tank is 6 metres height, with zone IV soil and soft soil types. A 5% modal damping is expected when using I=1 and OMRF. To be secured at the bottom. M30 concrete grade and Fe415 steel are the materials used. The investigation centres around of the tanks, encompassing parameters such as, shear force, bending moment, the research contributes valuable information to the understanding of water tank responses to seismic forces, aiding in improved design and construction practices.

Table 1: Model Specifications of the rectangular underground wate tank

Model Specification	
Component	**Size**
Shape of tank	Rectangular
Capacity of tank	3lack
Tank length	10m
Width of tank	6m
Height of tank	6m
No of bays along length	1
No of bays along width	1
No of bays along height	1
Plate Thickness	300mm
Free Board	200mm
Bearing capacity of soil	230KN/m2
Soil density	18KN/m3
Water density	10Mg/m3
Grade of concrete	M30
Grade of steel	415

Table 1 showing that the dimensions of a rectangular water tank with a 3 lack capacity are described in the model specification that is supplied. The tank has a single bay along each of its 10 metres of length, 6 meters of width, and 6 meters of height. It is constructed on soil that has a bearing capacity of 230 kilonewtons per square metre and consists of plates with a thickness of 300 millimetres and a freeboard of 200 millimetres. Water has a density of 10,

whereas soil has 18. The concrete used to make the tank is M30 grade, and it is reinforced with grade 415 steel. These standards guarantee the structural integrity and functionality of the tank by defining its size, composition, and foundational features.

3 Result and Discussion

Underground water tanks are designed to be buried beneath the ground's surface, offering a discrete and space-efficient solution for storing water. These tanks provide protection from weather elements, making them ideal for regions prone to extreme weather conditions or for areas where preserving the aesthetics of the surroundings is important. In highly crowded urban centres with limited surface area, underground water tanks are useful. They are also frequently used to store water while making the best use of available space in businesses, homes, and industrial facilities. In study to understand the behaviour of the structure when dead load, live load, and seismic load are applied to it, this study compares the evaluation of a rectangular water tank in zones IV and soft soil under earthquake and without earthquake. Applying the staad. Professional software completes the analysis and modelling. Undertakings: Rectangular underground water tanks in two different stages of fulling and emptying are studied to ascertain the realistic behaviour in the event of an earthquake with respect to the overall layout and elevation. Zone IV soil type and soft soil type are modelled for the water tank.

Table 2: Results of shear force in x y and z direction without earthquake

Condition	**Rectangular Water Tank**		
	FX KN	FY KN	FZ KN
Empty	130	872	65
Full	224	872	91

The Table 2 data provided outlines the forces performing on a rectangular water tank under different conditions: empty and full in without earthquake condition. In the empty condition, the forces exerted at the tank are as follows: an FX force of 130 kilonewtons (KN), an FY force of 872 KN, and an FZ force of 65 KN. Conversely, whilst the tank is full, these forces change. The FX force increases to 224 KN, indicating a greater force within the X direction likely due to the added weight of the water. However, the FY force remains constant at 872 KN, suggesting that the water's weight does not affect this direction. Similarly, the FZ force will increase to 91 KN, compared to the 65 KN when the tank is empty, demonstrating the additional load within the Z direction caused by the water. These force measurements are critical for engineering and structural evaluation, informing the layout of support systems able to withstanding the forces exerted by means of the water within the tank under various conditions.

Table 3: Results of maximum bending in x y and z direction without earthquake

Condition	**Rectangular Water Tank**	
	MX KN	MZ KN
Empty	298	328
Full	260	304

The Table 3 provided data outlines the moments exerted on a rectangular water tank under different conditions: empty and full in without earthquake condition. In the empty condition, the moments performing on the tank are specified as follows: an MX moment of 291 kilonewton-meters (KN-m), an MZ moment of 320 KN-m. Conversely, while the tank is full,

these moments revel in slight changes. The MX moment decreases to 287 KN-m, indicating a slightly decreased rotational force around the X-axis, probable because of modifications in weight distribution as a result of the added water. Similarly, the Z-axis. Extensively, the moment decreases to 304 KN-m, suggesting that the vertical rotational force remains changed the tank's water level. These moment measurements are crucial for structural engineers, informing them about the rotational forces exerted at the tank and assisting within the design of help systems capable of withstanding such forces underneath specific tank conditions.

Table 4: Results of maximum shear force in x y and z direction with earthquake

Condition	**Rectangular Water Tank**		
	FX KN	FY KN	FZ KN
Empty	145	1225	118
Full	245	1225	162

The Table 4 provided data outlines the forces acting on a rectangular water tank in both empty and full situations with earth quake condition. In the empty state, the forces exerted at the tank are specified as follows: an FX force of 145 kilonewtons (KN), an FY force of 1225 KN, and an FZ force of 118 KN. Upon filling the tank, these force values undergo changes. The FX force increases to 245 KN, suggesting a greater force performing along the X-axis because of the introduced weight of water. Conversely, the FY force stays constant at 1225 KN, indicating that the vertical force remains unaffected by the water level. Notably, the FZ force also increases to 162 KN, highlighting the extra downward force attributed to the increased water weight.

The Table 5 provided data outlines the moments exerted on a rectangular water tank in both empty and full in earthquake condition. When the tank is empty, the moments are as follows: an MX moment of 576 kilonewton-meters (KN-m), and an MZ moment of 685 KN-m. Upon filling the tank, these moments experience changes. The MX moment decreases to 536 KN-m, indicating a reduction in the rotational force across the X-axis, possibly due to alterations in weight distribution caused by the added water. Similarly, additionally, the MZ moment decreases barely to 662 KN-m. Although the change isn't as significant, it still shows a lower within the rotational force around the Z-axis.

Table 5: Results of maximum bending in x y and z direction with earthquake

Condition	**Rectangular Water Tank**	
	MX in KN	MZ in KN
Empty	576	685
Full	536	662

The Fig 1 provided outlines the forces performing on a rectangular water tank under different conditions: empty and full in without earthquake condition. In the empty condition, the forces exerted at the tank. The maximum value of shear force in FY direction as compared to FX and FZ in both empty and full tank condition. The maximum value of shear force in full tank when tank is empty, shear force is reduced. These force measurements are critical for engineering and structural evaluation, informing the layout of support systems able to withstanding the forces exerted by means of the water within the tank under various conditions.

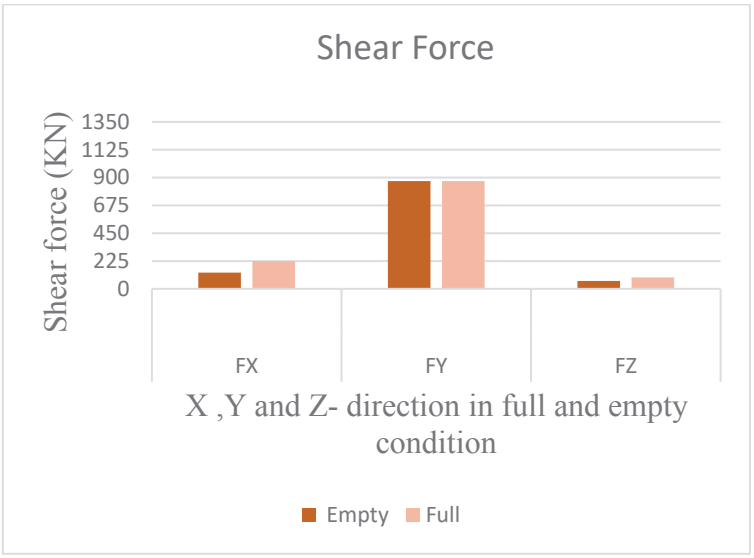

Fig. 1: Comparatively analysis of shear force in without earthquake for empty and full condition

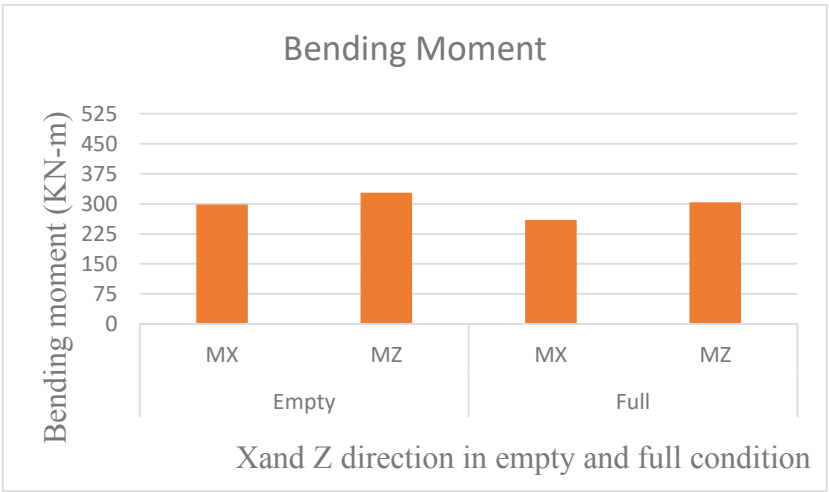

Fig 2: Comparatively analysis of bending moment in without earthquake for empty and full condition

The Fig 2 provided outlines the forces performing on a rectangular water tank under different conditions: empty and full in without earthquake condition. In the empty condition, the forces exerted at the tank. The maximum value of bending moment in MZ direction as compared to MX- direction in both empty and full tank condition. The maximum value of bending moment in empty tank when tank is full, moment is decreased. These moment measurements are crucial for structural engineers, informing them about the rotational forces exerted at the tank and assisting within the design of help systems capable of withstanding such forces underneath specific tank conditions.

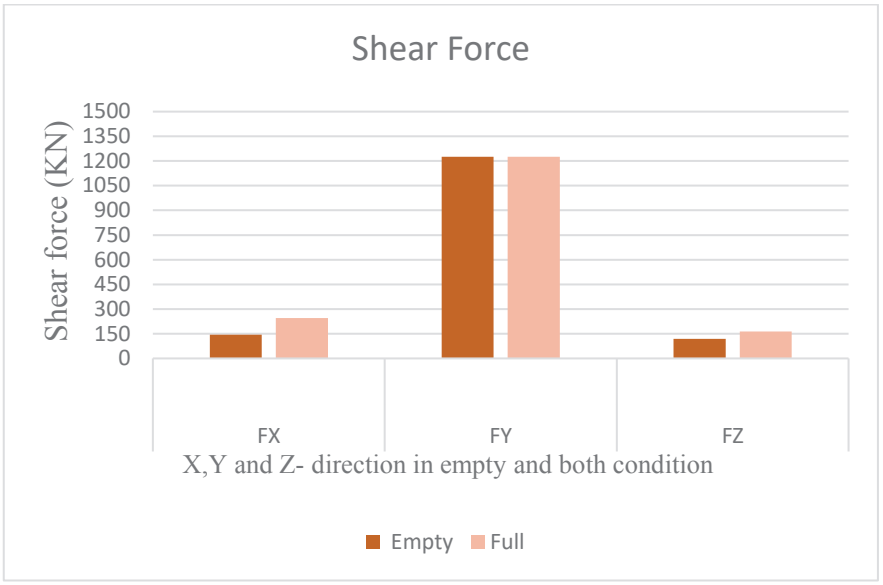

Fig 3: Comparatively analysis of shear force in with earthquake for empty and full condition

The Fig 3 provided outlines the forces performing on a rectangular water tank under different conditions: empty and full in with earthquake condition. In the empty condition, the forces exerted at the tank. The maximum value of shear force in FY direction as compared to FX and FZ in both empty and full tank condition. The maximum value of shear force in full tank when tank is empty, shear force is reduced. These force measurements are critical for engineering and structural evaluation, informing the layout of support systems able to withstanding the forces exerted by means of the water within the tank under various conditions.

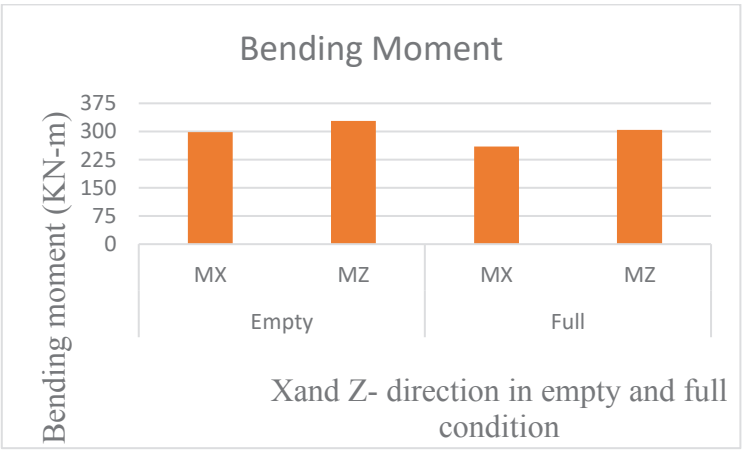

Fig. 4: Comparatively analysis of bending moment in with earthquake for empty and full condition

The Fig 4 provided outlines the forces performing on a rectangular water tank under different conditions: empty and full in with earthquake condition. In the empty condition, the forces exerted at the tank. The maximum value of bending moment in MZ direction as compared to MX- direction in both empty and full tank condition. The maximum value of bending moment in empty tank when tank is full, moment is decreased. These moment measurements

are crucial for structural engineers, informing them about the rotational forces exerted at the tank and assisting within the design of help systems capable of withstanding such forces underneath specific tank conditions.

4 Conclusion

Water tanks are an absolute necessity for both residential and commercial uses in order to meet their daily needs. These tanks are subjected to water pressure from inside and earth pressure from outside. Soil reaction from below and internal water pressure are applied to tank bases. In study to understand the behaviour of the structure when dead load, live load, and seismic load are applied to it, this study compares the evaluation of a rectangular water tank in zones IV and soft soil under earthquake and without earthquake. Applying the staad. Professional software completes the analysis and modelling. Undertakings: Rectangular underground water tanks in two different stages of fulling and emptying are studied to ascertain the realistic behaviour in the event of an earthquake with respect to the overall layout and elevation. Zone IV soil type and soft soil type are modelled for the water tank.

- Tank moment and shear force measurements: Empty and Full
- In without earthquake condition, Empty tank: FX force of 130 KN, FY force of 872 KN, and FZ force of 65 KN. When tank is full: FX force increases to 224 KN. FY force remains constant at 872 KN, FZ force increases to 91 KN, indicating additional load in the Z direction.
- In without earthquake condition Empty tank: MX moment of 291 KN-m, MZ moment of 320 KN-m. In Full tank: MX moment decreases to 287 KN-m, indicating decreased rotational force around X-axis due to water addition. Z-axis: MX moment decreases to 304 KN-m, indicating vertical rotational force remains, altering tank's water level.
- In with earthquake condition, Empty state: FX force of 145 KN, FY force of 1225 KN, FZ force of 118 KN. Filling state: FX force increases to 245 KN due to water weight. FY force remains constant at 1225 KN, indicating vertical force remains unaffected by water level. FZ force increases to 162 KN.
- In with earthquake condition Empty tank: MX moment of 576 KN-m, MZ moment of 685 KN-m. Filling tank: MX moment decreases to 536 KN-m, possibly due to water-induced weight distribution changes. MZ moment decreases to 662 KN-m, indicating a lower rotational force around the Z-axis.

References

1. Gadekar, Deepshikha, and Rakesh Patel. "Design and Analysis of Under Ground Water Tank Considering Different Fill Conditions Using STAAD. PRO: A Review." 6 (2022): 11-18.
2. Bhende, Amruta Arvind, and Prajakta B. Jamale. "Comparative Analysis of Different Shapes of Underground Water Tank." International Journal of Modern Developments in Engineering and Science 1,5 (2022): 19-21.
3. Chang, Chun, Zhiyong Wu, Helena Navarro, Chuan Li, Guanghui Leng, Xiaoxia Li, Ming Yang, Zhifeng Wang, and Yulong Ding. "Comparative study of the transient natural convection in an underground water pit thermal storage." Applied energy 208 (2017): 1162-1173.
4. Lotfy, Ayman M., Ashraf IG Elhetawy, Mahmoud M. Habiba, and Mohamed M. Abdel-Rahim. "A comparative study on the effects of seawater and underground saltwater on water quality, growth, feed utilization, fish biomass, digestive system development, and blood health in gilthead seabream, Sparus aurata." (2021): 1609-1621.

5. Gocke, Jessica. "The collateral damage of environmental federalism: A comparative study of underground storage tank policy in the United States." PhD diss., University of La Verne, 2012.
6. Bociort, Dalia, C. A. T. A. L. I. N. Gherasimescu, R. A. Z. V. A. N. Berariu, Romen Butnaru, Mihai Branzila, and Ion Sandu. "Comparative studies on making the underground raw water drinkable, by coagulation-flocculation and adsorption on granular ferric hydroxide processes." Revista de Chimie 63, 12 (2012): 1243-1248.
7. Jindal, Bharat Bhushan, Ajay Goyal, and Devinder Sharma. "Comparative Study Of Design Of Rectangular Water Tanks With Reference To Is 3370."
8. Johnston, Moira. "A critical and comparative analysis of the under regulation of underground storage tanks in South Africa and the attendant consequences for environmental resources." (2014).
9. Chang, Ni-Bin, Marty Wanielista, Ammarin Daranpob, Zhemin Xuan, and Fahim Hossain. "New performance-based passive septic tank underground drainfield for nutrient and pathogen removal using sorption media." Environmental Engineering Science 27, 6 (2010): 469-482.
10. Lee, Ho Yeol, Gyu Tae Seo, and Taek Soon Lee. "Comparative Analysis of the Storm Sewer Expansion Methodology and Underground Rainwater Storage Tanks for Urban Flood Control." Journal of Korean Society on Water Environment 29, 6 (2013): 754-761.
11. Wang, Huajun, and Chengying Qi. "Performance study of underground thermal storage in a solar-ground coupled heat pump system for residential buildings." Energy and Buildings 40, 7 (2008): 1278-1286.
12. PATEL, CHIRAG N., and Mehul S. Kishori. "Analytical and Software Based Comparative Analysis of on Ground Circular Water Tank." International Journal of Civil Engineering (IJCE), 5 (3) (2016).
13. Singh, Himmat, Sanjeev Kumar Gupta, Kumar Vikram, Rekha Saxena, and Amit Sharma. "The impact of mosquito proof lids of underground tanks “tanka” on the breeding of Anopheles stephensi in a village in western Rajasthan, India." Malaria journal 20 (2021): 1-10.
14. Rangrej, Junaid, and Hitesh Kodwani. "A Review of Analysis of Underground Water Tanks Considering Different Conditions." International Journal of Innovative Research in Technology and Science 12, 2 (2024): 235-239.
15. Tateishi, Akira. "A study on seismic analysis methods in the cross section of underground structures using static finite element method." Structural Engineering/Earthquake Engineering 22, 1 (2005): 41s-54s.
16. Andreolli, Marco, Nicola Albertarelli, Silvia Lampis, Pierlorenzo Brignoli, Nazaninalsadat Seyed Khoei, and Giovanni Vallini. "Bioremediation of diesel contamination at an underground storage tank site: a spatial analysis of the microbial community." World Journal of Microbiology and Biotechnology 32 (2016): 1-12.

Results in Engineering 23 (2024) 102607

Contents lists available at ScienceDirect

Results in Engineering

journal homepage: www.sciencedirect.com/journal/results-in-engineering

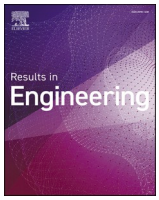

Split injection timing optimization in ammonia/biodiesel powered by RCCI engine

Elumalai Pv [a,b,c,*], Krishnaiah Ravi [d,**], Ramachandran Elumalai [d], Chan Choon Kit [e], Suresh Kumar K [f,***], Krishnasamy Karthik [g,****], M. Satyanarayana Gupta [h], Mohammad Asif [i]

[a] Department of Mechanical Engineering, Aditya University, Surampalem, India
[b] Research Fellow, Faculty of Engineering. Shinawatra University, Thailand
[c] Department of Mechanical Engineering, Saveetha School of Engineering, Saveetha Institute of Medical and Technical Sciences (SIMATS), Chennai, Tamil Nadu, 602105, India
[d] School of Mechanical Engineering, VIT University, Vellore, India
[e] Faculty of Engineering and Quantity Survey INTI International University, Persiaran Perdana BBN, Putra Nilai, 71800, Nilai, Negeri Sembilan, Malaysia
[f] Department of Mechanical Engineering, Faculty of Engineering and Technology, SRM Institute of Science and Technology, Kattankulathur, Chennai, 603203, Tamilnadu, India
[g] Vel Tech Rangarajan Dr Sagunthala R&D Institute of Science and Technology, Avadi, Chennai, 600 062, India
[h] Department of Aeronautical Engineering, MLR Institute of Technology, Hyderabad, Telangana, India
[i] Department of Chemical Engineering, King Saud University, P.O. Box 800, Riyadh, 11421, Saudi Arabia

ARTICLE INFO

Keywords:
Reactivity controlled compression ignition
Carbon free ammonia as IC engine fuel
Low carbon foot print algal biodiesel
Split injection strategy
Pollution

ABSTRACT

Employing carbon-neutral (NH_3) and low carbon footprint (biodiesel) fuels in Reactivity Controlled Compression Ignition (RCCI) engine mode is one possible method for minimizing carbon emissions in diesel engines. In this study, a Compression Ignition (CI) engine was customized to run in RCCI mode, employing High Reactive Fuel (HRF) as biodiesel and Low Reactive Fuel (LRF) as ammonia (NH3). Based on our earlier findings, the proportion of ammonia in premixing is fixed at 40 %. In the first phase, the primary injection timing of the algal biodiesel varied between 12 and 21°CA bTDC at a preset pre-injection timing of 46°CA bTDC. In the next phase, the pre-injection time varied between 46 and 54°CA bTDC, with the optimal main injection time being 18°CA. The result suggested that the optimal main and pre-injection at 18 and 58°CA bTDC increased the Cylinder Pressure (CP) by 30.1 %, and peak HRR and combustion phase angle were advanced. Brake Thermal Efficiency exhibited an 11 % enhancement, with Brake Specific Energy Consumption decreasing by 24.1 %. Nitrogen Oxide levels saw an increase of around 39.5 %. In contrast, reductions of 19.2 %, 23.5 %, 39.7 %, and 21.7 % were observed in Hydrocarbons, Carbon Monoxide, smoke emissions, and Exhaust Gas Temperature, respectively, compared to the single injection under full load conditions.

1. Introduction

1.1. Low temperature combustion (LTC)

According to research, greenhouse gases (GHG) released by human activities are intimately associated with global climate change, natural environment degradation, and energy resource scarcity [1]. Reduced usage of fossil fuels, aggressive development of renewable energy, mitigation of climate change, and the development of a low-carbon economy have established worldwide consensus [2–4]. Transportation-related carbon emissions totaled 896 million tons in 2020 [5]. Essentially, the use of fossil fuels in internal combustion engines (ICEs) is the primary source of CO_2 emissions in the transport sector. ICEs are not only the most thermally efficient technology, but

* Corresponding author.
** Corresponding author.
*** Corresponding author.
**** Corresponding author.
E-mail addresses: elumalaimech89@gmail.com (E. Pv), ravi.krishnaiah@vit.ac.in, ravikrish97@gmail.com (K. Ravi), sureshkk@srmist.edu.in (S.K. K), karthikmeed@gmail.com (K. Karthik), masif@ksu.edu.sa (M. Asif).

https://doi.org/10.1016/j.rineng.2024.102607
Received 9 March 2024; Received in revised form 20 July 2024; Accepted 22 July 2024
Available online 23 July 2024
2590-1230/© 2024 The Authors. Published by Elsevier B.V. This is an open access article under the CC BY-NC license (http://creativecommons.org/licenses/by-nc/4.0/).

also an important base industry that supports the rapid expansion of new industries in the world and continues to lead the way [6]. As a result, low-carbon and zero-carbonization of ICEs justifies continuous effort. Among these ICEs, CI engines are extensively used as sources of power in transportation and energy supply owing to their great fuel economy and sturdiness, but their usage has been limited due to rigorous pollution restrictions [7]. Therefore, significant improvements have been achieved in reducing NOx and smoke emissions, mainly from CI engines [8]. To fulfill rigorous emissions rules, certain combustion techniques like RCCI, PCCI and HCCI have been developed in recent years. These techniques are known as LTC [9]. Decreasing the combustion temperature and minimizing the fuel rich regions may significantly decrease NOx emissions in LTC [10]. Chemical kinetics entirely govern the LTC combustion process [11].

1.2. RCCI combustion

The RCCI engine is superior to other combustion concepts in terms of operating range, thermal efficiency, and emission value improvements without the need for aftertreatment [12]. RCCI permits the injection of two different reactivity fuels using various injection techniques to develop a reactivity gradient inside the cylinder. Premixed LRF is fed into the cylinder via the intake port. The HRF is delivered straight into the cylinder. When the cylinder temperature is high enough during the end of compression stroke, the combustion process begins where there are higher concentrations of HRF and disseminates throughout the remainder of the combustion chamber [13,14]. The type and proportion of LRF in RCCI mode have a notable effect on flame development [15]. Research compares RCCI combustion to Conventional Diesel Combustion (CDC). The findings demonstrate that enhancing the fraction of low-reactivity fuel energy from 10 % to 60 % enhanced CP owing to accelerated combustion timing and volumetric energy discharge. In the cumulative heat release analysis, RCCI mode exhibited higher energy release compared to CDC mode [16]. For instance Okcu et al. [12] used octanol and heptanol as LRF and diesel as HRE. According to the research, modifying the type and proportion of LRF might result in better controlled combustion. They were able to observe that, the increase in CO and HC emissions remains a concern at lower loads. As a result, substantial research into LRF for use in RCCI operations is required to minimize unburned emissions. The effects of diesel main injection timings on the RCCI engine were meticulously explored in a study by Liu J et al. The results reveal that by advancing the main injection from 15 to 27°CA bTDC, the peak CP rises, the knock propensity lowers greatly, and CO, HC and soot emissions are decreased by 55.6 %, 43.1 %, and 28.8 %, respectively [17]. In an experimental investigation, natural gas was advocated for usage in RCCI engines due to its greater octane number and reduced carbon to hydrogen ratio. According to reports, these qualities reduced the peak CP and produced incomplete combustion emissions [18]. In an investigation, it was studied that the petrol/biodiesel RCCI mode may achieve efficient combustion by delaying direct injection time in conjunction with later intake valve closing timing. Moreover, the Brake Thermal Efficiency (BTE) of the RCCI mode rose by 15 % following the addition of exhaust gas recirculation technology [19]. Research was conducted to compare the engine combustion, performance, and emission analysis of LTC modes, namely RCCI and PCCI, with the CI combustion mode. The results reveal that at greater engine loads, RCCI mode combustion achieved significantly enhanced BTE than CI and PCCI combustion modes. Another significant conclusion of this research was that RCCI combustion had a much lower EGT than PCCI and CI combustion modes [20]. A study was conducted to explore the influences of the RCCI engine with biodiesel blends as the HRF and ethanol as the LRF. Results revealed that HC and CO emissions rose while significant NOx emissions decreased [21]. Research investigated the combustion, performance, and emission characteristics of PCCI and RCCI. According to the study's findings, RCCI has a 3.9 % greater thermal efficiency than PCCI. Furthermore, RCCI outperforms PCCI in terms of HC, CO, NOx, and soot emissions [22]. Rangasamy et al. [23] examined the emissions characteristics of the methanol/biodiesel and the methanol/diesel RCCI operations. The methanol/biodiesel RCCI mode was more stable than the methanol/diesel RCCI mode because the ignition delay (ID) was shorter, and the reactivity gradient was wider when the cetane of the LRF was higher. Also, the HC, CO, and smoke emissions of the methanol/biodiesel operation improved, whereas the NOx decreased. Additionally, a number of studies have been done employing fossil fuels with high octane numbers as LRFs in RCCI operations. These fuels are observed to cause significantly greater CO and HC emissions [24].

1.3. Split injection technique

The split injection technique involves dividing the main injection pulse into two or more injections, enhancing the reaction zone between the combustion chamber air and the flame boundary while reducing the fuel-rich zone [25]. High-viscosity biodiesel with a mechanical injection system reduces thermal efficiency while increasing smoke and hydrocarbon emissions. Adapting the fuel injection system can address the challenges posed by increased viscosity. Common-Rail Direct Injection (CRDI) systems, in contrast to mechanical injection, enhance thermal efficiency and diminish emissions of Hydrocarbons (HC) and smoke [26]. The effect of the most important factors on RCCI engine combustion, including injection timing and injection duration, was numerically analyzed in a methane/natural gas-powered RCCI engine. The results show that delaying the commencement of single-stage injection increases HC, CO, and NOx emissions. The findings for different double injection schedules show that the cylinder temperature and rate of heat release decrease. Moreover, increasing the injection duration (from 55° to 70°CA) also decreases CO, NOx, and HC emissions [9]. In light of this, CRDI stands as a proven method for boosting engine performance while lowering exhaust pollutants. It also enables the implementation of split injection strategies and adjustments to split injection ratios to achieve further emission reductions. Split injection is proposed as a viable approach to enhancing in-cylinder combustion and emission traits without the need for extensive engine modifications [27]. Kakaee et al. [28] examined the utilization of CH_4 in RCCI engines. According to reports, natural gas was used as LRF and diesel as HRF in the RCCI operation using the split injection technique. Another research investigated the influence of injection timing on mixture reactivity and stratification by using various diesel injection techniques. The research found that advancing diesel injection enhances reactivity within the cylinder mixture, whereas delaying injection enhances mixture stratification. Moreover, the dual injection method proves more effective in scenarios with lower premixed energy ratios, while the single injection strategy performs better in cases with higher energy premixing levels [29]. According to the research, engine load and fuel premix ratio had an impact on engine characteristics. The effects of pilot mass, split diesel fuel injection timings, and the amount of pre-mixed natural gas on RCCI operation were investigated. The results showed that engine thermal efficiency could be increased, and smoke and NOx could be decreased by altering the experiment settings. Additionally, there are fewer emissions of HC and CO [30]. Yousefi et al. [31] investigated the use of the split injection technique to enhance BTE and lower emissions in an ammonia diesel powered dual-fuel CI engine. The results indicates that split injection increases indicated thermal efficiency by 39.72 % while simultaneously reducing engine exhaust emissions.

1.4. Ammonia as ICE fuel

The significant growth in GHG concentrations over the last millennia has raised the world average temperature, which may create climatic difficulties and have an influence on our humanity [32]. Because of the challenges and hazards associated with conventional carbon-based fossil energy, carbon offsets in transportation are increasingly necessary. The

increase in CO_2 emissions from the transportation sectors contributes significantly to the rise in GHG concentrations [33]. Controlling the CO_2 emissions of ICEs may therefore aid in GHG reduction [34]. Widening the usage of carbon-free fuels is one strategy to lower the ICE's carbon emissions. Carbon-free sources like hydrogen and ammonia help to mitigate environmental problems caused by GHG emissions [35]. The use of H_2 in ICEs has been extensively studied and has performed well [36,37]. But, because of its strong reactivity, hydrogen easily explodes when combined with air. Hydrogen is an excellent source of energy and a cleaner fuel with a better heating value than fossil fuel. However, improved storage methods are necessary, and the complexity of liquidation raises storage and transportation costs. As a result, hydrogen as a carbon-neutral alternative fuel in ICEs has limits [38]. Apart from hydrogen, ammonia, which is a hydrogen carrier, is an excellent energy source for transportation vehicles owing to its availability and storage capabilities [39,40]. As a result, ammonia usage in ICEs has been a major topic of study recently in an effort to reduce carbon emissions. Using carbon-free fuels like ammonia may aid in the decarburization of ICEs [41]. A study demonstrated the effects of substituting diesel fuel with ammonia in an ammonia-diesel blend dual-fuel engine. The results demonstrate that ammonia can deliver 84.2 % of the input energy, while increasing the diesel replacement increases thermal efficiency. Moreover, augmenting the ammonia energy content transitioned the combustion phase in dual fuel mode from diffusion to premixed combustion. This adjustment resulted in a 6.8°CA reduction in combustion duration and a shift of 32°CA in combustion phasing. While ammonia effectively decreased CO_2 and CO emissions, it also led to an increase in NO_X emissions [42]. Forby N et al. [43] investigated the ammonia energy in the dual fuel engine as LRF and n-heptane as HRF. Exhaust emissions are decreased due to increased ammonia combustion efficiency with split injection of direction injection fuel. Therefore, the investigation suggested that multi-injection and advance injection of HRF were two conceivable possibilities for ammonia combustion. Moreover, the work's innovation is highlighted by the split injection parameters calibration of the CRDI engine employing RCCI impact among the operating parameters.

1.5. Biodiesel as ICE fuels

The reason for an alternate source of energy is the energy security problem with traditional crude-based fuels as well as increased exhaust gas emissions from the CI engine, which operates on diesel fuels. Biofuels, which are produced from diverse biomass feedstocks, are the ideal replacement for renewable and ecologically beneficial fuels [44]. Renewable sources of energy like biofuels have great potential to displace fossil fuels. They provide plenty of benefits, including reusability, sustainability, a decrease in GHG emissions, and regional development [45]. The most popular biofuel is biodiesel because it has qualities that are extremely comparable to diesel fuel and can be used with only minor engine modifications [46,47]. When compared to petroleum-based diesel, biodiesel has several advantages, including being oxygenated, environmentally friendly, having an elevated flash point (storage), being biodegradable, emitting fewer emissions, and being produced from an abundance of resources, such as vegetable, algal, and waste oils [48,49]. There are also disadvantages to using biodiesel in addition to these specific benefits [50–52]. Their poor cold flow and spray qualities, greater viscosity, lower heating value, higher NOx emission levels, engine power losses, and increase in BSEC may all be listed as severe drawbacks [53,54]. Therefore, reducing biofuel and increasing the use of carbon-free fuels will sustain the CI engine.

2. Aims and aspirations in the current research

The investigation is based on a four-stroke, electronically regulated common-rail CI engine altered to use NH_3 as fuel. Ammonia usage in CI engines significantly affects exhaust characteristics. However, ammonia has certain shortcomings in terms of combustion characteristics and compatibility. Hence, recommending its adoption as a substitute for fossil fuels, relying solely on engine performance metrics, requires further scrutiny. It is necessary to evaluate the pre- and main-injection strategies to address the deficiencies of NH_3 combustion, resulting in an improved early Start of Combustion (SoC) of algal biodiesel. Consequently, a substantial study has been conducted into the effects of NH_3 on CI engines. The investigation's goal is to decrease engine emissions by minimizing biodiesel and improving carbon-free fuels for CI engine combustion. As a result, low-carbonization and zero-carbonization of ICE require continuous effort. On the contrary, ammonia demonstrates the lowest adiabatic flame temperature, superior latent heat of vaporization, and diminished combustion efficiency. Therefore, partitioning the primary injection of biodiesel into pre- and main injections with ammonia would augment combustion efficiency. The initial injection of biodiesel plays a pivotal role in this process by effectively delaying the ignition, a critical aspect of the combustion process.

To achieve optimal combustion efficiency for ammonia/biodiesel mixtures in CI engines, an in-depth analysis of RCCI dynamics using adjustable split injection is imperative. This study concentrates on performance metrics, combustion processes, and emission profiles across diverse load scenarios at a steady engine speed of 1500 rpm. Contemporary research examines the combustion traits of ammonia when amalgamated with other fuels, underscoring the prospective advantages and difficulties inherent in these blends. Also, the utilization of NH_3/biodiesel mixtures in RCCI mode-operated engines using biodiesel split injection has yet to be extensively examined. According to our previous investigations, maintaining an NH_3 premixing ratio of 40 % in RCCI mode is ideal; any deviation from this ratio tends to diminish the engine's thermal efficiency. By analyzing the combustion dynamics, performance metrics, and emission characteristics associated with pre-and main-injection timings in RCCI engines, our research suggests that fine-tuning these parameters can significantly improve the combustion efficiency of NH_3 when used as a fuel in RCCI engines. The current research focuses on how various biodiesel pre- and main-injection angles burn 40 % premixed ammonia with the 45 % biodiesel split ratio (45 % pre-injection and 55 % main-injection) by measuring combustion, performance, and emissions factors. Initially, the engine test rig was configured to operate in a dual-fuel mode with 40 % NH_3 and biodiesel, utilizing a single biodiesel injection approach across different load conditions. Subsequently, the engine continued to run in the 40 % NH_3/biodiesel dual-fuel mode and scrutinized the impacts of pre- and main injection of biodiesel under varying load scenarios.

3. Experimental methodology

3.1. Ammonia supply system

A 150-pound NH_3 cylinder was utilized to store the liquid NH_3, with its temperature maintained at 38 °C via a heating blanket affixed to the cylinder. Gaseous ammonia from the cylinder is routed through a pressure regulator and a mass flow meter to quantify the ammonia flow rate before reaching a solenoid injector within the intake manifold. A gas reservoir was installed upstream of the ammonia injectors to dampen flow fluctuations caused by pressure swings. Vaporized NH_3 is dispensed into the intake manifold using an electronically regulated port fuel injection system. An electronic control unit (ECU) governed the pulse width, injection pressure, and timing of the injections. The NH_3 energy premixing percentage was obtained by adjusting the injector's input voltage. The pressure regulator moderates high inlet pressures to suitable output levels and controls the flow of NH_3 gases. Additionally, it strives to uphold consistent exit pressure despite fluctuations in input pressure. The mass flow rate of gaseous NH_3 is meticulously regulated by passing it through a precision flow control valve before reaching the NH_3 mass flow meter. 40 % of the ammonia's energy contribution was introduced via the port injection method, while the remaining biodiesel

fuel was delivered using an ordinary fuel injection method.

3.2. Energy fraction methodology

According to equation (1), the energy share of NH_3 is calculated as the ratio of the energy from ammonia to the total energy provided for combustion:

$$\%NH_3 = \frac{(m_{NH3} \times CV_{NH3})}{(m_{BD} \times CV_{BD}) + (m_{NH3} \times CV_{NH3})} \times 100 \quad (1)$$

Where m_{NH3} and m_{BD} are the ammonia and biodiesel mass flow rates, respectively. The calorific values of NH_3 and biodiesel fuels are represented as CV_{NH3} and CV_{BD}, respectively. The tests incorporated into the scope of the research were performed under varying loads and at 1500 rpm. The test engine was thermally stabilized to 80 °C to ensure consistent operating conditions. Experimental trials were conducted in triplicate to mitigate data acquisition discrepancies, and the outcomes were averaged for precision. Tables 1 and 2 outline NH_3 and algae biodiesel fuels' properties and flow metrics.

3.3. Experimental setup

For this investigation, a 4-stroke mono-cylinder constant-speed common-rail injection system was designated from the Kirloskar research engine. Table 3 delineates the comprehensive engine parameters and specifications. The adaptable engine setup is rigidly placed on the test bench, with mechanical linkage to an eddy current dynamometer. A strain gauge load cell is employed to measure the applied load. A water-cooling arrangement is utilized to maintain optimal temperatures for both the dynamometer and engine. To examine the temperature of the exhaust emission, a K-type thermocouple sensor is correctly positioned at the appropriate junction. The CP with respect to crank angle (CA) data is necessary for the investigation of fuel combustion behavior. Moreover, a piezoelectric transducer and a charge amplifier are installed to collect pressure data. The airflow sensor, calorimetric fuel sensor, and thermal model FT1 flowmeter are used to detect the rate of consumption of intake air, directly injected fuel, and port-injected ammonia by the engine at each cycle for performance analysis. Fig. 1 illustrates a schematic representation of the experimental engine configuration. Furthermore, the engine control system is adjusted to manual mode for experimentation, incorporating a customizable control feature for injection timing. The MCAR software package's ECU, which is controlled by NIRA, was launched to allow this to happen. The data acquisition system makes use of the observed data. Further, it is utilized to determine the different combustion and performance parameters by applying thermodynamic principles. The AVL gas analyzer assesses exhaust emissions like HC, CO, and NOx, while the AVL 444 smoke meter model evaluates smoke opacity. A moisture trap and filtration system safeguard the gas analyzer from moisture and particulates.

Table 1
Properties of test fuels.

Properties	Unit	Algae biodiesel	NH_3
Viscosity @ 40 °C	cSt	5.07	–
Density @ 20 °C	g/ml	0.88	0.73
Flame velocity	m/s	0.3	0.32
Calorific value	MJ/kg	41.08	18.5
Cetane number	–	42	–
Octane number	–	–	130
Mass diffusivity in air	cm^2/s	–	0.22
Latent heat of vaporization	kJ/kg	306	1371
Minimum ignition energy	mJ	–	8
Auto ignition	K	523	651
Flash point	°C	91	132
Fire point	°C	121	148
Flammability limit	% vol	0.6–7.5	14–33.8
Stoichiometric A/F ratio	–	–	6.06

3.4. Uncertainty

To compute the uncertainties of measured parameters with $+2\sigma$ confidence levels, the Gaussian-distribution method was utilized. To evaluate variability, measurements were done under similar operating conditions. The uncertainties of the experiment are shown in Table 4.

Thus, any measured parameter uncertainty is computed as $(\Delta Xi) = 2\sigma_i / \overline{X_i} * 100$

To give accurate error limitations for the estimated parameters, the root-mean-square approach is utilized, and the degree of inaccuracy is expressed in equation (2).

$$\Delta R = \sqrt{\{(\partial R/\partial X_1) * \Delta X1)^2 + ((\partial R/\partial X_2) * \Delta X2)^2 + \ldots\ldots + ((\partial R/\partial Xn) * \Delta Xn)^2\}} \quad (2)$$

The experimentation overall uncertainty is calculated as follows:

$$= \sqrt{0.7^2 + 1.67^2 + 0.79^2 + 0.8^2 + 0.1^2 + 0.5^2 + 0.58^2 + 0.58^2}$$
$$= 2.33\%$$

4. Results and discussion

4.1. Combustion characteristics

4.1.1. In-cylinder pressure

4.1.1.1. Main-injection strategy. The peak CP for the single injection of dual fuel combustion along with the different main-injection timings of the biodiesel split injection are shown in Fig. 2. The rate of combustion of premixed fuel affects in-cylinder pressure. We observe that the CP rises when the pre-injection time is held constant at 46 °CA bTDC and the main injection is simply advanced from 12 to 18 °CA bTDC. The significant peak CP for a single injection of 40 % ammonia in dual fuel operation was 57.86 bar. Similarly, the various crucial main injection timings at 12, 15, 18, and 21°CA bTDC for 40 % ammonia-fueled operation with the 45 % split ratio peak pressures were 60.3 bar, 63 bar, 66.9 bar, and 65.6 bar, respectively. The maximum CP obtained among various main-injection timings is 18°CA bTDC, which is 15.6 % higher peak pressure than the 40 % ammonia-biodiesel dual fuel single injection operation at 26°CA bTDC injection timing.

It can be attributed to the port induction of ammonia and the pre-injection of biodiesel, which lengthens the mixing period with air and help the mixture become homogenous. The main biodiesel injection acts as the source of ignition for the homogeneous mixture. The homogeneous charge makes it easy to initiate the phenomenon of prompt multipoint auto ignition, which leads to intensified combustion pressure [17]. The dual-fuel combustion process continues to advance with the advancement of the main injection angle; peak CP increases progressively; their corresponding phases shift towards TDC; and the combustion period tends to reduce [55]. As a result, the peak CP increases. But with further advancement of the main injection to 21°CA bTDC, the peak CP was reduced. As the main injection angle advances, the cylinder air and biodiesel mixture gets more homogeneous and reduces the local equivalency ratio when cylinder temperature and pressure reach auto ignition condition [56].

4.1.1.2. Pre-injection strategy. The CP for the optimized main injection along with the different pre-injection timings of the biodiesel split injection are shown in Fig. 3. We observe that the CP rises when the main-injection time is held constant at 18 °CA bTDC and the pre-injection timing is simply advanced from 46 to 54°CA bTDC. The peak CP of various pre-injection timings at 46°CA, 50°CA, 54°CA, and 58°CA bTDC for 40 % ammonia-fueled operation with the 45 % split ratio were 66.9 bar, 69.6 bar, 75.3 bar, and 72.4 bar, respectively. The highest CP

Table 2
Experimental matrix and mass flow rates of fuels of dual fuel operation.

Test No	Operating mode	PortNH_3 (%)	Split angle (°CA bTDC) pre/main	Split ratio (%) pre/main	Mass flow rate (kg/h) for 40 % NH_3 and 60 % biodiesel										Acronym
					20 %		40 %		60 %		80 %		100 %		
					NH_3	BD	NH_3	BD	NH_3	BD	NH_3	BD	NH_3	BD	
1	Single injection	40	–	0/100	0.278	0.184	0.475	0.315	0.595	0.395	0.681	0.452	0.779	0.517	IT = 26 bTDC
2	Split injection	40	46/12	45/55	0.275	0.182	0.466	0.309	0.577	0.383	0.653	0.433	0.815	0.541	SIT = 46:12 bTDC
			46/15		0.272	0.181	0.456	0.303	0.560	0.372	0.626	0.416	0.780	0.518	SIT = 46:15 bTDC
			46/18		0.267	0.177	0.438	0.291	0.527	0.350	0.577	0.383	0.728	0.483	SIT = 46:18 bTDC
			46/21		0.269	0.179	0.447	0.297	0.543	0.360	0.601	0.399	0.749	0.497	SIT = 46:21 bTDC
			50/18		0.263	0.175	0.429	0.285	0.511	0.339	0.554	0.368	0.700	0.464	SIT = 50:18 bTDC
			54/18		0.256	0.170	0.412	0.274	0.481	0.319	0.511	0.339	0.646	0.429	SIT = 54:18 bTDC
			58/18		0.261	0.173	0.421	0.279	0.496	0.329	0.532	0.353	0.676	0.449	SIT = 58:18 bTDC

Table 3
Experimental engine setup.

Parameters	Details
Make	Kirloskar
Engine	CI
Cooling type	Water cooling
Power output	3.5 kW @ 1500 rpm
Compression Ratio (CR)	17.5
SoI (direct injection)	24 °CA bTDC
Bore × stroke	87.5 mm × 110 mm
Fuel Injection	Common rail direct injection
Torque	23.5 N-m

obtained from the various pre-injection timings is 54°CA bTDC, which is 12.5 % higher peak pressure than optimal main-injection operation at 18°CA bTDC for the 45 % biodiesel split ratio and 30.05 % higher than 40 % ammonia-biodiesel single injection operation at 26°CA bTDC injection timing. The peak CP apparently increased, and the corresponding phase shifted towards TDC. With the advance of the biodiesel pre-injection angle, when the main injection angle is optimum, the HR of ammonia-biodiesel combustion continues to increase, and the phases of combustion are further advanced. The peak values of CP further advanced to TDC and reached their maximum. Since the advancement of the pre-injection angle allows the pre-injected biodiesel sufficient time for physical delay and diffusion, thus progressively increasing the combustion auto-ignition point, when the main injection starts and the premixed combustion phase is constantly enhanced, more intense combustion occurs with improved peak CP [57]. But further advancement of the pre-injection angle to 58°CA bTDC, the maximum CP was further advanced closer to constant volume combustion [58]. The peak CP decreases as the pre-injection angle further advances. When the pre-injection angle is earlier than 54 °CA bTDC, there will be noticeable compression negative work, which causes the BSEC to fluctuate.

4.1.2. Heat release rate

4.1.2.1. Main injection strategy. The heat release (HR) for the single injection of dual fuel operation along with the different main-injection timings of the biodiesel split injection are shown in Fig. 2. We observe that the peak HRR rises when the pre-injection angle is held constant at 46 °CA bTDC and the main injection is simply advanced from 12 to 18 °CA bTDC. Double-peak HRR amplified noticeably, and the corresponding CA shifted towards TDC. The HRR of split injection shifts to a single peak HRR; this effect is attributed to pre-injected biodiesel, which enhances the premixed combustion. Earlier main biodiesel injection advances the start of combustion (SoC) and enhances the peak HRR in comparison to the 40 % ammonia-biodiesel single injection at 26°CAbTDC. With the advance of the early main injection of biodiesel from 12 to 18°CA, BTDC causes a higher quantity of biodiesel mixed with air, which develops combustion earlier. Advancing main injection also enhances the peak of HRR because more premixed charge is formed, resulting in a higher rate of combustion at premixed combustion phase [59]. But further advancement of the main injection to 21°CA bTDC, the phase of HRR was retarded. It can be attributed to the in-cylinder air temperature and pressure being lower, so ID increased and peak HRR was somewhat reduced and delayed [60]. When the injection timing is away from TDC, as the main injection angle advances, the cylinder air and biodiesel mixture gets more homogeneous and reduces the local equivalency ratio when cylinder temperature and pressure reach auto ignition conditions. Poor combustion might occur if the injection angle is increased or decreased beyond a specific limit [56,61].

4.1.2.2. Pre injection strategy. A dual-fuel operation pre-injection angle is a crucial variable, and useful technique for enhancing the enhancement of the combustion kernel throughout the in-cylinder. The HRR for the optimized main injection along with the different pre-injection timings of the biodiesel split injection are illustrated in Fig. 3. As the pre-injection advanced, the premixed combustion phase of HRR was noticeably enhanced noticeably, and the corresponding CA further moved towards TDC. However, by increasing the pre-injection angle to 58°CA bTDC, the HRR phase was delayed. It is evident that the pre-injection angle also has an important influence on how well the main biodiesel injection burns. The combustion process of the pre-injected biodiesel in the elevated temperature zone improved the SoC and flame development of the main-injected biodiesel in a suitable range, which ranges from 46°CA bTDC to 54°CA bTDC, and the cylinder charge approaches ignition conditions sooner, the combustion phases advance, and HRR becomes closer to constant-volume combustion [62]. The primary peak of HRR is dependent on the pre-biodiesel injection angle; by advancing the pre-biodiesel injection, the pre-injected biodiesel has ample time to create a homogeneous combination with ammonia and air. The SoC was further advanced, and the pre-injected biodiesel almost began to burn with the biodiesel main injection. According to this finding, the premixed combustion phase is improved, whereas the diffusion combustion phase is decreased. Moreover, as the pre-injection angle progressively advanced to 58°CA bTDC, the primary peak of the HRR curve increased and the corresponding CA further advanced, which is attributed to the negative compression work [63].

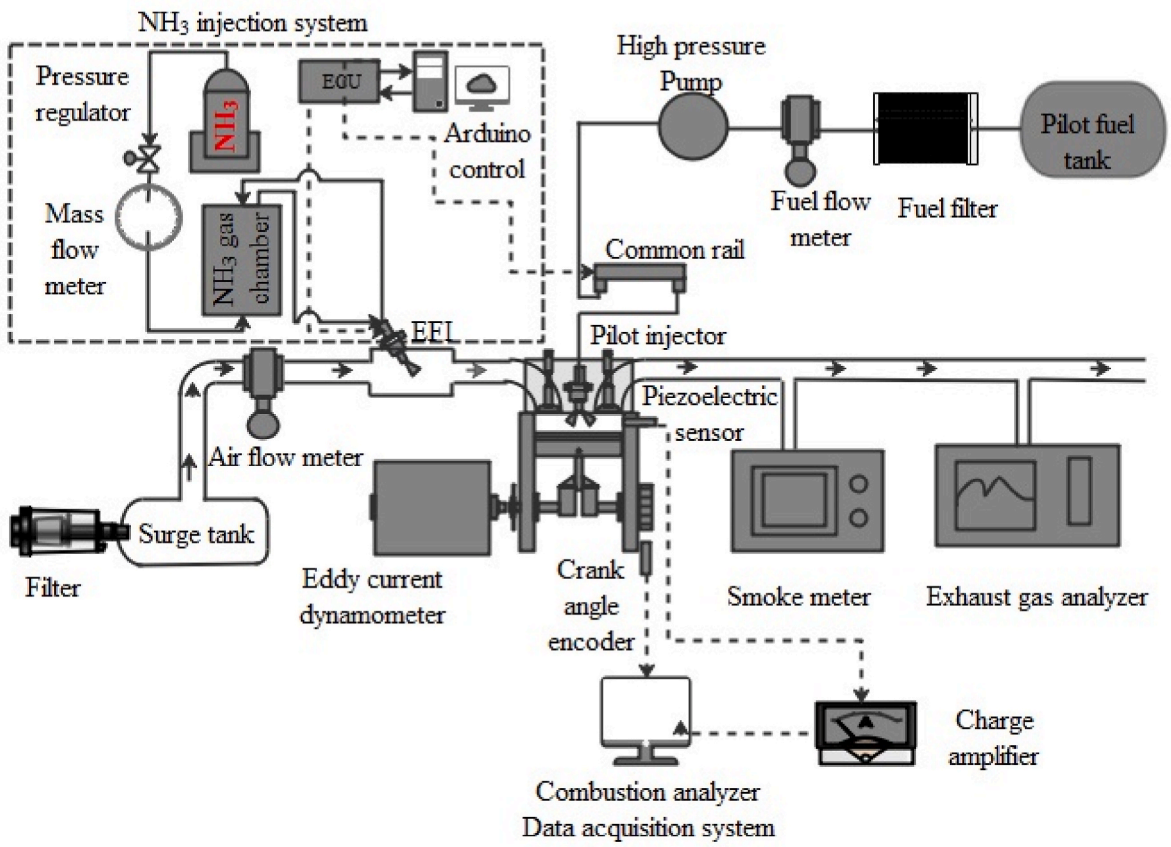

Fig. 1. Schematic of an experimental setup.

Table 4
Uncertainty particulars.

Parameters	Accuracy	% Uncertainty
Brake power (BP) (kW)	±0.5	±0.7
Pressure (bar)	±0.1	±1.67
Fuel consumption (kg/h)	±0.001	±0.79
Hydrocarbon (HC) (ppm)	±1.25	±0.8
Carbon monoxide (CO) (% vol.)	±0.08	±0.1
Nitrogen oxides (NOx) (ppm)	±1	±0.5
Smoke opacity (%)	±1.33	±0.58
Exhaust gas temperature (°C)	±1.1	±0.52

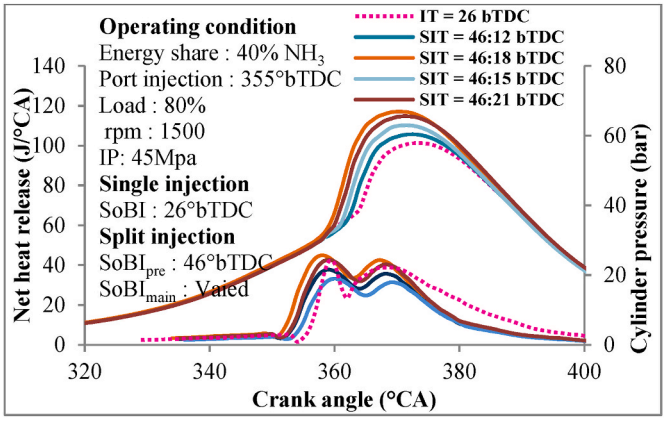

Fig. 2. Effects of main-injection angle on CP and HRR.

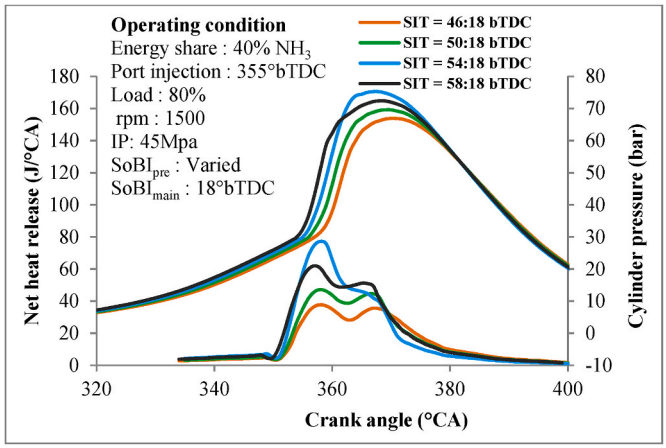

Fig. 3. Effects of pre-injection angle on CP and HRR.

4.2. Performance characteristics

4.2.1. Brake Thermal Efficiency and brake specific energy consumption

4.2.1.1. Main-injection strategy. Brake thermal efficiency and brake specific energy consumption are always one the inverse of the other. The performance of the IC engine that indicates a successful conversion of the fuel's chemical energy into useable power output is described as BTE. Fig. 4 demonstrates the difference in BTE and BSEC with regard to load for various main injection angles with the single injection of 40 % ammonia biodiesel in dual fuel operation mode for comparison. It increases with the gradual rise in load. It was noted that the BTE for a

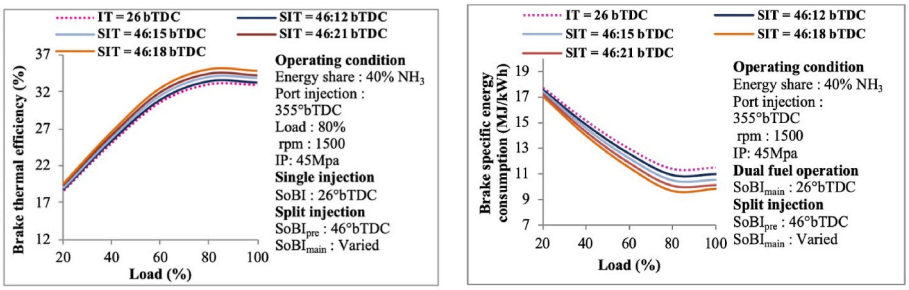

Fig. 4. Effects of main-injection angle on BTE and BSEC.

single-injected dual-fuel operation was 32.82 % at peak load conditions. Similarly, the BTE of different main injection timings at 12, 15, 18, and 21°CA bTDC operation for 40 % ammonia-fueled operation with the 45 % split ratio were 33.2 %, 33.8 %, 34.7 %, and 34.2 %, respectively. The maximum BTE obtained is 18°CA bTDC, which is 5.8 % higher than 40 % ammonia-biodiesel dual fuel single injection operation at 26°CAbTDC injection timing. Similarly, at peak load conditions, the average BSEC for a single injection of 40 % ammonia energy share in dual fuel operation was 11.5 MJ/kWh. Similarly, the BSEC of various main injection timings at 12, 15, 18, and 21 bTDC for the 40 % ammonia premixed split injection operation with the 45 % split ratio were 11, 10.5, 9.8, and 10.1 MJ/kWh, respectively. As related to single injection operations, the BSEC of 12, 15, 18, and 21°CA bTDC operations dropped by 4.3 %, 8.5 %, 14.5 % and 12.0 %, respectively. As main injection further advances to 21°CA bTDC, due to the reduced global temperature, the diffusion combustion phase increases, reducing the thermal efficiency. The main injection of 18°CA bTDC was chosen as the optimal main injection and may be utilized for further research based on acceptable performance and fuel attributes. Advancing of main injection angle from 12 to 18°CA bTDC, premixing is enhanced, which reduces the ID and thereby reduces fuel consumption. Further advancing the main injection to 21°CA bTDC, it was observed that the CP and temperature remained low at that time, the portion of the fuel could not be mixed with air, and an over-rich zone was created, resulting in inefficient combustion and higher energy consumption [64,65].

4.2.1.2. Pre-injection strategy. Fig. 5 exhibits the variation of BTE with regard to load for various pre-injection angles with optimum main injection of 40 % ammonia biodiesel dual fuel operation mode for the comparison. At peak load conditions, the maximum BTE for different pre-injection timings at 46°CA, 50°CA, 54°CA, and 58°CA bTDC for the 40 % ammonia premixed split injection operation with the 45 % split ratio were 34.7 %, 35.3 %, 36.4 %, and 35.8 %, respectively. As advancing the pre-injection to 54°CA bTDC rises the thermal efficiency remarkably by 4.9 % compared to optimum main injection operation at 18°CA bTDC and 11 % higher than 40 % ammonia-biodiesel dual fuel single injection operation at 26°CA bTDC injection timing. This might be due to the earlier SoC. Advancing both the pre- and main-injection timings further does not offer significant benefits and instead results in a decrease in Brake Thermal Efficiency (BTE) [56,64]. Similarly, at peak load conditions, the BSEC for different pre-injection timings at 46°CA, 50°CA, 54°CA, and 58°CA bTDC for the 40 % ammonia premixed split injection operation with the 45 % biodiesel split ratio were 9.9, 9.5, 8.7, and 9.1 MJ/kWh, respectively. As advancing the pre-injection angle to 54°CA bTDC, the highest reduction of BSEC is remarkably by 11.2 % than optimum main injection operation at 18°CA bTDC and 24.1 % higher than the 40 % ammonia-biodiesel dual fuel single injection operation at 26°CA bTDC injection timing. At an advanced pre-injection timing of 58°CA bTDC, the Peak Rate of Pressure Rise (PRR) at the end of the compression stroke increases, leading to higher negative compression work. This results in decreased thermal efficiency due to reduced net work output and increased fuel consumption. While advancing the injection timing initially enhances Brake Thermal Efficiency (BTE) and reduces energy consumption, there is a threshold beyond which these benefits diminish. Ultimately, the optimal injection timing for maximizing engine efficiency depends on the combustion characteristics of the specific fuel being used [55]. On further advancement, pre-injection leads to pre-auto ignition, which causes more fuel to get burned before TDC and significant heat loss, indicating that more fuel is needed to produce the same amount of power [66].

4.3. Emission characteristics

4.3.1. Unburned hydrocarbon emission

4.3.1.1. Main-injection strategy. The operating parameters of the engine, the fuel chemical composition, the fuel injection timing, and the air-fuel interaction inside the cylinder all affect the quantity of unburned hydrocarbon (UBHC) in the exhaust. Fig. 6 exhibits the difference in HC emissions with regard to load for the dual fuel single injection and various main-injection angles of split injection operations. The reduction in UBHC emission for main injection operation as compared to single main injection operation was found to be 3.8 % for 12°CA bTDC, 7.3 % for 15°CA bTDC, 13.4 % for 18°CA bTDC, and 10.2 % for 21°CA bTDC. The source of hydrocarbon emission is only from biodiesel combustion because ammonia doesn't contain carbon structure. The

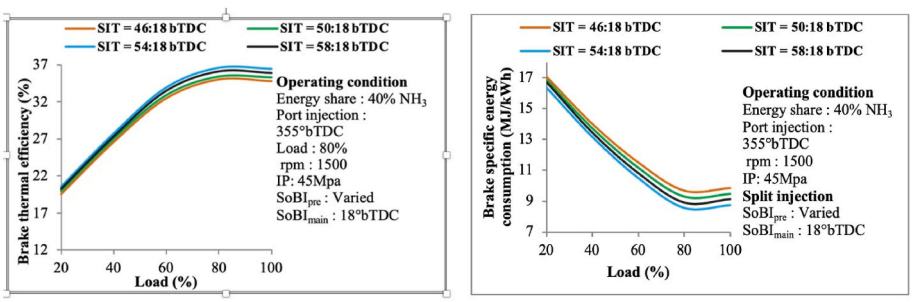

Fig. 5. Effects of pre-injection angle on BTE and BSEC.

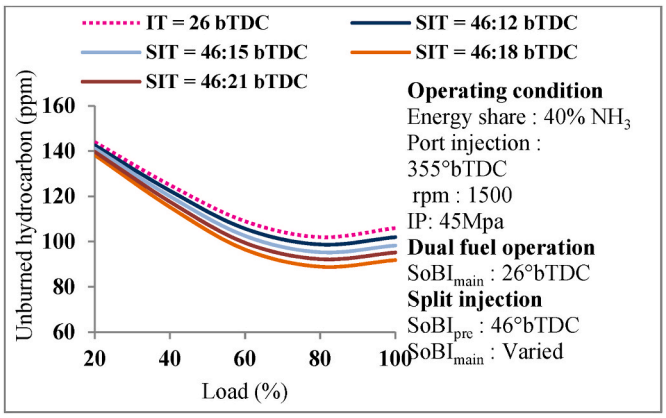

Fig. 6. Effects of main-injection angle on HC.

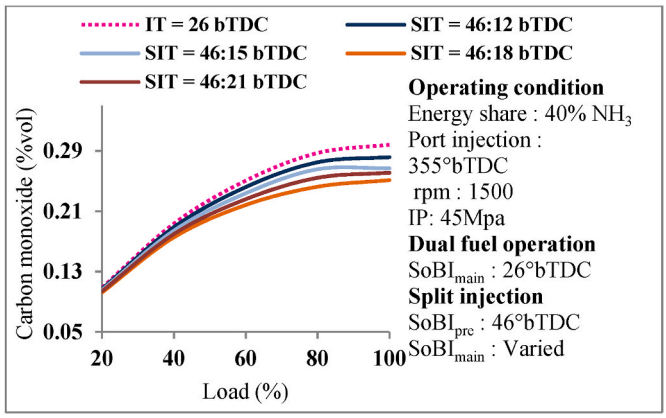

Fig. 8. Effects of main-injection angle on CO.

amount of UBHC emissions is decreased by improved biodiesel combustion efficiency. Furthermore, at peak loads, the HC emissions are reduced regardless of the injection angle due to combustion temperature, which enhances the oxidation of UBHC emission [67]. Improved atomization ratio is the primary factor in lower HC emissions at peak engine load. Simultaneously, high engine loads also contribute to turbulence or accelerated intake air flow. This promotes fuel atomization, homogenizes the mixture, and decreases HC emissions [68].

4.3.1.2. Pre-injection strategy. Fig. 7 shows the variation of HC emissions with respect to load for the optimum main injection and various pre-injection angles. The UBHC emissions noted for pre-injection timings of 46°CA bTDC, 50°CA bTDC, 54°CA bTDC, and 58°CA bTDC are 92 ppm, 89 ppm, 86 ppm, and 83 ppm. In contrast to the optimal main injection strategy, the UBHC of pre-injection is 3.2 %, 6.8 %, and 9.8 % reduced, respectively. Advancing pre-injection from 46 to 54 °CA bTDC results in reduced UBHC emissions. This is because of the advancement of the pre-injection effect; there was a longer dwell time, greater atomization, evaporation, and an enhanced air-fuel combination, which resulted in effective combustion [69]. Further advancement to 58 °CA bTDC elicited a shorter ID, due to which early SoC, which promotes constant-volume combustion and increases the cylinder temperature, results in a higher reduction of UBHC emissions.

4.3.2. Carbon monoxide emission

4.3.2.1. Main-injection strategy. The CI engine's CO emissions demonstrate poor fuel combustion. The CO release is another sign of improper fuel combustion. Fig. 8 indicates the difference in CO emissions with regard to load for various main injection angles with the single injection of 40 % ammonia biodiesel in dual fuel operation mode. The CO emission with the no pre-injection case (injection timing 26°CA bTDC) is much higher because the ID is extremely high in this situation. At peak load conditions, the observed highest CO emission for the single injection operation is 0.298 % vol. Similarly, for the main injection operationat12°CA bTDC was 0.282 % vol., 15°CA bTDC was 0.267 % vol., 18°CA bTDC was 0.251 % vol., and21°CA bTDC was 0.261 % vol. The drop in CO emissions as compared to dual fuel single injection was found to be 5.5 %, 10.5 %, 15.7 %, and 12.4 %, respectively.

The main causes of CO emissions include a heterogeneous charge mixture, insufficient oxygen, shorter resident time, and inefficient CO_2 promotion. Among them, the air-fuel ratio has a significant impact on CO emissions. At maximum load, CO emissions were high. This might be attributable to a rich air-fuel combination that hindered CO oxidation [70]. As explained earlier main injection advances the SoC and combustion phase, but further advanced the combustion efficiency is reduced because of cylinder temperature and pressure, which are not conducive for the auto ignition of main injected biodiesel. As a consequence of the delayed combustion, injected fuel may not have sufficient time to burn entirely, resulting in higher CO emissions [57,71].

4.3.2.2. Pre-injection strategy. Fig. 9 illustrates the difference in CO emissions with regard to load for different pre-injection angles with optimum main injection of 40 % ammonia biodiesel in dual fuel operation mode. The CO emissions found for the advanced pre-injection angle at 46, 50, 54, and 58°CA bTDC are 0.251, 0.239, 0.228, and 0.218 % vol. It was discovered that the 58°CA bTDC emits minimal CO, around 0.218 % vol., under the same working conditions. Compared with optimal main injection and the dual fuel single injection operation, the CO emissions for the 58°CA bTDC were reduced by 13.3 % and 26.9

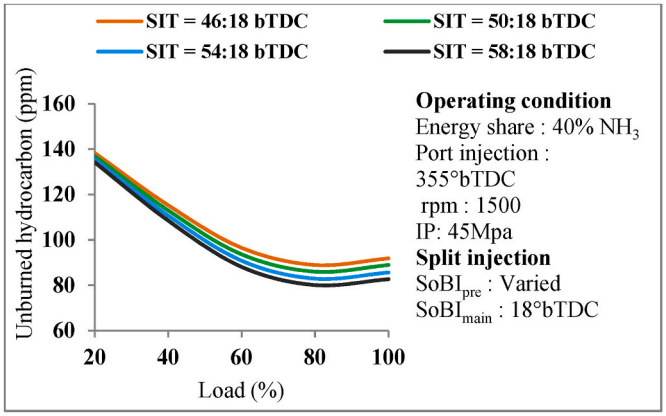

Fig. 7. Effects of pre-injection angle on HC.

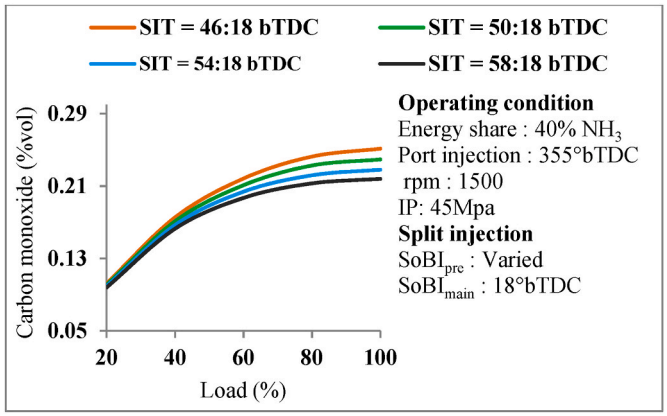

Fig. 9. Effects of pre-injection angle on CO.

%, respectively. Due to prolonged and sluggish combustion and the accompanying lower average in-cylinder temperature, CO emissions are considerable with single injection. With an increase in pre-injection time from 46 to 54°CA bTDC, resulting in greater oxidation levels and lower CO emissions. Because of the lower cylinder temperatures, pre-injection extends its ID time and forms a stoichiometric mixture, resulting in a greater combustion rate when main injection begins [63]. Further advancing to 58°CA bTDC, the CO oxidation is reduced. This can be attributed to higher fuel consumption due to negative compression work and insufficient time for complete combustion, which leads to increased CO emission [72].

4.3.3. Nitrogen oxides emission

4.3.3.1. Main-injection strategy. Nitrogen and oxygen actively interact together, resulting in nitrogen oxide (NOx) emission under high cylinder temperature regimes. Combusting the air-fuel mixture under stoichiometric conditions significantly contributes to NO_X formation. Similarly, NOx emissions were found to be greater around the maximum load state. Fig. 10 shows the difference in NOx emissions with regard to load for the dual fuel single injection and various main injection angle operations. The NOx emission for the dual fuel single injection operation was 456 ppm. Similarly, for the main injection operation at 12°CA bTDC was 482 ppm, 15°CA bTDC was 509 ppm, 18°CA bTDC was 538 ppm, and 21°CA bTDC was 509 ppm. As related to the dual fuel single injection operation, the NOx emissions for the 12, 15, 18, and 21°CA bTDC operations were increased by 5.6 %, 11.5 %, 25.2 %, and 17.9 %, respectively. It demonstrates a general law that NOx always grows as the main injection time advances. The fundamental reason is that it raises the combustion temperature as well as the residence time of high-temperature-burned gas, where NOx is aggressively formed [73]. As earlier explained, by further increasing main injection to 21°CA bTDC, NOx was reduced.

4.3.3.2. Pre-injection strategy. Fig. 11 illustrates the trend of NOx emissions with regard to load for various pre-injection timings with optimum main injection timing. The NOx emissions found for the pre-injection strategies such as46°CA, 50°CA, 54°CA, and 58°CA bTDC with 40 % ammonia-fueled operationsare572 ppm, 602 ppm, 637 ppm, and 671 ppm, respectively, compared with the optimum main injection, which has 5.2 %, 11.5 %, and 17.3 % higher NOx emissions. NOx emissions grow consistently as pre-injection timing advances. Because the advanced fuel injection timing results in an extended ID phase, the biodiesel may be properly mixed at the SoC, resulting in a more concentrated HR process and enhanced combustion perfection [74].

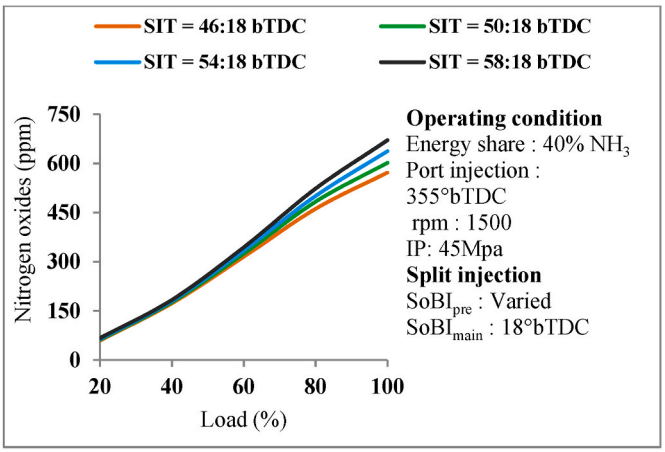

Fig. 11. Effects of pre-injection angle on NOx.

4.3.4. Smoke emission

4.3.4.1. Main-injection strategy. Smoke emission results from incomplete combustion, influenced by an improper air-fuel mixture, ineffective fuel burning, limited oxygen supply, and low combustion temperatures. Fig. 12 shows the variation of smoke opacity with respect to load for the dual fuel single injection and various main injection angle operations. The highest smoke emissions is for dual fuel single injection operation, which is 21.6 %. Similarly, the smoke emission of various main injection timings of 12, 15, 18, and 21°CA bTDC operation were 19.9 %, 17.1 %, and 18.5 %, respectively. The decrease in smoke emission for the dual fuel different main injection operation as compared to dual fuel single injection was found to be 8 % for 12°CA bTDC, 14.2 % for 15°CA bTDC, 27.1 % for 18°CA bTDC, and 21 % for 21°CA bTDC. Biodiesel has a beneficial effect on reducing smoke emissions due to its incomplete evaporation properties. However, as the engine load increases, there is a marked rise in smoke opacity emissions for the test fuel. The higher engine load increases fuel consumption, and the incomplete combustion of the injected fuel leads to elevated smoke emissions [75].

At the same time, the exhaust smoke emissions were reduced when the main injection angle advanced from 12 to 18°CA bTDC at high load conditions, because when the main injection is advanced, the cylinder temperature raises, which improves fuel and oxygen reactions. Another probable cause is the existence of ample time for the fuel vaporization and form a homogeneous charge, which reduced the intensity of the exhaust smoke [76]. Further advancement of the main injection increases smoke emissions because the combustion efficiency decreases.

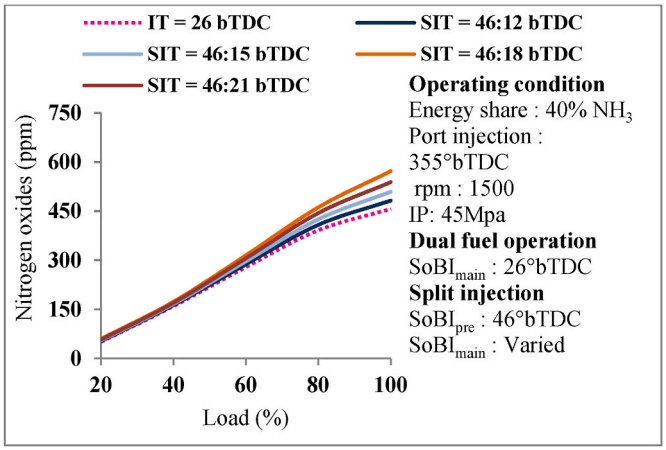

Fig. 10. Effects of main-injection angle on NOx.

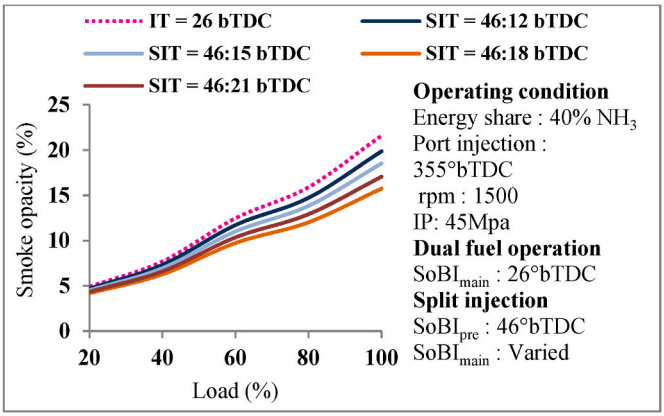

Fig. 12. Effects of main-injection angle on smoke.

4.3.4.2. Pre-injection strategy. Fig. 13 shows the difference in smoke opacity with regard to load for various pre-injections with optimum main injection timing. At peak load conditions, the smoke opacity for different pre-injection angles of 46, 50, 54, and 58°CA bTDC split injection operations was 15.8 %, 14.5 %, 13 %, and 13.5 %, respectively. The study showed a reduction in smoke intensity as advancing the pre-injection up to 54°CA bTDC, highest decrease of smoke opacity by 17.36%compared to optimum main injection operation and 39.73 % than dual fuel single injection operation. With the advancement of biodiesel pre-injection, the ID of the primarily injected biodiesel increased, and a more combustible charge formed, which resulted in higher ignition points and greater ignition energy inside the cylinder, resulting in an increase in CP. Simultaneously, the pre injection causes combustion to begin sooner, and the smoke produced by combustion has a longer duration for oxidation processes, resulting in lower smoke emissions [77]. Further advancing pre-injection to 54°CA bTDC, greater fuel consumption reduced the cylinder temperature, and fuel was not completely combusted, resulting in more smoke emissions. As a consequence, both injection techniques will result in decreased levels of smoke emissions within the region.

4.3.5. Exhaust gas temperature

4.3.5.1. Main-injection strategy. The exhaust gas temperature (EGT) demonstrates how well a fuel's thermal energy is utilized. Heat loss or a rise in exhaust gas temperature indicate that the thermal energy in the fuel has been converted to work [78]. The effects of main-injection timing on EGT with respect to load are shown in Fig. 14. The noticed EGT for the dual fuel single injection operation was 458 °C. Similarly, for the main injection operation at 12°CA bTDC, it was 436 °C, 15°CA bTDC was 420 °C, 18°CA bTDC was 389 °C, and 21°CA bTDC was 407 °C. As related to the dual fuel single injection operation, the EGT for the 12, 15, 18 and 21°CA bTDC operations were reduced by 4.8 %, 8.2 %, 11.2 %, and 11.2 %, respectively. The decreased level of exhaust temperature might be explained by the fact that ammonia has a lower calorific value and a greater cetane number than biodiesel. Because of the greater cetane number, which resulted in a lower exhaust temperature, ID occurred for shorter periods. Simultaneously, since biodiesel has a greater density and viscosity, spray penetration in dual fuel single injection produces a poor atomization rate [79,80]. Therefore, some fuel tends to combust later in the expansion stroke, subsequently, after burning happens, these factors increase the EGT [81]. Regardless of injection timing, the EGT increases at full loads; this might be because of greater amounts of fuel being consumed at greater loads to fulfil the power requirements and better combustion, which would raise the EGT [82]. EGT is greater in single-injection dual-fuel operation; this may be owing to a longer physical delay time, which results in combustion at a later expansion stroke.

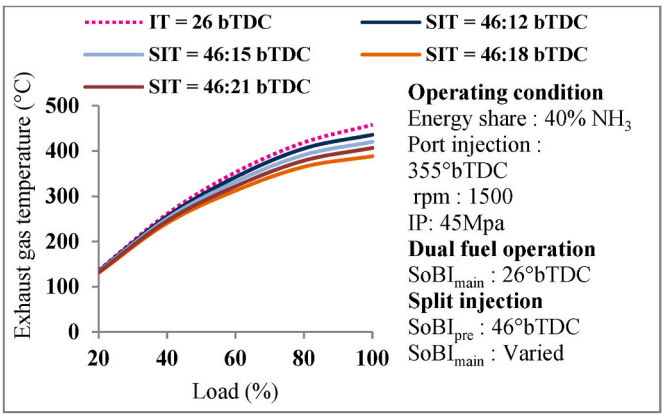

Fig. 14. Effects of main-injection angle on EGT.

4.3.5.2. Pre-injection strategy. The effects of pre-injection on EGT with respect to load are shown in Fig. 15. At peak load conditions, the EGT found for the pre-injection strategies such as 46°CA, 50°CA, 54°CA, and 58°CA bTDC split injection operations is389, 371, 358, and 350, respectively, compared with the optimum main injection timing, which is 18.9 %, 21.7 %, and 23.6 % lower EGT. As the advancement of pre-injection angle from 46 to 54°CA bTDC indicates the low EGT indicates that the pre-injection of biodiesel burned successfully and converted into a beneficial work. Further advancing the pre injection 58°CA bTDC, it was noted that the wall heat loss is higher due to prior combustion in the cycle, and it also makes negative compression work. For this condition, the heat energy is converted into negative work, thereby reducing the exhaust gas temperature [83]. When compared to dual fuel single injection, the reduced engine EGT shows that the biodiesel split injection efficiently burns in the cylinders [84,85].

5. Conclusion

In this research, initially the main injection angle of biodiesel was adjusted from 12 to 21°CA bTDC, and the pre-injection angle was fixed at 46°CA bTDC. From the initial investigation, the optimal main injection time was found to be 18°CA. In the next step, the pre-injection angle was adjusted from 46 to 58°CA bTDC, with the optimal main injection angle at 18°CA. and results were compared with 40 % ammonia-biodiesel dual fuel RCCI mode with a single injection at 26° bTDC. The optimal pre-injection timing is established as 54°CA. The results are as follows.

- From the initial investigation, the optimal main injection time of 18°CA bTDC increased the CP by 15.6 %, and the peak HRR and

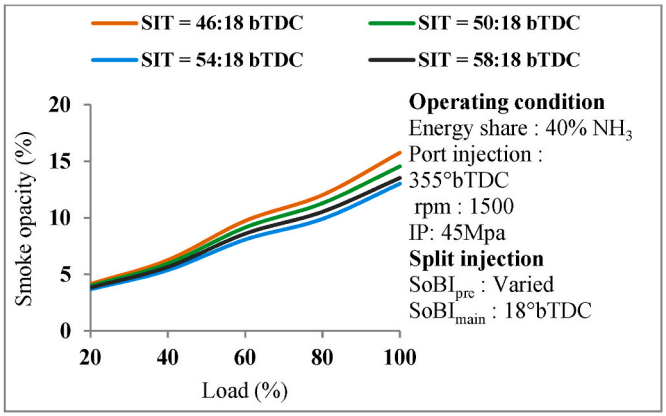

Fig. 13. Effects of pre-injection angle on smoke.

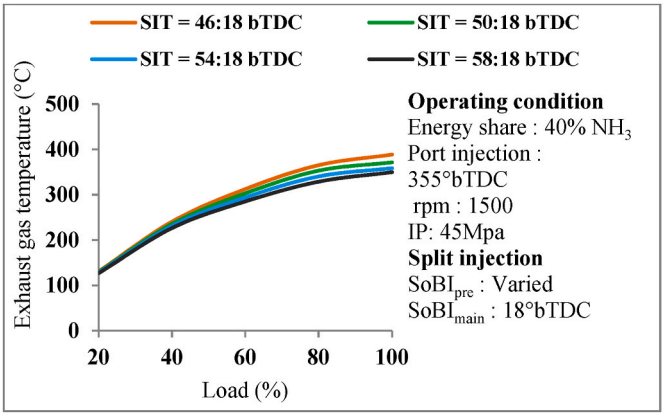

Fig. 15. Effects of pre-injection angle on EGT.

corresponding phasing angle were advanced. BTE was improved by 5.8 %, BSEC was reduced by 14.5 %, the NOx level was significantly increased by about 25.2 %, and HC, CO, smoke, and exhaust temperature were reduced by 13.4 %, 15.7 %, 27.1 %, and 15.2 % in comparison to the 40 % ammonia-biodiesel single injection mode at full load condition.

- In the next stage, the optimal pre-injection time of 54°CA bTDC increased the CP by 12.59 %, and the peak HRR and corresponding phasing angle were further advanced. BTE was improved by 4.9 %, BSEC was reduced by 11.3 %, the NOx level was significantly increased by about 11.4 %, and HC, CO, smoke, and exhaust temperature were reduced by 6.8 %, 9.25 %, 17.4 %, and 7.7 % in comparison to the optimal main injection mode at full load conditions.
- Overall, in contrast to dual fuel single injection operation, the optimal main and pre-injection angle of 18 and 54°CA bTDC increased the CP by 30.1 %, and the peak HRR and combustion phase angle were advanced. BTE was improved by 11 %, BSEC was reduced by 24.1 %, the NOx level was significantly increased by about 39.5 %, and HC, CO, smoke, and exhaust temperature were reduced by 19.2 %, 23.5 %, 39.7 % and 21.7 % at full load conditions.

CRediT authorship contribution statement

Elumalai Pv: Data curation. **Krishnaiah Ravi:** Writing – original draft, Supervision. **Ramachandran Elumalai:** Writing – original draft, Conceptualization. **Chan Choon Kit:** Formal analysis. **Suresh Kumar K:** Funding acquisition. **Krishnasamy Karthik:** Formal analysis. **M. Satyanarayana Gupta:** Data curation. **Mohammad Asif:** Funding acquisition.

Declaration of competing interest

The authors declare that they have no known competing financial interests or personal relationships that could have appeared to influence the work reported in this paper.

Data availability

Data will be made available on request.

Acknowledgments

We appreciate the financial support from the Researchers Supporting Project (RSP2024R42) at King Saud University in Riyadh, Saudi Arabia.

References

[1] M. Mehrpooya, B. Ghorbani, F.K. Bahnamiri, M. Marefati, Solar fuel production by developing an integrated biodiesel production process and solar thermal energy system, Appl. Therm. Eng. 167 (2020) 114701, https://doi.org/10.1016/j.applthermaleng.2019.114701.

[2] S. Muntasir Shovon, F. Ahamed Akash, M. Abdur Rahman, W. Rahman, P. Chakraborty, M.U. Monir, S.M. Sarkar, A. Abd Aziz, S. Chowdhury, Advancements in hydrogen generation, storage, and utilizations: a comprehensive review of current trends in Bangladesh, Energy 292 (2024) 130477, https://doi.org/10.1016/j.energy.2024.130477. Elsevier BV.

[3] X. Lu, Application of artificial intelligence algorithms in precision marketing with flow data analysis models, in: 2024 5th International Conference on Mobile Computing and Sustainable Informatics (ICMCSI), IEEE, 2024, https://doi.org/10.1007/s10973-023-12750-9.

[4] S.A. Jourabchi, S. Gan, H.K. Ng, Comparison of conventional and fast pyrolysis for the production of Jatropha curcas bio-oil, Appl. Therm. Eng. 99 (2016) 160–168, https://doi.org/10.1016/j.applthermaleng.2016.01.045. Elsevier BV.

[5] M. Zhao, T. Sun, Dynamic spatial spillover effect of new energy vehicle industry policies on carbon emission of transportation sector in China, Energy Pol. 165 (2022) 112991, https://doi.org/10.1016/j.enpol.2022.112991.

[6] J. Liu, H. Ma, L. Wang, W. Liang, Q. Ji, P. Sun, et al., Effects of EGR on combustion and emission characteristics of PODE/methanol RCCI mode at high load, Appl. Therm. Eng. 223 (2023) 120036, https://doi.org/10.1016/j.applthermaleng.2023.120036.

[7] Y. Yamineva, S. Romppanen, Is law failing to address air pollution? Reflections on international and <scp>EU</scp> developments, Review of European, Comparative & International Environmental Law 26 (3) (2017) 189–200, https://doi.org/10.1111/reel.12223. Wiley.

[8] V. Soloiu, A. Rivero-Castillo, M. Muinos, M. Duggan, S. Harp, W. Peavy, et al., Simultaneous reduction of NOX and Soot in a diesel engine through rcci operation with PFI of n-butanol and di of cottonseed biodiesel, SAE Tech Pap 1 (2014), https://doi.org/10.4271/2014-01-1322.

[9] M. Armin, M. Gholinia, Comparative evaluation of energy, performance, and emission characteristics in dual-fuel (CH4/Diesel) heavy-duty engine with RCCI combustion mode, Results Eng 16 (2022) 100766, https://doi.org/10.1016/j.rineng.2022.100766.

[10] V. Soloiu, J.D. Moncada, R. Gaubert, M. Muiños, S. Harp, M. Ilie, et al., LTC (low-temperature combustion) analysis of PCCI (premixed charge compression ignition) with n-butanol and cotton seed biodiesel versus combustion and emissions characteristics of their binary mixtures, Renew. Energy 123 (2018) 323–333, https://doi.org/10.1016/j.renene.2018.02.061.

[11] P. Berwal, S. Kumar, B. Khandelwal, A comprehensive review on synthesis, chemical kinetics, and practical application of ammonia as future fuel for combustion, J. Energy Inst. 99 (2021) 273–298, https://doi.org/10.1016/j.joei.2021.10.001.

[12] M. Okcu, M. Fırat, Y. Varol, Ş. Altun, F. Kamışlı, O. Atila, Combustion of high carbon (C7-C8) alcohol fuels in a reactivity controlled compression ignition (RCCI) engine as low reactivity fuels and ANN approach to predict RCCI emissions, Fuel 319 (2022), https://doi.org/10.1016/j.fuel.2022.123735.

[13] J.J. Thomas, G. Nagarajan, V.R. Sabu, C.V. Manojkumar, V. Sharma, Performance and emissions of hexanol-biodiesel fuelled RCCI engine with double injection strategies, Energy 253 (2022) 124069, https://doi.org/10.1016/j.energy.2022.124069.

[14] X. Liu, W. Zhong, P. Jiang, L. Dai, Z. He, Q. Wang, Optimizing RCCI combustion for improved engine performance under low load conditions: impact of low-reactivity fuel and direct injection timing, Fuel 351 (2023) 128871, https://doi.org/10.1016/j.fuel.2023.128871.

[15] S.P. Wategave, N.R. Banapurmath, M.S. Sawant, M.E.M. Soudagar, M.A. Mujtaba, A. Afzal, et al., Clean combustion and emissions strategy using reactivity controlled compression ignition (RCCI) mode engine powered with CNG-Karanja biodiesel, J. Taiwan Inst. Chem. Eng. 124 (2021) 116–131, https://doi.org/10.1016/j.jtice.2021.04.055.

[16] A.K. Subramani, G. Duraisamy, N. Govindan, A. Krishnasamy, Understanding the combustion mode transition from CDC to RCCI and RCCI to CDC – an experimental approach, Energy Convers. Manag. 270 (2022), https://doi.org/10.1016/j.enconman.2022.116233.

[17] J. Liu, Y. Liu, Q. Ji, P. Sun, X. Zhang, X. Wang, et al., Effects of split injection strategy on combustion stability and GHG emissions characteristics of natural gas/diesel RCCI engine under high load, Energy 266 (2023) 126542, https://doi.org/10.1016/j.energy.2022.126542.

[18] E. Arslan, N. Kahraman, The effects of hydrogen enriched natural gas under different engine loads in a diesel engine, Int. J. Hydrogen Energy 47 (2021) 12410–12420, https://doi.org/10.1016/j.ijhydene.2021.09.016.

[19] H. Wang, D. Liu, T. Ma, L. Tong, Z. Zheng, M. Yao, Thermal efficiency improvement of PODE/Gasoline dual-fuel RCCI high load operation with EGR and air dilution, Appl. Therm. Eng. 159 (2019) 113763, https://doi.org/10.1016/j.applthermaleng.2019.113763.

[20] A.P. Singh, V. Kumar, A.K. Agarwal, Evaluation of comparative engine combustion, performance and emission characteristics of low temperature combustion (PCCI and RCCI) modes, Appl. Energy 278 (2020) 115644, https://doi.org/10.1016/j.apenergy.2020.115644.

[21] M.Z. Is, Analysis of Ethanol RCCI Application with Safflower Biodiesel Blends in a High Load Diesel Power Generator Mehmet Zerrakki Is, vol. 184, 2016, pp. 248–260, https://doi.org/10.1016/j.fuel.2016.07.017.

[22] G. Xu, H. Duan, Y. Cai, Y. Li, M. Jia, Potential of the Reverse-Reactivity Controlled Compression Ignition (R-RCCI) Combustion for Maintaining Ultra-low Emissions and Enhanced Thermal Efficiency, vol. 280, 2023.

[23] G. Duraisamy, M. Rangasamy, N. Govindan, A comparative study on methanol/diesel and methanol/PODE dual fuel RCCI combustion in an automotive diesel engine Conventional Mode of Operation, Renew. Energy 145 (2020) 542–556, https://doi.org/10.1016/j.renene.2019.06.044.

[24] M.R. Saxena, R.K. Maurya, Effect of premixing ratio, injection timing and compression ratio on nano particle emissions from dual fuel non-road compression ignition engine fueled with gasoline/methanol (port injection) and diesel (direct injection), Fuel 203 (2017) 894–914, https://doi.org/10.1016/j.fuel.2017.05.015.

[25] N. Ganesan, K. Viswanathan, S.V. Karthic, P. Ekambaram, W. Wu, D.V.N. Vo, Split injection strategies based RCCI combustion analysis with waste cooking oil biofuel and methanol in an open ECU assisted CRDI engine, Fuel 319 (2022) 123710, https://doi.org/10.1016/j.fuel.2022.123710.

[26] A. Ramanathan, A. Santhoshkumar, Feasibility analysis of pyrolysis waste engine oil in CRDI diesel engine, Energy Proc. 158 (2019) 755–760, https://doi.org/10.1016/j.egypro.2019.01.201.

[27] S. Ramalingam, D. Babu, A. Santhoshkumar, R. Deepakkumar, D. Ravikanth, Impact of exhaust gas recirculation and split injection strategy combustion behavior on premixed charge compression ignition engine fuelled with moringa oleifera methyl ester, Fuel 319 (2022) 123702, https://doi.org/10.1016/j.fuel.2022.123702.

[28] A. Kakaee, P. Rahnama, A. Paykani, Journal of Natural Gas Science and Engineering in fl uence of fuel composition on combustion and emissions

characteristics of natural gas/diesel RCCI engine, J. Nat. Gas Sci. Eng. 25 (2015) 58–65, https://doi.org/10.1016/j.jngse.2015.04.020.
[29] A. Kumar, G. Duraisamy, N. Govindan, An innovative method of ammonia use in a light- duty automotive diesel engine to enhance diesel combustion , performance , and emissions, Int. J. Hydrogen Energy (2023), https://doi.org/10.1016/j.ijhydene.2023.06.183.
[30] A. Paykani, A. Kakaee, P. Rahnama, R.D. Reitz, Effects of diesel injection strategy on natural gas/diesel reactivity controlled compression ignition combustion, Energy 90 (2015) 814–826, https://doi.org/10.1016/j.energy.2015.07.112.
[31] A. Yousefi, H. Guo, S. Dev, S. Lafrance, B. Liko, A study on split diesel injection on thermal efficiency and emissions of an ammonia/diesel dual-fuel engine, Fuel 316 (2022) 123412, https://doi.org/10.1016/j.fuel.2022.123412.
[32] A. Sánchez, E. Castellano, M. Martín, P. Vega, Evaluating ammonia as green fuel for power generation: a thermo-chemical perspective, Appl. Energy 293 (2021) 116956, https://doi.org/10.1016/j.apenergy.2021.116956.
[33] E. Perumal Venkatesan, A. Kandhasamy, A. Sivalingam, A.S. Kumar, K. M. Ramalingam, P james thadhani Joshua, et al., Performance and emission reduction characteristics of cerium oxide nanoparticle-water emulsion biofuel in diesel engine with modified coated piston, Environ. Sci. Pollut. Res. 26 (2019) 27362–27371, https://doi.org/10.1007/s11356-019-05773-z.
[34] H. Kobayashi, A. Hayakawa, K.D.K.A. Somarathne, E.C. Okafor, Science and technology of ammonia combustion, Proc. Combust. Inst. 37 (2019) 109–133, https://doi.org/10.1016/j.proci.2018.09.029.
[35] Y. Feng, J. Zhu, Y. Mao, M. Raza, Y. Qian, L. Yu, et al., Low-temperature auto-ignition characteristics of NH3/diesel binary fuel: ignition delay time measurement and kinetic analysis, Fuel 281 (2020) 118761, https://doi.org/10.1016/j.fuel.2020.118761.
[36] H. Derikvand, M. Shafiey Dehaj, H. Taghavifar, The effect of different sampling method integrated in NSGA II optimization on performance and emission of diesel/hydrogen dual-fuel CI engine, Appl. Soft Comput. 128 (2022) 109434, https://doi.org/10.1016/j.asoc.2022.109434.
[37] C. Kurien, M. Mittal, Review on the production and utilization of green ammonia as an alternate fuel in dual-fuel compression ignition engines, Energy Convers. Manag. 251 (2022) 114990, https://doi.org/10.1016/j.enconman.2021.114990.
[38] Ø. Skreiberg, T. Li, E. Vantaggiato, L. Wang, M. Bugge, T. Løvås, An evaluation of effects of operational parameters on NOx emissions through detailed chemical kinetics simulations, Energy Proc. 158 (2019) 103–110, https://doi.org/10.1016/j.egypro.2019.01.053.
[39] P. Dimitriou, R. Javaid, A review of ammonia as a compression ignition engine fuel, Int. J. Hydrogen Energy 45 (2020) 7098–7118, https://doi.org/10.1016/j.ijhydene.2019.12.209.
[40] E.C. Blanco, A. Sánchez, M. Martín, P. Vega, Methanol and ammonia as emerging green fuels: evaluation of a new power generation paradigm, Renew. Sustain. Energy Rev. 175 (2023) 113195, https://doi.org/10.1016/j.rser.2023.113195.
[41] S. Mi, H. Wu, X. Pei, C. Liu, L. Zheng, W. Zhao, et al., Potential of ammonia energy fraction and diesel pilot-injection strategy on improving combustion and emission performance in an ammonia-diesel dual fuel engine, Fuel 343 (2023) 127889, https://doi.org/10.1016/j.fuel.2023.127889.
[42] E. Nadimi, G. Przybyła, M.T. Lewandowski, W. Adamczyk, Effects of ammonia on combustion, emissions, and performance of the ammonia/diesel dual-fuel compression ignition engine, J. Energy Inst. 107 (2023), https://doi.org/10.1016/j.joei.2022.101158.
[43] N. Førby, T.B. Thomsen, R.F. Cordtz, F. Bræstrup, J. Schramm, Ignition and combustion study of premixed ammonia using GDI pilot injection in CI engine, Fuel 331 (2023) 125768, https://doi.org/10.1016/j.fuel.2022.125768.
[44] A.S. Mohammed, S.M. Atnaw, A.V. Ramaya, G. Alemayehu, A comprehensive review on the effect of ethers, antioxidants, and cetane improver additives on biodiesel-diesel blend in CI engine performance and emission characteristics, J. Energy Inst. 108 (2023) 101227, https://doi.org/10.1016/j.joei.2023.101227.
[45] M. Elkelawy, H.A.E. Bastawissi, E.A. El Shenawy, M.M. Shams, H. Panchal, K. K. Sadasivuni, et al., Influence of lean premixed ratio of PCCI-DI engine fueled by diesel/biodiesel blends on combustion, performance, and emission attributes; a comparison study, Energy Convers. Manag. X 10 (2021) 100066, https://doi.org/10.1016/j.ecmx.2020.100066.
[46] B. Ashok, K. Nanthagopal, Eco Friendly Biofuels for CI Engine Applications, Elsevier Ltd., 2019, https://doi.org/10.1016/b978-0-08-102728-8.00015-2.
[47] K. Simhadri, P. Srinivasa Rao, M.K. Paswan, Effect of changing injection pressure on Mahua oil and biodiesel combustion with Ceo2 nanoparticle blend on Ci engine performance and emission characteristics, SSRN Electron. J. (2022), https://doi.org/10.2139/ssrn.4181180.
[48] N. Ganesan, T.H. Le, P. Ekambaram, D. Balasubramanian, V.V. Le, A.T. Hoang, Experimental assessment on performance and combustion behaviors of reactivity-controlled compression ignition engine operated by n-pentanol and cottonseed biodiesel, J. Clean. Prod. 330 (2022) 129781, https://doi.org/10.1016/j.jclepro.2021.129781.
[49] B. Maleki, Y. Kalanakoppal Venkatesh, Ashraf Talesh S. Siamak, H. Esmaeili, S. Mohan, G.R. Balakrishna, A novel biomass derived activated carbon mediated AC@ZnO/NiO bifunctional nanocatalyst to produce high-quality biodiesel from dairy industry waste oil: CI engine performance and emission, Chem Eng J 467 (2023) 143399, https://doi.org/10.1016/j.cej.2023.143399.
[50] S.P. Wategave, N.R. Banapurmath, M.S. Sawant, M. Elahi, M. Soudagar, M. Reza, A. Elfasakhany, A.M. Sajjan, Clean combustion and emissions strategy using reactivity controlled compression ignition (RCCI) mode engine powered with CNG-karanja biodiesel, J. Taiwan Inst. Chem. Eng. 000 (2021) 1–16, https://doi.org/10.1016/j.jtice.2021.04.055.
[51] S.S. Kumar, K. Rajan, V. Mohanavel, M. Ravichandran, P. Rajendran, A. Rashedi, A. Sharma, S.A. Khan, A. Afzal, Combustion , performance , and emission behaviors of biodiesel fueled diesel engine with the impact of alumina nanoparticle as an additive, Sustainability 13 (2021) 12103, https://doi.org/10.3390/su132112103.
[52] A. Afzal, R.G. Roy, C.P. Koshy, A. Y, M. Abbas, E. Cuce, A. Razak Rk, S. Shaik, C. A. Saleel, Characterization of biodiesel based on plastic pyrolysis oil (PPO) and coconut oil: performance and emission analysis using RSM-ANN approach, Sustain. Energy Technol. Assessments 56 (2023) 103046, https://doi.org/10.1016/j.seta.2023.103046.
[53] A. Devaraj, M. Nagappan, D. Yogaraj, O. Prakash, Y.A. Rao, A. Sharma, Influence of nano-additives on engine behaviour using diesel-biodiesel blend, Mater Today Proc 62 (2022) 2266–2270, https://doi.org/10.1016/j.matpr.2022.03.598.
[54] A. Sharma, Y. Singh, N. Kumar Singh, A. Singla, H. Chyuan Ong, W.H. Chen, Effective utilization of tobacco (Nicotiana Tabaccum) for biodiesel production and its application on diesel engine using response surface methodology approach, Fuel 273 (2020) 117793, https://doi.org/10.1016/j.fuel.2020.117793.
[55] B. Yang, K. Zeng, Effects of natural gas injection timing and split pilot fuel injection strategy on the combustion performance and emissions in a dual-fuel engine fueled with diesel and natural gas, Energy Convers. Manag. 168 (2018) 162–169, https://doi.org/10.1016/j.enconman.2018.04.091.
[56] R. Sindhu, G. Amba Prasad Rao, K. Madhu Murthy, Effective reduction of NOx emissions from diesel engine using split injections, Alexandria Eng J 57 (2018) 1379–1392, https://doi.org/10.1016/j.aej.2017.06.009.
[57] Y. Shekar Kuppili, P. Kumar, S. Singh Sandhu, A critical review of the impacts of split injection strategies on the performance, combustion and emissions characteristics of a diesel engine fueled with low carbon alcohol fuels, Mater Today Proc 72 (2023) 2928–2932, https://doi.org/10.1016/j.matpr.2022.08.020.
[58] K.P. Shrestha, C. Lhuillier, A.A. Barbosa, P. Brequigny, F. Contino, C. Mounaïm-Rousselle, et al., An experimental and modeling study of ammonia with enriched oxygen content and ammonia/hydrogen laminar flame speed at elevated pressure and temperature, Proc. Combust. Inst. 38 (2021) 2163–2174, https://doi.org/10.1016/j.proci.2020.06.197.
[59] P.S. Shelke, N.M. Sakhare, S. Lahane, Investigation of combustion characteristics of a cottonseed biodiesel fuelled diesel engine, Procedia Technol 25 (2016) 1049–1055, https://doi.org/10.1016/j.protcy.2016.08.205.
[60] A.M. Elzahaby, M. Elkelawy, H.A.E. Bastawissi, S.M. El Malla, A.M.M. Naceb, Kinetic modeling and experimental study on the combustion, performance and emission characteristics of a PCCI engine fueled with ethanol-diesel blends, Egypt J Pet 27 (2018) 927–937, https://doi.org/10.1016/j.ejpe.2018.02.003.
[61] K. Panda, A. Ramesh, Parametric investigations to establish the potential of methanol based RCCI engine and comparison with the conventional dual fuel mode, Fuel 308 (2022) 122025, https://doi.org/10.1016/j.fuel.2021.122025.
[62] Y. Zhang, W. De Ojeda, D. Wickman, Computational study of combustion optimization in a heavy-duty diesel engine using in-cylinder blending of gasoline and diesel fuels, SAE Tech Pap 8 (2012), https://doi.org/10.4271/2012-01-1977.
[63] J. Liu, P. Wu, Q. Ji, P. Sun, P. Wang, Z. Meng, et al., Experimental study on effects of pilot injection strategy on combustion and emission characteristics of diesel/methanol dual-fuel engine under low load, Energy 247 (2022) 123464, https://doi.org/10.1016/j.energy.2022.123464.
[64] S. Park, H.J. Kim, D.H. Shin, J.T. Lee, Effects of various split injection strategies on combustion and emissions characteristics in a single-cylinder diesel engine, Appl. Therm. Eng. 140 (2018) 422–431, https://doi.org/10.1016/j.applthermaleng.2018.05.025.
[65] S. Kokjohn, R.D. Reitz, D. Splitter, M. Musculus, Investigation of fuel reactivity stratification for controlling PCI heat-release rates using high-speed chemiluminescence imaging and fuel tracer fluorescence, SAE Int J Engines 5 (2012) 248–269, https://doi.org/10.4271/2012-01-0375.
[66] B. Yang, K. Zeng, Effects of natural gas injection timing and split pilot fuel injection strategy on the combustion performance and emissions in a dual-fuel engine fueled with diesel and natural gas, Energy Convers. Manag. 168 (2018) 162–169, https://doi.org/10.1016/j.enconman.2018.04.091.
[67] P. Saiteja, B. Ashok, Study on interactive effects of CRDi engine operating parameters through RSM based multi-objective optimization technique for biofuel application, Energy 255 (2022) 124499, https://doi.org/10.1016/j.energy.2022.124499.
[68] M. Canakci, A.N. Ozsezen, E. Arcaklioglu, A. Erdil, Prediction of performance and exhaust emissions of a diesel engine fueled with biodiesel produced from waste frying palm oil, Expert Syst. Appl. 36 (2009) 9268–9280, https://doi.org/10.1016/j.eswa.2008.12.005.
[69] D. Babu, R. Karvembu, R. Anand, Impact of split injection strategy on combustion, performance and emissions characteristics of biodiesel fuelled common rail direct injection assisted diesel engine, Energy 165 (2018) 577–592, https://doi.org/10.1016/j.energy.2018.09.193.
[70] T. Ravichandran, M. Nagappan, A novel technique and detailed study of concepts of low-cost hybrid vehicle design, Int. J. Ambient Energy 42 (2021) 1252–1257, https://doi.org/10.1080/01430750.2019.1592777.
[71] J. Liu, X. Zhang, Y. Liu, P. Sun, Q. Ji, X. Wang, et al., Experimental study on in-cylinder combustion and exhaust emissions characteristics of natural gas/diesel dual-fuel engine with single injection and split injection strategies, Process Saf Environ Prot 172 (2023) 225–240, https://doi.org/10.1016/j.psep.2023.02.013.
[72] M. Xu, W. Cheng, H. Zhang, T. An, S. Zhang, Effect of diesel pre-injection timing on combustion and emission characteristics of compression ignited natural gas engine, Energy Convers. Manag. 117 (2016) 86–94, https://doi.org/10.1016/j.enconman.2016.02.054.

[73] V. Bykov, M. Stein, U. Maas, Study of mechanism of ammonia decomposition and oxidation: from NOx reduction to ammonia auto-ignition problem, Proc. Combust. Inst. 0 (2022) 1–9, https://doi.org/10.1016/j.proci.2022.07.048.
[74] M. Nibin, J.B. Raj, V.E. Geo, Experimental studies to improve the performance, emission and combustion characteristics of wheat germ oil fuelled CI engine using bioethanol injection in PCCI mode, Fuel 285 (2021) 119196, https://doi.org/10.1016/j.fuel.2020.119196.
[75] N. Murugan, H. Venu, J. Jayaraman, P. Appavu, Emission and performance characteristics study on nanographene oxide additives doped palm oil methyl ester blend in a diesel engine, Int. J. Ambient Energy (2019) 1–7, https://doi.org/10.1080/01430750.2019.1697361, 0.
[76] H.G. How, H.H. Masjuki, M.A. Kalam, Y.H. Teoh, Influence of injection timing and split injection strategies on performance, emissions, and combustion characteristics of diesel engine fueled with biodiesel blended fuels, Fuel 213 (2018) 106–114, https://doi.org/10.1016/j.fuel.2017.10.102.
[77] H.G. How, H.H. Masjuki, M.A. Kalam, Y.H. Teoh, Influence of injection timing and split injection strategies on performance, emissions, and combustion characteristics of diesel engine fueled with biodiesel blended fuels, Fuel 213 (2018) 106–114, https://doi.org/10.1016/j.fuel.2017.10.102.
[78] C.C. Enweremadu, H.L. Rutto, Combustion, emission and engine performance characteristics of used cooking oil biodiesel - a review, Renew. Sustain. Energy Rev. 14 (2010) 2863–2873, https://doi.org/10.1016/j.rser.2010.07.036.
[79] K. Kalaimurugan, S. Karthikeyan, M. Periyasamy, G. Mahendran, T. Dharmaprabhakaran, Experimental studies on the influence of copper oxide nanoparticle on biodiesel-diesel fuel blend in CI engine, Energy Sources, Part A Recover Util Environ Eff 0 (2019) 1–16, https://doi.org/10.1080/15567036.2019.1679290.
[80] A. Atmanli, Comparative analyses of diesel-waste oil biodiesel and propanol, n-butanol or 1-pentanol blends in a diesel engine, Fuel 176 (2016) 209–215, https://doi.org/10.1016/j.fuel.2016.02.076.
[81] E. Ansari, M. Shahbakhti, J. Naber, Optimization of performance and operational cost for a dual mode diesel-natural gas RCCI and diesel combustion engine, Appl. Energy 231 (2018) 549–561, https://doi.org/10.1016/j.apenergy.2018.09.040.
[82] G. Sakthivel, Prediction of CI engine performance, emission and combustion characteristics using fish oil as a biodiesel at different injection timing using fuzzy logic, Fuel 183 (2016) 214–229, https://doi.org/10.1016/j.fuel.2016.06.063.
[83] S. Jindal, Effect of injection timing on combustion and performance of a direct injection diesel engine running on Jatropha methyl ester, Int. J. Energy Environ. 2 (2011) 113–122.
[84] P. Murugesan, P.V. Elumalai, D. Balasubramanian, S. Padmanabhan, N. Murugunachippan, A. Afzal, P. Sharma, K. Kiran, J.S. Femilda Josephin, E. G. Varuvel, et al., Exploration of low heat rejection engine characteristics powered with carbon nanotubes-added waste plastic pyrolysis oil, Process Saf. Environ. Prot. 176 (2023) 1101–1119, https://doi.org/10.1016/j.psep.2023.06.051.
[85] S.V. Khandal, Ü. Ağbulut, A. Afzal, M. Sharifpur, K. Abdul Razak, N. Khalilpoor, Influences of hydrogen addition from different dual-fuel modes on engine behaviors, Energy Sci. Eng. 10 (2022) 881–891, https://doi.org/10.1002/ese3.1065.

Journal of Physics: Conference Series

PURPOSE-LED PUBLISHING™

PAPER • **OPEN ACCESS**

Evaluation of mechanical properties and energy absorption of polyurethane foam core sandwich panels with kevlar/basalt-epoxy laminates as face sheets

To cite this article: S Keerthana *et al* 2024 *J. Phys.: Conf. Ser.* **2837** 012017

View the article online for updates and enhancements.

You may also like

- Anti-impact behavior of a novel soft body armor based on shear thickening gel (STG) impregnated Kevlar fabrics
Chunyu Zhao, Chenhui Xu, Saisai Cao et al.
- Evaluating the tribological and mechanical properties of filament wound composite incorporated with PTFE fibers and tungsten carbide filler applicable for self-lubricating bearings
Fatemeh Shahramforouz, Seyed Mahdi Hejazi and Aboozar Taherizadeh
- Investigation of the mechanical behaviour of hybrid fiber reinforced composite with aluminium laminates
Ramesh R and Nalla Mohamed M

This content was downloaded from IP address 106.0.37.90 on 21/10/2024 at 11:21

Journal of Physics: Conference Series **2837** (2024) 012017 doi:10.1088/1742-6596/2837/1/012017

Evaluation of mechanical properties and energy absorption of polyurethane foam core sandwich panels with kevlar/basalt-epoxy laminates as face sheets

Keerthana S[1], Kohila P[1], Pavithra A.S[1], Sagar K.S[1], Jensin Joshua J[1], Arunkumar K[2], Seralathan S[1,*]

[1]Department of Aeronautical Engineering, Hindustan Institute of Technology and Science, Chennai 603 103, Tamil Nadu, India
[2]Department of Aeronautical Engineering, MLR Institute of Technology, Hyderabad, Telangana, India

* Corresponding Author: siva.seralathan@gmail.com

Abstract. Sandwich panels are extensively used in aeronautical field due to its high strength-to-weight ratio and better energy absorption. In this study, the sandwich panels are fabricated with Kevlar (K) and basalt (B) fibres as face sheets as it has high strength, and thermal stability with polyurethane (PU) foam as core material and investigations are performed to evaluate the energy absorption and mechanical properties of the sandwich panels. The plates are fabricated using compression moulding method. Tests such as inter laminar shear strength test, edge wise compression test, flammability test, drop-weight impact test are performed, and the obtained results are compared. Plate 2 (Kevlar/Kevlar/PU Foam/Kevlar/Kevlar) shows a better shear strength as 4.38N/mm^2 and better energy absorption capability whereas, Plate 3 (Basalt/Kevlar/PU Foam/Kevlar/Basalt) shows more compressive strength with value of 13.4N/mm^2. Plate 1 (Basalt/Basalt/PU Foam/Basalt/Basalt) shows faster propagation speed when it is in contact with fire.

Keywords: Kevlar, basalt, polyurethane foam, energy absorption, mechanical properties.

1. Introduction

Composite panel is used due to its unique characteristics, such as a high strength-to-weight ratio along with remarkable energy absorption capabilities. Composite sandwich panels are utilized extensively in variety of engineering applications. A sandwich panel comprises one core component in the centre, two face sheets at the bottom and top, and two face sheets in between. Here, the face sheets are composed of Kevlar and basalt, and the centre part is made of Polyurethane (PU) foam. PU foam is extensively utilized as the core material in the sandwich panels because of its excellent energy absorption capacity and low density. The core material has a sizable impact on the overall mechanical behavior and energy absorption capabilities of these panels.

Kevlar and basalt fibers combined with epoxy resin have improved the performance of sandwich panel face sheets. A thorough literature review on the utilization of composite sandwich structures in aviation products/sectors is detailed here. The high strength-to-weight ratio, stiffness, and resistance to fatigue of these structures emphasize its significance in the aviation sector. Composite sandwich

Content from this work may be used under the terms of the Creative Commons Attribution 4.0 licence. Any further distribution of this work must maintain attribution to the author(s) and the title of the work, journal citation and DOI.
Published under licence by IOP Publishing Ltd

constructions are being used in aeronautical sectors such as aircraft wings, fuselages, and rotary rotor blades. Oana Alexandra Mocian *et al*. [1] used panels which contained of two identical aluminium face sheets as well as a foam core. Polyurethane and polystyrene foam were employed as the sandwich panel's core materials. With the help of the Instron CEAST 9340 testing device, impact tests were performed. In comparison to those with polystyrene foam cores, those with polyurethane foam cores absorbed more impact pressures with fewer indentations. Stanley Samlal and R. Santhanakrishnan [2] created sandwich structure with two face sheets and a core constructed of low-density foam. The peak loads carrying capability of foam core sandwich panels was increased by adding a layer of Kevlar to the facing sheet. The use of inter-play and intra-ply hybrid Kevlar face sheets improved the impact-resistant qualities of carbon fiber face sheet sandwich composites. The maximum load carrying capability of the foam core sandwich panel was increased by adding a Kevlar sheet to the facing sheet.

Sandwich composites with honeycomb cores and foam cores were utilized by Nicolae Constantin *et al.* [3] to determine the damage at low velocity impact. To assess the materials' resistance to damage, non-destructive examinations and mechanical destructive testing were used. Sandwich material with a honeycomb core experienced minimal deformations and was shielded against impacts with low velocities. On the hand, the foam core got exposed at large deformations and was not prevented from low velocity impact events. The honeycomb structure was better than the foam core structure. Frederick Laurin and Anthony J. Vizzini [4] stated that energy absorption played a major role in the panels to withstand impact. Uniaxial quasi static loading was used to determine the effect of reinforcement. The authors provided a general review on the sandwich structure as energy absorption. Face sheet and core improved the impact resistance. Ranjith Kumar Pathipaka *et al.* [5] prepared the honeycomb core using 3D printed technology. 3D-printed poly-lactic acid honeycomb and cross-linked polyethylene foam served as the core of sandwich composites, while GFRP served as the face sheet. For all impact energies, sandwich specimen with a foam core absorbed additional energy than those with honeycomb core. Comparing foam core sandwich specimen to honeycomb core sandwich specimen, contact force was higher.

Ramesh and Anand [6] investigated the composites made of natural and synthetic fibers. Sandwich material with a foam core was subjected to substantial deformations and could not shield itself from low-velocity impact events while, sandwich materials with a core made from honeycomb experienced no excessive deformations. The flexural strengths and tensile strengths of the composites comprising Kevlar (K) and basalt (B) fibers in mat foam was compared. The KBKBKBK hybrid composites strengthened with a total of three layers of basalt fiber and four layers of Kevlar had the maximum flexural strength of 188MPa along with the highest tensile strength of 174MPa [7]. A new kind of sandwich composite panel was studied by Victor Avisek Chatterjee *et al*. [8] employing 3D-mats consisting linked channels sandwiched between Kevlar layers. To investigate its impact on enhancing the material's ability to dissipate energy, high-performance 600nm silica-based shear thickening fluids (STF) were injected into the core of the panels. The sandwich composite panels with STF integrated were found to absorb 96.30% of the incident energy, which is almost 67.40% additional energy. Upon comparison with hollow sandwich composite panels, 61.27% increase in absorbed energy per unit and an increase in weight were also recorded. Sandwich composite panels with STF technology were therefore a viable material because of its improved energy absorption. The manner of collapses and overall crushing responses of sandwich panels were significantly influenced by the under edgewise compressive load [9]. The most efficient method of absorbing crash energy was the progressive end-crushing modes, which were characterized by a variety of micro collapse mechanisms of the sandwich constituent materials and contributed to higher average crushing loads, energy dissipation, and uniform compressive loads [10, 11]. When compared to foam cores or aluminium cores, the damage initiation and fracture processes for the hybrid fabric honeycomb core sandwich panels were more appealing. The specimen significantly reduced the quantity of impact damage and significantly increased energy absorption capacity [12].

By maintaining a constant overall core thickness and mass, Kazemi [13] investigated how variations in foam core density affected the quasi-static penetration processes in sandwich panels with

aluminium face sheets. More contact force was produced by sandwich panels with thinner foam core. Kevlar sheets were sandwiched between 3D mats with connecting passages to create an innovative type of sandwich composite panel. In the centre of the panels, 600nm silica based STF was administered to investigate the influence on the material's capacity to disperse energy. Sandwich composite panels with STF inserted demonstrated the ability to withstand 96.30% of incident energy, which was nearly 67.40% additional energy than hollow sandwich composite paneling. More contact force was produced by sandwich panel with a decreasing foam core density [14]. Zhou *et al.* [15] had mentioned that it was possible to boost perforation resistance by contrasting sandwich panels where the higher-density foam was positioned against the top surface skin and those where it is in contact with the distal surface. The outcomes demonstrated that foam core sandwich structures had a strong impact resistance and had the capacity to absorb a sizable quantity of energy [16]. When the total thickness of sandwich panels stayed constant, the front-to-back face sheet thickness ratio was efficiently increased to increase the energy absorption capacities and impact resistances [17]. When built in a sandwich configuration, the material utilization efficiency had significantly increased [18]. The polyurethane panels exhibited a stiffer behavior, a longer history of impact forces along with more intricate pattern of damage [19]. According to Faris Tarlochan [20], the sandwich structure's strong polyurethane foam core was surrounded by glass fiber composite face sheets. The criteria for ballistic performance were significantly impacted by density of the core material. The core shouldn't be overly soft or rigid. This was related to the foam's cell wall thickness and strut. Feng and Aymerich [21] mentioned that an increase in density of foam core led to a decrease in the contact force and duration of impact, as well as a reduction in the deformation of the face sheets and core. The authors attributed these results to the augmented stiffness and strength of the foam core at higher densities.

These understandings on the detailed literature reviews aid us in the development of lightweight and robust sandwich panels with the capability to absorb energy in event of a collision or impact which is essential for a wide range of industrial applications, including automotive, and aerospace sectors. A combination of Kevlar, basalt and polyurethane (PU) foam has not been previously explored.

Furthermore, the innovation lies in integrating PU foam core sandwich panels with Kevlar/basalt epoxy laminates as face sheets for aerospace engineering. This design offers lightweight yet robust structural elements which are crucial for aircraft and spacecraft applications where weight reduction is paramount. The mechanical properties of the PU foam core provide excellent strength-to-weight ratio, while the Kevlar/basalt epoxy laminates enhance the durability and energy absorption capabilities which are vital for withstanding impact as well as stress during flight or space missions. This combination ensures an enhanced structural integrity, fuel efficiency, and improved overall performance, making it a significant advancement in aerospace engineering for building lighter and more efficient vehicles.

Therefore, the purpose of this investigations is to determine the mechanical characteristics with energy absorption behavior of the sandwich panels made with polyurethane foam cores and Kevlar/basalt-epoxy laminates as face sheets. The sandwich panels with varying orientations are fabricated to conduct the test to estimate the stiffness, strength, and energy absorption capacity of the panels by performing inter-laminar shear strength test, edgewise compression test, flammability test, and drop-weight impact test.

2. Methodology

The materials used in this study are Kevlar, basalt, and polyurethane (PU) foam. These are stacked on each other in the following stacking sequences: - Plate 1: Basalt/Basalt/PU Foam/Basalt/Basalt. Plate 2: Kevlar/Kevlar/PU Foam/ Kevlar/ Kevlar. Plate 3: Basalt/Kevlar/PU Foam/ Kevlar/ Basalt. These plates named as Plate 1, Plate 2, and Plate 3 are created using the compression molding technique and these are displayed in Figure 1. The thickness of all the three plates are maintained same as 6mm.

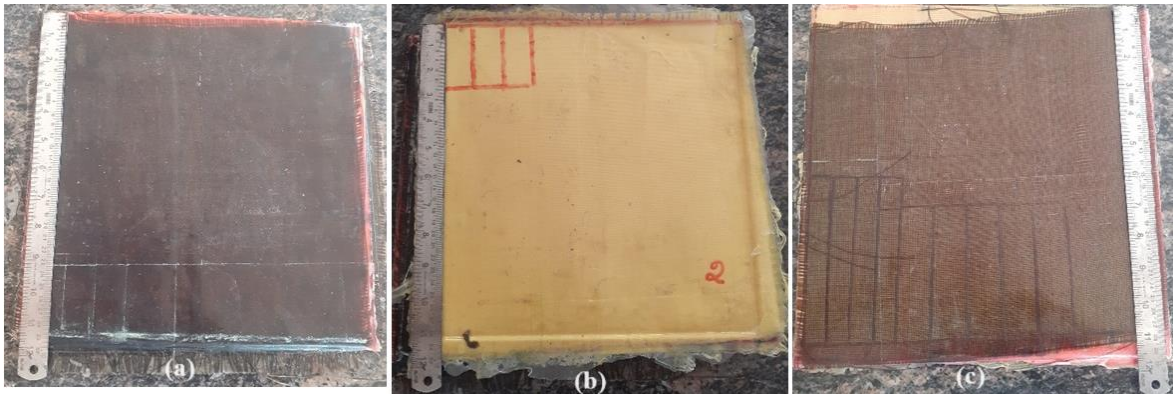

Fig. 1 (a) Plate 1 - Basalt/Basalt/PU Foam/Basalt/Basalt **(b)** Plate 2 - Kevlar/Kevlar/PU Foam/ Kevlar/ Kevlar **(c)** Plate 3 - Basalt/Kevlar/PU Foam/ Kevlar/ Basalt

2.1. Inter laminar shear strength (ILSS) test

ILSS test is performed to understand the shear strength between the composite laminates. Shear testing indicates how well the material holds up to the impact of a constant load that is parallel to its surface. The specimens are cut out based on ASTM D2344 standards. The images of the specimens being held in the universal testing machine during the tests being performed are presented in Figure 2(a) and 2(b) respectively.

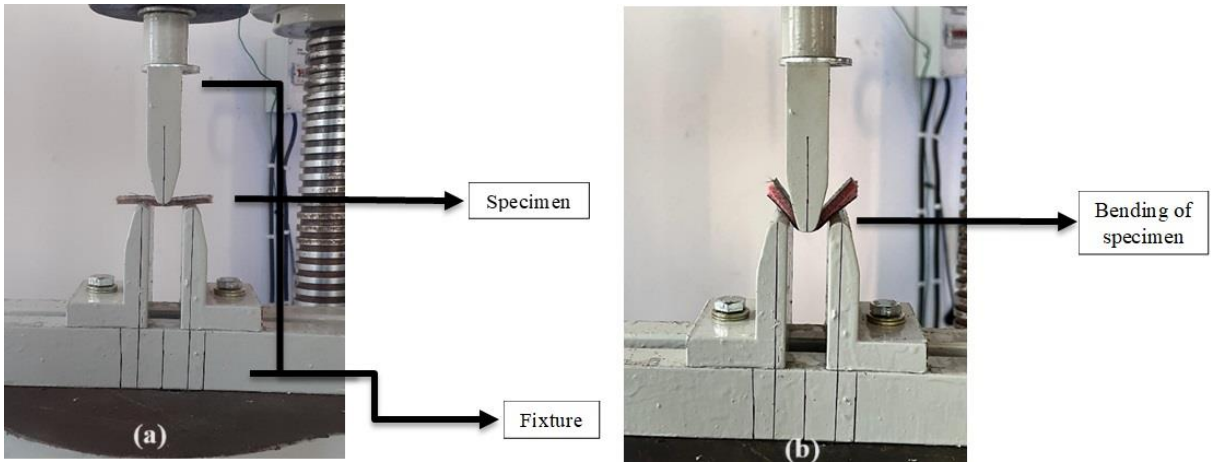

Fig. 2 (a) Test setup of ILSS test **(b)** ILSS test

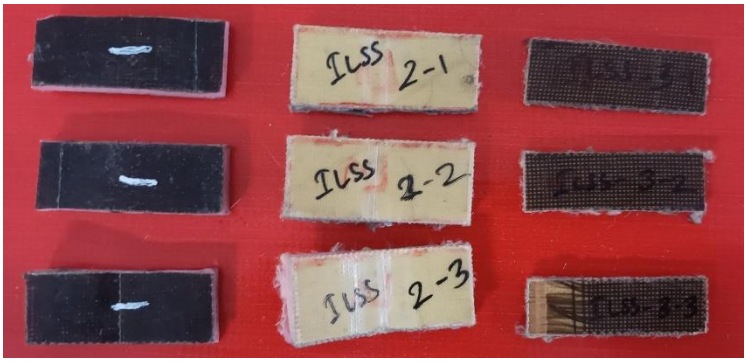

Fig. 3 Specimens after performing the test

Figure 3 represents the test specimens after the tests are completed. Equation (1) lists the formula used to estimate the shear strength between the composite laminates.

$$\sigma_{max} = \frac{3P}{4bt} \quad \text{----} \quad (1)$$

where P is load in Newton, b is the breadth of the specimen and t is the thickness of the specimen.

2.2. Edgewise compression test

This test is performed to assess the compressive capacity of the composite's sidewalls. The specimens are cut out according to the ASTM C364 standards and edgewise compression tests are performed. The samples prior to conducting the tests are shown in Figure 4. The specimens are held in the UTM as shown in Figure 5(a) and during the execution of the test is shown in Figure 5(b). Equation (2) lists the formula used to estimate the edgewise compression.

$$\sigma_c = \frac{P}{A} \quad \text{----} \quad (2)$$

where 'P' is the load in Newtons and 'A' is the area of the specimens.

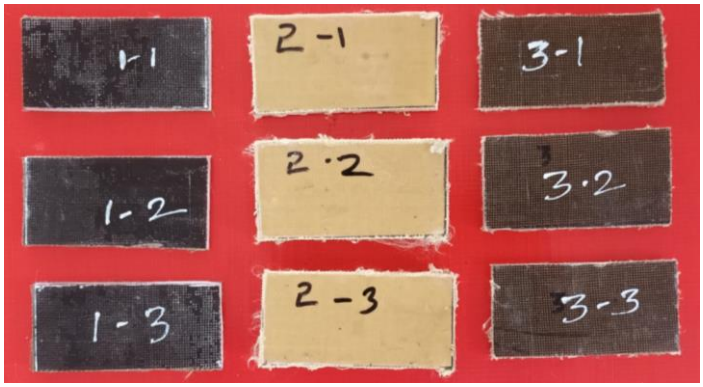

Fig. 4 Specimens before performing the test

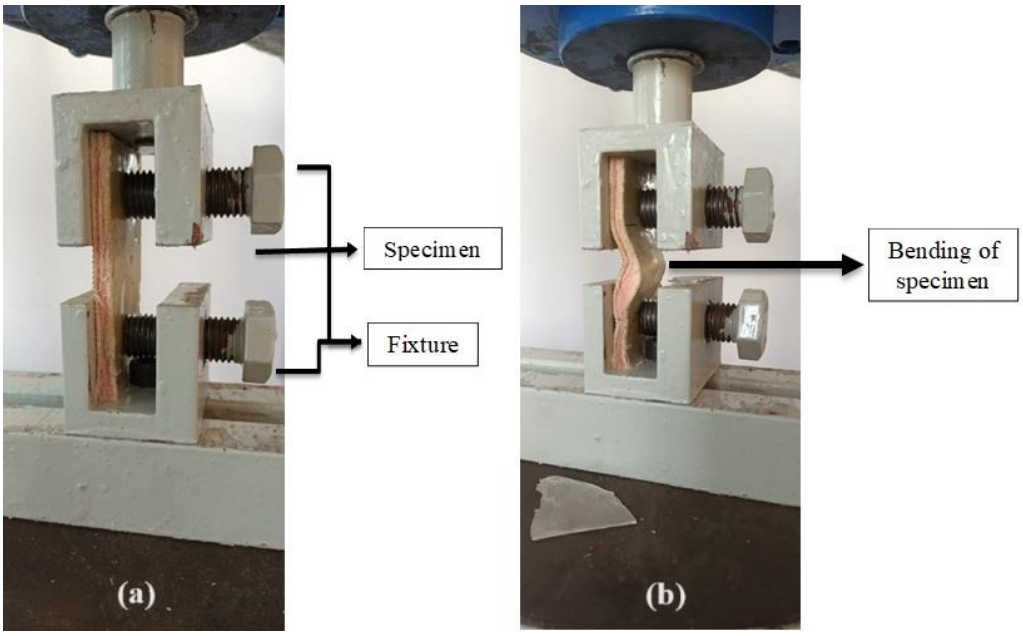

Fig. 5 (a) Test setup of edge wise compression test **(b)** While performing the test

The properties and strength of the foam core are crucial in deciding how a sandwich panel would collapse and how it will respond overall when subjected to edgewise compressive pressure. The progressive end-crushing mode, which is characterized by many micro-collapse processes of the sandwich constituent materials that contribute to energy dissipation, a higher average crushing load, and compressive load uniformity, is the most effective for absorbing impact energy [9]. Evaluation of panel design properties, and material specifications are all aided by the findings of the edgewise compression tests. Furthermore, the compressive characteristics of structural sandwich construction in a direction parallel to the sandwich-facing plane are covered by this test method [11].

2.3. Flammability test

This test is carried out to determine how quickly the materials emit heat and smoke when exposed to a specific amount of radiant heat. As seen in Figure 6(a) and 6(b), the specimen is placed in a vertical stand and ignited with a Bunsen burner for approximately 10 seconds. The ASTM D 3014 standards is followed in cutting out the specimens and the flammability test is carried out.

Sandwich composites takes longer time to ignite in the horizontal configuration when compared to a vertical orientation. Also, when kept in horizontal direction, it reveals itself intact with little damage at the ignited end. However, it when it is oriented in the vertical direction, it increases the ignition time and burning rates, showing a substantial burn damage in comparison with horizontal orientation. Moreover, the vertical orientation causes the face skins of sandwich composites to delaminate. By testing the composite laminate material's flammability, it is understood that how well it will stop a fire from spreading inside or outside. The composite laminate materials are exposed to flame for 60 seconds, and the panels are exposed for 12 seconds [10, 11].

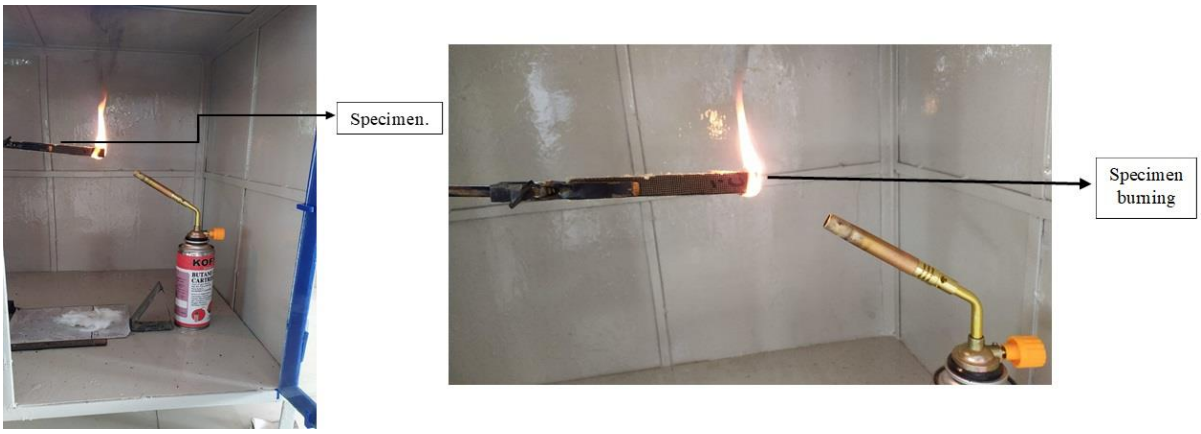

Fig. 6 (a) Test setup of flammability test **(b)** While performing the test

2.4. Drop-weight impact test

The purpose of this test is to estimate the material's ability to withstand maximum impact load, absorb energy, and damage caused. According to ASTM D7136 standards, the specimens are cut out, and the drop weight impact test is carried. Figure 7 shows the specimen prior to the test. Figure 8(a) shows the setup used to conduct the drop weight impact test, and Figure 8(b) shows the specimens after the tests are performed. The impactor head is 12.70mm and the applied energy is 25J. The drop tower height (h) is 1m and the mass (m) is 2.50kg. Equation (3) which is used to calculate the energy absorption is given by,

$$\text{Energy absorption} = m \times g \times (h\text{-}h_1) \quad \text{---- (3)}$$

The foam, which accounts for more than 40% of the energy absorbed, plays a crucial function [14].

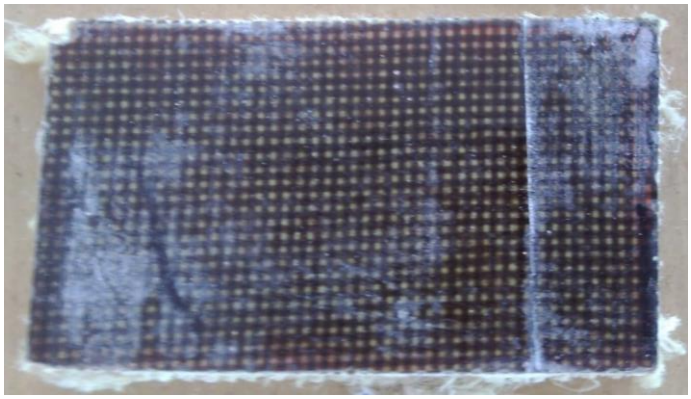

Fig. 7 Specimen before performing the test

3. Results and discussion

The findings from all the tests are analyzed and provided in this section to understand the outcomes of foam-core sandwich panels which had three different orientations and its energy absorption capacity and mechanical properties, such as shear strength and compressive strength of the specimens.

3.1. Inter laminar shear strength (ILSS)

Table 1 represents the readings obtained while performing the inter laminar shear strength testing of composite laminates namely, Plate 1, Plate 2, and Plate 3. The data listed in Table 1 illustrates the specimen's ability to withstand higher loads and shows the shear strength. Plate 2 has more inter-laminar shear strength due to Kevlar's high strength-to-weight ratio, which makes it an excellent material for applications requiring high stiffness and strength. On the other hand, basalt has comparatively lesser strength and stiffness than Kevlar and it is more suitable for high-temperature applications. Since Kevlar is present in Plate 3 along with basalt, it gives a similar strength as Plate 2.

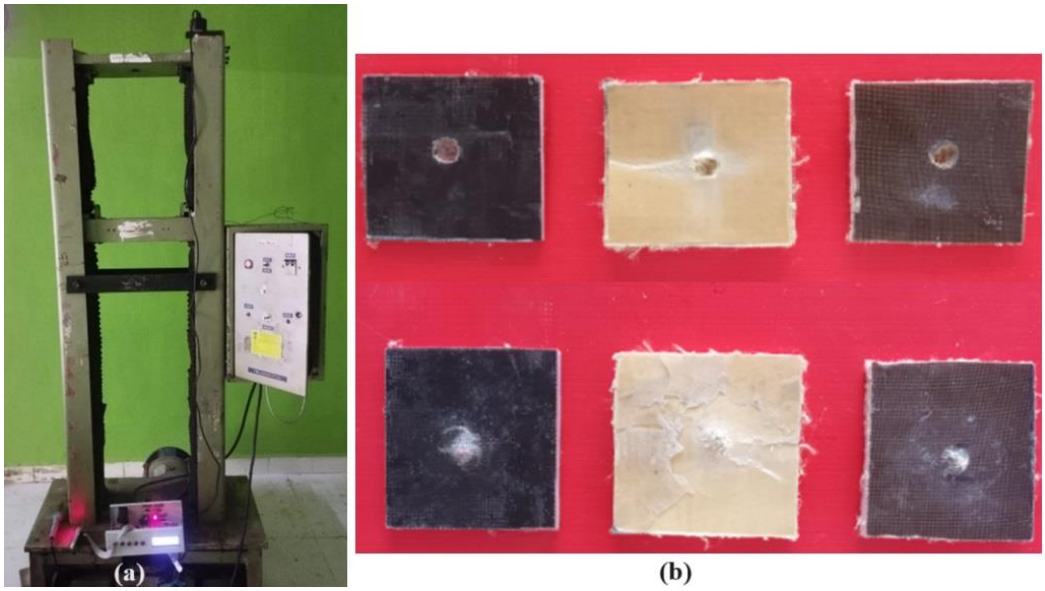

Fig. 8(a) Setup of drop weight impact test **(b)** Specimens after performing the test (front and back)

Table 1. ILSS test data

Specimen	Length (mm)	Breadth (mm)	Thickness (mm)	Load (N)	Shear strength (N/mm^2)	Average
Plate 1-1	62	23.40	6	300	1.64	2.12
Plate 1-2	62	24.50	6	500	3.4	
Plate 1-3	62	24.54	6	200	1.33	
Plate 2-1	62	26.54	6	1450	6.4	5.02
Plate 2-2	62	26.70	6	1100	4.35	
Plate 2-3	62	26.10	6	1350	4.31	
Plate 3-1	62	21.30	6	600	5.93	4.82
Plate 3-2	62	19.52	6	400	3.84	
Plate 3-3	62	18.74	6	500	4.71	

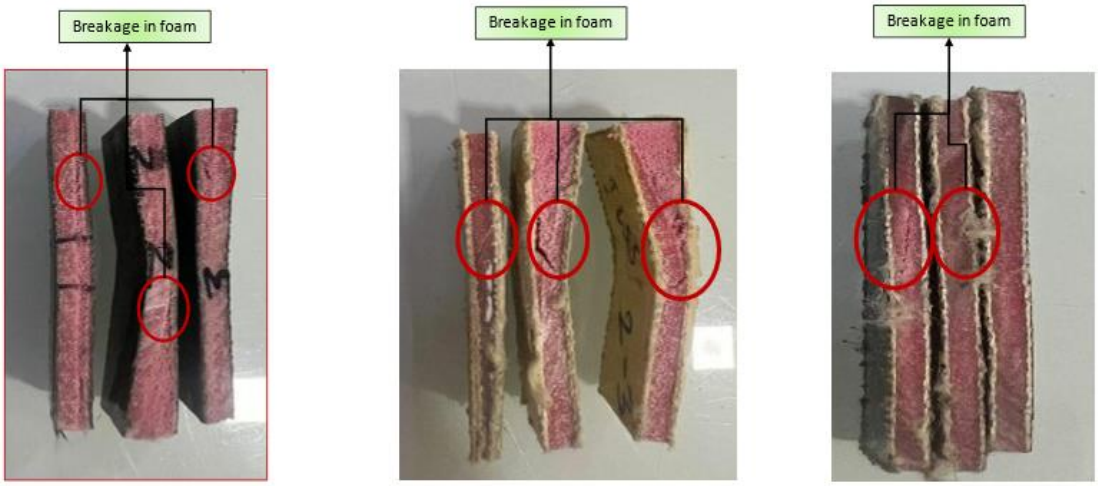

Fig. 9 ILSS test specimens after testing

Figure 9 shows that there are more visible cracks and deformation present in Plate 2 as Kevlar can withstand more load, and the PU foams tend to tear and leave a more visible crack on the side surface. While Plate 1 tends to have a slight tear as it can withstand only less weight. Plate 3 mostly has no cracks as it is a combination of Kevlar and basalt which gives a stronger surface.

3.2. Edgewise compression test

Table 2 represents the readings obtained while performing the edgewise compression test of composite laminates namely, Plate 1, Plate 2, and Plate 3. The data listed in Table 2 indicates the capability of each specimen to withstand a higher loads and shows a greater compressive strength. The sandwich panels with the material combinations presented here tend to collapse in three different modes under edgewise compressive loads. Sandwich-structured composites with PU foam and basalt fibers thereby strengthening the insulating sheets with an innovative structure and the material withstand the average crash of 13.4 N/mm^2 (refer plate 1). In plate 2, Kevlar with foam core exhibits an average crash of 8.74 N/mm^2 as the Kevlar has the property of high tensile strength and low elongation to break. In case of the combination of Kevlar /Basalt foam core (refer Plate 3), it has both properties of Kevlar and basalt, and it withstands with a high energy absorption of 17.08 N/mm^2 when compared to other plates. This is due to the arrangement of fiber and the fiber stacks.

Table 2. Edgewise compression test data

Specimen	Length (mm)	Breadth (mm)	Thickness (mm)	Area (mm^2)	Load (N)	Compression (N/mm^2)	Average
Plate 1-1	101	49	6	289.1	3300	11.76	13.4
Plate 1-2	101	48.74	6	287.56	4200	14.61	
Plate 1-3	102	47.74	6	281.66	3700	13.85	
Plate 2-1	102	50	6	295	200	6.78	8.74
Plate 2-2	102	52	6	323.44	500	1.55	
Plate 2-3	102	52	6	323.44	400	1.24	
Plate 3-1	100	49	6	220.5	4200	19.04	17.08
Plate 3-2	100	52	6	305.76	6200	20.37	
Plate 3-3	100	51	6	295.8	3500	11.83	

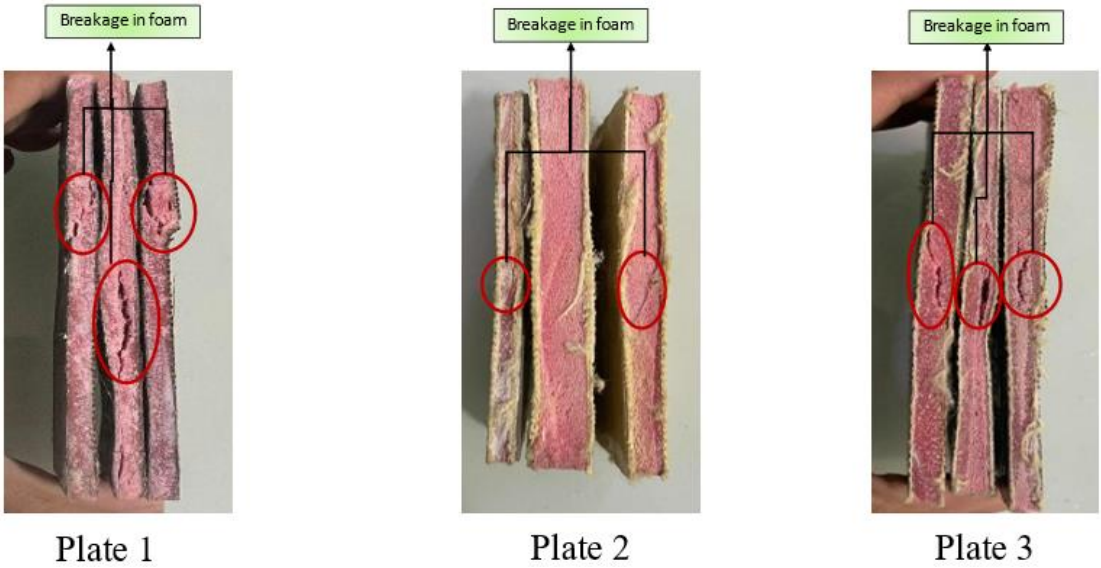

Fig. 10 Edgewise compression test specimens after testing

Figure 10 shows that there are more visible cracks and deformation present in Plates 1 and 3 as Kevlar can withstand more loads, and the PU foams tend to tear and leave a more visible crack on the side surface. While Plate 2 tends to have a slight tear as it can withstand only less weight. Plate 3 which has the combination of Kevlar and basalt gives a stronger surface.

3.3. Flammability test

Table 3 represents the readings obtained while performing the flammability test of the composites Plate 1, Plate 2, and Plate 3**.** The data listed in Table 3 identifies the specimen with a greater propagation speed. Plate 2, which has Kevlar, is inherited to fire resistance. So, it has an average flammability of 36.73mm/minute. In Plate 3, the effects of surface modification is done through basalt/Kevlar fiber-based epoxy composites. The traction and compression resistances of the PU foam core are reduced by adding basalt fiber, while the density and thermal stability of the foam are increased. As basalt is naturally fire resistant, its ability to self-extinguish and act as a flame retardant is strengthened. PU foam formulations are strengthened with basalt to increase their rigidity, hardness, and thermal resistance. The average flammability of basalt-PU foam is 59.2mm/minute. Plate 3, i.e., Kevlar-basalt-PU foam-based composite has a low flammability of 48.86mm/minute and is highly

unsaturated due to its high carbon to hydrogen atom ratio. Figure 11 shows the deformation that occurred in the specimens and how much the PU foam has withstood the fire burn.

Table 3. Flammability test data

Specimen	Propagation speed (mm/min)	Falling drops	Cotton lightens	UL-94 V Rating
Plate 1-1	62.6	N-1	N-0	V-1
Plate 1-2	58.2	N-1	N-0	V-1
Plate 1-3	56.8	N-1	N-0	V-1
Plate 2-1	38.2	N-1	N-0	V-1
Plate 2-2	36.3	N-1	N-0	V-1
Plate 2-3	35.7	N-1	N-0	V-1
Plate 3-1	51.2	N-1	N-0	V-1
Plate 3-2	48.8	N-1	N-0	V-1
Plate 3-3	43.6	N-1	N-0	V-1

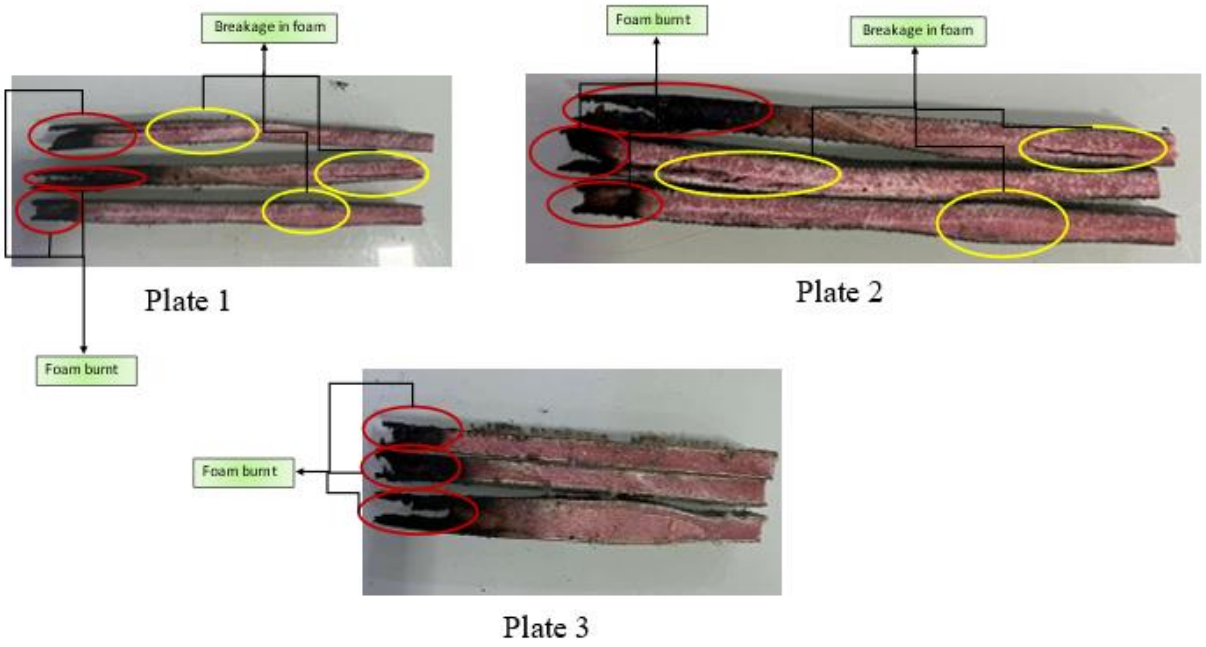

Fig. 11 Flammability test specimens after testing

As per UL-94 ratings, V0, V1 and V2 represent good flammable resistance, medium flammable resistance, and poor flammable resistance respectively. Similarly, N-0 represents frequent drops and N-1 represents frequent drops as per flammability test based on UL-94 ratings.

3.4. Drop-weight impact test

Table 4 represents the readings taken while performing the drop-weight impact test of composite laminates namely, Plate 1, Plate 2, and Plate 3. Table 4 shows the specimen ability with higher energy absorption when an impact load is applied to the specimen. The energy absorbed is more in Plate 2 as Kevlar has a long chain of molecular properties and bonding properties linked together by the amide bonds creating a strong intermolecular force between the chains.

Table 4. Readings of drop-weight impact test

Specimen	Height, h_1 (m)	Energy absorption (J)
Plate 1	0.654	8.5
Plate 2	0.518	11.8
Plate 3	0.649	8.6

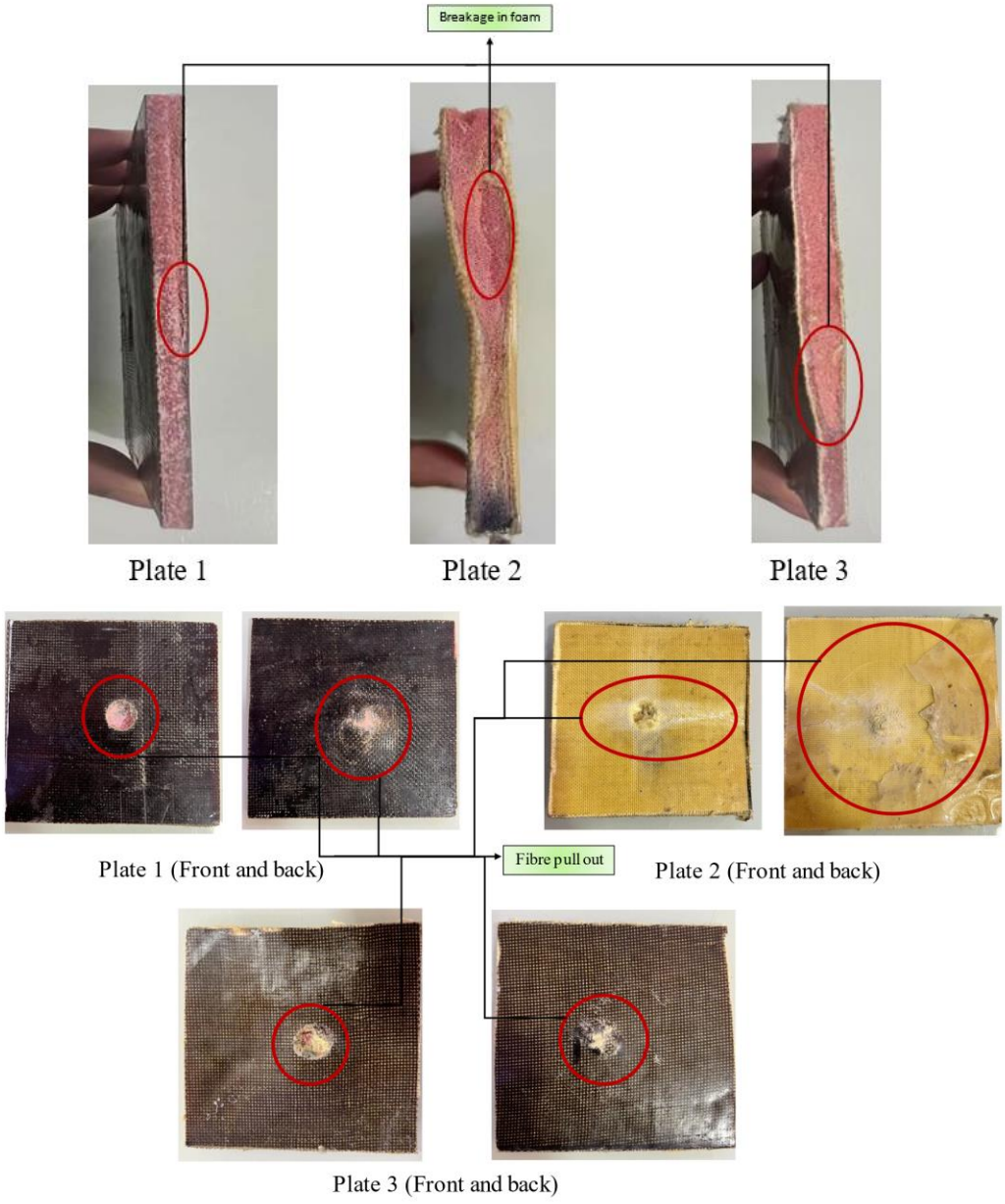

Fig. 12 Drop weight impact test specimens

Figure 12 shows the composite laminates after undergoing the drop weight impact test. When the load is applied to Kevlar fibers, due to impact, these intermolecular forces resist deformation and help to distribute the weight over a larger area, allowing the material to absorb more energy before failure. Since the energy absorbed is larger as fiber pull-outs in Plate 2 (refer Figure 12), the impact has travelled to a larger area.

4. Conclusion

This study investigates the effects of incorporating a polyurethane foam core with Kevlar and basalt face sheets in the constructions of three different plates with varying orientations. Plate 2 (Kevlar/Kevlar/PU foam/Kevlar/Kevlar) orientation exhibits better shear strength, while Plate 3 (Basalt/Kevlar/PU Foam/Kevlar/Basalt) orientation demonstrated high compressive strength. Plate 2 also absorbed more energy during impact testing and Plate 1 (Basalt/Basalt/PU Foam/Basalt/Basalt) demonstrated a faster propagation speed when exposed to fire. Finally, the combination of Kevlar, Basalt, and Polyurethane foam offers better shear strength and is light in weight. Moreover, it has low flammability, and high energy absorption ability making it suitable for applications such as bulletproof wings in aircraft and insulation of aircraft materials near the engine.

References

[1] Oana Alexandra Mocian, Dan Mihai Constantinescu and Andrei Indreş, Assessment on energy absorption of foam core sandwich panels under the low velocity impact, Macromolecular Symposia, 2021, 396(1), 2000300, 10 pages. https://doi.org/10.1002/masy.202000300

[2] Stanley Samlal and R. Santhanakrishnan, Low-velocity impact behaviour of foam core sandwich panels with inter-ply and intra-ply carbon/Kevlar/epoxy hybrid face sheets, Polymers, 2022, 14(5), 1060, 8 pages. https://doi.org/10.3390/polym14051060

[3] Nicolae Constantin, Marin Sandu, Adriana Sandu and Mircea Gavan, Damage identification and mechanical assessment of impacted Sandwich Composites, Procedia Engineering, 2017, 188, pp. 178-185. https://doi.org/10.1016/j.proeng.2017.04.472

[4] Frederick Laurin and Anthony J. Vizzini, Energy absorption of sandwich panels with composite-reinforced foam core, Journal of Sandwich Structures & Materials, 2005, 7(2), pp. 113-132. https://doi.org/10.1177/1099636205047888

[5] Ranjith Kumar Pathipaka, Kiran Kumar Narmala and Chennakesava Rao Bandaru, Damage characterization of sandwich composites subjected to impact loading, Journal of Sandwich Structures & Materials, 2020, 22(7), pp. 2125–2138. https://doi.org/10.1177/1099636218792717

[6] V. Ramesh and P. Anand, Evaluation of mechanical properties on Kevlar/basalt fiber reinforced hybrid composites, Materials Today: Proceedings, 2021, 39(4), pp. 1494–1496. https://doi.org/10.1016/j.matpr.2020.05.406

[7] Bruno Castanie, Christophe Bouvet and Malo Ginot, Review of composite sandwich structure in aeronautic applications, Composites Part C: Open Access, 2020, 1, 100004, 10 pages. https://doi.org/10.1016/j.jcomc.2020.100004

[8] Victor Avisek Chatterjee, Sanjeev Kumar Verma, Debarati Bhattacharjee, Ipsita Biswas and Swati Neogi, Enhancement of energy absorption by incorporation of shear thickening fluids in 3D-mat sandwich composite panels upon ballistic impact, Composite Structures, 2019, 225, 111148, 8 pages. https://doi.org/10.1016/j.compstruct.2019.111148

[9] A.G. Mamalis, D.E. Manolakos, M.B. Ioannidis and D.P. Papapostolou, "On the crushing response of composite sandwich panels subjected to edgewise compression: experimental," Composite Structures, 2005, 71(2), pp. 246–257. https://doi.org/10.1016/j.compstruct.2004.10.006

[10] M. Zarei Mahmoudabadi and M. Sadighi, Experimental investigation on the energy absorption characteristics of honeycomb sandwich panels under quasi-static punch loading, 2019, 88, pp. 273-286. https://doi.org/10.1016/j.ast.2019.02.035

[11] Muhammad Imran Khan and Mehmet Karahan, Testing of Natural Fiber Composites. In: Nawab, Y., Saouab, A., Imad, A., Shaker, K. (eds) Natural Fibers to Composites, Engineering Materials, Springer, 2023. https://doi.org/10.1007/978-3-031-20597-2_7

[12] A. Florence, M. Arockia Jaswin and A. Pal Pandi, Drop-weight impact behaviour of hybrid fiber/epoxy honeycomb core sandwich composites under hemi-spherical impactor, Fibers and Polymers, 2020, 21, pp. 1152–1162. https://doi.org/10.1007/s12221-020-9872-1

[13] M. Kazemi, Experimental investigation on the energy absorption characteristics of sandwich panels with layering of foam core under quasi-static punch loading, Mechanics of Advanced Materials and Structures, 2022, 29(21), pp. 3067–3075. https://doi.org/10.1080/15376494.2021.1885770
[14] D. Zangani, M. Robinson and A.G. Gibson, Energy absorption characteristics of web-core sandwich composite panels subjected to drop-weight impact," Applied Composite Materials, 2008, 15, pp. 139–156. https://doi.org/10.1007/s10443-008-9063-5
[15] J. Zhou, Z.W. Guan and W.J. Cantwell, The impact response of graded foam sandwich structures," Composite Structures, 2013, 97, pp. 370–377. https://doi.org/10.1016/j.compstruct.2012.10.037
[16] G. Caprino and R. Teti, Impact and post-impact behaviour of foam core sandwich structures, Composite Structures, 1994, 29(1), pp. 47–55. https://doi.org/10.1016/0263-8223(94)90035-3
[17] Guangyong Sun, Erdong Wang, Hongxu Wang, Zhi Xiao and Qing Li, Low-velocity impact behaviour of sandwich panels with homogeneous and stepwise graded foam cores, Materials & Design, 2018, 160, pp. 1117–1136. https://doi.org/10.1016/j.matdes.2018.10.047
[18] Xintao Huo, Hao Liu, Quantian Luo, Guangyong Sun, Qing Li, On low-velocity impact response of foam-core sandwich panels, International Journal of Mechanical Sciences, 2020, 181, 105681, 10 pages. https://doi.org/10.1016/j.ijmecsci.2020.105681
[19] Oana Mocian, Dan Mihai Constantinescu, Marin Sandu and Stefan Sorohan, Experimental and numerical analyses of the impact response of lightweight sandwich panels," Materials Today: Proceedings, 2018, 5(13), Part 2, pp. 26634–26641. https://doi.org/10.1016/j.matpr.2018.08.128
[20] Faris Tarlochan, Sandwich structures for energy absorption applications: a review, Materials, 2021, 14(16), 4731. https://doi.org/10.3390/ma14164731
[21] D. Feng and F. Aymerich, Effect of core density on the low-velocity impact response of foam-based Sandwich Composites," Composite Structures, 2020, 239, 112040. https://doi.org/10.1016/j.compstruct.2020.112040

Hybrid Wind-Solar System with UPQC

Abhishek Saxena[1], *Rajesh* Gundlapalle[2*], *Manish* Gupta[3], *Ediga* Poornima[4], *Harjeet* Singh[5], *Ali* Albawi[6], *K* Arunkumar[7]

[1]Department of Mechanical Engineering, ABES Engineering College, Ghaziabad - 201009, UP, India.
[2]Department of Electronics and Communication Engineering, New Horizon College of Engineering, Bangalore, India
[3]Lovely Professional University, Phagwara, India.
[4]Department of AI&ML, GRIET, Bachupally, Hyderabad, Telangana, India.
[5]Lloyd Institute of Engineering & Technology, Knowledge Park II, Greater Noida, Uttar Pradesh, India.
[6]Radiology Techniques Department, College of Medical Technology, The Islamic University, Najaf
[7]Department of Aeronautical Engineering, MLR Institute of Technology, Hyderabad, Telangana, India-500081

Abstract. The hybrid wind-solar system is a combination of renewable energy sources, specifically wind and solar, that is utilized for power generation. While wind power has historically been used for various purposes such as sails, windmills, and wind pumps, it is now predominantly used for electricity generation. This system incorporates solar panels and small wind turbine generators to produce electricity. The advantage of hybrid systems is that they can generate electricity as needed, taking into account the varying peak working hours of solar and wind systems throughout the year. To ensure a stable power system, UPQC (Unified Power Quality Conditioner) is employed. This multipurpose power conditioner serves multiple functions, including preventing harmonic load current from entering the power system, rectifying voltage fluctuations, and compensating for voltage disturbances from different power sources. It is specifically designed to minimize interference with sensitive or critical loads. With its series and shunt compensation capabilities, UPQC effectively manages power flow, reactive power, harmonics, and voltage disturbances. In this paper, the work addresses the issue of electricity quality that arises from the installation of wind turbines in the grid. To get over this issue, the suggested course of action demonstrates how to install a BESS and a unified power quality conditioner (UPQC) at the connection point. Even though wind power fluctuates, the use of battery energy storage technology helps to provide a constant power supply. With the power system block established in MATLAB/SIMULINK, one can simulate the UPQC control method of a grid-connected wind energy generating plant. As a result, the power's quality will increase. When the recommended approach lowers the load's and the induction generator's reactive power requirements, it is successful.

* Corresponding author: gundlapallerajesh@gmail.com

© The Authors, published by EDP Sciences. This is an open access article distributed under the terms of the Creative Commons Attribution License 4.0 (https://creativecommons.org/licenses/by/4.0/).

Furthermore, the plan for raising the grid's power quality criteria and developing the grid coordination rule are also provided.

Keyword-: -: Power Quality, Generator, Solar PV, Unified Power Quality Conditioner, Wind Energy.

1 Introduction

Since the demand for power is increasing at a very rapid rate, connecting to the distribution network necessitates the utilization of alternative energy sources. The primary drawbacks of alternative energy sources are their seasonal and erratic power production [1] [2]. Numerous alternative sources are connected in order to address these issues. A diode rectifier that supplies RL loads (non-linear-load) is employed to investigate the concept of compensation, different techniques of control, and overall performance of the UPQC. The theory, methodology, and application of a single power quality conditioner are documented in paper [4]. Effective participation in a remote island microgrid that makes use of solar-powered turbines requires combining the control of the battery storage with the management of the maximum power point of the tracking (MPPT). In order to maximize power generation, this integrated approach combines battery storage control with MPPT approaches, such as the perturb and observe method developed by the paper's author [6]. "The UPQC, as described in article [7], incorporates active power filters (APFs) in both series and shunt configurations to mitigate harmonics in the supply voltage and load power. Although a proportional-integral (PI) controller is included into the shunt APF control scheme, it is used in the series APF control scheme to relieve harmonic currents induced by nonlinear loads." By comparing and contrasting two UPQC models, the writers in [8] were able to determine which interface dramatically improved power quality. This paper's authors have come up with a number of different approaches to shunt active power filters that are used in three-phase systems [9]. The control methods for parallel active power filters that correct for current harmonics and voltage source inequality were thoroughly described by the authors of paper [10]. "In paper [11], authors have devised an effective voltage sag detection approach for an active voltage restorer. The experimental configuration and modeling of a shunt active power filter, which attempts to account for reactive power as well as harmonics, have been disclosed by the authors in paper [12]."The method described above has the advantage of maintaining a steady DC connection voltage. Wind energy could be able to provide the UPQC with the necessary power to run when sunlight isn't present. The main flaw with UPQC is that it cannot adjust for voltage interruptions; however, the recommended method can perform all of UPQC's duties and compensate for voltage interruptions.

2 Related Work

According to authors of study [12], the 21st century demands energy since renewable energy sources are widely used, easily accessible, and inexpensive. However, the volatility, round-the-clock accessibility, and other drawbacks of these fuels in their pure form can be mitigated by hybrid energy sources. They are essentially composed of numerous combinations of energy from renewable sources. They provide efficient responses to power issues, harmonic evaluations, voltage, and frequency fluctuations in stand-alone systems. Hybrid electrical systems retain the lowest possible unit cost, minimize energy variations brought on by DPSP (deficient power supply probability), and decrease complications with the help of appropriate design, increased quick reaction, good optimization, and control feasibility. This paper provides a brief description of hybrid wind and solar energy systems. The utilization of the

model served two purposes: firstly, to assess the technological viability of PV-wind hybrid systems within a defined load requirement range, and secondly, to conduct a cost-effective analysis for standalone PV, standalone wind, and PV-wind hybrid systems**.**

In order to aid decision-makers in their examination of the various elements involved in the creation of a hybrid solar-wind power system (HSWPS) for grid-connected applications, authors devised a decision support method. These elements primarily encompass advancements in social, political, and technical aspects, as well as improvements in economic and technological factors. The Analytic Hierarchy Process (AHP) is employed to assess the numerous disparities in beliefs, actions, and events that contribute to uncertainty and confusion during the development of HSWPS. More than one plan is made through the trade-off risk technique used to consider future 16 scenarios which lastly involve the development of respective curves of the trade-off. The current model was applied for two applications: one, for the technological feasibility evaluation of a PV-wind hybrid system within the span of a given specific load size; and two, for the cost-effective analysis for the stand-alone PV, the stand-alone wind, and the hybrid system of PV-wind [6].
Authors developed a decision support method to assist the decision-makers in analyzing the following of different factors associated with the development of an HSWPS for grid connected applications. Factors are primarily associated with social and political advancements, technical improvements, economic, and technological factors. In this regard, a number of discrepancies in beliefs are viewed as inducing uncertainty and confusion into the development of HSWPS, for which the application of the Analytic Hierarchy Process is employed [8]. Through the utilization of the trade-off risk technique, multiple plans are generated to account for 16 potential future scenarios, resulting in the creation of corresponding trade-off curves. Authors in this paper explored various methods of communication that can be employed to incorporate renewable energy sources into the power grid. Since renewable energy sources are often sporadic, it is crucial to integrate a substantial portion of them into the framework of a power grid. Currently, power is transmitted from centralized facilities to consumers through a single pathway. While a conventional power plant may have a greater capacity compared to a renewable energy facility, it is essential to recognize the potential of renewable energy as an emerging resource [9].
According to a study conducted by authors in paper [12], there is a projected rise in the adoption of renewable energy systems in the coming years. This shift is driven by the negative environmental consequences associated with conventional energy sources, as well as the escalating expenses of electricity [13-16]. Solar and wind energy power are complimentary; hence some strain on the energy grid can be alleviated. It has a note, however, that independently verified responses are on their own unpredictable and not, therefore, very reliable [17]. However, studies showed that a PV/WT hybrid energy system with autarkic features is comparably feasible and cost-effective to deliver electricity to remote customers worldwide. The work at hand provides a comprehensive introduction towards system setup, modeling, and renewable energy generation, optimum sizing estimation, hybrid system optimization criteria, and control techniques. A similar comparative study conducted concerning the Barwani, India, case states that the PV-Wind-Battery-DG hybrid system is the most cost-effective and environmentally friendly option compared with other freestanding hybrid combinations for application in remote areas. As an expansion of the discussion, the paper highlights some developments that will potentially further help in increasing the financial attractiveness and customer support of these approaches in the future [18-21].

3 Control Strategies of the UPQC System

To determine the UPQC reference voltage and current, a number of control mechanisms are possible.

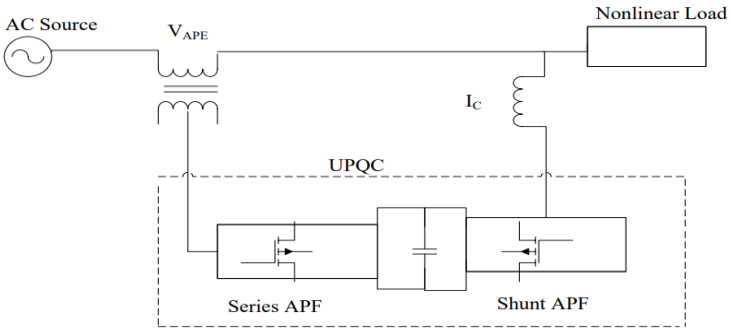

Fig. 1: Block Diagram of UPQC.

The block diagram for the control mechanism of the UPQC system is displayed in Figure 1. In the context of compensation and dependability, FACTS (Flexible AC Transmission System) equipment is essential to the power system. “Similar to the Unified Power Flow Controller, the Unified Power Quality Conditioner (UPQC) is intended for the electric power the system's distribution side. Shunt filters and series filters are both of them categories of active filters [22].

Shunt active power filters can help reduce harmonics caused by load current, while series active power filters can compensate for voltage disturbances such as voltage spikes and voltage sags. Energy exchange by connecting DC link capacitors to shunt and series active power filters in a back-to-back configuration.

3.1 Series/ Voltage Source Converter

It reduces voltage variations by connecting the voltage source converter in series with the AC line. As a result of nonlinear loads, parallel branches are formed to absorb harmonic currents so that voltage fluctuations will be avoided. The series converter voltage is often regulated using sinusoidal pulse width modulation (SPWM) [24-27]. An evaluation of a high frequency triangular signal and a voltage reference input is required to generate the gate pulses necessary for the converter to operate.

3.2 Shunt Converter

In order to control the reactive current of the load, correct for current distortion, and lower the power factor, this parallel source of voltage converters may also be utilized as an energy source [28]. Additionally, it controls the DC bus voltage, which considerably lowers the DC capacitors' power. A shunt converter's output current can be adjusted using a dynamic hysteresis range that stays in a predetermined hysteresis band and conforms with the reference signal by changing the state of the semiconductor switches [29-32].

3.3 DC Capacitor Bank Connected to Ground at the Midpoint

It is split into two series-connected groupings. The secondary transformer's neutral conductor is directly linked to the middle of the intermediate circuit [33]. The primary winding of the series transformer in a three-phase transformer connected in Y/Yo receives zero voltage to make up for the supply network's zero voltage. On either transformer's main side, there is no residual current flowing [34]. This guarantees that even when there are voltage fluctuations, the system current stays balanced.

3.4 Low-pass Filter

Low-pass filters pass signals below cutoff frequencies through while they attenuate sounds above cutoff frequencies [35]. Filters respond to frequencies differently depending on their structure. In electrical circuits, low-pass filters are used to filter audio hiss, improve acoustics, blur images, smooth data sets, and condition signals prior to analog-to-digital conversion [36]. In sectors such as banking, moving averages are used as low-pass filters. The investigation of this filter can also be done using signal processing techniques that are also available for investigating other low-pass filters. In order to smooth out a signal, low-pass filters can be used, which can eliminate short-term fluctuations while preserving a longer-term trend, so the signal can be provided with a rounded appearance. There is a possibility of using it to reduce the high-frequency elements at the output of a series converter that are caused by high-frequency switching [37-41].

3.5 High-pass Filter

When applied to electrical signals, high-pass filters (HPFs) allow those frequencies beyond a certain cutoff while reducing the volume of those frequencies below it. The design of the filter dictates the amount of attenuation that each frequency receives. A linear time-invariant system is often used to mimic a high-pass filter. It goes by a several names in the world of audio engineering, including low-cut and bass-cut filters. High-pass filters are useful for several things, one of which is shielding devices from non-zero average DC voltages, such as electronics or radio frequency equipment. They are versatile enough to be used in the construction of both low-pass and band-pass filters. Positioned near the shunt converter's output, it dampens ripples caused by current switching.

4 Result Analysis

MATLAB simulation of UPQC models in the field of wind/solar energy, including series AF, shunt AF, solar PV, wind energy, and boost converters is illustrated in Figure 1.

4.1 Equivalent Circuit

A UPQC consists of two voltage source converters, which can be arranged in a single-phase, three-phase, or four-phase configuration, as shown in Figure 2. All of these converters are interconnected by a DC intermediate circuit. A voltage link inverter is connected between the source and the load at the point of common coupling (PCC).

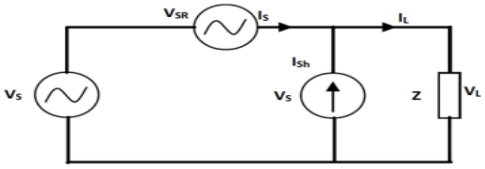

Fig. 2. Equivalent circuit for UPQC.

V_S : Voltage at power supply

V_SR : Voltage compensation by Series Active Power Filter (APF),

V_L : Load voltage and

I_Sh : Current compensation and VSR compensation by Shunt Active Power Filter (APF)

The voltage distortions may result in harmonic as well as negative phase sequence components in the structure of the system.

The source voltage in Figure 2 may often be written as:

V_s+V_SR=V_L (1)

To obtain a constant amplitude sinusoidal load voltage, V, the voltages that are output of the series-APF have to be supplied by:

V_SR=(V-V_lp)sin(ωt+θ_1P)-V_Ln (t)-∑_R^z=2V_k (t) (2)

Where, V_lp : Fundamental frequency of positive sequence voltage amplitude.

θ_1p : Initial phase angle of the positive sequence voltage.

V_Ln : Negativesequence component

A parallel APF functioning as a regulated current source must generate harmonic, reactive, and negative sequencing elements in its output in order to balance these numbers inside a load current. This is accomplished by matching the load component (as indicated by the following equation) with the output current of the parallel APF (Ish):

(&I_L=I_(l_p) cos(ωt+θ_IP)sinφ_1 P+I_Ln+∑_K^q=2@&ϕ_1P=φ_1P-θ_1P@&) (3)

Where, φ_1P: Initial phase of current for positive sequence.

The above equation shows that the power supply does not receive any harmonics, reactive power, or negative sequence currents." Therefore, the phase voltage at the load connection and the terminal source current have the same phase angle and are harmonic-free sinusoids-

(I_S&=I_L-I_Sh@&=I_1p sin⁡(ωt-θ_1P)cos⁡φ_1 p) (4)

4.2 Implementation and Discussions

A BESS, or battery energy storage system, is the energy storage element used in voltage regulation. STATCOM works well with BESS because of its reactive power injection and absorption capabilities, which help to stabilize the grid system and naturally keep the DC capacitor voltage constant. Additionally, it provides extremely fast control options for power transmission and distribution networks. With BESS, power fluctuations in the system can be compensated by operating during charging and discharging phases.

The DC capacitors and battery of STATCOM are linked in parallel. With capacitors on its DC terminals, the STATCOM is a three-phase voltage source inverter connected at a common coupling point. The STATCOM provides a compensation current with programmable frequencies and amplitudes elements at the standard coupling point.

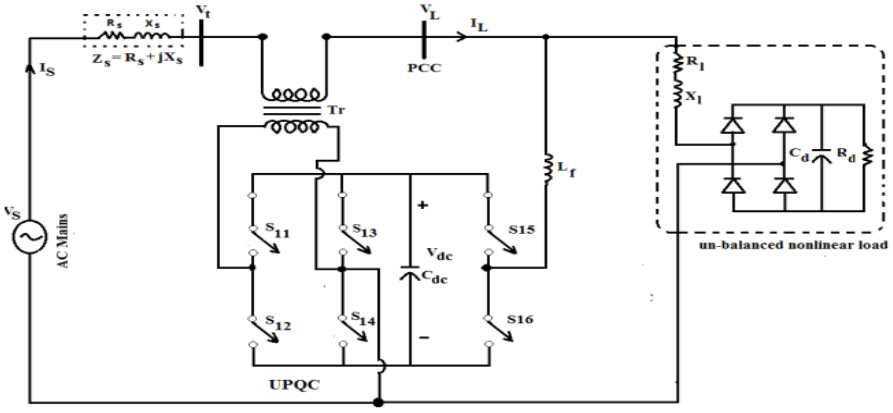

Fig. 3: System Operational Scheme in UPQC

The block diagram for the control mechanism of the UPQC system is displayed in Figure 1. In the context of compensation and dependability, FACTS (Flexible AC Transmission System) equipment is essential to the power system. The Unified Power Quality Conditioner (UPQC) is designed for the distribution side of the electric power system and functions similarly to the Unified Power Flow Controller. One kind of active filter is the shunt filter, while another is the series filter.

4.3 Simulation Model

Pitch controls, induction generators and wind turbines are used to generate wind power. Due to its simplicity and cost-effectiveness, induction generators are preferred over other types of machines in this case. The pitch angle of the turbine blades is adjusted by a pitch angle

controller to maintain a constant rotational speed regardless of wind speed. Additionally, the IM acts as a generator, receiving reactive power from the parallel capacitor bank.

Each time a sampling interval is completed, record the rms values of the resulting voltage and current, calculate the power, and trace the waveforms with an oscilloscope. In the figure, the timer is used to assign the wind speed to three different states, which are linearized after multiple loop operations.

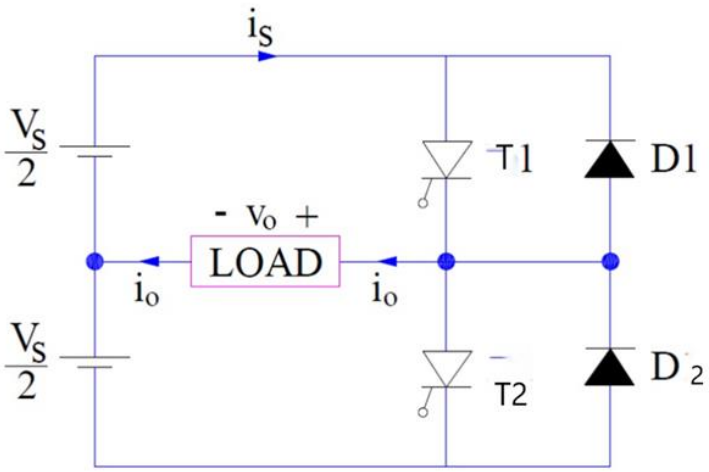

Fig. 4: Voltage Source Inverter with Battery

A voltage source inverter (VSI), which changes DC voltage into AC voltage, is shown in Figure 4. Another name for this gadget is a voltage-fed inverter, or VFI. A DC power source, switching transistors (such as IGBTs, MOSFETs, and thyristors), and a DC link capacitor—which reduces fluctuations and serves as a filter—make up the VSI. The VSI utilizes a voltage sensing interface (VSI) to maintain a consistent voltage throughout its operation.

Table 1: Different parameters and their ratings to carry out the simulation work.

Equipment/Specification	Specification Value
Voltage of Grid	315 V
Frequency of Operation	50 Hz
Specifications of Induction Generator	3.35 KVA, 415 V, 60 Hz
Rotational Speed	1240 rpm
Resistance - Rotor (Rr)	0.01 Ω
Resistance - Stator (Rs)	0.015 Ω
Inductance (Ls and Lr)	0.06 H
Voltage - DC Link (Inverter)	700 V
Capacitance - DC Link	100 µF
Frequency of Switching	2 kHz
Load (Non-linear)	15 KW

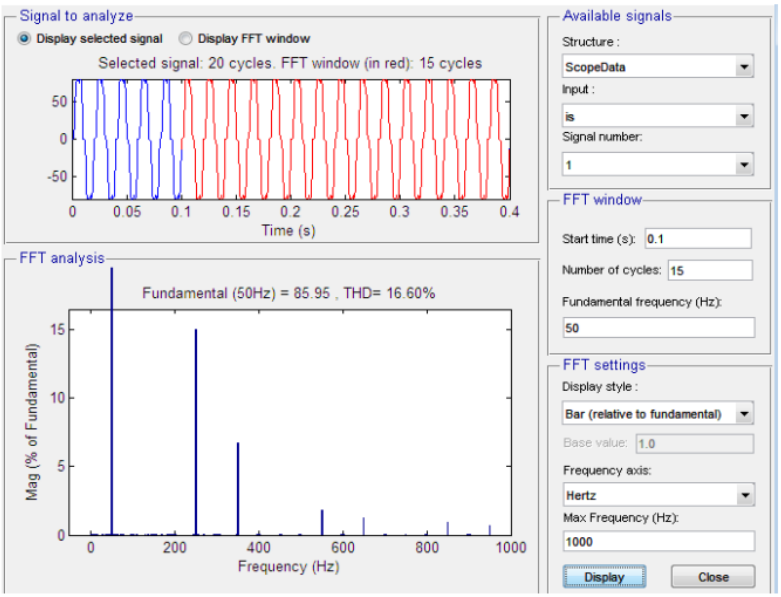

Fig. 5: Harmonics analysis without shunt APF.

The above figure 5 shows that harmonic analysis involves examining the harmonic content of voltage and current wave forms within a power system. Problems like better losses, equipment over heating, and interference with sensitive equipment can arise from harmonics produced by non-linear hundreds like rectifiers, electricity electronics, and variable velocity drives if a shunt APF isn't always used. Engineers may measure the effects of these harmonic distortions on the gadget's performance using harmonic evaluation.

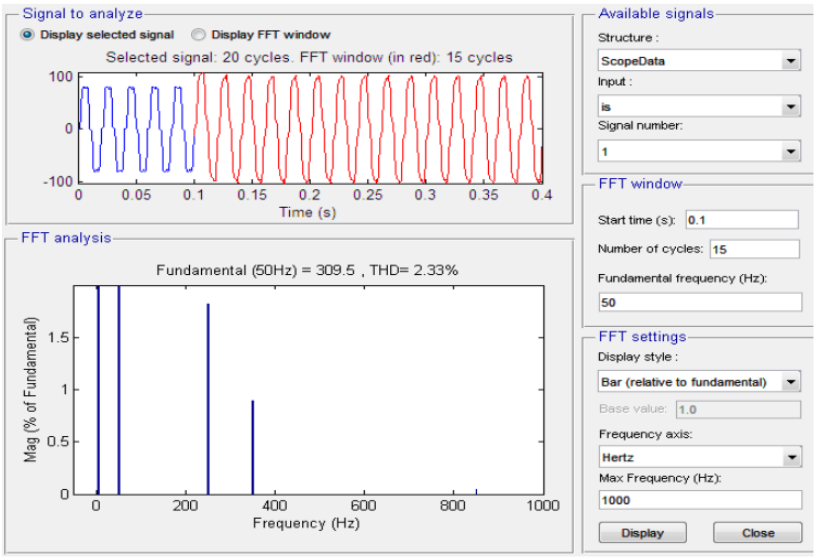

Fig. 6: Harmonics analysis with shunt APF.

As shown in figure 6, engineers can evaluate the effectiveness of an active electricity filter out (APF) in compensating for harmonic distortions through combining harmonic evaluation with a shunt APF. In order to reap the desired stage of harmonic mitigation, this method enables the optimization of APF manage settings and modifications.

Engineers can also achieve access to system performance blessings through integrating harmonic evaluation with shunt APFs. Improvements in strength first-class, stability, and total harmonic distortion (THD) discount need to be assessed. Also, it is beneficial for finding any harmonic issues that would necessitate further mitigating measures.

5 Conclusion

This paper proposes a FACTS- primarily based manage method for grid-connected wind generators operating underneath non-linear loads and with stepped forward power excellent (UPQC). The paper delves into electricity exceptional problems and the way they effect each utilities and customers. Power pleasant should be maintained by using modeling the UPQC control system in MATLAB/SIMULINK. it filters out the harmonics inside the load current.The opportunity to increase the transmission line load issue arises whilst the supply voltage and contemporary remain in section, the reactive power requirements of the wind generators are satisfied, and the demand at the PCC inside the grid gadget is met. Consequently, the performance of installing FACTS with BESS and wind power to preserve the specified voltage distribution is notable. Consequently, the proposed grid-linked device answer keeps the grid voltage free of distortion and harmonic seven as meeting Energy high-quality standards

References

1. Ashish S. Ingole*, Prof. Bhushan S. Rakhonde, “Hybrid Power Generation System Using Wind Energy and Solar Energy” International Journal of Scientific and Research Publications, Volume 5, Issue 3, March 2015.
2. Karim Mousa1, Hamzah AlZu’bi2, Ali Diabat3, “Design of a Hybrid Solar-Wind Power Plant Using Optimization”
3. Medugu, D. W. & Michael, E., “Integrated Solar – Wind Hybrid Power Generating System for Residential Application”, Global Journal of Researches in Engineering: F Electrical and Electronics Engineering , Volume 14 Issue 4 Version 1.0 Year 2014.
4. Rashid Al Badwawi, Mohammad Abusara & Tapas Mallick, “A Review of Hybrid Solar PV and Wind Energy System”, Smart Science Vol. 3, No. 3, pp. 127-138(2015).
5. Rashid Al Badwawi1,*, Mohammad Abusara1 and Tapas Mallick1, “A Review of Hybrid Solar PV and Wind Energy System”, Smart Science Vol. 3, No. 3, pp. 127-138(2015).
6. R. Chedid, “A Decision Support Technique For The Design Of Hybrid Solar-Wind Power System”, IEEE Transactions on Energy Conversion, Vol. 13, No. 1, March 1998.
7. Sandeep Kumar1, Vijay Kumar Garg2, “A Hybrid Model Of Solar-Wind Power Generation System”, International Journal of Advanced Research in Electrical, Electronics and Instrumentation Engineering, Vol. 2, Issue 8, August 2013.
8. Vaibhav J. Babrekar, Shraddha D. Bandawar, Ashwini R. Behade, “Review Paper on Hybrid Solar-Wind Power Generator”, International Journal of Computer Applications (0975 – 8887) Volume 165 – No.5, May 2017

9. Chandragupta Mauryan.K.S, Nivethitha.T, Yazhini.B, Preethi.B, “Study on Integration of Wind and Solar Energy to Power Grid”, Nivethitha.T et al Int. Journal of Engineering Research and Application,Vol. 4, Issue 5(Version 1), May 2014.
10. V. K. Gajbhiye1, Prof. A. A. Kanaskar2, Prof. S. S. Jawre, “Solar Wind Hybrid System-A Review”, International Journal of Research in Advent Technology, Vol.5, No.5, May 2017.
11. J. Barros, M. de Apraiz, and R. I. Diego, “Measurement of Subharmonics In Power Voltages”, Power Tech, IEEE Lausanne, Page(s): 1736 – 1740, 2007.
12. Mahesh Singh and Vaibhav Tiwari, “Modeling analysis and solution of Power Quality Problems”,
13. Chellali Benachaiba and Brahim Ferdi, “Voltage Quality Improvement Using DVR”, Electrical Power Quality and Utilisation, Journal Vol. XIV, No. 1, 2008.
14. R.N.Bhargavi, “Power Quality Improvement Using Interline Unified Power Quality Conditioner”, 10th International Conference on Environment and Electrical Engineering (EEEIC), Page(s): 1 - 5, 2011.
15. K. Palanisamy, J Sukumar Mishra, I. Jacob Raglend and D. P. Kothari, “Instantaneous Power Theory Based Unified Power Quality Conditioner (UPQC)”, 25th Annual IEEE Conference on Applied Power Electronics Conference and Exposition (APEC), Page(s): 374 – 379, 2010.
16. G. Siva Kumar, P. Harsha Vardhana and B. Kalyan Kumar, “Minimization of VA Loading of Unified Power Quality Conditioner (UPQC)”, Conference on POWERENG 2009 Lisbon, Portugal, Page(s): 552 - 557, 2009.
17. V. Khadkikar , A. Chandra, A.O. Barry and T.D Nguyen, “Conceptual Study of Unified Power Quality Conditioner (UPQC),” IEEE International Symposium on Industrial Electronics, Vol. 2, Page(s): 1088 –1093, 2006.
18. V. Khadkikar , A. Chandra, A.O. Barry and T.D. Nguyen, “Power quality enhancement utilising single-phase unified power quality conditioner: digital signal processor-based experimental validation” Conference on Power Electronics, Vol. 4, Page(s): 323 –331, 2011.
19. V. Khadkikar , A. Chandra, A.O. Barry and T.D.Nguyen, "Application of UPQC to Protect a Sensitive Load on a Polluted Distribution Network", IEEE PES General Meeting, 2006.
20. Ahmed M. A. Haidar, Chellali Benachaiba, Faisal A. F. Ibrahim and Kamarul Hawari, “Parameters Evaluation of Unified Power Quality Conditioner”, IEEE International Conference on Electro/Information Technology (EIT), page(s):1 - 6, 2011.
21. M. Tarafdar Haque, and S.H. Hosseini, "A Novel Strategy for Unified Power Quality Conditioner (UPQC)", Conference on Proceedings of Power Electronics Specialists, Vol. 1, Page(s): 94 - 98, June 2002.

Construction and Seismic Performance Evaluation of Concrete Water Tanks

Koushal Dhamija[1], *OSD* Hima Bindu[2], *N V* Uma Reddy[3*], *Rajeev* Sobti[4], *Q*. Mohammad[5], *Ravi* Kalra[6], *B Nagaraj* Goud[7]

[1]Lloyd Institute of Management and Technology, Greater Noida, Uttar Pradesh, India.
[2]Department of Civil, GRIET, Bachupally, Hyderabad, Telangana, India.
[3]Department of Artificial Intelligence and Machine Learning, New Horizon College of Engineering, Bangalore, India
[4]Lovely Professional University, Phagwara, India
[5]Hilla University College, Babylon, Iraq
[6]Lloyd Institute of Engineering & Technology, Greater Noida, Uttar Pradesh, India.
[7]Department of Aeronautical Engineering, MLR Institute of Technology, Hyderabad, Telangana, India-500094

Abstract- The construction of concrete water tanks is a crucial aspect of water distribution structures, ensuring dependable water supply at predetermined elevations for numerous purposes. Municipalities and corporations closely depend upon these tanks to store water, combustible fluids, and synthetic compounds. However, the safety of these tanks, especially during seismic events, is paramount. To address this, robust support structures inclusive of reinforced concrete (RC) propped outlines, metallic frameworks, RC shafts, and masonry platforms are employed. The RC casing approach could be the most common support system due to its effectiveness and durability. This paper gives a FEM based technique the use of Staad.pro employed inside the construction and evaluation of concrete water tanks.

Keyword-: Water tank, FEM, Stad.pro, concrete, support systems

1 Introduction

A raised water tank serves as a vital factor in water distribution systems, presenting a reliable supply of water at a predetermined elevation. Those tanks are important for ensuring adequate water stress and availability for numerous purposes. Municipalities and companies depend on fluid garage tanks not only for water but additionally for storing flamable fluids and synthetic compounds. But, it is critical to note that tanks containing unsafe or flammable substances pose widespread protection concerns, particularly for the duration of seismic events. To mitigate risks, these tanks are prepared with strong help structures, together with bolstered concrete (RC) propped outlines, metal frameworks, RC shafts, and masonry structures [1]. Every assist machine is designed to resist the load of the tank and its contents

* Corresponding Author: nvumareddy@gmail.com

© The Authors, published by EDP Sciences. This is an open access article distributed under the terms of the Creative Commons Attribution License 4.0 (https://creativecommons.org/licenses/by/4.0/).

at the same time as maintaining structural integrity, even under seismic pressure. Amongst these help systems, the RC casing approach is the maximum commonly followed due to its validated effectiveness and sturdiness, as shown in Fig.1. In the course of seismic events, making sure the integrity of fluid garage tanks is paramount to prevent leakage or spillage of risky materials. Proper layout and production techniques, along with everyday preservation and inspection, are essential for boosting the resilience of those tanks in opposition to seismic forces. By way of enforcing suitable aid systems and adhering to protection protocols, the risk of loss or damage to tank contents may be minimized, safeguarding each human life and the environment [2].

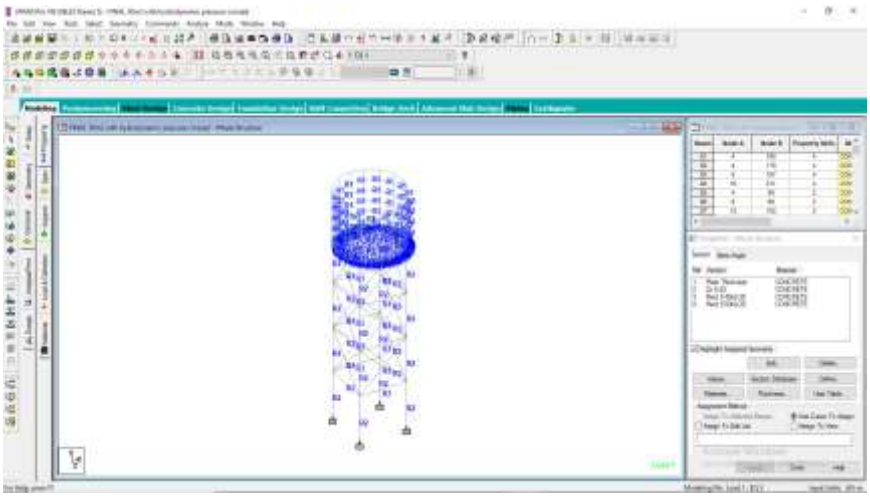

Fig. 1: Elevated Water Tank Supported by Inclined Columns

Component of factories, fireplace structures, and civic water structures is the raised water tank. Damage from earthquakes can threaten the provision of easy drinking water, positioned out fires, and result in financial loss. It is vital to investigate the seismic behavior of these buildings so one can fulfil safety requirements and shop constructing and maintenance charges. Using ANSYS software program, the study examined the response behavior of a raised RCC rectangular water reservoir under numerous water fill situations. The reactions of the tanks expanded with water height, according to the consequences [3]. Although concrete water tanks need to meet stringent requirements for serviceability, severe fractures can compromise their integrity and result in leaks. A 30 x 20 x 3.6 m water tank near the Arabian Gulf has cracks, according to a discipline exam [4-7]. To decide the problem and placed a restore plan into conduct, diagnostics research, outdoor inspections, lab testing, and 3-d modeling have been carried out. The study examined the properties of the concrete mix's heat of hydration using a semi-adiabatic calorimeter. It turned into discovered that tank walls cracked because of tensile loads which have been too amazing due to shrinkage lines and temperature. To get functionality backwards, a repair plan was counseled [8]. The use of non-corrosive reinforcing in reinforced concrete tanks of water and wastewater treatment centers is investigated in this study. It compares four substances—glass-fiber strengthened polymer (GFRP), stainless steel, epoxy-covered steel, and black iron—using existence-cycle cost evaluation [9]. The findings display that, despite its high preliminary cost, GFRP begins getting inexpensive following 35 years, suggesting that it is able to be a viable alternative for lengthy-time period concrete durability. In step with the have a look at, the internet cutting-edge cost of GFRP-strengthened concrete become 43% much less than that of black metal-bolstered concrete. Stainless steel was much less economical but had a twenty-five percent

decrease NPC. Epoxy coated metal confirmed a 15-12 months' growth in lifespan and an 11% discount in NPC [10-13]. The study discusses the design processes, building specifics, leakage testing, and monitoring outcomes for the world's first reinforced-concrete water chlorination tank. The purpose of the tank is to solve corrosion issues in RC tanks triggered by particular substances or treatment techniques' tank for a new water treatment facility is being built in Thetford Mines, Quebec, Canada. With a capacity of more than 2,500 m3, the tank satisfies the serviceability and durability specifications of ACI 350/350R-06, CAN/CSA S806-12, and ACI 440.1R-06. It is reinforced with GFRP bars [14]. Using non-destructive testing, this research assesses the state of brought up cement water tanks, including the development of cracks. Requirements for environmental quality influence tank design and construction. Water line cracks can pollute groundwater and harm storage tanks [15]. The research looks at leaks' causes and consequences. In addition to visual evaluations, hammer checks, design checks, cement compression tests, and Ultrasonic Pulse Velocity testing on tank construction parts was also part of the inquiry. Results included higher bending that planned, over time drying shrinkage cracks on the diagonally of the floor foundation, and flex type fractures in the centered span and diagonally beams of the main beam [16]. The behaviour of an elevated concrete water tank under seismic stress is investigated in this work by means of artificial seismic stimulation. It contrasts seven instances using models from the finite element strategy, mechanical designs, and actual dynamic analysis. Findings indicate that the axial power, overturning moment, or shear force at the tank's base are significantly impacted [17-20]. For big water tanks used in water treatment plants, in specific, the study revisits the application of iron cement in the construction of civil engineering. It is an appealing substitute that is particularly appropriate for poor nations, despite its low cost and plastic potential. Improving design methods and material comprehension is the goal of current study [21]. At order to compare different finite element models with experimental data, this study looks at numerical and experimental tests on big fibrocement tanks at Indianapolis, Brazil. The focus is on modeling accuracy and homogeneity procedures [22].
One world is becoming more aware of the problems associated with construction and civil engineering systems, especially as they relate to building water tanks. For the sake of economy, sustainability, as well as quality control, hybrid fiber concrete is the main focus of concrete manufacturing. Using this method will improve the quality of the finished product whereas building water reservoirs in Malaysian [23]. This study examines the nonlinear seismic response of raised water tanks made of reinforced concrete (RC), with an emphasis on a variety of tank sizes and RC pedestal measurements. Then takes a methodical approach, choosing and creating 48 model configurations, and then does linear static analysis utilizing a finite element technique. Research is being done to establish seismic reaction parameters for raised water tanks and to produce pushover curves for models [24]. The characteristics that are evaluated include the seismic design category, tank size, height to diameter ratio, and basic frequency. It shows that two cracking patterns are seen and that the size of the tank is important in seismic reaction [25]. The study investigates the application of water tanks as passively adjusted liquid dampers to reduce seismic activity in reinforced concrete structures. Tests were conducted on three 4-story models using a shaking table with different water levels. According to the study, for Models 1 and 2, water masses of 3.5 and two percent, respectively, provided the least reaction velocity and deflection [26-30]. In this essay, precast concrete water tanks and the R.C. water tanks are contrasted. It creates R.C.C. water tanks with an average size and uses MS Excel programming to compare the outcomes. RCC water tanks are more affordable for smaller-diameter tanks, but not for bigger ones, according to the results. The study highlights how crucial it is to choose the appropriate construction method for certain situations and building types [31]. Utilizing a probabilistic approach grounded on FAME P695, a research verifies the response modification factor of reinforced concrete pedestals in raised water tanks. Using incremental dynamic analysis, the likelihood

of collapse under various seismic loading situations is calculated for ten models that have different tank abilities and pedestal elevations. The nature of linear earthquakes is shown to be greatly influenced by tank size, with larger, heavier tanks being more susceptible [32-34]. Following sixty years of functioning, the highest possible and serviceability limit states for a reinforced concrete water towers tank are examined in this research. It consists of experimental research, site surveys, and computations to evaluate the load-bearing capacity, crack widths, and technical state of the tank and suggest structural repairs [35].

2 Problem Identification and Loading condition

This study aimed to evaluate the seismic performance of RCC elevated water tanks with columns positioned at various slant degrees. Loading conditions, including dead weight, seismic load, and hydrodynamic load under full water conditions, were considered. Altering the placement of columns can mitigate tensional modal analysis in circular tanks. Despite circular tanks being more cost-effective, rectangular tanks require a larger number of nodes for structural modelling. Structural modelling and analysis were conducted using the analytical software STAAD.Pro.

Concrete utilized in construction is of M30 grade, while reinforcement bars are of FE500 quality. The modulus of elasticity is measured at 1.95 x 10^5 Mega Pascals (MPa), with an ultimate tensile strength of 1860 MPa. The soil type is categorized as medium, while wind pressure is recorded at 39 meters per second. Hydraulic pressure considerations encompass tension and stress factors. Finally, seismic loads are accounted for within Zone II parameters. Those material residences serve as foundational facts crucial for design and construction levels, ensuring structural integrity and protection requirements are met.

The geometrical facts for the tank consists of a peak of 3.5 meters and a staging top of 8 meters. The tank's base diameter measures 4.4 meters, matching the diameter of the field. Supported by four columns, the tank is constructed the use of M30 grade concrete and reinforced with FE415 grade steel. Each column has a length of 500 square millimetres, even as beams degree 350 through 250 millimetres. Plate thickness is about at 800 millimetres, with wall thickness at 450 millimetres. For added support, bracing is furnished through I.S.M.B. 100 individuals. These specs offer important facts for the layout and construction stages, ensuring structural integrity and adherence to safety standards throughout the challenge.

3 Proposed Methodology

Study results were evaluated in many steps in order to ensure comprehensiveness and accuracy. A literature review was conducted as the first step to gather pertinent data and insight from previous studies regarding the underlying case. To comprehend the context and background of the study, existing literature, studies, and reviews were reviewed. Based on the results of this investigation, upcoming research and investigation are needed to address limitations or gaps in current studies. Analytical software STAAD.pro was used to prepare a geometrical shape for the study. The word STAAD refers to Structural Analysis and Design. One well-known program for assessing and developing structures, including buildings, towers, highways, industrial use, modes of transport, and functionality structures, is called STAAD Pro. These models were used to create digital versions of the water tank, columns, beams, and other structural elements. The superior features and competencies of STAAD.pro were leveraged to ensure realistic and reliable results. In the third step, the model's structural

sections were given material properties. There were specifics that were provided in regard to the concrete, metals, and any other materials that were to be used in the construction, as well as their properties. STAAD.pro will be able to simulate and analyze the structural behavior of the model appropriately after accurately defining the material properties, such as power and elasticity.

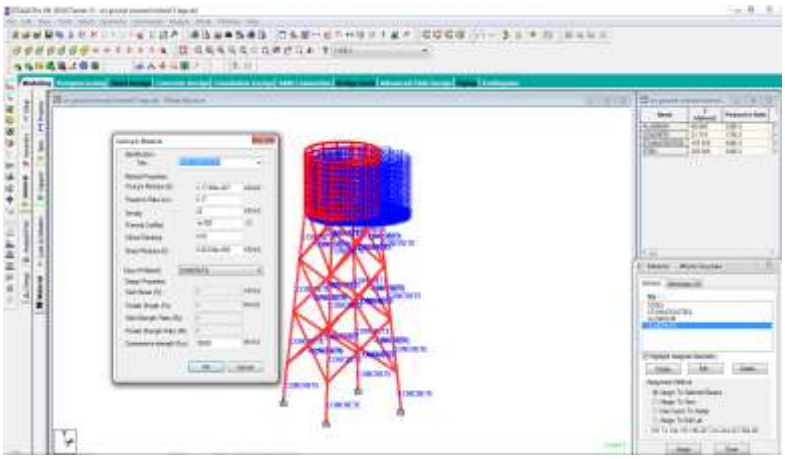

Fig. 2: Assigning Material Properties

As part of step 4, section properties were defined for the structural factors in the model, including geometric characteristics and mechanical characteristics. This step covered specifying the cross-sectional dimensions, including width, intensity, and thickness, of beams, columns, and other structural participants. Moreover, material properties such as modulus of elasticity, yield electricity, and remaining strength had been assigned to appropriately represent the behaviour of the materials underneath load. Through meticulously defining these phase homes, the structural response of the model to diverse loading situations will be accurately expected. This step performed a vital position in making sure the constancy and accuracy of the structural evaluation carried out the use of analytical software program like STAAD.pro.

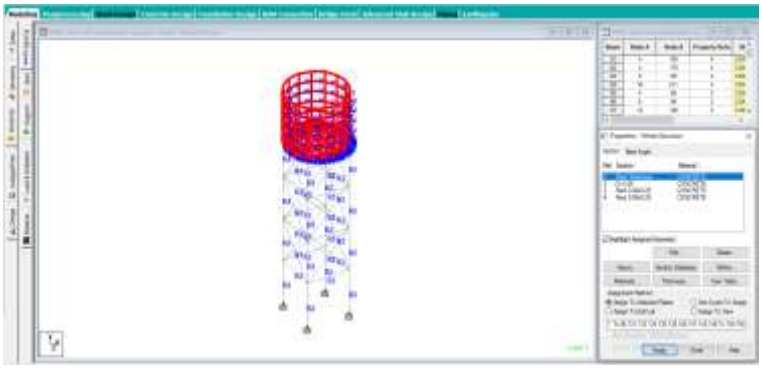

Fig. 3: Sectional Data

Step 5: in this step, weak springs were assigned at the base beams and cylindrical surface of the shape. Susceptible springs, additionally referred to as boundary springs, are virtual elements used to represent the relationship between the shape and its basis or assist machine. By means of assigning weak springs at strategic locations, which includes the bottom beams and cylindrical surface, the interaction between the structure and its surroundings could be

appropriately modeled. Those vulnerable springs mimic the flexibility and resilience of the foundation, allowing for a extra realistic simulation of the structural reaction to external loads, which include seismic forces. This step is crucial for capturing the dynamic behavior of the shape and ensuring that the analysis consequences replicate real-world situations appropriately**.**

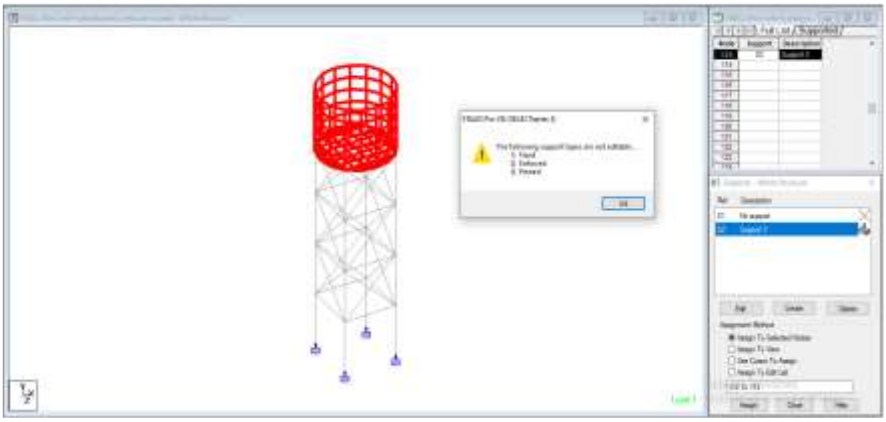

Fig. 4: Assigning Surface

Step 6: Assigning hydrostatic pressure in complete circumstance includes accounting for the strain exerted by way of water when the tank is at full capability. This step is important for as it should be simulating the structural reaction of the tank underneath hydrostatic loading conditions. By way of assigning hydrostatic pressure to the model, the distribution of forces appearing at the tank's walls and base may be appropriately represented. This consists of considering the weight of the water as well as any extra strain exerted because of the intensity of the water column.

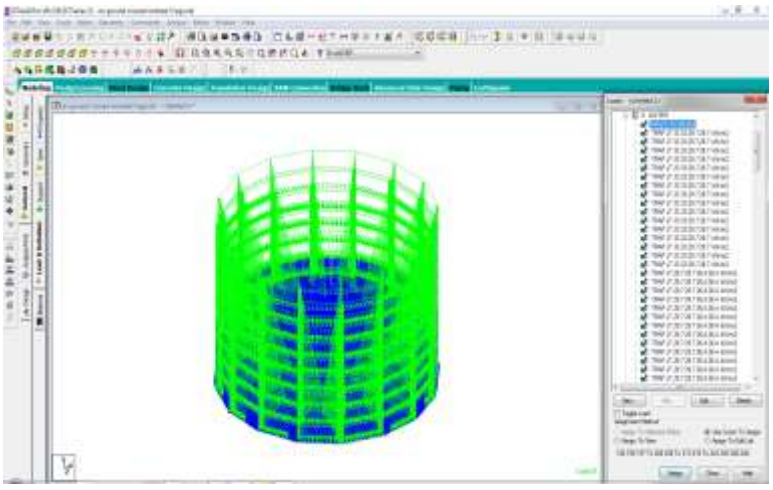

Fig. 5: Assigning Hydrostatic Load

Step 7: Assigning wind pressure as consistent with IS 875-III: 2015, with a wind velocity of 39 m/s, and seismic load as according to IS 1893-I: 2016, involves incorporating external environmental elements into the structural analysis. Wind pressure, according with the relevant code, is applied to the model to simulate the results of wind loading on the shape.

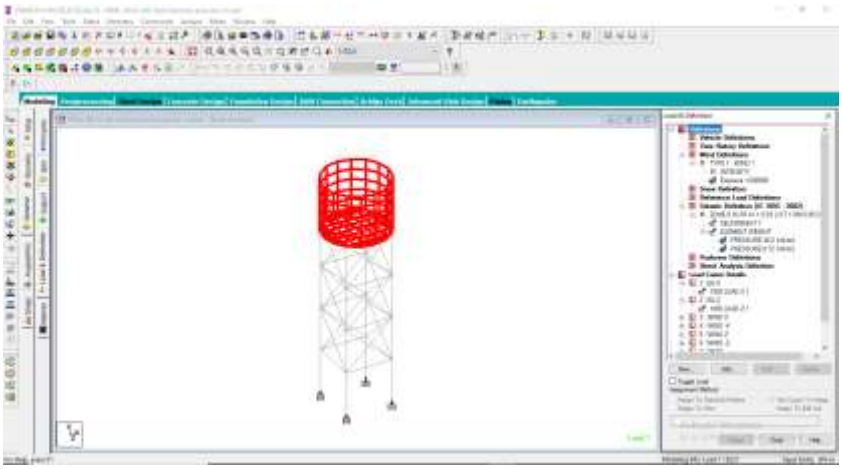

Fig. 6: Assigning Lateral Loads namely wind load and seismic load

Step 8: The Finite element method (FEM) analysis of the structure the use of the analytical application STAAD.pro includes accomplishing a comprehensive computational evaluation to assess the structural conduct and response below numerous loading situations. STAAD.pro utilizes superior numerical techniques to discredited the structure into finite elements, taking into consideration the accurate representation of complex geometries and material behaviours.

4 Results and Discussion

After conducting the FEM analysis the usage of STAAD.pro, the effects were evaluated and post-processed the usage of MS Excel. In this phase, the output records from STAAD.pro, consisting of stresses, displacements, and different structural responses, have been imported into Excel for similarly analysis and visualization.

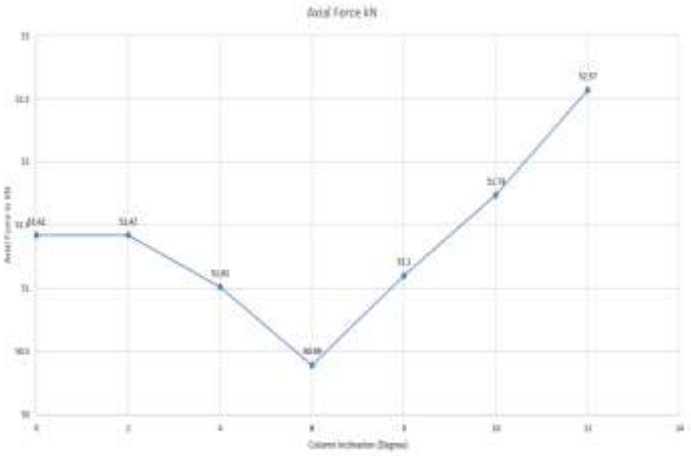

Fig. 7: Axial Force at Top Beam

Fig. 7 indicates the inner force exerted alongside the longitudinal axis of the beam at its uppermost segment. This force can be either compressive (pushing together) or tensile (pulling aside), relying on the loading and structural configuration. Evaluating the axial force

facilitates verify the beam's capability to resist vertical loads and contributes to determining its overall structural integrity and stability.

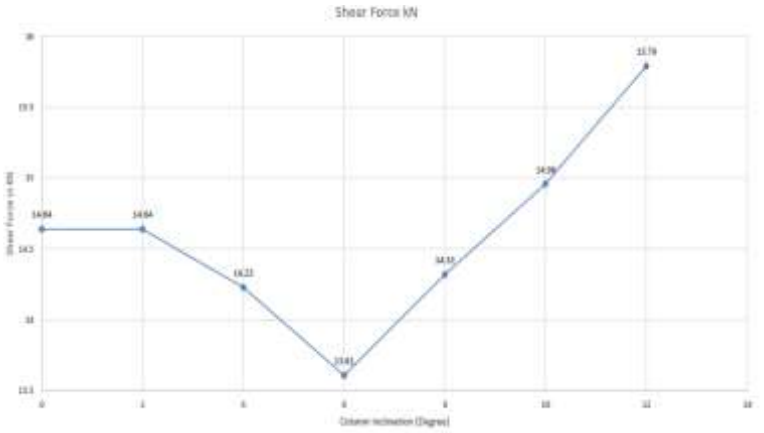

Fig. 8: Shear Force at Top Beam

Fig. 8 suggests the inner force performing parallel to the cross-sectional region of the beam at its uppermost part. This force represents the tendency of one part of the beam to slip or shear beyond another element. Evaluating the shear pressure facilitates determine the beam's resistance to lateral forces and contributes to determining its ordinary structural stability and performance.

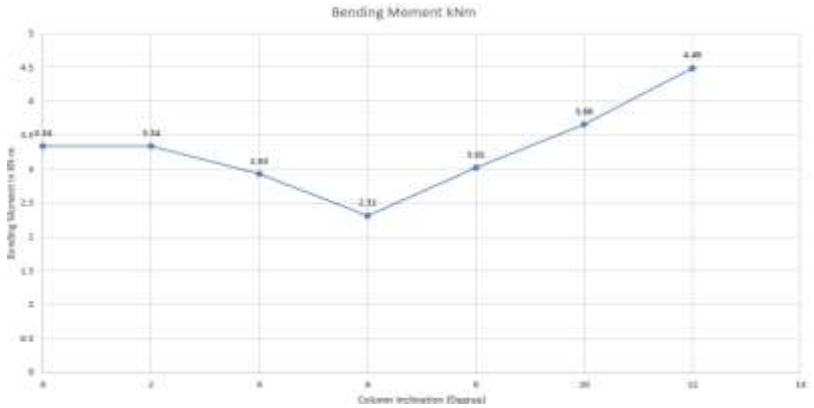

Fig. 9: Bending Moment at Top Beam

Fig. 9 shows the internal second or torque exerted at the beam at its uppermost section because of external loads. This moment induces curvature or bending inside the beam, inflicting it to deflect. Evaluating the bending moment facilitates assess the beam's capacity to resist bending and contributes to determining its usual structural energy and balance.

Fig. 10 shows the force exerted by means of a structural assist, such as a column or foundation, in response to the burden applied to the structure. This reaction pressure acts perpendicular to the help surface and is equal in value and opposite in path to the carried out load. Evaluating help reactions is crucial for studying the structural stability and ensuring that the aid machine can efficaciously bring and distribute the hundreds to the foundation or ground below.

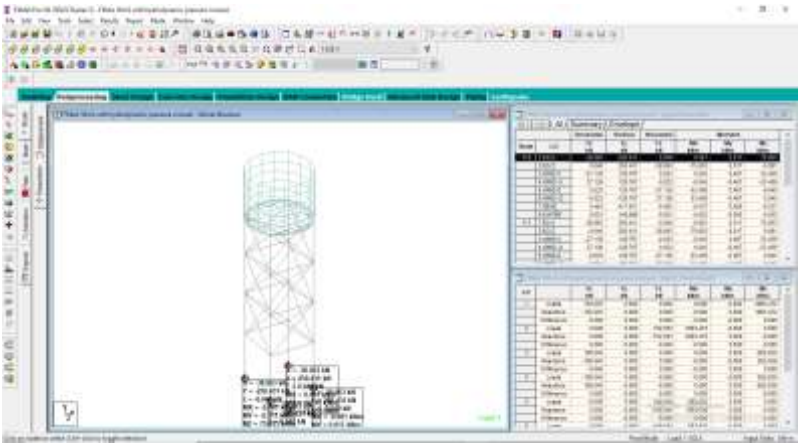

Fig. 10: Support Reaction

5 Conclusion

Concrete water tanks play a essential role in ensuring reliable water supply and storage. By using appropriate support structures and adhering to safety protocols, the risk of harm or leakage all through seismic occasions may be minimized. Numerous studies have explored unique elements of concrete water tank production, along with layout, fabric selection, and seismic overall performance evaluation. These research make contributions treasured insights to the continued efforts to beautify the safety, sturdiness, and efficiency of concrete water tanks. Further studies in this vicinity is important to address emerging challenges and improve the resilience of water garage infrastructure against natural dangers.

References

1. Mohammed, Hasan Jasim. "Economical design of water concrete tanks." European journal of scientific research 49, no. 4 (2011): 510-520.
2. MorVyankatesh, K., and T. More Varsha. "Comparative study on dynamic analysis of elevated water tank frame staging and concrete shaft supported." IOSR Journal of Mechanical and Civil Engineering (IOSR-JMCE) 14, no. 1 (2017): 38-46.
3. George, Raji Ruth, and Asha Joseph. "Dynamic analysis of elevated cement concrete water tank." Int J Innov Res SciTechnol 3 (2016).
4. Saeed, Muneer K., Muhammad K. Rahman, Mohammed H. Baluch, and Lutf A. Tooti. "Cracking in concrete water tank due to restrained shrinkage and heat of hydration: field investigations and 3D finite element simulation." Journal of Performance of Constructed Facilities 34, no. 1 (2020): 04019100.
5. Younis, Adel, Usama Ebead, PrannoySuraneni, and Antonio Nanni. "Cost effectiveness of reinforcement alternatives for a concrete water chlorination tank." Journal of Building Engineering 27 (2020): 100992.
6. Mohamed, Hamdy M., and BrahimBenmokrane. "Design and performance of reinforced concrete water chlorination tank totally reinforced with GFRP bars: Case study." Journal of Composites for Construction 18, no. 1 (2014): 05013001.
7. Kumar A., Sharma H., Gaur N., Nanthaamornphong A., "PAPR analysis in OTFS using the centre phase sequence matrix based PTS method," Results in Optics, vol. 15, 2024, doi: 10.1016/j.rio.2024.100664.

8. Ramaprabha J., Prema P., Gunasekar S., "HealthApex: Complete Healthcare Assistance With Consent Based Analytics," 2023 International Conference on System, Computation, Automation and Networking, ICSCAN 2023, , 2023, doi: 10.1109/ICSCAN58655.2023.10395884.
9. Roja Ramani D., Rachna P., Pavan G., Reddy R., Huzaifa M., "Agrobot: Agricultural Robot using IoT and Machine Learning (ML)," Proceedings - 2023 3rd International Conference on Smart Data Intelligence, ICSMDI 2023, , pp. 497-500, 2023, doi: 10.1109/ICSMDI57622.2023.00094.
10. Navya R., Bv S.K., Rawat A., Satheeshkumar S., "Cardiac Arrhythmia - Prediction and Classification using Support Vector Machine," 2023 International Conference on System, Computation, Automation and Networking, ICSCAN 2023, , 2023, doi: 10.1109/ICSCAN58655.2023.10394774.
11. Govindaraj M., Asha V., Saju B., Sagar M., Rahul, "Machine Learning Algorithms for Disease Prediction Analysis," Proceedings - 5th International Conference on Smart Systems and Inventive Technology, ICSSIT 2023, , pp. 879-888, 2023, doi: 10.1109/ICSSIT55814.2023.10060987.
12. Ramesh Babu, M., Mohana Roopa, Y., "Component-based self-adaptive middleware architecture for networked embedded systems," International Journal of Applied Engineering Research, vol. 12.0, no. 12, pp. 3029.0-3034.0, 2017.
13. De Poures M.V., Sudhir Chakravarthy K., Jabihulla Shariff M.D., Srinivasa Reddy Y., Siva Prasad V., Sreenivasa Rao K., Kaliyaperumal G., Venkatesh R., Kishore Kumar V., "Excellence of Nano SiC on Mechanical Behaviour of Low Density Polyethylene Hybrid Nanocomposite," Journal of The Institution of Engineers (India): Series D, , 2024, doi: 10.1007/s40033-024-00713-9.
14. Shivangi, Sah R.K., Shreeyam, Florance G., Nirmala M., "CNNCalc - An Implementation of a Handwritten Mathematical Equation Solver," Proceedings of the 7th International Conference on Intelligent Computing and Control Systems, ICICCS 2023, , pp. 638-645, 2023, doi: 10.1109/ICICCS56967.2023.10142278.
15. Yogitha, Rachana P., Milina M., Sabhahit N.G., Ainain M., "Breast Histopathology Image Classification: A Comparative Evaluation of SVM, Random Forest and CNN," 2023 3rd International Conference on Intelligent Technologies, CONIT 2023, , 2023, doi: 10.1109/CONIT59222.2023.10205567.
16. Bandi, G.N.S., Rao, T.S., Ali, S.S., "Data Analytics Applications for Human Resource Management," 2021 International Conference on Computer Communication and Informatics, ICCCI 2021, , 2021, doi: 10.1109/ICCCI50826.2021.9402300.
17. Rajendra Prasad, K., Mohammed, M., Narasimha Prasad, L.V., Anguraj, D.K., "An efficient sampling-based visualization technique for big data clustering with crisp partitions," Distributed and Parallel Databases, vol. 39.0, no. 3, pp. 813.0-832.0, 2021, doi: 10.1007/s10619-021-07324-3.
18. Deepak, D., Cornelio, J.A.Q., Midhun Abraham, M., Shiva Prasad, U., "Numerical analysis of the effect of nozzle geometry on flow parameters in abrasive water jet machines," Pertanika Journal of Science and Technology, vol. 25.0, no. 2, pp. 497.0-506.0, 2017.
19. Anitha A., Vinoth Kumar K., Bedant A., Madhav Reddy C., Abhisek K., "Non-Invasive Method of Detecting Anemia using AI & IoT," International Conference on Innovative Data Communication Technologies and Application, ICIDCA 2023 - Proceedings, , pp. 805-808, 2023, doi: 10.1109/ICIDCA56705.2023.10099915.
20. Srikrishnan, S., Dash, P.K., "2d cfd analysis of deflagration to detonation transition in closed pipe using different blockage," International Journal of Mechanical Engineering and Technology, vol. 8.0, no. 6, pp. 447.0-454.0, 2017.

21. Chaturvedi R., Darokar H., Patil P.P., Kumar M., Sangeeta K., Aravinda K., Kadhim A.A., "Maximizing towards the Sustainability: Integrating Materials, Energy, and Resource Efficiency in revolutionizing Manufacturing Industry," E3S Web of Conferences, vol. 453, 2023, doi: 10.1051/e3sconf/202345301036.
22. Manjunatha B., Kumar K.D., Goundar S., Kavin B.P., Seng G.H., "Sustainable waste management OOA-Enhanced MobileNetV2-TC model for trash image classification," Computational Intelligence for Green Cloud Computing and Digital Waste Management, , pp. 227-247, 2024, doi: 10.4018/979-8-3693-1552-1.ch012.
23. Sonia P., Srinivas R., Kansal L., Abdul-Zahra D.S., Reddy U., Kumari V., "Bioinspired Composites a Review: Lessons from Nature for Materials Design and Performance," E3S Web of Conferences, vol. 505, 2024, doi: 10.1051/e3sconf/202450501024.
24. Reddy, V.A., Solanki, C.H., Kumar, S., Reddy, K.R., Du, Y.-J., "Comparison of limestone calcined clay cement and ordinary Portland cement for stabilization/solidification of Pb-Zn smelter residue," Environmental Science and Pollution Research, vol. 29.0, no. 8, pp. 11393.0-11404.0, 2022, doi: 10.1007/s11356-021-16421-w.
25. Gantala, A., Vijaykumar, G., Telagam, N., Anjaneyulu, P., Phaniram, B., "Design of smart sensor using Linux-2.6.29 kernel," International Journal of Applied Engineering Research, vol. 12.0, no. 18, pp. 7891.0-7896.0, 2017.
26. Ganesan S., Dhanalakshmi, Asuti M., Kapadnis A.V., Saloni Belliappa B., "Augmented Reality as a Visual Aid for Classrooms: Supplemented by a Case Study," 14th International Conference on Advances in Computing, Control, and Telecommunication Technologies, ACT 2023, vol. 2023-June, pp. 1625-1635, 2023.
27. TaufiqRochman, Suhariyanto. "State of the art of tank structural evaluation review: A case study of an elevated concrete water tank concerning crack initiation." Journal of Southwest Jiaotong University 56, no. 5 (2021).
28. Algreane, G. A., SitiAminah Osman, O. Karim, and AnuarKasa. "Behavior of elevated concrete water tank subjected to artificial ground motion." EJGE 16 (2011): 387-406.
29. Moita, Gray F., Estevam B. de Las Casas, Edgar V. Mantilla Carrasco, and Sávio N. Bonifácio. "Experimental and numerical analysis of large ferrocement water tanks." Cement and Concrete Composites 25, no. 2 (2003): 243-251.
30. Azizan, M. A., N. Z. Noriman, N. Ishak, and H. Desa. "Application of Hybrid Fibre Concrete As Advanced Material For Concrete Water Tank Construction." In IOP Conference Series: Earth and Environmental Science, vol. 920, no. 1, p. 012012. IOP Publishing, 2021.
31. Ghateh, R., M. R. Kianoush, and W. Pogorzelski. "Seismic response factors of reinforced concrete pedestal in elevated water tanks." Engineering Structures 87 (2015): 32-46.
32. Ahmad, Muhammad Jamil, Qaiseruz Zaman Khan, and Syed Muhammad Ali. "Use of water tank as tuned liquid damper (TLD) for reinforced concrete (RC) structures." Arabian Journal for Science and Engineering 41 (2016): 4953-4965.
33. Sameer, Riyaz, A. R. Mundhada, and SnehalMetkar. "Comparison of RCC and prestressed concrete circular water tanks." Int. J. Emerging Technol. Advan. Eng 2, no. 12 (2012): 394-397.
34. Ghateh, Razmyar, Reza Kianoush, and Wes Pogorzelski. "Response modification factor of elevated water tanks with reinforced concrete pedestal." Structure and Infrastructure Engineering 12, no. 8 (2016): 936-948.
35. Dyba, Marcin, and Lukasz Slaga. "Technical Condition Assessment, Ultimate and Serviceability Limit States of the Water Tower Reinforced Concrete Tank after its Operation Lifetime." In IOP Conference Series: Materials Science and Engineering, vol. 471, no. 5, p. 052084. IOP Publishing, 2019.

Journal of Physics: Conference Series

PURPOSE-LED PUBLISHING™

PAPER • **OPEN ACCESS**

Numerical investigations of the buckling behaviour of an integrated stiffened panel

To cite this article: E. S. Elumalai *et al* 2024 *J. Phys.: Conf. Ser.* **2837** 012063

View the article online for updates and enhancements.

You may also like

- Influence of loading type and rectangular opening on the behaviour of GFRP stiffened panels
S. Anitha Priya Dharshani, A. Meher Prasad and R. Sundaravadivelu
- Effect of low velocity impact on residual compressive strength of stiffened panel with welding residual stress
Hui Liu, Zhenkun Lei, Zhenfei Guo et al.
- Ultimate strength of typical stiffened panels in container ships with comparison of hull girder bending analysis
Jinju Cui and Deyu Wang

This content was downloaded from IP address 106.0.37.90 on 21/10/2024 at 11:18

Journal of Physics: Conference Series **2837** (2024) 012063 doi:10.1088/1742-6596/2837/1/012063

Numerical investigations of the buckling behaviour of an integrated stiffened panel

E. S. Elumalai[1], R. Asokan[1], C. M. Thejus[1], N. Uday Ranjan Goud[2], Seralathan Sivamani[1] *

[1]Department of Aeronautical Engineering, Hindustan Institute of Technology and Science, Chennai 603 103, Tamil Nadu, India.
[2]Department of Aeronautical Engineering, MLR Institute of Technology, Hyderabad, Telangana, India.

* Corresponding Author: siva.seralathan@gmail.com

Abstract. Stiffened panels are used to reduce the displacement by loading. This study deals with the numerical simulation of stiffened panels in which the stiffeners are integrated to the panel. The panel is subjected to compressive load along the stiffener axis. This induces buckling stress in the structure. In this study, a Tee shaped stiffener is used for analysis. The focus of the study is to investigate the deformation as well as structural integrity of an integrated stiffened panel by performing buckling analysis and all the comparisons are made with conventional stiffened panel using ANSYS software. The simulation reveals that the integrated stiffened panel gives an improved performance than the conventional design. The integrated stiffened panel shows around 1.2% higher strain rate, stress capacity higher by nearly 4.864% and around 20.25% deformation resistance variation compared to the conventional panel. Therefore, the integrated stiffened panel is found to be an acceptable alternative to the conventional stiffened panel design.

1. Introduction

Thin structures are predominantly used elements in the aircraft industry, and they are used for skin sections. These sections are mostly subjected to traction at the edges. This results in buckling. To improve the buckling strength of the elements, stiffener is used with the plate section as stiffened panels. In general, for an aircraft, weight is always a crucial factor. Integrated stiffened structures are effective as they are high strength construction and light in weight. With advancement in manufacturing processes, renewed interest is created among researchers as well as manufacturers in integrating metallic structures for aircraft applications. With the advancements in the manufacturing processes, the proposed integrated stiffened panel can be manufactured by additive manufacturing. A precise computer aided design and drawings of the stiffened integrated panel is created using CATIA and through digital twin technologies, the integrated stiffened panel can be produced with the chosen material. CAD models are sliced and converted into a layer-by-layer code (G Code) which can be read by the 3D printer which produces the integrated stiffened panel structure of the chosen additive manufacturing techniques.

Quinn *et al.* [1] has experimentally demonstrated on the integrally machined stiffener panels to increase its structural efficiency. An increase in the buckling of the panel with the sub-stiffening was

Content from this work may be used under the terms of the Creative Commons Attribution 4.0 licence. Any further distribution of this work must maintain attribution to the author(s) and the title of the work, journal citation and DOI.
Published under licence by IOP Publishing Ltd

observed in comparison with the conventional panel of equivalent mass. Brot *et al.* [2] performed crack growth testing both analytically and experimentally for the integrally stiffened metallic structures. Wilckens *et al.* [3] used the IBUCK model for analyzing the buckling as well as post-buckling behavior of the stiffened panel. To approximate the deformation patterns during post-buckling as well as buckling, trigonometric functions were utilized for both local and global buckling, based on the stringers. The analysis commenced with a linear buckling eigen value analysis, where various buckling eigen modes were calculated. A combination of these modes was chosen as an imperfection to introduce initial geometric imperfections into the structure. Quinn *et al*. [4] studied with the objective of understanding how different constraints affected the weight and performance of the panels. Designing and optimizing aerospace structures was a complex task due to the intricate nature of the structural configurations and the wide range of possible loading and boundary conditions. To address this complexity, Marc Fischer *et al.* [5] and Fischer *et al.* [6] proposed a multilevel optimization approach. The study and design of aircraft structures was done using the VICONOPT panel design code, particularly stiffened wing panels along the longitudinal axis, offering a fast and efficient tool. Kevin S. Van Dooren and Chiara Bisagni [7] focused on the investigation of welded multi-stringer panels and their behavior in terms of buckling and skin-stringer separation and to observe and compare with that of the fuselage section. Jeff W.H. Yap *et al.* [8] created a FEM tool to quickly as well as reliably assess the effects of flaws and damage in composite structures on multi-rib, curved, T-stiffened composite panels that were frequently utilized in aerospace primary components. The skin-to-stiffener debonding defect, which was frequently present and considerably reduced the composite structures performance with integral or secondary bonded stiffeners, was the focus of the damage evaluation.

Dan Wang and Mostafa M. Abdalla [9] focused on grid-stiffened composite structures and investigated both local as well as global buckling phenomena in isogrid-stiffened as well as orthogrid-stiffened composite panels. These structures offered weight advantages over the conventional stiffened constructions and sandwich shells while also exhibiting superior damage tolerance properties. Broderick H. Coburn *et al*. [10] proposed a unique blade stiffened buckling analysis with Variable Angle Tow (VAT) panel to take advantage of the potential for improved buckling performance compared to traditional straight fiber laminates. A generalized Rayleigh-Ritz process was devised as an analytical technique to examine the pre-buckling and buckling behavior of a typical piece of the blade reinforced VAT panel. Eyassu Wodesenbet *et al*. [11] analyzed the buckling behavior of an iso-grid stiffened composite cylinders using an improved smearing approach. By examining the moment as well as force impacts of the stiffeners on unit cell, the model considered the stiffness contributions of the stiffeners into account. Combining the stiffness contributions of the shell yields and the stiffeners, the equivalent stiffness of the stiffener/shell panel was found. Shahriar Setoodeh *et al.* [12] suggested generalized a reciprocal approximation approach for laminated composite panels with variable stiffness to attain the highest buckling load. The inverse of the stiffness tensor was used to increase the buckling load. Due to its separability for discrete panels, this approximation had the benefit of enabling independent maximizing at each discrete node. This characteristic made the algorithm suitable for parallel processing.

Degenhardt *et al.* [13] investigated on the POSICOSS and COCOMAT project which focused to reduce the costs in the European aircraft industry by accurately simulating post-buckling behavior and exploiting the weight-saving potential in primary fiber composite fuselage structure. These projects resulted in improved analysis tools which were validated through extensive experiments. The design process involved simulation tools, and the research focused on DLR's understanding in designing as well as analyzing stringer stiffened CFRP panels. Mohsen Nasihatgozar *et al.* [14] focused on examining the buckling behavior of piezoelectric cylindrical composite panels reinforced with carbon nanotubes under axial loads. In order to construct correlations between stress and displacement that covered both mechanical and magnetic variables, the classic laminated plate theory (CLPT) was used. Taking into account on the existence of carbon nanotubes, the ‘Mori-Tanaka’ method was chosen to calculate the stress-strain equations for these panels. The findings showed that volume fraction

increments of nanotubes caused the buckling load to rise. Fiber orientation variations were proposed by Gurdal *et al.* [15] for flat rectangular composite laminates with varying stiffness properties. The author analyzed the in-plane and buckling responses, demonstrating the advantages of stiffness variation in different directions. The results indicated improvements in buckling load due to favorable stress distributions. The idea of variable stiffness gave the designers the flexibility in maximizing panel performance by allowing trade-offs between buckling load and overall stiffness.

On the basis of continuum damage mechanics, Faggiani and Falzon [16] simulated an intra-laminar damage model for carbon fiber composite structures. The model was built in a finite element program together with interface elements, and it was used to understand the reaction of a stiffened composite panels to a low velocity impacts. The numerical results demonstrated an excellent agreement with experimental data, including the energy absorbed, impactor force, and damage detection. The model accurately captured the interlaminar damage mechanisms, delamination, and post-impact permanent indentation. Falzon *et al.* [17] studied a unique failure mechanism involving mid-plane delamination at the free edge of the post-buckled stiffener web by experimentally examining the post buckling behavior of a panel with blade-stiffeners incorporating tapered flanges. Nagendra *et al.* [18] addressed the challenges of designing composite structures against buckling. The study highlighted the discrete nature of the laminate stacking sequence design and the need to find multiple local optima. Genetic algorithms were applied and modifications to the algorithm were proposed to enhance computational efficiency and reliability, thereby presenting improved designs for stiffened composite panel. Robert Vitali *et al.* [19] investigated the design study for optimizing the upper cover panel of a blended wing body transport aero plane. The optimization process utilizing response surfaces led to significant weight reduction compared to uniform cross-section design.

The literature studies reveal that the analysis of components for buckling is a predominant one for structural applications. But it is understood that the use of conventional stiffeners attached using fasteners, causes a major drawback in the design with respect to stress distribution. With the advancements in manufacturing processes like additive manufacturing, using integrated stiffened panel will be advantageous in terms of cost as well meeting the desired design requirements. As a result, the present numerical investigation is carried out with the objective to perform buckling analysis on an integrated stiffened panel made of aluminum alloy and compare the outcomes with those of the traditional stiffened panels.

2. Methodology

The modelling of the geometries of both conventional and integrated stiffened panels is done using ANSYS software. In this study, a Tee shaped stiffener is used for analysis. The geometry of both conventional and integral models is given in Figures 1 and 2 respectively. The dimensional details of both stiffened types of panel designs are given in Table 1. Figure 3 and Figure 4 show the cross-sectional view of the conventional and integral panels respectively. Quad meshing is chosen, and the meshing details are listed in Table 2. The models are meshed with 10mm sized elements. The meshed domains of both conventional and integrated stiffened panels are given in Figures 5 and 6 respectively to carry out the finite element analysis (FEA). Using ANSYS Workbench software, the FEA is carried out, and the buckling behavior is examined for both conventional and integrated stiffened panels.

Table 1. Dimensional details

Panel thickness	2.20mm
Panel length	440mm
Panel breadth	590mm
Stiffener thickness	2.80mm
Stiffener length	28mm
Stiffener breadth	590mm
Width between stiffeners	167mm

Table 2. Meshing details

Content	Conventional	Integrated
Element size	10mm	10mm
Elements	3658	3658
Nodes	11931	11931

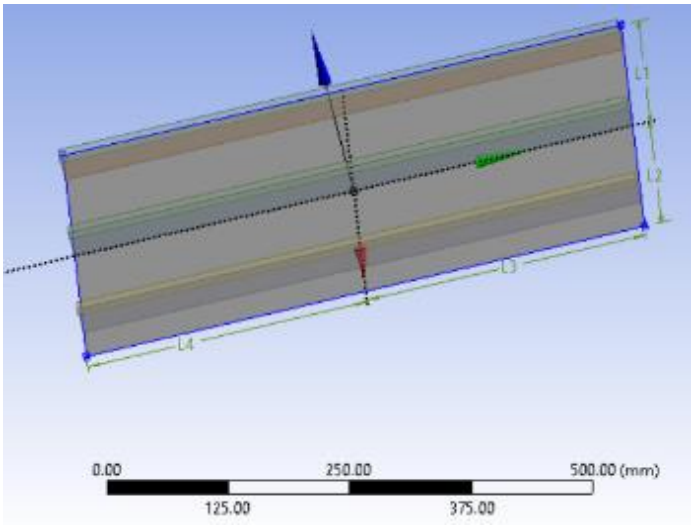

Figure 1. Geometry of conventional stiffened panel

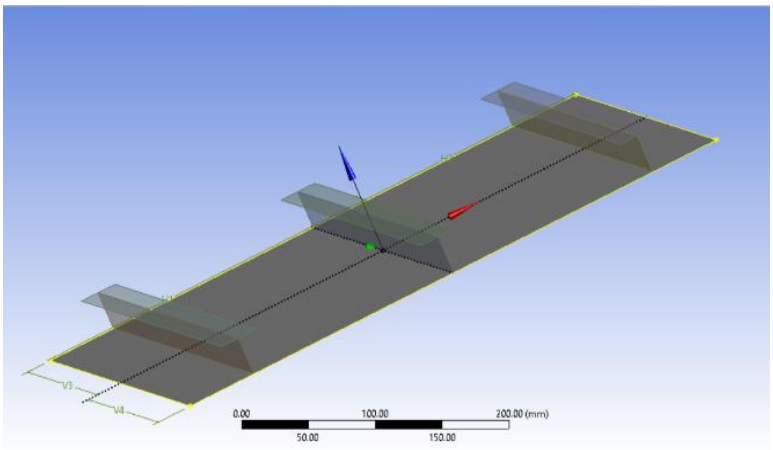

Figure 2. Geometry of integrated stiffened panel

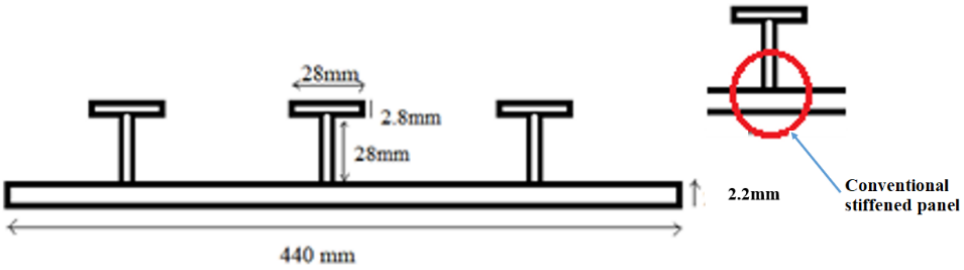

Figure 3. Structure of conventional stiffened panel

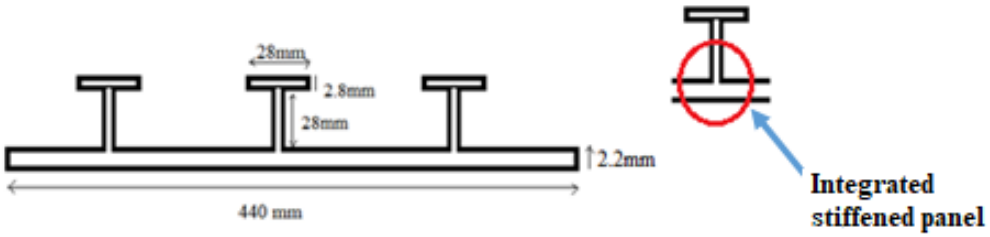

Figure 4. Structure of integrated stiffened panel

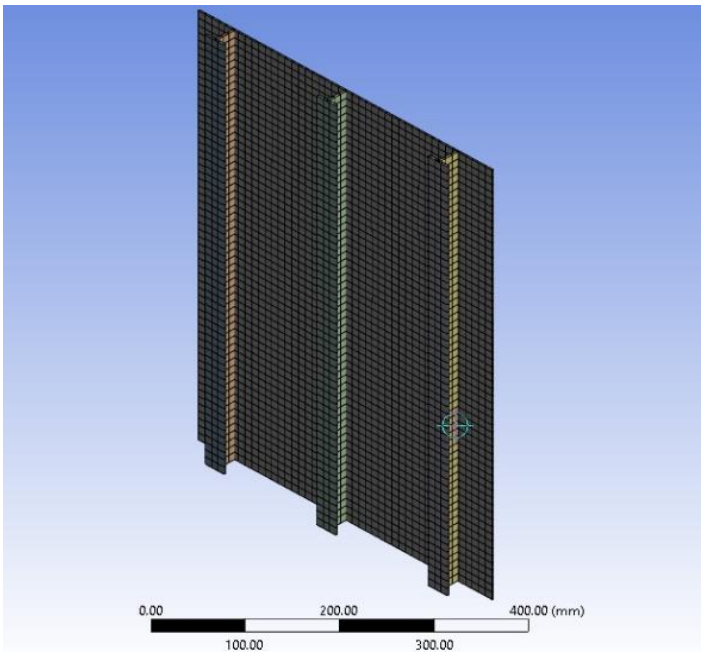

Figure 5. Meshed domain of conventional stiffened panel

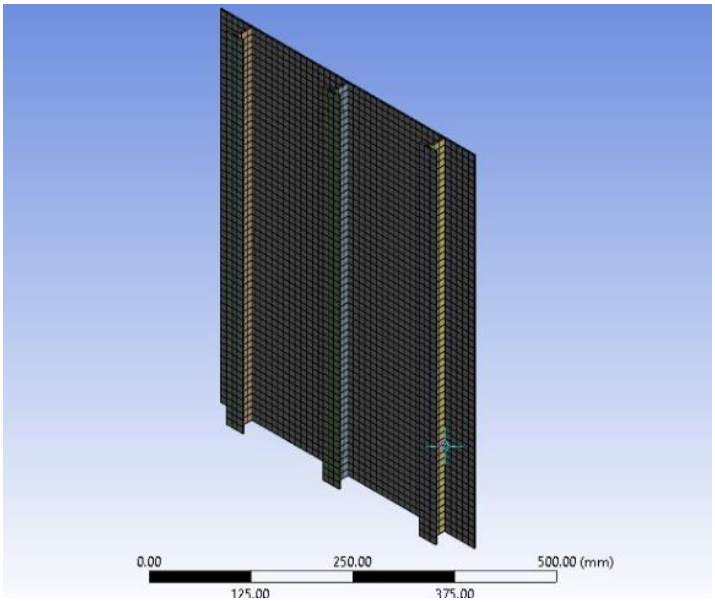

Figure 6. Meshed domain of integral stiffened panel

Table 3. Material properties of the panel

Description	Value
Young's modulus (MPa)	73700MPa
Density (kg/m^3)	2780Kg/m^3
Yield strength (MPa)	324
Ultimate strength (MPa)	471
Poisons ratio	0.33

The compressive load is applied to the stiffened panels using ANSYS Workbench to simulate the effect of buckling behavior. In both cases, the stiffener and one edge of the panel are fixed, and the other end is susceptible to compressive loading. The opposite sides of the panels are modeled and presumed to be as simply supported. Loads are applied to the free end to determine the deformation that occurred in the stiffened panels. Eigen-Buckling analysis is used to evaluate the buckling resistance of different stiffened panel designs, and the results are compared to identify the best one. The reliability and accuracy of the simulation results are ensured by specifying precise material properties and finite element modeling. Table 3 lists the material properties specified for the panels.

The governing equation for buckling of the panel is given as

$$\sigma_{cr} = \frac{k\pi^2 E}{12(1-\mu^2)} \left(\frac{t}{d}\right)^2 \qquad \text{---- (1)}$$

where σ_{cr} is the buckling stress of panel, k is co-efficient depending on the degree edge support, 'a' is the panel length in mm, 'b' is the width between stiffeners in mm, 'E' is the Young's modulus in MPa, μ is Poisson's ratio, 't' is thickness of the panel, 'w' is the effective width of panel.

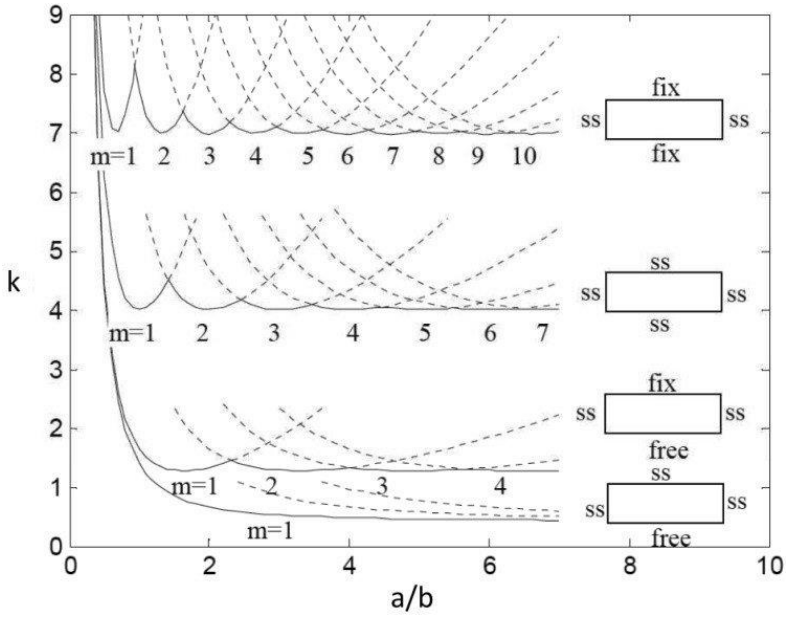

Figure 7. Buckling co-efficient versus aspect ratio [20]

Assuming all the edges are simply supported for the conventional stiffened panel, as observed from Figure 7, for a/b = 440/167 = 2.6, the value of 'k' is 4. Similarly, assuming two edges as fixed, and two edges simply supported for integral stiffened panel, from Figure 7, for a/b = 440/167 = 2.6, the value of 'k' is 7.

The effective width is estimated using equation (2) as given below,

$$w = \pi t \sqrt{\frac{kE}{12(1-\mu^2)\sigma_{cy}}} \qquad \text{---- (2)}$$

The effective width for both the conventional and integral stiffened panels is found to be 68mm. Using equation (1), the buckling stress for both conventional and integral stiffened panels is found to be $(\sigma_{cr})_{con} = 76.48\ MPa$ and $(\sigma_{cr})_{int} = 82.55\ MPa$ respectively. As the analytical findings of the buckling stress for both conventional and integral stiffened panels are closer, the viability of the proposed integrated stiffened panel design can be studied in detail by simulation.

3. Results and discussion

The comparative curves for the equivalent strain, equivalent stress, and total deformation for the conventional and integrated stiffened panels are shown in Figures 8 to 16. The strain contour for conventional and integrated stiffened panels is shown in Figure 8 and Figure 9 respectively. The maximum strain taken by integrated stiffened panel is 0.012452 mm/mm, whereas the maximum equivalent strain taken by the conventional stiffened panel is 0.012301 mm/mm.

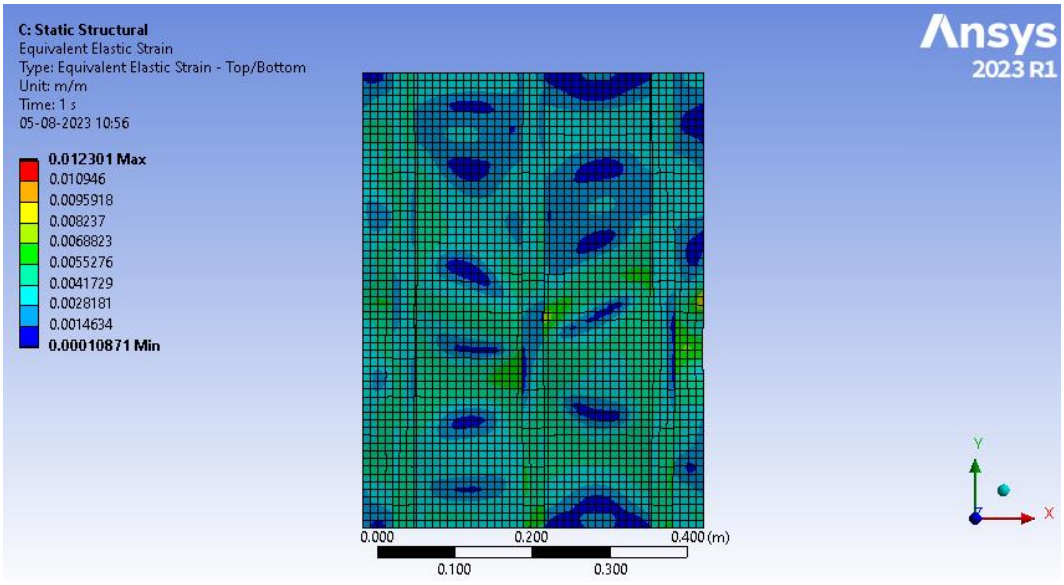

Figure 8. Strain contour for conventional stiffened panel

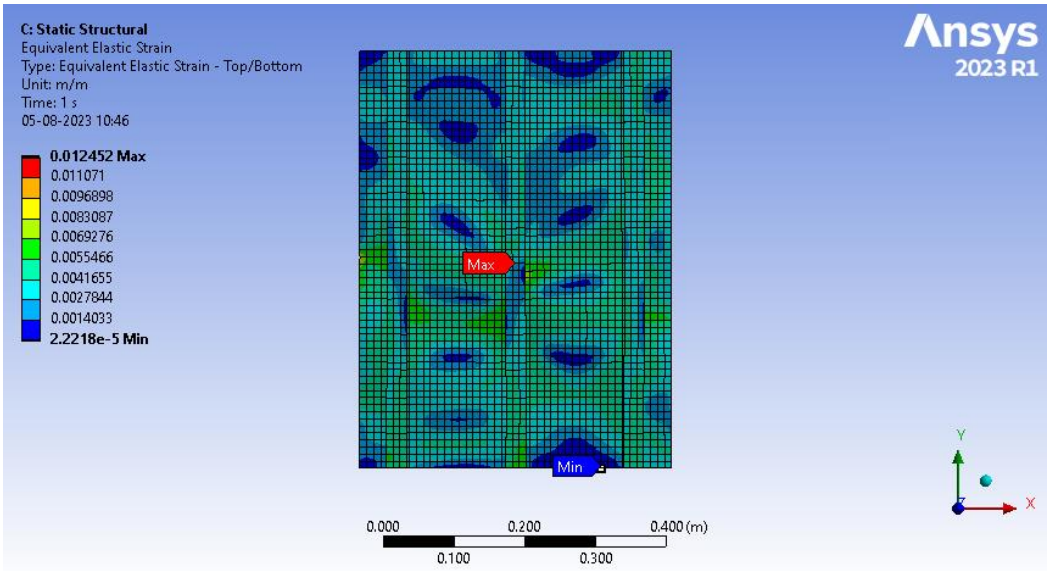

Figure 9. Strain contour for integrated stiffened panel

Figure 10 shows the equivalent strain with respect to time. As can be observed in the Figure 10, the maximum strain taken by integrated stiffened panel is 0.012452 mm/mm, whereas the maximum equivalent strain taken by the conventional stiffened panel is 0.012301 mm/mm. This clearly shows that the integrated stiffened panel has more fatigue life. Moreover, the strain capacity of the integrated panel is around 1.20% more in comparison with the conventional panel. Therefore, this is evident of the improved performance of the integrated stiffened panel with respect to conventional stiffened panel. The load of 10kN is acting on both the stiffened panels to observe the maximum stress acting on it.

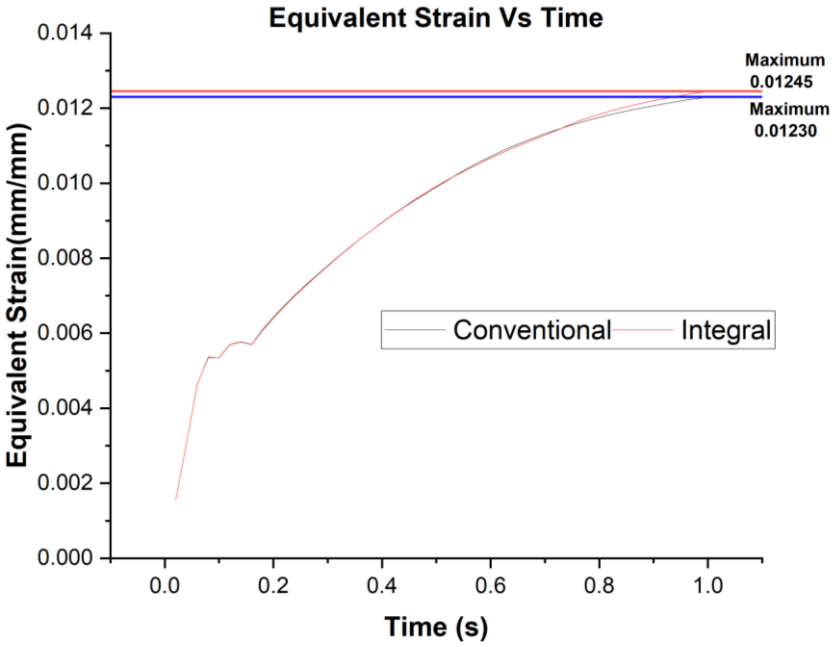

Figure 10: Equivalent strain versus time

The observed 1.2% higher strain rate in the integrated stiffened panel compared to the conventional design carries significant implications for structural performance and design considerations. The 1.2% higher strain rate suggests that the integrated stiffened panel experiences slightly more deformation under a given load or stress compared to the conventional design. This difference may seem small but can have notable effects on structural behaviour. Higher strain rates can influence the strength and durability of a structure. The increased strain rate indicates differences in stiffness or deformation characteristics between the integrated stiffened panel and the conventional design. The design aims to optimize weight, stiffness, and manufacturing efficiency by combining stiffeners and panels into a unified structure. The higher strain rate is the result of this integration, affecting how forces distribute and deform across the structure. The interaction between stiffeners and panels plays a crucial role in structural behaviour. Integrated designs improves load transfer between stiffeners and panels, enhancing overall stiffness, and reducing the stress concentrations.

Figures 11 and 12 shows the stress contour contour for conventional and integrated stiffened panels respectively. As can be seen in the Figure, the maximum stress observed for the conventional stiffened panel is 80.1MPa and by integrated stiffened panel, it is 84MPa. The contours shows that the stress distribution on both the panels are uniform yet there is considerable improvement in the integrated panel by 4.8% in case of induced stress.

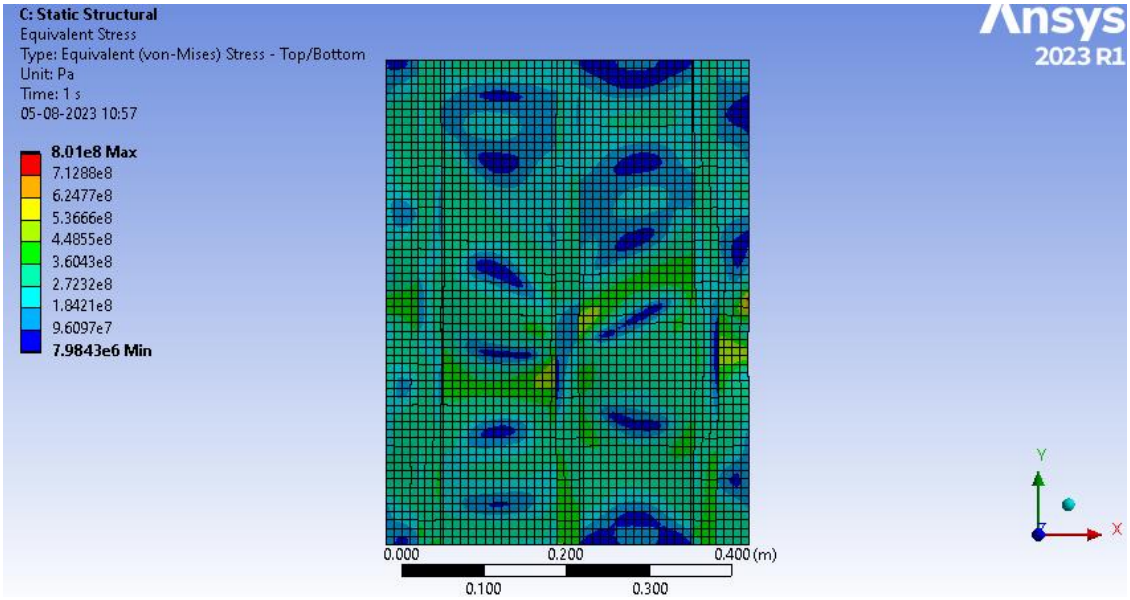

Figure 11. Stress contours for conventional stiffened panel

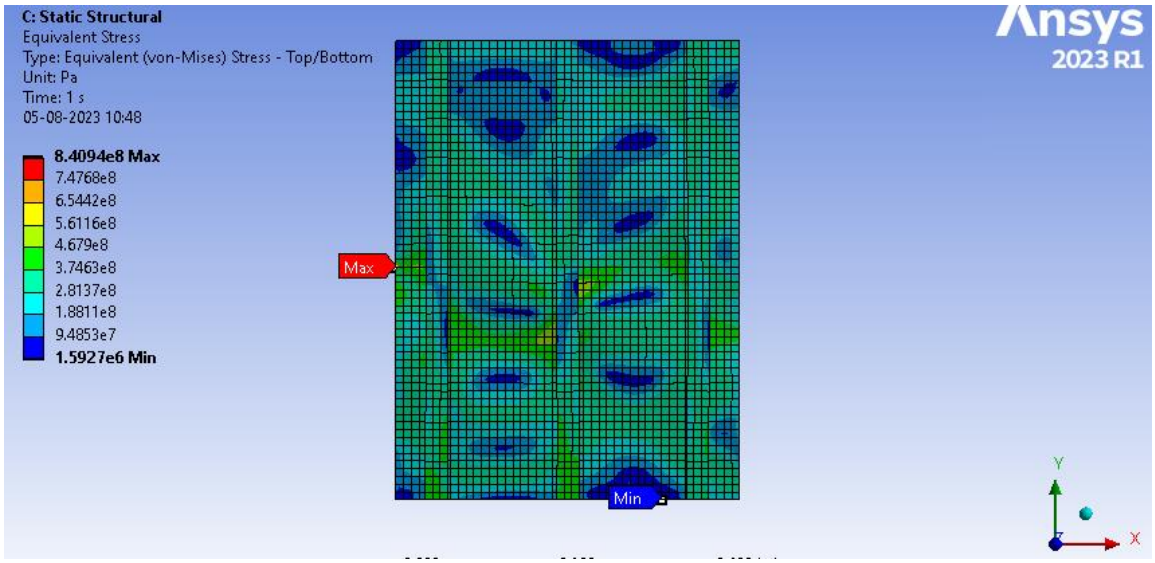

Figure 12. Stress contours for integrated stiffened panel

Figure 13 shows the variations of equivalent stress with respect to time. As can be observed in Figure 13, the maximum equivalent stress taken by integrated stiffened panel is 8.4094e8 Pa, whereas the maximum equivalent stress taken by the conventional stiffened panel is 8.01e8 Pa. This is evident that the integrated stiffened panel has more fatigue life. Moreover, the stress capacity of the integrated stiffened panel is around 4.864% more compared to conventional stiffened panel. The increase in stress bearing capacity of the integrated panel is not much to the expected outcomes but the design moderation in the panel insists it as a valid substitution for existing conventional design.

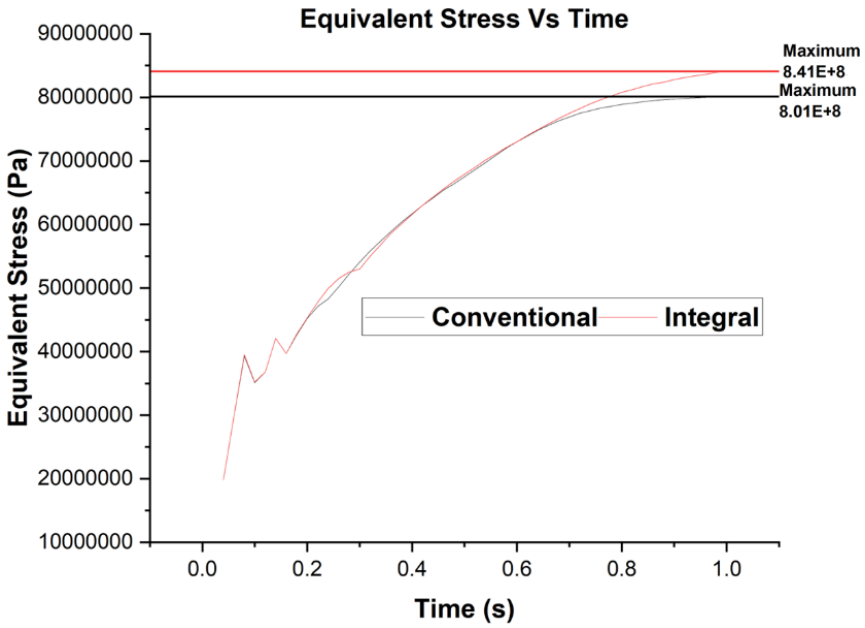

Figure 13: Equivalent stress versus time

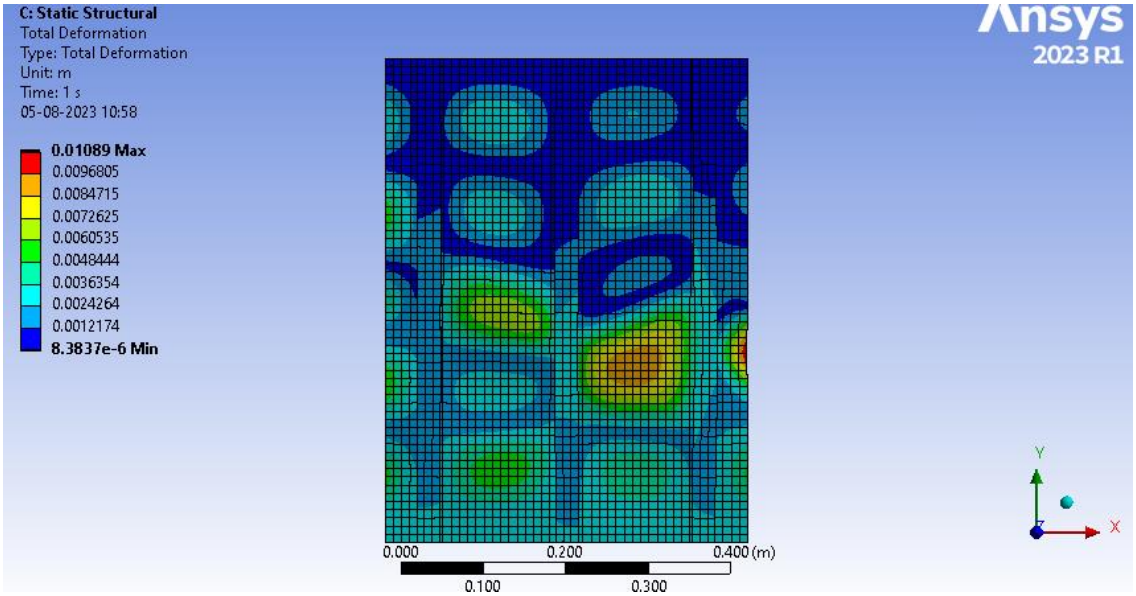

Figure 14. Total deformation contours for conventional stiffened panel

The distribution of total deformation of integrated and conventional stiffened panels is shown in Figures 14 and 15 respectively after the application of a 10kN load. The maximum deformation observed for the conventional stiffened panel is 10.8mm and for the integrated panel, it is 8.88mm. The integrated stiffened panels show considerable improvement in reduced the deformation. The contour shows drastic improvement in deformation of integrated panel compared to the conventional design. The integrated structures has high resistance to displacement.

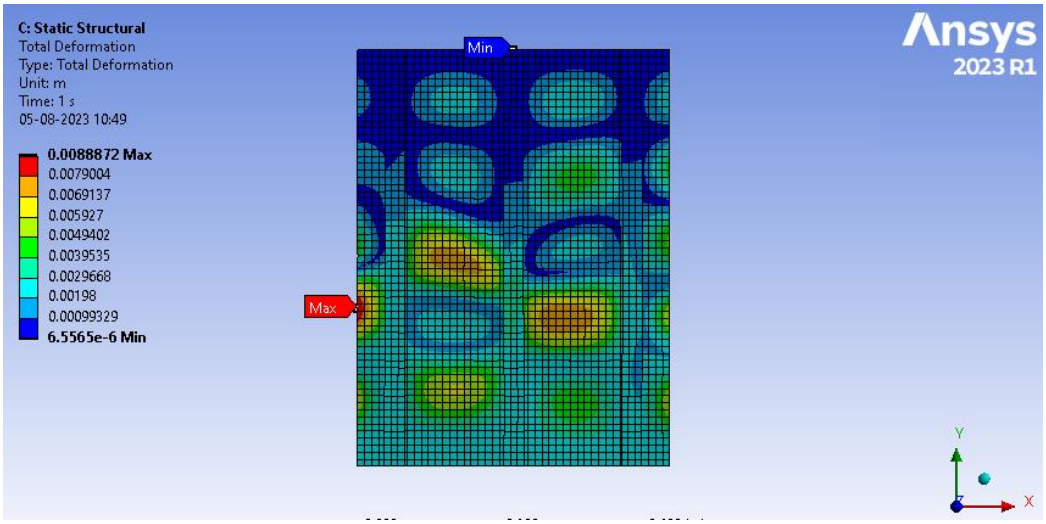

Figure 15. Total deformation contours for integrated stiffened panel

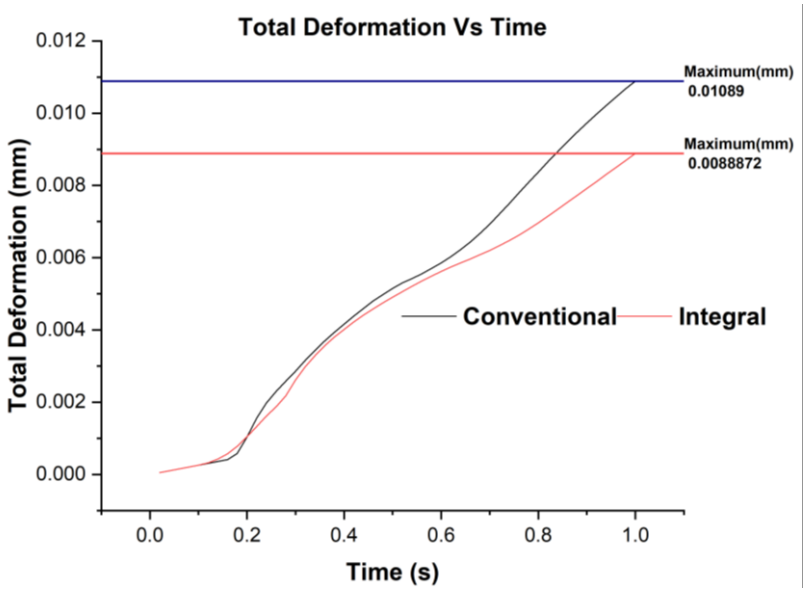

Figure 16. Total deformation versus time

Figure 16 illustrates the total deformation with respect to time. As can be observed in Figure 16, the maximum deformation observed in the integrated stiffened panel is 0.0088872mm, whereas the maximum deformation observed in the conventional stiffened panel is 0.01089mm. This is evident that integrated stiffened panel has more deformation resistance. Moreover, the deformation in conventional stiffened panel is 20.25% more in comparison with the integrated panel.

The limitations encountered in this numerical investigations are geometric complexity and modelling simplifications. These limitations may have affected the accuracy and comprehensiveness of the findings. Therefore, these limitations requires attention which would be considered in further studies so as to enhance the accuracy and reliability of the results.

4. Validation

With the finite element analysis carried out using simulation software ANSYS workbench, the data from this analysis is compared with the results based on theoretical analysis. Table 4 presents the comparison of results based on FEA analysis by simulation and theoretical analysis. Information on

the deviations observed in the analysis results. The buckling strength values of both theoretical and simulation results are compared for the conventional stiffened panel design, and it is observed to have a deviation of 4.62%. On the other hand, the deviation for the proposed integrated stiffened panel design has a deviation of around 1.84%. As standard deviation of values for both the conventional and integrated stiffened panels are less than 5%, it reinforces the outcomes of the simulations carried out in this study.

Table 4. Comparison of numerical and theoretical outcomes

Stiffened Panel Type	Buckling Strength		Standard Deviation
	Theoretical Values (MPa)	Numerical Values (MPa)	
Conventional	76.48	80.1	4.62%
Integrated	82.55	84.09	1.84%

5. Conclusion

Numerical investigations are carried out on the integrated stiffened panel design as it is found to be advantages over the conventional stiffened panel design. Based on the study, the following findings are observed and listed here.

- The integrated stiffened panel can withstand a maximum equivalent strain of 0.012452mm/mm, whereas the conventional stiffened panel can withstand a maximum equivalent strain of 0.012301 mm/mm. The integrated stiffened panel can withstand strain rate 1.2% higher than the conventional stiffened panel.
- The maximum equivalent stress the integrated stiffened panels can withstand is 84.09 MPa, whereas conventional stiffened panels can withstand a maximum equivalent stress of 80.1 MPa. The integrated stiffened panel has a greater stress life and has a stress withstanding capacity of almost 4.864% higher than that of conventional stiffened panel.
- The maximum deformation of integrated stiffened panel is 8.8872 mm. But the conventional stiffened panel maximum deformation is 10.89 mm. Again, this demonstrates the integrated stiffened panel greater resistance to distortion. Compared to an integrated panel, the conventional stiffened panel deforms by 20.25% more.

Thus, the integrated stiffened panel is found to be the suitable alternative to the existing conventional stiffened panel in terms of improved buckling resistance, ability to sustain greater loads at lesser weight, and ease of production with reduced cost.

References

[1] D. Quinn, A. Murphy, W. McEwan and F. Lemaitre, “Stiffened panel stability behaviour and performance gains with plate prismatic sub-stiffening”, Thin-Walled Structures, Vol. 47(12), 2009, pp. 1457-1468. https://doi.org/10.1016/j.tws.2009.07.004

[2] A. Brot, Y. Peleg-Wolfin, I. Kressel and Z. Yosef, “The damage-tolerance behavior of integrally stiffened metallic structures”, Proceedings of the Israel Annual Conference on Aerospace Sciences, 2008, 12 pages.

[3] D. Wilckens, R. Degenhardt, K. Rohwer, J. Tessmer and P. Bürmann, “IBUCK - A fast simulation tool for the design of CFRP aerospace structures”, Proceedings of the 2nd International Conference on Buckling and Postbuckling Behaviour of Composite Laminated Shell Structures, September 2008, 4 pages.

[4] D. Quinn, A. Murphy, M.A. Price and M. Mullan, “Impact of composite manufacturing constraints on aerospace stiffened panel design”, Proceedings of the 18th International Conference on Composite Materials, 2011, 6 pages.

[5] Marc Fischer, David Kennedy, and Carol A. Featherston, "Multilevel optimization of aerospace and lightweight structures", Proceedings of the ICAS 2002 Congress, 2002, 9 pages.
[6] M. Fischer, D. Kennedy and C.A. Featherston, "Multilevel framework for optimization of lightweight structures", Proceedings of the Institution of Mechanical Engineers, Part G: Journal of Aerospace Engineering, Vol. 226, Issue 4, 2012, pp. 380-394. doi:10.1177/0954410011411637
[7] Kevin S. Van Dooren and Chiara Bisagni, "Design and analysis of thermoplastic welded stiffened panels in post-buckling", Proceedings of the 36th Technical Conference of the American Society for Composites, 2021, pp. 406-471. DOI: 10.12783/asc36/35771
[8] Jeff W.H. Yap, Murray L. Scott, Rodney S. Thomson, and Dieter Hachenberg, "The analysis of skin-to-stiffener debonding in composite aerospace structures", Composite Structures, Vol. 57, Issues 1–4, 2002, pp. 425-435. https://doi.org/10.1016/S0263-8223(02)00110-1
[9] Dan Wang and Mostafa M. Abdalla, "Global and local buckling analysis of grid-stiffened composite panels", Composite Structures, Vol. 119, 2015, pp. 767-776. https://doi.org/10.1016/j.compstruct.2014.09.050
[10] Broderick H. Coburn, Zhangming Wu and Paul M. Weaver, "Buckling analysis of stiffened variable angle tow panels", Composite Structures, Vol. 111, 2014, pp. 259-270. https://doi.org/10.1016/j.compstruct.2013.12.029
[11] Eyassu Wodesenbet, Samuel Kidane, Su-seng Pang, "Optimization for buckling loads of grid stiffened composite panels", Composite Structures, Vol. 60, Issue 2, pp. 159-169, 2003. https://doi.org/10.1016/S0263-8223(02)00315-X
[12] Shahriar Setoodeh, Mostafa M. Abdalla, Samuel T. Ijsselmuiden and Zager Gurdal, "Design of variable-stiffness composite panels for maximum buckling load", Composite Structures, Vol. 87, Issue 1, 2009, pp. 109-117. https://doi.org/10.1016/j.compstruct.2008.01.008
[13] R. Degenhardt, A. Kling, K. Rohwer, A.C. Orfici and R. S. Thomson, "Design and analysis of stiffened composite panels including post-buckling and collapse", Computers & Structures, Vol. 86, Issue 9, 2008, pp. 919-929. https://doi.org/10.1016/j.compstruc.2007.04.022
[14] Mohsen Nasihatgozar, Vahid Daghigh, Milad Eskandari, Kamran Nikbin and Andy Simnoeau, "Buckling analysis of piezoelectric cylindrical composite panels reinforced with carbon nanotubes", International Journal of Mechanical Sciences, Vol. 107, 2016, pp. 69-79. https://doi.org/10.1016/j.ijmecsci.2016.01.010
[15] Z. Gurdal, B.F. Tatting and C.K. Wu, "Variable stiffness composite panels: Effects of stiffness variation on the in-plane and buckling response", Composites Part A: Applied Science and Manufacturing, Vol. 39, Issue 5, 2008, pp. 911-922. https://doi.org/10.1016/j.compositesa.2007.11.015
[16] A. Faggiani and B.G. Falzon, "Predicting low-velocity impact damage on a stiffened composite panel", Composites Part A: Applied Science and Manufacturing, Vol. 41, Issue 6, 2010, pp. 737-749. https://doi.org/10.1016/j.compositesa.2010.02.005
[17] B.G Falzon, K.A. Stevens and G.O Davies, "Postbuckling behaviour of a blade-stiffened composite panel loaded in uniaxial compression", Composites Part A: Applied Science and Manufacturing, Vol. 31, Issue 5, 2000, pp. 459-468. https://doi.org/10.1016/S1359-835X(99)00085-8
[18] S. Nagendra, D. Jestin, Z. Gurdal, R.T. Haftka and L.T. Watson, "Improved genetic algorithm for the design of stiffened composite panels", Computers & Structures,Vol. 58, Issue 3, 1996, pp. 549-555. https://doi.org/10.1016/0045-7949(95)00160-I
[19] Robert Vitali, Oung Park, Raphael T. Haftka and Bhavani V. Sankar, "Structural optimization of a hat stiffened panel by response surface techniques", AIAA-97-1151, 1997.
[20] Structural stability research council, 2009, Chapter 4: Plates, USA.

Journal of Physics: Conference Series

PURPOSE-LED PUBLISHING™

PAPER • **OPEN ACCESS**

Analysis and Fabrication of Aluminium Composite with SiC and Graphite Using Stir Casting Method (MMC).

To cite this article: Sreekanth Sura *et al* 2024 *J. Phys.: Conf. Ser.* **2837** 012067

View the article online for updates and enhancements.

You may also like

- Design and Analysis of Work Holding Device for Convex Milling
J. Krishnaraj, V. Venkata Phani Babu, C. S N S Ganesh et al.
- Investigation of various winglets using computational fluid dynamics for subsonic aircraft
R Jayanth, Chiraag M Sagar, T K Rajashekar et al.
- Analysis of Implication of Phase Change Material Enclosed Design on Thermal Performance of Solar Collector
V Rathinam, S Seenivasan, V Velliyangiri et al.

This content was downloaded from IP address 106.0.37.90 on 21/10/2024 at 11:23

Journal of Physics: Conference Series **2837** (2024) 012067 doi:10.1088/1742-6596/2837/1/012067

Analysis and Fabrication of Aluminium Composite with SiC and Graphite Using Stir Casting Method (MMC).

Sreekanth Sura, B Nagaraj Goud, A.Gowtham Reddy, E.Veeraprathap, T.Jaikanth, U.Yashwanth

Department of Aeronautical Engineering, MLR institute of technology, Hyderabad, India.

Abstract: Composites, as we all know, are used to reduce weight while boosting strength, stiffness, and other material properties as required by the application. Material science and engineering have sparked a lot of curiosity in the contemporary era. There has been a huge impact since the invention of composite materials. As a result of its high strength and durability. Low weight is the winning combination that propels composite materials towards the future. new frontiers Composites are commonly used to substitute natural materials like wood. Steel, iron, and other metals are distinguished by their surface properties. Metal Matrix was discovered in the literatures. Traditional materials are being phased out of the aerospace and automotive industries, while composites are being seriously studied. Because of their mechanical properties, Aluminum alloy MMCs are becoming increasingly used in a wide range of industrial applications. Using the stir casting method, the main theme of this project is to produce and fabricate composite materials based on aluminium alloy (A1-2024) reinforced with 15% volume fraction of silicon carbide Particulates (SiC) and 5% volume fraction of graphite particulates, taking into account the aforementioned factors and the following. As a result, the major purpose is to show that traditional metals may be used instead of composites in aircraft and vehicle applications. As a result, the project involves Metal Matrix Composite MMC testing and analysis, in which the produced composite is put to the test to assess its strength, hardness, and other physical attributes. Additionally, cracking and composite behaviour were investigated using Ansys Software. Finally, the final findings are compared to traditional material quality, demonstrating that composites are the best alternative.

1. INTRODUCTION

Composite substances at the moment are utilized in quite a few engineering structures, which include spacecraft technology, aeroplane technology, car technology, marine technology, light-weight sports-associated device with great requirements, long-lasting bridges and homes with excessive power and stiffness. Because of its most helpful and amazing vital properties, composite materials are now widely used in the research industry, consisting of excessive precise required power and excessive precise required hardness with required power to weight ratio and excessive hardness to weight ratio. The majority of shafts are made of sturdy or hollow round tubes formed from metal or aluminium, as may be observed. At least two composition constituent components, one of which must be a metallic component, are required in a metallic matrix composite (MMC). and the polar opposite is most likely a distinctive metallic or fabric, made up of a ceramic fabric or a natural related chemical.MMCs are usually created via way of means of combining a lightweight metallic matrix, consisting of aluminum(al), magnesium(mg), or titanium(Ti), with reinforcement elements, consisting of silicon carbide metallic(SiC), boron carbide metallic (B4C), aluminium oxide, graphite, granite, and so on.

A composite shaft has greater high strength, stiffness, and hardness as compared to typically used standard shafts. The composites shaft was designed and built in response to industry demands for greater satisfaction and efficiency in the aerospace and high-performance automotive sectors. Three fundamental techniques were used to develop the MMC: solid metal state processing, liquid metal state processing, and in-situ processing.We chose to build composite shafts utilising a liquid metal state technology, namely the stir casting process, in this study. MMCs offer much better strength and rigidity than the aluminium and steel materials now in use, allowing the composite shaft to achieve a variety of benefits, including decreased weight and the removal of concerns like as excessive noise and big vibrations.

Content from this work may be used under the terms of the Creative Commons Attribution 4.0 licence. Any further distribution of this work must maintain attribution to the author(s) and the title of the work, journal citation and DOI.
Published under licence by IOP Publishing Ltd

2.DESIGN PARAMETERS

The effective design process of a composite drive shaft is dependent on a set of certain factors, which can be attained. The outer radius and subsequently the length of the composite shaft are the major shaft factors to design. However, the current study aims to produce the design AA 2024/SiC-graphite of a high strength and stiffness composite shaft, which was successfully designed and evaluated using the ANSYS simulation tool for aerospace industry applications.

Design parameters of the specimen shaft:

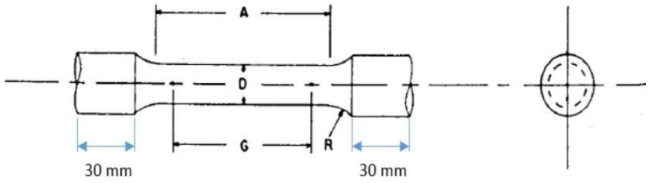

Fig1 Specimen Dimensions

Gauge length of the specimen(G) = 50mm.
Inner diameter of the specimen(Di) = 10mm.
Length of the specimen(L) = 1300mm.
Outer diameter of the specimen(Do) = 25mm.
The poisson's ratio of composite specimen = 0.3.
Density of the composite specimen = 2.9 g/cc.
Moment applied on the specimen = 1000Nm.

3.FABRICATION OF SPECIMEN

3.1 STIR CASTING

Casting is a process in which a liquid substance is poured into a mould having a hollow hole in the desired shape and then hardened. solidified piece, also known as a casting, is discharged or broken out of the mould to complete the process. A mould is created in the shape of a desired part's geometric shape. The mould is then filled with molten metal. As the substance solidifies, the mould keeps it in form. It's made into a metal case. Although it appears to be a straightforward operation, metal casing manufacture is both a science and an art. The mechanical stirrer generates a vortex that helps the reinforcing elements fed into the melt mix better. The stirrer is made up of the impeller blade and the stirring rod. Impeller blades are available in numerous range of variety we opted for flat blade with three numbers.. Because flat blades with three numbers generate an axial flow pattern in the crucible while wasting less energy, they were chosen. This stirrer is connected to variable-speed motors, and the motor's regulator controls the stirrer's spinning speed. The feeder is connected to the furnace and feeds reinforcing powder into the melt.

Fig2.Stir Casting Equipment

4.COMPOSITION OF MATRIX AND REINFORCEMENTS:

4.1 Composition of pure Al2024:

Material	Al2024	SiC	Graphite
1.Material (in %)	100	0	0
2.Weight(grams)	150	0	0

4.2 Composition of AL2024+Sic+Graphite:

Material	Al2024	SiC	Graphite
1.Material (in %)	80	15	5
2.Weight(grams)	120	22.5	7.5

Fig3.Al2024 with 10%SiC

Fig4.Al2024 with 15%SiC&5%graphite

5.TENSILE TEST

Tensile testing is a destructive test method that determines the metallic material's tensile strength, yield strength, and ductility. It calculates the amount of force required to break a composite or plastic specimen, as well as how far the specimen must stretch or elongate to achieve that breaking point.

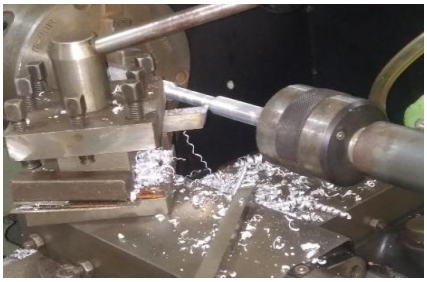

Fig5.Specimen Preparation for tensile test

6.TENSILE TEST RESULTS

6.1 TENSILE TEST RESULTS OF Al2024 /10% SiC

Al2024 /10% SiC	Value
Maximum force applied	1014N
Cross section area	79.485 mm^2
Gauge length	50mm
Ultimate Tensile Strength	132.41Mpa
% of elongation	4.2
Max Load	7820N
Equivalent stress	98.72Mpa

6.2 TENSILE TEST RESULTS OF Al2024/15%SiC/5%GRAPHITE

Al2024/15%SiC/5%GRAPHITE	Value
Maximum force applied	1140N
Cross section area	80.1 mm^2
Gauge length	50mm
Ultimate Tensile Strength	146.26Mpa
% of elongation	3.42

Max Load	8600N
Equivalent stress	107.42Mpa

7. BRINELL HARDNESS TEST

Brinell's hardness test is used to determine the materials' hardness. Structures with a high-course or high-rough-surface surface are put to the test. In this approach, a load is delivered to the specimen to ascertain the hardness number, a fixed diameter carbide ball is used to test, and the force is applied for a specified amount of time before being withdrawn. A brinell microscope, which has a specifically developed optical system that covers at least two diameters, is used to measure the resultant imprint.

$$\mathbf{BHN} = {}^{2L}\Big/_{\pi D(D-\sqrt{(D^2-d^2)})}$$

Al2024/SiC10%

Al2024/SiC15%/5% graphite

Fig6.Specimen for hardness test

8. HARDNESS TEST RESULTS

Material	Applied force(Kgf)	Hardness number
Al2024/SiC 10%	100	74
Al2024/SiC15%/Graphite 5%	100	80

Fig7 Brinell hardness equipment

Fig8. Indentation location

9. STRUCTURAL ANALYSIS

9.1. Composite Test specimen cylindrical in CatiaV5

The below fig is the obtained model of test specimen designed in Catia software which is further imported into the Ansys workbench for analysis.

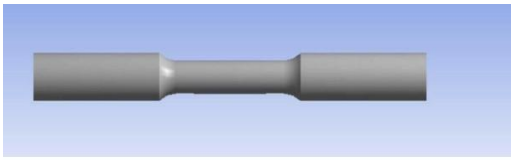

Fig 9. Catia V5 model

9.2 Ansys Workbench explicit Dynamic Simulation Results:

- The boundary conditions used in this analysis where inserted one end with fixed support and other end with load or displacement.
- We applied a moment force as 1000N or either displacement in y direction up to 2 mm.

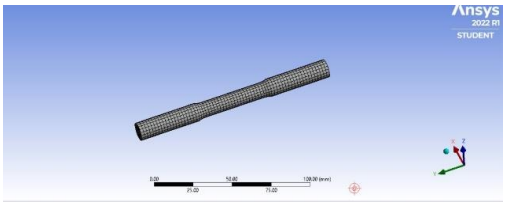

Fig10. meshed model of fine size

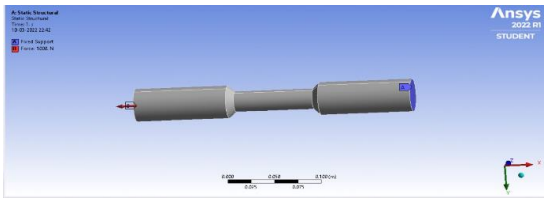

Fig11.Applied boundary condition

10.EXPERIMENTAL RESULTS OF ANSYS WORKBENCH

10.1.Analysis results of Al2024+10%SiC:

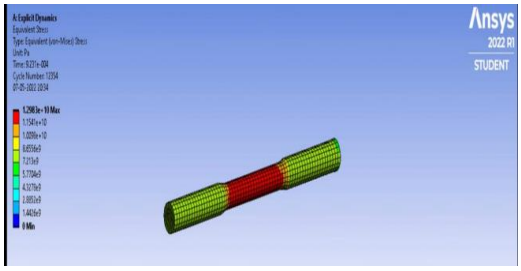

Fig 12.Total deformation

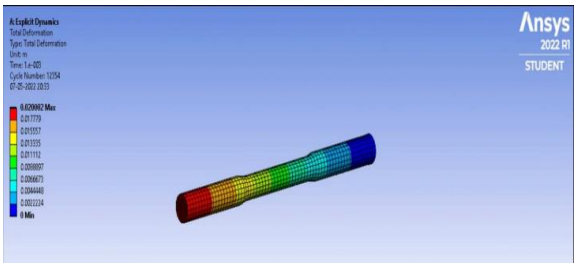

Fig13. Equivalent Stress (von Moises)

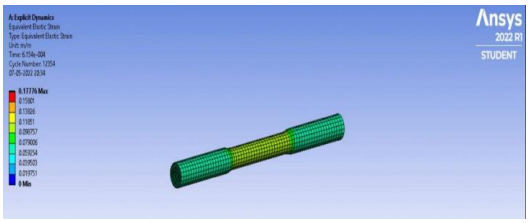

Fig14.Equivalent Elastic Strain (von Moises)

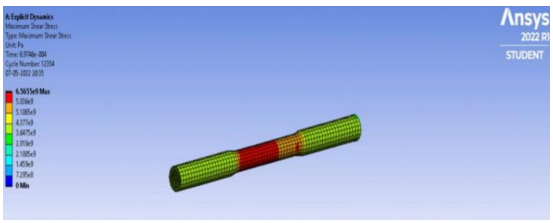

Fig 15.Max Shear Stress

10.2.Analysis results of Al2024+SiC+Gr MMC

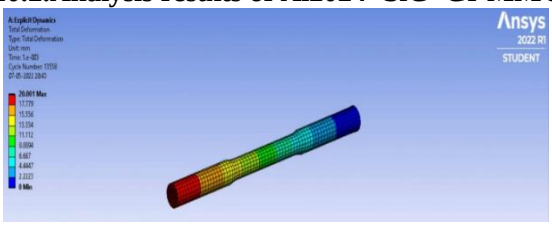

Fig 16.Total Deformation

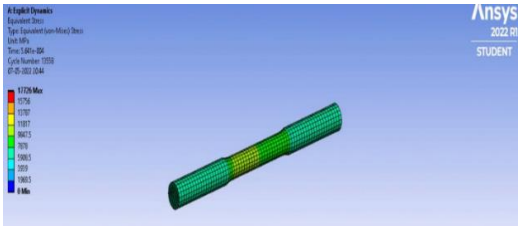

Fig 17.Equivalent stress (Von Moises)

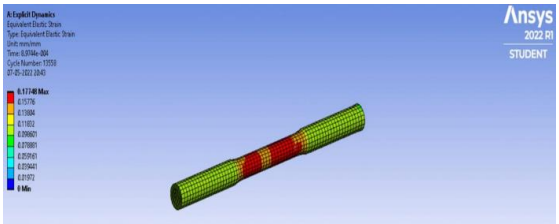

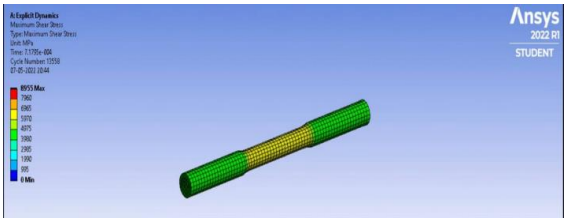

11. ANALYSIS RESULTS

11.1 RESULTS OF Al2024 /10% SiC

Al2024 /10% SiC	Value
Max Load	7820N
Equivalent stress	98.72Mpa
Ultimate Tensile Strength	145.02Mpa
% of elongation	4.2
Total deformation	53.10mm

11.2 RESULTS OF Al2024/15%SiC/5%GRAPHITE

Al2024/15%SiC/5%GRAPHITE	Value
Max Load	8600N
Equivalent stress	107.42Mpa
Ultimate Tensile Strength	155.63Mpa
% of elongation	3.42
Total deformation	51.71mm

12. RESULTS

We are comparing the two constructed models in this project work by adjusting the Wt % of Sic and B4C, and the results are displayed below.

Tensile Strength of first specimen(Al2024+SiC10%) = 132.41N/mm2.
Tensile strength of second Specimen (Al2024+SiC15%+5%graphite) = 146.26N/mm2.
Brinell Hardness Number of first specimen = 74
Brinell Hardness Number of second Specimen = 80

12.1 TEST RESULTS

S.no	**Tensile strength (N/ mm^2)**	**Brinell hardness number**
1.Specimen 1	132.41	74
2.Specimen 2	146.26	80

Aluminium matrix composites (AMCs) with silicon carbide (SiC) content (10%) and silicon carbide 15% +graphite (5%) were created in this experiment utilising the stir casting manufacturing process. The produced composites' microstructural, hardness, and tensile strength properties were investigated. The following results can be phrased as follows based on experimental examination.

- In the microstructures, clustering and non-homogeneous dispersion of silicon carbide (SiC) particles in Al matrix were detected. and porosities were discovered.

- The addition of silicon carbide (SiC) to the Al matrix boosted composite hardness and tensile strength when compared to unreinforced Al. 2024, The specimen with 15% silicon carbide (SiC) content and 5% graphite content aluminium matrix composites (AMCs) demonstrated the highest hardness and tensile strength.

- With increasing silicon carbide (SiC) concentration in Al matrix, wear resistance of aluminium matrix composites (AMCs) increased.

- By adding of graphite to the aluminium with silicon carbide we have seen that the increase in hardness.

13. CONCLUSION

After analysing the results and comparing them to the test results, it was discovered that the MMC model Shaft had the following results and properties. As a result, it is widely utilised and applicable/suitable in the automotive industry for a variety of applications, particularly in automobiles and aircraft. According to the analytical and experimental results, at a specific volume % of silicon carbide, the composite material tends to enhance its mechanical qualities such as tensile strength, compressive strength, and hardness. 15 % silicon carbide is the most effective volume fraction for improving the mechanical characteristics of the aluminium metal matrix composite. Mechanical qualities are reduced if the volume fraction increases above 15 % silicon carbide.

And also we have seen that with increase in graphite volume fraction above 6% the hardness and tensile strengths were decreased so we have concluded that the effective volume fraction for increasing tensile strength and hardness is 5%for graphite & 15%silicon carbide. These increased tensile strength and hardness increase the wear resistance of the material so that we can use them as surfaces for aircraft and automobile applications.

14. REFERENCES

[1]Chawla, N., 2006. Metal matrix composites in automotive applications. Adv. Mater. Processes., 164: 29-31.
[2]Abhijith R, Harish . T. M, 2016, Fabrication & Analysis of Aluminium (Al-2024) and Tungsten Carbide (WC) Metal Matrix Composite by in-Situ Method, http://dx.doi.org/10.17577/IJERTV5IS080332
[3] Arunkumar K N , Dr. G B Krishnappa, 2022, Mechanical Properties of Aluminum Metal Matrix Composites – A Review, International Journal Of Engineering Research & Technology (Ijert) Volume 11, Issue 03 (March 2022).
[4] Mr. P. Raju, M. Arunnadevi, P. Kokula Sandhiya, R. Krishnan, R. Manikandan, 2019, Fabrication and Analysis of Aluminium based Metal Matrix Composites Reinforced with Aluminium Oxide, INTERNATIONAL JOURNAL OF ENGINEERING RESEARCH & TECHNOLOGY (IJERT) ETEDM.

[5] Dr. M SatyanarayanaGupta, K Veeranjaneyulu, "Fabrication and Analysis of Adhesive joints Used in Aircraft Structures" International Conference on Advancements in Aeromechanical Materials for Manufacturing (ICAAMM-2016International MLRIT, Hyderabad July 9-11, 2016.

[5] M.Satyanarayana Gupta, “Fabrication and comparision of AA7005/SiC-Al2O3 and other composite materials using different methods”, AIP Conference Proceedings 2317, 020030 (2021); https://doi.org/10.1063/5.0036139.

[7] B. Nagaraj Goud, K. Shiva Shankar, B. Manideep, K. Veeranjaneyulu “Experimental Test on Glare Composite of an Aircraft Structure under Tensile Strength Failure”, International Journal of Engineering and Advanced Technology (IJEAT) ISSN: 2249 – 8958, Volume-9 Issue-2, December, 2019.

[5] Sidney H.Avner.,(1986); Introduction to physical metallurgy, McGraw-Hill.
[6] Introduction to Composite Materials, F.C. CampbellStructural Composite Materials.
[7] Traina , A. Hernandez , T. Scheck , C. Etuk , J. Peters ,E.W. Lee , J. Ogren , O.S. Es-Said (2005) On the correlation of mechanical and physical properties of 7075-T6 Al alloy, Engineering Failure Analysis
[8] Walter D. pilkey "peterson's stress concentration factors", 2nd edition. Wiley Interscience (1997)
[9] Vikram Singh and R.C Prasad, 2004 "Tensile and Fracture Bchavior of 6061 AlISic, Metal Matrix Composite", International symposium of research on materials science and engineering
[10] Vidya Sagar Avadutala, 2005, "Dynamic Analysis of Cracks in Composite Materials" Wiley Interscience
[11] P. Rohatgi, 1991, "Cast Aluminum Matrix Composites for Automotive Applications" Journal of Metals.
[12] Abis, S., (1989), "Characteristics of an aluminium alloy/Alumina Metal Matrix composite", Composites science and technology, Vol.35. pp.1-11.
[13] Brian Terry and Jones Glyn..(1990), Metal matrix composite, Elsevier Science Publishers Ltd., England, pp.41-47.
[14] Boopathi, M. & Arulshri, K.P. & Natesan, Iyandurai. (2013). Evaluation of mechanical properties of Aluminium alloy 2024 reinforced with silicon carbide and fly ash hybrid metal matrix composites. American Journal of Applied Sciences. 10. 219-229. 10.3844/ajassp.2013.219.229.
[15]. Carreño, Caleb & Estrada, Ivanovich & López-Meléndez, C. & Martínez-Sánchez, R.. (2014). Dispersion of silicon carbide nanoparticles in a AA2024 aluminum alloy by a high-energy ball mill. Journal of Alloys and Compounds. 586. S68-S72. 10.1016/j.jallcom.2013.03.232.
[16]. N, Mohan & C, Jayabalan & M, Siva & B, Ramesh. (2022). A Novel Manufacturing Process for Nanosilica Carbide Reinforced Al2024 Matrix Composites. ECS Transactions. 107. 4089-4098. 10.1149/10701.4089ecst.
[17]. Sunderraj, D. & Raj, J. & Kathiresan, Arun Vasantha Geethan & Singh, Prathap & Narayanamoorthy, K.. (2021). Study of tribological behavior of Al2024 by power metallurgy method. AIP Conference Proceedings. 2395. 040008. 10.1063/5.0068796.

Journal of Physics: Conference Series

PURPOSE-LED PUBLISHING™

PAPER • **OPEN ACCESS**

Comparative Study on Effect of Material on structural Performance of a Quadcopter Drone with ‘X- Frame’

To cite this article: Chitkula Harika *et al* 2024 *J. Phys.: Conf. Ser.* **2837** 012099

View the article online for updates and enhancements.

You may also like

- Analysis of Mapping Area of Flood With Drone Type Multicopter in Girimulyo, Kulonprogo
I. Suroso
- Strategic framework of using drone in cities disaster response
H. Zahir, M.S. Fathi and A.F. Tharima
- Drone data reveal heterogeneity in tundra greenness and phenology not captured by satellites
Jakob J Assmann, Isla H Myers-Smith, Jeffrey T Kerby et al.

This content was downloaded from IP address 106.0.37.90 on 21/10/2024 at 11:23

Journal of Physics: Conference Series **2837** (2024) 012099 doi:10.1088/1742-6596/2837/1/012099

Comparative Study on Effect of Material on structural Performance of a Quadcopter Drone with 'X- Frame'

Chitkula Harika [1,a)] , A Sai Kumar [1,b)] and M V Raghavendra Rao[2, c)]

[1] Department of Aeronautical Engineering, MLR Institute of Technology, Hyderabad, India.
[2] Department of Automobile Engineering, Godavari Institute of Engineering & Technology, Rajahmundry, India.

[a)] harikareddie04@gmail.com, [b)] ask.mraj@gmail.com, [c)] raghavendram@giet.ac.in

Abstract: Drones have become most important parts of the day-to-day life from a hobby to serious research. But, the operation and maintenance cost of these drones is very high due to multiple failures while flying. The most common component that experience heavy loads and undergo failure is frame of the drone. Hence, there is a need to address the best shape and material that can be used to reduce the operation cost due to catastrophic failures. The present work deals with design of a micro-drone frame which must withstand a load of at least 2 kgs. The 'X'-shaped frame, were modelled and analysed at various load conditions for glass fiber, carbon fiber, aluminum alloy, and plastic materials. The results obtained for the different materials were compared and it was observed that carbon fiber is the preferred material for load-bearing applications but the cost for manufacturing and maintenance is very high. Aluminum alloy shows good strength and is cost effective. The ease of manufacturing and make it more suitable for drones. Plastic, though flexible and easy to fabricate, does not meet the required strength to weight ratio.

Keywords: Drone, Materials.

1. Introduction

Quadcopters are simple flying mechanisms with four arms and motors attached to propellers. They are not stable and require a flight controller for control. UAV technology has gained interest in it, with drones being used for crime scenes, surveillance, and more. They can use sensors like laser, infrared, and optical to monitor their environment and navigate autonomously. The evolution of drone technology, including high-resolution cameras, flight capabilities, and battery life, highlights the increasing importance of mini drones in surveillance and data acquisition. The project aims to enhance the quadcopter's design, structural integrity, and material selection, contributing to ongoing progress in drone technology. Advancements in technology have led to new applications in agriculture, engineering, research, military use, and mineral exploration. Drones can also guide disabled people, map buildings, and perform various tasks in various fields. **Fig 1** represents sketch of a Quadcopter with camera mounted at the bottom of the frame.

Content from this work may be used under the terms of the Creative Commons Attribution 4.0 licence. Any further distribution of this work must maintain attribution to the author(s) and the title of the work, journal citation and DOI.
Published under licence by IOP Publishing Ltd

Fig 1. Quadcopter

1.1 Objectives

The present focuses on designing a quad copter frame of required dimensions which can be successfully withstand the loads that it encounters during it operation. The purpose of the drone is image capture or provide platform for loads such as emergency medical supplies, speaker, etc. The work also emphasizes the importance of frame materials, particularly glass fiber and carbon fiber, in determining the quadcopter's weight, strength, and resilience. The work also emphasizes on improving the strength to weight ratio by using weight optimization in Ansys Workbench.

2. Literature Survey

N. Muralidharan, et.al, 2021 [1] explores the importance of assessing the structural integrity and performance of Unmanned Aerial Vehicles (UAVs), including quadcopters. It explores various methodologies and techniques, including finite element analysis, stress analysis, and computer-aided simulations. The study also considers load types, such as static and dynamic loads, and material properties, such as modulus of elasticity, density, and tensile strength, to predict the frame's response to various load conditions.

Gavireddi Abhinava Bharat, et.al,[2] Quadcopter frame design is crucial for the performance, stability, and functionality of unmanned aerial vehicles (UAVs). It involves creating a structure that supports components and optimizes mission execution. Frame design affects stability, maneuverability, payload capacity, and aerodynamic efficiency, which directly correlates with energy consumption and flight performance. This major project focuses on quadcopter frame design, which is essential for a quadcopter's overall performance.

Khaled Hassan Mostafa 2021 et.al, [3] the X-frame design of a quadcopter improves stability but increases aerodynamic disturbance vulnerability. It requires more material due to the arms sandwiched between main plates, limiting hardware space. The motor, fuel tanks, flight controls, and cargo must fit in, causing vibration problems. The X-frame's proximity to the flight controller and camera increases vibration. Stacking components would require more structural material and increase the quadcopter's weight.

3. Methodology

The project aims to create a detailed model of a quadcopter frame with an 'X'-shaped structure, utilizing ANSYS software for structural analysis [4]. The model will serve as the foundation for subsequent analyses, comparing the suitability of glass fiber and carbon fiber frame materials. The load-bearing assessment will assess the frame's ability to withstand dynamic loads during operation. The project's ultimate goal is to provide practical recommendations for optimizing frame material selection, structural design, and overall performance, focusing on fulfilling image capture missions. The X-frame design, with more weight concentrated at the center of gravity, improves stability but increases vulnerability to aerodynamic disturbances [5]. The True X design, with equal perpendicular distance between motor centers, provides equal stability on all axes.

3.1 Quadcopter Frame Modelling

The Quadcopter Frame Modeling process is crucial for a project's success. It involves creating a detailed three-dimensional model of the quadcopter's structural frame, incorporating every component, dimension, and geometric property. Visual aids and images are used to provide a clear understanding of the structure. Advanced software tools facilitate this modeling, creating a virtual representation that mirrors the actual frame [6-8]. This digital blueprint serves as a dynamic foundation for the project's phases, ensuring stability and optimal aerodynamic performance during image capture missions.

3.2 Software Tools: SOLIDWORKS

The project uses advanced software tools, such as SolidWorks, to create a detailed three-dimensional model of the quadcopter frame. These tools allow the team to design the frame with precision, considering every component, dimension, and geometric property [9]. They provide a comprehensive representation of the quadcopter's structural framework, ensuring accuracy and completeness. These tools also facilitate further structural analyses, load-bearing assessments, and material selection, ultimately enhancing thequadcopter's performance and stability during critical image capture missions.

3.2.1 'X'-Shaped Frame Design

The 'X'-shaped frame design is a key component in a quadcopter project, balancing structural stability and aerodynamic efficiency. It provides a stable platform for the quadcopter, allowing it to navigate through various environments with ease. This design minimizes aerodynamic resistance, enhancing maneuverability and efficiency during image capture missions [11]. The frame's specific dimensions and geometric properties ensure optimal weightdistribution, stability, and control during flight. It is a dynamic solution for the quadcopter's performance.

3.3 Dimensions and Specifications

The quadcopter frame's dimensions, now at 250x250 mm, are crucial to the project's objectives. These measurements ensure stability and aerodynamic efficiency during image capture missions [10]. The frame's geometric properties promote an even distribution of weight, promoting stability and precise control. The updated specifications align with the project's commitment to precision and performance during image capture missions.

4. Setup and Structural Analysis

4.1 ANSYS

ANSYS software is crucial for the "Structural Analysis" phase of a project, allowing for comprehensive structural analysis and simulations [2,12]. It helps assess the quadcopter frame's response to various load scenarios, identifying potential weak points and stress accumulation areas. ANSYS also facilitates stress and strain analysis, ensuring the frame's reliability during image capture missions. This data-driven approach informs decisions related to frame design, material selection, and load-bearing capabilities.

4.2 Load Scenarios

Load scenarios are crucial in the "Structural Analysis"phase of a quadcopter project. They involve subjecting the frame to simulated conditions and forces to evaluate its structural response [14]. These scenarios, including static and dynamic loads, aerodynamic forces, and gravitational effects, help identify potential weaknesses and guide decisions on material selection,structural enhancements, and overall frame design. This comprehensive evaluation ensures the frame's structural integrity and reliable performance during image capture missions.

4.3 Material Properties

The "Structural Analysis" phase of a project involves evaluating the properties of materials like glass fiber and carbon fiber to predict their response to dynamic forces [14-16]. Key properties include

modulus of elasticity, density, and tensile strength. The analysis compares these properties under various conditions to determine the most suitable material for the frame. The objective is to select a material that balances lightweight construction with high structural integrity, ensuring the chosen material aligns with the project's objectives of structural stability and reliable performance during dynamic conditions.

4.4 Boundary Conditions

Boundary conditions are crucial in the "Structural Analysis" phase of a project, defining constraints and environmental factors that influence the quadcopter frame's behavior [17-19]. They include fixed displacement, loads, and constraints, which simulate the frame's interactions with components and external forces. Accurate and precise boundary conditions guide decisions related to frame design, material selection, and load-bearing capabilities, ensuring the quadcopter's structural integrity and reliable performance during dynamic events like image capture missions [20].

4.5 Meshing and Analysis Setup

Meshing and analysis setup are crucial in the "Structural Analysis" phase of a quadcopter project. Meshing involves breaking down the 3D model into smaller elements, allowing for a detailed analysis. Analysis setup involves setting parameters, defining load scenarios, and specifying constraints. These steps ensure the project aligns with real-world scenarios, providing valuable insights into stress and strain distribution within the frame [3,7,10]. This helps ensure the quadcopter's structural integrity and performance during dynamic scenarios.

5. Results and Discussion

5.1 Frame Modelling and Design

The study focused on frame modeling and design using SolidWorks software, specifically using carbon fiber for its lightweight and superior strength properties. The frame size was 250mm, aiming to enhance structural integrity and performance under various conditions.

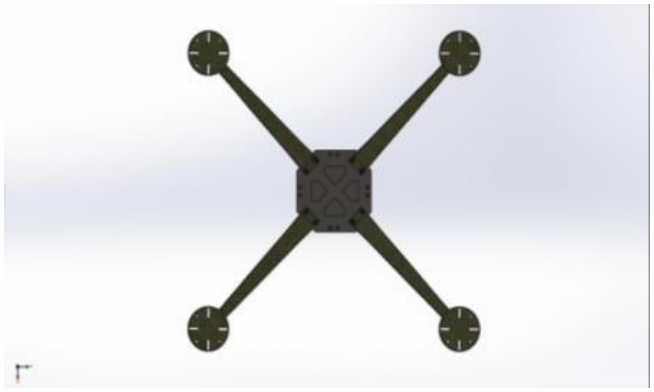

Fig 2. Model in Solidworks

Figure 2 represents the 3d frame, made of 250x250 millimeters carbon fiber, is lightweight and strong, ideal for load-bearing applications. Its weight is estimated using the density of carbon fiber, and its dimensions and geometric properties guide design considerations, ensuring the frame meets desired performance criteria. Fig 3. Represents the draft of Model.

Calculation: Volume = Length x Width x Height Volume = 25 cm x 25 cm x 0.3 cm (assuming a 3mm thickness) Using the density, we can then estimate the weight: Weight = Volume x Density Weight = (25 cm x 25 cm x 0.3 cm) x 1.75 g/cm³ These dimensions and the weight estimation provide crucial information for further analysis and design considerations, ensuring the frame meets the desired criteria for strength, weight, and overall performance, particularly in the context of quadcopter applications.

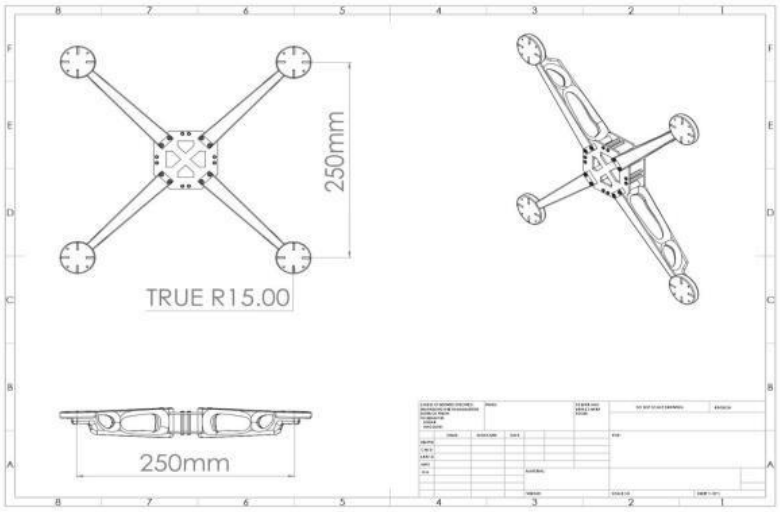

Fig 3. Draft sheet for Model

5.2 Results for Carbon Fiber

5.2.1 Load Distribution for carbon fiber

Load Distribution is a crucial aspect of frame analysis, influencing the frame's structural integrity and ability to support intended loads. Factors like material properties, geometry, and external forces influence load distribution. Understanding this distribution is essential for assessing the frame's performance.

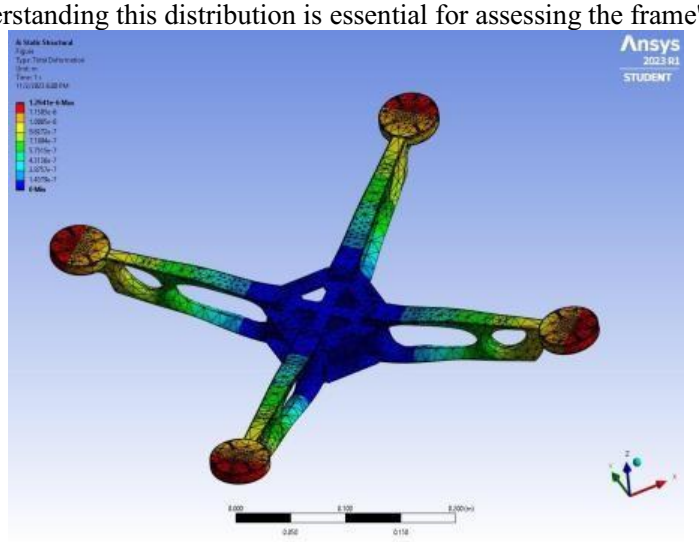

Fig 4. Load Distribution for carbon fiber

The quadcopter's structure's maximum deformation after applying a force of 4.905 newtons at four points is 1.2941×10^-6 millimeters, equivalent to 1.2941 micrometers as shown in **Fig 4**. This small deformation is typical for lightweight aerospace vehicles like quadcopters. The analysis provides insights into the quadcopter's response to external forces, crucial for ensuring its structural integrity and performance. The deformationvalue is 1.611×10^-6 meters.

5.2.2 Displacement Analysis for carbon fiber

Displacement Analysis at Two Motor Mounting Points is a crucial part of frame assessment, assessingthe frame's response to forces and loads at specific motor mounting points. This analysis helps maintain stability and alignment in the frame under dynamic forces. **Fig 5.** Indicates the quadcopter's maximum

deformation was 1.5503×10^-6 meters, while the average deformation was 3.7732×10^-7 meters. These deformation values indicate the structure's response to the applied force, with the maximum being the most significant point. These deformations are small, typical for lightweight aerospace vehicles like quadcopters, making this analysis crucial for understanding the structure's response to external forces, ensuring its structural integrity and performance.

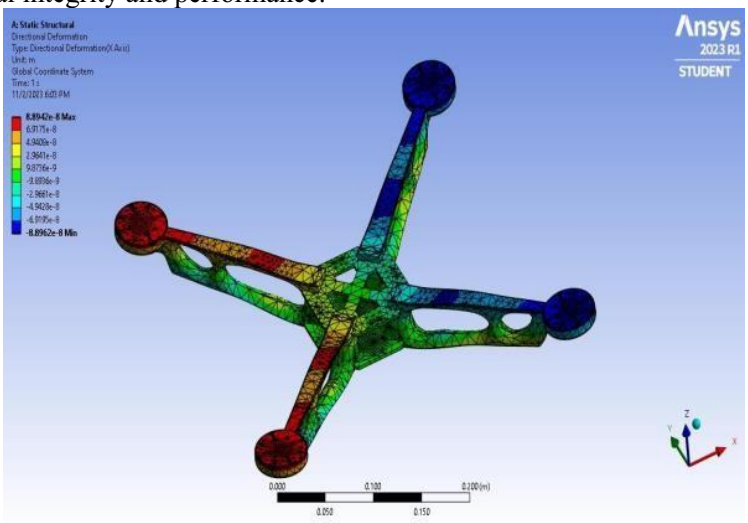

Fig 5. Displacement Analysis for carbon fiber

5.2.3 Stress and Strain Analysis for carbon fiber

Stress and strain analysis is a crucial part of evaluating a frame's structural performance. It assesses the frame's ability to withstand external loads and its material's response to these loads. Stress analysis identifies areas of excessive stress, while strain analysis examines the material's deformation under these forces. These results help identify safety margins, potential weak points, and aid in design optimization. **Fig 6.** Indicates the maximum shear strain as 2.5113×10^5. Understanding and analyzing shear strain is vital for assessing the frame's structural integrity and material behavior.

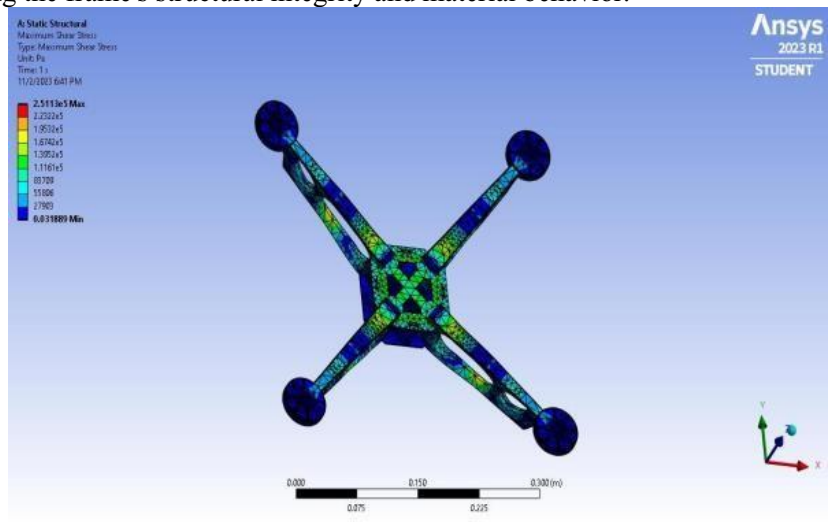

Fig 6. Stress and Strain Analysis for carbon fiber

5.2.4 Maximum shear elastic strain for carbon fiber

The quadcopter structure's maximum shear elastic strain, measured at 3.2647×10^{-6}, Fig 7. Indicates the material's deformation in response to shear forces during analysis.

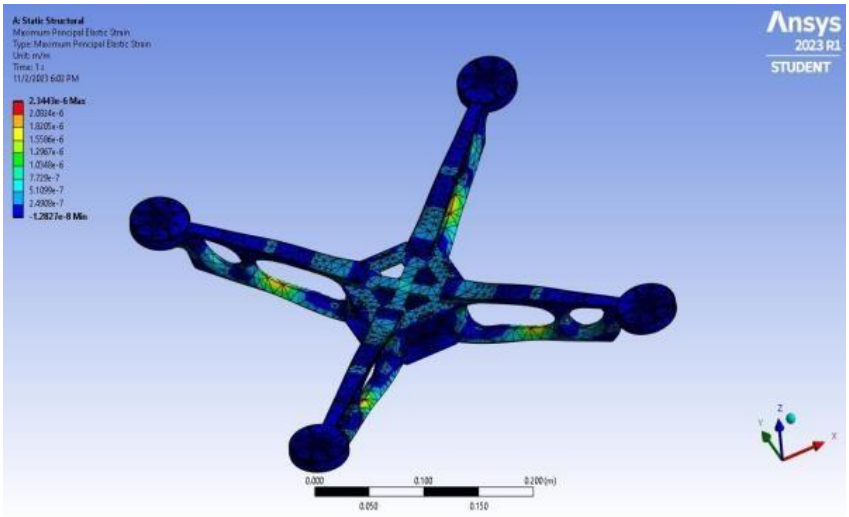

Fig 7. Maximum shear elastic strain for carbon fiber

5.3 Results for Aluminum Alloy

5.3.1 Total deformation for aluminum alloy

A uniform 4.905 Newton's force applied uniformly to the quadcopter's aluminum alloy frame resulted in a total deformation of 1.9787e-006 m as shown in Fig 8., assessing its structural response to external forces.

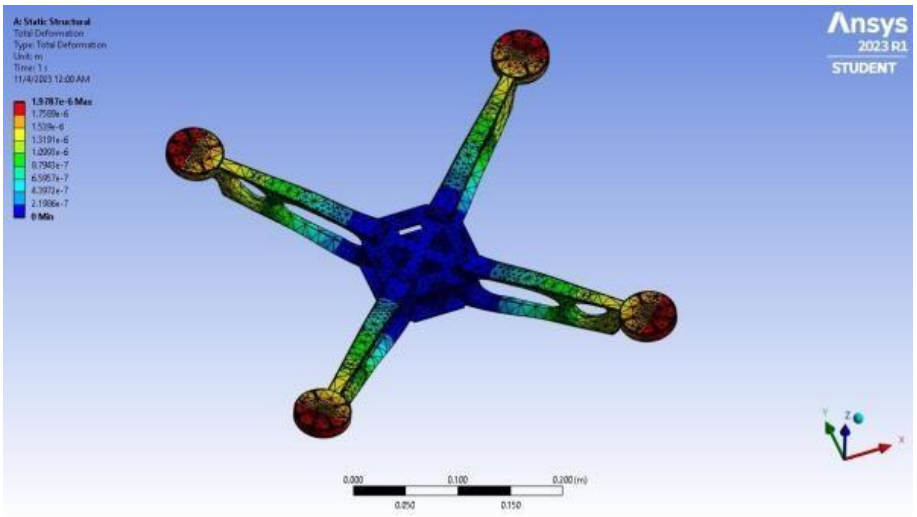

Fig 8. Total deformation for aluminum alloy

5.3.2 Maximum shear elastic strain for aluminum alloy

The quadcopter's aluminum alloy frame underwent uniform 4.905 Newton's force, resulting in a total deformation of 1.9787e-006. The maximum shear elastic strain was 4.9918e-006, as shown in Fig 9. The material's ability to withstand shearing forces and assess its structural performance under different loading conditions.

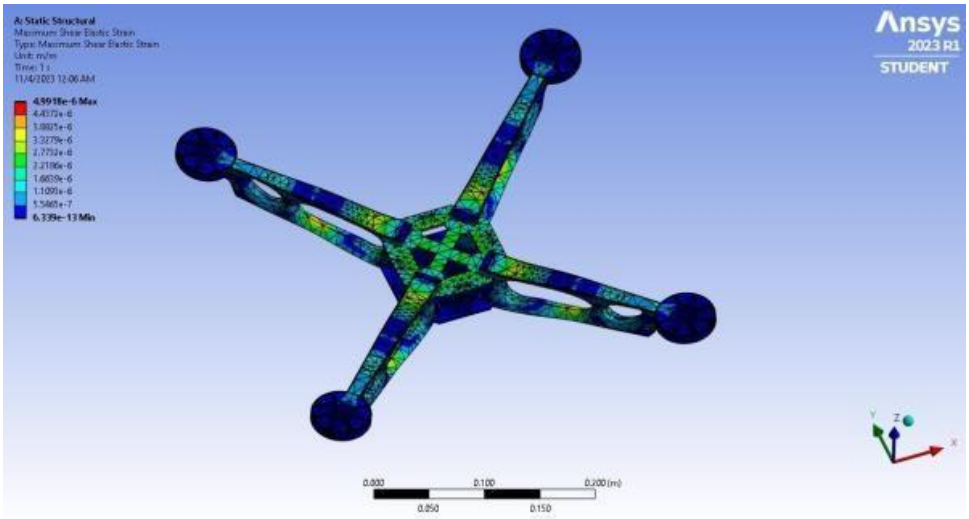

Fig 9. Maximum shear elastic strain for aluminum alloy

5.3.3 Maximum shear stress for aluminum alloy

The aluminum alloy frame of a quadcopter was subjected to a uniform force of 4.905 Newton's, resulting in a total deformation of 1.9787e-006 m as shown in Fig 10. The material's maximum shear elastic strain and stress were measured, providing insights into its structural response, flexibility, and with standability for quadcopter frame construction.

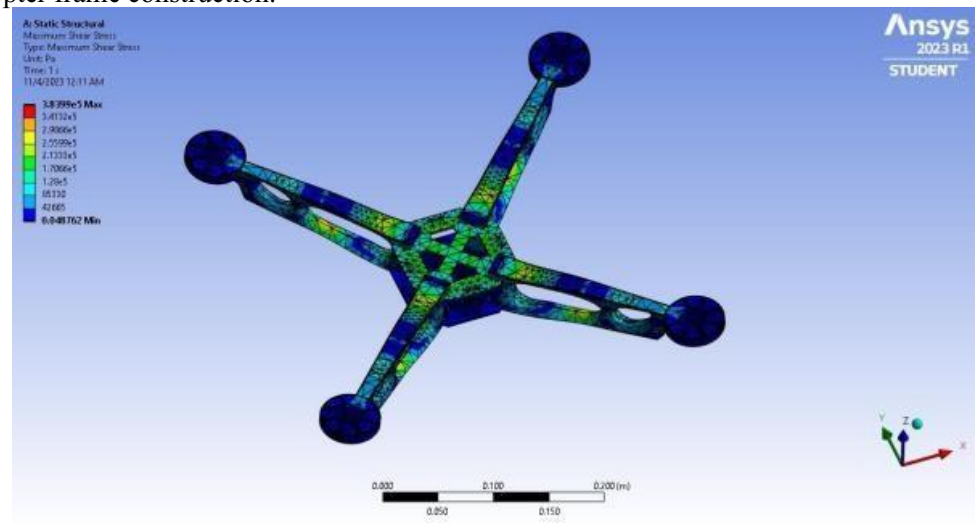

Fig 10. Maximum shear stress for aluminum alloy

5.4 Results for Plastic

5.4.1 Total deformation for plastic

The plastic frame of a quadcopter underwent a uniform force of 4.905 Newton's, resulting in a total deformation of 3.166e-006 m Fig 11., indicating its flexibility and structural performance. This higher deformation may affect its suitability for quadcopter design.

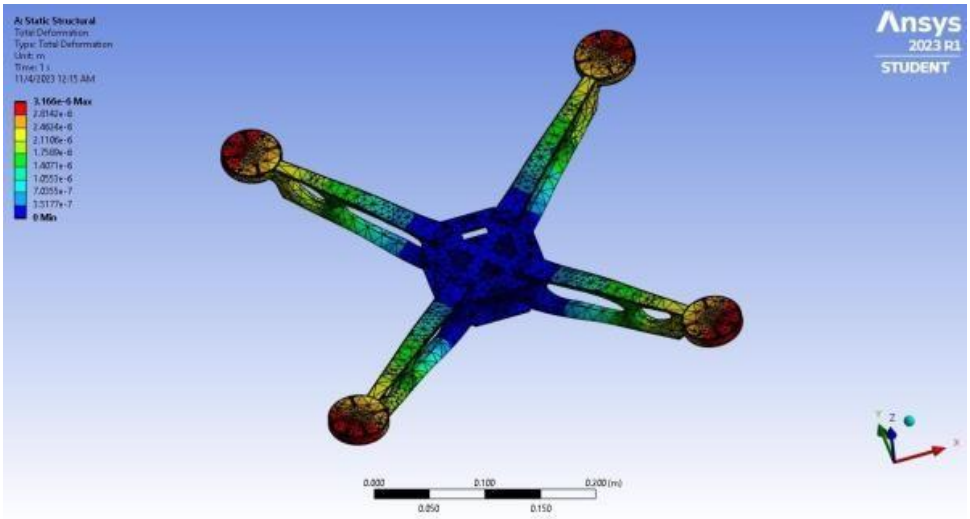

Fig 11. Total deformation for plastic

5.4.2 Maximum shear stress for plastic

The plastic quadcopter frame underwent a uniform force of 4.905 Newton's, resulting in a total deformation of 3.166e-006 meters and a maximum shear elastic strain of 7.9869e-006 m/m, indicating its ability to withstand shearing forces and deformation under load as shown in Fig 12.

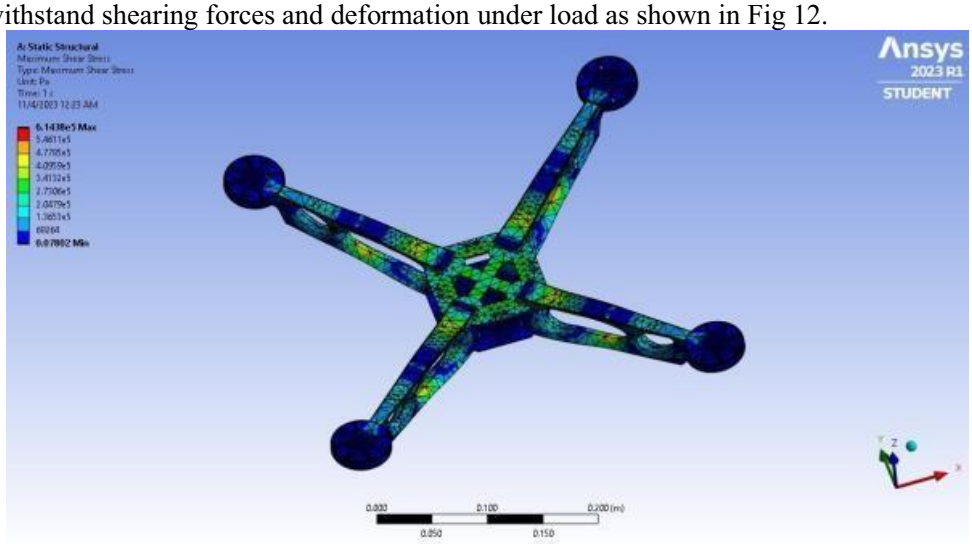

Fig 12. Maximum shear stress for plastic

5.5 Glass Fiber

5.5.1 Total deformation for Glass Fiber

The quadcopter frame's glass fiber frame underwent auniform force of 4.905 Newton's, resulting in a total deformation of 2.3745e-006 m as shown in Fig 13. This deformation value is crucial for assessing structural performance, suggesting a balance between flexibility and rigidity, making it suitable for quadcopter frame construction.

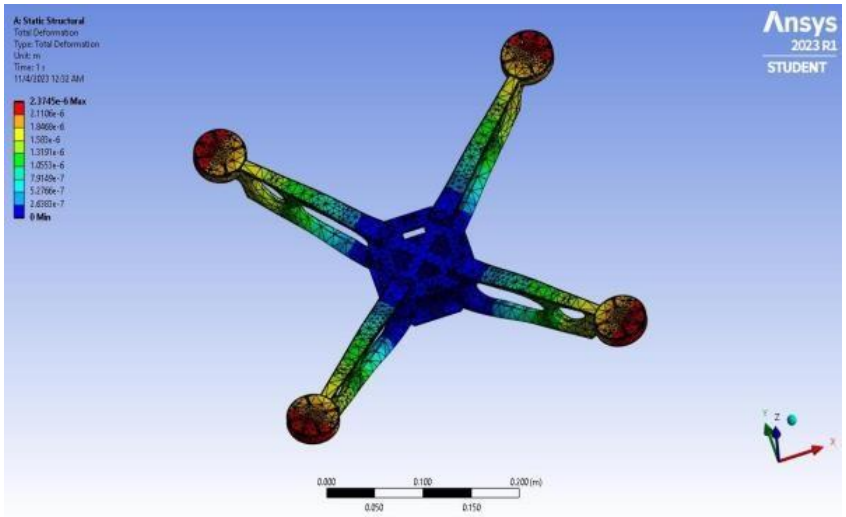

Fig 13. Total deformation for Glass Fiber

5.5.2 Maximum shear elastic strain for Glass Fiber

The quadcopter frame's glass fiber frame underwent uniform force application, resulting in a total deformation of 2.3745e-006 and a maximum shear elastic strain of 5.9902e-006 as shown in Fig 14, indicating its ability to withstand shearing forces and respond to deformation under load, a balance between flexibility and rigidity.

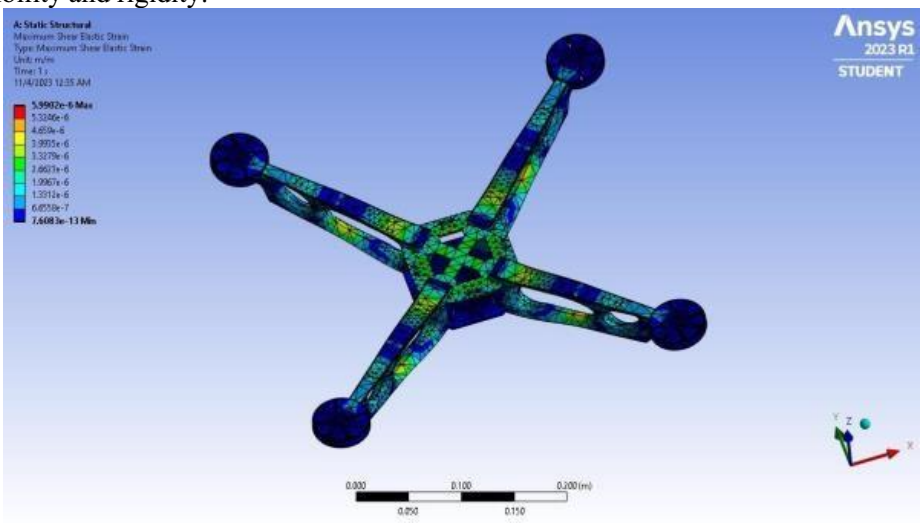

Fig 14. Maximum shear elastic strain for Glass Fiber

5.5.3 Maximum shear stress for Glass Fiber

The quadcopter frame's glass fiber material withstands shearing forces and deformation under load, exhibitinga balance between flexibility and rigidity. A uniform force of 4.905 Newton's applied to all four sides resulted in a total deformation of 2.3745e-006 m as shown in Fig 15.The material's maximum shear elastic strain and stress reached 4.6078e+005 mm, making it a suitable choice for quadcopter frame construction.

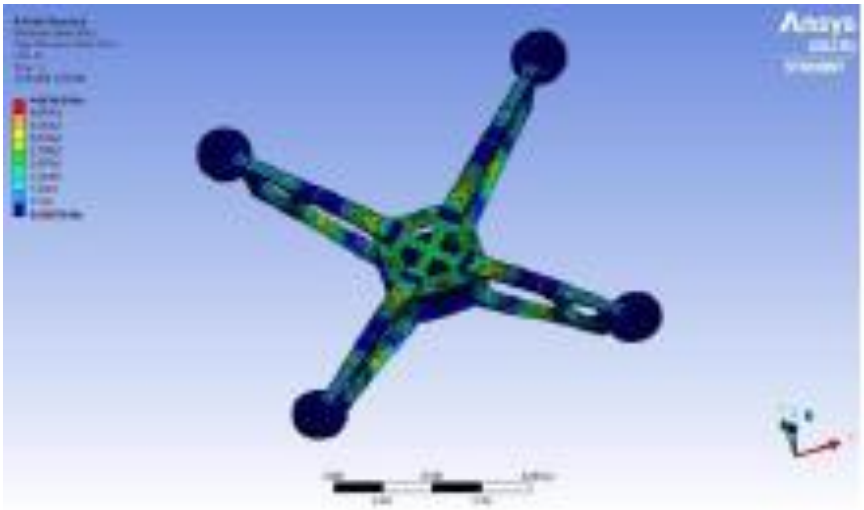

Fig 15. *Maximum shear stress for Glass Fiber*

5.6 Frame Material Comparison

The study compares four materials for quadcopter frame construction, including carbon fiber, aluminum alloy, plastic, and glass fiber. The results show that carbon fiber and aluminum alloy exhibit lower deformations, while plastic and glass fiber show higher deformations and significant differences in shear elastic strain and shear stress. This information helps in selecting the most suitable material for quadcopter frame construction based on specific project requirements.

The displacement analysis reveals that carbon fiber exhibits minimal deflection at motor mounting points, which is crucial for quadcopter applications. This ensures stability and precise alignment, even when subjected to dynamic forces generated by the motors. Carbon fiber's exceptional strength-to-weight ratio allows it to withstand various loads with minimal deformation, making it ideal for applications where structural robustness is paramount.

The suitability of carbon fiber for load-bearing is also a crucial factor, as it ensures the frame can support the weight of the quadcopter and any additional equipment without compromising structural integrity. This suitability significantly contributes to the overall success of the quadcopter in terms of stability, control, and performance.

Conclusions

It is evident that carbon fiber as the frame material has a positive impact on quadcopter performance. Its exceptional strength-to-weight ratio, minimal deflection, and ability to endure higher loads with minimal deformation significantly enhance the quadcopter's stability, control, and reliability. Overall, carbon fiber's suitability for demanding quadcopter applications is a strategic decision that positively influences the quadcopter's overall performance.

The study reveals that carbon fiber is the preferred material for load-bearing applications, such as quadcopters, due to its exceptional strength-to-weight ratio. This material offers stability and precision, with minimal deflection at motor mounting points ensuring reliability and performance. Carbon fiber's ability to withstand higher loads with minimal deformation also enhances structural integrity and quadcopter performance.

The study's recommendations for frame material selection align with these findings, emphasizing the significant impact of selecting carbon fiber as the frame material. This choice optimizes quadcopter performance, ensuring stability, control, and reliability in demanding operational scenarios.

The structural integrity of the frame is crucial for quadcopter operation. Carbon fiber's exceptional strength-to-weight ratio minimizes the risk of structural failure, even in challenging operational

conditions. The minimal deflection observed in carbon fiber frames enhances structural stability, improving control and precision in maneuvers.
The load-bearing capacity of carbon fiber is also crucial for ensuring structural integrity. The study's significance lies in its implications for engineering and design, particularly in aerospace and robotics. By comparing and recommending carbon fiber over other materials, the study contributes to the advancement of structural design across various applications, optimizing performance while maintaining structural integrity.

Future Study:
The process of enhancing a drone's flight capabilities involves a thorough analysis and optimization of the system, identifying weaknesses and making incremental improvements. This involves a thorough testing plan covering functionality, performance, and security, as well as validation against industry standards and user feedback. The integration of high- resolution cameras, which are crucial for aerial photography, surveying, or monitoring, is another crucial step. The drone's hardware and software should be compatible with the new cameras, and efficient image processing and data storage solutions should be implemented. The flight capabilities can be improved through hardware and software enhancements, such as motors, sensors, and propellers, fine-tuning flight control algorithms, and implementing safety features and fail-safes. Regular testing and validation of these enhancements are essential to ensure safety and performance standards are met, leading to a morereliable and capable system.

References
[1] N. Muralidharan, V.G. Pratheep, A. Shanmugam, A. Hariram, P. Dinesh, B. Visnu, Structural analysis of mini drone developed using 3D printing technique, Materials Today: Proceedings, Volume 46, Part 17, 2021, Pages 8748-8752, ISSN 2214-7853
[2] Abhinava Bharat, G, Nandini, AS, & Prasad, MJ. "Generative Design of a Quad-Copter Frame." Proceedings of the ASME 2021 Conference on Smart Materials, Adaptive Structures and Intelligent Systems. ASME 2021 Conference on Smart Materials, Adaptive Structures and Intelligent Systems. Virtual, online. September 14–15, 2021. V001T05A004. ASME. https://doi.org/10.1115/SMASIS2021-67487
[3] Mostafa, Khaled Hassan, Ayman Shehata Thabet, and Abdelrady Okasha Elnady. "Design and Manufacturing of X-Shape Quadcopter." (2021).
[4] Parandha, Sai Mallikarjun, and Zheng Li. "Design and analysis of 3d printed quadrotor frame." International Advanced Research Journal in Science, Engineering and Technology 5.4 (2018): 66-73.
[5] Patel, Brijesh, R. P. Sukhija, and R. P. S. Kumar. "Structural analysis of arm of multicopter with various loads." International Journal of Emerging Technology and Advanced Engineering 8.4 (2018): 215-223.
[6] Abazari, Amirali. Design, fabrication, and soft impact modeling and simulation of a collision resilient foldable micro quadcopter. Diss. Bilkent Universitesi (Turkey), 2022.
[7] Rahul Singh, Rajeev Kumar, Abhishek Mishra, Anshul Agarwal, Structural Analysis of Quadcopter Frame, Materials Today Proceedings, Vol. 22, Part 4, pp. 3320-3329, 2020, https://doi.org/10.1016/j.matpr.2020.03.295
[8] K. Venkatesan, K. Ramanathan, R. Vijayanandh, et al., Comparative structural analysis of advanced multi- layer composite materials, Materials Today: Proceedings, Volume 27, Part 3, 2020, pp. 2673-2687, https://doi.org/10.1016/j.matpr.2019.11.247
[9] K. Naveen Kumar, R. Vijayanandh, G. Raj Kumar, B. Sanjeev, Hariharan Balachander and S. Guru Prasad, Comparative Approaches for Fatigue Life Estimation of Aluminium Alloy for Aerospace Applications, Int. J. Vehicle Structures & Systems, 10(4), 282-286, 2018, doi: 10.4273/ijvss.10.4.11
[10] Vijayanandh R, Venkatesan K, Ramesh M, Raj Kumar G, Senthil Kumar M, Optimization of Orientation of Carbon Fiber Reinforced Polymer Based On Structural Analysis, International

Journal of Scientific & Technology Research, ISSN 2277-8616, Volume 8, Issue 11, pp. 3020-3029, 2019.

[11] Ramesh M, Vijayanandh R, Raj Kumar G, Vijayakumar Mathaiyan, P Jagadeeshwaran, Senthil Kumar M, Comparative Structural Analysis of Various Composite Materials based Unmanned Aerial Vehicle's Propeller by using Advanced Methodologies, IOP Conf. Series: Materials Science and Engineering, 1017, 012032, 1-10, 2021, doi:10.1088/1757- 899X/1017/1/012032

[12] Anamika Bhandari, Faraz Ahmad, Pushpendra Kumar, Pravin P. Patil, Design and Vibration Characteristics Analysis of Quadcopter Body Frame, International Journal of Applied Engineering Research, Vol. 14, No. 9, pp. 66 - 70, 2019.

[13] Bright, Jerrin, et al. "Optimization of quadcopter frame using generative design and comparison with DJI F450 drone frame." IOP Conference Series: Materials Science and Engineering. Vol. 1012. No. 1. IOP Publishing, 2021.

[14] Ahmed, MD Faiyaz, Mohd Nayab Zafar, and J. C. Mohanta. "Modeling and analysis of quadcopter F450 frame." 2020 international conference on contemporary computing and applications (IC3A). IEEE, 2020.

[15] Kalyan, Chokkarapu Sai, Mudumbai Srujana, A. Nikhil Reddy, and P. Pavan. "Design and Static Structural Analysis of a Quadcopter."

[16] Daud, Mohd Ehsanul Hafizi, Mohd Shariff Ammoo, Iskandar Shah Ishak, and Shabudin Mat. "Design and Structural Analysis of a Quadrotor." Jurnal Mekanikal (2018).

[17] Elmeseiry, Nourhan, et al. "Design and analysis of a reliable quadcopter UAV for wireless communication purposes." 2021 3rd Novel Intelligent and Leading Emerging Sciences Conference (NILES). IEEE, 2021.

[18] Tatale, Omkar, Nitinkumar Anekar, Supriya Phatak, and Suraj Sarkale. "Quadcopter: design, construction and testing." International Journal for Research in Engineering Application & Management 4 (2018): 1-7.

[19] Pilli, Aren, Bhuvanesh Pabbathi, Yeshwanth Gokarakonda, Thota Pramod, Mohammad Sami, Venkata Nori, and Prakash Jadhav. "Structural analysis of agricultural drone." In AIP Conference Proceedings, vol. 2788, no. 1. AIP Publishing, 2023.

[20] Sreeramoju, Srawanee, and M. Sreenivasa Rao. "Design and Analysis of Quad Copter Chassis Using Shape Optimization Technique.

Journal of Physics: Conference Series

PURPOSE-LED PUBLISHING™

PAPER • **OPEN ACCESS**

Mechanical Properties of Natural Composites: Hemp Fiber and Polypropylene Resin

To cite this article: G Pavani and A Shashidhar 2024 *J. Phys.: Conf. Ser.* **2837** 012002

View the article online for updates and enhancements.

You may also like

- Behaviour of Fly Ash and Silica Fume based Composite Fiber (Glass and Polypropylene) reinforced High-Performance Concrete under Acid Attack
Sachin Patil, H. M. Somasekharaiah, H. Sudarsana Rao et al.
- Physical and Mechanical Properties of Self-Compacting Concrete (SCC) with Pineapple Leaf Fibre and Polypropylene
Hanoora Sarah Anindita Hendrian, Saloma, Hanafiah et al.
- Investigation of Mechanical Properties of M-sand concrete with Polypropylene and Steel fibers
Naga Venkata Vamsi Krishna Tadiboina and U V Narayana Rao

This content was downloaded from IP address 106.0.37.90 on 21/10/2024 at 11:25

Journal of Physics: Conference Series **2837** (2024) 012002 doi:10.1088/1742-6596/2837/1/012002

Mechanical Properties of Natural Composites: Hemp Fiber and Polypropylene Resin

G Pavani [1], A Shashidhar [1]

[1] Department of Aeronautical Engineering, MLR Institute of Technology, Hyderabad, Telangana, India.

*Corresponding author email: aadhyasreegopi1@gmail.com

Abstract. Natural composite is a material, formed by combining natural fibers, such as hemp or flax, with a synthetic matrix, often composed of polymers like Epoxy Resin, Polyester Resin, Polyethylene Resin, Polypropylene Resin and Polypropylene Resin. The natural fibers contribute strength and environmental sustainability, while the synthetic matrix enhances durability and structural integrity, resulting a versatile composite material for various applications and unique properties of both components for improved overall performance. These composites are considered as environmentally friendly alternatives to traditional materials due to the renewable nature of hemp and the recyclability of polypropylene. The focus is on understanding how these materials behave when combined, with their mechanical properties and materials respond to applied forces for assessing their structural performance. In this research, computational analysis is done by using ANSYS 2024R1 software is to investigate the mechanical properties of the hemp fiber and polypropylene resin combine composite. The simulation involves setting up the virtual environment, applying boundary conditions, and running simulations to predict the behaviour of the composite material respond to applied forces. Although no manufacturing process is undertaken in this study, the computational analysis allows us to gain insights into how the materials might interact and perform in real-world applications.

Keywords: Natural composites, hemp fiber, polypropylene resin, computational analysis, ANSYS 2024R1, mechanical properties, structural performance, environmental sustainability, renewable materials, recyclability.

1. Introduction

Natural composite materials that are sustainable are becoming more and more popular. Materials that are not only durable and dependable but also environmentally friendly are gaining popularity. The usage of natural composites—such as those derived from plant fibers and environmentally benign resins—is growing in popularity as a means of producing robust and adaptable materials without heavily depending on conventional, more polluting sources.[1-5] Composite materials hold great promise when natural fibers like hemp are combined with synthetic resins like polypropylene. Plant-based hemp fibers are strong and environmentally friendly, promoting sustainability. Conversely, synthetic resin

Content from this work may be used under the terms of the Creative Commons Attribution 4.0 licence. Any further distribution of this work must maintain attribution to the author(s) and the title of the work, journal citation and DOI.
Published under licence by IOP Publishing Ltd

polypropylene increases strength and adaptability. Sustainable natural composite materials are becoming more and more popular. Environmentally friendly materials are becoming more and more appealing to people in addition to being robust and dependable. [6] Natural composites are becoming more popular because they provide a means of producing robust and adaptable materials without heavily depending on conventional, more polluting sources. Examples of these materials include those constructed from plant fibers and environmentally friendly resins.[7] Innovative possibilities in composite materials are created when natural fibers, such as hemp, are combined with synthetic resins, such as polypropylene. The plant-based material known as hemp offers durability and environmental friendliness, promoting sustainability. On the other hand, synthetic resin polypropylene increases adaptability and durability.

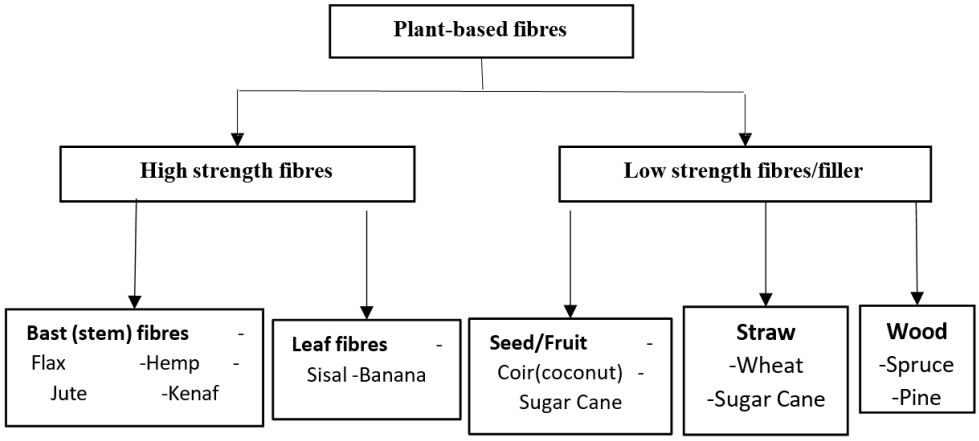

Figure 1. Plant fibre types [8]

2 Materials and Method:

2.1 Hemp Fibers:

Hemp fibers are produced from the stalk of the hemp plant and contain several unique properties. Their main claim to fame is their incredible strength.[9] Because these fibers are strong and able to withstand a great deal of tension, they are helpful in circumstances where durability is crucial. Hemp fibers are more versatile because they are lightweight as well. They are also biodegradable, which supports the sustainability of the environment. [8] Hemp fibers are known to be used to make a wide variety of textiles and goods. The mechanical properties of hemp fiber are Mechanical Characteristics Density is 1.35 g/cm^3, Poisson ratio is 0.4, and Youngs modulus, E, is 70 Gpa.

2.2 Polypropylene:

The synthetic resin polypropylene is utilized extensively in many different industries due to its characteristics. Durability is one of its main qualities [10]. Because of its resilience to deterioration, polypropylene prolongs the life of materials that include it.[11] It is also well-known for being chemically resistant, which makes it appropriate for uses where exposure to various contaminants is a problem.[12] Because it is lightweight, polypropylene is more appealing to businesses where weight is an important consideration. Moreover, it is a thermoplastic, which allows for flexibility in manufacturing processes by allowing it to be molded and reshaped when heated. As a matrix resin, polypropylene has the following mechanical properties: density is 0.92 g/cm^3, Youngs modulus, E is 1.6 Gpa, and Poisson ratio is 0.4.

2.3 Compatibility:

When these hemp and polypropylene fibers are mixed together to create a composite material, their individual qualities enhance one another's qualities [13]. Polypropylene offers strength and moldability, whereas hemp fibers offer environmental advantages and strength [14]. The resultant composite is a viable choice for a number of applications since it can provide a well-balanced mix of strength, flexibility, and sustainability [15].

Natural fibre
- Strength
- Eco friendly

Synthetic resin
- Durability
- Moldability

Natural composite
- Strength
- Flexibility
- Sustainability

2.4 Environmental Considerations:

Hemp is a renewable resource with a lower environmental impact Because it grows quickly and requires few pesticides. Despite being synthetic, polypropylene has an eco-friendly profile because it is recyclable.[16] Together, these materials form a composite that satisfies the growing need across multiple industries for sustainable substitutes.

2.5 Geometry and boundary conditions:

Examine a thin, rectangular, stiffened plane panel with dimensions of 1000 mm in width, 2000 mm in length, and 10 mm in thickness, as depicted in the figure.

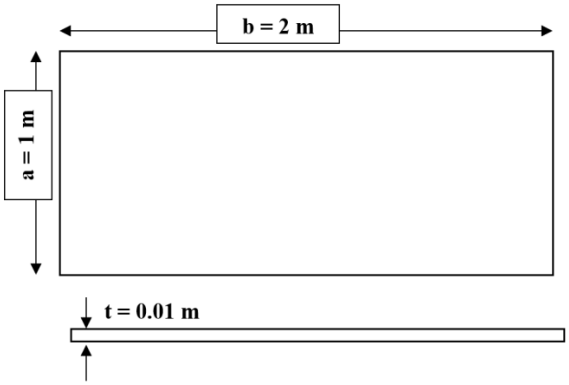

Figure 2. Rectangular stiffened plane panel

Loading condition:

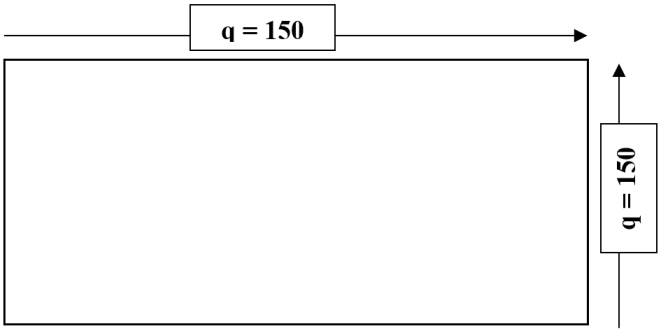

Figure 3. Load applied in Rectangular stiffened plane panel

Symmetric Boundary conditions:

At top and bottom,	at left and right,
displacement of z = 0	displacement of z = 0
Rotation of y = 0	Rotation of x = 0

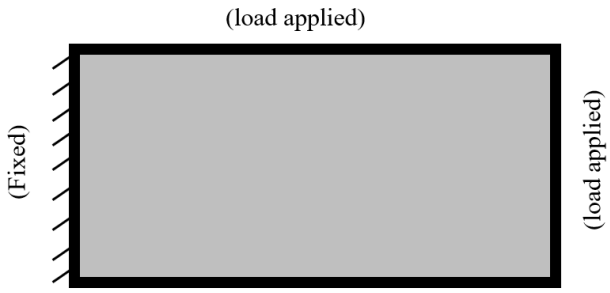

Figure 4. Boundary conditions applied in Rectangular stiffened plane panel

2.6 Computational Analysis (Ansys):

Methodology

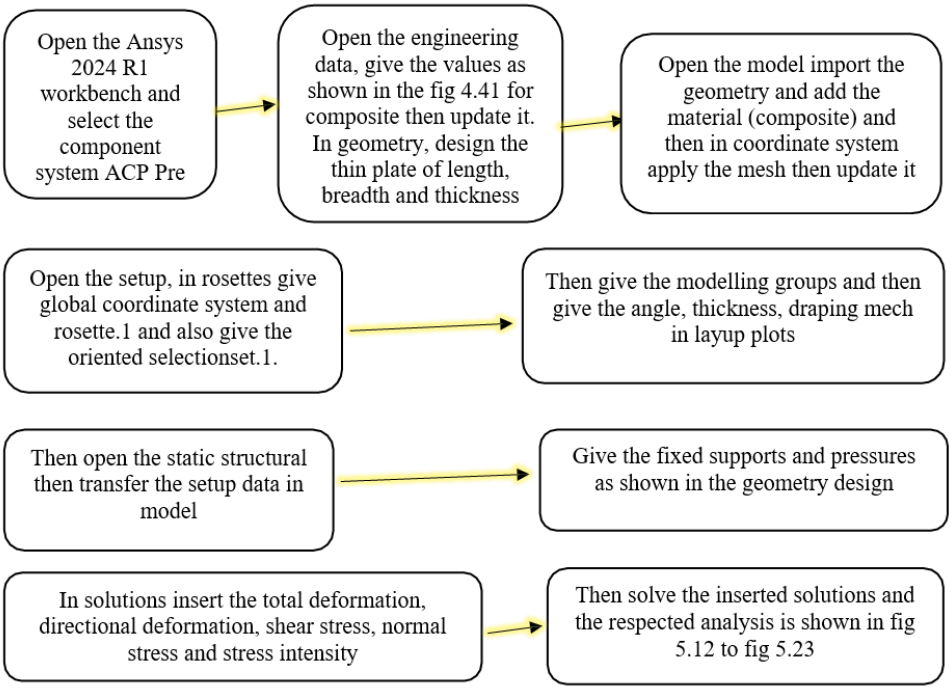

Result:

2.7 Acp Analysis simulation (Deformation)

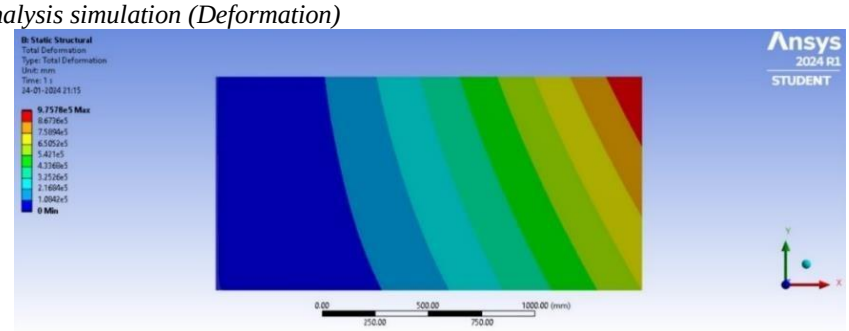

Figure 5. maximum deformation resulting from pressure or load is indicated by the red color orientation as Y axis using Ansys is depicted

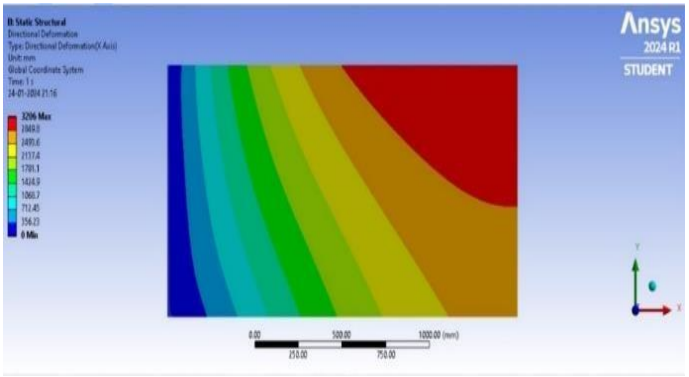

Figure 6. thin plate directed deformation orientation as X axis is depicted

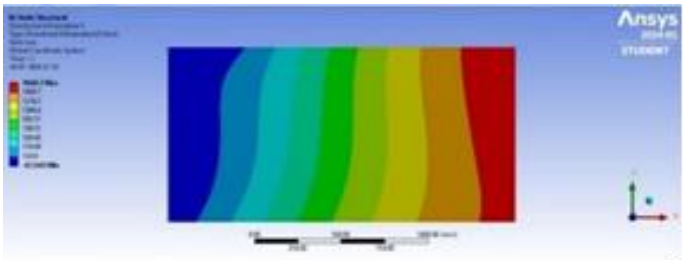

Figure 7. thin plate directed deformation orientation as Y axis using Ansys is depicted

- As indicated in figure, the plane panel's left edge is fixed, and loads are given to its top and right edges.The maximum deformation resulting from pressure or load is indicated by the red color in figure 5 of the thin plate total deformation utilizing the Ansys work bench. This maximum deformation is 20 Mpa W = 9.7578e5mm.

- If the X-axis is selected as the orientation for the direction deformation type, the deformation will differ somewhat from the total deformation as depicted in figure. The thin plate directed deformation orientation as X axis is depicted in figure 6 using Ansys. The maximum deformation resulting from pressure or load is indicated by the red color, and it is 15 Mpa Wxy = 3206mm (according to Ansys).

- If the Y-axis is selected for the direction deformation type, the deformation will differ somewhat from the total deformation as depicted in figure. The thin plate directed deformation orientation as Y axis using Ansys is depicted in figure 7. The maximum deformation resulting from pressure or load is indicated by the red color, and it is 15 Mpa Wyz = 1660.7mm (according to Ansys).

2.8 Acp Analysis simulation (Stress)

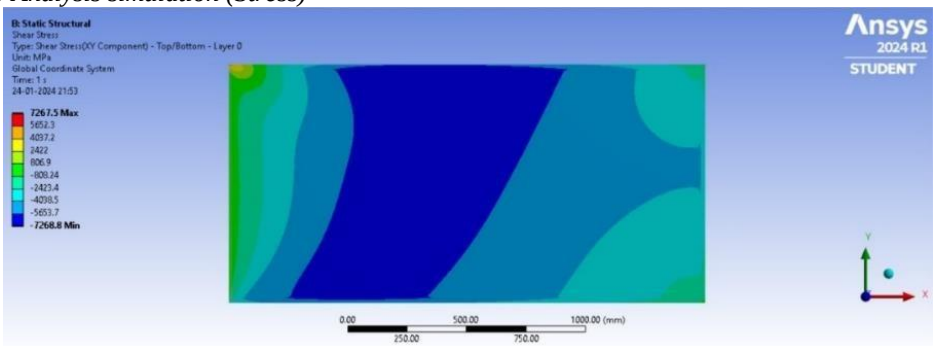

Figure 8. maximum shear stress resulting from pressure or load is indicated by the red color

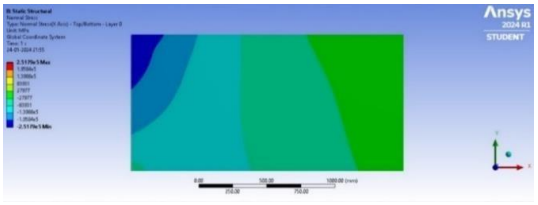

Figure 9. the normal stress (x component) is provided for the plane panel

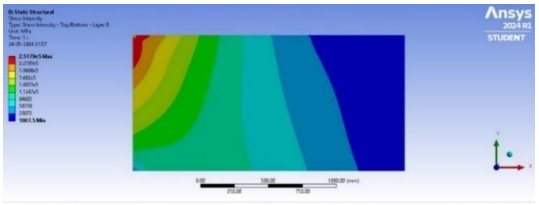

Figure 10. maximal stress intensity caused by pressure or load

- As seen in figure, the shear stress (xy component) is provided for the plane panel's top edge, right edge, and left edge fixed and applied load. The maximum shear stress resulting from pressure or load is indicated by the red color in Figure 8. Shear stress (xy component) using Ansys, and it is 15 Mpa τxy= 7267.5 mm (from Ansys).

- As seen in figure, the normal stress (x component) is provided for the plane panel's left edge fixed and applied load in the top edge and right edge. As depicted in figure 9. The highest normal stress resulting from pressure or load is indicated by the red color in the normal stress (x component) using Ansys. This value is 15 Mpa τx = 2.5179e5 mm (according to Ansys).

- According to figure, the stress intensity is provided for the plane panel's left edge fixed and applied load in the top edge and right edge. The maximal stress intensity caused by pressure or load is indicated by the red color in Figure 10. Stress intensity using Ansys, and it is equal to 15 Mpa τi = 2.5179e5 mm (according to Ansys)

Table 1. Orthotropic Elasticity Properties of combine composite:

Properties	Values	Units
E1	49480	MPa
E2	9679	MPa
E3	2937	MPa
G12	2937	MPa
G23	3301.3	MPa
G31	2937	MPa
μ1	0.4	-
μ2	0.39999	-
μ3	0.46615	-
Density, $\boldsymbol{\rho}$	$1.221e^{09}$	t mm^{-3}

2.9 Mesh of composite:

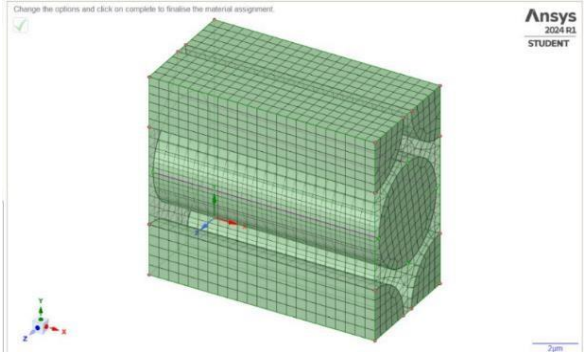

Figure 10. Mesh of green composite

3 Discussion:

Natural composites with a compelling combination of mechanical qualities include those made of hemp fiber and polypropylene resin. Because of its natural stiffness and strength, hemp fiber strengthens the composite, increasing its tensile and flexural strength while also lowering its weight. Furthermore, hemp fibers have a high level of resistance to environmental deterioration, which increases the composite's long-term endurance. The resulting composite strikes a balance between stiffness and toughness when mixed with polypropylene resin, which offers cohesion and flexibility. This makes it appropriate for a variety of applications. In addition to improving the mechanical qualities, the complementary relationship between hemp fiber and polypropylene resin provides a greener substitute for traditional synthetic composites, addressing sustainability issues in material development and production.

4 Conclusion:

By using computational analysis as a sophisticated tool, we are able to forecast the performance of the hemp fiber and polypropylene composite without the need to create physical prototypes. This helps us create a material with the best possible strength, durability, and environmental friendliness while also saving time and resources. It helps us make more informed and environmentally friendly decisions by providing a glimpse into the future of materials.Conducting practical studies would be beneficial for future research in order to verify our computational results and the hemp fiber and polypropylene composite's real-world performance. To confirm the accuracy of our forecasts, this may entail producing prototypes and putting them through various tests.

5 References

[1] Aziz, S. H. and Ansell, M. P. (2004a). The effect of alkalization and fibre alignment on the mechanical and thermal properties of kenaf and hemp bast fibre composites: Part 1 - polyester resin matrix. Compos. Soi. Technol., 64,12

[2] Bai, S. L., Li, R. K. Y., Wu, L. C. M., Zeng, H. M. and Mai, Y. W. (1998). Tensile failure mechanisnris of sisal fibers in composites. J. Mater. Sci. Lett, 17, 18

[3] Bos, H. L., Van den Oever, M. J. A., Peters O. C. J. J. (2002) Tensile and compressive properties of flax fibres for natural fibre reinforced composites. J. Mater. Sci., 37, 16

[4] Chand, N., Sood, S., Rohatgi, P.K. and Satyanarayana, K. G. (1984). Resources, structure, properties and uses of natural fibres of Madhya Pradesh. J. Sci. Ind. Research, 43, 48

[5] Contat-Rodrigo, L. and Ribes Greus, A. (2002). Biodégradation studies of LDPE filled with biodegradable additives: Morphological changes. 1. J. Appi Polym. Sci., 83, 16

[6] David, C., De Kesel, C., Lefebvre, F. and Weiland, M. (1994). The biodegradation of polymers: Recent results. Angew. Makromol. Chem., 216 (1),

[7] llison, G. C., Mcnaught, R. and Eddleston, E. P. (2000). The use of natural fibres in nonwoven structures for applications as automotive component substrates. Research and Development Report prepared for the Ministry of Agriculture, Fisheries and Food, UK

[8] Ruys, D., Crosky, A. and Evans, W. J. (2002). Natural Bast Fibre Structure. Int. J. Mater. Prod. Tec., 17 (1/2)

[9] H.,Soumya, G., Bhavana, P.H.S., Chandrashekhar, S., Anand, A.V. Mechanical properties of green composites with hemp/sisal fiber and novolac resi Porwal, AIP Conference Proceedings, 2023, 2492, 040009.

[10] Suardana NPG, Piao Y, Lim JK. Mechanical properties of hemp fibers and hemp/pp composites: effects of chemical surface treatment. Mater Phys Mech 2011;11.

[11] Khan, M.A., Bhanuprakash, L., Anand, A.V. Magnesium matrix reinforced with zirconium, garnet and graphite for improved mechanical properties AIP Conference Proceedings, 2023, 2492, 040077.

[12] Evans, W. J., Isaac, D. H., Suddell, B. C. and Crosky, A. (2002). Natural fibres and their composites: A global perspective. In Proceedings of the 23rd Riso Int. Symposium on Materials Science: Sustainable Natural and Polymeric Composites - Science and Technology, Denmark 2002.

114.
[13] Kellersztein I, Dotan A. Chemical surface modification of wheat straw fibers for polypropylene reinforcement. Polym Compos 2016;37:21.
[14] Notta-Cuvier D, Lauro F, Bennani B, Nciri M. Impact of natural variability of flax fibres properties on mechanical behaviour of short-flax-fibre-reinforced polypropylene. J Mater Sci 2016;51:29.
[15] M.U., Sudha, S., Reddy, Y.Y., Sahasrarchith, N., Anand, A.V. Mechanical properties of hybrid composite sandwich structure with sisal and e glass fiber Sree, AIP Conference Proceedings, 2023, 2492, 040008.
[16] Gandhi, S. and Lyon, R. E. (1998). Health hazards of carbon fibers from burning composite materials. In Proceedings of the International SAMPE Symposium and Exhibition: Materials and Process Affordability - Keys to the Future

Journal Pre-proof

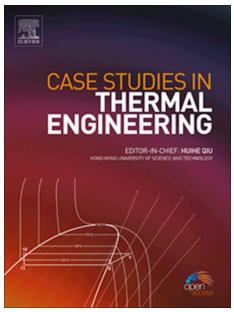

Significance of Darcy–Forchheimer Flow Casson Fluid Past a Non-Permeable Curved Stretching Sheet with the Impacts of Heat and Mass Transfer

Kavita Jat, Kalpna Sharma, Prasun Choudhary, Pooja Soni, Rifaqat Ali, M. Ganesh

PII: S2214-157X(24)00938-9

DOI: https://doi.org/10.1016/j.csite.2024.104907

Reference: CSITE 104907

To appear in: *Case Studies in Thermal Engineering*

Received Date: 20 May 2024

Revised Date: 3 July 2024

Accepted Date: 30 July 2024

Please cite this article as: K. Jat, K. Sharma, P. Choudhary, P. Soni, R. Ali, M. Ganesh, Significance of Darcy–Forchheimer Flow Casson Fluid Past a Non-Permeable Curved Stretching Sheet with the Impacts of Heat and Mass Transfer, *Case Studies in Thermal Engineering*, https://doi.org/10.1016/j.csite.2024.104907.

This is a PDF file of an article that has undergone enhancements after acceptance, such as the addition of a cover page and metadata, and formatting for readability, but it is not yet the definitive version of record. This version will undergo additional copyediting, typesetting and review before it is published in its final form, but we are providing this version to give early visibility of the article. Please note that, during the production process, errors may be discovered which could affect the content, and all legal disclaimers that apply to the journal pertain.

© 2024 Published by Elsevier Ltd.

Journal Pre-proof

Significance of Darcy–Forchheimer Flow Casson Fluid Past a Non-Permeable Curved Stretching Sheet with the Impacts of Heat and Mass Transfer

Kavita Jat[1], Kalpna Sharma[1,*], Prasun Choudhary[2,*], Pooja Soni[1], Rifaqat Ali[3,] and M. Ganesh[4]

[1]*Department of Mathematics and Statistics, Manipal University Jaipur, Jaipur, Rajasthan 303007, India.; kavitakumari3299@gmail.com and kalp_aali@yahoo.co.in; poojasoni4001@gmail.com*

[2]*Department of Mathematics, University of Rajasthan, Jaipur, Rajasthan 303002, India.; prasun.iimet@gmail.com*

[3]*Department of Mathematics, Applied College in Mohayil Asir, King Khalid University, Muhayil 61413, Abha, Saudi Arabia.; rrafat@kku.edu.sa*

[4] *Department of Aeronautical Engineering, MLR Institute of Technology, Hyderabad, Telangana, India.; ganesh.manikonda@gmail.com*

[*]*Corresponding author*

Journal Pre-proof

Abstract: Casson fluid flow based on a curved surface has been mathematically modeled using Brownian motion and the Darcy-Forchheimer equation of porosity. Similarity variables are applied to convert flow-anchored partial differential equations into basic ordinary differential equations. The MATLAB solver "Bvp4c" is utilized to derive numerical responses for the problem under consideration. During the numerical approach, all parameters have been set to their values based on reviewed literatures and numerical solutions for all flow fields have been obtained against the concerned parameters. Additionally, a variety of graphs are created utilizing numerical extractions to discuss the results. The curvature parameter ($K = 1.5, 2.5, 3.5, 4.5$) results in an improvement in velocity distribution ($f'(\eta = 1) = 0.32564, 0.360142, 0.378247, 0.385401$). The reason is that for higher values of the curvature parameter, the radius of a curved sheet decreases. Hence, a smaller region of sheet will be in contact, which produces a small amount of resistance towards fluid particles, so that the velocity profiles show an enhancement. Increasing inputs of Forchheimer number imply stronger inertial effects and it introduce an additional resistance to flow that's why fluid

velocity decreased. Additionally, for a curved stretched sheet, a higher drag force is required compared to a flat plate because curved sheet has a larger surface area while flat plate has a minimal surface area in contact with the fluid.

Keywords: Casson fluid, Curved surface, Darcy Forchheimer flow, Brownian motion.

Nomenclature

Bi_1	Thermal Biot number
Bi_2	Solutal Biot number
Br	Brinkmann number
c	Stretching rate (s^{-1})
c_p	Specific heat ($Jkg^{-1}K^{-1}$)
C	Concentration (kgm^{-3})
C_b	Drag coefficient
C_∞	Free stream Concentration (kgm^{-3})
C_w	Concentration of fluid at sheet (kgm^{-3})
C_{fs}	Coefficient of local skin friction
Cr	Chemical reaction parameter
D_{Br}	Coefficient of Brownian diffusion (m^2s^{-1})
D_{Th}	Thermophoresis diffusion (m^2s^{-1})
Ec	Eckert number
Fr	Local Forchheimer parameter
Ha	Hartmann number
k_p	Constant permeability factor (m^2)
K	Curvature Parameter
K_1	Constant rate chemical reaction (s^{-1})
Nu_s	Local Nusselt number
p	Fluid Pressure (Nm^{-2})
R	Radius of curvature
Sh_s	Local Sherwood number
T	Temperature of fluid (K)
T_∞	Free stream temperature (K)
T_w	Temperature of sheet (K)
u_w	Velocity of the stretching sheet in s - direction (m^1s^{-1})
v	Fluid velocity in r -direction (m^1s^{-1})
Pr	Prandtl number
q_r	Radiative heat flux (W)
Rd	Radiation parameter
Re_s	Local Reynolds number
(r, s)	Curvilinear coordinates

Greek symbols:

η	Similarity transformation
κ	Thermal conductivity $\left(Wm^{-1}K^{-1}\right)$
k^*	Mean absorption coefficient (m^{-1})
ϕ	Dimensionless concentration
ψ	Stream function
ρ	Density of fluid (kgm^{-3})
ρc_p	Heat capacity ($Jm^{-3}K^{-1}$)
μ_B	Dynamic viscosity $\left(kgm^{-1}s^{-1}\right)$

Journal Pre-proof

P	Porous medium parameter	υ_B	Kinematic viscosity $\left(m^2 s^{-1}\right)$
P_1	Dimensionless Pressure	τ_{rs}	Shear wall stress $\left(Nm^{-2}\right)$
q_m	Wall mass flux $\left(kgm^{-2}s^{-1}\right)$	σ^*	Stefan-Boltzmann constant $(Wm^{-2}K^{-4})$
q_w	Wall heat flux $\left(Wm^{-2}\right)$		

1. Introduction

Casson fluid flow refers to the flow behavior of fluids referred by the Casson model. This model is a rheological model that is employed to characterize the flow of certain types of non-Newtonian fluids, specifically those with a force named yield stress. Variable viscosity is exhibited by non-Newtonian fluids based on the imposed stress or shear rate, in comparison with Newtonian fluids, which have a constant viscosity across all shear rates. This model is commonly used in the study of certain biological fluids, such as blood, and in industrial applications where yield stress is a significant factor in the fluid's behavior. Understanding the flow properties of Casson fluids is essential for various engineering and medical applications. Batra and Jena [1] presented an analysis in a curved tube with Casson fluid. Mukhopadhyay et al. [2] addressed about Casson fluid movement across stretched surface in context of time dependent flow. Anantha Kumar et al. [3] assessed the consequences of Casson fluid movement on an exponentially curved geometry. Amjad et al. [4] mentioned thermal study of micropolar nanofluid movement through a porous curved surface. Nagaraja and Gireesha [5] and Roja et al. [6] reported numerical research regarding Casson fluid flow through distinct geometries. Maity and Kundu [7] investigated Casson nanofluid movement past a curved surface in appearance of driven force. Aljuaydi et al. [8] offered numerical outcomes of ion slip and magnetic impacts for the movement of Casson fluid in the appearance of pore media, employing non-Fourier double diffusion concepts via ANNs (Artificial neural networks). Nadeem et al. [9] evaluated nanofluid simulation based on Reynolds of Casson fluid movement that transports exponential nanoparticles over a sheet. Mahabaleshwar et al. [10] explained how the radiation affects the movement of Casson nanofluid across a stretching geometry.

A curved surface in context of fluid flow and temperature distribution likely refers to a surface or boundary that is not flat but has a curved or contoured shape. This can be relevant in various engineering and scientific applications where fluid dynamics and heat transfer are considered. In fluid flow, curvature of a surface can affect the behavior of the fluid as it moves over or

around the curved object. The curvature can influence factors such as pressure distribution, velocity profiles, and the generation of vortices. Engineers and scientists study these effects to understand the aerodynamics of curved surfaces, which is crucial in designing efficient and aerodynamic structures, such as aircraft wings or car bodies. Murthy [11] examined consequences of flow characteristics on MHD movement of Casson fluid across a stretching surface with a curved contour. A report offered by Amjad et al. [12] talked about the impacts of Lorentz force on the flow of Casson nanofluid across a curved surface which was porous. The radiative Williamson fluid research across a stretchable surface was explored by Raza et al. [13]. Shi et al. [14] investigated computation for flow of micropolar fluid towards an exponential bended sheet utilizing an analytical approach named as Keller Box technique. The Phenomena of production of entropy and mixed convection movement of Casson fluid was published by Yusuf et al. [15] and Naveed et al. [16] past moving surfaces. Some numerical approaches were explored by Dawar et al. [17], Mumtaz et al. [18] and Nagaraja et al. [19] on curved surfaces to explore flow characteristics. Sakkaravarthi and Reddy [20] offered a comparative study in context of shape factors.

The Forchheimer equation is employed to model non-Darcy flow in spongy media, where the resistance to flow is not solely proportional to the square of the velocity, as in Darcy's law. This equation is particularly relevant in situations where inertial effects become significant, such as high flow velocities or the presence of complex geometries. In fluid dynamics, Darcy's law is often employed to justify fluid flow through porous media. Darcy's principle states that a decline in pressure across a porous substance is directly equal to the square of the velocity. However, this assumption breaks down under certain conditions, such as high flow velocities or in situations where the porous medium has complex geometries. The Forchheimer equation extends Darcy's law to account for additional inertial effects that become important under non-Darcy flow conditions. Examples include fluid flow in packed beds, filters, and porous media with irregular structures. Understanding non-Darcy flow is crucial in optimizing processes involving fluid flow through porous materials to improve accuracy in predictions and design. Using a finite elements methodology, Murali et al. [21] provided an explanation of Darcy Forchheimer equation for an uneven channel flow. Khan et al. [22] explored an analysis for modeling of micropolar ferrofluid slip flow with Darcy–Forchheimer concept at second order velocity. Gireesha et al. [23] analysed the implications of exponential heat production on the non-Darcy-Forchheimer movement of water-based carbon nanotubes caused by a curve-shaped stretching surface. Afterwards, Kumar et al. [24] and Raja et al. [25] explored two crucial

reports on Darcy Forchheimer flow. By utilizing cubic autocatalyzed chemical reactions, Wang et al. [26] improved entropy flow of Darcy-Forchheimer viscous fluid. Ali and Jubair [27] described the rheological aspects of hybrid nanofluid movement over a twisted slippery surface utilizing thermal emission and a heat source. A latest report on micropolar hybrid-nanofluid was discussed by Shah et al [28] to understand rotationally symmetric movement with melting heat transfer phenomena over a disk which is porous and rotating.

Brownian motion is a fundamental aspect of fluid dynamics, influencing particle dynamics, dispersion, diffusion, suspension stability, and various transport phenomena. Understanding and accounting for Brownian motion are crucial for accurately modeling and predicting about dynamics of particles in various fluid processes. Brownian motion regulates a major role in dispersion of small particles in a fluid. The random motion of particles due to Brownian motion promotes mixing and helps in achieving a more uniform distribution of particles within the fluid. Brownian motion is a manifestation of random thermal motion of particles. This random motion goes up to the diffusion of particles through a fluid. The diffusion coefficient is related to the intensity of Brownian motion and is crucial in predicting how particles spread and disperse in a fluid. In existence of Brownian motion, Abdel-Wahed et al. [29] analyzed flow implications past a surface with nonlinear velocity and variable thickness in nanofluids. Regarding the significance of velocity in the context of Brownian motion, Genthon [30] detailed its evolution. The utilization of nanofluid in channels by Saghir and Rahman [31] highlighted the thermophoretic consequences and Brownian motion as a two-phase model. Flow features taking thermally Brownian motion with different fluids and distinct flow geometries were researched by Tawade et al. [32], Alharbi et al. [33] and Khan et al. [34]. Sharma et al. [35] assessed the implications of thermophoresis features in their study on movement of nanofluid through a stretching Riga plate under convective conditions and zero nanoparticle mass flux.

In summary, Casson fluid models are often used to describe the flow of blood in arteries and veins. In environmental engineering, knowledge of curvature effects is vital for understanding and mitigating issues like sediment transport in rivers and erosion control. Curved buildings optimize natural light and ventilation, potentially reducing energy consumption for heating, cooling, and lighting.

1.1. *Novelty of current work*

Despite this, the above referenced literatures indicate that many reports on the flow and heat performance of two-phase models have been discussed utilizing various types of geometries and Newtonian fluids to check the dynamics of this model. In light of the extensive range of applications and possibilities associated with non-Newtonian fluids, we made the decision to assess the present fluid problem by utilizing the Casson fluid flow over a curved surface, choosing Darcy Forchheimer term both in momentum and energy equation. Hence, the key focus and contribution of the current study will be:

- What are the outputs by curvature parameter on all fluid profiles?
- What are the Casson fluid parameter's implications for the velocity field?
- How Forchheimer parameter affects velocity and temperature profiles?
- Consequences of thermal and mass Biot number on temperature and concentration field.
- Visualization of profiles of all three physical quantities with key parameters of flow problems.

1.2. *Outline of the current work*

To answer these research questions, our paper structured as:

- The authors developed a mathematical model in the section titled as "Mathematical Modeling".
- We developed a solution process in the section titled as "Method of solution".
- Validation of current work was provided in "Code validation" section.
- Findings and debate of the current work were summarized in section titled as "Result and discussion".
- "Conclusion" was used to conclude the discussed problem.
- Finally, future guidance of this analysis was included in section titled as "Future recommendations".

2. Mathematical modeling

2.1. *Flow description*

Journal Pre-proof

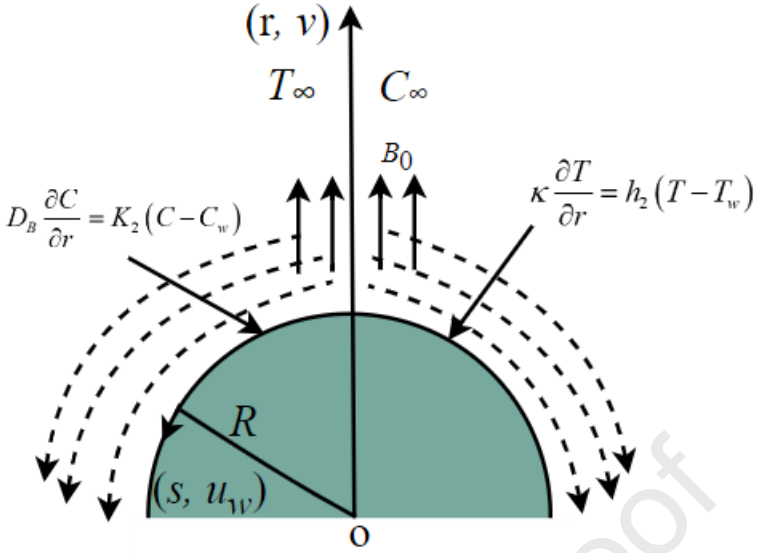

Fig. 1(a). Curved geometry of flow problem

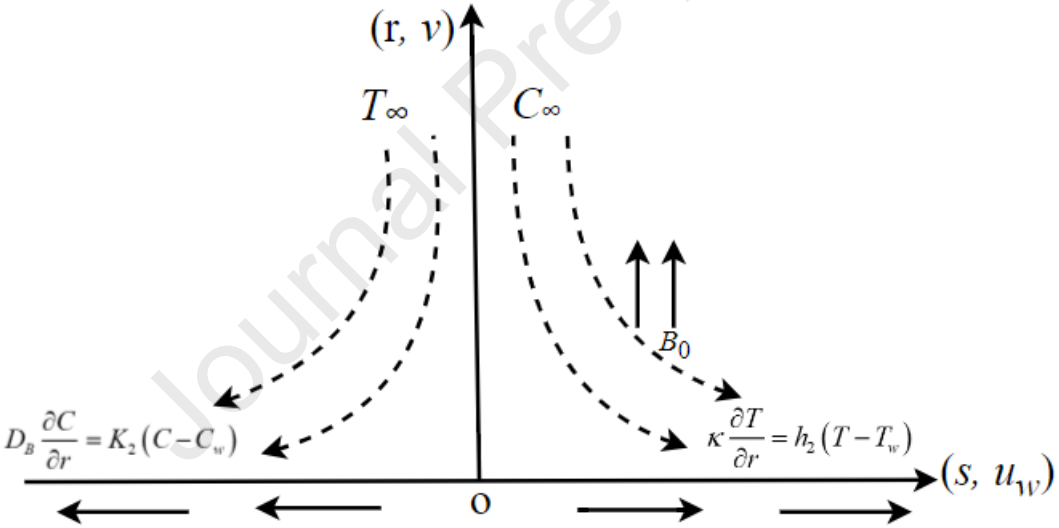

Fig. 1(b). Flat plate geometry for flow problem

Figure 1. Flow diagram

Assume the steady two-dimensional incompressible Casson fluid flow over a curved stretched sheet. Here, in curvilinear coordinates (r, s), $u_w = cs$ is stretching sheet velocity along s - axis while v is the normal velocity to the curved sheet in the r - direction. Due to two equal and opposing forces acting in s - direction, the sheet is stretched. The radius of curved stretching sheet is R with coiled shape as shown in Figure 1(a) and if $R \to \infty$ then curved surface is reduced into a flat plate as depicted in Figure 1(b). The uniform magnetic field of

strength B_0 is assumed normal to flow direction. Considering that our magnetic Reynolds number is very small, we have ignored the consequences of an induced magnetic field. Additionally, the applied electric field is considered to be zero. In this model, the investigation of fluid flow and heat transfer is analyzed through porous media and thermal radiation. In addition, Brownan motion and thermophoresis properties are associated with mass and heat transfer phenomena.

2.2. *Flow model*

Using an isotropic and incompressible flow model of a Casson fluid, the following is the rheological equation of state (Vyas et al. [41] and Sharada and Shankar [42]):

$$\tau_{ij} = \begin{cases} 2\left(\mu_B + \dfrac{P_y}{\sqrt{2\pi}}\right)e_{ij}, \pi > \pi_c \\ 2\left(\mu_B + \dfrac{P_y}{\sqrt{2\pi_c}}\right)e_{ij}, \pi < \pi_c \end{cases}. \tag{1}$$

where $\pi = e_{ij}e_{ij}$ and e_{ij} is deformation rate of $(i,j)^{\text{th}}$ component, π is product of deformation rate component with itself, π_c signifies the product critical value based on non-Newtonian model, μ_B is plastic dynamic viscosity of non -Newtonian fluid, and p_y is yield stress of fluid. Viscosity of Casson fluid is expressed by

$$\mu = \mu_B + \frac{p_y}{\sqrt{\pi}}, \text{ where } p_y = \frac{\mu_B\sqrt{2\pi}}{\beta}. \tag{2}$$

and kinematic viscosity of Casson fluid is expressed as

$$\upsilon = \frac{\mu_B}{\rho}\left(1+\frac{1}{\beta}\right) = \upsilon_B\left(1+\frac{1}{\beta}\right). \tag{3}$$

where $\upsilon_B = \dfrac{\mu_B}{\rho}$ and β is Casson parameter

2.3. *Governing equations and boundary conditions of flow model*

Based on this principle, the governing equations of above flow model are (Sajid et al. [36], Abbas et al. [37], Nield and Bejan [38], Hayat et al. [39] and Varun et al. [40]):

$$\frac{\partial(r+R)v}{\partial r}+R\frac{\partial u}{\partial s}=0. \tag{4}$$

$$\begin{aligned} v\frac{\partial u}{\partial r}+\frac{Ru}{(r+R)}\frac{\partial u}{\partial s}+\frac{uv}{(r+R)} &= -\frac{1}{\rho}\frac{R}{(r+R)}\frac{\partial p}{\partial s}+\upsilon_B\left(1+\frac{1}{\beta}\right)\left(\frac{\partial^2 u}{\partial r^2}+\frac{1}{(r+R)}\frac{\partial u}{\partial r}-\frac{u}{(r+R)^2}\right) \\ &\quad -\frac{\sigma B_0^2}{\rho}u-\frac{\upsilon_B}{k_p}\left(1+\frac{1}{\beta}\right)u-\frac{C_b}{\sqrt{k_p}}u^2 \end{aligned}. \tag{5}$$

$$\begin{aligned} \left(\rho c_p\right)\left(v\frac{\partial T}{\partial r}+\frac{Ru}{(r+R)}\frac{\partial T}{\partial s}\right) &= \kappa\left(\frac{\partial^2 T}{\partial r^2}+\frac{1}{(r+R)}\frac{\partial u}{\partial r}\right)-\frac{1}{(r+R)}\frac{\partial(r+R)q_r}{\partial r}+\sigma B_0^2u^2 \\ &\quad +\frac{\mu_B}{k_p}\left(1+\frac{1}{\beta}\right)u^2+\left(\rho c_p\right)_s\left\{D_{Br}\left(\frac{\partial T}{\partial r}\frac{\partial C}{\partial r}\right)+\frac{D_{Th}}{T_\infty}\left(\frac{\partial T}{\partial r}\right)^2\right\} \\ &\quad +\frac{\rho C_b}{\sqrt{k_p}}u^3+\mu_B\left(1+\frac{1}{\beta}\right)\left(\frac{\partial u}{\partial r}-\frac{u}{(r+R)}\right)^2 \end{aligned}. \tag{6}$$

$$v\frac{\partial C}{\partial r}+\frac{R}{(r+R)}u\frac{\partial C}{\partial s}=D_{Br}\left(\frac{\partial^2 C}{\partial r^2}+\frac{1}{(r+R)}\frac{\partial C}{\partial r}\right)+\frac{D_{Th}}{T_\infty}\left(\frac{1}{(r+R)}\frac{\partial T}{\partial r}+\frac{\partial^2 T}{\partial r^2}\right)-K_1\left(C-C_\infty\right). \tag{7}$$

with associated boundary conditions of the present model written as

$$\left.\begin{aligned} &u=u_w=cs, \quad v=0, \quad \kappa\frac{\partial T}{\partial r}=h_2\left(T-T_w\right), \quad D_{Br}\frac{\partial C}{\partial r}=K_2\left(C-C_w\right) && \text{at} \quad r=0; \\ &u\to 0, \quad \frac{\partial u}{\partial r}\to 0, \quad T\to T_\infty, \quad C\to C_\infty && \text{at} \quad r\to\infty. \end{aligned}\right\}. \tag{8}$$

Here, σB_0^2u and $\sigma B_0^2u^2$ are the magnetic field terms in momentum and energy equations respectively, c is the stretching constant whose dimension is s^{-1}, R is the radius of curved stretching sheet and h_2, K_2 are uniform constant convective heat and mass transfer coefficient respectively.

In this model Rosseland approximation is denoted by q_r and its expression is given by (Hayat et al. [39]):

$$q_r=\frac{-4\sigma^*}{3k^*}\frac{\partial T^4}{\partial r}=\frac{-16\sigma^*T_\infty^3}{3k^*}\frac{\partial T}{\partial r} \tag{9}$$

Now, using equation (9) into equation (6), we get the following equation

Journal Pre-proof

$$\nu\frac{\partial T}{\partial r}+\frac{Ru}{(r+R)}\frac{\partial T}{\partial s}=\frac{\kappa}{\rho c_p}\left(\frac{\partial^2 T}{\partial r^2}+\frac{1}{(r+R)}\frac{\partial u}{\partial r}\right)+\frac{16\sigma^* T_\infty^3}{3k^*\rho c_p}\left(\frac{\partial^2 T}{\partial r^2}+\frac{1}{(r+R)}\frac{\partial T}{\partial r}\right)+\frac{\sigma B_0^2}{\rho c_p}u^2$$
$$+\frac{(\rho c_p)_s}{\rho c_p}\left\{D_{Br}\left(\frac{\partial T}{\partial r}\frac{\partial C}{\partial r}\right)+\frac{D_{Th}}{T_\infty}\left(\frac{\partial T}{\partial r}\right)^2\right\}+\frac{\mu}{k_p\rho c_p}\left(1+\frac{1}{\beta}\right)u^2 \quad . \quad (10)$$
$$+\frac{\rho C_b}{\rho c_p\sqrt{k_p}}u^3+\frac{\mu}{\rho c_p}\left(1+\frac{1}{\beta}\right)\left(\frac{\partial u}{\partial r}-\frac{u}{(r+R)}\right)^2$$

3. Method of solution

3.1. *Similarity transformations in flow model*

In this model, we apply the following similarity transformations in equations (4), (5), (8) and (10) (Sajid et al. [36] and Abbas et al. [37]):

$$\left.\begin{aligned} &u=csf'(\eta), \qquad v=\frac{-R}{r+R}\sqrt{c\upsilon_B}\,f(\eta), \quad \eta=\sqrt{\frac{c}{\upsilon_B}}r, \quad K=\sqrt{\frac{c}{\upsilon_B}}R,\\ &p=\rho c^2 s^2 P_1(\eta), \qquad \theta(\eta)=\frac{T-T_\infty}{T_w-T_\infty}, \qquad \phi(\eta)=\frac{C-C_\infty}{C_w-C_\infty}. \end{aligned}\right\} \quad (11)$$

$$\frac{\partial P_1}{\partial\eta}=\frac{f'^2}{\eta+K}. \quad (12)$$

$$\left(1+\frac{1}{\beta}\right)\left(f'''+\frac{1}{\eta+K}f''-\frac{f'}{(\eta+K)^2}\right)-\frac{2K}{\eta+K}P_1+\frac{K}{\eta+K}\left(ff''-f'^2+\frac{ff'}{\eta+K}\right)-Haf'$$
$$-\left(1+\frac{1}{\beta}\right)Pf'-Frf'^2=0 \quad . \quad (13)$$

$$(1+Nr)\theta''+\frac{1}{\eta+K}(1+Nr)\theta'+\frac{K}{\eta+K}Prf\theta'+Br\left(1+\frac{1}{\beta}\right)\left(f''-\frac{f'}{\eta+K}\right)^2$$
$$Pr\left(Nt\theta'^2+Nb\theta'\phi'\right)+Br\left(Haf'^2+\left(1+\frac{1}{\beta}\right)Pf'^2+Frf'^3\right)=0 \quad . \quad (14)$$

$$\phi''+\frac{1}{\eta+K}\phi'+Sc\frac{K}{\eta+K}f\phi'+\frac{Nt}{Nb}\left[\theta''+\frac{\theta'}{\eta+K}\right]+\frac{K}{\eta+K}Scf\phi'-Sc.Cr\phi=0. \quad (15)$$

Reduced boundary conditions are

$$\left.\begin{aligned} &f(\eta)=0, \quad f'(\eta)=1, \quad \theta'(\eta)=Bi_1(\theta-1), \quad \phi'=Bi_2(\phi-1) \quad at \quad \eta=0;\\ &f'(\eta)\to 0, \quad f''(\eta)\to 0, \quad \theta(\eta)\to 0, \quad \phi\to 0 \quad as \quad \eta\to\infty. \end{aligned}\right\} \quad (16)$$

Journal Pre-proof

Differentiating equation (13) with respect to variable "η" then we get the following equation:

$$\left(1+\frac{1}{\beta}\right)\left(f''''-\frac{2}{(\eta+K)^2} f''+\frac{1}{\eta+K} f'''+\frac{2}{(\eta+K)^3} f' \right)+\frac{K}{\eta+K}\left(ff'''- f' f''\right)-2Frf' f'' \\ -\frac{2K}{(\eta+K)^3} ff'+\frac{K}{(\eta+K)^2} f'^2-\left\{ Ha+\left(1+\frac{1}{\beta}\right)P \right\} f''=\frac{K}{\eta+K}\frac{\partial P_1}{\partial \eta}-\frac{2K}{(\eta+K)^2}P_1 \quad . \quad (17)$$

Now, to remove pressure P_1 from equations (17) we put value of P_1 and $\frac{\partial P_1}{\partial \eta}$ from equations (12) and (13), the following equation is obtained:

$$\left(1+\frac{1}{\beta}\right)\left(f''''-\frac{f''}{(\eta+K)^2}+\frac{2}{\eta+K} f'''+\frac{f'}{(\eta+K)^3} \right)+\frac{K}{\eta+K}\left(ff'''- f' f''\right)-\frac{K}{(\eta+K)^3} ff' \\ +\frac{K}{(\eta+K)^2}\left(ff''- f'^2\right)-\left\{ Ha+\left(1+\frac{1}{\beta}\right)P \right\}\left(f''+\frac{1}{\eta+K} f' \right)-Fr\left(2f' f''+\frac{1}{\eta+K} f'^2 \right)=0 \quad . (18)$$

In equations, (12) to (18), the following dimensionless parameter are obtained as:

Hartmann number $Ha=\frac{\sigma B_0^2}{\rho c}$, Casson fluid parameter $\beta=\mu_B\frac{\sqrt{2\pi}}{p_y}$, Porosity parameter $P=\frac{\upsilon_B}{k_p c}$, Prandtl number $Pr=\frac{\mu_B c_p}{\kappa}$, Eckert number $Ec=\frac{u_w^2}{c_p\left(T_w-T_\infty\right)}$, Brinkman number $Br=Pr.Ec$, Radiation parameter $Nr=\frac{16\sigma^* T_\infty^3}{3k^*\kappa}$, Local Forchheimer number $Fr=\frac{C_b s}{\sqrt{k_p}}$, Thermophoresis parameter $Nt=\frac{\left(\rho c_p\right)_s D_{Th}}{\left(\rho c_p\right)\upsilon_B T_\infty}\left(T_w-T_\infty\right)$, Schmidt number $Sc=\frac{\upsilon_B}{D_{Br}}$, Brownian motion $Nb=\frac{\left(\rho c_p\right)_s D_{Br}}{\left(\rho c_p\right)\upsilon_B}\left(C_w-C_\infty\right)$, Curvature $K=\sqrt{\frac{c}{\upsilon_B}}R$, Chemical reaction parameter $Cr=\frac{K_1}{c}$.

3.2. *Physical quantities of flow model*

Journal Pre-proof

The surface formulae for localized estimates of skin friction coefficient C_{fs} , Nusselt number Nu_s and Sherwood number Sh_s are provided by

$$C_{fs} = \frac{\tau_{rs}}{\rho u_w^2}. \tag{19}$$

$$Nu_s = \frac{sq_w}{\kappa\left(T_w - T_\infty\right)}. \tag{20}$$

$$Sh_s = \frac{sq_m}{D_{Br}\left(C_w - C_\infty\right)}. \tag{21}$$

where $\tau_{rs} = \mu_B\left(1+\frac{1}{\beta}\right)\left(\frac{\partial u}{\partial r} - \frac{u}{r+R}\right)\Big|_{r=0}$, $q_w = -\kappa\frac{\partial T}{\partial r} + q_r\Big|_{r=0} = -\kappa\frac{\partial T}{\partial r} - \frac{16\sigma^* T_\infty^3}{3k^*}\frac{\partial T}{\partial r}\Big|_{r=0}$,

$q_m = -D_{Br}\frac{\partial C}{\partial r}\Big|_{r=0}$.

The coefficient of local skin-friction, which measures the surface shear stress, local Nusselt number, which measure the nondimensional heat transport rate at curved stretching surface, and local Sherwood number, which measure mass transfer rate at surface to fluid are the physical quantities of engineering significance for current model which are expressed as-

$$C_{fs}\left(Re_s\right)^{1/2} = \left(1+\frac{1}{\beta}\right)\left(f''(\eta) - \frac{f'(\eta)}{K}\right)\Big|_{\eta=0}. \tag{22}$$

$$Nu_s\left(Re_s\right)^{-1/2} = -\left(1+Nr\right)\left(\theta'(\eta)\right)\Big|_{\eta=0}. \tag{23}$$

$$Sh_s\left(Re_s\right)^{-1/2} = -\phi'(\eta)\Big|_{\eta=0}. \tag{24}$$

where $Re_s^{1/2} = \sqrt{\frac{c}{\upsilon_B}}s$.

3.3 *Numerical scheme*

The obtained dimensionless governing equations (18), (14) and (15) are coupled and non-linear in nature. Here, MATLAB solver "bvp4c" is employed to provide responses for related characteristics to these coupled nonlinear differential equations with associated properties (16). This bvp4c function is created utilizing the 3-stage Lobatto IIIa formula and the finite

difference programme, with fourth order exactness. The essential syntax for this function is sol = bvp4c(@odefun, @bcfun, solinit, options), with a relative tolerance of 10^{-4}. Figure 2.2 displays a flow chart of the computing technique.

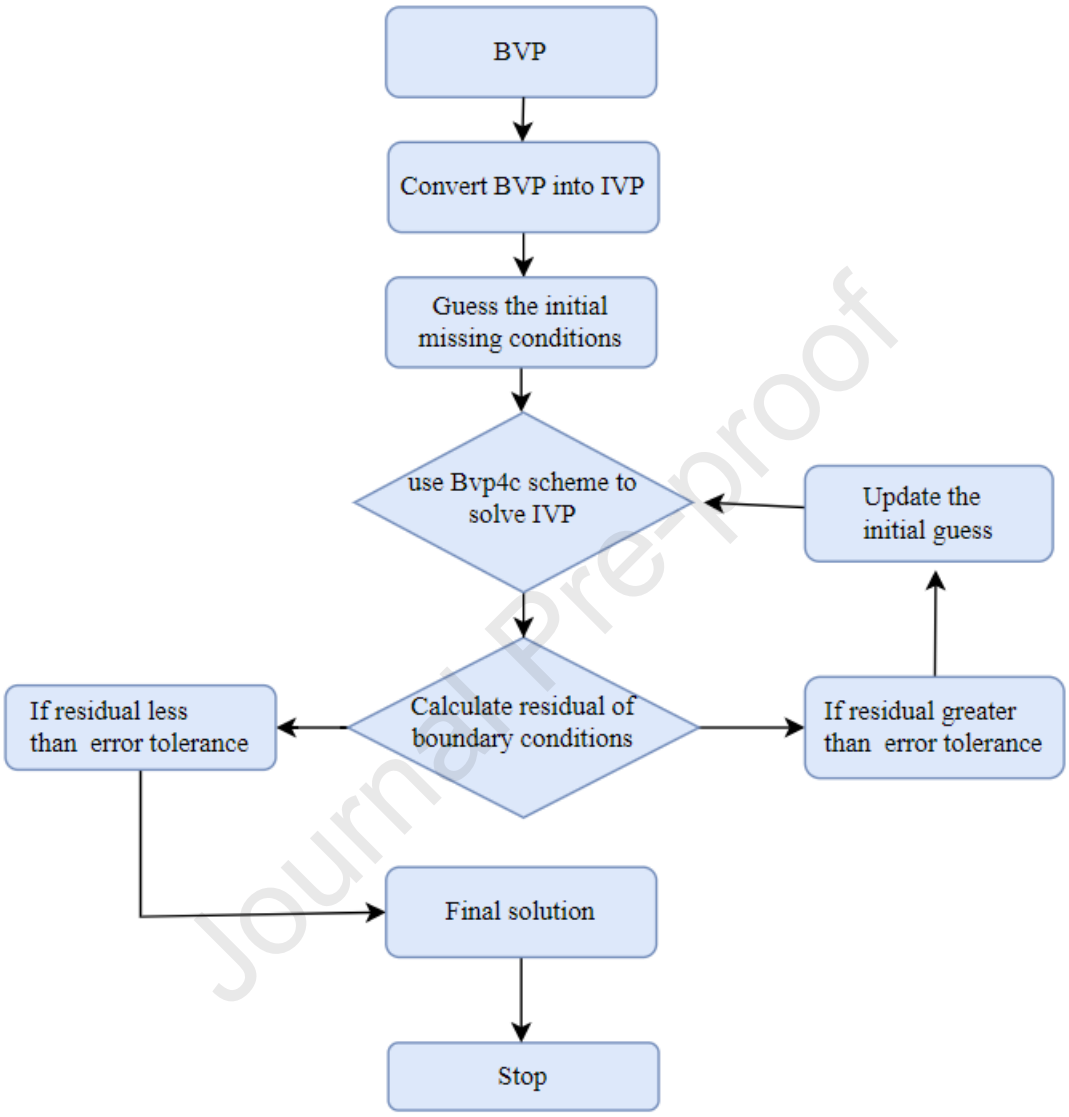

Figure 2. Flow chart of the problem

To solve the system via bvp4c, first we convert this system of boundary value equations (14)-(18) to a system of initial value equations as follows:

Let $f = f_1$, $\theta = f_5$ and $\phi = f_7$ then

$$
\left.\begin{aligned}
&f_1' = f_2;\\
&f_3' = f_4;\\
&f_4' = \frac{-1}{\left(1+\frac{1}{\beta}\right)}\left\{\begin{aligned}&\left(1+\frac{1}{\beta}\right)\left(\frac{2f_4}{\eta+K}-\frac{f_3}{(\eta+K)^2}+\frac{f_2}{(\eta+K)^3}\right)+\frac{K}{\eta+K}\left(f_1f_4-f_2f_3\right)\\&+\frac{K}{(\eta+K)^2}\left(f_1f_3-f_2^{\,2}\right)-\frac{K}{(\eta+K)^3}f_1f_2-\left(Ha^2+P\right)\left(f_3+\frac{f_2}{\eta+K}\right)\\&-Fr\left(2f_2f_3+\frac{f_2^{\,2}}{\eta+K}\right)\end{aligned}\right\};\\
&f_5' = f_6;\\
&f_6' = \frac{-1}{(1+Nr)}\left\{\begin{aligned}&\frac{(1+Nr)f_6}{\eta+K}+\frac{K}{(\eta+K)}Prf_1f_6+\left(1+\frac{1}{\beta}\right)Br\left(f_3-\frac{f_2}{\eta+K}\right)^2\\&+Br\left(Ha^2+\left(1+\frac{1}{\beta}\right)P+Frf_2\right)f_2^{\,2}\end{aligned}\right\};\\
&f_7' = f_8;\\
&f_8' = (-1)\left\{\frac{f_8}{\eta+K}+\frac{Nt}{Nb}\left(f_6'+\frac{f_6}{\eta+K}\right)-Sc.Crf_7+Sc\frac{K}{\eta+K}f_1f_7\right\}.
\end{aligned}\right\}. \qquad (25)
$$

and boundary conditions are

$$
\left.\begin{aligned}
&f_1(0)=0,\ f_2(0)=1,\ f_3(0)=\varepsilon_1,\ f_4(0)=\varepsilon_2,\ f_6(0)=\varepsilon_3,\ f_6(0)=Bi_1(f_5(0)-1),\\
&f_8(0)=\varepsilon_4,\ f_8(0)=Bi_2(f_7(0)-1).
\end{aligned}\right\}. \qquad (26)
$$

and here additional boundary conditions are

$$
f_2(\eta_\infty)=0,\ f_3(\eta_\infty)=0,\ f_5(\eta_\infty)=0,\ f_7(\eta_\infty)=0. \qquad (27)
$$

Now, we select suitable guess values of $f_3(0)$, $f_4(0)$, $f_6(0)$ and $f_8(0)$ i.e., $\varepsilon_1, \varepsilon_2$, ε_3 and ε_4, so that, when the preceding system of first-order differential equations is integrated, the boundary conditions mentioned in equation (27) are kept absolutely. For calculation point of view, here we take $\eta_\infty = 6$ for velocity profiles, $\eta_\infty = 30$ for temperature profiles and $\eta_\infty = 12$ for concentration profiles, where η_∞ denotes $\eta \to \infty$ and interval is subdivided using step size $h = 0.01$. We use the bvpinit command to generate initial boundary condition predictions. The bvpfcn(x,y) command encodes first order differential equations (25) to differential functions, while the bcfcn(ya,yb) command encodes boundary conditions. Then we address the problem

employing sol=bvp4c(@bvpfcn, @bcfcn, solinit) and plot the result with plot(sol.x, sol.y) command.

The advantages of the bvp4c solver are: (i) it automatically adjusts the mesh to improve accuracy; (ii) it handles problems with or without singularities; and (iii) it provides solutions with high precision.

Limitations of the bvp4c solver are: (i) Poor guesses can lead to non-convergence or incorrect solutions; (ii) It is specific to MATLAB, which may not be accessible or preferable for all users or applications; (iii) Problems with complex or discontinuous boundary conditions can be challenging.

4. Code validation

Under some specific circumstances, the computational outputs are linked to those that are currently accessible in the literature which is provided in Table 1. The outputs are matched with Abbas et al. [37] and a comparison is also made with analytical methodology of OAFM (Optimal Auxiliary Function Method). Strong associations in the outcomes assure the exactness of our numerical findings and code.

Table 1. Comparison for skin frication $-\mathrm{Re}_s^{1/2} C_{fs}$ at $Ha = P = Fr = 0$.

K	Abbas et al. [37]	Present out comes	
		Bvp4c	OAFM
5.0	1.15763	1.1650	1.165175
10.0	1.07349	1.0765	1.076486
20.0	1.03561	1.0372	1.037177
30.0	1.02353	1.0247	1.024770
40.0	1.01759	1.0186	1.018695
50.0	1.01405	1.0149	1.015092
100.0	1.00704	1.0077	1.007980

5. Results and discussion

The proposed investigation addresses the consequences of Brownian motion and curvature on Darcy-Forchheimer flow of Casson fluid across a curved surface which is stretching. Using shooting approach, flow governing equations are computed. The graphs illustrate the

consequences on velocity, temperature, and concentration of fluid. The computational and graphical representations of skin friction coefficient, Nusselt and Sherwood number are also performed. In addition, subsequent control parameters are implemented in order to attain the desired analytical solution: Casson fluid parameter $0.2 \le \beta \le 0.5$, Hartmann number $0.5 \le Ha \le 3.5$, radiation parameter $2.0 \le Rd \le 5.0$, porosity parameter $0.3 \le P \le 1.2$, thermophresis parameter $0.1 \le Nt \le 0.4$, Brownian motion parameter $0.3 \le Nb \le 1.2$, chemical reaction parameter $0.5 \le Cr \le 2.5$, Schmidt number $0.1 \le Sc \le 0.7$, thermal Biot number $0.1 \le Bi_1 \le 0.4$, mass Biot number $0.2 \le Bi_2 \le 0.6$, Brinkman number $0.33 \le Br \le 0.66$, Prandtl number $1.1 \le Pr \le 4.1$, Forchheimer number $0.2 \le Fr \le 6.2$. Also, for the computational purpose $\beta = 0.4$, $Ha = 0.5$, $Rd = 5.0$, $Pr = 1.1$, $Br = 0.33$, $P = 0.3$, $Fr = 0.2$, $Nt = 0.1$, $Nb = 0.3, Cr = 0.5$, $Sc = 0.5$, $Bi_1 = 0.2$, $Bi_2 = 0.3$, $K = 1.5$ and $K \to \infty$ are fixed until stated separately. The mathematical solutions are achieved employing a fourth-order exactness programme (bvp4c), and findings are validated by comparing them to OAFM (Optimal Auxiliary Function Method). OAFM is an analytical technique that constructs an auxiliary function which optimizes the convergence of the solution series of the flow model.

5.1. *Velocity distribution profiles*

In this research paper, the velocity distribution against involved parameters is analyzed using the sketches in Figures 3(a-e). Figure 3(a) shows how the curvature parameter K behaves on a velocity distribution. Improvements in curvature parameter ($K = 1.5, 2.5, 3.5, 4.5$) provide a rise in velocity profiles ($f'(\eta = 1) = 0.32564, 0.360142, 0.378247, 0.385401$). As the curvature parameter increases, the surface geometry changes, which has a virtue to alter the way fluid flows over it. Increased curvature leads to higher gradients in the velocity field due to the more pronounced bending of the surface. This enhances velocity distributions. The implication of Hartman number Ha on velocity distribution is seen in diagram 3(b). A spike in Hartman number allows the velocity distribution to down. The reason for this is that Lorentz force results for higher inputs of Ha, which increases the fluid flow's resistance. Figure 3(c) illustrates how fluid parameter β alters the fluid velocity f ′(η). We noticed that the yield stress lowers with rising inputs of Casson fluid parameter β, and as an outcome, velocity and momentum boundary layer thickness decrease for improved inputs of Casson fluid parameter. Figure 3(d) demonstrates how the velocity profiles are affected by Forchheimer number. Increasing inputs of Forchheimer number imply stronger inertial effects and it introduce an

additional resistance to flow that's why fluid velocity decreased. Improvements in the porosity parameter P indicate the presence of more porous space, which enables fluid flow to encounter more resistance. As an outcome, increased inputs of porosity parameter cause the flow to decline, as depicted in Figure 3(e).

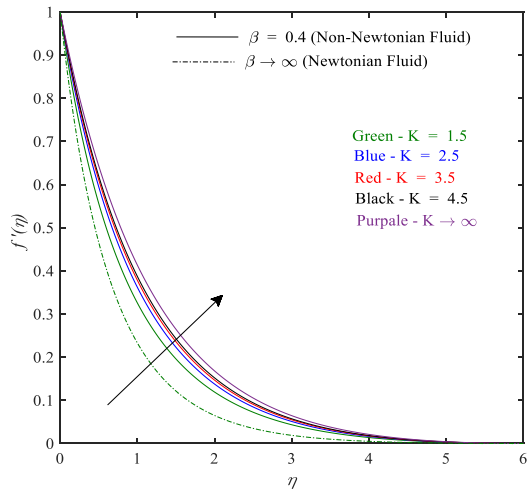

(a)

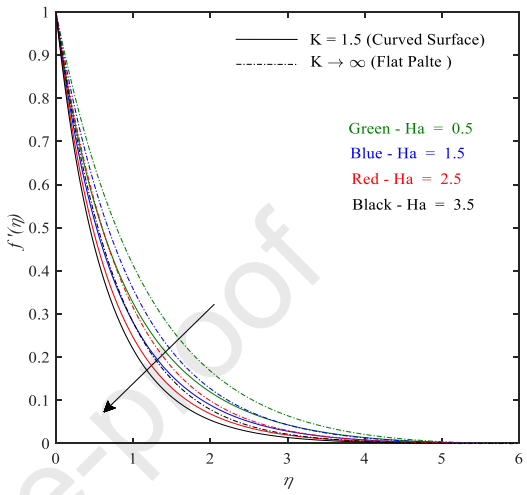

(b)

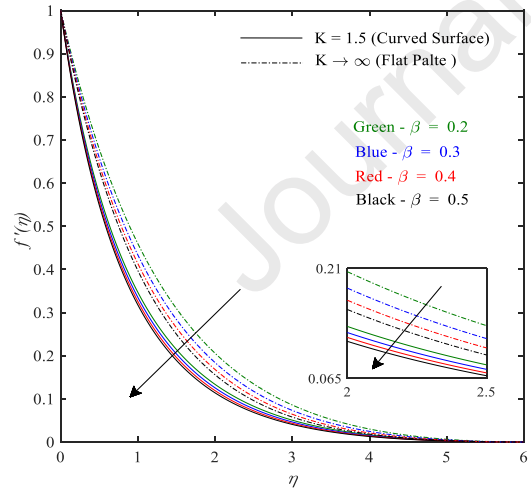

(c)

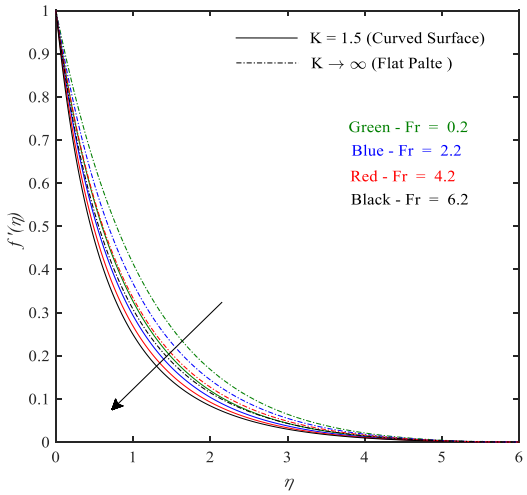

(d)

Journal Pre-proof

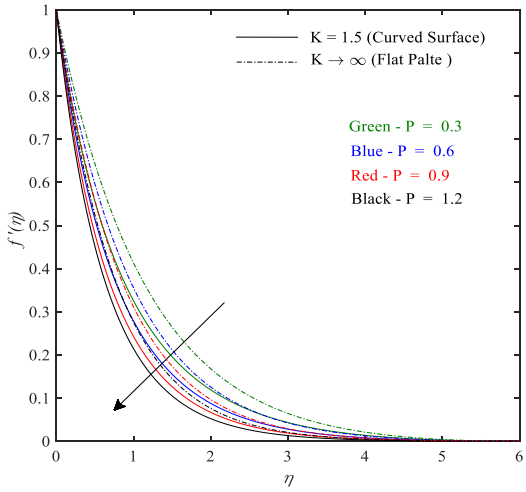

(e)

Fig. 3. Momentum profiles against inputs of **(a)** Curvature parameter K, **(b)** Hartmann number Ha, **(c)** Casson fluid parameter β, **(d)** Forchheimer number Fr, **(e)** Porosity parameter P.

5.2. *Temperature distribution profiles*

The temperature distribution is analyzed against the relevant factors in this study using the sketches in Figs. 4(a–g). Figure 4(a) depicts consequences of Prandtl number Pr on temperature region. Both temperature field and thickness of thermal layer shrink with rising inputs of Prandtl number Pr. As we know that, Prandtl number is a dimensionless number that characterizes the relative thickness of the momentum and thermal boundary layers in a fluid. It is described as the ratio of momentum diffusivity to thermal diffusivity. So, the connection between thermal diffusivity and Prandtl number Pr is reciprocal. There is less thermal diffusivity with larger Prandtl numbers Pr. Hence, temperature field and related thermal layer diminish as a result of this reduced diffusivity. Figure 4(b) illustrates outcomes of curvature parameter K on thermal field. It is observed that the thermal boundary layer thickness downs when curvature parameter is increased. A plot of Figure 4(c) shows how the variation in Forchheimer number Fr affects the temperature field. Temperature field enhancements have been noted in the presence of larger Forchheimer number augments. Actually, greater inputs of Forchheimer number Fr result in stronger resistive force between fluid particles, which improves temperature distribution. Figure 4(d) hints the implications of thermal Biot number Bi_1 on temperature. The temperature distribution declines by boosting estimates of thermal Biot number ($Bi_1 = 0.1, 0.2, 0.3, 0.4$). Weaker convection happens physically with a rise in

thermal Biot ($Bi_1 = 0.1, 0.2, 0.3, 0.4$), which downs the temperature field. Figure 4(e) displays the direct relationship between the temperature profile and the magnetic variable Ha. Temperature rises as a result of enhanced resistance between fluid particles caused by Lorentz force when inputs of Ha increase. The effect of Brinkman number Br on thermal distribution is demonstrated in Figure 4(f). It is important to note that temperature rises with greater inputs of Brinkman number ($Br = 0.33, 0.44, 0.55, 0.66$). Given that Brinkman number Br is associated with viscous dissipation, temperature improves as viscous effects become greater for bigger inputs of Brinkman number Br. The thermophoresis parameter dominates heat transference, as seen in Figure 4(g). The improvement in inputs of Nt, results in an improved profile of thermal distributions.

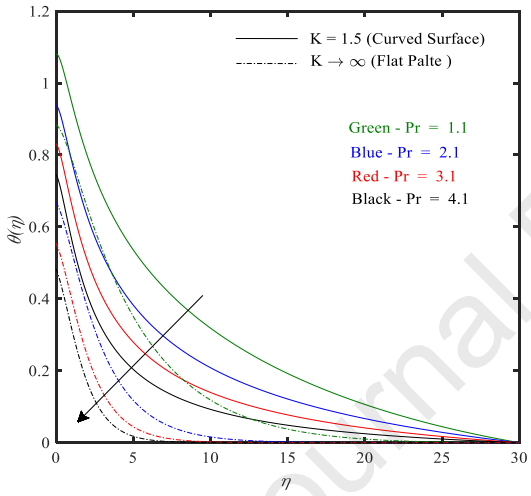

(a)

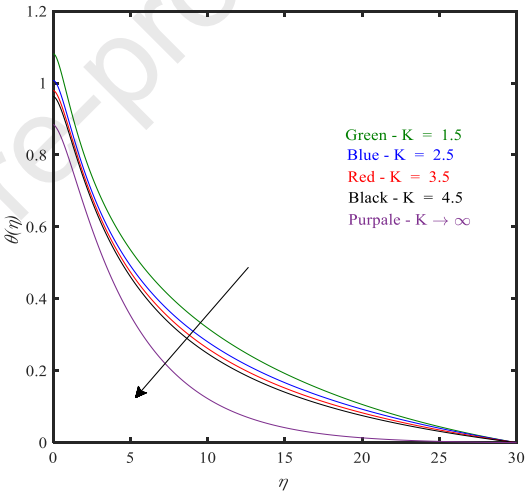

(b)

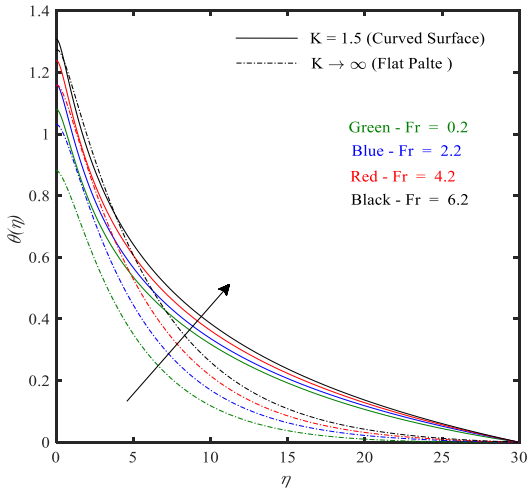

(c)

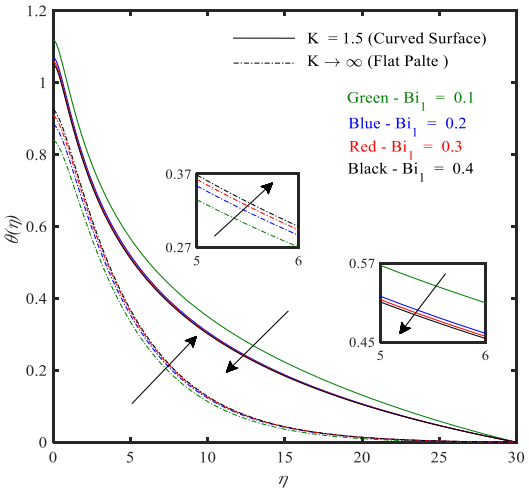

(d)

Journal Pre-proof

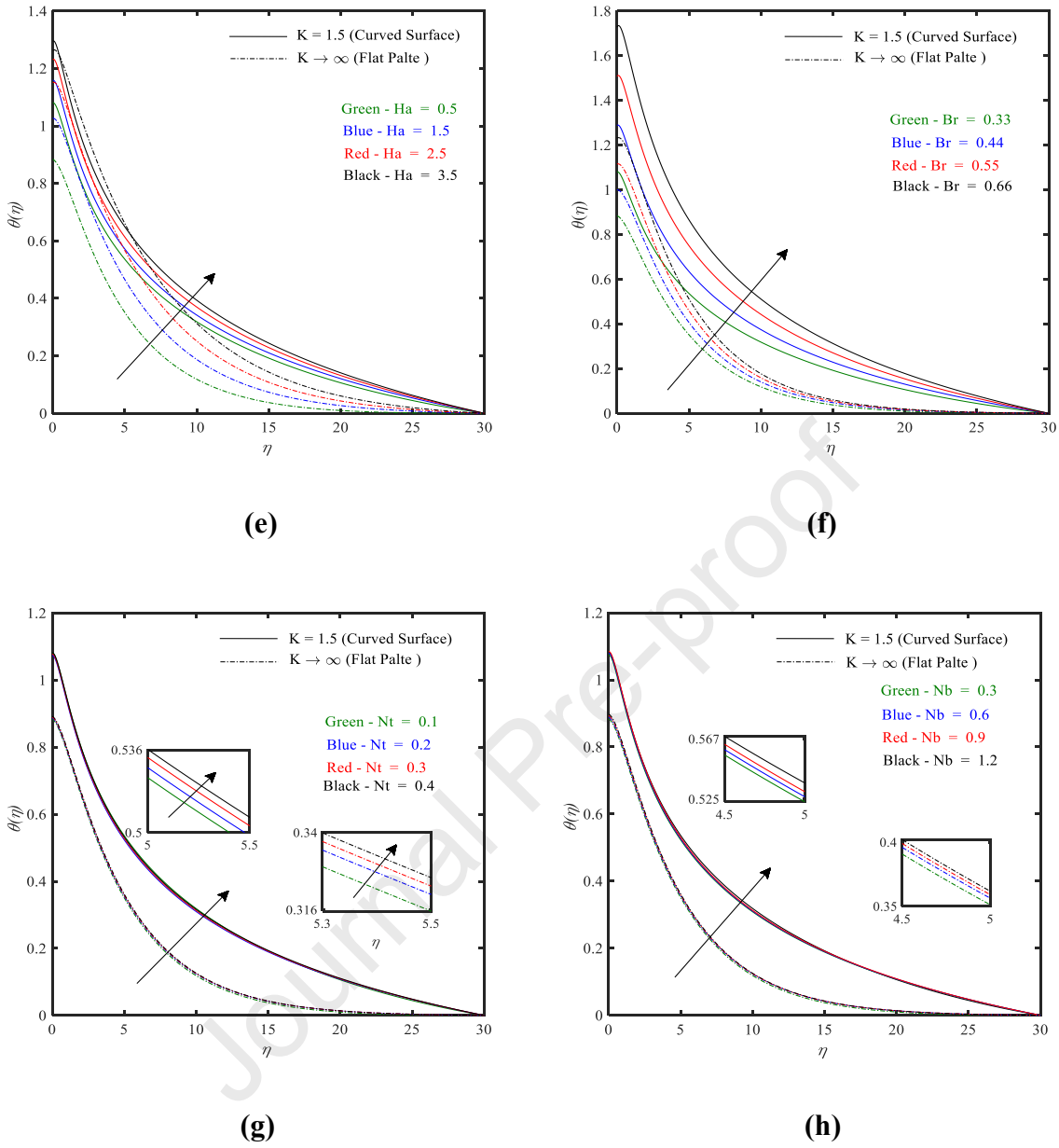

Fig. 4. Temperature profiles for various values of **(a)** Prandtl number Pr, **(b)** Curvature parameter K, **(c)** Forchheimer number Fr, **(d)** Thermal Biot number Bi_1, **(e)** Hartmann number Ha, **(f)** Brinkman number Br, **(g)** Thermophoresis parameter Nt.

5.3. *Concentration distribution profiles*

In the current paper, the concentration distribution against concerned parameters is analyzed using the sketches in Figs. 5(a–f). As the Schmidt number Sc is varied, Figure 5(a) shows how concentration field changes. The concentration field and concentration layer thickness reduce with advancing inputs of Schmidt number Sc. It happens because mass diffusivity and Schmidt number Sc have an opposing trend. So, concentration profile and layer thickness

decrease with improving inputs of Schmidt number Sc, which is associated with a lower mass diffusivity. We can observe in Figure 5(b) that the concentration profile rises when inputs of solutal Biot number ($Bi_2 = 0.3, 0.4, 0.5, 0.6$) grows. It happens because, with a rise in the mass Biot number, the internal resistance to mass transfer becomes more significant compared to the external resistance and it leads to an enhanced concentration distributions i.e., steeper concentration gradients. Sketched depicting the action of thermophoresis parameter Nt on concentration profile is seen in diagram 5(c). The results from this figure indicate a decline in both concentration and corresponding thickness of boundary layer. Figure 5(d) illustrates that concentration profile declines as inputs of Hartmann number Ha increases. It happens because mass and density of fluid particles are reduced on the improved inputs of Hartmann number Ha. Figure 5(e) depicts that concentration profile are enhanced with augmented inputs of curvature parameter K. The feature of chemical reaction parameter on concentration field is explained in Figure 5(f). This graph illustrates how the concentration gradient becomes less determined with increased chemical reaction parameter Cr inputs. Physically, a stronger chemical reaction results in the decay of the reactant species, which is a noteworthy negative effect. As a result, for increased chemical reaction parameter Cr, the concentration gradient falls.

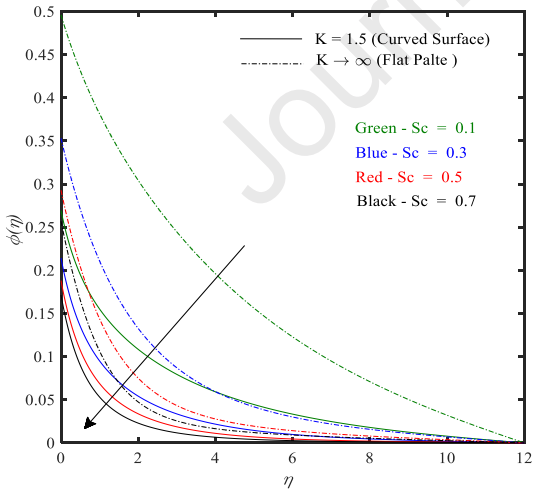

(a)

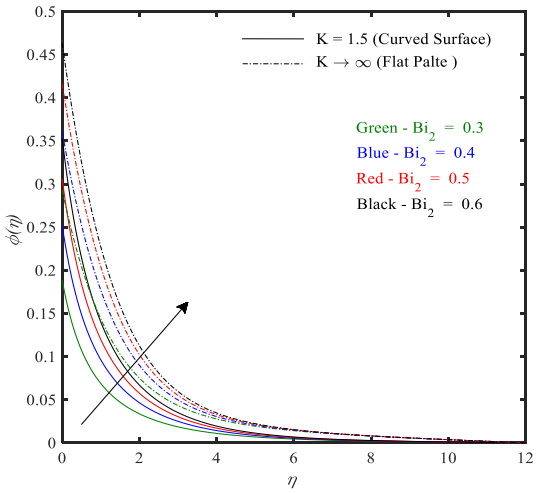

(b)

Journal Pre-proof

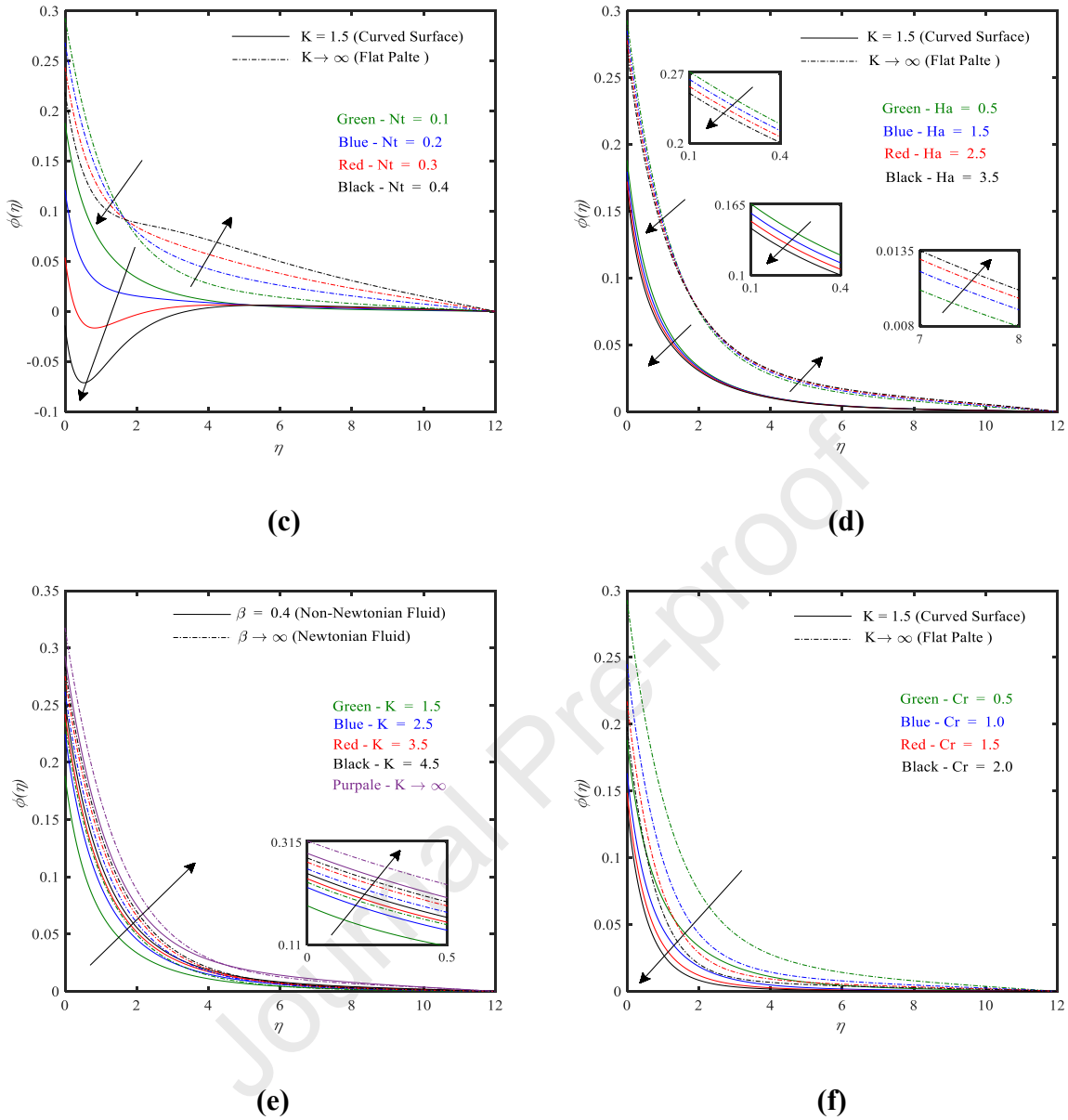

Fig. 5. Concentration profiles for various inputs of **(a)** Schmidt number Sc, **(b)** Mass Biot number Bi_2, **(c)** Thermophoresis parameter Nt, **(d)** Hartmann number Ha, **(e)** Curvature parameter K, **(f)** Chemical reaction parameter Cr.

Figs. 6-8 are plotted using the least squares technique (LSM) (Animasaun et al. [43]). For linear regression with the best slope through the data point, the least squares method is helpful. The line that best illustrates the connection between a scatter plot's numerous data points (x_i^*, y_i^*) for $i > 2$ is used to characterize the plot. The line of greatest fit for the data shown above is denoted by $y^* = m_1 x^* + c^*$, where m_1 denotes slope and c^* denotes intercept.

$$m_1 = \frac{\sum\left(x_{av}^{*} - x_i^{*}\right)\left(y_{av}^{*} - y_i^{*}\right)}{\sum\left(x_{av}^{*} - x_i^{*}\right)^2} \tag{28}$$

$$c^{*} = y_{av}^{*} - m_1 x_{av}^{*} \tag{29}$$

where x_{av}^{*} and y_{av}^{*} are mean of the points in x^{*} and y^{*}, respectively.

5.4. *Skin friction coefficient profiles*

Figure 6 stands the display of skin friction coefficient $C_{fs}\left(Re_s\right)^{1/2}$ for distinct behavior of Hartmann number Ha, Forchheimer number Fr, porosity parameter P and Casson fluid parameter β. Hartmann number Ha on skin friction coefficient $C_{fs}\left(Re_s\right)^{1/2}$ via Forchheimer number Fr is depicted in diagram 6(a). Here magnitude of surface drag force lowers for improving inputs of both Hartmann number Ha and Forchheimer number Fr. Figure 6(b) illustrates the effects of porosity parameter P via Casson fluid parameter β on skin friction coefficient $C_{fs}\left(Re_s\right)^{1/2}$. Improving augments of Hartman number Ha lowers skin friction $C_{fs}\left(Re_s\right)^{1/2}$ while it enhances with growing inputs of Casson fluid parameter β.

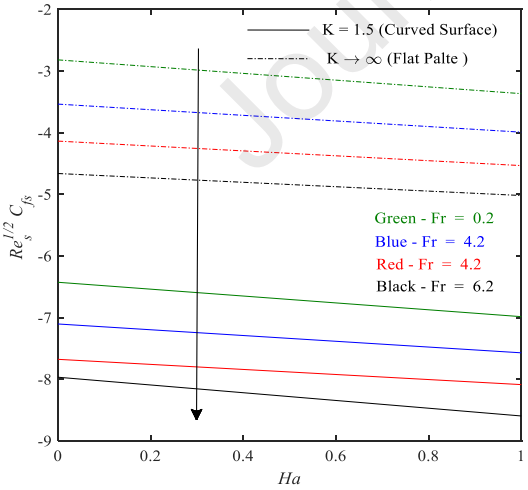

Fig. 6(a). $C_{fs}\left(Re_s\right)^{1/2}$ via Hartmann number Ha and Forchheimer number Fr.

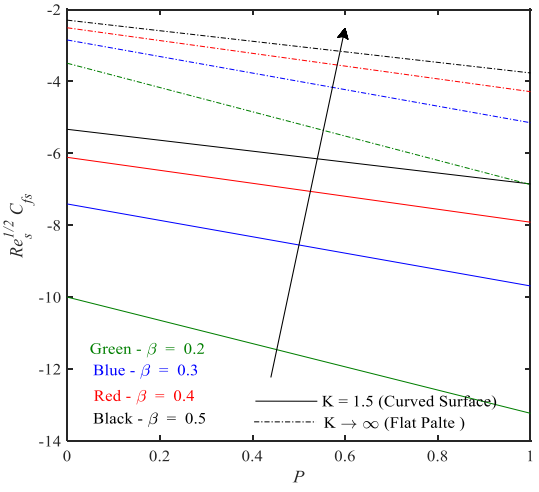

Fig. 6(b). $C_{fs}\left(Re_s\right)^{1/2}$ via Casson fluid parameter β and Porosity parameter P.

Fig. 6. Profiles of physical quantity $C_{fs}\left(Re_s\right)^{1/2}$ against non dimensionless parameters.

5.5. *Nusselt number profiles*

Figure 7 represents the plot of Nusselt number $Nu_s\left(Re_s\right)^{-1/2}$ for distinct outcomes of thermal Biot number Bi_1, Brinkman number Br, radiation parameter Rd and curvature parameter K. Figure 7(a) displays the behavior of thermal Biot number Bi_1 on Nusselt number $Nu_s\left(Re_s\right)^{-1/2}$ against Brinkman number Br. For higher inputs of thermal Biot number Bi_1 surface heat transfer rate $Nu_s\left(Re_s\right)^{-1/2}$ improves but it reduces with increased inputs of Brinkman number Br. Figure 7(b) indicates the influence of radiation parameter Rd through curvature parameter K. Nusselt number $Nu_s\left(Re_s\right)^{-1/2}$ improves for larger inputs of both radiation (Rd) and curvature (K) factors.

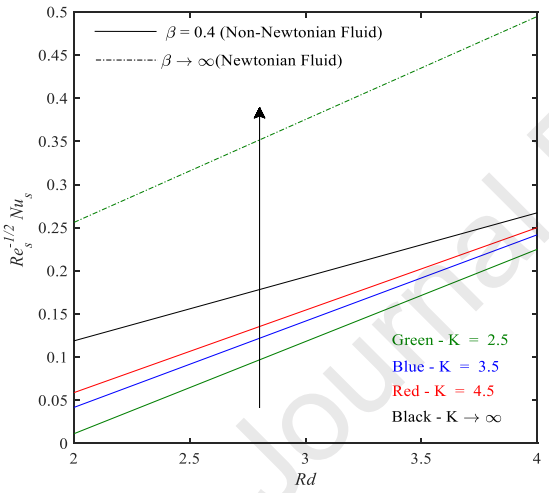

Fig. 7(a). $Nu_s\left(Re_s\right)^{-1/2}$ via Curvature parameter K and thermal radiation Rd.

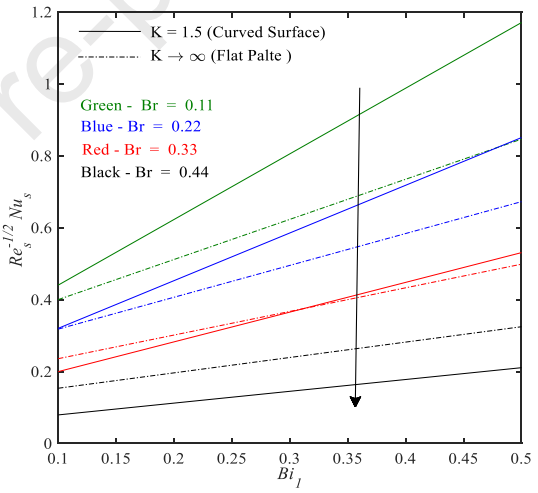

Fig. 7(b). $Nu_s\left(Re_s\right)^{-1/2}$ via Thermal Biot Bi_1 and Brinkman number Br.

Fig. 7. Profiles of physical quantity $Nu_s\left(Re_s\right)^{-1/2}$ against non dimensionless parameters.

5.6. *Sherwood number profiles*

Figure 8 represents the plot of the Sherwood number $Sh_s\left(Re_s\right)^{-1/2}$ for various outcomes of mass Biot number Bi_2, thermophoresis parameter Nt, chemical reaction parameter Cr and Brownian motion parameter Nb. Figure 8(a) illustrates the behavior of mass Biot number Bi_2 on Shwerwood number $Sh_s\left(Re_s\right)^{-1/2}$ against thermophoresis parameter Nt. Surface mass

transfer rate $Sh_s\left(Re_s\right)^{-1/2}$ improves not only for higher inputs of mass Biot number Bi_2 but also thermophoresis parameter Nt. Figure 8(b) illustrates the impact of chemical reaction parameter Cr via Brownian motion parameter Nb. It is noticed that Sherwood number Nb has opposite output for these two parameters.

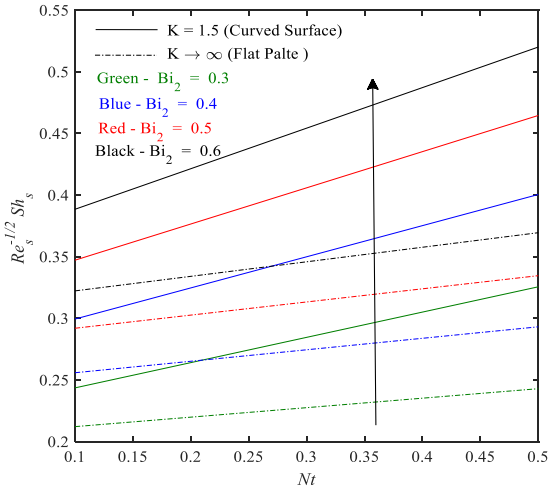

Fig. 8(a). $Nu_s\left(Re_s\right)^{-1/2}$ via mass Biot Bi_2 and Thermophoresis parameter Nt.

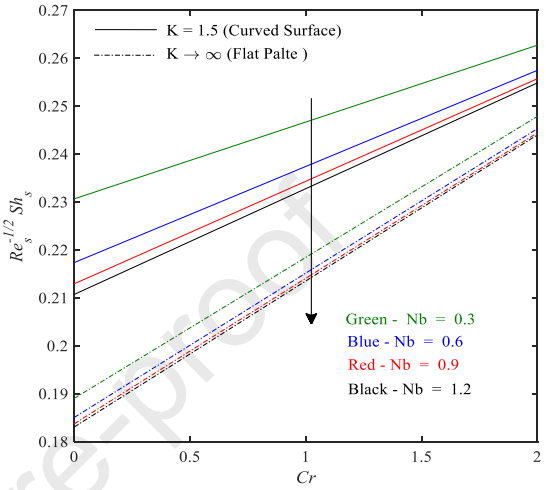

Fig. 8(b). $Nu_s\left(Re_s\right)^{-1/2}$ via Brownian motion Nb and Chemical reaction Cr.

Fig. 8. Profiles of physical quantity $Sh_s\left(Re_s\right)^{-1/2}$ against non dimensionless parameters.

5.7. *Variation of parameters on velocity contour*

Figure 9 illustrates the relationship between velocity contour and the parameters of curvature, porosity, and the Casson fluid. The curves depicted in Figs. 9(a-c) exhibit an asymptotic trend as the domain size increases. The flow rate displays a greater rise due to changes in the curvature parameter, as compared to the influence of porosity and the Casson fluid parameter.

Journal Pre-proof

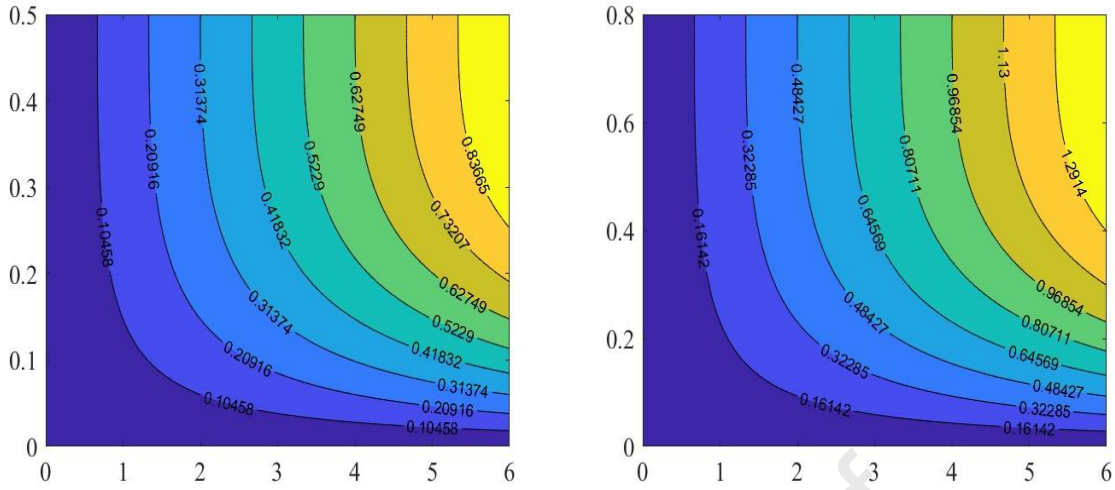

(a) **(b)**

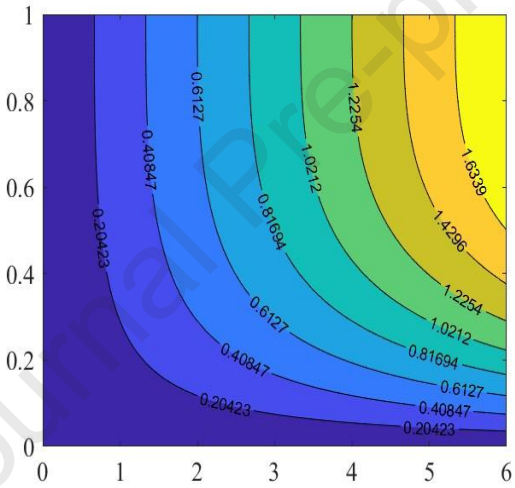

(c)

Fig. 9. Velocity contour for **(a)** Casson fluid parameter β, **(b)** Porosity parameter P and **(c)** Curvature parameter K.

Table 2. Computational findings for all physical quantities ($-\mathrm{Re}_s^{1/2} C_{fs}$, $\mathrm{Re}_s^{-1/2} Nu_s$ and $\mathrm{Re}_s^{-1/2} Sh_s$) via Table 2 and Table 3 for distinct parameters (Casson fluid parameter β, Forchheimer number Fr, Brownian motion Nb, Thermal Biot number Bi_1, Mass Biot number Bi_2) at $K = 1.5$.

	$-\mathrm{Re}_s^{1/2} C_{fs}$	$\mathrm{Re}_s^{-1/2} Nu_s$	$\mathrm{Re}_s^{-1/2} Sh_s$

β	Fr	Nb	Bi_1	Bi_2	$K=1.5$		
0.3	0.2	0.3	0.2	0.3	8.1705	0.1820	0.2483
0.5	0.2	0.3	0.2	0.3	5.8378	0.3671	0.2411
0.4	**2.2**	0.3	0.2	0.3	7.3419	0.2252	0.2467
0.4	**4.2**	0.3	0.2	0.3	7.8851	0.1631	0.2492
0.4	0.2	**0.6**	0.2	0.3	6.7133	0.2931	0.2338
0.4	0.2	**0.9**	0.2	0.3	6.7134	0.2885	0.2304
0.4	0.2	0.3	**0.3**	0.3	6.7133	0.3872	0.2437
0.4	0.2	0.3	**0.4**	0.3	6.7134	0.4559	0.2437
0.4	0.2	0.3	0.2	**0.4**	6.7133	0.2965	0.2997
0.4	0.2	0.3	0.2	**0.5**	6.7134	0.2955	0.3474

Table 3. Computational findings for all physical quantities ($-\mathrm{Re}_s^{1/2} C_{fs}$, $\mathrm{Re}_s^{-1/2} Nu_s$ and $\mathrm{Re}_s^{-1/2} Sh_s$) via Table 2 and Table 3 for different parameters (Casson fluid parameter β, Forchheimer number Fr, Brownian motion Nb, Thermal Biot number Bi_1, Mass Biot number Bi_2) at $K \to \infty$.

β	Fr	Nb	Bi_1	Bi_2	$-\mathrm{Re}_s^{1/2} C_{fs}$	$\mathrm{Re}_s^{-1/2} Nu_s$	$\mathrm{Re}_s^{-1/2} Sh_s$
					$K \to \infty$		
0.3	0.2	0.3	0.2	0.3	3.6210	0.2661	0.2142
0.5	0.2	0.3	0.2	0.3	2.7817	0.3529	0.2111
0.4	**2.2**	0.3	0.2	0.3	3.7683	0.1966	0.2154
0.4	**4.2**	0.3	0.2	0.3	4.3381	0.0916	0.2181
0.4	0.2	**0.6**	0.2	0.3	3.1000	0.3156	0.2086
0.4	0.2	**0.9**	0.2	0.3	3.1000	0.3107	0.2074
0.4	0.2	0.3	**0.3**	0.3	3.1000	0.3916	0.2121
0.4	0.2	0.3	**0.4**	0.3	3.1000	0.4404	0.2119
0.4	0.2	0.3	0.2	**0.4**	3.1000	0.3195	0.2560
0.4	0.2	0.3	0.2	**0.5**	3.1000	0.3186	0.2922

Journal Pre-proof

Table 2 is tabulated to see the numerical findings of all three physical quantities for different entries of dimensionless Casson fluid parameter β, Forchheimer number Fr, Brownian motion parameter Nb, thermal and mass Biot number (Bi_1 & Bi_2). It can be demonstrated from this table that both skin friction coefficient $C_{fs}\left(Re_s\right)^{1/2}$ and Nusselt number $\mathrm{Re}_s^{-1/2} Nu_s$ enhances as the dimensionless Casson fluid parameter β is increased while these two lowers with growing data of Forchheimer number Fr, Brownian motion parameter Nb and mass Biot number Bi_2. It is also noted that thermal Biot number Bi_1 has opposite behave with skin friction coefficient $C_{fs}\left(Re_s\right)^{1/2}$ and Nusselt number $\mathrm{Re}_s^{-1/2} Nu_s$. Furthermore, Sherwood number $\mathrm{Re}_s^{-1/2} Sh_s$ is improving with enhanced inputs of Forchheimer Fr and mass Biot number Bi_2 while it is lowering with Brownian motion Nb and Casson fluid parameter β. In Table 3, similar outputs are observed for Nusselt number $\mathrm{Re}_s^{-1/2} Nu_s$ for mentioned parameters as in Table 2. Behave of Sherwood number $\mathrm{Re}_s^{-1/2} Sh_s$ is similar with mentioned parameters in Table 2 except thermal Biot number Bi_1 for which Sherwood number $\mathrm{Re}_s^{-1/2} Sh_s$ profile is lowering as seen in Table 3. Also, skin friction coefficient $C_{fs}\left(Re_s\right)^{1/2}$ in Table 3 is enhancing with growing inputs of Casson fluid parameter β but decreasing with Forchheimer number Fr and it remains constant for rest three parameters named as Brownian motion Nb, thermal and mass Biot number (Bi_1 & Bi_2).

6. Conclusions

The Darcy Fochheimer movement of Casson fluid over a curved surface is the subject of this article. The discussion of this analysis involves the inclusion of the Darcy-Forchheimer term in both the velocity and temperature equations while analyzing Brownian motion. The nonlinear ordinary differential equations that are obtained are computed utilizing the Bvp4c MATLAB approach. The following are the primary discoveries:

- The curvature parameter results in an improvement in velocity distribution. The reason is that for higher values of the curvature parameter, the radius of a curved sheet decreases. Hence, a smaller region of sheet will be in contact, which produces a small amount of resistance towards fluid particles, so that the velocity profiles show an enhancement. For

the curvature parameter, similar patterns are observable in the concentration and temperature distributions.

- Casson fluids are characterized by yield stress. When the Casson fluid flows over a curved surface, the shear stress at the surface increases due to the curvature, which exceeds the yield stress of the fluid. As a result, the Casson fluid profiles go down with enhanced inputs of Casson fluid parameter.
- The association between the magnetic field and the fluid becomes more intense across a curved surface. As a result, the Lorentz forces produced by the magnetic field act to oppose the fluid motion more effectively, causing a reduction in velocity.
- Enhanced inputs of the Forchheimer number over a curved surface lead to increased turbulence and convective heat transfer in fluid flow which is a reason of rise in temperature distributions.
- Concentration trends associated with the curved surface for the thermophoresis parameter are declining and growing with the Brownian motion parameter.
- Surface drag force profiles are higher for flat plate as compared to curved surface for enhanced inputs of Forchheimer number, porosity, Hartmann number, and Casson fluid parameter.
- Profiles related to heat transfer rate are proportional to radiation parameter and temperature Biot number but show an anti-proportional nature with growing inputs of Brickman and Hartmann number.
- Sherwood number profiles for curved surface are dominating over flat surface for distinct parameters named as chemical reaction, Brownian motion, thermophoresis parameter and Biot number.

Real world applications

We can explore several areas where this research can be applied in real-world scenarios:

- Utilising the results, targeted devices can function more effectively in the field of medicine delivery.
- The findings can be applied to improve the efficiency of targeted drug delivery systems.
- The study can help to understand blood flows through arteries with varying curvatures, which is crucial in designing medical devices such as stents and artificial blood vessels.
- The findings can be applied to the study of contaminant transport in groundwater.

Journal Pre-proof

- The research can be beneficial in the petroleum industry for enhanced oil recovery techniques.

Future recommendations

According to the outcomes of this assessment, it is suggested that additional research should be attempted to expand the current research on the Catteno-Christov model of unsteady Casson fluid flow across a doubly curved surface using an analytic approach.

AUTHOR DECLARATIONS

Conflict of Interest: "The authors have no conflicts of interest to declare."

Acknowledgments: "The authors extend their appreciation to the Deanship of Scientific Research at King Khalid University for funding this work through large group Research Project under grant number RGP 2/206/45."

Data Availability: "The data that provide confirmation for the findings of this study can be obtained from the corresponding author upon request."

References

1. R.L. Batra, B. Jena, Flow of a Casson fluid in a slightly curved tube, Int. J. Eng. sci. 29 (1991) 1245-1258, https://doi.org/10.1016/0020-7225(91)90028-2
2. S. Mukhopadhyay, P.R. De, K. Bhattacharyya, G.C. Layek, Casson fluid flow over an unsteady stretching surface, Ain Shams Eng. J. 4 (2013) 933-938, https://doi.org/10.1016/j.asej.2013.04.004
3. K. Kumar Anantha, V. Sugunamma, N. Sandeep, Effect of thermal radiation on MHD Casson fluid flow over an exponentially stretching curved sheet, J. Therm. Anal. Calorim. 140 (2020) 2377-2385, https://doi.org/10.1007/s10973-019-08977-0
4. M. Amjad, I. Zehra, S. Nadeem, N. Abbas, Thermal analysis of Casson micropolar nanofluid flow over a permeable curved stretching surface under the stagnation region, J. Therm. Anal. Calorim. 143 (2021) 2485-2497, https://doi.org/10.1007/s10973-020-10127-w
5. B. Nagaraja, B.J. Gireesha, Exponential space-dependent heat generation impact on MHD convective flow of Casson fluid over a curved stretching sheet with chemical reaction, J.

Therm. Anal. Calorim. 143 (2021) 4071-4079. DOI: https://doi.org/10.1007/s10973-020-09360-0

6. A. Roja, B.J. Gireesha, B. Nagaraja, Irreversibility investigation of Casson fluid flow in an inclined channel subject to a Darcy-Forchheimer porous medium: a numerical study, Appl. Math. Mech. 42 (2021) 95-108, https://doi.org/10.1007/s10483-021-2681-9
7. S. Maity, P.K. Kundu, magnetically driven chemically reactive Casson nanofluid flow over curved surface with thermal radiation, Heat Transf. 51 (2022) 4882-4905, https://doi.org/10.1002/htj.22527
8. F. Aljuaydi, Z. Khan, S. Islam, Numerical investigations of ion slip and Hall effects on Cattaneo-Christov heat and mass fluxes in Darcy-Forchheimer flow of Casson fluid within a porous medium, utilizing non-Fourier double diffusion theories through artificial neural networks ANNs, Int. J. Thermofluids. 20 (2023) 100475, https://doi.org/10.1016/j.ijft.2023.100475
9. S. Nadeem, B. Ishtiaq, M.B. Ben Hamida, S. Almutairi, H.A. Ghazwani, S.M. Eldin, A.S. Al-Shafay, Reynolds nano fluid model for Casson fluid flow conveying exponential nanoparticles through a slandering sheet, Sci. Rep. 13 (2023) 1953, https://doi.org/10.1038/s41598-023-28515-1
10. U.S. Mahabaleshwar, T. Maranna, M. Mishra, M. Hatami, B. Sunden, Radiation effect on stagnation point flow of Casson nanofluid past a stretching plate/cylinder, Sci. Rep. 14 (2024) 1387, https://doi.org/10.1038/s41598-024-51963-2
11. M.K. Murthy, Effects of heat and mass flux conditions on magnetohydrodynamics flow of Casson fluid over a curved stretching surface, Defect Diffus. Forum. 392 (2019) 29-41, https://doi.org/10.4028/www.scientific.net/DDF.392.29
12. M. Amjad, I. Zehra, S. Nadeem, N. Abbas, A. Saleem, A. Issakhov, Influence of Lorentz force and induced magnetic field effects on Casson micropolar nanofluid flow over a permeable curved stretching/shrinking surface under the stagnation region, Surf. Interfaces. 21 (2020) 100766, https://doi.org/10.1016/j.surfin.2020.100766
13. R. Raza, F. Mabood, R. Naz, S.I. Abdelsalam, Thermal transport of radiative Williamson fluid over stretchable curved surface, Therm. Sci. Eng. Prog. 23 (2021) 100887, https://doi.org/10.1016/j.tsep.2021.100887
14. H.Q. Shi, T. Shabbir, M. Mushtaq, M.I. Khan, Z. Shah, P. Kumam, Modelling and numerical computation for flow of micropolar fluid towards an exponential curved surface: a Keller Box method, Sci. Rep. 11(1) (2021) 16351, https://doi.org/10.1038/s41598-021-95859-x

Journal Pre-proof

15. T.A. Yusuf, R.A. Kareem, S.O. Adesanya, J.A. Gbadeyan, Entropy generation on MHD flow of a Casson fluid over a curved stretching surface with exponential space-dependent heat source and nonlinear thermal radiation, Heat Transf. 51 (2022) 2079-2098, https://doi.org/10.1002/htj.22389
16. M. Naveed, Z. Abbas, M. Sajid, Mixed Convection Flow of a Casson Fluid over a Curved Stretching Surface with Nonlinear Rosseland Thermal Radiation, J. Eng. Thermophys. 32 (2023) 824-834, https://doi.org/10.1134/S1810232823040148
17. A. Dawar, S. Islam, Z. Shah, S.R. Mahmuod, A passive control of Casson hybrid nanofluid flow over a curved surface with alumina and copper nanomaterials: A study on sodium alginate-based fluid, J. of Mol. Liq. 382, (2023) 122018, https://doi.org/10.1016/j.molliq.2023.122018
18. M. Mumtaz, S. Islam, H. Ullah, A. Dawar, Z. Shah, A numerical approach to radiative ternary nanofluid flow on curved geometry with cross-diffusion and second order velocity slip constraints, Int. J. Heat Fluid flow 105 (2024) 109255, https://doi.org/10.1016/j.ijheatfluidflow.2023.109255
19. B. Nagaraja, B.J. Gireesha, F. Almeida, P. Kumar, A.R. Ajaykumar, Entropy analysis of Darcy-Forchheimer model of Prandtl nanofluid over a curved stretching sheet and heat transfer optimization by ANOVA-Taguchi technique, J. Appl. Comput. Mech. 10(2) (2024) 287-303. DOI: https://doi.org/10.22055/jacm.2023.44524.4229
20. K. Sakkaravarthi, P. Bala Anki Reddy, Entropy generation on MHD Eyring-Powell hybrid nanofluid flow over a curved stretching sheet with shape factors and the Cattaneo–Christov heat flux model: A comparative study, *Sci. Iran*. (2024), https://doi.org/10.24200/SCI.2024.61292.7237
21. K. Murali, V.K. Naidu, B. Venkatesh, Solution of Darcy–Brinkman–Forchheimer equation for irregular flow channel by finite elements approach, J. Phys. Conf. Ser. 1172 (2019) 012033, https://doi.org/10.1088/1742-6596/1172/1/012033
22. M.I. Khan, F. Alzahrani, A. Hobiny, Simulation and modeling of second order velocity slip flow of micropolar ferrofluid with Darcy–Forchheimer porous medium, J. Mater. Res. Technol. 9 (2020) 7335-7340, https://doi.org/10.1016/j.jmrt.2020.04.079
23. B.J. Gireesha, B. Nagaraja, S. Sindhu, G. Sowmya, Consequence of exponential heat generation on non-Darcy-Forchheimer flow of water-based carbon nanotubes driven by a curved stretching sheet, Appl. Math. Mech. 41 (2020) 1723-1734, https://doi.org/10.1007/s10483-020-2647-7

Journal Pre-proof

24. R. Kumar Naveen, R.P. Gowda, B.J. Gireesha, B.C. Prasannakumara, non-Newtonian hybrid nanofluid flow over vertically upward/downward moving rotating disk in a Darcy–Forchheimer porous medium, Eur. Phys. J. Spec. Top. 230 (2021) 1227-1237, https://doi.org/10.1140/epjs/s11734-021-00054-8
25. M. A. Z. Raja, Z. Khan, S. Zuhra, N. I. Chaudhary, W. U. Khan, Y. He, ... & M. Shoaib, Cattaneo-christov heat flux model of 3D hall current involving biconvection nanofluidic flow with Darcy-Forchheimer law effect: Backpropagation neural networks approach. Case Stud. Therm. Eng. 26 (2021) 101168 (2021), https://doi.org/10.1016/j.csite.2021.101168
26. F. Wang, S.A. Khan, S. Gouadria, E.R. El-Zahar, M.I. Khan, S.U. Khan, Y.M. Li, Entropy optimized flow of Darcy-Forchheimer viscous fluid with cubic autocatalysis chemical reactions, Int. J. Hydrog. Energy. 47 (2022) 13911-13920, https://doi.org/10.1016/j.ijhydene.2022.02.141
27. B. Ali, S. Jubair, Rheological properties of Darcy–Forchheimer hybrid nanofluid flow with thermal emission and heat source over a curved slippery surface, *Pramana*, *97* (2023) 127, https://doi.org/10.1007/s12043-023-02605-1
28. Z. Shah, M. Sulaiman, A. Dawar, M.H. Alshehri, N. Vrinceanu, Darcy–Forchheimer MHD rotationally symmetric micropolar hybrid-nanofluid flow with melting heat transfer over a radially stretchable porous rotating disk, J. Therm. Anal. Calorim. (2024)1-17, https://doi.org/10.1007/s10973-024-12986-z
29. M.S. Abdel-Wahed, E.M.A. Elbashbeshy, T.G. Emam, Flow and heat transfer over a moving surface with non-linear velocity and variable thickness in a nanofluids in the presence of Brownian motion, Appl. Mathe. Comput. 254 (2015) 49-62 https://doi.org/10.1016/j.amc.2014.12.087
30. A. Genthon, The concept of velocity in the history of Brownian motion: From physics to mathematics and back, Eur. Phys. J. H. 45 (2020) 49-105, https://doi.org/10.1140/epjh/e2020-10009-8
31. M.Z. Saghir, M.M. Rahman, M. M. Brownian motion and thermophoretic effects of flow in channels using nanofluid: A two-phase model, Int. J. Thermofluids, 10, (2021) 100085 https://doi.org/10.1016/j.ijft.2021.100085
32. J.V. Tawade, C.N. Guled, S. Noeiaghdam, U. Fernandez-Gamiz, V. Govindan, S. Balamuralitharan, Effects of thermophoresis and Brownian motion for thermal and chemically reacting Casson nanofluid flow over a linearly stretching sheet, Results Eng. 15 (2022) 100448, https://doi.org/10.1016/j.rineng.2022.100448

Journal Pre-proof

33. K.A.M. Alharbi, Z. Khan, S. Zuhra, S. Islam, A. Ali, E. Tag-Eldin, S.R. Mahmoud, Numerical study of the electromagnetohydrodynamic bioconvection flow of micropolar nanofluid through a stretching sheet with thermal radiation and stratification, ACS omega, 7(47) (2022) 42733-42751, https://doi.org/10.1021/acsomega.2c04145
34. Z. Khan, S. Zuhra, S. Islam, M. A. Z. Raja, A. Ali, Modeling and simulation of Maxwell nanofluid flows in the presence of Lorentz and Darcy–Forchheimer forces: toward a new approach on Buongiorno's model using artificial neural network (ANN). Eur. Phys. J. Plus, 138 (2023) 107, https://doi.org/10.1140/epjp/s13360-022-03583-w
35. R. P. Sharma, S.R. Mishra, G.K. Panda, P.K. Pattnaik, Effects of Brownian and thermophoresis on the nanofluid flow with zero nanoparticle mass flux and convective conditions through non-linearly expanding Riga plate, Mod. Phys. Lett. B, 38 (2024) 2450026, https://doi.org/10.1142/S021798492450026X
36. M. Sajid, N. Ali, T. Javed, Z. Abbas, Stretching a curved surface in a viscous fluid, Chi. Phys. Lett. 27 (2010) 024703, https://doi.org/10.1088/0256-307X/27/2/024703
37. Z. Abbas, M. Naveed, M. Sajid, Heat transfer analysis for stretching flow over a curved surface with magnetic field, J. Eng. Thermophys. 22 (2013) 337-345 https://doi.org/10.1134/s1810232813040061
38. D. A. Nield, A. Bejan, Convection in porous media, New York springer, 3 (2006) 629-982, https://doi.org/10.1007/978-3-319-49562-0
39. T. Hayat, S. Qayyum, M. Imtiaz, A. Alsaedi, Double stratification in flow by curved stretching sheet with thermal radiation and joule heating, J. Therm. Sci. Eng. Appl. 10 (2018) 021010, https://doi.org/10.1115/1.4037774
40. R.S. Varun Kumar, P. Gunderi Dhananjaya, R. Naveen Kumar, R.J. Punith Gowda, B.C. Prasanna kumara, Modeling and theoretical investigation on Casson nanofluid flow over a curved stretching surface with the influence of magnetic field and chemical reaction, Int. J. Comput. Meth. Eng. 23 (2022) 12-19, https://doi.org/10.1080/15502287.2021.1900451
41. P. Vyas, Gajanand, S. Khan, Irreversibility analysis for Casson thermo-fluidics inside a cone: Cattaneo–Christov heat flux, Heat Transf. 51 (2022) 4584-4619, https://doi.org/10.1002/htj.22514
42. K. Sharada, B. Shankar, MHD mixed convection flow of a Casson fluid over an exponentially stretching surface with the effects of soret, dufour, thermal radiation and chemical reaction, World J. Mech. 5 (2015) 165-177. https://doi.org/10.4236/wjm.2015.59017

Journal Pre-proof

43. I.L. Animasaun, N.A. Shah, A. Wakif, B. Mahanthesh, R. Sivaraj, O.K. Koríko, Ratio of momentum diffusivity to thermal diffusivity: introduction, meta-analysis, and scrutinization, *CRC Press* (2022).

Journal Pre-proof

Conflicts of Interest

"The authors declare that they have no conflicts of interest".

Journal Pre-proof

Journal of Physics: Conference Series

PURPOSE-LED PUBLISHING™

PAPER • **OPEN ACCESS**

Comparison Study on Experimental and Computational Structural Analysis for Kevlar Composite by Polyester resin.

To cite this article: B. Nagaraj Goud *et al* 2024 *J. Phys.: Conf. Ser.* **2837** 012010

View the article online for updates and enhancements.

You may also like

- Unhole and open hole compressive behaviours of hybrid Kevlar/glass fibre reinforced silica nanocomposites
Norazean Shaari and Aidah Jumahat
- Anti-impact behavior of a novel soft body armor based on shear thickening gel (STG) impregnated Kevlar fabrics
Chunyu Zhao, Chenhui Xu, Saisai Cao et al.
- A smart Kevlar-based triboelectric nanogenerator with enhanced anti-impact and self-powered sensing properties
Fang Yuan, Shuai Liu, Jianyu Zhou et al.

This content was downloaded from IP address 106.0.37.90 on 21/10/2024 at 11:04

Journal of Physics: Conference Series **2837** (2024) 012010 doi:10.1088/1742-6596/2837/1/012010

Comparison Study on Experimental and Computational Structural Analysis for Kevlar Composite by Polyester resin.

B. Nagaraj Goud [1], P. Aravind[2], B. Jawahar Lal[3], K. Sanskruti[4], Ch. Pavan[5]

[1]nagaraj2107@gmail.com
[2]aravindpaindla8@gmail.com
[3]jawaharlalbhogikar@gmail.com
[4]sanskruthikesarkar03@gmail.com
[5]chinthiralapavan@gmail.com

[1,2,3,4,5] Department of Aeronautical Engineering, MLR Institute of Technology, Hyderabad 500 043, India

Abstract. The finite element method was used to analyze Kevlar composite material under the most extreme conditions. The goal of the comparison study between experimental and computational studies of the tensile and flexural behavior of Kevlar woven fabric laminated composite was tested experientially under UTM. As a result, this work aims to approach the modelling of Kevlar composite material by focusing on material properties and failure criteria. The computational results agree well with the experimental results from the literature. The research is conducted utilizing the ANSYS (ACP) program and the finite element technique (FET). ANSYS (ACP) Software was used to model the fiber geometry and generate meshes and approaches to incorporate damage initiation and evolution. The experimental results of woven Kevlar fiber combined with polyester resin were obtained for six layers of the laminate by ASTM Standards, as well as mechanical properties of the woven Kevlar fiber. The CATIA V5 software is used to create the composites design model, and the modal responses are obtained via a simulation model that takes into account the individual layer effects of each Sample test specimen via the ANSYS static-structural module.

Key words: Kevlar composite, polyester resin, mechanical properties, stresses and deformation.

1. Introduction

Composite materials are a major concern in engineering applications, due to their superior features like as high strength-to-weight ratios, outstanding fatigue capabilities, excellent dynamics, and corrosion properties. The most recent advancements in composite materials and adaptable structures have enabled. To determine the accurate response of a product design, finite element (FE) modelling has been widely used in civil, aerospace, and mechanical engineering applications. Because of its ability to apply to irregular geometry in the form of shells or plates containing composite material properties, FE modelling has proven to be a powerful tool used in aerospace engineering applications [1]. Composites are primarily used in structural engineering for the construction of bridges, aircraft structures, and automotive structures, among other things. The strength-to-weight ratio When compared to reinforced concrete and steel, KFRP (Kevlar Fibre Reinforced Polymer) is better suited to handle peak loads than other composites. Kevlar fibre is a type of synthetic fibre that belongs to the Aramid family. It is widely used as a replacement for alloys and composites in all material manufacturing processes.

Content from this work may be used under the terms of the Creative Commons Attribution 4.0 licence. Any further distribution of this work must maintain attribution to the author(s) and the title of the work, journal citation and DOI.
Published under licence by IOP Publishing Ltd

1.1 Fibre orientation of composites

The orientation of fibres has a significant impact on the strength of a part. Unidirectional, random, bidirectional, and multi-directional are the four most common orientations in fibre-reinforced composites. [10] Fibre orientation, regardless of the direction of fibres within the material, can significantly improve the mechanical and chemical properties of an injection moulded part. The optimal structural arrangement of individual fibres in developing and manufacturing advanced composite materials (ACM) and fibre-reinforced composites is referred to as fibre orientation (FRC). The orientation of the fibre in the matrix will affect the composite's mechanical strength. The shape and size of structure constituents, as well as the distribution of natural fibre reinforced composites, are important factors in the overall composite appearance.

1.2 Kevlar fibre

Kevlar is an example of aramid fibre. It is woven into textile materials and is extremely strong and lightweight, with corrosion and heat resistance. It is used in a wide range of applications, including aerospace engineering (such as aircraft bodies), body armour, bulletproof vests, car brakes, and boats. Kevlar® fibre is more than a collection of threads. DuPont TM Kevlar® fibres are used to make clothing, accessories, and equipment safer and more durable. It's the go-to fibre for protective apparel and accessories, with five times the strength of steel based on equal weight. Kevlar® fibre and filament are available in a variety of forms, each with its own set of properties and performance characteristics tailored to specific protection requirements. Kevlar is available in three grades: Kevlar 29, Kevlar 49, and Kevlar 149. The table below depicts the differences in material properties between the various grades. It is most likely the Kevlar 49 version, which is widely available. The three versions are compared Tensile Modulus of Kevlar 29 = 83 G Pa, Tensile Strength = 3.6 GPA, Elongation = 4.0 percent Tensile Modulus of Kevlar 49 = 131 G Pa, Tensile Strength = 4.0 G Pa, Elongation = 2.8 percent Kevlar 149 has a tensile modulus of 186 G Pa, a tensile strength of 3.4 G Pa, and an elongation of 2.0 percent [5].

1.3 Polyester Resin

Polyesters are widely used in commercial applications, but their use in high-performance composites is limited. Polyester, while less expensive than epoxies, has a lower temperature capability. [7] Polyester is made up of at least three components: a polyester, a crosslinking agent like styrene, and an initiator. The crosslinking or curing agent used has a strong influence on the properties of the resulting polyester. One of the primary advantages of polyester is that it can be formulated to cure at either room or elevated temperatures, giving it great processing versatility [11].

1.4 Applications of composite

Aerospace, transportation, construction, marine goods, sporting goods, and, more recently, infrastructure are some of the applications. In general, high-performance but more expensive continuous fibre composites drove the development of much of the technology now used by other industries. Composites are used in both small and large commercial aircraft to reduce weight and improve fuel performance [8-10].

1.5 Composite laminate

A lamina is a lay-up that consists of a single-ply or a lay-up in which all of the layers or plies are stacked in the same orientation. The lay-up is known as a laminate when the plies are stacked at different angles. Continuous-fibre composites are typically laminated materials in which the individual layers, piles, or laminate are oriented to improve strength in the primary load direction [11-12]. The various types of composite laminate are Uni-directional lamina(ply) with continuous fibre, Uni-directional lamina with discontinuous fibre, Random orientation plane,3D- orientation short fibres/whisker, Woven fabric composite, Hybrid-fibre composite,3Dwoven/stitched/braided composite [13-18].

2. Analysis of Tensile Test.

To analyze the stress, strain and deflection for a rectangular beam of 250mm*25mm*3 with a load of 8720N and 12500N and 16220N.

2.1 Ansys Workbench

Open the engineering data and enter the data, Type of material used in this is Kevlar composite and polyester resin, also add the properties like (Density=1440kg/m-3, Youngs modulus=76000mpa, Poisson's ratio=0.3)

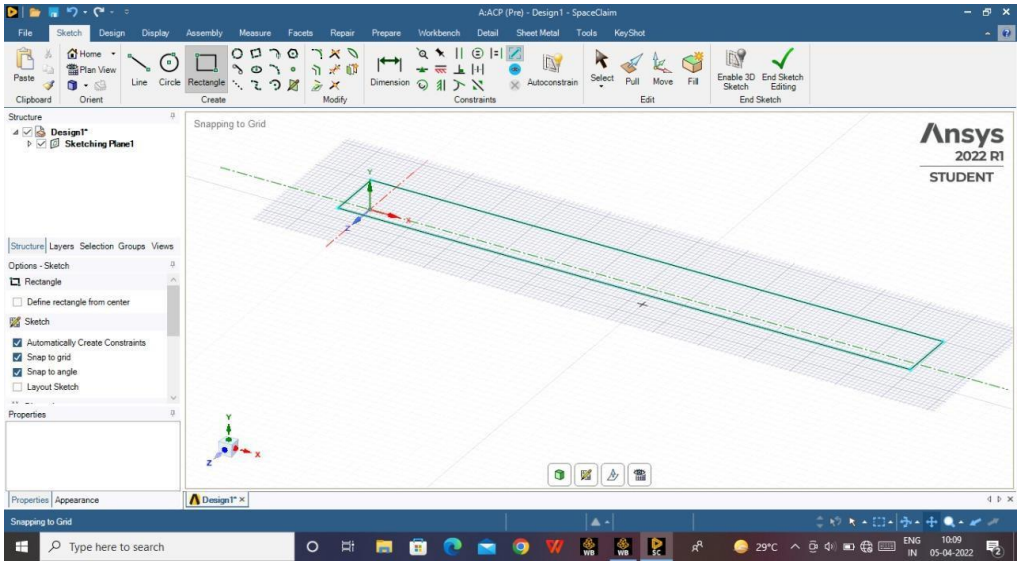

Figure1: Assigning Material Properties for tensile test

2.2 Geometry

Open the space claim designer and select the rectangle shape to draw the (250mm*25mm) rectangle

2.3 Modelling

Ansys is used to model the Kevlar fibre reinforced polymer (KFRP) composite with a sandwich structure. Right-click and go to the edit option, select geometry (ACP/Pre/surface) The dimensions of the 3D deformable solid body are Length=250, Width=25, and Thickness=3.

2.4 Meshing

Mesh is the process of transforming irregular shapes into more recognizable volumes known as elements. When using ANSYS simulation software, it is critical to determine which features of your model to use. Stimulation describes the relationship between two or more parts of your geometry. When your geometry shares nodes between common faces, you must decide whether it will be a conformal or non- conformal mesh. For parts joined by glue or welds, a conformal mesh is used. A non-conformal mesh is used to connect parts that are joined by contacts or joints.

Click on mesh→ update → insert → reinforcement →select geometry selection (select all) →apply →change reinforcement up to 3→generate mesh → update mesh part.

2.5 Set-up

Update the material data for the ACP model by right-clicking and selecting Kevlar composite and polyester resin. Choose fabric 1 and give it the name Kevlar. Take the material Kevlar composite and apply it. Choose fabric and give it the name Polyester resin. Take the material Polyester resin and apply it. Element set→ all element→ update. Rosette→ global co-ordinate system→ update. Go to the oriented selection set to start creating element set (all element) orientation (give 1for direction rosette (global coordinate system) apply ok. Create a modelling group by naming group one and apply it. Go to Modelling group one and create a ply for ply one by giving an oriented selection set one ply the material (Kevlar composite) ply angle (0.0) apply ok. Repeat for polyester resin by providing ply material and ply angle apply ok. Repeat the Kevlar material for six layers by changing the ply angle (0°,90°,0°,90°,0°,90°) apply ok. Apply resin in the same manner for six layers in between layers with ply angle (0) apply ok. Click on Solid model and create (solid model one element set (all elements) apply ok Update the configuration by selecting the ACP model static structural

Copy and paste static structural→ connect setup to static structural model (transfer solid composite shell)

2.6 Boundary conditions

Boundary conditions are essential components of a mathematical model. They direct the motion of flow which leads to a unique solution. In ANSYS we use standard boundary conditions such as inlet, outlet, wall, and symmetry. The main types of loading in FEA include force, pressure and temperature. These can be applied to

points, surfaces, edges, nodes and elements. The displacement and rotation of the model are constrained as per the conditions and a load of surface traction is applied in the composite.

Right -click →edit →static structural →insert →fixed support→ geometry (select the face 1side) → apply. Rotate the figure → insert →force/displacement→ geometry (select another face) →apply to →give the magnitude (1.706e+007 N) or (17.060KN)

3. Analysis of Flexural Test

To analyze the stress, strain and deflection for a rectangular beam of 130.56mm*13mm*3 with a load of 78.5N, 82N, 85.5N.

3.1 Ansys workbench

Open the engineering data and enter the data, Type of material used in this is Kevlar composite and polyester resin, also add the properties like (Density=1440kg/m-3, Youngs modulus=76000mpa, Poisson's ratio=0.3)

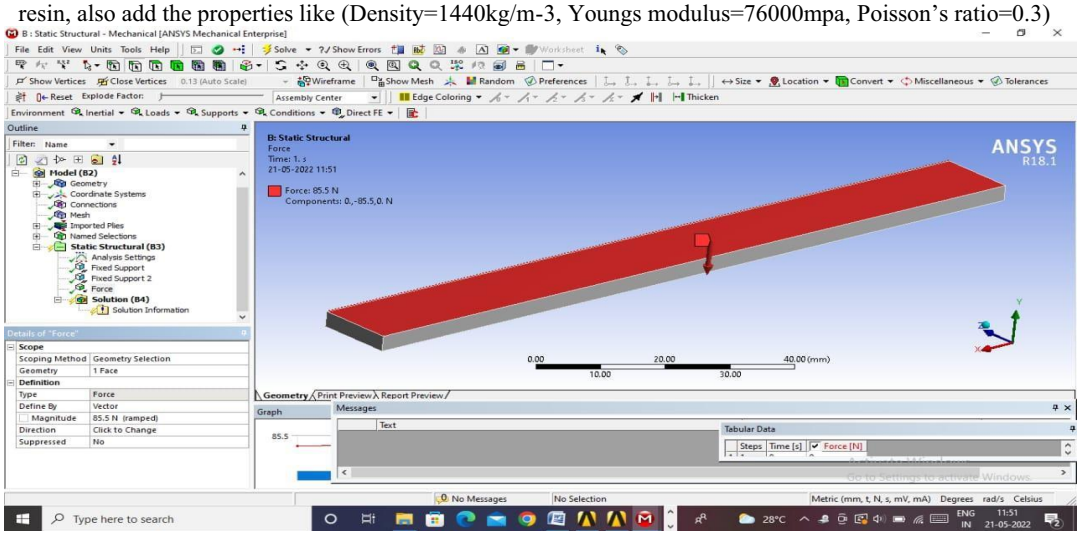

3.2 Geometry

Open the space claim designer and select the rectangle shape to draw the (130.56mm*13mm) rectangle

3.3 Modelling

ANSYS is used to model the Kevlar fibre reinforced polymer (KFRP) composite with a sandwich structure. Right-click and go to the edit option, select geometry (ACP/Pre/surface) The dimensions of the 3D deformable solid body are Length=130.56, Width=13, and Thickness=3

3.4 Meshing

Finite element mesh is done on the composite using mesh option, in order to obtain stress and deformation at different layers.

Click on mesh → update → insert → reinforcement → select geometry selection (select all) → apply → change reinforcement up to 3→generate mesh → update mesh part.

4. Results & Discussion

The experimental results of woven Kevlar fiber combined with polyester resin were obtained for six layers of the laminate by ASTM Standards, as well as mechanical properties of the woven Kevlar fiber and computational results agree well with the experimental results from the literature. The research is conducted utilizing the ANSYS (ACP) program and the finite element technique (FET). ANSYS (ACP) Software was used to model the fiber geometry and generate meshes and approaches to incorporate damage initiation was presented.

Table1. Experimental Results of Tensile test

Sample no	Ultimate Load (N)	Max Deflection (mm)	Percentage elongation (%)
01	8200	0.953	1.895
02	8720	0.984	1.953
03	12500	1.381	2.760
01	8200	0.953	1.895
02	8720	0.984	1.953

Table2. Experimental Results of Flexure test

Sample no	Ultimate Load (N)	Max Deflection (mm)	Percentage elongation (%)
01	780	1.724	75.69
02	820	1.751	86.09
03	850	1.823	87.52

Table 3. Computational Results of Tensile test and Flexural test

Load (N)	Sample no	Total deformation (mm)	Max Principal stress (M pa)	Shear stress (M pa)	Equivalent stress (mm)	Equivalent strain (mm)
Tensile test						
8720	01	0.662	279.72	34.616	248.2	0.0032
12500	02	0.949	400.97	49.621	355.8	0.0046
16200	03	1.231	520.27	64.351	461.74	0.0060
Flexural test						
78.5	01	0.704	36.06	19.936	215.36	0.00283
82	02	0.736	37.636	20.825	224.96	0.00296
85.5	**03**	**0.480**	**39.242**	**21.721**	**234.52**	**0.00308**

Table 4. Comparison of Experimental Results with Computational Results

S. no	Type of test	Sample test specimen number	Experimental (Max Deformation) mm	Computational (Max Deformation) mm
01	**Tensile**	1	0.953	0.662
		2	0.984	0.949
		3	1.381	1.231
02	**Flexural**	1	1.724	0.704
		2	1.751	0.736
		3	1.823	0.767

5. Conclusion

In this paper, we compared designed Kevlar laminates in this project. We used simulation software (ANSYS) ACP to provide the required boundary conditions and ply angle orientation. The loads were the same as in the experiment, a total of six samples are tested three for tensile and the other three for flexural, and dimensions are taken as per ASTM standards (D3039 & D7264). The three tensile test samples are of different loading conditions for that are (sample 1 (8720N), sample 2 (12500N), and sample 3 (16220N)), the highest deformation is observed in (sample 3) is 1.231mm and the lowest deformation is observed in (sample 1) is 0.662mm because the maximum load is of sample 3 and minimum load is of sample 1, Average deformation of three samples is 0.947mm which is same as sample 2 by this we can understand sample 2 performed better than other two and when we observe both the deformation of experimental and computational the difference found 0.5% to 1% among the three samples. Therefore, the results of experimental and computational for the tensile test are found very close.

The other three samples are of flexural test and their loads for each sample are (85.5N Sample1) (78.5N Sample2)

(82N sample3), the highest deformation is observed in sample 1 is 0.767mm and the lowest deformation is observed in sample 2 is 0.704mm because the maximum load is of sample 1 and minimum load is of sample 2, Average deformation of three samples is 0.735mm which is close to sample 3 and By observing the above deformation results of both Experimental and computational the difference found 0.2% to 0.6% among the three samples.
Therefore, the results of experimental and computational for the flexural test are found very close. Comparing both types of the test found that the results as been increased in experimental by 0.5 to 1% in tensile and 0.2% to 0.6% in flexural. Therefore, the strength of Kevlar has been increased practically.

6. References

[1] Ernnie Illyani Basri, Mohamed Thariq Hameed Sultan, Adi Azriff Basri, Faizal Mustapha & Kamarul Arifin Ahmad. Consideration of Lamination Structural Analysis in a Multi-Layered Composite and Failure Analysis on Wing Design Application, Materials2021,14,3705. *https://doi.org/10.3390/ma14133705*

[2] Raj Kumar, G. R., Vijayanandh, R., Venkatesan, K., Ramesh, M., Kumar, M. S., & Balaji, S. (2020, March). Comparative Investigations on the Main Elements of Carbon Fibre Based Composites Using Computational Structural Simulations. In Journal of Physics: Conference Series (Vol. 1504, No. 1, p. 012003). IOP Publishing.

[3] S Indira Prasanth1, K Kesavan1, P Kiran1, M Sivaguru1, R Sudharsan1, G Raj Kumar1 and R Vijayanandh. Fibre Oriental Optimization on Glass Fibre Reinforced Polymer Composite in Multi-Objective Perspective based on Computational Structural Analysis Journal of Physics Conference Series 1849 (2021) 012005 IOP Publishing doi:10.1088/1742-6596/1849/1/012005

[4] Talib, AR Abu, A. A. Ramadhan, AS Mohd Rafie, and R. Zahari. "Influence of cut-out hole on multi-layer Kevlar-29/epoxy composite laminated plates." Materials & design 43 (2013): 89-98.

[5] Manigandan, S. "Computational investigation of high-velocity ballistic impact test on Kevlar 149." Applied Mechanics and Materials 766 (2015): 1133-1138.

[6] Muthalagu, R., J. Murugesan, S. Sathees Kumar, and B. Sridhar Babu. "Tensile attributes and material analysis of kevlar and date palm fibres reinforced epoxy composites for automotive bumper applications." Materials Today: Proceedings 46 (2021): 433-438.

[7] Yahaya R, Sapuan SM, Jawaid M, et al. Effects of kenaf contents and fiber orientation on physical, mechanical, and morphological properties of hybrid laminated composites for vehicle spall liners. Polymer Composite 2014. DOI: 10.1002/pc.23053.

[8] Cheng, M., Chen, W., & Weerasooriya, T. (2005). Mechanical properties of Kevlar KM2 single fibre. Journal of Engineering Materials and Technology, Transactions of the ASME, 127, 197–203. https://doi.org/10.1115/1.1857937

[9] M. Ganesh, K. Shiva Shankar "Modelling And Analysis Of Scaffolding Structure Used In Aerospace Vehicle*"(IJSR)*Volume 4 Issue 5, May 2015,Issn (Online): 2319-7064.

[10] K. Veeranjaneyulu, M.S.N Gupta, Dhana Jayan Vamsi, Damage Analysis of Low Speed Impact On Composite Materials, International Journal of Civil Engineering & Technology (IJCIET).

[11] Alka Sawale, Nayani Uday Ranjan Goud, M.Srinikitha "Experimental Analysis of Stress Concentration on V-Notched Plate" International Journal of Innovative Technology and Exploring Engineering *(IJITEE)* ISSN: 2278-3075, Volume-9 Issue-2, December 2019, page No 3709-3712

[12] G. Dhanajayan, Veeranjaneyulu Kalavagunta, V. Vamshi, M. Satyanarana Gupta, Environmental Study on GFRP Composite Laminates, International Journal of Civil Engineering & Technology (IJCIET).

[13] Vemanaboina, H., Akella, S., Buddu, R.K., Yelamasetti, B., Matam, M.B., Salem, K.H., Saxena, K.K., Prakash, C., Buddhi, D "Prediction of thermal and residual stress distributions in SS304 materials for nuclear application using finite element analysis" (2023) International Journal on Interactive Design and Manufacturing,

[14] Shiva, A., Cheepu, M., Kantumuchu, V.C., Ravi Kumar, K., Venkateswarlu, D., Srinivas, B., Jerome, S. "Microstructure Characterization of Al-TiC Surface Composite Fabricated by Friction Stir Processing" (2018) IOP Conference Series: Materials Science and Engineering, 330 (1), art. no. 012060

[15] Ashok Reddy, K. "Non-Destructive Testing, Evaluation of Stainless-Steel Materials" (2017) Materials Today: Proceedings, 4 (8), pp. 7302-7312

[16] Vemanaboina, H., Babu, M.M., Prerana, I.C., Gundabattini, E., Yelamasetti, B., Saxena, K.K., Salem, K.H., Khan, M.I., Eldin, S.M., Agrawal, M.K. "Evaluation of residual stresses in

CO2 laser beam welding of SS316L weldments using FEA" (2023) Materials Research Express, 10 (1), art. no. 016509,

[17] Robert Xavier, A., Ravichandran, A.T., Ravichandran, K., Mantha, S., Ravinder, D. Sm doping effect on structural, morphological, luminescence and antibacterial activity of CdO nanoparticles (2016) Journal of Materials Science: Materials in Electronics, 27 (11), pp. 11182-11187

[18] Praveen, L., Geeta Krishna, P., Venugopal, L., Prasad, N.E.C Effects of pulse on and off time and electrode types on the material removal rate and tool wear rate of the Ti-6Al-4V Alloy using EDM machining with reverse polarity (2018) IOP Conference Series: Materials Science and Engineering, 330 (1), art. no. 012083.

Journal of Physics: Conference Series

PURPOSE-LED PUBLISHING™

PAPER • **OPEN ACCESS**

Composite Laminates with Epoxy Resin and E-Glass Fibers: Analysis of Mechanical Properties

To cite this article: K. Pranathi *et al* 2024 *J. Phys.: Conf. Ser.* **2837** 012008

View the article online for updates and enhancements.

You may also like

- Failure Analysis of Bypass Rupture of Flowmeter in Steam Pipeline
  Ting Yu, Bin Du, Fengping Zhong et al.
- Traditional ecological knowledge of the Moronene tribe: insights into forest conservation practice in Bombana Area, Southeast Sulawesi
  Basri, A Ferdinan, H Powatu et al.
- A Vortex Electromagnetic Wave Beam Control Method based on Amplitude-Modulated Concentric Circular Array
  Jiayue Sun, Qian Chen, Chaowei Fu et al.

This content was downloaded from IP address 106.0.37.90 on 21/10/2024 at 11:24

Journal of Physics: Conference Series **2837** (2024) 012008 doi:10.1088/1742-6596/2837/1/012008

Composite Laminates with Epoxy Resin and E-Glass Fibers: Analysis of Mechanical Properties

K. Pranathi [1], S MD Adib Ayub[1], CH Paul[1]

[1]Department of Aeronautical Engineering, MLR Institute of Technology, Hyderabad, Telangana, India

*Corresponding author email: pranathishree2003@gmail.com

Abstract

Polymer fibre-reinforced composites are extensively researched for their potential in high-performance industries such as aerospace, automotive, and ground transportation. These composites offer high strength and inertia. However, their use is hindered by inherent drawbacks, primarily the inability to absorb moisture and high flammability compared to natural fibres. Despite these challenges, composites made from glass and specialty synthetic fibres continue to be attractive due to benefits like a high strength-to-weight ratio and excellent resistance to heat and chemicals. To overcome the limitations of polymer fibres, natural fibres are often combined with synthetic ones. This combination aims to create materials that maintain high strength and stiffness while improving resistance to moisture absorption and fire hazards. Such composite materials offer the possibility of achieving enhanced performance at desired levels. Composite materials, particularly those with low thermal expansion, play a vital role in aerospace components due to their exceptional mechanical properties, including strength and stiffness-to-density ratios. This research focuses on composite laminates using epoxy resin and E-glass fibre reinforcement, analysed through Ansys software. The study characterizes the mechanical properties, such as compressive and tensile strength, of these laminates. The results reveal that laminates with synthetic fibres possess attributes favouring their selection for structural components. These findings highlight the potential of composite materials to meet the demanding performance requirements of industries like aerospace and automotive. Advancements in composite manufacturing processes and material science have led to significant improvements in the performance and versatility of polymer fibre-reinforced composites. Ongoing research aims to address remaining challenges, including enhancing resistance to moisture absorption and fire hazards, through strategies such as incorporating nanomaterials and developing novel fibre treatments. With continued progress, these composites are poised to play an increasingly significant role in various high-performance applications.

1. Introduction

The fluid that covers and binds the reinforcement phase, which is frequently made up of fibers, particles, or other forms is the matrix in composite materials. Whenever two or more different types of components are combined to create a new material with characteristics that are different from its individual components, the resulting material is commonly referred to as a composite [1-6]. The individual materials or phases, at times called as the components, could be made up of many kinds of materials like metals, ceramics, polymers, or a combination of these Glass fibres found within a polymer matrix typically polyester, epoxy, or vinyl ester resincompose the composite material known as fiberglass [7]. Fiberglass is used extensively in construction, automotive, aerospace, and other sectors because of its substantial strength-to-weight percentage, ability to withstand corrosion, and flexibility.

Content from this work may be used under the terms of the Creative Commons Attribution 4.0 licence. Any further distribution of this work must maintain attribution to the author(s) and the title of the work, journal citation and DOI.
Published under licence by IOP Publishing Ltd

Its insulating characteristics and moldability further add to its widespread adoption. Composite materials, renowned for their versatility, often demand a careful consideration of fiber types. In this section, we delve into the specific characteristics of E-Glass as a key reinforcing fiber and its implications for structural analysis [8].

2. Impact of e-glass on environment

E-Glass, a widely used synthetic fibre, has significant implications for environmental sustainability. Assessing its production, usage, and disposal processes is crucial [9]. While E-Glass is durable and corrosion-resistant, its manufacturing involves high-energy consumption. This prompts the exploration of more eco-friendly alternatives.

2.1 Comparison of E-Glass Fibre with Natural Fibre

2.1.1 E-Glass vs Sisal

E-Glass and sisal fibres stand at opposing ends of the spectrum regarding origin and properties. E-Glass, being a synthetic fiber, boasts high strength and resistance to chemicals [10]. Conversely, sisal, a natural fiber, offers a biodegradable and renewable alternative but may fall short in certain mechanical properties.

2.1.2 E-Glass vs Hemp

Contrasting E-Glass with hemp fiber unveils another facet of material selection. Hemp, a natural fiber, demonstrates excellent tensile strength and environmental friendliness [11]. However, E-Glass outshines it in terms of stiffness and resistance to harsh conditions. The choice between these fibers depends on specific application requirements.

2.2 E-Glass and Synthetic Fiber Integration

E-Glass can be effectively integrated with various synthetic fibers to create composite materials with tailored properties. This combination capitalizes on the strengths of both materials, providing a balanced approach to structural reinforcement [12]. The synergy between E-Glass and synthetic fibers enhances the overall performance and widens the application range of composite materials.

In conclusion, the selection of E-Glass as a fiber for composite materials involves a thorough evaluation of its environmental impact, a comparative analysis with natural fibers like sisal and hemp and exploring its compatibility with synthetic fibers. Balancing mechanical properties, environmental considerations, and application requirements is essential for making informed choices in composite material design.

3. Selection of Resin

In the realm of composite materials, the choice of resin is pivotal, influencing the mechanical properties, durability, and overall performance of the material. This section delves into the specifics of epoxy resin, a commonly used synthetic resin known for its versatility and adhesive properties.

3.1 Resin

While natural resins exist, epoxy resin distinguishes itself with exceptional characteristics suitable for a broad spectrum of applications [13]. Its synthetic nature provides precise control over formulation, ensuring consistent and reliable material properties. This aspect is particularly crucial in structural applications where predictability and performance are paramount.

3.2 Synthetic Resin - Epoxy Resin

Epoxy resin, a thermosetting polymer, is a cornerstone in composite material engineering fig 1. Its reputation stems from numerous positive properties: Versatility-Epoxy resin is versatile and can be tailored to meet specific requirements [14]. Its ability to be reinforced with various fibers allows for the creation of composites with a wide range of mechanical properties.

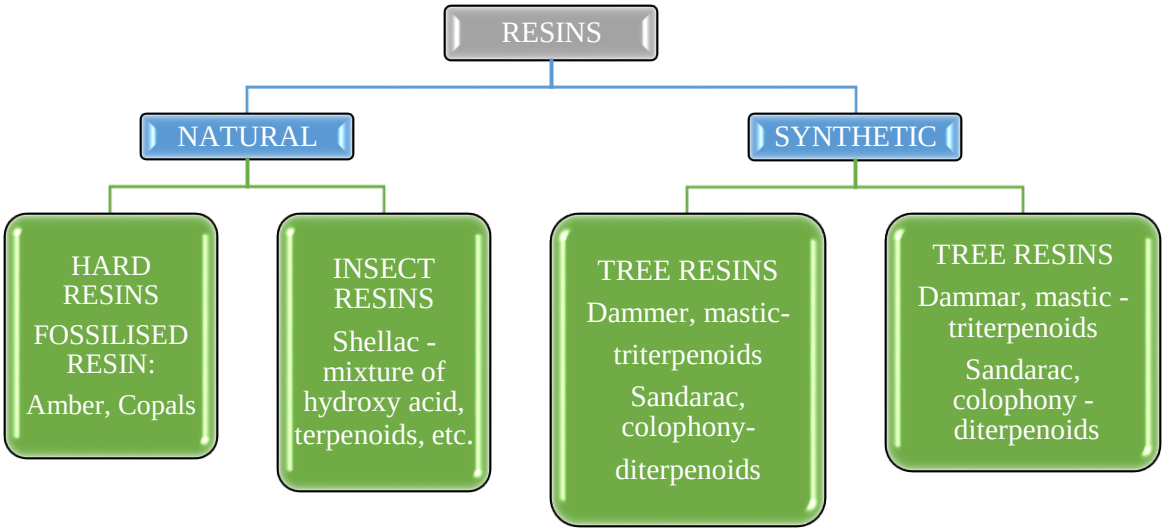

Fig 1. Types of resins

Durability: Epoxy resin is highly durable and resistant to environmental factors such as moisture, chemicals, and temperature fluctuations. This makes it suitable for applications where the material is exposed to challenging conditions.

3.3 Applications of Epoxy Resin in Composite Materials

Epoxy resin finds extensive use in various industries, including aerospace, automotive, and construction. Its versatility makes it an ideal choice for manufacturing components requiring high strength-to-weight ratios, corrosion resistance, and dimensional stability [15].

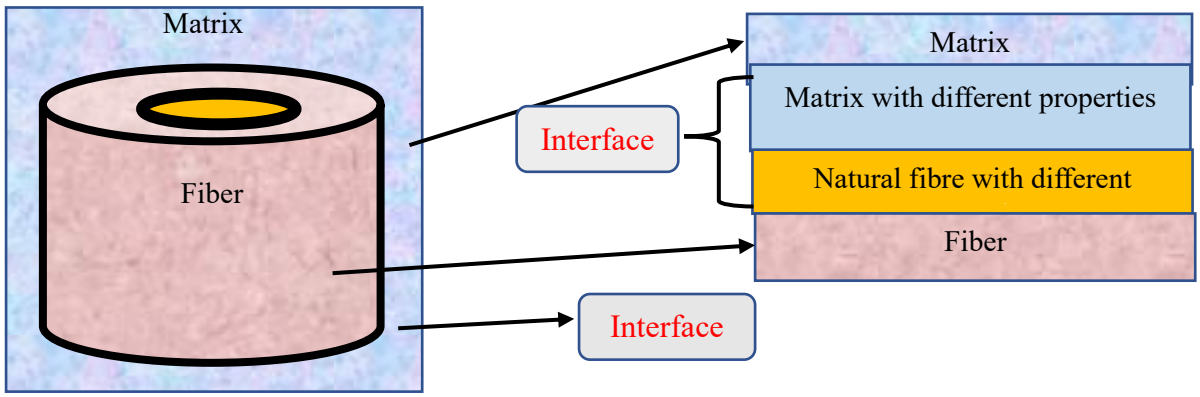

Fig 2. Schematic Illustration of Interphase in the Composite Materials

In real time, the selection of epoxy resin in composite materials is driven by its remarkable adhesive strength, durability, versatility, and wide-ranging applications. A suitable application for composite

laminates with epoxy resin and E-glass fiber reinforcement is in the manufacturing of aerospace structural components. These laminates offer a combination of high strength, stiffness, and lightweight properties, making them ideal for aerospace applications. Specifically, they can be used in aircraft fuselages, wings, empennage structures, and interior components. Their superior mechanical properties allow for reduced weight without compromising structural integrity, resulting in improved fuel efficiency and performance. Additionally, the corrosion resistance of composite materials makes them suitable for long-term use in harsh aerospace environments. Overall, these laminates offer significant advantages in aerospace engineering, contributing to safer, more efficient aircraft designs.

4. Analysis Procedure

Analysis is done using the Ansys 2024 R1 (ACP), Ansys Composite PrePost. The composite material is combined using the ACP engineering data and applied to the model of thin plate designed in the Ansys geometry and then it is meshed perfectly. The procedure is labelled below in fig 3.

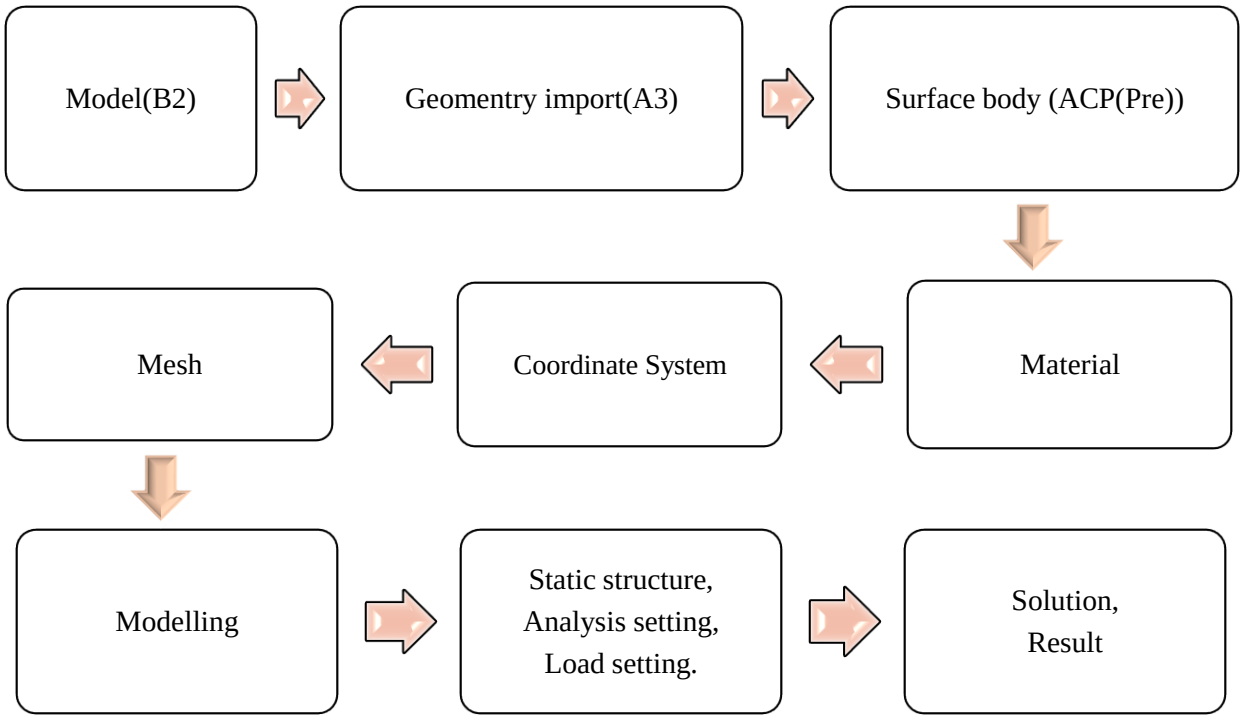

Fig 3. Ansys analysis procedure

In the case(i) fixed end is applied at the left end and the bottom end, the opposite side is fixed using box selection and nodes in static structure. In the case(ii) fixed end is applied at the left end only, load is applied on the opposite side is fixed using box selection and nodes in static structure. In static structure the following material properties are analyzed and snipped.

5. Result

The analysis of composite structure of E-glass and epoxy resin in Ansys are evaluated and the results of case(i) two ends fixed, opposite side the pressure is applied fig 4(a) and fig 4(b). Case(ii) one end is

fixed, opposite side the pressure is applied fig. In the second case the stress and strain loads are also applied to evaluate the stress and strain patterns fig4 - fig.

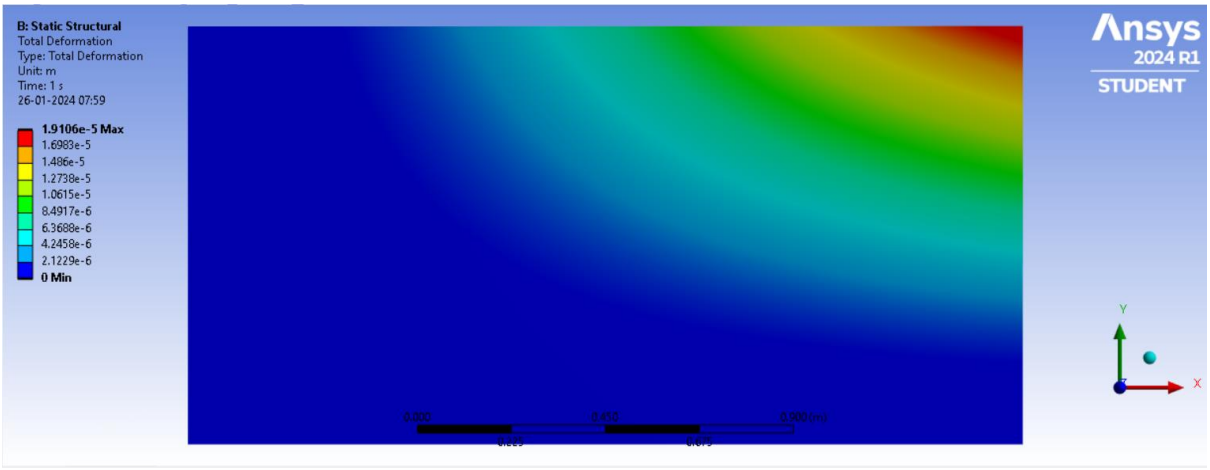

Fig 4(a). case(i) two end are fixed, total deformation

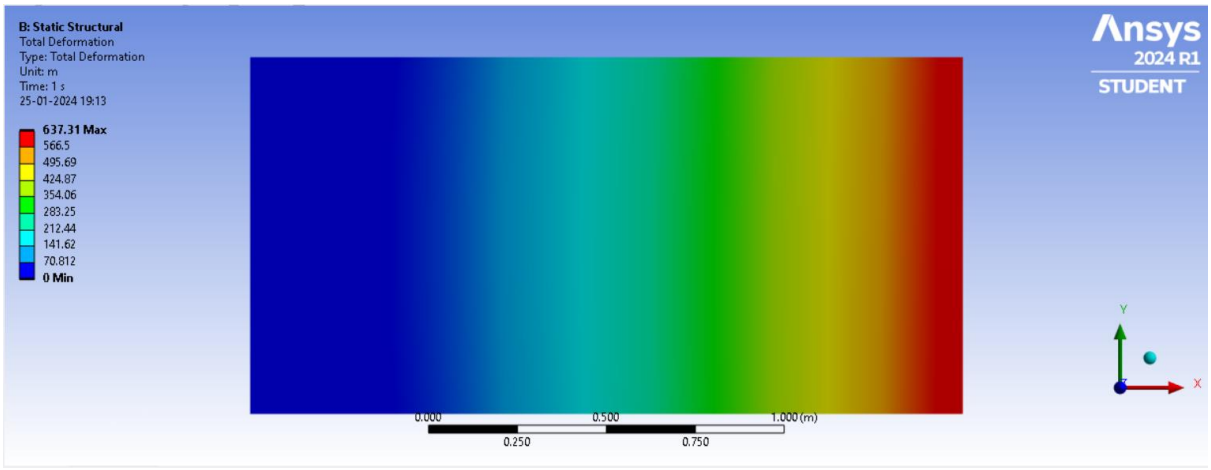

Fig 4(b). case(ii) one end is fixed, total deformation

Fig 4(a) case(i) two end are fixed and pressure is applied on opposite side the deformation is more at the point where the pressure is directly applied, and it is gradually decreasing. The total deformation is observed. fig 4(b) case(ii) one end is fixed and pressure is applied on the opposite end the deformation is more at the point where the pressure is directly applied, and it is gradually decreasing. The total deformation is observed.

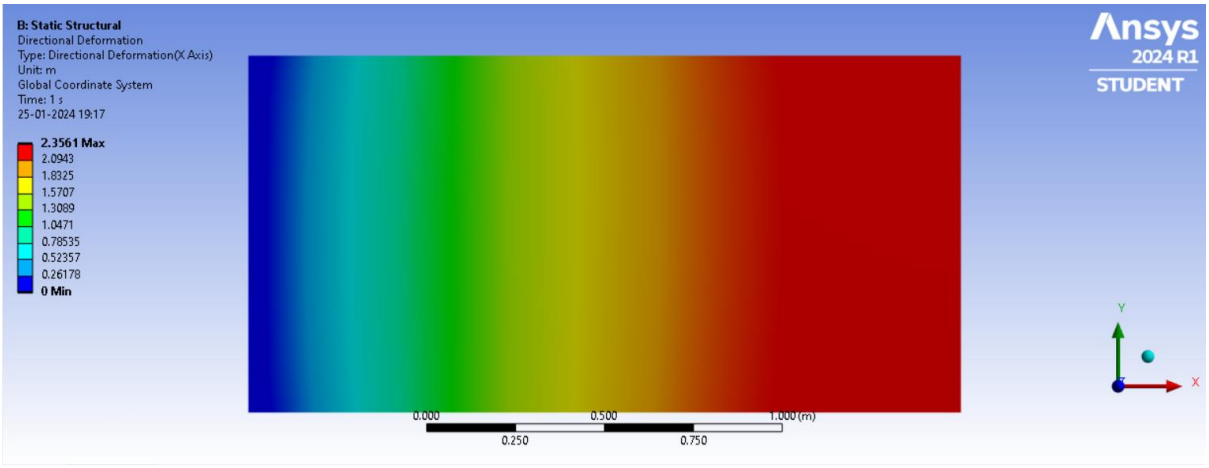

Fig 5(a). Directional deformation (X) direction

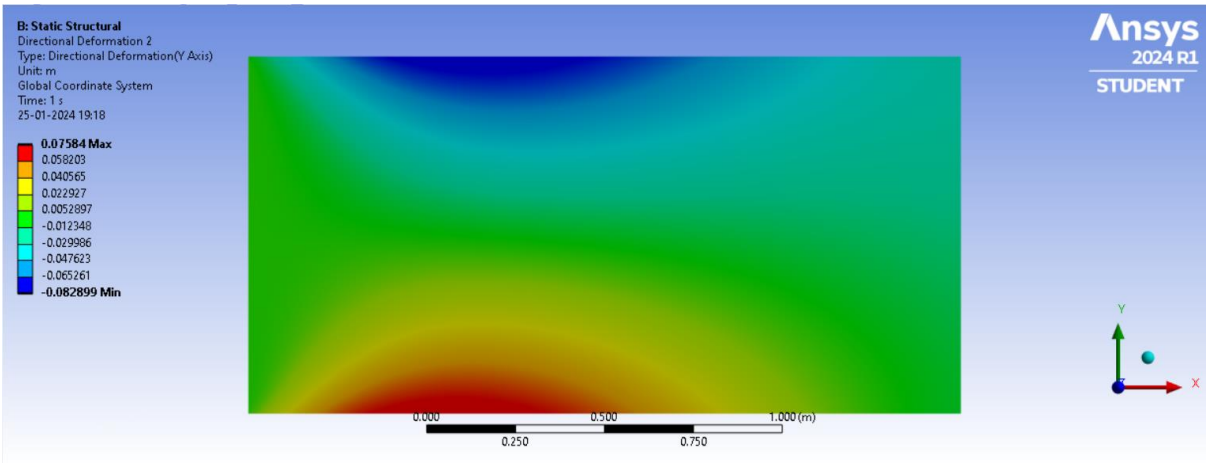

Fig 5(b). Directional deformation (Y) direction

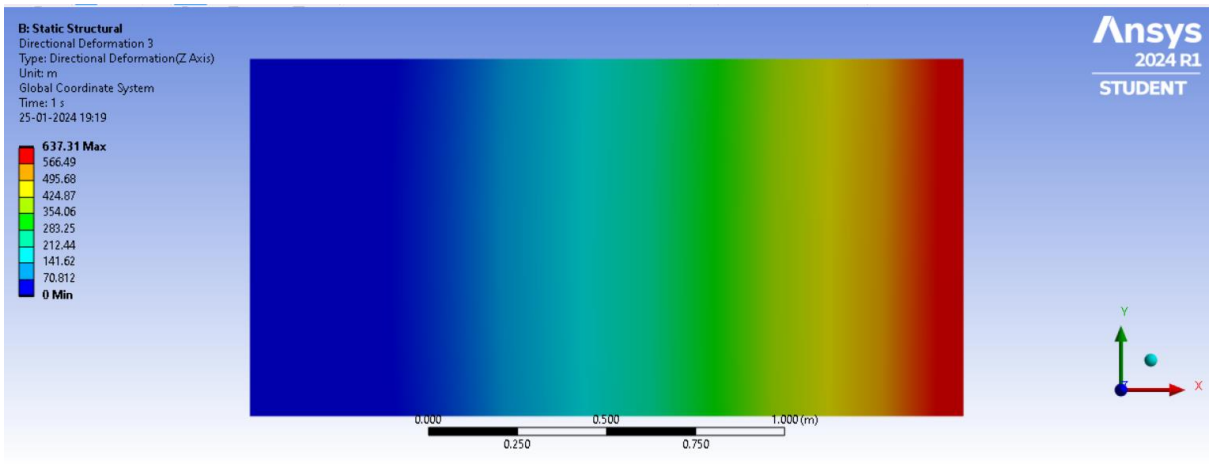

Fig 5(c). Directional deformation (Z) direction

In fig 5(a) case(ii) one end is fixed and pressure is applied on the opposite end the deformation is more at the point where the pressure is directly applied. The X- direction deformation is observed. fig 5(b) case(ii) one end is fixed, the Z- direction deformation is observed. In fig 5(c) case(ii) one end is fixed, and it is gradually decreasing. The Y- direction deformation is observed

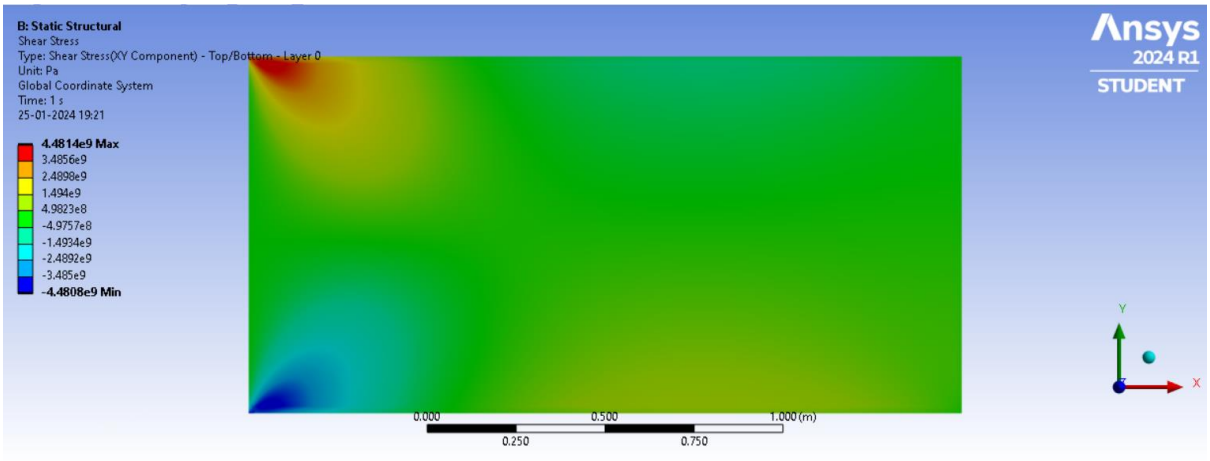

Fig 6(a). shear stress pattern

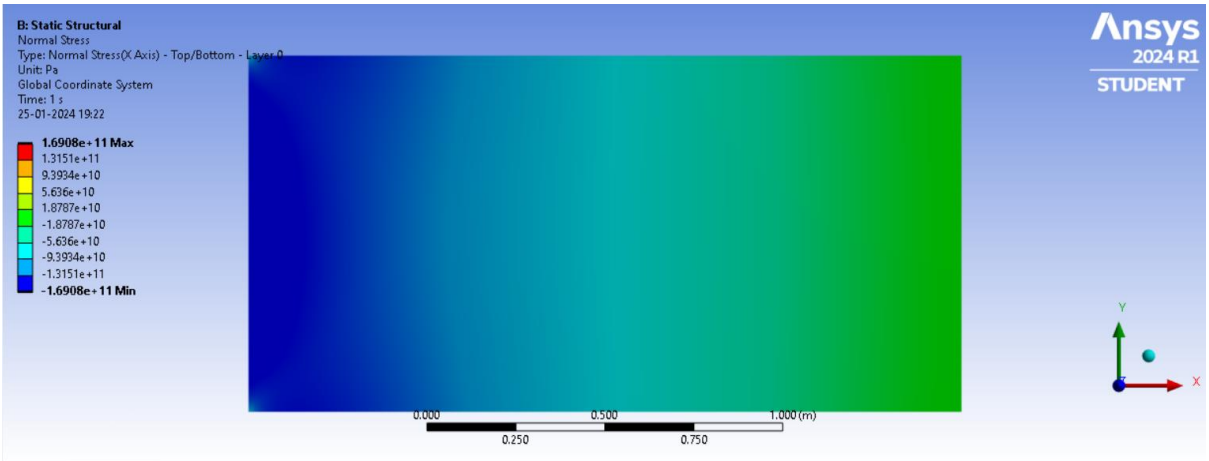

Fig 6(b). normal stress pattern

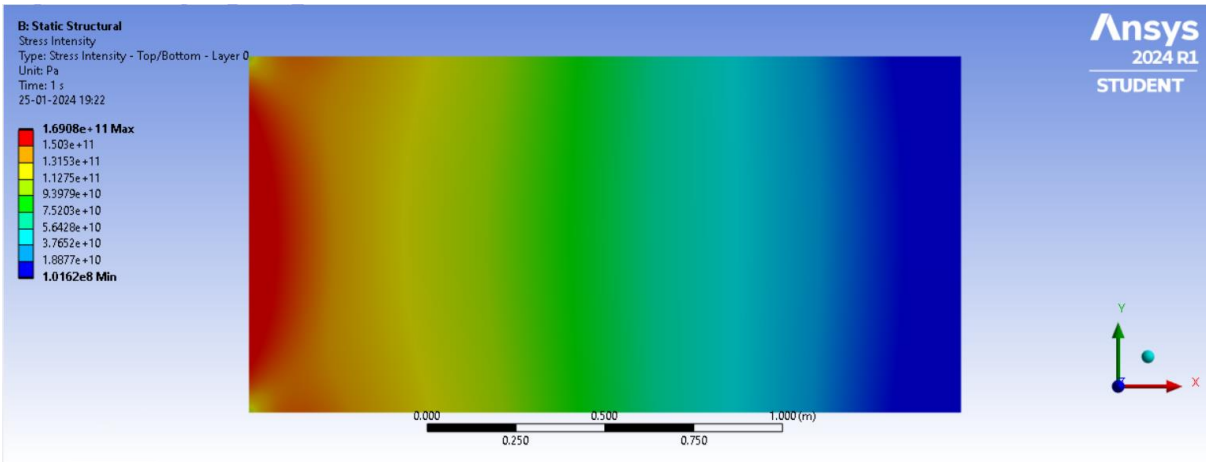

Fig 6(c). stress intensity pattern

In fig 6(a) case(ii) one end is fixed and pressure is applied on the opposite end. The shear stress is observed. In fig 6(b) case(ii) one end is fixed, the normal stress is observed. Fig 6(c) case(iii) one end is fixed, and it is gradually decreasing, the stress intensity is observed.

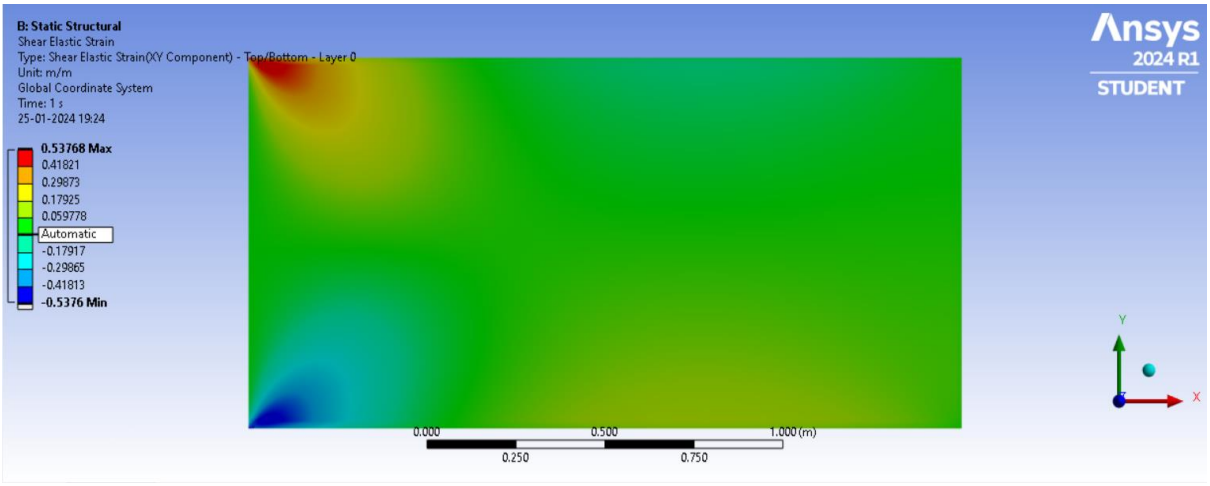

Fig 7(a) shear strain pattern

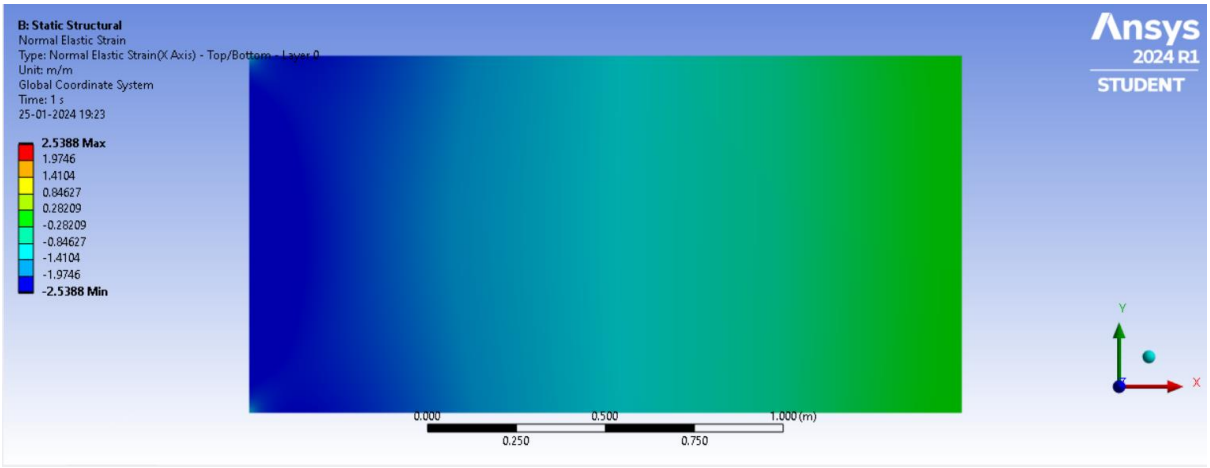

Fig 7(b) shear strain pattern

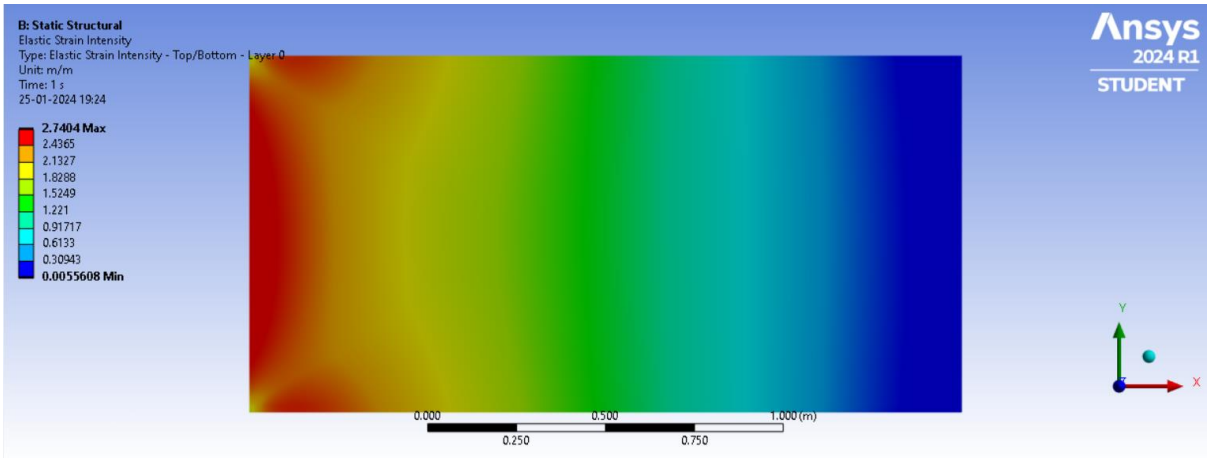

Fig 7(c) shear strain pattern

In fig 7(a) case(ii) one end is fixed and pressure is applied, the normal strain is observed. In fig 7(b) case(ii) one end is, the shear strain is observed. In fig 7(c) case(iii) one end is fixed and pressure is applied on the opposite end the deformation is more at the point where the pressure is directly applied, and it is gradually decreasing, the strain intensity is observed.

Table 1. Final Orthotropic Elasticity Results Obtained from Composite Structure

Young's Modulus X-direction (Pa)	Young's Modulus Y-direction (Pa)	Youngs Modulus Z-direction (Pa)	Poisson's Ratio XY	Poisson's Ratio YZ	Poisson's Ratio ZX	Shear Modulus XY (Pa)	Shear Modulus XY (Pa)	Shear Modulus XY (Pa)
6.57e+010	6.59e+010	6.62e+010	0.11273	7.0e+002	7.0e+002	8.3e+009	5.5e+009	8.3e+009

Table 2. Composite > Color

Red	Green	Blue
109	157	209

6. DISCUSSION

The analysis of composite laminates with epoxy resin and E-glass fiber reinforcement demonstrates their strong mechanical properties, crucial for structural applications. E-glass fibers significantly enhance strength and stiffness. While results align with prior studies, potential manufacturing defects and limitations in dynamic loading analysis remain. Future research should focus on optimizing manufacturing processes to minimize defects and investigate fatigue behavior for real-world applicability. These laminates hold promise for aerospace, automotive, and other industries due to their lightweight and high-strength characteristics. Further validation and optimization are essential for widespread adoption in structural components.

7. CONCLUSION

Extensive research is being carried out on polymer fiber-reinforced composites for use in high-performance goods, automotive, and aerospace industries. Composites made of glass and certain synthetic fibers have a high strength-to-weight ratio and good chemical and heat resistance. Unfortunately, limitations like as flammability and moisture absorption prevent polymer fibers from being used exclusively. Natural and synthetic fibers are frequently mixed to make composites with greater durability with the goal to solve this. The extraordinary strength-to-density ratios of composite materials—particularly those using epoxy resin and E-glass fiber reinforcement—make them crucial in the aerospace industry. Such composite laminates were studied using Ansys in a research that concentrated on mechanical properties such as compressive and tensile strength. The outcomes demonstrated the advantages of composite laminates based on synthetic fibers for structural elements in terms of strength and other mechanical features. The methodology for confirming the accuracy of the Ansys results will be described in the manuscript. This may involve validation against experimental data, comparison with analytical solutions, or sensitivity analysis.

8. REFERENCES

[1] Mechanical properties of green composites with hemp/sisal fiber and novolac resin
Porwal, H.,Soumya, G., Bhavana, P.H.S., Chandrashekhar, S., Anand, A.V.
AIP Conference Proceedings, 2023, 2492, 040009.

[2] Mechanical properties of hybrid composite sandwich structure with sisal and e glass fiberSree, M.U., Sudha, S., Reddy, Y.Y., Sahasrarchith, N., Anand, A.V. AIP Conference Proceedings, 2023, 2492, 040008.

[3] Magnesium matrix reinforced with zirconium, garnet and graphite for improved mechanical properties Khan, M.A., Bhanuprakash, L., Anand, A.V.
AIP Conference Proceedings, 2023, 2492, 040077.

[4] Macro Mechanical and Water Absorption Properties of Composite Laminates with Novolac Resin and E-Glass/Sisal Fibers Anand, A.V., Velmurugan, P., Singh, R.A., Rao, K.S.,Kumar, P.S.P.
AIP Conference Proceedings, 2022, 2446, 040012.

[5] P. M. S. P. Renuka Bulagoud and P. T. T. Hawal, "Synthetic,efect of natural and fbers on mechanical properties of epoxy resin," Int. J. Adv. Technol. Eng. Sci, vol. 02, no. 07, pp. 2348–7550, 2014.

[6] G. Cicala, G. Cristaldi, G. Recca, G. Ziegmann, A. El-sabbagh, and M. Dickert, "Properties and performances of various hybrid glass/natural fbre composites for curved pipes," Materials & Design, vol. 30, no. 7, pp. 2538–2542, 2009.

[7] S. Mosisa and B. Sirhabizu, "Study and characterization of fexural and tensile properties of hybrid bamboo/sisal fber reinforced epoxy composite," Journal of Materials Science and Engineering, vol. 8, no. 5, pp. 1–7, 2019.

[8] C. R. Ferreira, A. M. Ara´ujo, J. D. C. M. Fonseca, R. F. Leite, and ´I. A. D. P. E. Silva, "Mechanical properties of sisal/f- berglass reinforced composites," International Journal of Advanced Engineering Research and Science, vol. 7, no. 3, pp. 106–110, 2020.

[9] R. S. Rana, A. Kumre, S. Rana, and R. Purohit, "Character- ization of properties of epoxy sisal/glass fber reinforced hybrid composite," Materials Today: Proceedings, vol. 4, no. 4,pp. 5445–5451, 2017.

[10] M. Ramesh, K. Palanikumar, and K. H. Reddy, "Mechanical property evaluation of sisal-jute-glass fber reinforced poly- ester composites," Composites Part B: Engineering, vol. 48, pp. 1–9, 2013.

[11] K. Palanikumar, M. Ramesh, and K. Hemachandra Reddy, "Experimental investigation on the mechanical properties of green hybrid sisal and glass fber reinforced polymer com- posites," Journal of Natural Fibers, vol. 13, no. 3, pp. 321–331, 2016.

[12] M. Idicula, A. Boudenne, L. Umadevi, L. Ibos, Y. Candau, and S. Tomas, "Termophysical properties of natural fbre reinforced polyester composites," Composites Science and Technology, vol. 66, no. 15, pp. 2719–2725, 2006.

[13] S. Panthapulakkal and M. Sain, "Injection-molded short hemp fber/glass fber- reinforced polypropylene hybrid composites mechanical, water absorption and thermal properties," Journal of Applied Polymer Science, vol. 103, no. 4, pp. 2432–2441, 2007.

[14] K. John and S. V. Naidu, “Tensile properties of unsaturated polyester-based sisal fber– glass fber hybrid composites,” Journal of Reinforced Plastics and Composites, vol. 23, no. 17, pp. 1815–1819, 2004.

[15] A. V. Lima, J. L. Cardoso, and C. J. Lobo, “Research on hybridsisal/glass composites: a review,” Journal of Reinforced Plastics and Composites, vol. 38, no. 17, pp. 789–821, 2019.

[16] H. Ku, H. Wang, N. Pattarachaiyakoop, and M. Trada, “Areview on the tensile properties of natural fber reinforced polymer composites,” Composites Part B: Engineering, vol. 42,no. 4, pp. 856–873, 2011.

Journal of Physics: Conference Series

PURPOSE-LED PUBLISHING™

PAPER • **OPEN ACCESS**

Particle disseverment study in square-cylinder vortex separator by Centrifugal action in CFD

To cite this article: R Vivek *et al* 2024 *J. Phys.: Conf. Ser.* **2837** 012027

View the article online for updates and enhancements.

You may also like

- Structural, Optical, and Electrical Transformations in $Fe_xSi_{1-x}O$ Thin Films: The Role of Iron and Annealing
M Sudha, A Balamurugan, L Girisha et al.
- The passive control of three-dimensional flow over a square cylinder by a vertical plate at a moderate Reynolds number
S Malekzadeh, I Mirzaee, N Pourmahmoud et al.
- Vortex-induced vibrations of a square cylinder under linear shear flow
Wenjuan Sun, Dai Zhou, Jiahuang Tu et al.

This content was downloaded from IP address 106.0.37.90 on 21/10/2024 at 11:19

Journal of Physics: Conference Series **2837** (2024) 012027 doi:10.1088/1742-6596/2837/1/012027

Particle disseverment study in square-cylinder vortex separator by Centrifugal action in CFD

Vivek R [1]*, Venkatesh S [2], Satyanarayana Gupta M[3] Kavin Kumaar S S[4], Sivashri J T [5], Aswin G[6], Jagadheep A[7]

[1] Assistant professor - Mechanical Engineering Department, Sri Eshwar college of Engineering, Coimbatore , Tamilnadu, India.

[2] Associate professor - Mechanical Engineering Department, Sri Eshwar college of Engineering, Coimbatore Tamilnadu, India.

[3]Head of the Department – Aeronautical Engineering Department, MLR Institute of Technology, Telangana, India.

[4, 5, 6, 7] UG Students- Mechanical Engineering Department, Sri Eshwar College of Engineering, Coimbatore, Tamilnadu, India.

Email: vivek.r@sece.ac.in, kavinkumaar.ss2021mech@sece.ac.in

ABSTRACT: The particle collection performance of the square and cylindrical type of cyclone separator is reviewed for the study. The fabricated setup is designed and processed by Solid works and TIG welding respectively. The geometrical variations observed in the structure of setup sequentially arranged in parallel condition of Square-Cylinder- Square-Cylinder arrangement. The significant rise in pressure drop is observed with the study for collection efficiency. The performance carried out in larger scale for the conclusive segments with the aid of variable frequency diaphragm. The speed controlling device which optimize the speed condition for the setup through blower. The centrifugal action inside the separator will impinges the fine particles away from the surface and follows the vortex patter on the middle. The coarse particles will largely collected to the bottom of the vortex and collected on the bin. The variant's mixed configuration has a higher pressure drop and better collecting effectiveness. Only for tiny particles does the level of short circuiting particles ascend with an expansion in admission speed. There are recognizable errors in the assortment proficiency bends because of the way that when molecule size builds, the small amount of short circuiting particles declines all the more rapidly at higher admission speeds. The findings from the review research will allows to recommend the suitable arrangement setup for better collection efficiency and also provides the convene model to study of particulates.

KEYWORDS: Velocity and Flow pattern, Cyclone separator, Pressure drop, Speed Regulator

Content from this work may be used under the terms of the Creative Commons Attribution 4.0 licence. Any further distribution of this work must maintain attribution to the author(s) and the title of the work, journal citation and DOI.
Published under licence by IOP Publishing Ltd

1. PRESSURE DROP

The assessment of pressure drop holds significance as a pivotal factor in tornado design and performance evaluation, alongside separation efficiency. To comprehend the intricate interplay, an accurate numerical model that establishes the connection between pressure drop and tornado characteristics is essential. Adjusting the dimensions of a tornado can either increase or decrease the pressure reduction in a tornado separator. Employing a precise pressure drop equation is imperative for the effective design of a tornado. In the 1980s, statistical models emerged as an alternative method for calculating tornado pressure reduction. The size of the tornado separator and various operational factors play a crucial role in influencing tornado pressure drop. Changes in locale, wall contact, changes in stream bearing and vortex finder (power source tube) breakdown add to the decrease in strain across a tempest. The clarification truly ought to "pressure drop" wraps decreases in both static and dynamic strain. In additional direct terms, it suggests the decrease in pressure experienced by the stream between the data and result.

$$Hv=KHWDe\ 2\Delta P=12\rho gVi2Hv \quad (1)$$

Hv=pressure drop

K=Constant (K=12to18forastandardtangential-entrycyclone)

H = Height in millimeter.

W=Width in millimeter.

De = Diameter in meter.

ρg = Density in kg/m3.

Vi = Inlet velocity in m/s.

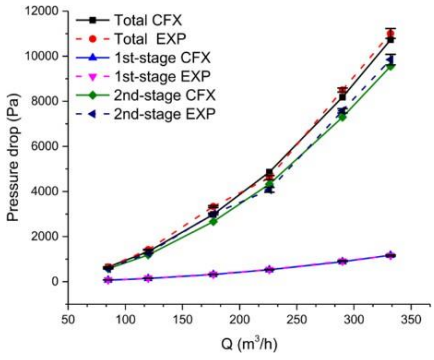

Figure1: Effect of 2-Stage Cyclone Separator's Performance on Inlet Air Volumetric Flow Rate

2. OPTIMIZATION OF CYCLONE DESIGN

This article examines two new, innovative designs for four-delta tornado separators, considering their show and stream illustrations [1]. Tornado separators are widely utilized for solid particle separation due to their favorable characteristics and simple manufacturing process. The author investigates the basic plan (s1) and two extra plans (c4 and n4) of four deltas, utilizing computational assessment with the discrete stage model

and Reynolds stress model (RSM) for fierce stream. The numerical model demonstrates dependable, with plan s1 displaying the most un-critical ordinary Euler number, while course of action c4 produces the briefest typical cut-off gauge (1.399 μm). The imaginative game plan n4 beats both s1 and c4, showing a 0.1% and 1% improvement, separately, in execution.

The assessment project focuses on a spiral tornado separator with extended ports on the cone-shaped section [2]. The study explores the effects of additional ports on pressure drop and collection capability. Results indicate that adding more ports to the cylindrical part improves efficiency by providing the required flow rate. Introducing particles through both the main inlet and additional ports results in comparable performance to the reference tornado separator, suggesting that adding more inlets to the tapered section could handle a higher particle flow rate, enhancing cost-effectiveness. The design of gas-particle filters emphasizes pressure reduction and separation efficiency [3]. The review enhances a middle stream type gas-molecule twister separator utilizing RSM and computational Fluid Dynamics (CFD).The optimized design achieves a 100% improvement in separation efficiency for 8-m particles and a 69.32% reduction in static pressure compared to the previous design. The balance between separation efficiency and static pressure drop is achieved through the optimal design. A tornado separator is investigated for moisture removal from compressed air in equipment susceptible to damage [4]. CFD is employed to analyze the vane's angle, with a focus on parameters such as liquid flows, compressed gaseous pressure, and velocity. The study identifies the vane angle that results in the best pressure drop and compressed airflow speed to prevent component deterioration. Sub-current leakage and tornadoes of various diameters are explored to enhance the separation of spray particles [5]. The study creates tornadoes with varying cylinder diameters and vortex finder depths. The HLG75 cyclone with a diameter of 75 mm and a vortex finder depth of 0.7D proves most efficient, reaching 95% efficiency at a flow rate of 35.5 m3/h. The study suggests controlling the gas at each tornado's sub-current outlet to improve gas-liquid cyclonic separation. In conclusion, these studies contribute valuable insights into the optimization and efficiency improvement of tornado separators for diverse applications, ranging from solid particle separation to moisture removal in compressed air and spray particle separation.

3. NUMERICAL SIMULATION OF CYCLONE SEPARATOR

This work presents a mathematical evaluation of the gas-powder stream inside an ordinary L-molded typhoon separator. The examination utilizes the Reynolds stress model to assess the aggravation in the gas stream. Consequently, the got strain and stream fields are used to reenact powder stream utilizing a stochastic Lagrangian model [6]. The review explores the effect of molecule size and gas speed on partition productivity, and the discoveries adjust well to exploratory outcomes. Various factors influencing the cyclone's performance are identified, including the interaction of gas streams and the occurrence of short-circuiting flow around the cyclone's chamber and channel intersection. The entry position of particles is recognized as a crucial factor affecting cyclone efficiency in large industries. Using the Large Eddy Simulation (LES) model,

this work explores the effects of vortex development in a reverse-step mandrel cyclone separator. Mathematical analysis establishes a clear relationship between vortex development, energy distribution, and flow properties in incompressible fluid. Additionally, they focus on the square twister separator, which is a powerful tool used in flowing fluidized bed boilers to distribute high-temperature gas. Limits such as atom mass stream rate, delta speed, cove temperature, and intake pressure are all analyzed using CFD. The ongoing study aims to propose an efficient design for the conventional square cyclone separator by replacing the single-cone channel-shaped part with a double counter-cone, resulting in improved separation efficiency. They further dives into the effect of cutting edge scattering and molecule wall crash models on productivity and corruption forecast, taking into account different scattering models and molecule sizes. Along with the "float revision," anisotropic ordinary and shear Reynolds stresses have a major impact on the dispersion model used in cyclone applications. Four crucial zones for degradation within a cyclone are revealed by the analysis, highlighting the significance of taking into account variable compensation coefficients in the particle-wall collision model and Saffman and Magnus lift forces on particles for precise separation efficiency prediction. Furthermore, it is discovered that wall hardness increases the pace at which massive particles partition by combining the effects of the "shadow impact" with the dynamic inner vortex on particles. Finally, the study explores the relationship between turbulent flow in cyclones and rapid self-adjustment, as well as molecular chaos, aiming to provide insights into improving separation performance and enhancing the utilization of cyclones. Investigation into cyclone geometric parameters and inlet gas velocity reveals their influence on the phase flow field, swirling, and high-speed self-turbulence of dispersed phase particles. The study establishes a theoretical foundation for advanced applications of cyclones in chemical processing and environmental engineering, particularly in pollutant removal on the outer surface of particles and in pores.

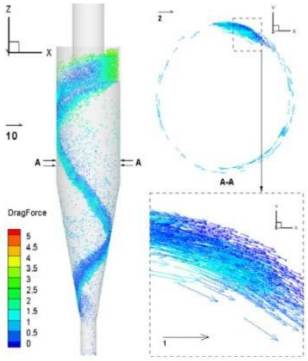

Figure 2. Spatial dispersion of the gas drag forces acting on the cyclone's particles

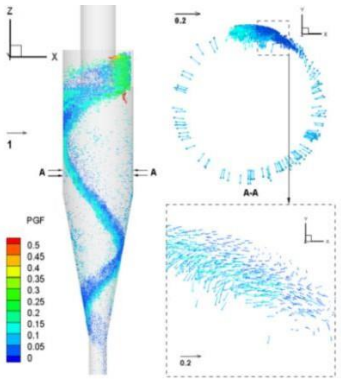

Figure 3. The geographic pressure gradient forces distribution and their effects on the cyclone's particle

4. TURBULANCE MODEL OF CYCLONE

4.1 MingGuo Using the theory of large-scale eddy duplication, the primary objective of this study is to thoroughly examine the effect of a chamber vortex stabilizer on the varying disturbance pattern of a Stairmand cyclone separator. Because of its simplicity, the chamber vortex stabilizer can be easily included with little modification into a variety of cyclone models. This adjustable feature is expected to mitigate problems associated with waste compartment particle entrapment and vortex end swing in the swirling flow. Three different versions with varying vortex stabilizer lengths and widths were used in mathematical simulations together with the Stairmand cyclone separator. The simulation results showed that the chamber vortex stabilizer significantly enhanced the suppression of fluctuating disturbances and reduced flow uncertainties. The idea is that the inner semi-confined vortex zone of the cyclone might effectively reduce needless turbulence by utilizing the chamber vortex stabilizer. Remarkably, as compared to the Stairmand cyclone, the cyclone model with the vortex stabilizer (width d/D: 0.12, length L/D: 6.5) showed a noteworthy decrease in the rotating first and second peak frequencies of 10.86% and 11.54%, respectively. Additionally, this redesigned cyclone model demonstrated a significant increase in flow stability with an approximate maximum reduction of 18.4% in the normalized flow angle, a decrease of 24.8% in the rotational kinetic energy in the particle collector, and an improvement of 14.2% in the cyclone main assembly.

4.2 Mohanasundaram When developing cyclone separators, the industrial sector benefits greatly from a well-defined framework that addresses particle material collecting efficiency and flow design. The goal of implementing different design concepts and tactics, such as the use of pollution control equipment, is to lessen the increasing levels of air pollution in industrial environments. Businesses frequently use cyclone separators to extract particle matter from tainted gas, especially in large furnaces. This review concentrates on the separation of gaseous solids from big furnaces,

even though cyclone separators are commonly used for the separation of vaporous and gaseous liquids. Results from various designs and studies show that although enhancing the overall performance of dual inlet cyclone separators, increasing the vortex locator's circular length reduces separation efficiency. It has also been shown that using a modified cone vortex locator improves separation efficiency and lowers pressure loss. The size range of particulate matter released by furnaces is 2.5 μm to 10 μm. Improvements in flow design and numerical properties further optimize the development assembly design's overall particle material collecting performance, which eventually results in a decrease in pressure loss. In conclusion, with continuous efforts to use efficient tactics and design principles to battle air pollution in industrial settings, a well-defined framework addressing particle material collection efficiency and flow design proves beneficial for the industry. Particularly in the context of big furnaces, cyclone separators continue to be essential tools for businesses in the extraction of particulate matter from tainted gas.

4 .3 Marek Wasilewski The multiphase flow dynamics inside the lower stage cyclone separator used in the clinker replication process were investigated and documented in detail in this research. Both experimental results and CFD techniques were employed in the inquiry. While these cyclone separators play a crucial role in the manufacturing of clinker, very few research has examined their basic functions and particular working circumstances. These cyclone separators involve intricate calculations that are substantially different from those of regular separators due to their distorted operating conditions. Additionally, the accuracy and consistency of the Large Eddy Simulation (LES) model and two turbulence models, k-ε RNG and RSM (RANS), were assessed. The most accurate model for estimating the efficiency of particle separation and reducing pressure in lower stage cyclone separators was found to be the LES model based on the data. Though with more pronounced variances, the RSM model also showed great precision, producing accurate separation efficiency estimates. The RNG model k-ε was found to exhibit more discrepancies. In this work, Marek Wasilewski provides a detailed investigation of the multiphase flow dynamics in the lower stage cyclone separator utilized in the clinker replication process. Both experimental results and CFD methodologies are used in the study. These kinds of cyclone separators received very little research attention, despite their peculiar working conditions and critical role in the clinker production process.. These cyclone separators involve intricate calculations that are substantially different from those of regular separators due to their distorted operating conditions. The study evaluates the accuracy and consistency of two turbulence models, k-ε RNG and RSM, as well as Large Eddy Simulation (LES), under the Reynolds-Averaged Navier-Stokes (RANS) paradigm. The findings indicate that for assessing particle efficiency and pressure reduction in lower stage cyclone separators, the LES model performs the best. Moreover, the RNG k-ε model shows more severe mistakes, whereas the RSM model shows outstanding precision and produces precise estimations of separation efficiency. The understanding and improvement of cyclone separators in clinker production processes is greatly aided by the current work.

4.4 S.Pirker The paper highlights the impact of disparity structure by providing a numerical

assessment of the collaboration between a gas phase and a particle phase. We study how bundle capacity in a typhoon separator is affected by the thickness of the cutoff layer and the cruelty structure. This work also investigates the impact of the Saffman force on particle flight. The parcel limit increases with decreasing impact power and falls with decreasing cutoff layer thickness, according to the results. Small particles' trajectory is changed by the Saffman force, which shortens their time spent inside the tornado. Furthermore, the paper explores the impact of discrepancy structure on the cooperative behavior of a particle and a gas phase, providing an extensive numerical evaluation. By analyzing the effects of cutoff layer thickness and cruelty structure on bundle capacity in a typhoon separator, the study clarifies important parameters influencing particle dynamics. Interestingly, the results show a significant decrease in parcel limit as disturbance strength increases, whereas the thickness of the cutoff layer shows the opposite relationship. Moreover, the examination of the Saffman force indicates that it plays a noteworthy function in modifying the path of minute particles, thereby decreasing their duration of stay in the tornado atmosphere.

4.5 Pantea Hadi Jafari The goal of the ongoing research is to lay the groundwork for a cyclone gasifier's design plan, which will enable it to explore many design possibilities with limited computing resources and accurately anticipate its flow field. To accurately simulate the responding flow inside a cyclone gasifier, a solid single-phase flow model is essential. In order to provide guidance for simulating multi-phase flow in cyclone separators/gasifiers, the research objectively evaluates popular turbulence modeling approaches for single-phase flow inside these devices. An extensive comparison of the mean speed and fluctuation components of the speed profiles between models and experimental data is provided, along with an analysis of the ways in which turbulence models fall short of accurately representing the real factors affecting the design of cyclone gasifiers.

5. GEOMENTRICAL AND DESIGN PARAMETERS

An exceptionally productive pressure gadget for high-temperature gas inside CFB boilers is the square tornado separator. Alongside, other operational aspects such as variations in particle loading and gas speed intermittently act as influential factors affecting liquid flow in gas cyclones, emphasizing the crucial need for capacity improvement. However, determining the most suitable operational configuration proves challenging due to a fundamental understanding of operational principles often overlooked within the existing framework. This study digs into the investigation of gas stream inside a square typhoon, using CF Parts to recognize boundaries like molecule mass stream rate, gulf speed, delta temperature, and tempestuous power. The Taguchi strategy fills in as an outline for the primer plan of tests (DoE), meaning to streamline practicality. The overall impact of each parameter to the performance of the gas cyclone is then evaluated using the Analysis of Variance (ANOVA). In the meantime, the Eulerian-Lagrangian method is used by the Volatile Reynolds-Averaged Navier-Stokes equations to track particle movement, with Discrete Random Walk (DRW)

handling speed fluctuation. The most significant factor, according to the Taguchi analysis, is input speed, whereas the particle mass flow rate from different environmental conditions has the least bearing on the performance of cyclones. The investigation results demonstrate that, individually, the optimal values for inlet speed, channel temperature, particle mass flow rate, and turbulent power are 20 m/s, 300 K, 180 g/min, and 4%, respectively. Suggested in the software affiliation point A little volume of pipeline process fluid is diverted by a cyclone separator in Design 31 for the mechanical seal cooling system. Regardless of its straightforwardness, this redirection course of action requests thorough plan thought to guarantee similarity with pressure drop and stream rate to the mechanical seal. In this appraisal, Programming Association Point 31 tornado separator mathematical boundaries were analyzed for their impacts on pressure drop and seal stream rates involving mathematical strategies in ANSYS Familiar programming. Changes in overflow and sub-current reach, chamber and cone-like structure lengths resulted in pressure drop reductions of 15.94%, 24.82%, 20.30%, and 11.42%, respectively. Meanwhile, increasing vortex finder length decreased the pressure drop by 7.77%. Progresses at the vortex finder's length and overflow caused the flow rate to increase by 9.63% and 43.79%, respectively. On the other hand, expanding under-stream reach and lengths of chamber and channel diminished the stream rate to seal by 71.92%, 6.41%, and 8.93%, individually. It's essential to take note of that the suspicion of a particular twister separator model isn't generally pertinent as it relies upon the typhoon separator's base plan itself, where all mathematical parts really add to compel drop and stream to seal. The assessment explores the impact of adding an extra component to the cyclone separator's design, such as a post with a round cross-section — in the center. Thirty numerical configurations, with variable parameters including post diameter and length, were utilized. Three methodologies were employed: preliminary analysis, physical model PIV, and CFD (which included LES and DPM models). The refinement of the design based on accepting the outcomes was made possible by the performance of these three evaluation models. The expansion of a post with a round cross-segment essentially further developed the typhoon separator's presentation (division productivity, Stk50, and Eu, generally). The most useful setup brought about a 25.5% drop in Stk50 and a 8.2% expansion in generally speaking detachment productivity. All designs created a lower worth of Eu than the base model because of strain drop (addressed as Eu); the best decrease noticed was 23.9% (contrasted with the base model). The typhoon separator's partition proficiency is affected by the easy route stream. To mimic a gas-strong two-stage stream, the LES model and molecule irregular voyaging were used. The examination of molecule development into two sections, to be specific molecule direction and home time, uncovered an underlying increment followed by a slow decrease in the detachment effectiveness of particles from 1 μm to 10 μm in size. At the point when the molecule size was more modest than 10 μm, the division effectiveness started to diminish. The partition effectiveness was above 80% when the molecule size was more than 3 μm, and it altogether diminished when the molecule size was more modest than 3 μm. An accumulation of the upper ash ring, particularly around the cyclone check at 130-180 degrees, where a high concentration of particles gathered, was observed. The top ash ring, with a semi-convulsive shedding characteristic and uneven distribution, became visible after adjusting the force of particles. Additionally, when the airflow turned, its center shifted sideways to the oncoming airflow, causing pressure fluctuations. These phenomena not only distributed particles, reducing the efficiency of separation and evened out the wear of the

wall but also introduced unpredictability.

6. CONCLUSION

As a result,

i) Forecasting effectiveness and strain decline is incredibly troublesome, particularly for minor twisters. Most models use conditions that are either completely or generally founded on exact information. The models decide the slice off size that compares to half viability by ascertaining adequacy. The math of typhoons, the entrained molecule size circulation of particles, and twister activity boundaries all influence how well they work.

ii) The effectiveness of cyclones has been predicted using a number of models. The operating parameters should be included in the modeling since it is generally accepted among scientists that they do, in fact, have an impact on cyclone performance. Numerous hypotheses explain particle diameter, density, gas velocity, and viscosity. Regarding the influence of geometry, for different scientists, there are differences in approaches.

iii) The cut size "d50," which represents the molecule breadth, is considered by most of speculations, as was recently referenced. The two most broadly involved procedures for estimating adequacy are The Power Equilibrium Hypothesis expresses that when drag is at its least, maximum speed is reached. The Static Molecule Approach [Barth] considers basic power adjusting, in which powers working on a molecule are identical to a few different powers, and claims that radial and forward powers are equivalent. Indeed, even exceptionally confounded ideas have been proposed, they basically lay on one of the two speculations.

7. REFERENCES:

[1] Chu, K.W., Bo Wang, D. L.Xu, Y.X.Chen, and A. B. Yu."CFD–DEMsimulationofthe gas–solid flow in a cyclone separator." Chemical Engineering Science 66, no. 5 (2011): 834- 847.

[2] Moiz Hussain, Mayur KM, Pradeep D,PrithviB SrinivasS, 2020.Designand Analysisof Cyclone Separator, International Journal of Scientific & Engineering Research Volume 11, Issue 6, ISSN 2229-5518.

[3] ChenJ, Jiang ZA, Chen J. Effect of Inlet Air Volumetric Flow Rate on the Performance of a Two-Stage Cyclone Separator. ACS Omega. 2018 Oct 15; 3(10):13219-13226.

[4] Vivek, R., S. Venkatesh, V. Manoj, and Manoj Kumar. "A brief review on improving materials particulates using cyclone separator by geometrical and turbulence factors." Materials Today: Proceedings (2022).

[5] Jihe Chen, Zhong-an Jiangand Jushi Chen, 2018. Effect of Inlet Air Volumetric Flow Rate on the Performance of a Two-Stage Cyclone Separator, ACS Omega, 3, 13219−13226.

[6] Barth W. 1956. Design and layout of the cyclone separator on the basis of new investigations. Brennstoff-Warme-Kraft

[7] Pandey, Satyanand, and Lakhbir Singh Brar. "On the performance of cyclone separators with different shapes of the conical section using CFD." Powder Technology 407 (2022): 117629.

[8] Zhou,L.X.,andS.L.Soo."Gas—solidflowandcollectionofsolidsinacyclone separator."Powdertechnology63, no.1 (1990):45-53.

[9] Venkatesh, S., S. P. Sivapirakasam, M. Sakthivel, S. Ganeshkumar, M. Mahendhira Prabhu, and M. Naveenkumar. "Experimental and numerical investigation in the series arrangement square cyclone separator." Powder Technology 383 (2021): 93-103.

[10] Wang, B., Xu, D.L., Chu, K.W., Yu, A.B., 2006. Numerical study of gas–solid flow in a cyclone separator. Applied Mathematical Modelling 30, 1326–1342.

[11] Fal, D. Introduction to Industrial Gas Cleaning; Academic Press: San Diego, CA, 1989; pp 55−90.

[12] Zhou, F.; Sun, G.; Zhang, Y.; Ci, H.; Wei, Q. Experimental and CFD study on the effects of surface roughness on cyclone performance. Sep. Purif. Technol. 2018, 193, 175−183.

[13] Venkatesh, S., S. P. Sivapirakasam, and M. Sakthivel. "Importance of Dust Collectors in Waste Management and Recycling in Industries." In Green Materials and Advanced Manufacturing Technology, pp. 23-34. CRC Press, 2020.

[14] Bogodage, S. G.; Leung, A. Y. T. CFD simulation of cyclone separators to reduce air pollution. Powder Technol. 2015, 286, 488−506.

[15] Balestrin, E.; Decker, R. K.; Noriler, D.; Bastos, J. C. S. C.;Meier, H. F. An alternative for the collection of small particles in cyclones: Experimental analysis and CFD modeling. Sep. Purif. Technol. 2017, 184, 54−65.

[16] Brar, L. S.; Sharma, R. P.; Elsayed, K. The effect of the cyclone length on the performance of Stairmand high-efficiency cyclone. Powder Technol. 2015, 286, 668−677.

[17] Cortes, C.; Gil, A. Modeling the gas and particle flow inside cyclone separators. Prog. Energy Combust. Sci. 2007, 33, 409−452.

[18] Haig, C. W.; Hursthouse, A.; Mcilwain, S.; Sykes, D. An empirical investigation into the influence of pressure drops on particle behavior in small scale reverse-flow cyclones. Powder Technol. 2015,275, 172−181.

[19] Huang, A.-N.; Ito, K.; Fukasawa, T.; Fukui, K.; Kuo, H.-P.Effects of particle mass loading on the hydrodynamics and separation efficiency of a cyclone separator. J. Taiwan Inst. Chem. Eng. 2018, 90, 61.

[20] Kashani, E.; Mohebbi, A.; Heidari, M. G. CFD simulation ofthe preheater cyclone of acement plant and the optimization of its performance using a combination of the design of experiments andmulti-gene genetic programming. Powder Technol. 2018, 327, 430.

[21] Luciano, R. D.; Silva, B. L.; Rosa, L. M.; Meier, H. F. Multiobjective optimization of cyclone separators in series based on computational fluid dynamics. Powder Technol. 2018, 325, 452−466.

[22] Vegini, A. A.; Meier, H. F.; Iess, J. J.; Mori, M. Computational Fluid Dynamics (CFD) Analysis of Cyclone Separators Connected in Series. Ind. Eng. Chem. Res. 2008, 47, 192−200.

[23] Mazyan, W. I.; Ahmadi, A.; Ahmed, H.; Hoorfar, M. Increasing efficiency of natural gas cyclones through addition of tangential chambers. J. Aerosol Sci. 2017, 110, 36−42.

[24] Venkatesh, Seenivasan, MurukesanSakthivel, Muthukumar Avinasilingam, Subramanian Gopalsamy, Eswaran Arulkumar, and Hari Prasanth Devarajan. "Optimization and experimental investigation in bottom

inlet cyclone separator for performance analysis." Korean Journal of Chemical Engineering 36, no. 6 (2019): 929-941.

[25] Launder, B. E. Second-moment closure: present... and futureInt. J.Heat FluidFlow1989, 10, 282−300.

[26] Ansys, Inc. ANSYS Workbench Help. Release 17.0; ANSYS, Inc: Canonsburg, Pennsylvania, 2017.

[27] Wang, H.; Nie, W.; Cheng, W.; Liu, Q.; Jin, H. Effects of air volume ratio parameters on air curtain dust suppression in a rock tunnel's fully mechanized working face. Adv. Powder Technol. 2018, 29, 230−244.

[28] Missoula, D.; Anderson, A. G.; Lundström, T. S. Effects of the inlet angle on the flow pattern and pressure drop of a cyclone with helical-roof inlet. Chem. Eng. Res. Des. 2015, 102, 307−321.

[29] Gao, X.; Chen, J.; Feng, J.; Peng, X. Numerical investigation of the effects of the central channel on the flow field in an oil−gas cyclone separator. Comput. Fluids 2014, 92, 45−55.

[30] Shi, Y.; Zhu, Z.; Fan, Y. New form of geodetic coordinate system taking two length quantities as coordinate parameters. Front.Architect. Civ. Eng. China 2009, 3, 105−110.

[31] Vivek, R., Rameshbabu, R., Tamilarasan, V. D., Arunachalam, P., & Anand, A. V. (2023). A Comparative study on Annealing and phase transition effect in SS 304 and SSLNA from low Nickel Austenite to Martensite. Materials Today: Proceedings.

[32] Huang, Y.; Zhang, M.; Lyu, J.; Liu, Z.; Yang, H. Effects of gas leakage on the separation performance of a cyclone. Part 1: Experimental investigation. Chem. Eng. Res. Des. 2018, 136, 900.

[33] Yang, J.; Sun, G.; Zhan, M. Prediction of the maximum efficiency inlet velocity in cyclones. Powder Technol. 2015, 286, 124−131.

[34] Yuu, S.; Jotaki, T.; Tomita, Y.; Yoshida, K. The reduction of pressure drop due to dust loading in a conventional cyclone. Chem.Eng. Sci. 1978, 33, 1573−1580.

[35] Madadi, Z.; Hassani besheli, F.; Esmaeili, S.; Hedayatifar, L.; Masoudi, A. A. Surface growth by cluster particles: Effects of diffusion and cluster's shape. J. Cryst. Growth 2017, 480, 56−61.

[36] De Oliveira, J. V.; Szabo, A.; de Castro, L. N. Particle Swarm Clustering in clustering ensembles: Exploiting pruning and alignment free consensus. Appl. Soft Comput. 2017, 55, 141−153.

[37] Wang,L.; Wu,C.; Ge,W.Effect of particle clusters on mass transfer between gas and Particles in gas-solid flows. PowderTechnol.2017,319,221−227.

[38] Wu, K.; Li, B.; Gao, L.; Yuan, Z.; Luo, D.; Guan, L.; Gu, C.Study on the distribution characteristics of flexible filamentous particle clusters in a fluidized bed dryer. Powder Technol. 2018, 331, 7−19.

[39] Venkatesh, S., M. Sakthivel, S. Sudhagar, and S. Ajith Arul Daniel. "Modification of the cyclone separator geometry for improving the performance using Taguchi and CFD approach." Particulate Science and Technology (2018).

[40] Muruganandhan, P., Jothilakshmi, S., Vivek, R., Nanthakumar, S., Sakthi, S., Mayakannan, S., & Girimurugan, R. (2023). Investigation on silane modification and interfacial UV aging of flax fibre reinforced with polystyrene composite. Materials Today: Proceedings.

[41] Liu, D.; Hsiao, T.-C.; Chen, D.-R.Performancestudyofaminiaturequadru-inletcyclone. J.AerosolSci.2015, 90,161−168.

[42] P.B. Fu, F. Wang, X.J. Yang, L. Ma, X. Cui, H.L. Wang, Inlet Particle-Sorting Cyclone for the

Enhancement of PM2.5Separation, Environmental Science & Technology, 51 (2017) 1587-1594.

[43] J.P. Yan, L.Q. Chen, Q. Lin, Removal of fine particles in WFGD system using the simultaneous a coustic agglomeration and supersaturated vapor condensation, Powder Technol., 315 (2017) 106-113.

[44] J.P. Yan, L.Q. Chen, L.J. Yang, Combined effect of acoustic agglomeration and vapor condensation on fine particles removal, Chemical Engineering Journal, 290 (2016) 319-327.

[45] Venkatesh, S., R.SureshKumar, S.P.Sivapirakasam, M.Sakthivel, D.Venkatesh, and S. Yasar Arafath. "Multi-objective optimization, experimental and CFD approach for performance analysis in square cyclone separator."Powder Technology371 (2020):115-129.

[46] Gowtham, S., Barath, G., Sudharsan, K., Thiyagarajan, V., & Balasubramani, S. (2023, December). Regenerative suspension system using linear magnet system. In AIP Conference Proceedings (Vol. 2914, No. 1). AIP Publishing.

[47] Aravinth, K., Kondusamy, V., Ramakrishnan, T., Tamilarasan, V. D., & Rasu, K. K. (2023). Investigation of mechanical properties on agave plant fiber composite by experimental and numerical methods. Materials Today: Proceedings.

[48] Utikar, Ranjeet, Nina Darmawan, Moses Tade, Qin Li, G. Evans, M. Glenny, and Vishnu Pareek. "Hydrodynamic simulation of cyclone separators." In *Computational fluid dynamics*, pp. 241-266. InTech, 2010.

[49] Misiulia, Dzmitry, Sergiy Antonyuk, Anders Gustav Andersson, and Tord Staffan Lundström. "High-efficiency industrial cyclone separator: A CFD study." *Powder Technology* 364 (2020): 943-953.

[50] Chu, K. W., Bo Wang, D. L. Xu, Y. X. Chen, and A. B. Yu. "CFD–DEM simulation of the gas–solid flow in a cyclone separator." *Chemical Engineering Science* 66, no. 5 (2011): 834-847.

[51] Cullivan, J. C., Richard A. Williams, and R. Cross. "Understanding the hydrocyclone separator through computational fluid dynamics." *Chemical Engineering Research and Design* 81, no. 4 (2003): 455-466.

[52] Tapkir, P., and Dinesh Kamble. "Analysis of cyclone separator using empirical models and CFD for variation of dimensions." *vol* 2 (2015): 225-233.

[53] Qian, Fu Ping, and Ming Yao Zhang. "Empirical model and numerical prediction for separation performance of cyclone separator." *Journal of Southeast University (natural science edition)(China)* 35 (2005): 35-39.

[54] Prasanna, N., and R. Ramachandran. "Development of an optimum CFBC Cyclone separator with REPDS for low pressure drop and denudation rates using [51] CFD." *International Journal of Applied Engineering Research* 10, no. 13 (2015): 2015.

[55] Venkatesh, Seenivasan, Murukesan Sakthivel, Muthukumar Avinasilingam, Subramanian Gopalsamy, Eswaran Arulkumar, and Hari Prasanth Devarajan. "Optimization and experimental investigation in bottom inlet cyclone separator for performance analysis." *Korean Journal of Chemical Engineering* 36 (2019): 929-941.

Journal of Physics: Conference Series

PURPOSE-LED PUBLISHING™

PAPER • **OPEN ACCESS**

3-Blade Propeller Design and Acoustical Analysis

To cite this article: Sreekanth Sura *et al* 2024 *J. Phys.: Conf. Ser.* **2837** 012093

View the article online for updates and enhancements.

You may also like

- Steering magnetic micropropellers along independent trajectories
Peter J Vach, Stefan Klumpp and Damien Faivre
- A micro-force measurement system based on high-temperature superconducting magnetic levitation
Wenjiang Yang, Yu Ji, Mao Ye et al.
- THE POPULATION OF PROPELLERS IN SATURN'S A RING
Matthew S. Tiscareno, Joseph A. Burns, Matthew M. Hedman et al.

This content was downloaded from IP address 106.0.37.90 on 21/10/2024 at 11:22

Journal of Physics: Conference Series **2837** (2024) 012093 doi:10.1088/1742-6596/2837/1/012093

3-Blade Propeller Design and Acoustical Analysis

Sreekanth Sura[1,a)], B Nagaraj Goud[1, b)], Raju Santhani[1,c)], Sathwik[1,d)], Manideep[1,e)]

[1] Department of Aeronautical Engineering, MLR Institute of Technology, Hyderabad, India.

[a)] sreekanthsuramlrit@gmail.com, [b)]nagaraj2107@gmail.com,
[c)]rajusanthani2000@gmail.com, [d)] sathvik.gogula@gmail.com,
[e)]Lukenikki2208@gmail.com

Abstract. In the recent time, the deployment and usage of small scale unmanned aerial vehicles (UAVs) have grown rapidly for a wide range of civilian and military applications. These applications range from racing, delivery and photography for civilians to land based reconnaissance operations for military purposes. The noise produced by the propellers is one of the major factors which are stopping its application in delivery of goods. As a lot of drones around the houses making annoying noises will lead to the frustration and stress to local residents. Even in the application of drone in military purpose for reconnaissance the noise generated by the propeller should be decreased to make the drone stealthy. This projects goal is to design a 3-blade propeller for a small size unmanned aerial vehicle (UAV) using propeller theories and to analyse its acoustical behaviour. The propeller design is validated by using two methods they are – Analytical, Experimental. Blade Element Theory is used for analytical analysis whereas experimental validation has been done using thrust stand. For acoustical analysis a python code has been developed based on Gutin & Deming theory. The parameters of a propeller like Diameter, RPM (Revolutions per minute), and Load distribution are iterated to design an efficient, low noise propeller which is capable to produce required amount of thrust.

Keywords: Unmanned aerial vehicle, Blade element theory, thrust stand etc.

1. Introduction

There have been the recent technological advances which have produced efficient, slow-flying unmanned aerial vehicles (UAVs), a great number of which have propellers as their propulsion system[1]. These technological advances also include improvements of silent electric motors. Propellers become a major source of noise after replacing the piston engines with silent electric motors, due to which reducing the noise generated by the propeller became very important [2].

Along with this the recent growth of UAV applications such as photography, aerial mapping, agriculture and deliveries in civil and for reconnaissance in military sector the need of low noise propeller has become mandatory [3,5,7]. As we all know that the noise generated by propeller is one off the major drawback which is stopping its growth in air deliveries, air taxis etc. The propeller acoustics of small UAVs has become a topic of interest as it is one of the recent subject area a lot of research is needed to understand the effect of different parameters on the noise generated by propeller.

Content from this work may be used under the terms of the Creative Commons Attribution 4.0 licence. Any further distribution of this work must maintain attribution to the author(s) and the title of the work, journal citation and DOI.
Published under licence by IOP Publishing Ltd

2. Aerodynamic Theories:

The theories which existed pre-war for the design of propellers are Betz's theory in 1919 [4]. Bet's theory proved that the efficient propeller will minimize induced power loses by having a constant induced velocity and a constant wake pitch in the propellers slipstream. Goldstein created a theory in 1920 to design a propeller that would meet Betz's condition. The other two major theories which mostly used are Momentum theory and Blade Element theory [4]. In Blade Element theory to study the forces acting on a propeller in detail the blade is divided in to elementary strips, and the forces on each element are calculated. The idea of division and analysis of forces on elements are published by William Froude in 1878.

The simple blade-element theory is referred to as the Drzewiecki theory, as Drzewiecki who put it into practical form and brought it into general use [6-9]. Also, he was the first person to sum up the forces on the blade elements to obtain the thrust and torque for a whole propeller and the first to introduce the idea of using airfoil data to find the forces on the blade elements. Where radius of propeller(R), elemental chord(b), radial distance(r), Section Lift(dL), Section Drag(dD), Blade pitch angle(β), Section angle of attack(α), Forward velocity(V).

The thrust & torque equations:

$$T = \frac{1}{2}\rho V^2 B \int_0^R T_c dr \tag{1}$$

$$Q = \frac{1}{2}\rho V^2 B \int_0^R Q_c dr \tag{2}$$

2.1 Acoustic Theory (Gutin & Deming):

The first successful analytical acoustic theory was developed by Gutin, who modeled the steady aerodynamic forces acting on a propeller (torque and thrust) as a ring of dipole source distributed over the propeller disc [10-12]. Following a similar procedure, Deming was the first to model the noise caused by finite blade thickness using the superposition of a continuous ring of sources and sinks in the propeller plane.

The aforementioned formulations for loading and thickness noise are presented. Discretized values for thrust and torque were used, rather than the effective radius approximation used by Gutin and Deming, to maintain a consistent aerodynamic input across all prediction methods [13].

$$P_{mL} = \frac{mB\cap}{2\sqrt{2}\pi cS}\int_{hub}^{tip}\left[\frac{dT}{dR}cos\,\theta - \frac{dQ}{dR}\frac{c}{\cap R^2}\right] {J_{mB}}^{dR} \tag{3}$$

$$P_{mT} = \frac{-\rho(mB\cap)^2 B}{3\sqrt{2\pi}\,S}\int_{hub}^{tip} bh{J_{mB}}^{dR} \tag{4}$$

$$J_{mB} = J_{mB}\left(\frac{mB\cap}{C}R\,sin\,\theta\right) \tag{5}$$

3. Code Description:

Python 3 was chosen as the programming platform due to its flexibility, ease of use and reasonable computational speed for matrix manipulation and mathematical operations [14]. The Gutin and Deming theory is used to develop the code so that fast and accurate results can be obtained.

Based on the design every propeller has four unique equations which have to be substituted in the code. These equations are based on Thrust, Torque, Thickness and Chord distributions of a propeller [14-15].

Equations of Design

Thickness: $y = -3992.2x^5 + 413.1x^4 - 0.8693x^3 - 0.7623x^2 - 0.0131x + 0.0031$ (6)

Chord: $y = -171167x^5 34179x^4 - 2522.4x^3 + 78.266x^2 - 0.7502x + 0.0152$ (7)

Thrust: $y = -1E + 07x^5 + 2E + 06x^4 - 106648x^3 + 3337.8x^2 - 38.953x + 0.1376$ (8)

$$Torque: y = -7E + 06x^5 + 1E + 06x^4 - 191161x^3 + 7479.9x^2 - 26.017 + 0.0908 \quad (9)$$

The inputs which are given in the code are RPM and number of blades, the output of the code i.e. the noise generated by the propeller is printed in the excel sheet.

```
import xlsxwriter
import sympy
from sympy import *
from math import acos,asin,pi,log,log10
from scipy.integrate import quad
workbook=xlsxwriter.Workbook('test_1.xlsx')
def fact(j):
    n=1
    for i in range(1,j+1):
        n=n*i
    return n
x=0.133
y=0.655
z=0
var('r')
B=int(input("Enter no. of blades of the propeller "))
rpm=int(input("Enter RPM of the propeller "))
rho=1.225
n=float(rpm/60)
c=343.2
Po=2*10**-5
S=sqrt(x**2+y**2+z**2)
theta=acos(x/S)
oh=2*pi*n
w=10
class Excel:
```

Figure 1. Python Code

4. Design & Modeling:

By using blade element theory, a 3-blade UAV propeller has been designed which is capable of providing required amount of thrust [15,16].

Table 1: Final Chord & Pitch Distribution

r/R	Chord(mm)	t/c	β
0.15	13	17	62.4
0.30	18.3	10	43.7
0.45	18.91	9	32.5
0.60	17.08	9	25.6
0.75	13	7	20.9
0.90	9	5	17.7

Table 2: Theoretical Thrust

Thrust (g)	429
Ƞ (%)	71

The Design Software- CATIA V5 has been used for modelling the propeller [17]. The Airfoils are Choose based on the criteria of BET, At every station of the propeller i.e. 15%, 45%, 60%, 75% and 90%.

Figure 2. CATIA Model

5. Prototyping:

For prototyping Stereo lithography (SLA) additive manufacturing process is used which belongs to the vat photo polymerization family. The technology uses a light source to cure a photopolymer reason. Grey Pro Resin material has been chosen as it is an Engineering Resin designed for high precision, moderate elongation, and low creep [18]. These mechanical properties make Grey Pro Resin a versatile material for a wide range of engineering applications, including concept modelling and functional prototyping.

Table 3: Grey resin material properties

	Green[2]	**Post-Cured**[2]
Tensile Properties		
Ultimate tensile strength	33 MPa	61 MPa
Tensile Modulus	1.4 GPa	2.6 Gpa
Elongation	33%	13%
Flexural Properties		
Flexural Stress at 5% strain	39 MPa	86 MPa
Flexural Modulus	0.9 GPa	2.2 GPa

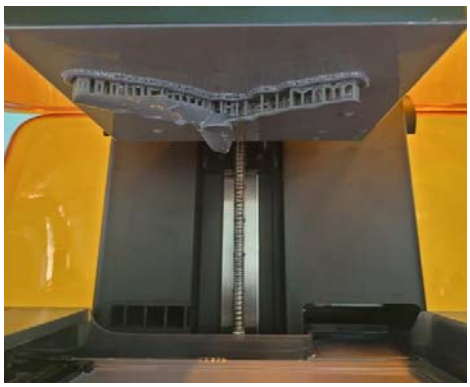

Figure 3. 3D Printing of Propeller

6. Experimental setup:

A test setup (thrust stand) is developed to test various parameters such as thrust, current, power consumed, RPM and noise produced, during testing if any structural failure occurs or design doesn't provide the required thrust or if it isn't matching the requirements then the R&D is carried out again.

After prototyping a propeller, it is balanced using propeller balancer [15]. The Thrust, RPM, are displayed on the monitor using Aurdino code and a wattmeter is used to measure the current, voltage and power consumed. The noise generated by the propeller is measured using sound meter.

Figure 4. Experimental Setup

7. Test Cases:

To analyze the effect of different parameters on the noise generated by a propeller a number of parameters such as Thrust distribution, Diameter and Pitch has been varied.

7.1 Test Case -1:

In this test case the thrust distribution on a propeller blade has been varied to understand the effect of thrust loading on the noise generated by a propeller. Two different designs has been made based upon the thrust distribution and the noise generated is calculated by using the propeller acoustical code.

7.2 Design – 1

In this the propeller blade is divided into ten sections i.e. 10%, 20%,…100%. The thrust generated by the each section has been gradually increased up to 90%.

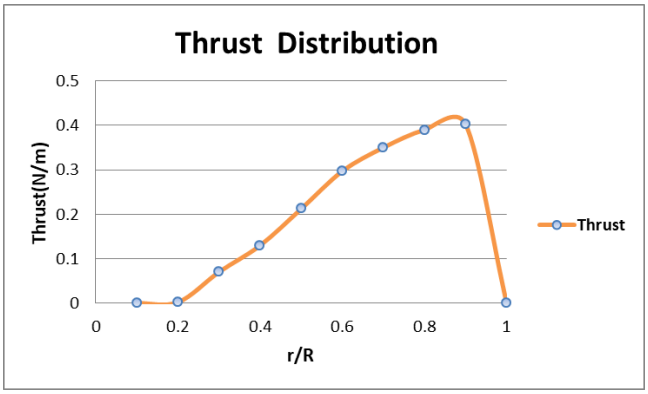

Figure 5. Thrust Distribution Over Design-1 Propeller

7.3 Design -2

In this the propeller blade is divided into ten sections i.e. 10%, 20%, 100%. The thrust generated by the each section has been gradually increased up to 60% and then decreased.

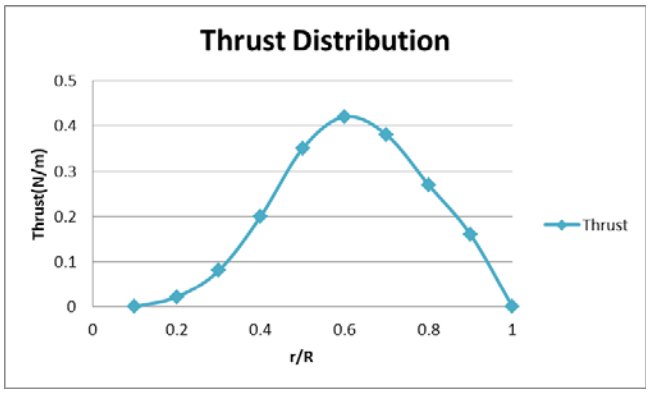

Figure 6. Thrust Distribution Over Design-2 Propeller

8. Test Case -2:

In this test case the Diameter of a propeller blade has been varied to understand the effect of thrust loading on the noise generated by a propeller. Two different designs has been made based upon the Diameter and the noise generated is calculated by using the propeller acoustical code.

8.1 Design-3

The diameter of the propeller is reduced from 5 inch to 4 inch by keeping the thrust generated by both the propellers same. Due to this the Thrust loading per unit area increases the effect of this change in noise generated by the propeller is determined.

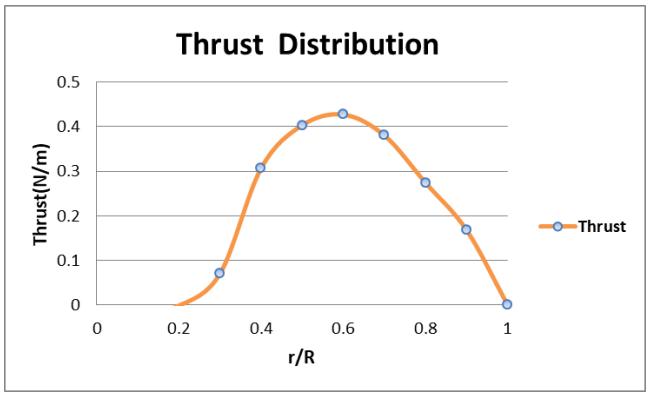

Figure 7. Thrust Distribution over Design-3 Propeller

8.2 Design-4

The diameter of the propeller is increased from 5 inch to 6 inch by keeping the thrust generated by both the propellers same. Due to this the Thrust loading per unit area decreases the effect of this change in noise generated by the propeller is determined.

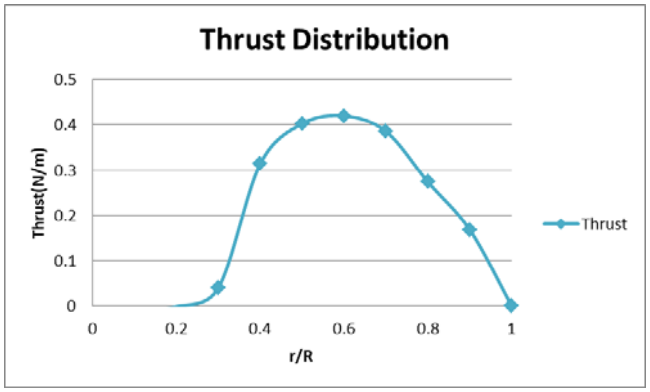

Figure 8. Thrust distribution over design-4 propeller

9. Test Case -3:

In this test case the Pitch of a propeller blade has been varied to understand the effect of thrust loading on the noise generated by a propeller. Two different designs has been made based upon the Pitch and the noise generated is calculated by using the propeller acoustical code.

9.1 Design-5

The pitch of the propeller is decreased from 4.5 inch to 3.5 inch by keeping the thrust generated by both the propellers same. Due to this the required rpm to generate the same amount of thrust increases the effect of this change in noise generated by the propeller is determined.

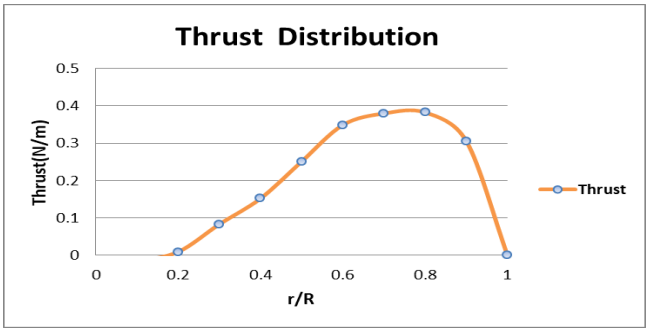

Figure 9. Thrust distribution over design-5 propeller

9.2 Design-6

The pitch of the propeller is decreased from 4.5 inch to 3.5 inch by keeping the thrust generated by both the propellers same. Due to this the required rpm to generate the same amount of thrust increases the effect of this change in noise generated by the propeller is determined.

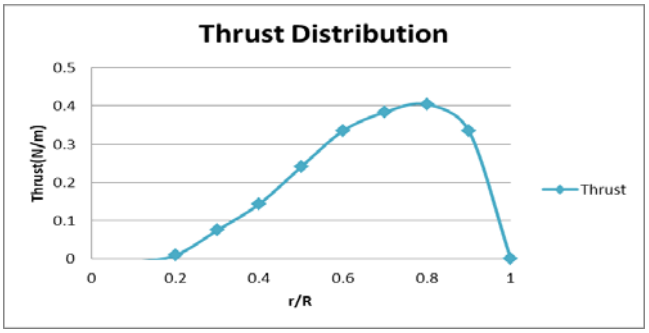

Figure 10. Thrust distribution over design-6 propeller

10. Results:

The result of experimental and Theoretical(Code) noises are compared in the table below the difference in theoretical and experimental is less than 10%, so the code has been validated and further used to determine the noise generated by the other propeller designs.

Table 4: Comparison Of Experimental & Theoretical (Code) Result`

Test Case	Design	Code SPL(dB)	Experimental SPL(dB)
1	1	86.28	88.15
	2	95.14	92.86

Table 5: Theoretical Result of Noise Generated By Different Designs

Test case	Design	Code SPL(dB)
1	1	86.28
	2	95.14
2	3	97.24
	4	84.12
3	5	97.18
	6	82.96

11. Conclusion:

After comparing different test case results, we can see that the effect of thrust loading has higher impact on acoustic noise generated by propeller when comparing to diameter change. As the loading on propeller decreases noise decreases. The Code can be used to determine the near field noises generated by a propeller as Experimental and Theoretical result has less than 10% error.

12. References:

[1] Text Book - “Aircraft Propeller Design”, by Brost, 2007.
[2] Text Book – “A Process for the and Design Manufacturing of Propellers for Small UAV” by Brain David Rutkay, 2014.
[3] Design and Analysis Software for Propellers by Prathpanayaka Rajeevalochanam,2013. Model Airplane Propeller, by W.B. Garner, 2009.
[4] Nomenclature for Aeronautics by National Advisory Committee for Aeronautics.
[5] Design and Development of Three Blade Propeller for Micro Air Vehicles by Viond kumar,CSIR-NAL,India.
[6] R. Peterson. Regional turboprop resurgence continues; jet demand shifts upward. Aircraft Engineering and Aerospace Technology, 80(2), 2004.

[7] Mr. Veeranjaneeyulu K Dr.Mohad Ali "Vibrational Analysis of Initially Stressed Laminated Plates using FEM." The Journal of Mechanical Engineering, College of Engineering, Defence University, Debre-zeit, Ethiopia.vol 2,2002, pp27-38.
[8] K Shiva Shankar, B Nagaraj Goud, Sreekanth Sura, Ch Harish, B Pravalika, "An UAV with Twin Propellers Driven by Single Motor", International Journal of Innovative Technology and Exploring Engineering (IJITEE), ISSN: 2278-3075, Volume-9 Issue-2, December 2019.
[9] Mr. Sreekanth Sura, Alka Sawale, M Satyanarayana gupta "Dynamic Analysis of Cantilever Beam" International Journal of Mechanical Engineering and Technology (IJMET), Date: 05-05-2017, Volume no:8
[10] M. S. Ryerson and M. Hansen. The potential of turboprops for reducing aviation fuel consumption. Transportation Research Part D: Transport and Environment, 2010.
[11] E. Franssen, C. van Wichen, N. Nagelkerke, and E. Lebret. Aircraft noise around a large international airport and its impact on general health and medication use. Occupational and Environmental Medicine, 61(5), 2004.
[12] H. Swift. A review of the literature related to potential health effects of aircraft noise. PARTNER-COE-2010-003, Partnership for Air Transportation Noise and Emissions Reduction, Cambridge, MA, July 2010.
[13] R. P. Woodward. Measured noise of a scale model high speed propeller at simulated take off approach conditions. NASA-TM-88920, Lewis Research Centre, Cleveland, OH, January 1987.
[14] J. H. Dittmar and R. J. Jeracki. Additional noise data on the SR-3 propeller. NASA-TM-81736, Lewis Research Centre, Cleveland, OH, May 1981.
[15] L. Gutin. On the sound field of a rotating propeller. NACA-TM-1195, National Advisory Committee for Aeronautics, Washington, DC, October 1948.
[16] C. Holsclaw. Stage 5 airplane noise standards. 81 FR 1923, Federal Aviation Administration, Washington, DC, January 2016.
[17] N. Dickson. ICAO noise standards. In ICAO Symposium on Aviation and Climate Change, Montreal, Canada, 2013.
[18] F. J. H. Lynam and H. A. Webb. The emission of sound by airscrews. Technical Report of the Advisory Committee for Aeronautics for the Year 1918-1919.

Journal of Physics: Conference Series

PURPOSE-LED PUBLISHING™

PAPER • **OPEN ACCESS**

Dynamic mechanical analysis, flammability and quasi-static test on Kevlar/basalt-epoxy hybrid composite laminates

To cite this article: Ruval P Parekh *et al* 2024 *J. Phys.: Conf. Ser.* **2837** 012025

View the article online for updates and enhancements.

You may also like

- Unhole and open hole compressive behaviours of hybrid Kevlar/glass fibre reinforced silica nanocomposites
Norazean Shaari and Aidah Jumahat
- Anti-impact behavior of a novel soft body armor based on shear thickening gel (STG) impregnated Kevlar fabrics
Chunyu Zhao, Chenhui Xu, Saisai Cao et al.
- A smart Kevlar-based triboelectric nanogenerator with enhanced anti-impact and self-powered sensing properties
Fang Yuan, Shuai Liu, Jianyu Zhou et al.

This content was downloaded from IP address 106.0.37.90 on 21/10/2024 at 11:16

Journal of Physics: Conference Series **2837** (2024) 012025 doi:10.1088/1742-6596/2837/1/012025

Dynamic mechanical analysis, flammability and quasi-static test on Kevlar/basalt-epoxy hybrid composite laminates

Ruval P Parekh[1], Ballina Rakesh[1], Chakrala Uttrani[1], Eekshit[1], Subramaniam Haginilaathan[1], Jensin Joshua J[1], Ganesh M[2], Seralathan S[1] *

[1]Department of Aeronautical Engineering, Hindustan Institute of Technology and Science, Chennai 603 103, Tamil Nadu, India
[2]Department of Aeronautical Engineering, MLR Institute of Technology, Hyderabad, Telangana

* Corresponding Author: siva.seralathan@gmail.com

Abstract. The composites made of Kevlar and basalt are studied individually. The experimental investigations aims to study the hybrid composites made from both materials. The present study examines the thermal as well as mechanical properties of the composites by conducting tests such as dynamic mechanical analysis (DMA), flammability (UL-94) and quasi-static tests on Kevlar, basalt, and Kevlar/basalt hybrid composites. The composite laminates are fabricated by hand-layup method and the results are compared to evaluate the thermal and mechanical properties. DMA test showed that Kevlar has a higher storage modulus, while basalt has a higher loss modulus. Quasi-static test showed basalt has the higher energy absorption capacity followed by the hybrid Kevlar/basalt composite. The hybrid Kevlar/basalt composite showed these values at par with pure Kevlar laminate. The flammability UL-94 test demonstrated that hybrid composite exhibited better flame retardancy properties. Based on the results, it is found that Kevlar/basalt hybrid composite is a better material for the applications of balanced mechanical properties with flame retardancy when compared to Kevlar or basalt individually.

1. Introduction

Composite materials are used in various industries because of their high strength-to-weight ratio, high fatigue resistance, and superior damage tolerance. Among various composite materials, Kevlar and basalt has gained attention due to its significant thermal and mechanical properties. Kevlar, a synthetic fiber, is known for toughness, high strength, and abrasion, whereas basalt, a natural volcanic fiber, is known for high temperature resistance as well as tensile strength. The outcome of this study gives an insight into the properties of the hybrid composites which can be helpful for the industries like aerospace, automotive and construction where high performance materials are required to withstand extreme conditions.

There are variety of methods in which the composites are fabricated, which includes hand lay-up method, vacuum infusion method and resin transfer molding [1]. In this study, hand lay-up method is chosen as it is simple, cost-effective method and is widely used in various industries. Hand lay-up method involves laying the material by hand on a mold and then, using a roller to consolidate the layers and remove any air bubbles. It is allowed to cure for 24 to 36 hours. Other methods such as

Content from this work may be used under the terms of the Creative Commons Attribution 4.0 licence. Any further distribution of this work must maintain attribution to the author(s) and the title of the work, journal citation and DOI.
Published under licence by IOP Publishing Ltd

resin transfer molding and vacuum infusion method have added advantages such as improved control over the resin distribution and reduced void content [1].

Although, there are research carried out on Kevlar/basalt hybrid composites, it is relatively limited when compared to the research on Kevlar and basalt composites individually. However, there are research that investigate the mechanical and thermal properties of various hybrid composites which are then compared to their individual composites.

Heitor Luiz Ornaghi Jr *et al.* [1] performed the dynamic mechanical analysis (DMA) on glass/sisal hybrid composite with various fiber loadings and volume ratios. The storage modulus decreased with increase in temperature and the storage modulus increased with intensification in the fiber loading. This was due to the robust fiber/matrix interactions and large elastic modulus values of the glass fiber. The drop in the modulus around glass transition temperatures (T_g) was smaller for high fiber loading and glass fiber content, whereas in loss modulus, the inclusion of glass fiber created a broadened loss modulus peak. This led towards reversal of the relaxation process within the composite. There was an apparent change in T_g towards higher temperature upon increase of the glass fiber contents and overall fiber content. The damping parameter (viz., tan δ) curve of the composite shifted toward higher values for high fiber content and had a lower peak height which indicated about the good interfacial adhesion and vice-versa. Moreover, the tan δ peak became broader on the addition of fibers.

Zachariah Oommen *et al.* [2] studied on the physically compatibilized natural rubber/poly methyl methacrylate blend by adding natural graft-poly methyl methacrylate and learnt about their dynamic, mechanical, and thermal properties. Using DMA, the authors found the degree of interpenetrating of PMMA and NR at the interfaces by evaluating the entanglement density. Ramesh and Anand [3] studied the Kevlar (K)/basalt (B) hybrid composite on various stacking sequence and analyzed the mechanical properties. The various stacking sequences such as BKBKBKB, KBKBKBK, BBKBKBB, KKBKBKK, BBKKKBB, and KKBBBKK were used and analyzed the fractured surface using morphological analysis and mechanical properties. The tensile strength and flexural strength of the composites were compared, and it was observed that KBKBKBK had the highest tensile strength of 174MPa along with highest flexural strength of 188MPa followed by KKBKBKK and KKBBBKK with a tensile strength of 151MPa and flexural strength of 114MPa. BBKBKBB had the least flexural and tensile strength of 77MPa and 132MPa respectively. The morphological test showed that KBKBKBK possessed lesser defects.

Akash *et al.* [4] investigated the horizontal and vertical flammability of sisal/coir fiber reinforced hybrid composites for various weight percentages. It was observed that increase in natural fiber led to the increase of its flammability. This was an indication that natural fiber had a bad flame retardant as a layer has generated due to pyrolysis. This layer behaved as a fire supporter, and it spread fire to the un-pyrolyzed substance. As the specimen got preheated in the vertical position, the flame speed was faster in the vertical position than in the horizontal position. Jensin Joshua *et al.* [5] studied on the Kevlar/glass-epoxy as well as Kevlar/basalt-epoxy intra woven composite laminates and found that the quasi-static impact strength of Kevlar/basalt was around 5.70 times higher than the Kevlar/glass which may be influenced by the weaving pattern of the composite laminate.

Ibrahim M. Alarifi *et al.* [6] studied the mechanical properties of natural fibers reinforced with polymer composites which improved with use of synthetic or natural fiber with a comparably enhanced elongation. Thingujam Jackson Singh and Sutanu Samanta [7] concluded that the improved impact properties of Kevlar composites were due to its ability to absorb higher impact energy dissipated during plastic deformations. Yunfu Ou *et al.* [8] stated that the maximum strain increased with increase in temperature and strain rate. The toughness increased with increase in strain rate, but it decreased at higher temperatures. Asim *et al.* [9] concluded that the combustion rate increased because of the incompatibility of both fibers with a matrix which revealed the uncovered cellulosic content of fiber. Vasudevan *et al.* [10] used theoretical modelling to envisage the damping parameters, storage modulus, and reinforcement coefficient. Activation energy was determined for the corresponding T_g and loss modulus. A good correlation existed between the experiment and theoretical values. With increase in frequency, the T_g values moved towards high-temperature regions. The temperature of peak

tan δ value was higher with respect to peak value of loss modulus. Srivatsava Madarvoni and Sreekanth P.S. Rama [11] mentioned that characterizations such as impact strength, hardness, flexural, and tensile were analyzed separately, along with viscosity properties and heat deflection of the epoxy composites.

Hilmar Koerner *et al.* [12] stated that the low-to-intermediate crosslink density provided adequate deformability and elasticity above T_g, and a higher glass transition temperature provided resistance to stress relaxation in the stored shapes. For similar specimen dimensional details, Hemant Chouhan *et al.* [13] found that K-PP composite performed better under quasi-static loading in comparison with dynamic loading. The peak stress of K-PP was 33% to 47% higher compared to dynamic tests. On the other hand, the test results of KPEI was quite opposite to that of K-PP results. Aswani Kumar Bandaru *et al.* [14] revealed the tailoring of 2D fabrics using basalt and Kevlar fabric. The use of intra-ply hybridization created a lighter weighing 2D fabrics compared to heavy weight 3D fabrics. The hybridization scheme highly influenced the composite material's dynamic response. The intra-ply hybrid composite was able to withstand higher strain rates in comparison with inter-ply hybrid composite. Mohd Firdaus Omar *et al.* [15] stated that strain rates applied influenced the mechanical properties of all tested polymeric. With increase in strain rate, the compressive strength, compression modulus, as well as yield stress got increased proportionally. Ramesh Velumayil and Anand Palanivel [16] stated that the microscopic examination revealed the excellent bonding among the reinforcements as well as matrix materials. The pure basalt/epoxy showcased a larger flexural as well as tensile strengths with respect to hybrid laminates and showcased values in between Kevlar/epoxy and pure basalt/epoxy laminates. An identical pattern was seen for the hardness and impact strength values for the fabricated composite laminates. Farzin Azimpour-Shishevan *et al.* [17] concluded that, in glassy state, the movement of chains were curtailed. The bonds between polymers and fibers along the interface regions influenced the values of storage modulus.

Many investigations on Kevlar were conducted on studying the mechanical properties and high strain properties [18-21]. But very few studies are available in open domain on the basalt and Kevlar/basalt hybrid composite. Based on the review of literatures, it is observed that few studies are carried out on the mechanical behavior as well as energy absorption properties of the Kevlar, basalt, and Kevlar/basalt hybrid composites. Thus, the focus of this study is on the estimation of thermal as well as mechanical properties of Kevlar/basalt hybrid composites by performing various tests such as dynamic mechanical analysis (DMA), flammability (using UL-94) and quasi-static test.

2. Material and fabrication

Epoxy resin LY556 along with the Hardener HY951 is used to fabricate the composites. Kevlar fabric of 220 GSM, plain weave with wrap and weft of 1000D, and 0.9mW and Basalt fabric of 200 GSM, plain weave of 1mW is used. The tensile modulus of Kevlar is 86GPa and the breaking strength is 226N. Also, a polyester film (Mylar sheet) of 75-micron, 125 GSM is used as a protective film so that the laminate is easy to extract from the mold [6]. Kevlar has an exceptional property due to which it is used in military and industrial applications. It is anisotropic in nature because of its high tensile-shear modulus ratio. Its dynamic properties such as young's modulus, tensile strength, toughness, and maximum strain is dependent on its strain rate [7]. The properties of basalt are dependent on the strain rate and temperature [8].

Table 1. Fabricated plates

Plate Number	Sequence	Denotation
Plate 1	KKKKKKKK	K- Kevlar B- Basalt
Plate 2	BBBBBBBB	
Plate 3	KKKBBKKK	

There are variety of methods in which the composites are fabricated, which includes hand lay-up method, vacuum infusion method and resin transfer molding (RTM) [1]. In this study, hand lay-up

method is used. It is simple, cost-effective method and is widely used in various industries. Hand lay-up method involves laying the material by hand on a mold and then using a roller to consolidate the layers and remove any air bubbles. It is then allowed to cure for 24 to 36 hours. Three plates are fabricated using hand lay-up method. Firstly, the fabric is cut to dimension of 300mm x 300mm and are placed on the mold one by one followed by the application of the resin-hardener mixture after each layer. The sequence of layer used for the various fabricated plates is shown in Table 1. As per ASTM Standards, the standard thickness of the specimen is 3mm [3, 21]. Therefore, all the specimens chosen in this study are maintained as 3mm thickness. Kelvar has comparatively a better abrasion resistance than basalt. Moreover, basalt is also an eco-friendly material. Hence, as in Plate 3, two layers of basalt are kept within the three layers of Kevlar on either side. Plates 1 and 2 are made of pure Kevlar and basalt with six layers each to attain 3mm thickness and to meet the ASTM standard.

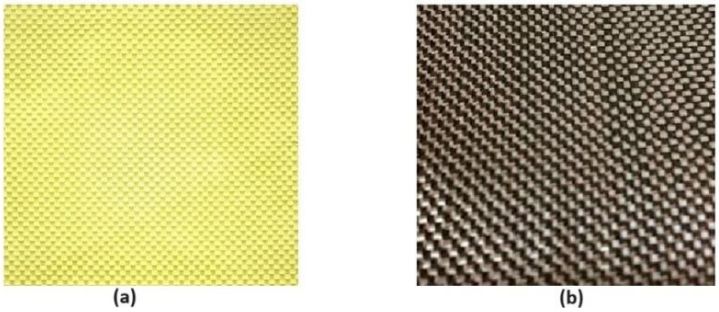

Fig. 1 (a) Kevlar fabric **(b)** Basalt fabric

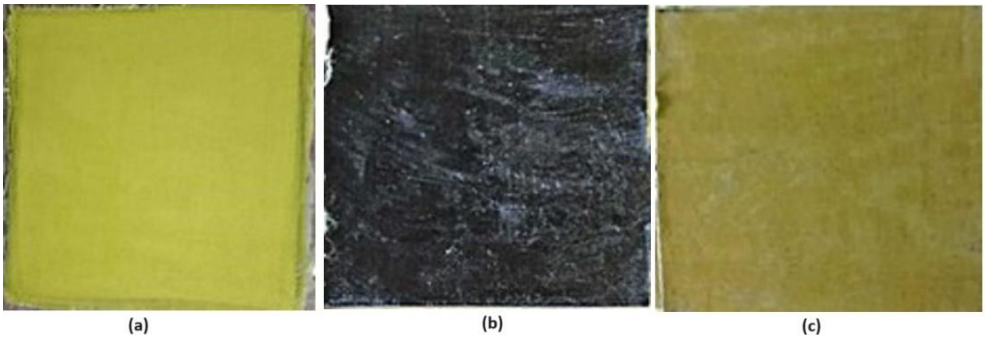

Fig. 2 (a) Plate 1 **(b)** Plate 2 **(c)** Plate 3

Figure 1 shows the Kevlar and basalt fabrics, and Figure 2 depicts the fabricated plates, namely Plate 1 (pure Kevlar), Plate 2 (pure basalt), and Plate 3 (Kevlar/basalt hybrid) as per the stacking sequences shown in Table 1. The sequence KKKBBKKK provides an average flexural and tensile strengths of both these materials and adding of more natural fibers reduces the flexural as well as tensile strengths of the hybrid composites and makes it a poor composite. An alternate layer of each fabric can also provide a better thermal as well as mechanical properties. However, the selection of the stacking sequence depends on the purpose of the intended application [3].

3. Methodology

3.1. Dynamic mechanical analysis (DMA)

Dynamic mechanical analysis is a technique used to study and characterize materials. Moreover, it is used for studying the viscoelastic behavior of polymers [17]. The DMA works by applying a sinusoidal deformation to a sample of known geometry. The sample can be subjected by a controlled stress or a controlled strain. For a known stress, the sample will then deform to a certain amount. The extent of deformation is related to its stiffness.

The testing process involves sample preparation in which the sample is prepared according to the ASTM D5026 standard for polymeric composite materials in tension mode. The sample is then mounted on the DMA instrument using clamps or grips. The load is applied through a sinusoidal force (stress σ) to the sample (input). This results in a sinusoidal deformation (strain ε; output). The DMA instrument records the force and displacement amplitudes as well as phase shifts with respect to time. The data collected from the DMA test is analyzed using software tools.

In this study, the test is carried out using Dynamic Mechanical Analyzer DMS 6100. A three-point bending at a frequency of 1 Hz between the temperature ranges from 26°C to 160°C is used to test the composites. The heating rate is 3°C/minute. The test samples are cut into the rectangular shapes of dimensions 50mm x 12.8mm x 3mm as per ASTM D5026 standard and the test specimens are shown in Figure 3(a). The curves of damping parameter (tanδ), loss modulus (E''), as well as storage modulus (E') with respect to temperatures are plotted. The tests are performed by following the ASTM D5026 procedures and the test set up used in the study is shown in Figure 3(b).

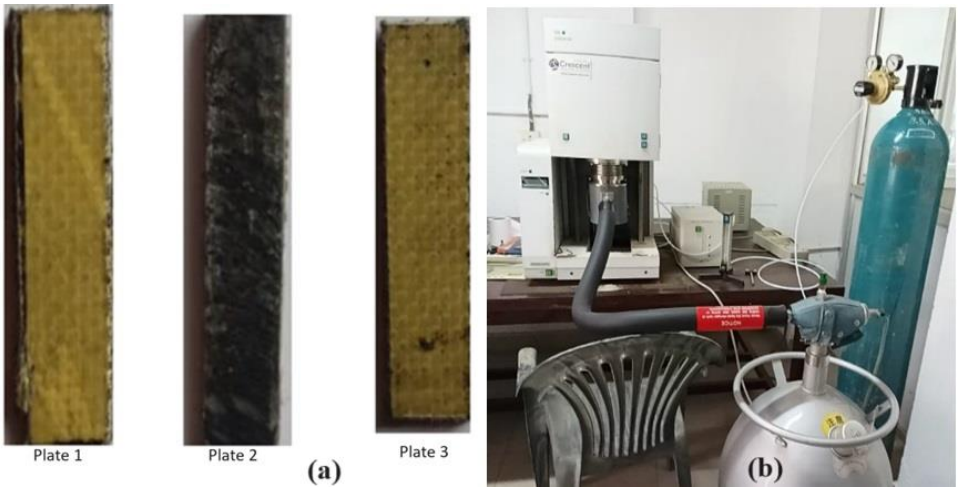

Fig. 3(a) DMA specimens **(b)** Dynamic mechanical analyzer - DMS 6100

3.2. Quasi-static indentation

The quasi-static test is performed to evaluate the quasi-static impact strength of the composites. The tests are performed using the Universal Testing Machine by following the ASTM D6264 standards [5]. The test samples are cut into a square shape, with dimensions of 100mm x 100mm x 3mm as per ASTM D6264 standard. The specimen is fixed over a circular opening, and the plate is subjected to load concentration using a hemispherical intender into the surface at a slow rate, with a cross head time (CHT) of 1mm/sec. Figure 4(a) shows the arrangement of the quasi-static test setup.

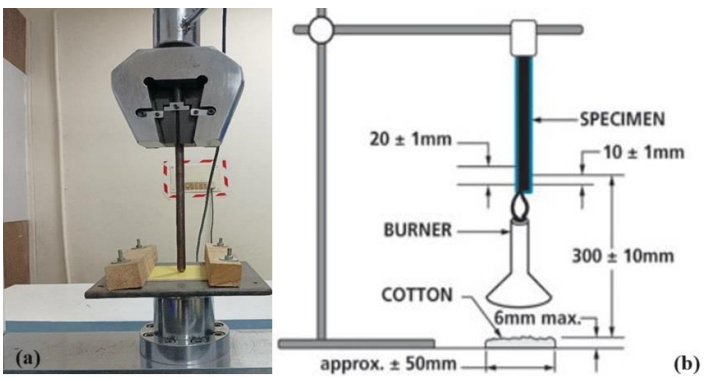

Fig. 4(a) Quasi-static test setup **(b)** UL-94 test setup

3.3. Flammability test

Flammability test is performed to evaluate the fire resistance of the composites. The test is performed using the UL-94 and following the ASTM D3801 standards [9]. The test samples are cut at a dimension of 127mm x 12.70mm x 3mm as per ASTM D3801 standard. It is then placed vertically in the UL-94 test chamber and exposed to a flame for about 10 seconds. The flame is then removed, and the specimen are observed for 30 seconds. This is repeated for at least three times for each specimen and the rating of each specimen is observed. Table 2 lists the rating criteria as per UL-94 standard. The UL-94 test set up used in this study is shown in Figure 4(b).

Table 2. UL-94 standard rating criteria

Rating	Burning time after each application (sec)	Dripping of the material
V0	≤ 10	Not Allowed
V1	≤ 30	Not allowed
V2	≤ 30	Allowed

4. Results and discussion

The Kevlar, basalt and Kevlar/basalt hybrid composites are studied through Dynamic Mechanical Analysis (DMA), Quasi-static testing, and Flammability (UL-94) based on ASTM D5026, ASTM D6264, and ASTM D3801 standards respectively and the outcomes are discussed here.

4.1. Dynamic mechanical analysis (DMA)

Based on the Dynamic Mechanical Analysis (DMA), the results of storage modulus (E'), loss modulus (E'') and damping parameter (tan δ) with respect to temperatures are plotted as seen in Figures 5 to 7. The comparison of all the composites considered in this study is depicted in Figure 8.

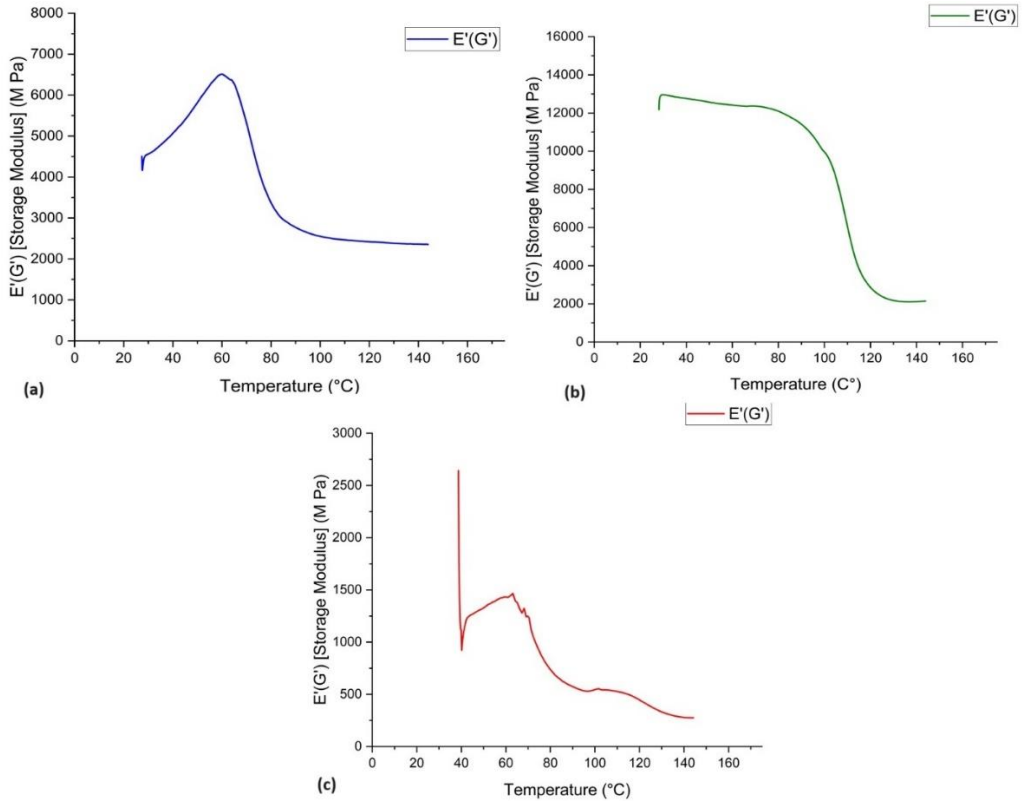

Fig. 5 Storage modulus versus temperature **(a)** Plate 1 - pure kevlar **(b)** Plate 2 - pure basalt **(c)** Plate 3 - hybrid kevlar/basalt laminate

The storage modulus (E') is a measure of the amount of energy per cycle that is stored by a material, and it relates to its elastic behavior [10]. As observed in Figure 5(a), the storage modulus of pure Kevlar laminate is 6.513GPa at a glass-transition temperature $(T_{gs})_{Kevlar}$ of 60.07ºC. This is an indication of superior load-carrying capacity as per the higher storage modulus value. This can be due to the strong mechanical interlocking between the polymer matrix and the bridging action that occurs at the Kevlar and epoxy interface. With respect to Figure 5(b), the storage modulus of pure basalt laminate is 12.335GPa at a glass-transition temperature $(T_{gs})_{Basalt}$ of 72.51ºC. With reference to Figures 5(a) and 5(b), the storage modulus of basalt is 1.894 times the Kevlar. The higher storage modulus results from multiple factors. These factors may include the rising molecular motion of the polymer matrix, the presence of stress concentrations at the fiber-matrix interface, and alterations in the composite's viscoelastic properties as it undergoes thermal transitions.

Figure 5(c) shows the variations in storage modulus with respect to temperatures for Plate 3. The storage modulus of hybrid Kevlar/basalt laminate is 1.465GPa at a glass-transition temperature $(T_{gs})_{KB}$ of 63.14ºC. The lower stiffness of the hybrid laminate on comparison with individual composites may be attributed to differences in the fiber's properties and their interfacial bonding. A lower stiffness can improve toughness or impact resistance, while a higher stiffness may be preferable for structural applications.

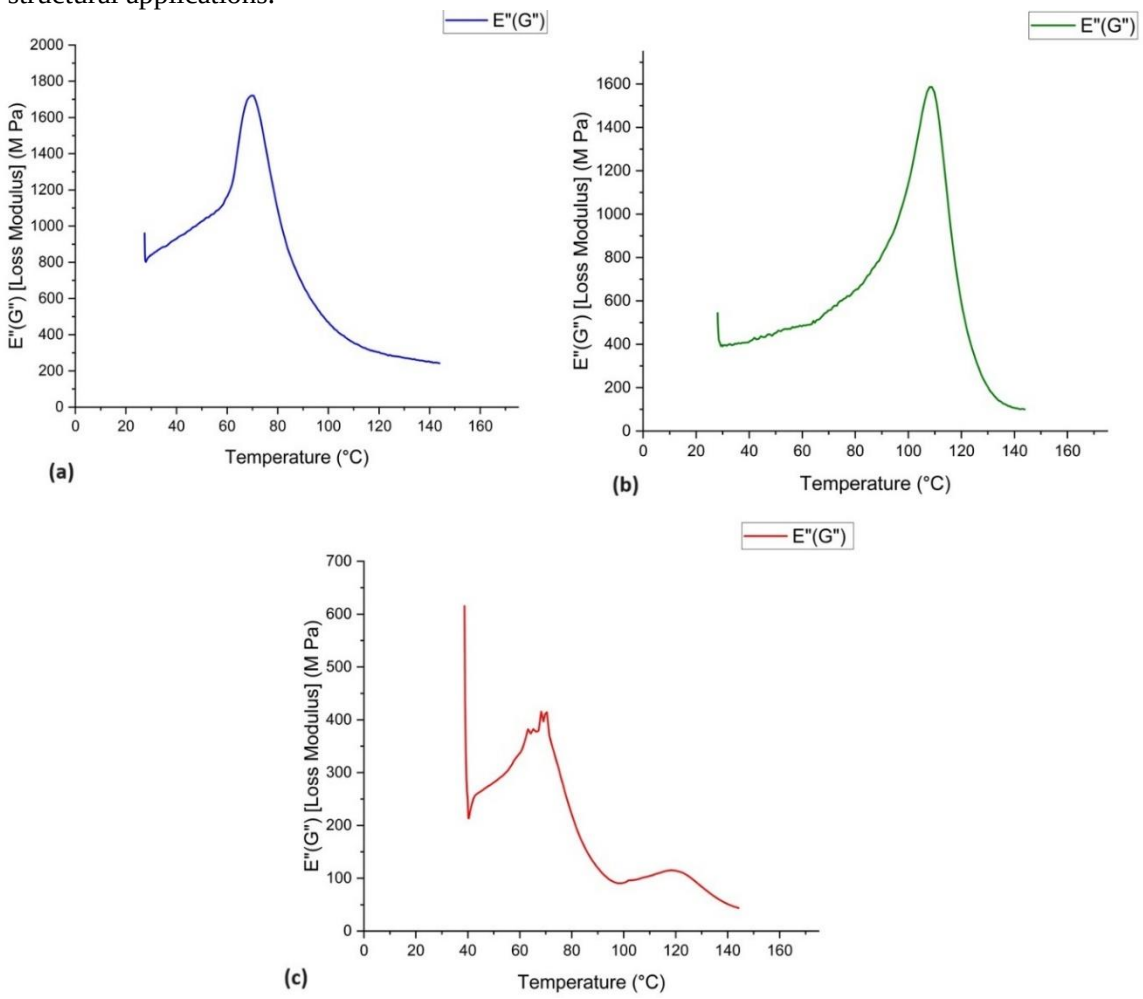

Fig. 6 Loss modulus versus temperature **(a)** Plate 1 - pure kevlar **(b)** Plate 2 - pure basalt **(c)** Plate 3 - hybrid kevlar/basalt laminate

The loss modulus (E'') measures the energy dissipated as heat, which is an indicative of the material's viscous behavior [10]. Figure 6(a) indicates the loss modulus of pure Kevlar laminate as 1.695GPa at a glass-transition temperature $(T_{gl})_{Kevlar}$ of 67.88ºC. The loss modulus is 3.84 times lesser than the storage modulus. The $(T_{gs})_{Kevlar}$ value obtained for the storage modulus is lower than the $(T_{gl})_{Kevlar}$ value obtained from the loss modulus. It may suggest that the material underwent microstructural changes, such as phase separation that may have impacted its mechanical characteristics. In these instances, the $(T_{gs})_{Kevlar}$ determined from the storage modulus may not be an accurate reflection of the material's overall T_g.

Figure 6(b) depicts the variations in loss modulus of plate 2 with respect to temperatures. It is observed that the loss modulus of pure basalt laminate is 1.586GPa at a glass-transition temperature $(T_{gl})_{Basalt}$ of 108.90ºC. The increment and decrement of loss modulus as a function of temperature in basalt laminate may be due to the combined effect of the matrix material's glass transition behavior and the relaxation behavior of the reinforcement fibers. The characteristics of the basalt laminate, including the resin type, reinforcement fiber properties, and manufacturing process can influence these properties.

The variations of loss modulus with respect to temperatures for plate 3 is shown in Figure 6(c). The loss modulus of hybrid Kevlar/basalt laminate is 0.415GPa at a glass-transition temperature $(T_{gl})_{KB}$ of 68.22ºC. With reference to the loss modulus curve, the residual stresses, strains relaxation and interfacial bonding relaxation will influence the material's mechanical properties, contributing to its viscoelastic behavior.

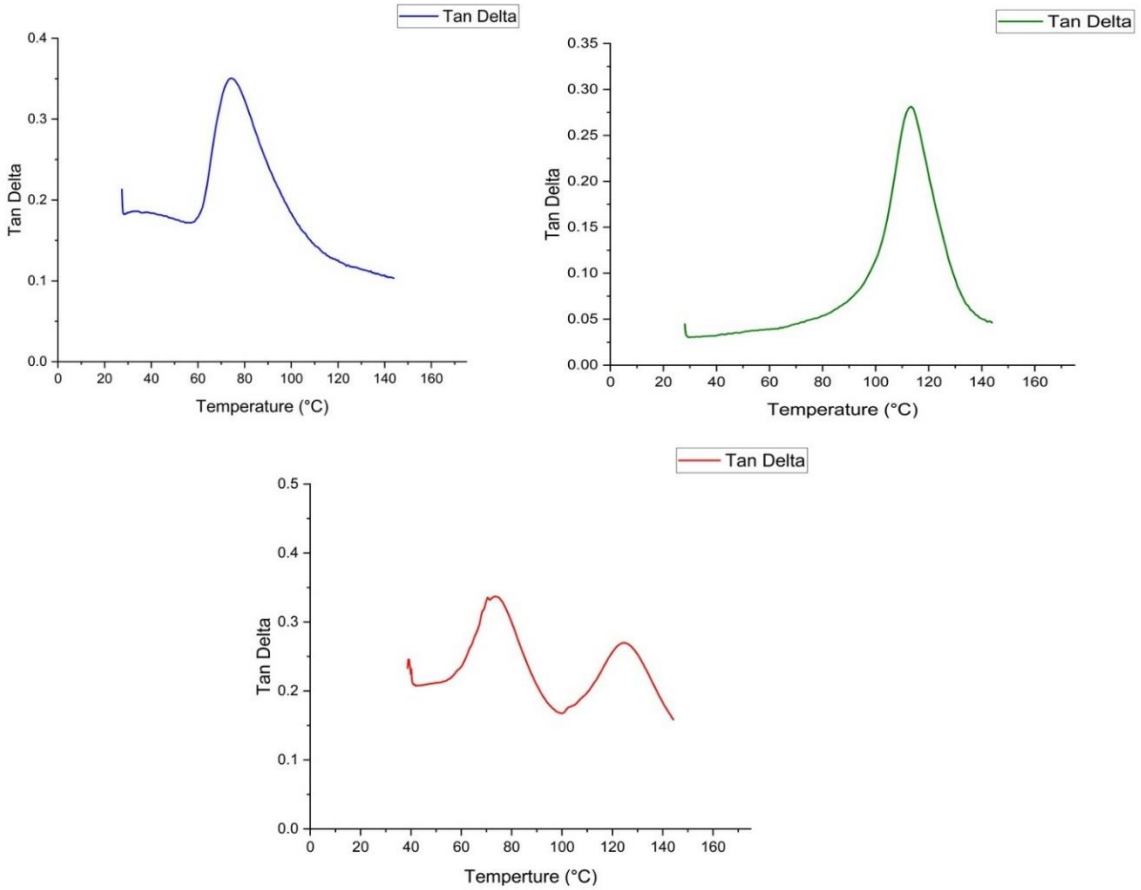

Fig. 7 Damping parameter versus temperature **(a)** Plate 1 - pure kevlar **(b)** Plate 2 - pure basalt **(c)** Plate 3 - hybrid kevlar/basalt laminate

As observed in Figure 7(a), the tan δ (i.e., damping parameter) of pure Kevlar laminate is 0.3506 at a glass-transition temperature $(T_{g\delta})_{Kevlar}$ of 73.978 ºC. A lower value of tan δ indicates more elasticity, while a higher value indicates better damping and energy dissipation [11]. With reference to Figure 7(b), the tan δ (i.e., damping factor) of pure basalt laminate is 0.2815 at a glass-transition temperature $(T_{g\delta})_{Basalt}$ of 113.34 ºC. The areas under the loss curves reflects the energy dissipation capabilities of the materials. The breadth of tan δ shows the distribution of local collective dynamics [12]. The damping capacity and loss modulus of basalt laminate are lower than those of Kevlar (refer Figures 7a and 6a). This is due to the slow increment and steep descent of the loss factor, which is caused by the relaxation behavior of basalt fibers with increasing temperature. As a result, the material becomes less energy-dissipative, leading to a decrease in the loss modulus.

Figure 7(c) shows the damping parameter with temperature for plate 3. Tan δ (i.e., loss factor) of hybrid Kevlar/basalt laminate is 0.337 at a glass-transition temperature $(T_{g\delta})_{KB}$ of 73.21ºC. The Kevlar/basalt hybrid epoxy laminate undergoes two relaxation processes as can be seen in Figure 7(c) with different energy dissipation magnitudes. The lower magnitude of the second cycle suggests that the material may have undergone irreversible changes during the first cycle, resulting in reduced energy dissipation capacity during the second cycle. This behavior is attributed to the progressive degradation due to cyclic loading or environmental factors. The material displays a complex viscoelastic property.

It is noticed that the storage modulus, loss modulus, and tan δ of the pure Kevlar laminate have an increasing glass transition temperatures (T_g) in that order, and it indicates that the material becomes stiffer and less deformable with increasing temperature.

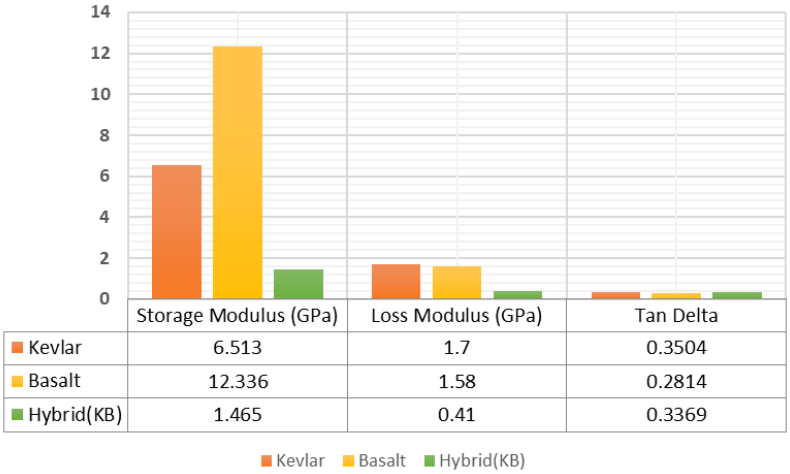

	Storage Modulus (GPa)	Loss Modulus (GPa)	Tan Delta
Kevlar	6.513	1.7	0.3504
Basalt	12.336	1.58	0.2814
Hybrid(KB)	1.465	0.41	0.3369

Fig. 8 Comparison of DMA results

Figure 8 shows the comparison of the DMA results. It is observed that basalt has the highest storage modulus than Kevlar. This indicates that basalt is stiffer, stronger, and more resistant to deformation. Kevlar shows the highest loss modulus than basalt, which depicts that Kevlar has better ability to dissipate energy when subjected to deformation. The delta values for all three materials are within a similar range, indicating that they all have similar levels of damping. Hybrid Kevlar/basalt laminate showed a comparatively lesser values of both storage and loss modulus. The lower value of storage modulus for the hybrid Kevlar/basalt is due to debonding of the matrix in the laminate in comparison with pure Kevlar and pure Basalt laminates. Moreover, Kevlar and basalt have varied material properties and when combined into as hybrid composite, they may not be compatible. Moreover, the distinct ways in which Kevlar and basalt responds to stress and temperature variations may result in reduction in storage modulus and loss modulus values for the hybrid Kevlar/basalt composite laminate. The maximum storage modulus of pure Basalt composite laminate is around

11.76 GPA and the same for the present study is around 12.31 GPA. The findings reported in the present study are in line with the outcomes of Konstantinos Karvanis *et al.* [22].

4.2. Quasi-static test

The results of the energy absorbed from the quasi-static testing are shown in the Figure 9. The impact strengths and damage areas of the specimens are calculated, and these are tabulated as shown in Table 3.

Figure 9(a) depicts the outcome of the quasi-static test for the Plate 1 (i.e., pure Kevlar). As can be seen in the Figure, the curve forms multiple peaks and irregular decrements due to its complex microstructure, outstanding tensile strength and resistance to impact and penetration. As the force increases, the material undergoes plastic deformation, which causes the decrease in the load value. The load value increases again as the fibers reorient themselves to withstand greater loads and deformation which leads to the second peak and the load value again decreases. This is due to the strain hardening property of Kevlar. Now, further increase in the load leads to the breaking of the fibers resulting with final peak. Then, the curve decreases rapidly.

Figure 9(b) depicts the load versus displacement curve for Plate 2 (i.e., pure basalt). As can be seen in the Figure, as it reaches the peak point, it corresponds to the elastic deformation. As the critical point is reached, it undergoes plastic deformation which leads to a sudden drop in the load due to the micro cracks.

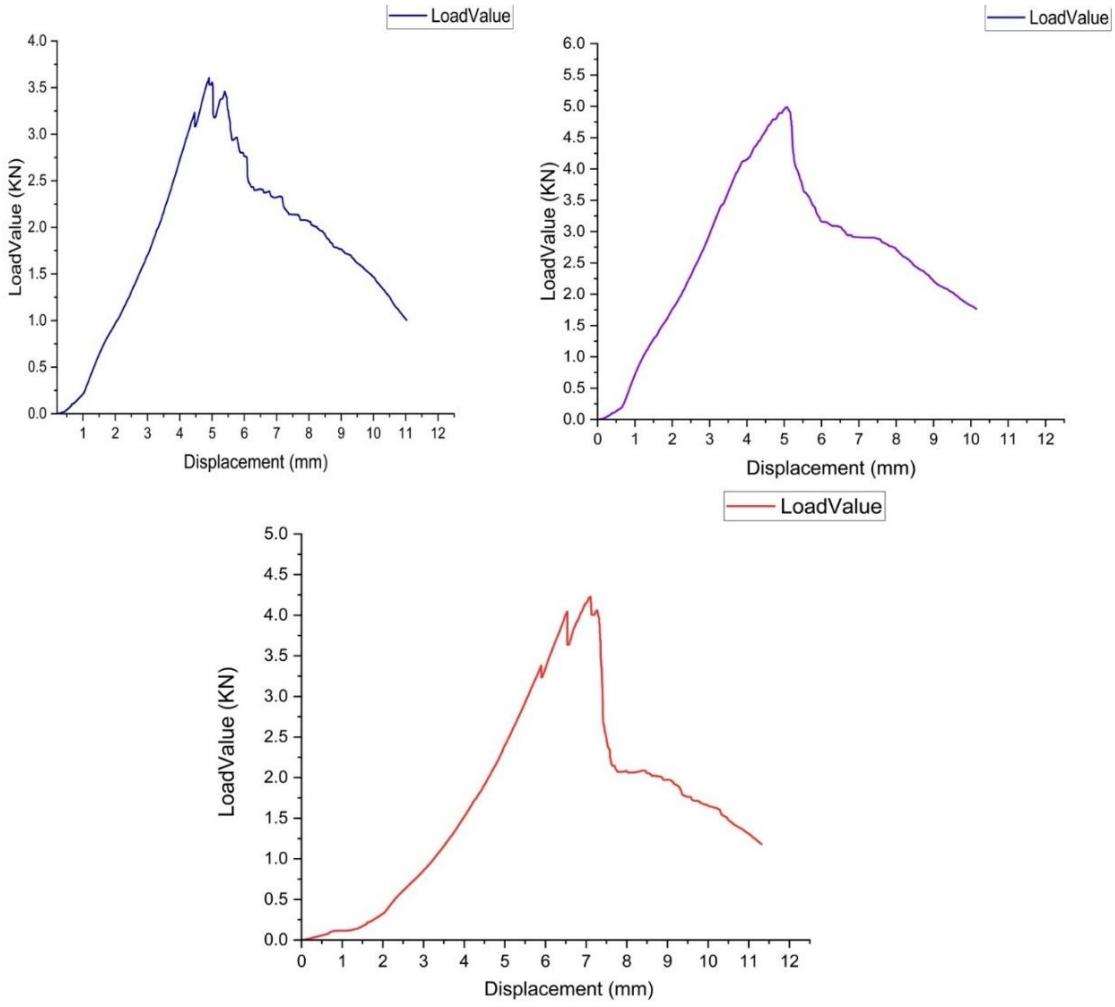

Fig. 9 Energy absorbed **(a)** Plate 1 - pure kevlar **(b)** Plate 2 - pure basalt **(c)** Plate 3 - kevlar/basalt hybrid

Afterwards, a steep decrement is seen. Furthermore, the continued plastic deformation occurs as the micro cracks propagates which leads to the progressive decrement of the curve. This deformation behavior is because of the anisotropic nature of its mineral constituents. Figure 9(c) showcase the load versus displacement curve of the Kevlar/basalt hybrid composite which is a combination of curves as seen in for pure Kevlar and pure basalt. It has multiple peaks, like that of the Kevlar composite, due to the strain hardening behavior of Kevlar. It means that as the fiber is deformed it becomes stiffer and stronger. The steep decrement is exhibited after the multiple peaks which is due to the failure of Kevlar. This may be because of the formation of micro cracks leading to a sudden drop in the load, thereby leading to steep decrement. Finally, it shows irregular progressive decrement which is due to the continued deformation of basalt fibers in the composite.

The energy absorption of the composites is the area under the curves as seen in Figure 9 and these values are tabulated as shown in Table 3. The area under the curves is calculated using Origin Plot software. The damaged areas of the sample plates are shown in Figures 10 to 12, and it is calculated using Image J software and these values are tabulated in Table 3.

The impact strength is calculated as the ratio of $\frac{AbsorbedEnergy}{DamagedArea}$ [5].

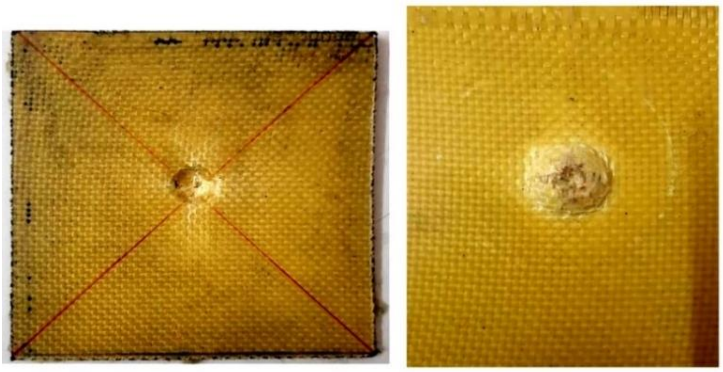

Fig. 10 Damaged area of kevlar composite (plate 1)

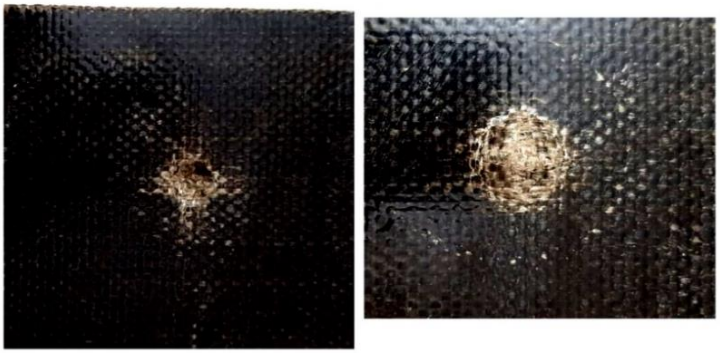

Fig. 11 Damaged area of basalt composite (plate 2)

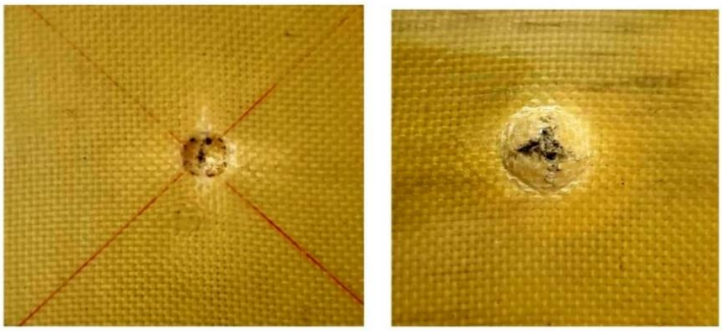

Fig. 12 Damaged area of kevlar/basalt hybrid composite (plate 3)

Table 3. Absorbed energy

	Composite Plate	Absorbed Energy (J)	Damaged Area (mm^2)	Impact Strength (J/mm^2)
Plate 1	Kevlar	19.906	237	0.08399
Plate 2	Basalt	26.541	326	0.08141
Plate 3	Kevlar/basalt Hybrid	19.303	279	0.08356

As listed in Table 3, it is observed that impact strength of Kevlar/basalt hybrid is relatively similar to that of Kevlar which is known for its high impact strength [13]. Since the impact strength of Kevlar/basalt hybrid is slightly lower than Kevlar but higher than basalt, it indicates that basalt fibers contribute to the overall impact strength, but the contribution is relatively small when compared to the Kevlar fibers. This suggests that Kevlar/basalt hybrid has a good combination of impact strength and makes it a potential candidate for the applications that require high strength and impact resistance such as aerospace components, protective gear, etc.

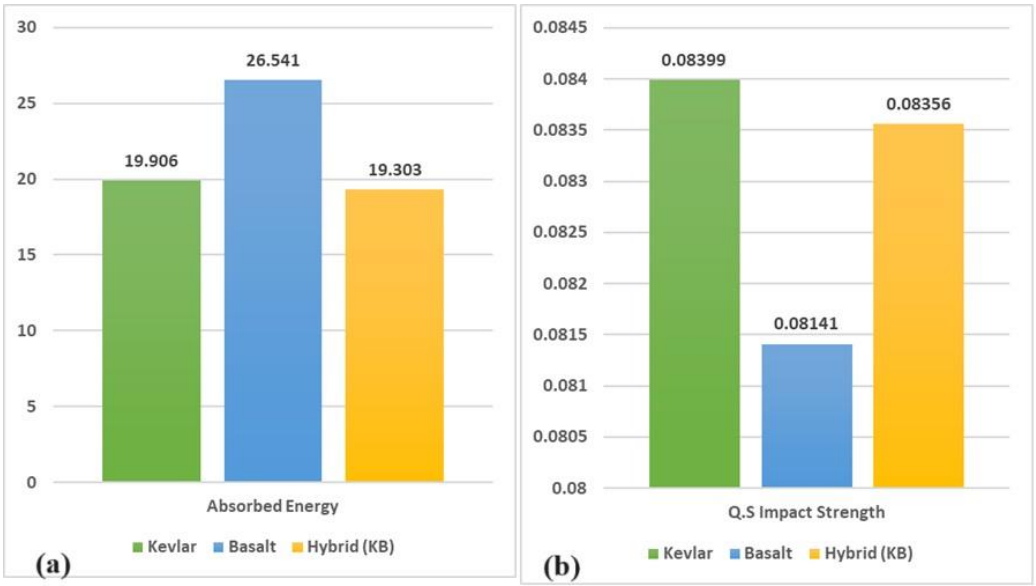

Fig. 13(a) Comparison of absorbed energy **(b)** Comparison of quasi-static impact strength

As depicted in Figures 13(a) and 13(b), basalt has the highest energy absorption and the lowest impact strength. This indicates that basalt can resist deformation and maintain its integrity under stress. Overall, the result from the above Figures shows that the Kevlar/basalt hybrid composite has an almost equivalent quasi static impact strength as well as energy absorption capabilities in comparison with pure Kevlar composite laminate. The Kevlar's intrinsic properties, its optimized orientation and its compatibility with a matrix may have ensured the values of quasi static strength and energy absorption of Kevlar/basalt hybrid composite to be at par with pure Kevlar composite laminate [14]. The introduction of Basalt in the hybrid composite has issues like material incompatibility, but this has not altered the impact resistance capability of the hybrid composite [23].

Table 4. UL-94 obtained ratings

	Plate	Total combustion time (sec)	UL-94V rating
Plate 1	Kevlar	92	V1
Plate 2	Basalt	203	V2
Plate 3	Kevlar/basalt hybrid	73	V1

4.3. Flammability test

The flame retardancy of the samples are found by carrying out the flammability tests and the obtained values are tabulated in Table 4. As per UL-94 standards, V0 indicates good flame resistance, V1 indicates moderate flame resistance and V2 indicates poor flame resistance. As listed in Table 4, it is seen that Kevlar/basalt hybrid composite shows the best flame retardancy and basalt has the poor flame retardancy.

Figure 14 shows the samples after flammability test. As seen in these Figures, it is visible that the basalt composite has burnt completely while Kevlar composite is moderately burnt. On the other hand, the Kevlar/basalt hybrid composite has burnt very less. This is because basalt is more susceptible to burning due to the presence of organic matter in it whereas, Kevlar has high resistance to flame and does not burn easily. The combination Kevlar/basalt hybrid provides a high flame retardancy than basalt alone due to the presence of Kevlar fiber which acts as a barrier and prevents the propagation of the flame. Therefore, in the Kevlar/basalt hybrid composite, the Kevlar and basalt fibers work together to enhance the overall flame retardancy of the composite. This is due to the synergistic effect between the two fibers.

Fig. 14 Samples after flammability test **(a)** Pure kevlar – plate 1 **(b)** Pure basalt – plate 2 **(c)** Kevlar/basalt hybrid – plate 3

5. Conclusion

A detailed investigation on the mechanical and thermal properties of the Kevlar/basalt hybrid composites is carried out. Based on the study, the findings from the dynamic mechanical analysis, quasi-static test and flammability test are listed.

- Dynamic mechanical analysis showed that basalt has the highest storage modulus indicating its remarkable ability to store elastic energy. Kevlar has the highest loss modulus highlighting its exceptional energy dissipation characteristics. Kevlar has a higher storage modulus of around 84% when compared with the hybrid Kevlar /basalt composite. The Kevlar/basalt hybrid composite shows 16% higher Tan δ value in comparison with the basalt composite laminate.
- Quasi-static test showed that basalt has highest energy absorption showcasing its superior ability to withstand and dissipate impact energy. The Kevlar/basalt hybrid composite also exhibited higher impact strength compared to basalt alone, indicating a positive blending effect between the two constituent materials. The Kevlar laminate shows only 0.50% increment in impact strength when compared with the Kevlar/basalt laminate.

- Pure basalt composite laminate shows 20% higher damage area when compared with hybrid Kevlar/Basalt hybrid composite laminate.
- Flammability test (UL-94) shows that Kevlar/basalt hybrid composite has a better flame retardancy which may be due to the synergistic effect between the Kevlar and basalt fibres. Though the flame resisting characteristics of pure basalt is very poor, it has increased by around 60% when Kevlar is added to it as seen in hybrid Kevlar/basalt composite laminate.
- Hybrid Kevlar/basalt composite laminate shows improved performance in comparison with pure Kevlar and pure basalt laminates. The addition of basalt with Kevlar results with nearly comparable properties of Kevlar. Moreover, the cost of the hybrid Kevlar/basalt laminate is reduced when compared with the pure Kevlar laminate.

Overall, the results from this study strongly suggest that the Kevlar/basalt hybrid composite offers a favorable combination of properties when compared to the individual composites. It exhibits excellent energy absorption, impact strength, and flame retardancy characteristics, making it a highly promising material for a wide range of applications across various industries.

References

[1] Heitor Luiz Ornaghi Jr, Alexandre Sonaglio Bolner, Rudinei Fiorio, Ademir Jose Zattera and Sandro Campos Amico, Mechanical and dynamic mechanical analysis of hybrid composites molded by resin transfer molding, Journal of Applied Polymer Science, 2010, Vol. 118 (2), pp. 887-896. https://doi.org/10.1002/app.32388

[2] Zachariah Oommen, Gabriel Groeninckx and Sabu Thomas, Dynamic mechanical and thermal properties of physically compatibilized natural rubber/poly (methyl methacrylate) blends by the addition of natural rubber-graft-poly(methyl methacrylate), Journal of Polymer Science Part B: Polymer Physics, 2000, Vol. 38 (4), pp. 525-536. https://doi.org/10.1002/(SICI)1099-0488(20000215)38:4%3C525::AID-POLB4%3E3.0.CO;2-T

[3] V. Ramesh and P. Anand, Evaluation of mechanical properties on Kevlar/Basalt fiber reinforced hybrid composites, Materials Today: Proceedings, 2021, Vol. 39 (4), pp. 1494-1496. https://doi.org/10.1016/j.matpr.2020.05.406

[4] Akash, K.G. Girisha, N.S. Venkatesha Gupta and K.V. Sreenivas Rao, A study on flammability and moisture absorption behavior of sisal/coir fiber reinforced hybrid composites, IOP Conference Series: Materials Science and Engineering, 2017, Vol. 191, 012003, 6 pages. DOI 10.1088/1757-899X/191/1/012003

[5] J. Jensin Joshua, Dalbir Singh Lohchab, A.R.S Nikhil Aanandhan, M. Ashwin, S. Keerthana, Rayala Sateesh, S. Seralathan, Evaluation of quasi static strength of Kevlar/Basalt-Epoxy and Kevlar/Glass-Epoxy Intra-woven composite laminate, Materials Today: Proceedings, 2023 (Article in Press). https://doi.org/10.1016/j.matpr.2023.04.249

[6] Ibrahim M. Alarifi, Majid Khorami, Tarek M.A.A. EL-Bagory and Ramazan Asmatulu, Dynamic Mechanical Analysis of Epoxy/Synthetic Fiber Composites. In: Mavinkere Rangappa, S., Parameswaranpillai, J., Siengchin, S., Thomas, S. (eds) Handbook of Epoxy/Fiber Composites . Springer, Singapore, 2022. https://doi.org/10.1007/978-981-15-8141-0_8-1

[7] Thingujam Jackson Singh and Sutanu Samanta, Characterization of Kevlar fiber and its composites: a review, Materials Today: Proceedings, 2015, Vol. 2 (4-5), pp. 1381-1387. https://doi.org/10.1016/j.matpr.2015.07.057

[8] Yunfu Ou, Deju Zhu, and Hang Li, Strain rate and temperature effects on the dynamic tensile behaviors of basalt fiber bundles and reinforced polymer composite, Journal of Materials in Civil Engineering, 2016, Vol. 28 (10), 04016101-1 to 04016101-10. https://doi.org/10.1061/(ASCE)MT.1943-5533.0001615

[9] M. Asim, M.T Paridah, M. Jawaid, M. Nasir and N. Saba, Physical and flammability properties of kenaf and pineapple leaf fibre hybrid composites. IOP Conference Series: Materials Science and Engineering, 2018, Vol. 368, 012018, 6 pages. DOI 10.1088/1757-899X/368/1/012018

[10] A. Vasudevan, S. Senthil Kumaran, K. Naresh, and R. Velmurugan, Experimental and

analytical investigation of thermo-mechanical responses of pure epoxy and carbon/Kevlar/S-glass/E-glass/epoxy interply hybrid laminated composites for aerospace applications. International Journal of Polymer Analysis and Characterization, 2018, Vol. 23 (7), pp. 591—605. https://doi.org/10.1080/1023666X.2018.1468599

[11] Srivatsava Madarvoni and Sreekanth P.S. Rama, Dynamic mechanical behaviour of graphene, hexagonal boron nitride reinforced carbon-kevlar, hybrid fabric-based epoxy nanocomposites, Polymers and Polymer Composites, 2022, Vol. 30, 12 pages. https://doi.org/10.1177/09673911221107289

[12] Hilmar Koerner, Robert J Strong, Matthew L Smith, David H Wang, Loon-Seng Tan, Kyung Min Lee, Timothy J White, Richard A Vaia, , Polymer design for high temperature shape memory: Low crosslink density polyimides, Polymer, 2013, Vol. 54 (1), pp. 391-402. https://doi.org/10.1016/j.polymer.2012.11.007

[13] Hemant Chouhan, Neelanchali Asija Bhalla, Aswani Kumar Bandaru, Shishay Amare Gebremeskel and Naresh Bhatnagar, , Quasi-static and high strain rate response of Kevlar reinforced thermoplastics, Polymer Testing, 2021, Vol. 93, 106964. https://doi.org/10.1016/j.polymertesting.2020.106964

[14] Aswani Kumar Bandaru, Hemant Chouhan, and Naresh Bhatnagar, High strain rate compression testing of intra-ply and inter-ply hybrid thermoplastic composites reinforced with Kevlar/basalt fibers, Polymer Testing, 2020, Vol. 84, 106407. https://doi.org/10.1016/j.polymertesting.2020.106407

[15] Mohd Firdaus Omar, Hazizan Md Akil and Zainal Arifin Ahmad,. Measurement and prediction of compressive properties of polymers at high strain rate loading, Materials & Design, 2011, Vol. 32 (8-9), pp. 4207-4215. https://doi.org/10.1016/j.matdes.2011.04.037

[16] Ramesh Velumayil and Anand Palanivel, Hybridization effect on mechanical properties of basalt/Kevlar/epoxy composite laminates, Polymers, 2022, Vol. 14 (7), 1382. https://doi.org/10.3390/polym14071382

[17] Farzin Azimpour-Shishevan, Hamit Akbulut and M.A. Mohtadi-Bonab,. Mechanical and thermal properties of carbon/basalt intra-ply hybrid composites. I. effect of intra-ply hybridization, Fibers and Polymers, 2020, Vol. 21, pp. 2579-2589. https://doi.org/10.1007/s12221-020-9843-6

[18] Hemant Chouhan, Neelanchali Asija Bhalla, and Naresh Bhatnagar, High strain rate performance of UHMWPE composites: Effect of moisture ingress and egress, Materials Today Communications, 2021, Vol. 26, 101709. https://doi.org/10.1016/j.mtcomm.2020.101709

[19] Aswani Kumar Bandaru, Vikrant V Chavan, Suhail Ahmad, R. Alagirusamy and Naresh Bhatnagar, Ballistic impact response of Kevlar reinforced thermoplastic composite armors, International Journal of Impact Engineering, 2016, Vol. 86, pp. 1-13. https://doi.org/10.1016/j.ijimpeng.2015.10.014

[20] Rajat Kapoor, Laxman Pangeni, Aswani Kumar Bandaru, Suhail Ahmad and Naresh Bhatnagar, High strain rate compression response of woven Kevlar reinforced polypropylene composites, Composites Part B: Engineering, 2016, Vol. 89, pp. 374-382. https://doi.org/10.1016/j.compositesb.2015.11.044

[21] K.A. Zakaria, R.H. Jimit, S.N.R. Ramli, A.A. Aziz, O. Bapokutty and M.B. Ali, Study on fatigue life and fracture behaviour of fiberglass reinforced composites, Journal of Mechanical Engineering Sciences, 2016, Vol. 10, Issue 3, pp. 2300-2310.

[22] Konstantinos Karvanis, Soňa Rusnáková, Ondřej Krejčí and Milan Žaludek, Preparation, thermal analysis, and mechanical properties of basalt fiber/epoxy composites, Polymers, Vol. 12, Issue 8, 1785, 2020. https://doi.org/10.3390/polym12081785

[23] Fabrizio Sarasini, Jacopo Tirillò, Luca Ferrante, Claudia Sergi, Pietro Russo, Giorgio Simeoli, Francesca Cimino, Maria Rosaria Ricciardi and Vincenza Antonucci, Quasi-Static and Low-Velocity Impact Behavior of Intraply Hybrid Flax/Basalt Composites, Fibers, 7(3), 26, 2019. https://doi.org/10.3390/fib7030026

Journal of Physics: Conference Series

PURPOSE-LED PUBLISHING™

PAPER • **OPEN ACCESS**

An Experimental Study on E-Glass Fiber Reinforced Epoxy with Nano-Silica for an Aircraft Structural Applications

To cite this article: B. Nagaraj Goud *et al* 2024 *J. Phys.: Conf. Ser.* **2837** 012004

View the article online for updates and enhancements.

You may also like

- Fabrication of highly sensitive and fast response flexible humidity sensor based on rGO/MoS_2 hybrid composite
Ningfeng Ke, Gengwu Ge, Hongliang Ma et al.
- Membership Study of Open Cluster NGC 6134 using HDBSCAN Clustering Algorithm
M Yusuf, D G Ramadhan, A T P Jatmiko et al.
- Evaluation of LM 43.8P blade performance at different hub height wind speeds using blade element momentum theory
G L Augusto, W H Chen and L A Gan Lim

This content was downloaded from IP address 106.0.37.90 on 21/10/2024 at 11:05

Journal of Physics: Conference Series **2837** (2024) 012004 doi:10.1088/1742-6596/2837/1/012004

An Experimental Study on E-Glass Fiber Reinforced Epoxy with Nano-Silica for an Aircraft Structural Applications

B. Nagaraj Goud [1], Vangari Vyshnavi [2], A.Nandhishwari [3], S.Govinda Rahul[4]

[1]nagaraj2107@gmail.com
[2] vangarivyshnavi2002@gmail.com
[3] nandhishwariajmeera @gmail.com
[4] govindsurnedi51216@gmail.com

[1,2,3,4,] Department of Aeronautical Engineering, MLR Institute of Technology, Hyderabad 500 043, India

Abstract. E-Glass composites have been broadly beneficial in various aerospace structural applications including aircraft, space vehicles and other automobiles applications etc. The advantage of using polymer-based composites are significance in the aircraft structural components such as fuselages, wings and tail sections etc, due to high resistance to corrosion, high specific strength, lightweight in structure, better tensile strength, ability to withstand relatively high temperatures, stiffness, and relatively low cost. A technique has been developed to enhance the strength of the 2D plain woven E-Glass fabric laminated composite under compression molding techniques and material cutting process will be performed by using CNC Milling machine. It will improve the structural stability with an accurate shape and size of the composite during the fabrication and provides the better binding properties. An attempt is made in this project work to compare the testing of composite with and without the inclusion of silica nanoparticle of composite laminated and material characterization will be performed including the response of the tensile strength, flexural strength tests will be conducted. Furthermore, experimental study results will be compared with the computational studies.

Key words: Glass fiber, silica nanoparticles, compression molding, tensile, flexural strength.

1. Introduction

A composite material is a mixture of two or more materials that results in better mechanical properties then the parent material used individually [1]. The synthetic fibers are used as reinforcement elements which increases the strength of the composite. As the flexural strength furnishings, randomes etc. because of its superior strength, stiffness, superior corrosion resistance, high specific strength, capacity to tolerate relatively high temperatures, lightweight design, and affordable price.[2].

1.1 E-glass Properties

The typical glass composition used for the majority of glass fibre oxides of silicon, , calcium, magnesium, aluminu m and boron is also referred to as electrical glass. It has the following mechanical properties can shown in the table

Content from this work may be used under the terms of the Creative Commons Attribution 4.0 licence. Any further distribution of this work must maintain attribution to the author(s) and the title of the work, journal citation and DOI.
Published under licence by IOP Publishing Ltd

Table 1. Mechanical properties of E-glass fiber

Properties	**E-glass**
Density (g/cm^3)	2.54
Specific gravity	2.60
Modulus (GPa)	70-73
Strength (MPa)	2000-3500
Tensile elongation in percentage	4.8
Co-efficient of thermal expansion (μm/m/°C)	5.0

It's common knowledge that the majority of sophisticated fibre composites have more tension (in the direction of the fibres) than compression. The characteristic is caused by the fact that microbuckling of fibre incorporated in the matrix controls the compressive strength of bidirectional composites. (Liu et al.,2017). When compared to other polymer matrix composites, optical fiber reinforced composites are the least expensive and most widely used due to their exceptionally high strength. SiO2 may also be added to glass fibers, either as continuous fibers or as staple fibers [3].

Figure1. 2D plain woven E-glass fiber

It is now commonly known that a polymer's mechanical characteristics, particularly its stiffness, may be significantly enhanced by the addition of a modest number of nanoparticles. A few attempts have been made to increase the composite's compressive strength by utilising the benefits of a matrix impregnated with nanoparticles [1-3]. It is now commonly known that a polymer's mechanical characteristics, particularly its stiffness, may be significantly enhanced by the addition of a modest number of nanoparticles. A few attempts have been made to increase the composite's compressive strength by using the matrix injected with nanoparticles[2-4].

In a different investigation, VARIM was used to create carbon epoxy composites with stiff nanoparticle-modified matrices and CTBN liquid rubber utilising unidirectional fiber fabrics. Using a hoover to aid with resin infusion, different concentrations of nanofillers (Such as silica, halloysite, and CTBN liquid rubber particles) were introduced to epoxy matrices reinforced by carbon fibre textiles. Using a hot-pressing tool, the impregnated laminate was allowed to cure. In order to clarify the mechanical characteristics of the changed matrices and the resultant composites and to confirm the impact of the different types of nanoparticles, analyses of compressive and flexural properties were conducted. The purpose of this investigation was to see if stiff nanofillers might be used to enhance the compressive and flexural properties of composite laminates made from altered matrices.

Cho et al. [4] noted thatBy adding 3 weight percent and 5 weight percent graphite nanoparticles to epoxy matrices, epoxy composites with a 55% fibre volume fraction saw improvements in longitudinal compressive strength of 10% and 16%, respectively.It has been demonstrated in this work that adding a modest quantity of stiff nanoparticles to a polymer matrix greatly improves its mechanical characteristics. There have been several attempts to improve the mechanical performance of fibre composites by utilising the benefit of the nanoparticle reinforced matrix.Numerous research employed nanoparticles to examine fracture toughness and tensile characteristics. The impact of nanoparticles on the compressive and flexural characteristics of fiber/epoxy

composites—specifically, those made using RTM and VARIM—has only been the subject of a small number of investigations. The primary goal of this work that makes nanosilica a novel possible candidate material for secondary reinforcement [5-7].

The researchers conducted a detailed analysis of the composite laminates' flexural characteristics. It's vital to remember that flexural strength and stiffness are the outcome of the material's basic compressive, shear, and tensile qualities working together rather than being inherent characteristics of the material. Put another way, when flexural pressure is applied to a multidirectional composite plate, all three of the material's primary stress states are introduced. The main compressive failures that occur during the three-point bending tests are microbuckling, splitting, Wrinkling, and kinking. As a result, the impact of stacking order on composite material's flexural properties rose to prominence. In this paper, it is improved the strength of unidirectional composite by adding the nanoparticles. They have been used standard DGEBA epoxy with silica nanoparticles to the composite**.** The modified epoxy's elastic modulus improved significantly in this compression test, increasing by 40%. Unidirectional E-glass fibre reinforced epoxy nanocomposites were made using a modified vacuum aided resin transfer moulding technique. Utilising a micro buckling model, the compression test findings were confirmed. [8-9].
They have shown that the carbon fiber/epoxy composites produced using a VARIM technique have both compressive and flexural characteristics. the steady rise brought on by the bulk materials' flexural and compressive characteristics. When compared to epoxies, the impact of various particles on the compressive property of epoxy/fiber composites was greater.Here, we learn that graphite nanoplatelets have been used to modify epoxy matrix carbon fiber/epoxy composites in order to increase their mechanical characteristics. Sonication was used to combine and distribute graphite nanoparticles throughout the epoxy matrix, and then a vacuum-assisted wet layup procedure was employed. The in-plane shear characteristics and compressive strength of the nanoparticle-reinforced composites were improved. a straightforward mathematical methodology for longitudinal compressive strength prediction.[9-10].

Transmission and scanning electron microscopy (SEM) were used to examine the morphology of nano clay suspended in acetone and distributed in resin. SEM and TEM images reveal resin intercalation in areas of randomly orientated exfoliated clay and gallery spaces of nano clay. Glass fibre reinforced composites' longitudinal compressive strengths significantly increased with the addition of nanoclay. Based on the matrix parameters, the compressive strength of fiber-reinforced composites was predicted using the elastic-plastic model.
The goal of this project is to characterize the damage to composite laminate reinforced with glass fiber and silica nanoparticles. They used weight ratios of 0%, 0.5%, 1%, and 3% for the nano silica particles and created a laminate by hand lay-up manual method consisting of 12 layers of 40% fiber volume fraction 2D woven glass fibers. The material characterization will involve tensile,compressive, quasi-static indentation test, 3-point bending, and ballistic impact test for silica nanoparticles in composite laminates. In comparison to other composites and nano silica particles, 0.5% nano silica reported greater ballistic limit, energy absorption, and quasi-static indentation test results.

The tensile fatigue behavior of an epoxy reinforced with glass fiber and silica nanoparticles is enhanced in this effort. Using a flexible tooling approach and hydride-cured thermosetting epoxy polymer, they created a laminate and added 10% weight of well-dispersed silica nanoparticles. Because of the silica nanoparticles, stiffness rose three to four times in the tensile fatigue characteristics.Investigating the effects of E-glass fiber reinforced epoxy with secondary nanosilica composite laminate was the aim of this project. In order to create the laminates, they employed 0.5, 0.75, 1, and 3 weight percent of nanosilica. Tensile, three-point bending, quasi-static indentation testing, and dynamic mechanical analysis were also carried out. As a result, compared to other composite and nano silica particle materials, the 0.75 weight percent silica nanoparticle reinforced composite laminate exhibits higher tensile and flexural strengths, a quasi-static indentation test, a lower glass transition temperature, and a higher storage module.

The mechanical characteristics of Kevlar composite laminate are the focus of this project. They used a 2D plain weave Kevlar fiber reinforced with polyester resin and a compression molding procedure at room temperature to create the composite laminate. A waterjet machine was used to cut the material, and tensile and flexural tests were conducted on a UTM. Improved structural stability of the composite laminate and increased tensile and flexural strength are the outcomes of using Kevlar composite [9].

2. Material and Methods

2.1 Material selection of composites

The glass fiber reinforced with epoxy composite specimen was created using a 2D woven glass fiber with an areal density of 200g/m^2. Spherical silica nanoparticles were added using a diameter of 100nm, a density of 2.2g/cc, and a surface area of 180-270 m^2/g to fabricate composite laminates.

2.2 ASTM D3039 Standard

For material characterization we use these ASTM standards for test method for Tensile properties of Polymer Matrix composite Materials. For the development of Epoxy composites, understanding of their respective tensile strength and modulus plays a vital role for structural applications[10-13]. The laminate was fabricated and designed with the cross section as shown in table 3. By using the 3 point or 4 point bending method for determining the flexural characteristics of composite with the required rectangular cross section.

2.3 ASTM D7264 Standard

The sample with the cross section as shown in table 3 was also performed 3 point bending for finding the flexural characteristics of a E glass fiber reinforced composite. The required resin will be placed in the compression molding at a required temperature.

Table 2. Dimensions of specimens used in tensile and flexural tests.

Test type	Length (mm)	Width (mm)	Thickness (mm)
Tensile	250	25	3
Flexural	120	13	3

2.4 Nano composites Preparation

Five layers of 2D plain woven glass fiber placed were layered inside a mold to create composite laminates with a thickness of 3mm and each lamina as 0.6mm thickness. The matrix was strengthened using nano silica at 0.5 weight percent with a hand tool, homogeneous dispersion of nanosilica in matrix was achieved. After that master batch put in compression moulding as shown in fig 1. This compression moulding is used for removing all of the air bubbles created during mixing of epoxy and nano silica particles. the mechanical properties of the composite laminate were impacted by the removal of these defects. The mold was then compressed to remove any remaining resin, and it was left to cure under compression for a full day. The general process used to manufacture glass fiber reinforced plastic (GFRP) laminates reinforced with nanosilica is shown in Figure 1. It should be mentioned that reinforcing nano fillers affects the matrix's ability to cure[14-15].

2.5 Hand layup Technique.

One popular and adaptable technique for creating composite materials, such as E-Glass composites containing silica nanoparticles, is hand lay-up. This approach is appropriate for small to medium-sized production runs and prototype manufacturing since it is quite easy to use and reasonably priced.

The E-Glass fibres are joined with a thermosetting resin, such as vinyl ester, polyester, or epoxy. The final composite's required qualities are taken into consideration while choosing the resin. The purpose of incorporating these nanoparticles into the resin matrix is to improve certain characteristics, such flame retardancy, mechanical strength, and heat resistance. Next, a mould is made using the ultimate composite product's dimensions and desired shape in mind. To make it easier to remove the cured composite from the mould, a release agent may be applied to it. The resin matrix is infused into the E-Glass fibres.

This can be done manually by laying the fibers into the mold and applying the resin using brushes or rollers. Silica nanoparticles are often dispersed in the resin beforehand or added layer by layer during the hand lay-up process. The hand-layup process involves building up multiple layers of E-Glass and resin until the desired thickness and structure are achieved. Once the desired thickness is achieved the composite is allowed to cure. after curing the composite is demolded and excess material is trimmed[15-16].

2.6 Compression moulding

This method is suitable for fabricating product of complex geometry in short period of time. It also eliminates secondary finishing operation such as forming, drilling and overall process can be automated. The mold compound is first placed in an open heated mold cavity [17-18]. After that, the mould is sealed and pressure is used to fill the hollow. Most often, a hydraulic wrap is used to generate enough force during the moulding process. Until the material cures, the pressure and heat are kept constant. The moulding temperature typically ranges from 130°C to 160°C, while the moulding pressure can fluctuate between 1.4 and 34.5 mpa.. To decrease the temperature which may chemical degradation and cause burning in the resin. To avoid this filler may be added

Figure2. Compression moulding

2.7 Fabrication process

Cut the E-Glass fibers to the required length. Arrange the fibers in the desired orientation . Apply a release agent to the mold surface to facilitate easy demolding. Measure the appropriate amounts of epoxy resin and hardner according to the manufacturer's, recommendations. Mix the resin and hardner thoroughly to ensure uniform curing. Brush the E-Glass fibers with the mixed epoxy resin to impregnate them thoroughly. Layer the impregnated E-Glass fibers in the mold according to the desired thickness and orientation. Repeat the process to create multiple layers if needed. Place the mold in a controlled environment to allow the epoxy to cure.After curing, carefully demold the composite part [19-20].

2.7.1 Cutting process of composite laminate

Material cutting process will be performed by using CNC Milling machine. A CNC (Computer Numerical drive) machine is one type of automated manufacturing equipment that drives machine tools using computer programs. These machines can do a wide range of tasks, including additive manufacturing, drilling, cutting, and milling. Here are some essential characteristics of CNC equipment: System of Control: CNC machines are operated by computerised systems that are capable of understanding numerical data. This data is usually generated by CAD and CAM systems.

2.7.2 Preparing the Materials

E-Glass Fiber: Made of alumino -borosilicate glass, e-glass fibers are glass fibers. They are renowned for having excellent electrical insulation qualities, a low weight, and strong strength. The purpose of adding nano-fillers to a composite material is to improve its mechanical, thermal, or electrical properties. Examples of these materials include carbon nanotubes, graphene, and other reinforcing agents.Making a Composite Matrix:- It is common practice to blend the E-glass fibers with a polymer matrix, like epoxy resin. Within this matrix, the nano-filler particles are distributed. It appears that you are explaining how to use epoxy resin and E-glass fabric to create a composite material.

3. Experimental Testing

For this specific experimental test, we used a UTM machine to perform two tests on an E-glass fibre reinforced epoxy composite to measure its tensile and flexural strength.Tensile test on composite laminate.

Tensile testing in accordance with ASTM D3039 is performed to determine the force necessary to fracture a polymer composite specimen and to extend the specimen until it elongates at that breaking point. Tensile modulus is therefore determined using the stress and strain diagram that is created by the tensile testing. Typically, the data is utilised for material specification, force application resistance component design, and quality assurance testing of the specific material composite. The specimens are first inserted into the UTM's grips at a certain grip separation, then they are pulled until they break. For ASTM D3039, The test speed may be ascertained using the material specification or the time to failure (1 to 10 minutes). A typical test speed for standard test specimens is 2 mm/min (0.05 in/min).

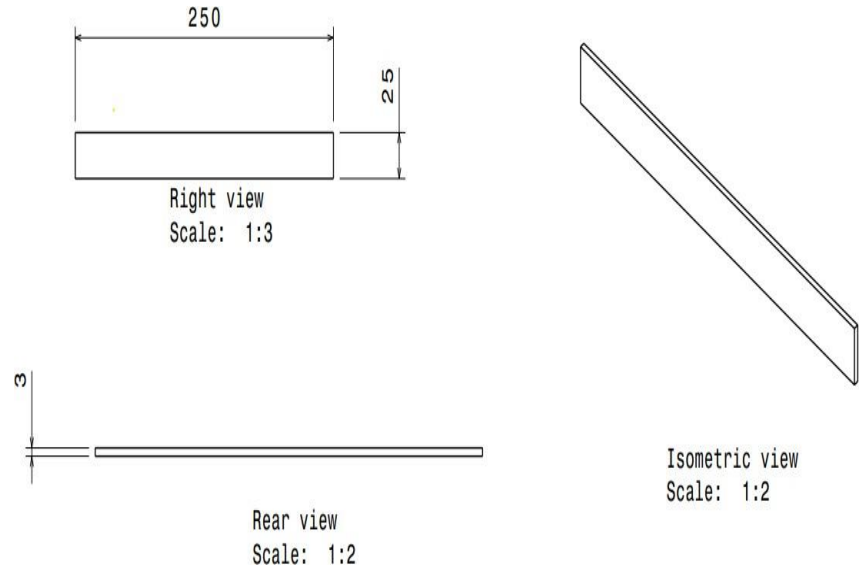

Figure3. Laminate dimension for tensile test

3.1. Flexural test on composite laminate

Important mechanical properties are discovered using flexural testing. The specimen's laminate is loaded with a compressive force on top and a tensile force at the bottom. The intermediate lamination planes get no force at all. The three point bending examinations: Maximum of [EN 2746], 10% to 50% Maximum of [EN 2562], 10% to 25% or strain limits [ISO and ASTM] are the ranges of values for the flexural modulus.Four-Point Exam for Flexural Strength: The advantage of the 4-point flexural test on composites is the shear-force-free area between 0.1% and 0.3% strain [ASTM D7264] or 0.05% and 0.25% strain [ISO 14125].

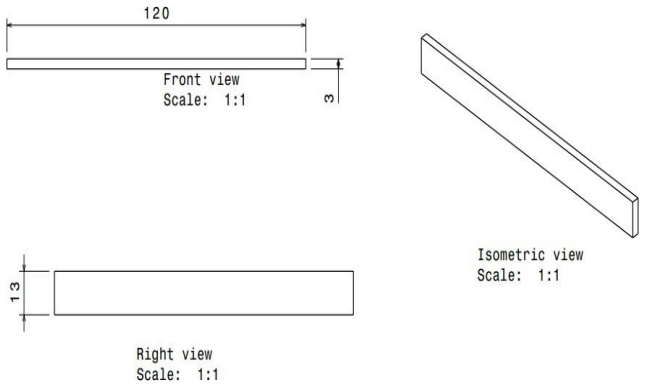

Figure 4. Laminate dimension for flexural test

4. Results & Discussion

To ascertain the force necessary for the composite laminate to fracture and the ensuing deformation at the fracture point, a tensile test was performed. This parameter is essential for determining the test sample's yield strength and young's modulus. The UTM setup is seen in the photo, and specimens measuring 250 mm by 25 mm by 3 mm were used in the studies.To ensure experimental homogeneity, the statistical correctness of the tensile test on polymer beams was determined using ASTM D3039M. Four samples were tested using the specimen size and test type specified by the ASTM standard.

.
.

Figure 5. Tensile Test Results

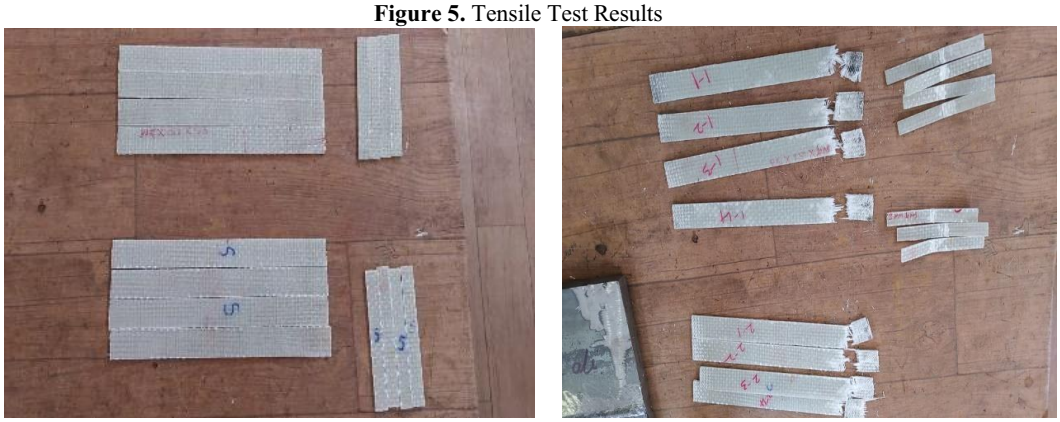

Figure 6. Tensile Test Results

The flexural examination was conducted to as certain the force required for the fracture of the composite specimen and the utmost bending at the point of fracture. This data is employes for computing the flexural strength and the highest deflection of the composite.

Table 3. Result of tensile test without nanoparticles

S.No.	Sample (1) Test specimen	Ultimate Load(KN)	Tensile Strength(Mpa)
1.	T1	25.794	352.302
2.	T2	21.504	295.710
3.	T3	24.696	337.529
4.	T4	28.102	381.808

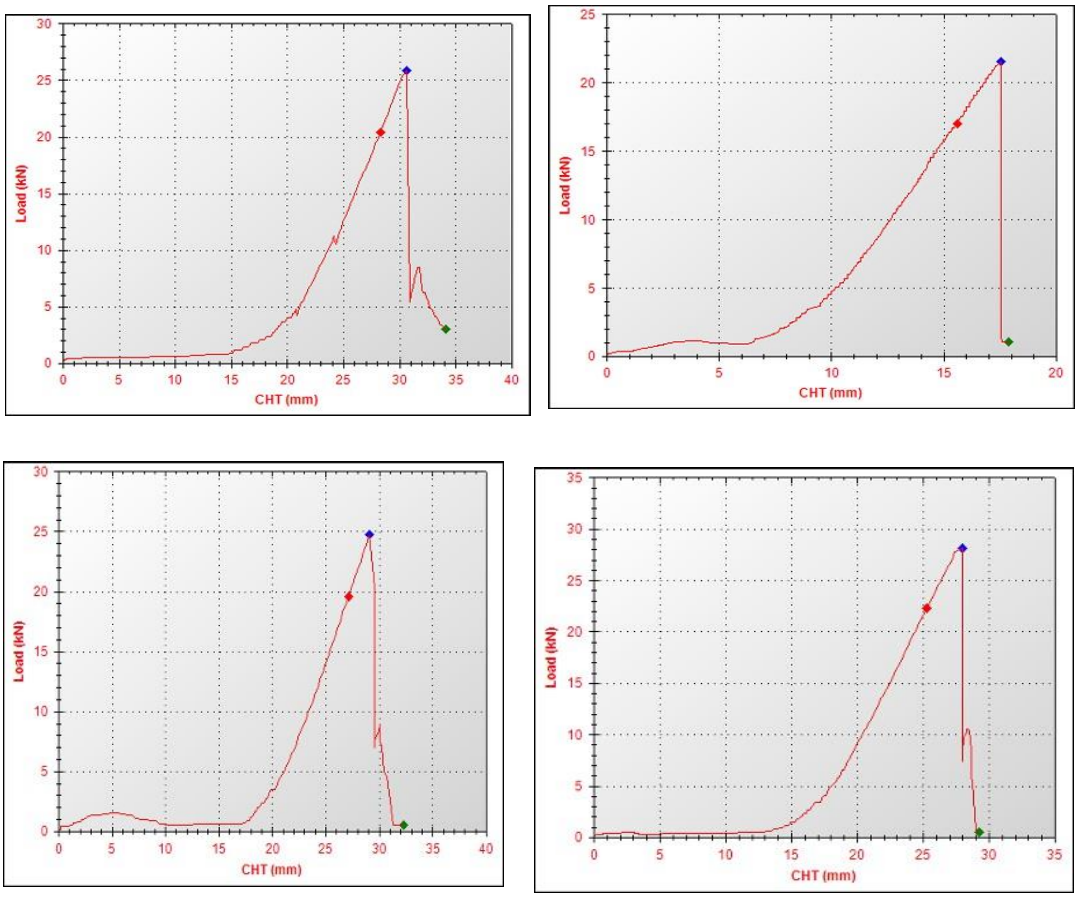

Figure 6 . Result graph of tensile test without nanoparticles

Table 4. Result table of flexural test without nano particles

S.NO.	SAMPLE ID	WIDTH(b) in mm	THICKNESS (d) in mm	LOAD(F) IN Newtons(N)	LENGTH OF SUPPORT SPAN (L) in mm	FLEXURAL STRENGTH(σ) in N/mm^2
1.	T1	13.08	3.14	330	30	115.148
2.	T2	12.96	3.0	340	30	131.172
3.	T3	13.05	3.05	388	30	143.825
4.	T4	12.98	3.01	310	30	118.622

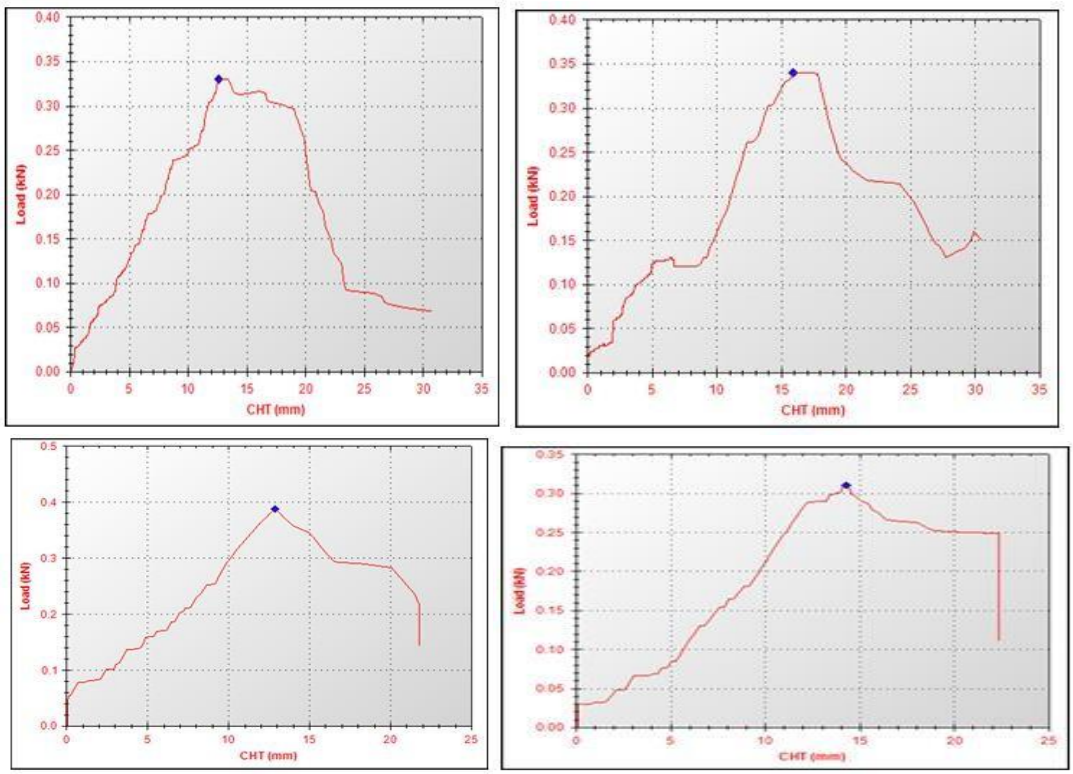

Figure 7 . Result graph of flexural test with nanoparticles

Table 5. Result table of flexural test with nano particles

S.NO.	SAMPLE ID	WIDTH(b) in mm	THICKNESS (d) in mm	LOAD(F) IN Newtons(N)	LENGTH OF SUPPORT SPAN (L) in mm	FLEXURAL STRENGTH(σ) in N/mm^2
1.	T1	13.15	2.97	370	30	143.541
2.	T2	13.14	3.01	334	30	126.250
3.	T3	13.24	2.97	428	30	164.913
4.	T4	13.29	2.99	392	30	148.467

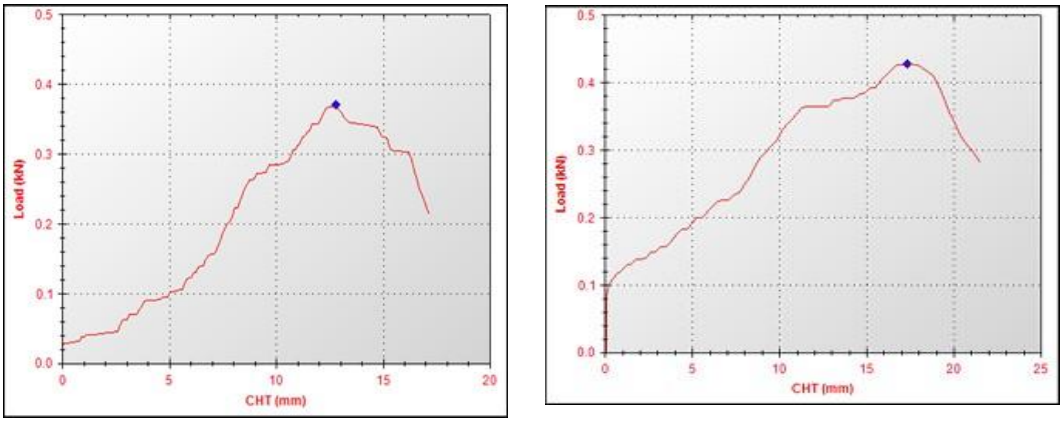

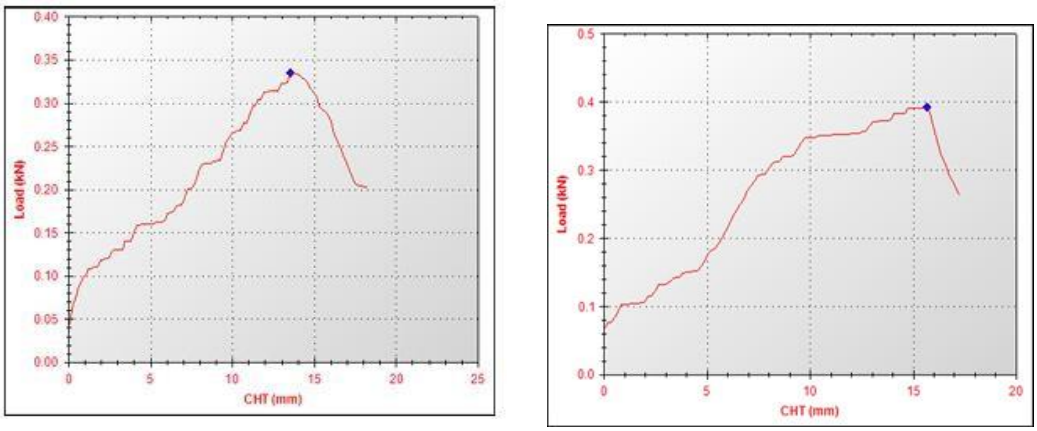

Figure 8. Result graph of flexural test without nanoparticles

5. Conclusion

Through tensile and flexural testing on the composite material, we were able to determine the tensile test findings about deformation without adding nano filler is at ultimate load of 28.104KN the tensile strength of specimen T4 is 381.808 MPa is maximum when compared to the tensile strength of specimen T1,T2,T3 respectively. Now let us examine the tensile strength of composite material with nano filler at ultimate load of 21.658KN the tensile strength of specimen is 386.171 MPa is maximum when compared to the tensile strength of specimen T1,T2,T3 respectively. The deformation we have obtained the results for flexural test without nano filler at ultimate load of 388KN the flexural strength is 143.825MPa is maximum for sample T3 when compared to the flexural strength of samples T1,T2,T4.Now let us examine the flexural stress of the composite with nano particles the flexural strength at load of 428KN is 164.913MPa for T3, when compared to the sample T1,T2,T3

6. References

[1] Uddin, M. F., & Sun, C. T. (2008). Strength of unidirectional glass/epoxy composite with silica nanoparticle-enhanced matrix. *Composites Science and Technology*, *68*(7–8), 1637–1643.

[2] Subramaniyan, A. K., & Sun, C. T. (2006). Enhancing compressive strength of unidirectional polymeric composites using nanoclay. *Composites Part A: Applied Science and Manufacturing*, *37*(12), 2257–2268.

[3] Liu, F., Deng, S., & Zhang, J. (2017). Mechanical Properties of Epoxy and Its Carbon Fiber Composites Modified by Nanoparticles. *Journal of Nanomaterials*, *2017*, 14–16.

[4] Cho, J., Chen, J. Y., & Daniel, I. M. (2007). Mechanical enhancement of carbon fiber/epoxy composites by graphite nanoplatelet reinforcement. *Scripta Materialia*, *56*(8), 685–688.

[5] Manjunatha, C. M., Taylor, A. C., Kinloch, A. J., & Sprenger, S. (2010). The tensile fatigue behaviour of a silica nanoparticle-modified glass fibre reinforced epoxy composite. *Composites Science and Technology*, *70*(1), 193–199.

[6] Afrouzian, A., Movahhedi Aleni, H., Liaghat, G., & Ahmadi, H. (2017). Effect of nano- particles on the tensile, flexural and perforation properties of the glass/epoxy composites. *Journal of Reinforced Plastics and Composites*, *36*(12), 900–916.

[7] Sapiai, N., Jumahat, A., Jawaid, M., Midani, M., & Khan, A. (2020). Tensile and flexural properties of silica nanoparticles modified unidirectional kenaf and hybrid glass/kenaf epoxy composites. *Polymers*, *12*(11), 1–11.

[8] Lazar, P. J. L., Sengottuvelu, R., & Natarajan, E. (2018). Assessments of secondary reinforcement of epoxy matrix-glass fibre composite laminates through nanosilica (SiO2). *Materials*, *11*(11).

[9] Nagaraj Goud, B., Sura, S., Aravind, P., Jawahar Lal, B., Sanskruti, K., & Pavan, C. (2022). An

experimental study on mechanical properties of Kevlar composite for aircraft structural applications. *Materials Today: Proceedings*, *64*, 909–916.

[10] Morampudi, P., Namala, K. K., Gajjela, Y. K., Barath, M., & Prudhvi, G. (2020). Review on glass fiber reinforced polymer composites. *Materials Today: Proceedings*, *43*, 314– 319.

[11] M. Ganesh, K. Shiva Shankar "Modelling And Analysis Of Scaffolding Structure Used In Aerospace Vehicle*"(IJSR)*Volume 4 Issue 5, May 2015,Issn (Online): 2319-7064.

[12] K. Veeranjaneyulu, M.S.N Gupta, Dhana Jayan Vamsi, Damage Analysis of Low Speed Impact On Composite Materials, International Journal of Civil Engineering & Technology (IJCIET).

[13] Alka Sawale, Nayani Uday Ranjan Goud, M.Srinikitha "Experimental Analysis of Stress Concentration on V-Notched Plate" International Journal of Innovative Technology and Exploring Engineering *(IJITEE)* ISSN: 2278-3075, Volume-9 Issue-2, December 2019, page No 3709-3712

[14] G. Dhanajayan, Veeranjaneyulu Kalavagunta, V. Vamshi, M. Satyanarana Gupta, Environmental Study on GFRP Composite Laminates, International Journal of Civil Engineering & Technology (IJCIET).

[15] Vemanaboina, H., Akella, S., Buddu, R.K., Yelamasetti, B., Matam, M.B., Salem, K.H., Saxena, K.K., Prakash, C., Buddhi, D "Prediction of thermal and residual stress distributions in SS304 materials for nuclear application using finite element analysis" (2023) International Journal on Interactive Design and Manufacturing,

[16] Shiva, A., Cheepu, M., Kantumuchu, V.C., Ravi Kumar, K., Venkateswarlu, D., Srinivas, B., Jerome, S. "Microstructure Characterization of Al-TiC Surface Composite Fabricated by Friction Stir Processing" (2018) IOP Conference Series: Materials Science and Engineering, 330 (1), art. no. 012060

[17] Ashok Reddy, K. "Non-Destructive Testing, Evaluation of Stainless Steel Materials" (2017) Materials Today: Proceedings, 4 (8), pp. 7302-7312

[18] Vemanaboina, H., Babu, M.M., Prerana, I.C., Gundabattini, E., Yelamasetti, B., Saxena, K.K., Salem, K.H., Khan, M.I., Eldin, S.M., Agrawal, M.K. "Evaluation of residual stresses in CO2 laser beam welding of SS316L weldments using FEA" (2023) Materials Research Express, 10 (1), art. no. 016509,

[19] Robert Xavier, A., Ravichandran, A.T., Ravichandran, K., Mantha, S., Ravinder, D. Sm doping effect on structural, morphological, luminescence and antibacterial activity of CdO nanoparticles (2016) Journal of Materials Science: Materials in Electronics, 27 (11), pp. 11182-11187

[20] Praveen, L., Geeta Krishna, P., Venugopal, L., Prasad, N.E.C Effects of pulse on and off time and electrode types on the material removal rate and tool wear rate of the Ti-6Al-4V Alloy using EDM machining with reverse polarity (2018) IOP Conference Series: Materials Science and Engineering, 330 (1), art. no. 012083.

Journal of Physics: Conference Series

PURPOSE-LED PUBLISHING™

PAPER • **OPEN ACCESS**

A Study on the Bending Strength of Ultra Double-Sided Polypropylene Arc Welded Using Stainless Steel Sheets

To cite this article: Tankeswar Prasad *et al* 2024 *J. Phys.: Conf. Ser.* **2837** 012101

View the article online for updates and enhancements.

You may also like

- Effect of secondary phases on 475 °C embrittlement of 1.4462 and 1.4501 duplex stainless steels at short-term heat treatment conditions
Alptekin Kisasoz, Gokhan Ozer and Ahmet Karaaslan
- Analysis of structure property relationship of super duplex stainless steel AISI 2507 weldments for severe corrosive environments
V Paranthaman, K Shanmuga Sundaram and A Vinoth Jebaraj
- Effect of temperature on microstructure evolution and localized corrosion resistance of high tungsten hyper duplex stainless steel
Nithin Raj P, Sekar K and M A Joseph

This content was downloaded from IP address 106.0.37.90 on 21/10/2024 at 11:24

Journal of Physics: Conference Series **2837** (2024) 012101 doi:10.1088/1742-6596/2837/1/012101

A Study on the Bending Strength of Ultra Double-Sided Polypropylene Arc Welded Using Stainless Steel Sheets

Tankeswar Prasad[1], K Srinivasa Reddy[1], Aruna Kunda[2], JM Durga[3], A Sai Kumar[4]

[1]Department of Mechanical Engineering, Godavari Institute of Engineering &Technology (Autonomous), Rajahmundry-533296, AP, India
[2]Department of Automobile Engineering, Godavari Institute of Engineering & Technology (Autonomous), Rajahmundry-533296, AP, India
[3]Department of Mining Engineering, Godavari Institute of Engineering & Technology (Autonomous), Rajahmundry-533296, AP, India
[4]Department of aeronautical engineering, MLR Institute of Technology, Hyderabad, India

Correspondence author email ID: tjayanandak@gmail.com

Abstract. In this research, a micro-plasma arc welding technique is used to butt weld super duplex stainless steel sheets with a thickness of 0.33mm. While roughness and strength of tensile are referred to as output qualities, welding input factors included pulse width, pulse rate, peak current, and base current. Applications requiring both strong fatigue strength and resistance to corrosion are increasingly using super-duplex stainless steels. Welded joint tensile strength (868.28MPa) is 6.28 percent less than the fundamental metal tensile strength (923.16MPa). The microstructure of welded super duplex stainless steels has a strong correlation with their tensile strength (SDSS), and ANSYS has been utilized to do FEA analysis for different profiles that have also been investigated. This work includes a detailed investigation of the effects of various welding circumstances on super duplex stainless steel.
Keywords: SDSS, Ansys, UTS, Stainless steel, UNS32750

1. Introduction

In both onshore and offshore applications wherever strong durability, good corrosion resistance, and exceptional resistance to fatigue are needed, super duplex stainless steel is

Content from this work may be used under the terms of the Creative Commons Attribution 4.0 licence. Any further distribution of this work must maintain attribution to the author(s) and the title of the work, journal citation and DOI.
Published under licence by IOP Publishing Ltd

widely employed. Austenitic and ferritic stages are combined within these materials' distinctive microstructures in roughly equal amounts, giving them a remarkable combination of characteristics. The mechanical properties of these substances, such as durability, tenacity, and resistance to fatigue, are largely dependent on their microstructure, that welder may significantly alter. Therefore, in order to produce superior welds with ideal qualities, it is essential to research welding behavior, welding methods, and welding variables. The fatigue strength of duplex and super-duplex stainless steel was measured using the 4R technique, and it was discovered that the microstructure of these substances had a major effect on this property. It was also noted that the super-duplex stainless steel's fatigue strength was higher than the duplex stainless steel's because of its finer microstructure [1]. The mechanical and corrosion properties of SAF 2507 super duplex stainless steel joints were examined, and it was shown that the microstructure significantly affected these properties [2]. Investigations into the effects of thermal input on the microstructure and corrosive behavior of duplex stainless steel shielded metal arc welding revealed that the microstructure became coarser and the susceptibility to corrosion decreased with increasing heat input [3]. The conductivity of lasers and the plasma arc welding processes with duplex and super-duplex stainless steels revealed this, with regard to of the mechanical characteristics of the connections, the plasma arc welding procedure produced superior results than the laser process for welding [4]. examined the effects of the thermal inputs, the quantity of progresses, and the degree of heat throughout the passes on the microstructure, mechanical properties, and corrosion resistance of the welds during multi-pass arc welding operations [5]. Tensile overloading was shown to cause the beginning of additional breaks and accelerate the propagation of existing cracks in 2205 duplex stainless steel fatigue crack behavior [6]. Low intensity electromagnetic interaction was used to study the fatigue resistance of AL6XN super-austenitic stainless steel while gas metal arc melting. It was found that this electromagnetic connection significantly boosted the welded connections' resistance to fatigue [7]. When the variables of pulsing current flux arc welding were optimized for the ferrite stage in DSS welds, it was discovered that the ferrite content of the welds was highly influenced by both the rate of welding and the pulse frequency [8]. Because of their special mechanical qualities and ability to withstand corrosion, DSS can be used in hostile situations [9]. The mechanical characteristics, microstructure, and texture of AISI 2507 SDSS steel were examined, along with the effects of welding variables such as gas circulation percentage, laser energy, and velocity of welding on the process [10]. The microstructure and corrosion resistance of DSS welding are strongly impacted by heat input [11]. a few the key factors influencing the fatigue behavior of DSS is the fatigue procedure, that has been modeled beneath both very high-cycle fatigue (VHCF) and high-cycle fatigue (HCF) loading conditions [12]. Along with contributing to the thermal input, the welding technique themselves can have a substantial impact on the microstructure and mechanical qualities of DSS welders. Lower heat input resulted in a finer microstructure and improved corrosion resistance [13]. Present gas tungsten arc welding generated welding with greater mechanical strength and less deformation than pulse current gas tungsten arc welding [15]. When concentrating on various aspects of the material's properties and fatigue efficiency, the friction stir-treated SDSS (SAF-2507) fatigue crack formation behavior significantly boosts the material's resistance to fatigue formation of cracks [16]. According to torsional loads, the cyclic deformation behavior and failure process of S32205 were examined. It was discovered which the DSS failure mechanism during cyclic loading is complex and includes a number of distinct deformation types [17]. The microstructure and the existence of defects were discovered to have an impact on the joints durability when the metallurgical effect and fatigue efficiency of electron beam welding DSS connections were assessed [18]. Examining how laser welding affected the substance's tensile strength, fatigue behavior, and microstructure showed that the procedure significantly affected DSS2205's mechanical properties and microstructure [19]. It was found that the procedures for fatigue

crack development and growth are different from the ones observed under traditional fatigue loading when the behavior of short fatigue cracks over extremely high cycle fatigue of DSS was investigated [20].

2. Methodology

For this project, UNS S32750 super duplex stainless steel sheets with a thickness of 0.33 mm were joined using a pulsed current micro plasma arc welding technique. To examine their effects on the fatigue strength of the welded joints, welding parameters including pulse rate, welding flow, and rate of welding were changed.

Materials and Methods

An autogenous square butt junction is used to attach Super Duplex stainless steel sheets with measurements of 200x20x0.33 mm, as specified by UNS S32750. UNS S32750 super duplex stainless steel's mechanical properties and chemical makeup are shown in Tables 1 and 2.

Table1. UNS S32750 chemical composition (Weight %)

C	Cr	Mn	Cu	Fe	Ni	Mo
0.03	25.04	1.0	0.45	64.02	6.68	3.26

Table2. UNS S32750 mechanical characteristics

Elongation (%)	Ultimate Tensile strength(MPa)	Vickers Hardness (VHN)
21.8	923.16	259.8

When welding, ultrapure argon (99.99%) is utilized as an insulating and follower gas to prevent nitrogen and oxygen from escaping into the atmosphere. Table 3 lists the welding variables that were used during the welding process.

Table 3. Conditions for Welding

Power Source	Secheron Micro Plasma Arc Machine
Polarity	DCEN
Mode of operation	Pulse mode
Electrode diameter	1 mm
Electrode	2% throated tungsten electrode
Plasma gas flow rate	6 Lpm
Plasma gas	Argon & Hydrogen
Shielding gas	Argon
Shielding gas flow rate	0.6 Lpm
Purging gas flow rate	0.6 LpmArgon
Purging gas	
Nozzle to plane diameter	1 mm
Copper Nozzle distance	1 mm
Welding Speed	240 mm/min
Operation type	Automatic
Torch Position	Vertical

In an Unbroken Stream Based to the MPAW research, which is displayed in table 4, the most important parameters to take into account when assessing the welding performance are the highest current, base voltage, pulse size, and pulse rate. Trial experiments and material

thickness were used to determine the welding parameter ranges. Base flow, peak flow, pulse dimension, and pulse rate constraints had been established in reaction.

Table 4. Limitations of process parameters

	Multiple Levels					
Input facto	Units	-2	-1	0	+1	+2
Base Current	A	8	9	10	11	12
Peak current	A	18	19	20	21	22
Pulse width	%	30	40	50	60	70
Pulse rate	Pulses	20	30	40	50	60

After welds, wire cutting electro discharge machining (EDM) was used to divide the sheets into dog-bone forms. It occurred in order to produce tension welding samples that, as shown in figure 1, complied with ASTM E8M-04 criteria.

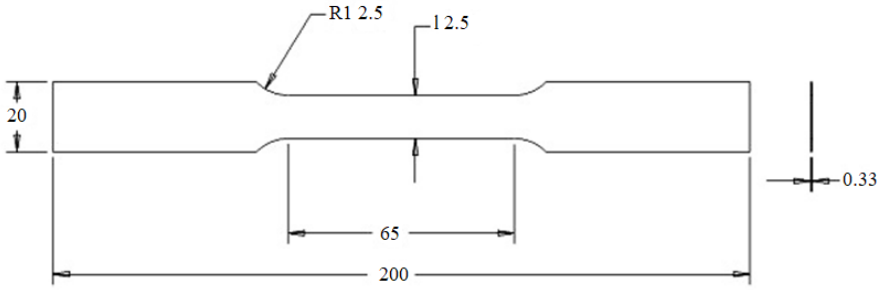

Figure1. Tensile sample in accordance with ASTM E8M-04

3. Results & Discussions

3.1 Microstructure Analysis

3.1.1 Measurement of the grain size in the fusion zone

An essential first step in assessing the performance of a welded joint is determining the grain size of the fusion zone. The toughness and strength of the joint can be impacted by the fusion zone's grain size. The installation and setup procedures for the samples follow ASTM E 3-1 guidelines. Utilizing a belt grinder, the transverse faces of the samples are first cleaned with a piece of emery paper in the mesh sizes of 1/0 (245), 2/0 (425), and 3/0 (515).

The size of the grains in this zone can have a major impact on the mechanical properties of the weld. The fusion zone grain can be found by preparing a cross-section of the welding junction and then etching its surface to reveal the microstructure. After that, the grain size can be examined under a microscope and contrasted with predetermined parameters. Non-destructive testing techniques like X-ray or ultrasonic inspection can also be utilized to assess the fusion zone and determine the grain size. By using these techniques, you may evaluate the weld quality without endangering the welded junction.

The grain size and microstructure of the weld zone can be seen by varying the etching period. when magnified 100 times. A micrograph displaying the fusion zone, heat-affected zone, and parent metal, as depicted in figures 2, 3, and 4, in that order.

The base metal SDSS 2507's microstructure reveals small ferrite and austenite grains with dark and light hues, respectively, along with a small amount of dark patches caused by slag inclusions. The base metal SS 316L's microstructure displays some slag

inclusions and coarse austenite grains as black patches. Whereas the heat-affected zone of SDSS 2507 displays a thin fusion line with coarse ferrite grains as dark zones and coarse austenite grains as light zones, the heat-affected zone of SS 316L displays coarse austenite grains. The structure of widemanstaten ferrite with fine grains is visible in the weld metal.

Figure 2. Micro structure of Parent metal of SDSS

The grade of the material chosen was SDSS 2507. Duplex stainless steel is a type of steel that is composed of two phases: ferrite and austenite. Its good qualities as both austenite and ferrite result from this, setting it apart from other materials. These substances are more ductile and strong. In order to improve both the strength and the weldability, nitrogen is added. It is extremely duplex due to its superior corrosion resistance and pitting resistance equivalent number of more than 40.

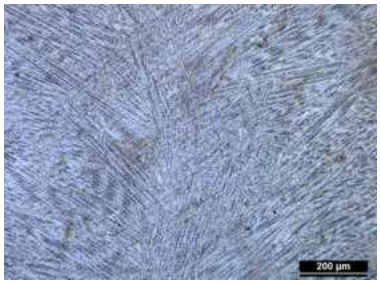

Figure 3. Heat-affected zone

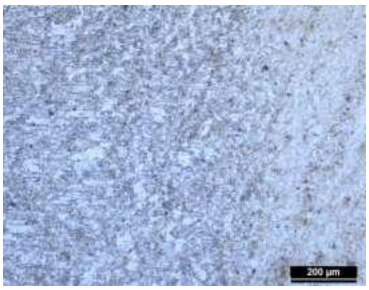

Figure 4. Fusion zone microstructure

3.2 Evaluation of the fusion zone hardness

This technique for measuring microhardness makes a mark in the material using a diamond indenter. Vickers hardness number is derived from the resistance of the material to depression and the measured size of the indentation. The fusion area in welded joints is one example of a tiny area of substance whose firmness can be assessed using Vickers hardness testing.

Vickers microhardness testing apparatus (Manufactured by Banbros Engineering Pvt Ltd., India; Model: VHS 1000) As per ASTM E384, the brittleness of the area of fusion can be evaluated by applying a 0.5 kg weight on the welded samples and waiting for 10 seconds. The average values of the three harshness readings for each sample are shown in Table 5.

3.3 Measurement of ultimate tensile strength (UTS)

A common test protocol for tensile testing metallic materials is ASTM E8M-04. This standard describes how to use a universal testing equipment and a standard test specimen to determine the ultimate tensile strength of metallic materials. The test specimen must be prepared in accordance with precise measurements and specifications, such as the gauge length and cross-sectional area, as stated in the ASTM E8M-04 standard. After that, the specimen is fastened onto the UTM's grips and steadily stressed until it breaks.

Continuous measurements are made of the load and the specimen's associated extension or distortion throughout the examination. A stress-strain curve, which illustrates the connection between stress and strain when the material is loaded, is created using this data. Finding the greatest position on the stress-strain curve, which indicates the highest stress the material can bear before shattering, yields the UTS. The stress unit used to report this number is either psi or MPa. These specifications aid in guaranteeing that the test's outcomes are dependable, exact, and comparable across various testing environments and labs.

3.4 Tensile and Hardness test results

Tensile tests are performed with a short extensometer connected to a universal testing apparatus with computer aid that has a 100kN capability.(Star Testing Systems, Model No. 9036TD, Senior No. STS-522). Tensile specimens deform as a result of the specimens being loaded steadily at a rate of 1.5 kN/min in compliance with ASTM regulations. It is feasible to ascertain the maximum allowable tensile strength for the weld joints utilizing the stress-strain curve (Figure 5).

The highest tensile strength (868.28MPa) and hardness strength (252.2 VHN) are found in experimentation result number 6. It displays the ideal welding parameters.

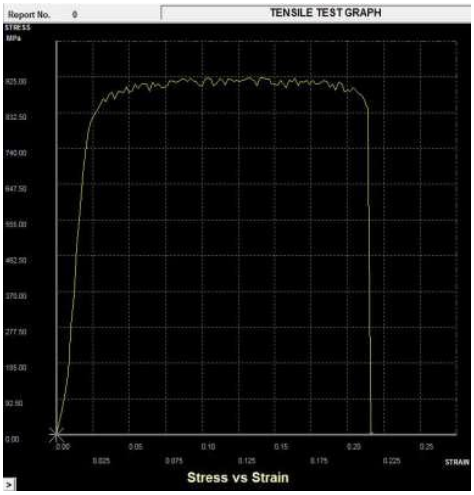

Figure 5. Stress- Strain diagram for Base metal of SDSS Analysis

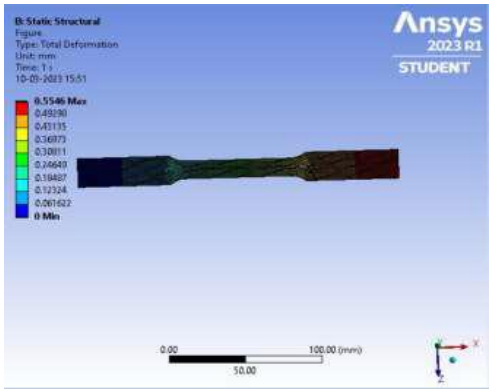

Figure 6. Total Deformation

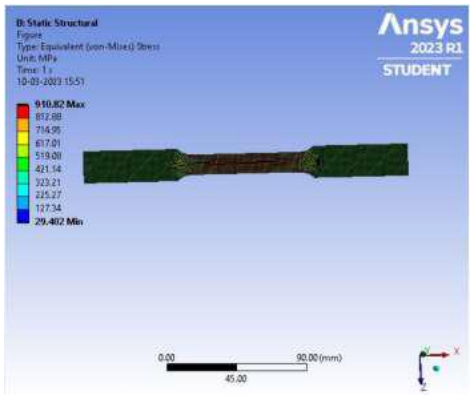

Figure 7. Equivalent Stress

After statistical structural analysis using the Ansys workbench, the overall displacement and corresponding stress levels of the super duplex stainless steel material are shown in Figures 6 and 7.

Table 5. FEA Input parameters

Properties	Standard
Poisson's ratio	0.3
Young's modulus	2E+05 MPa
Yield Strength	655.6 Ma
Tensile ultimate strength	868.2 MPa

Table 6. Tensile test results for both welded joints and base metal of SDSS

S. No	Material	UTS (MPa)
Experimental results	Base Metal	923.16
FEA analysis	PAW joint	868.29
Error percentage experiment result and FET Results	Base Metal	910.84

4. Conclusion

These deductions were made based on the study's results. The greatest tensile strength (868.28 MPa) and hardness strength (252.2 VHN) are shown in Experimental outcome number 6 of Table 5. Therefore, when employing micro plasma arc welding to join super duplex stainless steel sheets, such welding settings work well. Based on the FEA evaluation, learners should feel confident in this method before moving on to more complex models because of the close acceptance in tensile strength measurements for basic metals between ANSYS (910.82 Mpa) and the experiment results (923.16 Mpa).

5. References

[1] Björk, T., Mettänen, H., Ahola, A., Lindgren, M., &Terva, J. (2018). Fatigue strength assessment of duplex and super-duplex stainless steels by 4R method. Welding in the World, 62, 1285-1300.

[2] Wang, Q., Gu, G., Jia, C., Li, K., & Wu, C. (2023). Investigation of microstructure evolution, mechanical and corrosion properties of SAF 2507 super duplex stainless steel joints by keyhole plasma arc welding. Journal of Materials Research and Technology, 22, 355-374.

[3] Gupta, A., Kumar, A., Baskaran, T., Arya, S. B., &Khatirkar, R. K. (2018). Effect of heat input on microstructure and corrosion behavior of duplex stainless steel shielded metal arc welds. Transactions of the Indian Institute of Metals, 71, 1595-1606.

[4] Taban, E., &Kaluc, E. (2011). Welding behaviour of duplex and superduplex stainless steels using laser and plasma arc welding processes. Welding in the World, 55, 48-57.

[5] Arun, D., Ramkumar, K. D., &Vimala, R. (2019). Multi-pass arc welding techniques of 12 mm thick super-duplex stainless steel. *Journal of Materials Processing Technology*, *271*, 126-143.

[6] Zhang, W., Jiang, W., Li, H., Song, M., Yu, Y., Sun, G., ...& Huang, Y. (2019). Effect of tensile overload on fatigue crack behavior of 2205 duplex stainless steel: Experiment and finite element simulation. International Journal of Fatigue, 128, 105199.

[7] Cortés-Cervantes, I. S., López-Morelos, V. H., Miyashita, Y., García-Hernández, R., Ruiz-Marines, A., & Garcia-Renteria, M. A. (2018). Fatigue resistance of AL6XN super-austenitic stainless steel welded with electromagnetic interaction of low intensity during GMAW. The International Journal of Advanced Manufacturing Technology, 99, 2849-2862.

[8] Palandi, M., Magudeeswaran, G., &Harikannan, N. (2019). Optimization of pulsed current flux cored arc welding parameters for ferrite phase in duplex stainless-steel welds. J Balk TribolAssoc, 25(4), 865-881.

[9] Chaudhari, A. N., Dixit, K., Bhatia, G. S., Singh, B., Singhal, P., &Saxena, K. K. (2019). Welding behaviour of duplex stainless Steel AISI 2205: AReview. Materials Today: Proceedings, 18, 2731-2737.

[10] Köse, C., &Topal, C. (2022). Texture, microstructure and mechanical properties of laser beam welded AISI 2507 super duplex stainless steel. Materials Chemistry and Physics, 289,

[11] Verma, J., &Taiwade, R. V. (2017). Effect of welding processes and conditions on the microstructure, mechanical properties and corrosion resistance of duplex stainless-steel weldments—A review. Journal of Manufacturing Processes, 25, 134-152.

[12] Dönges, B., Fritzen, C. P., & Christ, H. J. (2018). Fatigue mechanism and its modeling of an austenitic-ferritic duplex stainless steel under HCF and VHCF loading conditions. Fatigue of Materials at Very High Numbers of Loading Cycles: Experimental Techniques, Mechanisms, Modeling and Fatigue Life Assessment, 111-131.]

[13] Yousefieh, M., Shamanian, M., & Saatchi, A. (2011). Influence of heat input in pulsed current GTAW process on microstructure and corrosion resistance of duplex stainless-steel welds. Journal of iron and steel research, international, 18(9), 65-69.

[14] Xie, X. F., Li, J., Jiang, W., Dong, Z., Tu, S. T., Zhai, X., & Zhao, X. (2020). Nonhomogeneous microstructure formation and its role on tensile and fatigue performance of duplex stainless steel 2205 multi-pass weld joints. Materials Science and Engineering: A, 786, 139426.

[15] Neissi, R., Shamanian, M., &Hajihashemi, M. (2016). The effect of constant and pulsed current gas tungsten arc welding on joint properties of 2205 duplex stainless steel to 316L austenitic stainless steel. *Journal of Materials Engineering and Performance*, *25*, 2017-2028.

[16] Arafat, E., Merah, N., Al-Badour, F. A., Bello, I. T., &Albinmousa, J. (2021). Fatigue crack growth behavior of friction stir processed super duplex stainless steels (SAF-2507). *Materials Today Communications*, *26*, 101937.

[17] Li, B., Zheng, Y., Shi, S., Zhang, Z., & Chen, X. (2020). Cyclic deformation behavior and failure mechanism of S32205 duplex stainless steel under torsional fatigue loadings. *Materials Science and Engineering: A*, *786*, 139443.

[18] Singh, J., &Shahi, A. S. (2019). Metallurgical, impact and fatigue performance of electron beam welded duplex stainless-steel joints. *Journal of Materials Processing Technology*, *272*, 137-148.

[19] Odermatt, A. E., Ventzke, V., Dorn, F., Dinsé, R., Merhof, P., &Kashaev, N. (2021). Effect of laser beam welding on microstructure, tensile strength and fatigue behaviour of duplex stainless steel 2205. *Journal of Manufacturing Processes*, *72*, 148-158.

[20] Krupp, U., Giertler, A., Söker, M., Fu, H., Dönges, B., Christ, H. J., ...& Ludwig, W. (2015). The behavior of short fatigue cracks during Very High Cycle (VHCF) Fatigue of duplex stainless steel. *Engineering Fracture Mechanics*, *145*, 197-209.

Comparative Analysis of Various Bracing Configurations and Their Impact on Elevated Water Tank Performance

Jisha P K[1*], *Atul* Singla[2], *Voruganti* Sreevani[3], *Ravi* Shankar Raman[4], *Manoj* Kumar Vishkarma[5], *Ali* Albawi[6], *M* Ganesh[7]

[1]Department of Applied Science, New Horizon College of Engineering, Bangalore, India.
[2]Lovely Professional University, Phagwara, India.
[3]Department of CSBS, GRIET, Bachupally, Hyderabad, Telangana, India.
[4]Department of Mechanical Engineering, ABES Engineering College, Ghaziabad-201009, UP, India.
[5]Lloyd Institute of Engineering & Technology, Knowledge Park II, Greater Noida, Uttar Pradesh, India.
[6]Radiology Techniques Department, College of Medical Technology, The Islamic University, Najaf, Iraq
[7]Department of Aeronautical Engineering, MLR Institute of Technology, Hyderabad, Telangana, India-500085

Abstract. During a few extremely distressing earthquakes in India, R.C.C. elevated water tanks suffered significant damage or collapsed. This may have been brought on by incorrect staging geometry as well as ignorance of how the tank's supporting system should behave in the event of an earthquake. The elevated water tank is made up of structural components such as footings, beams, columns, and slabs. Subjected loads are passed between these components and ultimately to the soil's sub-grade. When an overhead tank is advantageously analysed, the elevated water tank behaves differently for distinct types of loadings (Dead, Live, and Seismic). Various combinations of loads that support the possibility of occurrence are indicated by the codes for Indian standards. The primary goal of this research is to improve performance during earthquakes and complement conventional staging by better understanding the behaviour of various bracing systems. Equivalent static analysis of various bracing system types applied to the elevated circular water tank staging in the seismic zone are carried out using STAAD Pro. The axial force and maximum bending moment of the circular water tank are examined in the X, Y, and Z axes. Several models are used to calculate the axial force and maximum bending moment for staging with cross bracing, diagonal bracing, and alternating diagonal bracing.

* Corresponding author: Jishasab13@gmail.com

© The Authors, published by EDP Sciences. This is an open access article distributed under the terms of the Creative Commons Attribution License 4.0 (https://creativecommons.org/licenses/by/4.0/).

Keywords. Elevated water tanks, Earthquakes in India, R.C.C. elevated water tanks, Damage or collapse, Incorrect staging geometry.

1 Introduction

Humans require water to survive on a daily basis. The design of a water tank at a particular location determines how well water is distributed. A big water storage tank known as an elevated water tank is designed to keep water supplies at a specific height in order to induce the water distribution system [1]. Many inventions and creative concepts have led to the development of different methods for storing water and other liquid components. There are several ways to store liquid, including elevated, underground, and ground-supported methods [2]. Liquid storage tanks are widely used by enterprises and municipalities to store flammable liquids such as water and chemicals. For this reason, water tanks are essential to both public service and industrial structure [3-4]. Water tanks are essential components of a lifeline. They are crucial element of many industrial sites' water storage systems, municipal water supplies, and firefighting apparatuses [5]. There are three main types of water tanks: elevated, underground, and resting on the ground. The earth immediately supports the stationary tanks that are sitting on the ground, such as settling tanks, aeration tanks, and clear water reservoirs [6-7]. The walls of these tanks are under pressure, and the bases are susceptible to water weight and ground pressure [8]. The tops of the tanks might be covered. From a design perspective, the tanks can be categorised based on their shape: round, spherical, conical bottom, Intze type, rectangular, and suspended bottom tanks [9]. When modest capacity tanks are needed, rectangular tanks are offered [10]. Due to the high expense of the formwork, circular tanks are not cost-effective for smaller capacities. From an economic standpoint, the rectangular tanks should ideally have a square layout. It is preferable if the longer side is no more than twice as long as the smaller side [10]. Vibrations from earthquakes provide a special danger of damage to the liquid storage tanks [11]. Many above water tanks sustained damage in the last earthquake. A small number of them were on-frame staging, while the majority were shaft staging [12]. An elevated water tank failing during an earthquake is mostly caused by the massive water mass at the top of a thin staging. Strategically significant and indispensable construction are elevated water tanks [13]. When these structures sustain damage during an earthquake, the availability of safe drinking water may be compromised, fighting big fires may become more challenging, and substantial financial losses may ensue. Given that elevated tanks are frequently used in seismically active regions, a detailed analysis of their seismic behaviour is required [14]. Due to the ignorance of the supporting system, some of the water tanks broke or sustained serious damage. Therefore, while using alternative supporting systems that are both more robustly engineered, it is vital to consider the seismic safety of lifeline structures [15]. A high degree of accuracy should be used in the design of new tanks and the safety assessment of existing tanks because the failure of such structures, especially during an earthquake, may be catastrophic. The hydrodynamic pressures that tanks experience during seismic activity are a significant factor in tank design. Elevated water tanks are susceptible to significant horizontal forces and overturning during an earthquake [16]. Because of its basic design, which consists of a massive mass concentrated at the top with a relatively slender supporting structure, these tanks are highly susceptible to damage during earthquakes [17]. In regions with strong seismic activity, the design of these structures is mostly governed by earthquake forces when the tank is operating at maximum capacity [18]. Making ensuring that necessities like the water supply are not harmed during earthquakes is crucial. Tanks shall not topple over wholesale in the worst situation [19]. The main aim of this study is to try to understand the behavior of different bracing systems for the purpose of strengthening of the conventional staging and make it more effective during earthquake

conditions. Equivalent static analysis carried out to the elevated circular water tank staging in the seismic zone for different types of bracing systems [20].

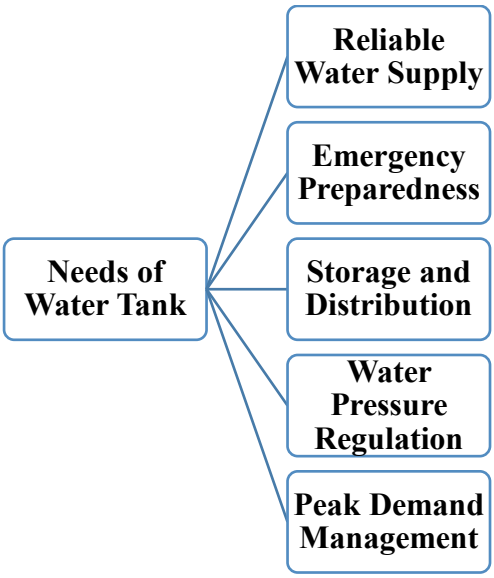

Fig 1: Needs of water supply

2 Methodology

The purpose of the introduced study is to carry out detailed research on the behavior exhibited by increased circular water tanks under seismic activity. This study presents research for the improvement of the knowledge base regarding the dynamic behavior of elevated circular water tanks by experimental study of the structural behavior of increased circular water tanks in seismic conditions. Braced circular water tanks of three different bracing types—cross bracing, diagonal bracing, and alternate diagonal bracing—are taken up for research. The project gives the comparative study to find out reasonable behavior for recognition of general design and height. The heights and capacities of the water tanks are well-designed with fixed support using Staad Pro. The height of the tank is 5 meters, whereas the staging height is 12 meters. Three kinds of bracing have been incorporated into the model: cross bracing, diagonal bracing, and alternative diagonal bracing. The structural materials used here are Fe500-grade steel and M30-grade concrete. This paper presents very complex reactions in circular elevated water tanks, caused by unique bracing arrangements, and it helps in understanding the dynamic behavior of such tanks, with some of the extremely important information for seismic-resistant design considerations.

Table shows that a total of 8 columns and 20 bays along the periphery are taken into account during modelling. The structure also has four bays along the length of it. The tank's geometric measurements are as follows: 4.5 metres for the radius, 5 metres for height, and 12 metres for the staging height. We have carefully defined the structural characteristics to meet the given size specifications. This comprehensive method provides an appropriate representation in the model by generating and assigning attributes for beams, columns, and plate thicknesses. The section parameters have been properly defined, with the tank bottom beam measuring 450 x 600 mm, the floor beams measuring 300 x 450 mm, the columns measuring 500 x 500 mm, and certain plate thicknesses taken into account. The thickness of the bottom plate is 250 mm, and the wall and ceiling have 180 mm and 150 mm thicknesses, respectively,

for the three types of bracing trees: cross, diagonal, and alternate diagonal bracing. The Staad-Pro model captures the subtle dimensions and structural features necessary for an in-depth and accurate structural analysis by integrating these specific section qualities

Table 1: The geometry of the braced elevated water tank

Shape of tank	**Circular**
Size Capacity	3 lack litters
Roof Slab Thickness	150 mm
Thickness of wall	180 mm
Thickness of Floor Slab	250 mm
Bottom Beam Size	450mm x 600 mm
Floor Beam Size	300mm x 450 mm
Size of Braces	300mm x 450 mm
Column Size	500mm x500mm
Height of Tank	5 m
Tank Diameter	9m
Staging Height	12 m
Type of Staging	Frame Staging
Free Board	0.3 m
Concrete Grade	M30
Steel Grade	Fe 500
Bearing capacity of soil	230KN/m2
Soil density	18KN/m3
Water density	10Mg/m3

3 Results and Discussion

Water tanks serve as vital structures for storing liquids used for various purposes essential in our daily lives. They are indispensable for drinking water, firefighting, irrigation, rainwater collection, and storage of chemicals and gases in industrial sectors. The elevated water tank is build-up of structural components such as footings, beams, columns, and slabs. Subjected loads are passed between these components and ultimately to the soil's sub-grade. The elevated water tank exhibits distinct behaviours depending on the type of loading (Dead, Live, and Seismic). The overhead tank analysis is helpful. Indian standards codes recommend different load combinations that support the probability of an occurrence. The results for analysis of a circular elevated water tank with varying bracing configurations, including cross bracing, diagonal bracing, and alternate diagonal bracing, with same height and capacity. The study primarily focused on a comparative evaluation of critical structural parameters, namely maximum axial force, maximum bending moment, The obtained results are presented below, providing a comprehensive overview of the tank's performance under different bracing scenarios. This comparative study offers valuable insights into the nuanced variations in structural behaviour, facilitating a deeper understanding of the implications of each bracing type on the tank's overall stability and resilience.

Table 2 presents the maximum bending moments experienced through specific columns, every diagnosed through a completely unique column number. These are bending moments of the column in kilonewton-meters (kNm) and provide useful information about the structural performance under the action of the applied loads on it. Column 6 is registered with the highest bending moment of 288 kNm, meaning considerable bending stress for such a special column. Column 14 shows a decreased bending moment of 93 kNm, whereas Column

22 registers a bending moment of 29 kNm, and Column 30 has a value of 15 kNm, with the lowest of all. Additionally, this information aids in refining structural fashions and optimizing designs to decorate average structural overall performance and resilience.

Table 2: maximum bending moment of circular elevated water tank with cross bracing for 3 lack litters

S No	Column No.	Max Bending Moment in KNm
1	6	288
2	14	93
3	22	29
4	30	15

Table 3: maximum axial force of circular extended water tank with cross bracing for 3 lack litters

S No.	Column No.	Max Axial Force in KN
1	6	1225
2	14	775
3	22	572
4	30	354

The Table 3 gives insights into the maximum axial forces experienced by specific columns, every identified through the use of a unique column range. These axial forces, measured in kilonewtons (kN), are important indicators of the compression or tension exerted along the longitudinal axis of the columns under applied loads. Column 6 demonstrates the highest recorded axial force of 1225 kN, suggesting significant compression alongside its longitudinal axis. In assessment, Column 14 experiences a lower axial pressure of 775 kN, accompanied by way of Column 22 with 572 kN, and Column 30 with the lowest axial pressure of 354 kN furthermore, this statistic allows the refinement of structural models and optimization of designs to enhance common structural overall performance and resilience.

Table 4: Maximum bending moment of circular elevated water tank with diagonal bracing for 3 lack litters

S No.	Column No.	Max Bending Moment in KNm
1	6	322
2	14	96
3	22	34
4	30	25

The Table 4 offers the maximum bending moments experienced by specific columns, every identified by a unique column number. these bending moments, measured in kilonewton-meters (KNm), indicate the significance of bending stress that every column undergoes under applied loads. Column 6 exhibits the highest recorded bending moment of 322 KNm, indicating significant bending stress along its length. In comparison, Column 14 experiences a lower bending moment of 96 KNm, followed by Column 22 with 34 KNm, and Column 30 with the lowest bending moment of 25 KNm. Moreover, this fact assists in refining structural models and optimizing designs to enhance overall structural performance and resilience.

Table 5: Maximum axial force of circular elevated water tank with diagonal bracing

S No.	Column No.	Max Axial Force in KN
1	6	1420
2	14	1382
3	22	915
4	30	625

The given table 5 shows the maximum axial forces the specific columns—each identified by a highly unique column number—can experience. These axial forces, expressed as kilonewton (kN), indicate the level of compression or tension along each column's longitudinal axis when loads are applied. With an axial force of 1420 kN, Column 6 has the highest recorded value and appears to have undergone severe compression along its length. Considering carefully, Column 14 undergoes an examination with a significant axial force of 1382 kN, whereas Columns 22 and 30 undergo relatively less axial forces of 915 kN and 625 kN, respectively. Engineers can ensure that column are safely constructed and reinforced to bear predicted loads while maintaining safety standards by employing this research of these axial forces.

Table 6: Maximum bending moment of a circular elevated water tank with alternating diagonal bracing with 3 lack litters

S No.	Column No.	Max Bending Moment in KNm
1	6	340
2	14	98
3	22	53
4	30	45

The Table 6 provide highest bending moments that particular columns have encountered are displayed in the table, each column being uniquely designated by a number. These bending moments, which are measured in kilonewton-meters (KNm), are the maximum bending moment that each column encounters when a load is applied. Column 6 exhibits significant longitudinal bending stress, with a maximum bending moment of 340 KNm. As per the assessment, Column 14 exhibits the highest bending moment of 98 KNm, whereas Column 22 and Column 30 have the lowest bending moments of 53 KNm and 45 KNm, respectively. This determine is essential for structural engineers because it offers invaluable knowledge insights about the load-bearing capacity and structural behaviour of columns within a structure.

Table 7: Maximum axial force of a circular elevated water tank with three lack litters and alternating diagonal

S No.	Column No.	Max Axial Force in KN
1	6	2195
2	14	2160
3	22	1035
4	30	720

The Table 7 provides information on the maximum axial forces that particular column, each identified by a distinct column number have to withstand. These axial forces, measured in kilonewtons (kN), constitute the importance of compression or tension along the longitudinal axis of each column under applied loads. Column 6 demonstrates the highest recorded axial

force of 2195 kN, indicating significant compression along its period. Following closely, Column 14 experiences a substantial axial force of 2160 kN in comparison, Columns 22 and 30 experience relatively lower axial forces of 1035 kN and 720 kN, respectively.

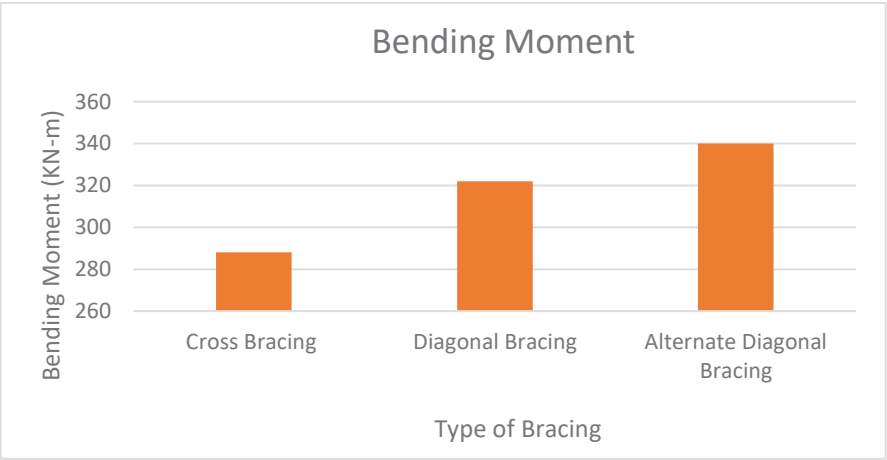

Fig. 2: Comparatively result of bending moment for cross bracing, diagonal bracing and alternate diagonal bracing

The Fig 2 presents a comparative analysis of the maximum bending moments experienced under three different bracing configurations: cross Bracing, Diagonal Bracing, and alternate Diagonal Bracing. Bending moments are crucial indicators of the bending stresses exerted on structural elements, such as columns due to applied loads. Diagonal Bracing results in slightly higher bending moments in comparison to cross Bracing, with the values consistently higher throughout all scenarios. Similarly, alternate Diagonal Bracing induces the highest bending moments among the three configurations, with values constantly exceeding those of cross Bracing and Diagonal Bracing.

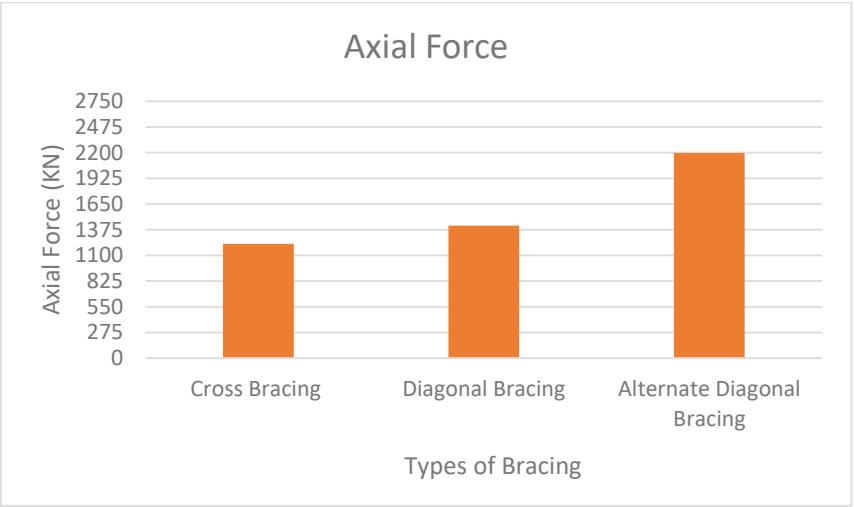

Fig. 3: Comparatively result of axial force for cross bracing, diagonal bracing and alternate diagonal bracing

The Fig 3 provided a comparative analysis of the maximum axial forces experienced under three different bracing configurations: cross Bracing, Diagonal Bracing, and alternate Diagonal Bracing. Axial forces represent the compression or tension exerted along the longitudinal axis of structural members, such as columns or beams, due to applied loads. Diagonal Bracing results in higher axial forces as compared to cross Bracing, with values consistently exceeding those of cross Bracing across all scenarios. Similarly, change Diagonal Bracing induces the highest axial forces among the three configurations, continually yielding values better than the ones of cross Bracing and Diagonal Bracing

4 Conclusion

This study undertakes a comprehensive analysis of the behaviours exhibited by elevated circular water tanks when subjected to seismic conditions. The primary goal of this research is to better understand how various bracing patterns behave in order to reinforce traditional staging and improve performance during earthquakes. An equivalent response study was conducted for the elevated circular water tank staging in zone III, utilising several bracing system types. The results for analysis of a circular elevated water tank with varying bracing configurations, including cross bracing, diagonal bracing, and alternate diagonal bracing, with same height and capacity. The study primarily focused on a comparative evaluation of critical structural parameters, namely maximum axial force, maximum bending moment.

- Analyze behavior of elevated circular water tanks under seismic conditions. Focuses on understanding bracing patterns to enhance conventional staging.
- Conducts equivalent response analysis for staging with different bracing systems. analyze varying bracing configurations (cross, diagonal, alternate diagonal) with same height and capacity.
- The alternate diagonal bracing experiences the highest axial force of 2195 kN, whereas under diagonal Bracing, it's 1420 kN, and under Cross Bracing, it's 1225 KN.
- The alternate diagonal bracing" configuration induces the highest bending moment of 340 KNm, followed by diagonal bracing with 322 KNm and cross bracing with 288 KNm.
- The alternate diagonal bracing" consistently yields the highest bending moments as compared to diagonal bracing and cross bracing.

References

1. Gandhi, Manish N., and Ancy Rajan. "Earthquake Resistant Analysis of Circular Elevated Water Tank with Different Bracings in Staging." IJISET-International Journal of Innovative Science, Engineering & Technology 3, no. 11 (2016): 255-259.
2. MAHENDRA, PRASAD. "Effect Of Defferent Bracing Configuration On The Seismic Performance & Economy Of Intz Water Tanks." (2007).
3. Pathak, Ajay Kumar, and Abhishek Mishra. "Seismic assessment of different vertical bracing systems in staging of elevated liquid retaining tank." Materials Today: Proceedings (2023).
4. Varughese, Shirley Susan, and Vivek Philip. "Effect of Bracing system on Seismic Behavior of Rectangular Elevated RC Water Tank." International Research Journal of Engineering and Technology 4, no. 05 (2017): 3200-3203.
5. Patel, Hardik V., Jasmin A. Gadhiya, and Abhishek Raturi. "Analysis of Elevated Square Water Tank with Different Staging System."

6. Adhikari, Sneha, Imtiyaz A. Parvez, and Kiran Kamath. "Study of Tank with Inclined Braced Staging." International Journal of Innovative Research in Science, Engineering and Technology 5, no. 9 (2016): 66-72.
7. Dutta, Somnath, Aparna Mandal, and Sekhar Chandra Dutta. "Soil–structure interaction in dynamic behaviour of elevated tanks with alternate frame staging configurations." Journal of sound and vibration 277, no. 4-5 (2004): 825-853.
8. Workeluel, Nathnael, Purnachandra Saha, Selemon Matiyas, and Tribikram Mohanty. "A comparative study on analysis and design of RC C elevated water tank using different country codes." Materials Today: Proceedings (2023).
9. Mor Vyankatesh, K., and T. More Varsha. "Comparative study on dynamic analysis of elevated water tank frame staging and concrete shaft supported." IOSR Journal of Mechanical and Civil Engineering(IOSR-JMCE) 14, no. 1 (2017): 38-46.
10. Sandeep, T. D. "A comparative study on elevated water tank due to dynamic loading." international research journal of engineering and technology (irjet) 4, no. 05 (2017): 2000-2004.
11. Dixit, Abhishek. "Comparative Seismic Analysis Between Elevated Circular Water Tanks Using Equivalent Static Method and Response Spectrum Method." In Advances in Geotechnics and Structural Engineering: Select Proceedings of TRACE 2020, pp. 373-384. Singapore: Springer Singapore, 2021.
12. Sharma, Vaibhav, and Abhilash Shukla. "Comparison of Square and Circular Water Tanks." (2016).
13. Khedikar, Amey R., and Abhishek Pandey. "Seismic Analysis and Comparative Study of Elevated Storage Tank by GSDMA Guidelines."
14. Patil, Ankita R., and S. A. Bhalchandra. "Effect of Different Staging Configurations on Seismic Performance of Circular Elevated Water Tank." International Journal of Engineering Research and Applications 4 (2014): 39-43.
15. Rana, Yogesh, and Abbas Jamani. "Comparative Study of Annular Raft Foundation & Solid Circular Raft Foundation for Different Diameter of Water Tank." International Research Journal of Engineering and Technology 5, no. 04 (2018): 3428-3436.
16. Soniwala, Anik N. "Comparative Study on Effect of Different Configuration of Horizontal Bracings on the Performance of Elevated Water Tank." (2020).
17. Mali, Amit K., and Harsh Desai. "Performance of Various Staging Systems for Elevated Water Tank."
18. Singh, Vaibhav, Manik Seth, and Anirban Dhulia. "Analysis and Design of Elevated RCC Water Tank." (2021).
19. Atalkar, Gaurav, and Anand Gharad. "Comparative Analysis Of Elevated Water Storage Structure Using Different Types Of Bracing Patterns In Staging." i-Manager's Journal on Structural Engineering 3, no. 1 (2014): 1.
20. Anjum, Tayyaba, and Mohd Zameeruddin. "Evaluation of Efficacy of the Elevated Water Tank Under the Seismic Loads." International Journal of Civil Engineering 8 (2021): 20-26.

Journal of Physics: Conference Series

PURPOSE-LED PUBLISHING™

PAPER • **OPEN ACCESS**

Design and Structural Analysis of an Aircraft Landing Gear strut under Static Loading Condition

To cite this article: B. Nagaraj Goud *et al* 2024 *J. Phys.: Conf. Ser.* **2837** 012066

View the article online for updates and enhancements.

You may also like

- Research on the control technology of aircraft landing gear buffer variable stroke
Xin Dai, Lu Liu, Qing Xu et al.
- Stress analysis of Landing gear of light Unmanned Aerial Vehicle
Plabita Sonowal, Soumik Das, Durgesh Kumar Mishra et al.
- New control logic based on mechanical energy conservation for aircraft landing gear system with magnetorheological dampers
Ji-Young Yoon, Byung-Hyuk Kang, Joo-Hyung Kim et al.

This content was downloaded from IP address 106.0.37.90 on 21/10/2024 at 11:03

Journal of Physics: Conference Series **2837** (2024) 012066 doi:10.1088/1742-6596/2837/1/012066

Design and Structural Analysis of an Aircraft Landing Gear strut under Static Loading Condition

B. Nagaraj Goud [1]S Soniya sai[2], K S Bhavan[3], B Bhavana[4], L Murali Krishna[5],

[1,2,3,4,5] Department of Aeronautical Engineering, MLR Institute of Technology, Hyderabad 500 043, India

[1]nagaraj2107@gmail.com
[2]soniyasai143@gmail.com
[3]ksbhavan67@gmail.com
[4]bhavanabommalapally06@gmail.com
[5]muralikrishna81435@gmail.com

Abstract. Aircraft Landing gear strut is major structural components which takes various types of loads. Main landing gear bears with impact load while the nose landing gear bears side, break and impact loads. In aerospace industry, weight reduction is an important aspect and use of composite plays a major role by providing better strength to weight ratio. In this work, weight of landing gear strut. A light weight aircraft is selected for the analysis. The design of landing gear strut is carried out as per the CS-23 Certification specification. Computational analysis is carried out on the existing design with appropriate loading and boundary conditions to arrive at optimized landing gear strut cross section. Fatigue life for the composite landing gear strut is also estimated using SN curve approach. With the optimization of existing titanium alloy landing gear strut, mass of the strut is reduced by only 4.5%. Stresses and deflections under all loading conditions are within the acceptable limit. The static structural analysis was carried out to compare with different materials and as per dimensions of the strut. Maximum Stresses of strut performances for aircraft landing gear is very significant role for determination of safety and stability of structural assemblies The design of Boeing 747 nose landing gear structure and using FEA package of ANSYS workbench is carried the static structural analysis is done and determined the deformation and stresses for various material with comparison of selected material such as Titanium alloy, Aluminum alloy and Steel alloy and studied their material characteristic to design a landing gear structure to improve the strength and stiffness.

Key words: Landing gear, strut, strength, stiffness, stresses and deformation

1.Introduction

Aircraft structural component is required to exist design of the landing gear, frequently considered to be an undercarriage support system of an entire aircraft. The major component of landing gear structure is uses for not flying and it also provides the good maneuverability such as landing and take-off [1]. In general landing gear supports the compressive force, drag force and side force. The major function of an aircraft landing gear structure is to prevent from the excess damage to the aircraft components under tension and compression of an airframe and other structural components during applied load conditions. The dynamic and static loading is supported by structure to withstand these loads. The load under static

Content from this work may be used under the terms of the Creative Commons Attribution 4.0 licence. Any further distribution of this work must maintain attribution to the author(s) and the title of the work, journal citation and DOI.
Published under licence by IOP Publishing Ltd

force, energy absorption is significant in the design standard. For the aircrafts, the lip type of spring used for landing gear that normally enough to resist the impact energy. An oleo strut of landing gear is used for heavy loaded aircraft. High-speed aircrafts have made with retractable system of landing gear, which fold ups for the period of flight to decrease air resistance. The aircraft landing gear consists of hydraulic suspension system, oleo struts and wheels the runs on rough surfaces[2].

The Landing gear was primary constructed for taxing on surface of the runway, but it was not only optimized for the long duration of flight. Since beginning 1920, aerospace industry becomes further organized and industrial new innovative technologies on landing gear system. Thus, the aircrafts went more rapidly the retractable edition constructs its smooth appearance and which helps to decreases the drag force. Different materials have been designed and build up to improve the innovative technology, such as high resistance steels, various composites, hydraulic systems and pneumatic systems.

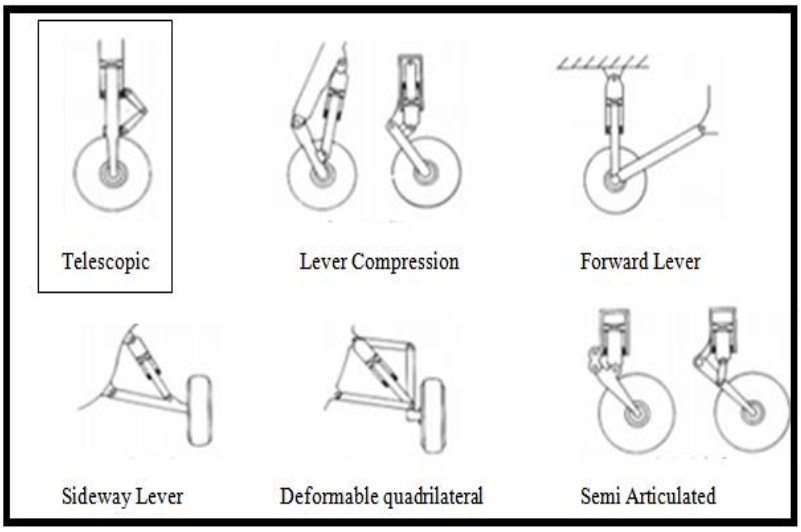

FIGURE1.Configurations of landing gears
Ref Source :(Young, 1986)

Carbon fiber reinforced material behaviour is more difficult to predict than steel. Numerical Equations are used to predict the material behaviour of high resistance steel although as the composite materials are latest technologies, consequently, the to test the material and material [3].

1.1 Types of the Landing Gear Systems Uses for Different Aircrafts

The Landing gear systems are connected to the aircraft under the various locations with the requirements of aircraft design. It would be connected under wing structure, under the fuselage structure or in between of the fuselage and wing. Various types of landing gear system configurations as such as Single main system, Bi-cycle system, Tricycle system, Tail gear system, Quadricycle system and Multi-bogey system [13].

1.1.1 Single Main Landing Gear

The single main system is the basic design of landing gear. this type of assemble needs the location of the landing gear near to CG and which performs the main landing gear and it carries entire the weight of the aircraft.

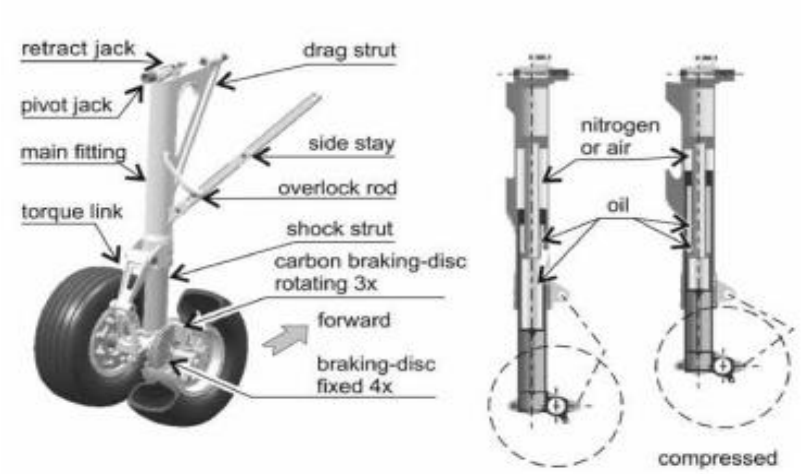

FIGURE2. Configuration of main type landing gear with section view
Ref Source :(Lernbeiss and Plöchl, 2007)

1.1.2 Bi-cycle Landing Gear

The Bi-cycle landing gear construction, two equal size of landing gear is one frontward and the other aft, almost central from CG of the aircraft location. due to this an extension of single landing gear provides modesty and decline in weight. Though, the instability of ground is a critical issue for this arrangement.

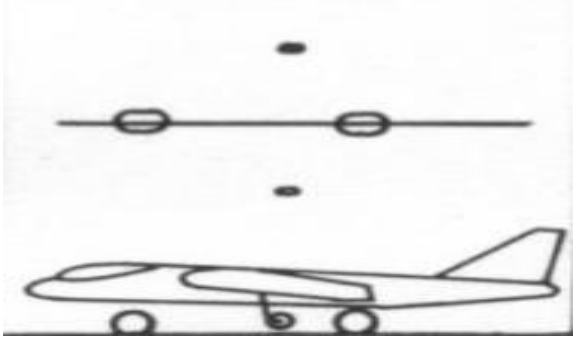

FIGURE3.Bi-cycle landing gear
Ref Source image :(Wang, Wang and Wang, 2016)

1.1.3 Tricycle Landing Gear

This type of configuration is used with two wheels carried the aircraft mass equally position aft to the CG of the aircraft along with the nose located at position nearby the nose. the aircraft is level on the position the ground with main landing and nose landing gear is with equal height and with flat floor position.

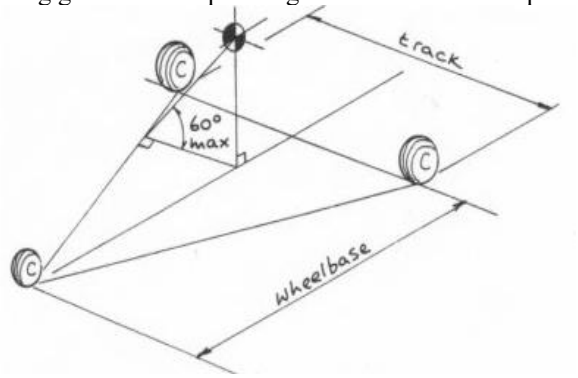

FIGURE4.Configurations of Tricycle landing gear
Ref Source image :(Wang, Wang and Wang, 2016)

Flugge et.al have explained impact loads on landing gear structure. Both impact of the landing and the ground taxiing loads has been measured, but the drag forces have also excluded [4]. The numerical solution and differential equations have been formulated by the, studying of nonlinear physical properties of oleo strut. the method is exposed on how these dimensions are measured by determined the specified load-time diagram. And also, the review study of German literature on landing-gear structure impact was presented

Jocelyn et.al have explained issues facing by the aircraft communal in the dynamics of landing gear, particularly brake-induced vibration and shimmy. The survey of literature exposed the variety of modelling, testing, analyses and landing gear simulation [5]. Experimental investigation and validation of shimmy and brake-induced vibration are reported for the aircraft landing gear. The aircraft vibration research commenced in 1970s and the development of turbofan engines, vibrations of airframe have become the major structural component in the overall vibrations caused by the aircraft in the configuration of landing gear system

Amit Goyal et.al published the paper on the design of Light weight Landing Gear. Under the process of development phase, buckling analysis and the non-linear analysis of stress was done [6]. The use of FEA software ANSYS for the designing of Light Landing Gear structure. Several experimental investigations were conducted using with different loads and different type of orientations. He was also pointed out that, the important features of this analysis were carried out the optimization of thickness and orientation with buckling, stresses and various failure conditions. He was mentioned that, the material should be highly elasticity and high storage of strain energy. The main characteristics of the landing gear are lightweight, high strength, highly elasticity and high storage of strain energy, medium stiffness. The role of the landing gear is to absorb the kinetic energy of the vertical landing velocity.

2. Design Considerations.

The static structural analysis was carried out as per the dimensions and selected material for the landing gear system to evaluate the various stresses and structure deformation under the static load of 200kN applied on under the landing gear strut. The Boeing 747 Aircraft landing gear design and analysis is done using FEA tool and studied the material characteristics and selection of different material and carried out of results of various stresses.The design work in this research plans on construction and expansion the abilities of those computational tools by proposed methodology to improve modelling, optimization, effective, analysis and design and development, while designing of the landing gear entirely or designing of its discrete required components. The landing gear strut was modelled by using CATIA Part design work individually and assembled in the work bench to make a combined nose landing gear model.

Table 1. Geometry of Nose Landing Strut.

Item Name	Specifications
Length of the Strut	0.65107m
Outer Diameter	0.175m
Internal Diameter	0.150m
Thickness	0.25m
Material Used	Titanium Alloy
Density	4.750mg/m^3
Length of The Strut	0.65107m

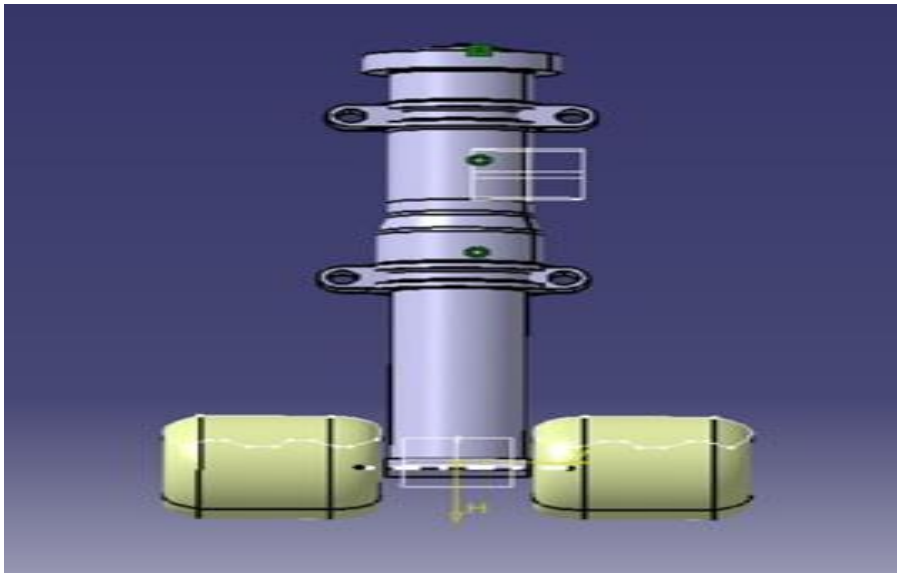

FIGURE5. Design of Nose Landing Gear Strut

3.Simulation Results

The static analysis of landing gear was performed in ANSYS Workbench extensively and design was imported from CATIA as per the specified dimensions. Select the materials from the engineering data and its material properties for the landing gear structure in the Ansys tool[10-12]. The process followed by meshing, applied boundary conditions, it was supported fixed on top of the trunnion and support on the strut with frictionless. Analysis have been conducted with static load 200KN applied under landing gear struct and obtained results are presented for deformation and various failure stresses[14-19].

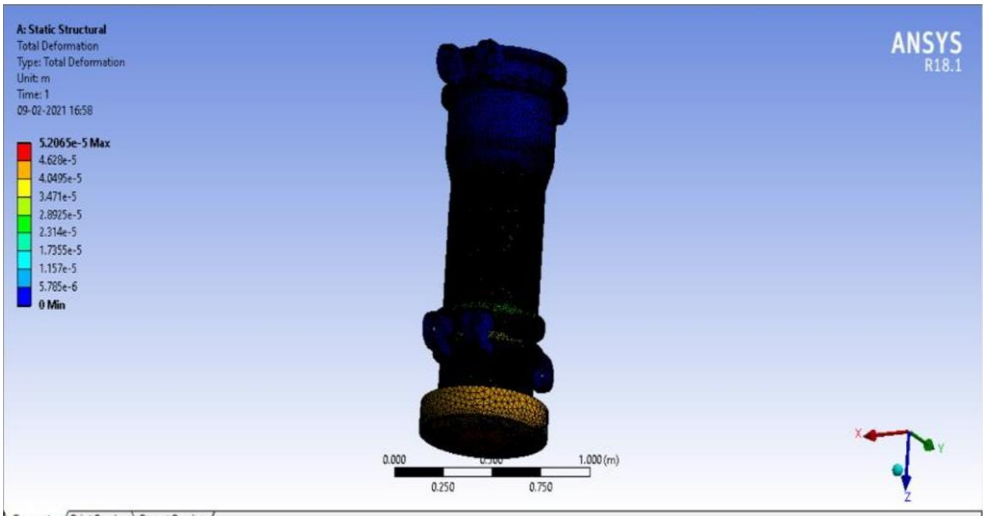

FIGURE 6. Deformation

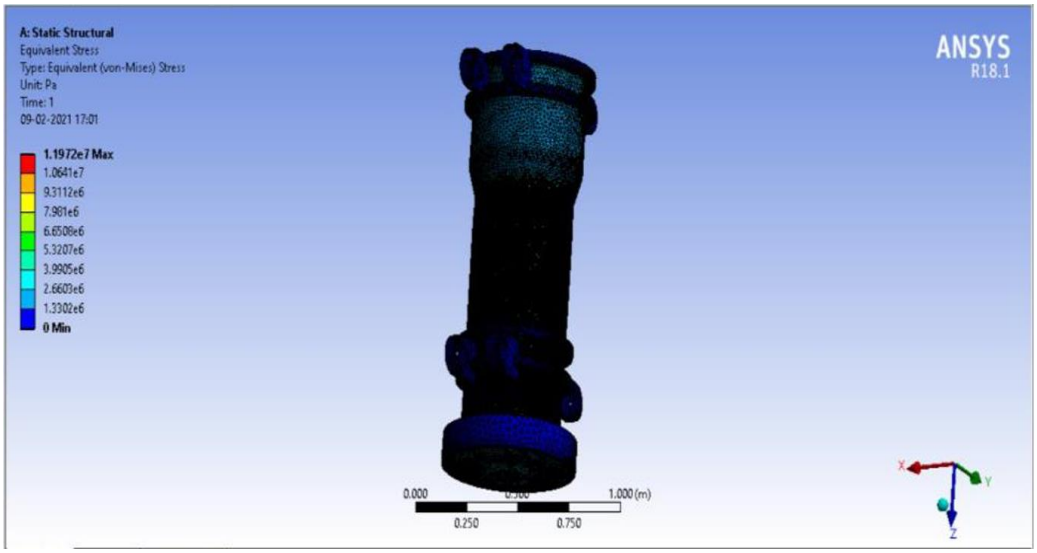

FIGURE7. Equivalent Stress

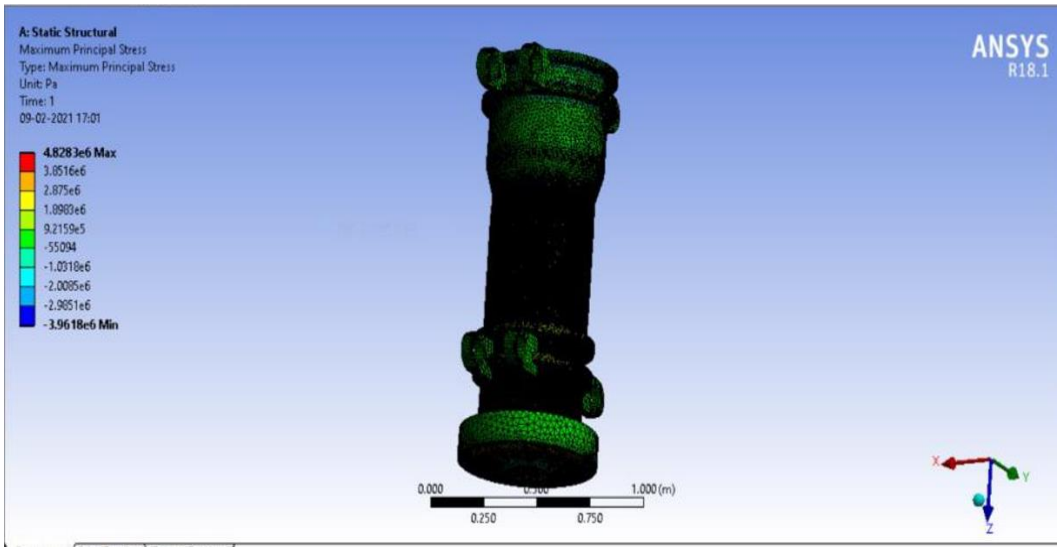

FIGURE8. Maximum Principal Stress

TABLE2.Stresses and Deformation results

Materials	Maximum Deformation (mm)	Von Misses Stresses (Mpa)
Titanium alloy	2.05	72.2
Aluminium alloy (A2040)	6.5	125
Steel alloy (Ferrium m54)	0.65	65.5

TABLE3. Parameter's v/s performance of materials

Parameters	Aluminium Alloy	Titanium Alloy	Steel Alloy
Strength	Low	Medium	High
Mass	Low	Medium	High
Cost	Low	High	Medium
Machinability	low	Medium	High
Stiffness	High	Medium	Low

4. Conclusion

The landing gear strut structure was analyzed under 200KN of static load applied under the struct. The complete summary the research work as followed. Primarily the geometry was design by using Catia software as per the dimensions. The geometry was imported to Ansys workbench and the static structural analysis have done for 200KN loads for deformation and Maximum stresses development. The analysis results were shown for different materials such as Titanium alloy, Aluminium alloy and Steel alloy. The maximum principal stresses are induced in the landing gear strut is found of 72.2 Mpa for titanium alloy and it can compare with other material such as Aluminium alloy which is found 125MPa and both materials can be compare with steel alloy which is less stresses found 65MPa. The various material results were present that concluded the highest strength of material is steel alloy that can withstand minimum deformation values compared with other material.

5. References

[1] Wang, H., Wang, Y. and Wang, M. (2016) 'On the development of a landing gear design method in aircraft multidisciplinary design environment', *2016 IEEE International Conference on Aircraft Utility Systems (AUS)*, pp. 403–407.
[2] Young, D. W. (1986) 'Aircraft Landing Gear_The Past, Present and Future', Proceedings of the Institution of Mechanical Engineers, Part D: Journal of Automobile Engineering, 200, pp. 75–92.
[3] Lernbeiss, R. and Plöchl, M. (2007) 'Simulation model of an aircraft landing gear considering elastic properties of the shock absorber', *Proceedings of the Institution of Mechanical Engineers, Part K: Journal of Multi-body Dynamics*, 221(1), pp. 77–86. doi: 10.1243/1464419JMBD63.
[4] Flugge W. "Landing Gear Impact", *NACA*, TN2743, 9016,1952,
[5] Jocelyn I. Pritchard, "An Overview of Landing Gear Dynamics", *NASA/TM*-1999-209143 ARL-TR-1976.
[6] Amit Goyal, Dr.H.V.Lakshminarayan "Design ,analysis and simulation of a composite main landing gears for a light aircraft" Coventry university postgraduate study centre *MSRSAS*,Bangalore.
[7] R. C. Fordham, "Airport Planning in the Context of the Third London Airport," *Econ. J.*,vol. 80, no. 3183, pp. 307–322, 1970
[8] L. News, "Updating the A380: the prospect of a new version and what's involved," pp. 1–5,2014.
[9] A. Kharina and D. Rutherford, "Fuel efficiency trends for new commercial jet aircraft: 1960 to2014," *Int. Counc. Clean Transp*. August, 2015.
[10] M. Ganesh, K. Shiva Shankar "Modelling And Analysis Of Scaffolding Structure Used In Aerospace Vehicle*"(IJSR)*Volume 4 Issue 5, May 2015,Issn (Online): 2319-7064.
[11] 'Nayani Uday Ranjan Goud', 'Alka Sawale', 'Bhupal Rakham', "Buckling Load Predictions of Panel and Shell using Vibration Correlation Technique", International Journal of Engineering and Advanced Technology *(IJEAT),* ISSN: 2249 – 8958, Volume-9 Issue-2, December, 2019

[12] Alka Sawale, Nayani Uday Ranjan Goud, M.Srinikitha "Experimental Analysis of Stress Concentration on V-Notched Plate" International Journal of Innovative Technology and Exploring Engineering *(IJITEE)* ISSN: 2278-3075, Volume-9 Issue-2, December 2019, page No 3709-3712

[13] G. Roloff, "Aircraft Landing Gear: The Evolution," *Airbus, .* April, p. 92, 2002.

[14] Vemanaboina, H., Akella, S., Buddu, R.K., Yelamasetti, B., Matam, M.B., Salem, K.H., Saxena, K.K., Prakash, C., Buddhi, D "Prediction of thermal and residual stress distributions in SS304 materials for nuclear application using finite element analysis" (2023) International Journal on Interactive Design and Manufacturing,

[15] Shiva, A., Cheepu, M., Kantumuchu, V.C., Ravi Kumar, K., Venkateswarlu, D., Srinivas, B., Jerome, S. "Microstructure Characterization of Al-TiC Surface Composite Fabricated by Friction Stir Processing" (2018) IOP Conference Series: Materials Science and Engineering, 330 (1), art. no. 012060

[16] Ashok Reddy, K. "Non-Destructive Testing, Evaluation of Stainless Steel Materials" (2017) Materials Today: Proceedings, 4 (8), pp. 7302-7312

[17] Vemanaboina, H., Babu, M.M., Prerana, I.C., Gundabattini, E., Yelamasetti, B., Saxena, K.K., Salem, K.H., Khan, M.I., Eldin, S.M., Agrawal, M.K. "Evaluation of residual stresses in CO2 laser beam welding of SS316L weldments using FEA" (2023) Materials Research Express, 10 (1), art. no. 016509,

[18] Robert Xavier, A., Ravichandran, A.T., Ravichandran, K., Mantha, S., Ravinder, D. Sm doping effect on structural, morphological, luminescence and antibacterial activity of CdO nanoparticles (2016) Journal of Materials Science: Materials in Electronics, 27 (11), pp. 11182-11187

[19] Praveen, L., Geeta Krishna, P., Venugopal, L., Prasad, N.E.C Effects of pulse on and off time and electrode types on the material removal rate and tool wear rate of the Ti-6Al-4V Alloy using EDM machining with reverse polarity (2018) IOP Conference Series: Materials Science and Engineering, 330 (1), art. no. 012083

Interactions (2024) 245:163
https://doi.org/10.1007/s10751-024-02004-x

RESEARCH

Performance of jack fruit methyl ester and pine oil blends with coconut shell nanoadditive biodiesel for automobile applications

G. Hima Bindu[1] · M. Ganesh[2] · S. Sathees Kumar[1] · Pravat Ranjan Pati[3] · Jayant Giri[4] · T. Sathish[5] · Emad Makki[6,7]

Accepted: 7 July 2024
© The Author(s), under exclusive licence to Springer Nature Switzerland AG 2024

Abstract
Biodiesel made from oil-bearing crops including Jatropha, Pongamia, Calophyllum Inophyllum, and others has elisions been the subject of extensive research over the past ten years. Still, not much research has been done on the idea of using oilseeds like jackfruit to make biodiesel. The objective of the experiment is to enhance the efficiency and downgrade emission by identifying the NOx and reducing it. In this experimental work, diesel and various blends such as (pine oil (PO), Jack Fruit Methyl Ester (JFME), Low cetane Jack fruit oil, mixture of Pine Oil, coconut shell nano additives with Pine oil and Jack Fruit Methyl Ester (JFOPOCS)) were utilised for investigating the performance of diesel engine. The effects signify that PO20 and JFO40 are both useful. There were no modifications made to the diesel engine. Conversely, NO_X has been identified. All blends of pine oil and biodiesel rise consistently when compared to diesel. With the exception of nitrogen oxides, tertiary blends and the application of break thermal efficiency in the third phase can reduce all other emissions. Finally, comprehensive examination of the significant testing outcomes, it was determined that JFO40PO20CS60 could be utilised as an appropriate biofuel mixture for diesel engines functioning at optimal performance levels Nano Coconut Shell Additive. A biofuel mixture of Pine Oil 20%, Jack Fruit Oil 40%, and Coconut Shell Nano additive 60 ppm is a sustainable choice for usage in a Common Rail Direct Injection (CRDi) engine with the optimal parameters, according to extensive testing.

Keywords Coconut shell nano additive · Jack fruit methyl ester · Pine oil · CRDI engine · Smoke emission · Carbon monoxide emission · NO_x · HC emission · Break thermal efficiency

Extended author information available on the last page of the article

Published online: 18 July 2024

1 Introduction

The energy situation has now spread and improved the exploration of non-conventional, renewable, and environmentally beneficial fuels. It is obvious that the planet has some assets of fossil fuels. Several experts and academicians have determined that natural gas can survive for 63 years, oil for 14 years, and coal for up to 218 years [1]. The demand and supply of conventional fuels are increasing due to increased population, extensive growth, and rising living standards in many urbanized countries [2]. If developing countries succeed, their dependency on other countries will inevitably diminish, cutting the cost of petroleum imports. Additives enhance the performance, combustion, diesel emissions, and CI engines that run on biodiesel, according to Hemmerlein et al. [3]. In order to address the challenging technological issue of diesel engine clean combustion, the development of biodiesel, additives, and engine modifications is currently required. Previously, researchers employed a variety of vegetable oils. There are numerous oils that are suitable for human consumption [4]. As a result, there will be insufficient food because vegetable oils are widely used in cooking. In context with the present crisis of energy, non-edible oils have been identified, two examples being pine oil and jackfruit oil. Transesterification of vegetable oils produces biodiesels, which are then tested. To begin, consider functionality, emissions, and combustion. By examining their chemical and physical characteristics, these trans esterified vegetable oils' attributes are determined. According to Hawkins et al. [5], natural gas, crude oil, coal, and nuclear energy can all be used to meet the world's energy needs. These resources might soon run out because they are non-renewable. Among these, diesel fuel is widely utilised for the transportation of agricultural and industrial items, as well as machinery such as diesel generators and tractors. As a result of the increased energy needs of the transportation and industrial sectors, fossil fuel use is increasing dramatically, harming the environment with pollution. As a result, we need to prioritise studies regarding the use of renewable energy. Many biofuels are now being researched in order to meet severe emission criteria for pollution control [6]. Nonetheless, there's enough potential here to warrant more investigation. Fuls et al. [7] addressed its energy needs; India needs to set short-term targets by 2030 that can be incremental steps toward achieving energy security by that year, as well as a long-term plan by 2050. The need for petroleum products will rise due to the rapid development of autos, as stated by Azam et al. [8]. This demand is expected to exceed 340 million metric tonnes by 2024–2025, and to reach around 650 million metric tonnes by 2030–2031, assuming rapid expansion in output. Rather than evaluating the performance of the diesel engine using diesel, Jacobus et al. [9] employed diesel and different mixtures. Considering these literatures, for the first time, blends of coconut shell nano additives, jack fruit (JF) methyl ester, and pine oil (PO) were introduced to carry out the characteristics of diesel engines. There were many research work carried on the same domain but there was no perfect result been found to reduce NOx and smoke emission. In this research the NOx and smoke emissions have been reduced by adding coconut shell nano additive to the blended fuel. Due to which the environment will be free from pollution which will increase the life span of the population in India.

2 Characteristics of engine operation using fuels added with nanoparticles

According to Pavuluri et al. [10], a single-cylinder, 4 stroke CI engine with ratios of compression of 17.5%, 18.5%, and 19.5% was studied to see how the engine performed, burned, and released emissions. Kumar and Sharma [11] tested the four different combinations of ethanol (10, 20, 30, and 40). To keep the ethanol-biodiesel combination homogeneous and avoid phase separation, it was combined with 1% diethyl carbonate, 1% ethyl acetate, and 2% emulsifier. High compression ratio ethanol increases brake thermal efficiency (BTE), as demonstrated by Kumar et al. [12]. Diesel engines perform better and had more efficient combustion when the compression ratio is higher. Cerium oxide nanoparticles mixed to ethanol and biodiesel were the subject of an analysis by Selvan et al. [13] to better understand the emission behaviour of a CI engine. A castor oil biodiesel emulsion was produced using ultrasonic bath stabilization. Bhattacharyya and Reddy [14] stated that diesel-biodiesel ethanol blends have a greater BSFC than diesel. Diesel outperformed diesel-biodiesel ethanol mixes in terms of BTE at all loads, whereas diesel-ethanol blends showed a modest improvement when cerium oxide was added. Cerium oxide reduced the diesel ignition delay but ethanol increased it, as reported by Altın et al. [15]. Cerium oxide produces less heat and speeds up combustion. Pramanik [16] blends of biodiesel containing cerium oxide significantly diminished emissions of CO, HC, smoke, and NOx. Utilising jatropha biodiesel with alumina nanoparticles. Basha and Anand [17] performed a DI single cylinder, 4 stroke CI engine function, emission, and combustion analysis. To make a homogenous mixture containing the jatropha biodiesel, distilled water and wetting agent were combined utilising a mechanical agitator. Tween 80 poly-xyethylenesorbitane mono-oleate and Span 80 sorbitans mono-oleate are the surfactants that the authors chose to create a stable emulsion. Initially, a mechanical agitator was employed by Nwafor [18] to fuse Span80 and Tween80 together at a 2% volume ratio. In accordance with Shaheed and Swain [19], the mixture of surfactant and distilled water with a volume proportion of 15% was mixed for about 30 min at different speed rates of 1500, 2000, 2500, and 3000 rpm at 30 °C atmosphere temperature. Finally, biodiesel is produced. Kayisoglu et al. [20] was experimented on alkyl esters which are chemically produced when alcohol and plant oils react to produce biodiesel, a replacement for CI engines. It can be utilized alone or in combination with diesel in CI engines that have not been upgraded, according to a comprehensive 14 research and demonstration study. Government subsidies and growing gas prices have recently raised interest in biodiesel [21]. While the current supply of plant oil limits the amount of petroleum that biodiesel can replace, the potential for alternative oil yields to increase biodiesel's role as a major source of supports.

3 Synthesis, mixing, and characteristics of biodiesel

The comprehensive research plan that is implemented to meet the stated objectives and results is provided below in Fig. 1.

Table 1 shows the characteristics of Pine oil where as in Table 2 illustrates the chemical compositions of Jack Fruit Methyl Ester's in which the acids give the percentage values such as 9.54%, 11.34%, 4.35%, 3.03%, and 69.55% for Palmitic, Linoliec, Stearic, Myristic,

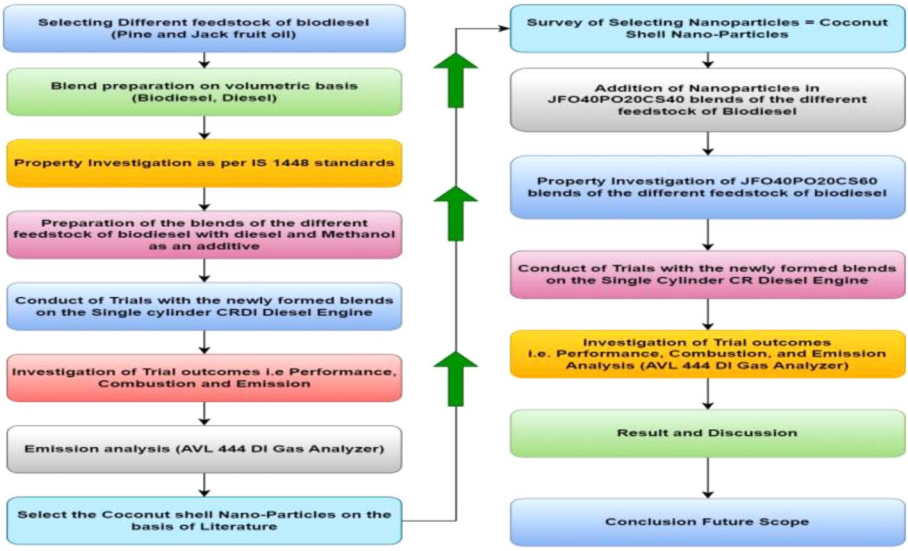

Fig. 1 Methodology of the research work

Table 1 Characteristics of pine oil

Compound	Pine Seed Oil
Density (kg/m^3)	846.29
Calorific Value (kJ/kg)	43,012
Kinematic viscosity at 40^{o}C	1.80
Cetane Index	14
Flash Point in ^{o}C	145

Table 2 Jack fruit methyl ester's chemical composition

Acids / Compounds	% composition
Palmitic (16:0)	9.54
Linoliec (18:2)	11.34
Stearic (18:0)	4.35
Myristic	3.03
Oliec (18:1)	69.55

Oliec acids. One of the most effective methods for producing nanoparticles is the mechanical ball milling process. Because coconut shell nanoparticles are used in the research, it is evident how they are made, tested for qualities, and listed in the Tables 3 and 4. The chemical compositions of elements such as carbon, hydrogen, sulphur are 49.62, 7.31 and 0.10% respectively. 0.1% of coconut shell nano additive is added to one litre of biodiesel until the desired concentration is obtained. Numerous components included in the coconut shell nanoparticles have been identified by the use of EDAX. It is also mentioned that, based on CHNS analysis, biodiesel has no sulphur content and an oxygen concentration of 10.16% observed from Table 5. It should be mentioned, though, that diesel fuel includes 0.18% sul-

Table 3 JFOME and Jack Fruit fuel blends' attributes

Properties	Diesel	JFO	JFME	JFO 10%	JFO 20%	JFO 30%	JFO 40%
Density (g/m^3)	0.839	0.90	0.80	0.83	0.84	0.84	0.8
Kinematic viscosity	2.9	32.7	3.9	2.9	3.1	3.2	3.3
Calorific value (MJ/kg)	42.49	39.09	38	42.8	42.6	42.1	41.7
Saponification value	-	178.06	174	-	-	-	-
Cetane Index	48	40	54	47.9	48.9	48.9	50.0
FlashPoint^{0}C	54	172	167	66	77	88	97
Boiling point(^{0}C)	180–340	243–328	240–340	-	-	-	-
Iodine value (gI_2/100 g)	-	122	113	-	-	-	-

Table 4 JFOME with pine oil fuel blend characteristics

Properties	Measurement Standards	Diesel	JFO-20PO20	JFO-30PO20	JFO-40PO20
Density (g/m^3)	ASTMD1298	0.83	0.84	0.85	0.86
Flash Point ^{0}C	ASTMD92	55	82	94	105
Calorific Value (MJ/kg)	ASTMD240	42.4	39.3	39.0	38.6
Cetane Index	ASTMD4737	48	43.2	43.4	44.2
Kinematic Viscosity(Cst)	ASTMD445	2.8	3.2	3.4	3.4

Table 5 Coconut shell nanoparticle components

Components	Coconut Shell Observed	
	Atomic %	Wt. %
C	56.8	49.0
Al	0.17	0.32
O	42.04	48.38
K	0.16	0.46
Ca	0.12	0.35
Si	0.70	1.41
Total	**100.00**	**100.00**

Table 6 The characteristics of JFOME and fuel blends with pine oil and coconut shell

Properties	Measurement Standards as per ASTM	Diesel	JFO40PO20	JFO40PO20CS40	JFO-40PO20CS60
Kinematic Viscosity	D445	2.9	3.31	3.32	3.33
Calorific Value in MJ/kg	D240	42.5	38.6	39.5	40.0
Flash Point in °C	D92	54	103	104	106
Density in g/m^3	D1298	0.8	0.86	0.86	0.86
Cetane Index	D4737	48	44.1	44.5	46

phur. The characteristics of JFOME and fuel blend with pine oil and coconut shell is seen in Table 6.

4 Proportion of diesel and blends

Diesel and pine oil (PO) mixtures are equipped by various volume proportions like PO10, PO20, PO30, and PO40. The selection of biofuels was done by 10, 20, 30, 40% that is by increasing for 10%. If we select 5% we may not get more variation and may get similar values due to which we selected increase by 10% to get varied values. Furthermore, Diesel and Jack Fruit (JF) Methyl Ester, designated JFO10, JFO20, JFO30, and JFO40, and evaluating them in a diesel engine. Additionally, volume-based Diesel, Pine Oil, and Jack Low cetane pine oil is used in the production of Fruit Methyl Ester blends, which are designated PO20JFO20, PO20JFO30, and PO20JFO40. The best combination for additional study is established by contrasting the test results with typical diesel operation. Phase two involves creating volume-based blends of Diesel and Jack Fruit (JF) Methyl Ester, designated JFO10, JFO20, JFO30, and JFO40, and accessing them in a diesel engine. In the third step, volume-based Pine Oil, Diesel and Jack Low cetane pine oil is used in the production of Fruit Methyl Ester blends, which are designated PO20JFO20, PO20JFO30, and PO20JFO40. This enhances the fuel blends' optimal replacement of conventional fuel diesel without sacrificing performance. In the fourth phase, volume blends of diesel, pine oil, coconut shell nano additives, and Jack Fruit Oil Methyl Ester are created and labelled JFO40PO20, JFO40PO20CS40, and JFO40PO20CS60, respectively. The features of ideal operating parameters were investigated. The fuel combination JFO40PO20CS60 produces 5.04% less NOx than diesel at advanced BMEP conditions. The gasoline mixtures JFO-40PO20CS40 and JFO40PO20CS60 emit 24.07 and 27.7 HSU of smoke, respectively. The oxygen-to-fuel ratio rises with the addition of coconut shell nanoparticles. The primary factor increasing the cetane number is oleic acid. Essential oil contains a variety of oxygenated chemicals as well as hydrocarbons related to terpenes, unlike biodiesel. More thorough research is required on essential oils as there are still not many of them. According to ASTM guidelines, the thermophysical characteristics of Pine Oil Ester and Jack Fruit Methyl are evaluated. Pine oil biofuel, jackfruit methyl ester, and a coconut shell nano additive are used in the CRDi diesel engine to enhance its functioning, combustion features, and emissions. There are several factors to take into account, including the ones that follow: inside-cylinder pressure, ignition delay period, heat release rate (HRR), exhaust gas, brake-specific energy consumption (BSEC), temperature (EGT), and brake. There are four processes involved in the calculations for Thermal Efficiency (TE), HC, CO, NOx, and Smoke Emissions. Fabrication of Coconut Shell Nano Particles and Transesterification setup are shown in Figs. 2 and 3 respectively.

5 Testing setup

A Kirloskar water-cooled CRDi engine fitted with control and measurement instruments immediately connects to the eddy current test bench. The components of the CRDi system include an injector that is managed by a solenoid valve, a common rail, and a pressure sen-

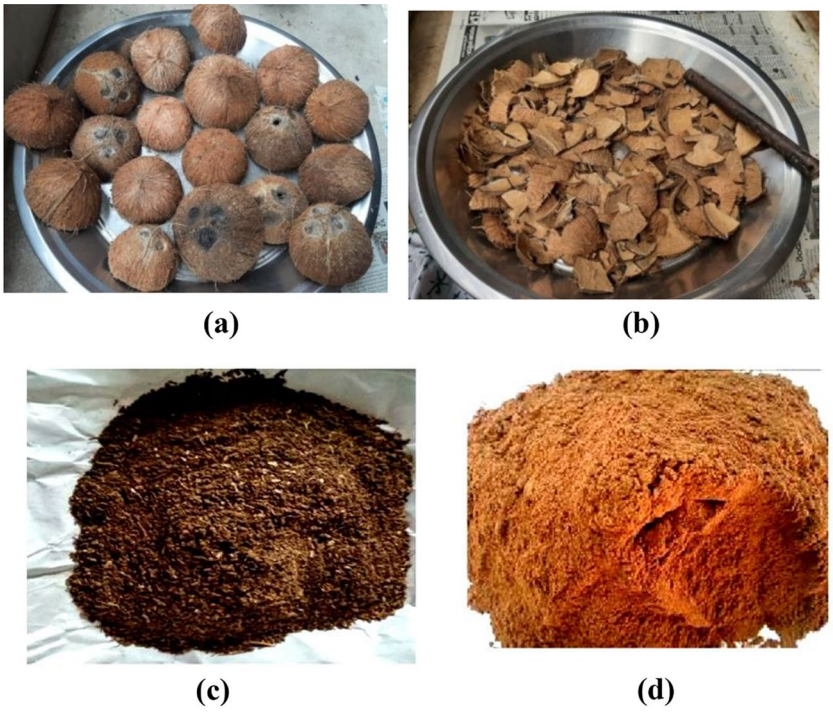

Fig. 2 Fabrication of nanoparticles from coconut shell. (**a**) Coconut shells. (**b**) Broken coconut shells (**c**) Powdered coconut shell. (**d**) Nano particles from coconut shell

Fig. 3 Transesterification setup

Fig. 4 Photo view of the test configuration

Table 7 CRDi engine technical specifications

Details	Specifications
Power	5.2 kW
Bore	87.5 mm
Stroke	110 mm
Capacity	661 cc
Compression Ratio	12–18 or 17.5:1
Speed	1500 RPM
Dynamometer Arm	185 mm
Method of Cooling	Water

sor that gauges the common rail pressure. The rail pressure sensor continuously provides pressure data to the Nira i7r control unit, which it utilizes to modify injection parameters and keep the common rail pressure constant.

The engine runs at a nominal speed of around 1500 rpm, producing 5.2 kW. The operational details of the engine are displayed in Table 7. The diesel engine configuration for experimentation is shown in Fig. 4.

When evaluating engine properties in a CRDI engine using mixes of Pine oil and JFOME, different approaches were employed. A fuel blend of JFO40PO20 with a 40–60 ppm coconut shell nano additive was added during engine operating optimization.

6 Results and discussion

6.1 Brake Thermal efficiency (BTE)

As shown in Fig. 5, PO20 has the greatest observed BTE whereas PO40 has the lowest. In comparison to diesel, the BTE of the PO20 blend was 4.64% greater. Diesel has a BTE 3.91% higher than the JFO40 blend.

Considering the biodiesel pine oil blend has less energy than other blends, JFO40PO20 produced lower BTE. The BTE of JFO40PO20CS60 is 6.8% greater than diesel when operating at optimal settings.

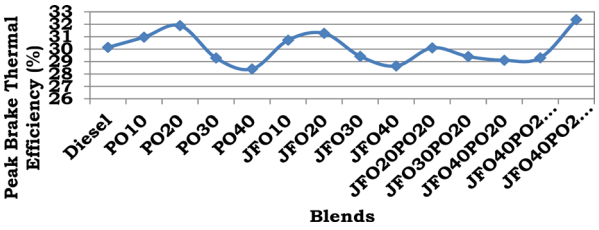

Fig. 5 Brake thermal efficiency variations for several blends

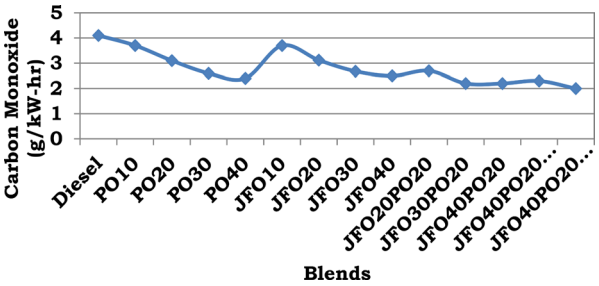

Fig. 6 Variation of carbon monoxide emission for several blends

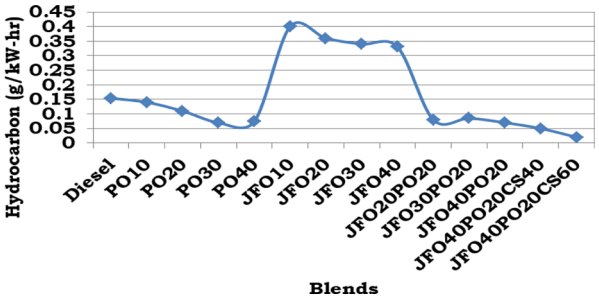

Fig. 7 Hydrocarbon emission variations for several blends

6.2 Carbon monoxide emission

As compared with diesel, Fig. 6 illustrates that all pine oil mixes have reduced CO_2 emissions. Because biodiesel naturally contains oxygen, JFO40 blends help reduce CO_2 emissions. In addition to producing less carbon dioxide than JFO40, JFO30PO20 and JFO40PO20 supply larger emission reductions. JFO40PO20CS60 has lower emissions than JFO40PO20 and reduces CO_2 emissions by 45.05%.

6.3 Hydrocarbon emission

Compared to JFO40PO20CS60, the other blends emit more HC. Figure 7 illustrates how coconut shell nano additive, which is added to the fuel blend to help minimize HC emissions, has high activation energy.

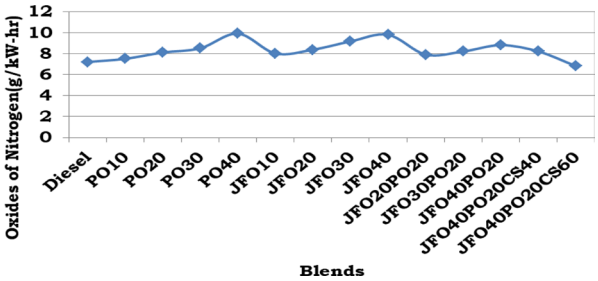

Fig. 8 Variation in NOx emission for several blends

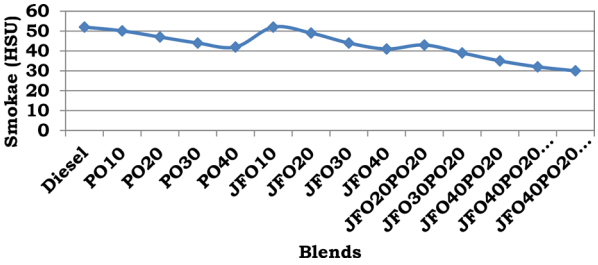

Fig. 9 Smoke emission variation for several blends

6.4 Oxides of nitrogen emission

All of the pine oil blends clearly show greater NOx emissions in Fig. 8. Specifically, compared to diesel, the NOx emissions from PO20 mixes are 11.12% higher. In a similar vein, the JFO40 blend releases 2.48% more NOx and 27.64% more than the PO40 blend. Higher NOx emissions are caused by JFO40PO20's higher peak heat release rate compared to diesel.

This raises the temperature of the cylinder, which ultimately results in increased NOx emissions. Conversely, JFO40PO20CS60 exhibits a 5.04% decrease in NOx emissions when contrasted with diesel. This is explained by the absorptive quality of coconut shell nano additive, which lowers the temperature of the cylinder by absorbing heat and thereby reducing NOx emissions.

6.5 Smoke emission

Figure 9 represents the smoke emission for different blends. JFO40PO20 emits 35.19% less smoke than diesel at higher BMEP conditions, while JFO40PO20CS60 emits less smoke and lowers smoke emission by 27.7%.

7 Conclusions

This study focuses on the utilization of JFME and PO as biofuels in a CRDi diesel engine. The investigation of the engine's performance, combustion, and emission characteristics when utilizing mixes of PO and JFME led to the following findings.

- The BTE has enhanced by 3.16% as a result of using a nano additive in CS60 ppm.

This is because the additive improves combustion through its catalytic activity. Diesel, JFO40PO20, JFO40PO20CS40, and JFO40PO20CS60 generate 2.92, 2.39, 2.28, and 4.12 g/kw-hr of CO, respectively.

- In contrast to diesel as the standard fuel, the fuel mix JFO40PO20CS60 has been determined to emit 45.05% less CO emissions than diesel at advanced BMEP conditions. By holding and releasing oxygen, the coconut shell nano material functions as an oxygen buffer, facilitating efficient oxidation and thus lowering CO emissions.
- Under higher BMEP circumstances, the fuel blend JFO40PO20CS60 reduces HC emissions by 37.23% when compared to diesel. This decrease is explained by the fuel blend's high activation energy of the coconut shell nano addition, which improves carbon particle combustion at cylinder wall temperature and lowers HC emissions under all BMEP circumstances.
- The primary reason for the drop in HC emissions is the high ratio of surface area to volume of the nanoparticles, which promotes a higher oxidation rate and burning. Additionally, the fuel mix JFO40PO20CS60 exhibits a 5.04% decrease in NOx emissions is measured under better BMEP settings relative to the baseline fuel diesel.
- The extensive experimental study leads to the conclusion that the fuel blend JFO40PO20CS60, which contains nanoparticles of coconut shell, significantly reduces smoke emission as compared to diesel by roughly 24.07 and 27.7 HSU. JFO40PO20CS60 is a viable biofuel mix for diesel engines because of this improvement in the oxygen/fuel ratio, especially when paired with optimal operating settings.
- The major applications of the present work are identified as follows: The bio fuel can be used in 4 stoke water cooled diesel engine, and this blend can directly be used in automobile engines for reducing the pollution and increase the efficiency by slightly decreasing the NO_x.

Author contributions G. Hima Bindu, M. Ganesh: Wrote the paper with input from all authors, Contributed to the design and implementation of research, to the analysis of result and to the writing of the manuscript; S. Sathees Kumar, Pravat Ranjan Pati: Contributed to the design and implementation of research; Jayant Giri, T Sathish, Emad Makki: Contributed to the design and implementation of research.

Data availability No datasets were generated or analysed during the current study.

Code availability Not applicable.

Declarations

Ethical approval Not applicable.

Consent to participate Not applicable.

Consent for publication Not applicable.

Competing interests The authors declare no competing interests.

References

1. Bruwer, J.J., Boshoff, B., Hugo, F.J.C., Fuls, J., Hawkins, C., Walt, A.N., Engelbrecht, A., du Plessis, L.M.: Utilization of sunflower seed oil as a renewable fuel for diesel engines. ASAE national energy symposium (United States) 6518435 (1981)
2. Barsic, N.J., Humke, A.L.: Performance and emissions characteristics of a naturally aspirated Diesel Engine with vegetable oil fuels. SAE Tech. Paper **810262** (1981)
3. Hemmerlein, N., Korte, V., Richter, H., Schröder, G.: Performance, Exhaust emissions and Durability of Modern Diesel engines running on Rapeseed Oil. SAE Tech. Paper **910848** (1991)
4. Labeckas, G., Slavinskas, S.: The effect of rapeseed oil methyl ester on direct injection Diesel engine performance and exhaust emissions. Energy Convers. Manag. **47**, 1954–1967 (2006)
5. Hawkins, C.S., Fuls, J., Hugo, F.J.C.: Engine durability tests with Sunflower Oil in an Indirect Injection Diesel Engine. SAE Tech. Paper **831357** (1983)
6. Wang, Y.D., Al-Shemmeri, T., Eames, P., McMullan, J., Hewitt, N., Huang, Y., Rezvani, S.: An experimental investigation of the performance and gaseous exhaust emissions of a diesel engine using blends of a vegetable oil. Appl. Therm. Eng. **26**, 1684–1691 (2006)
7. Fuls, J., Hawkins, C.S., Hugo, F.J.C.: Tractor engine performance on sunflower oil fuel. J. Agric. Eng. Res. **30**, 29–35 (1984)
8. Azam, M.M., Waris, A., Nahar, N.M.: Prospects and potential of fatty acid methyl esters of some non-traditional seed oils for use as biodiesel in India. Biomass Bioenergy. **29**, 293–302 (2005)
9. Jacobus, M.J., Geyer, S.M., Lesfz, S.S., Taylor, W.D., Risby, T.H.: Single-cylinder Diesel Engine Study of four Vegetable oils. SAE Tech. Paper **831743** (1983)
10. Pavuluri, S., Reddy, B.S., Prasad, B.D.: An experimental investigation on the performance, Combustion and Emission characteristics of CI Diesel Engine at various Compression ratio with different ethanol-biodiesel blends. Int. J. Adv. Sci. Technol. **29**, 2215–2226 (2020)
11. Kumar, A., Sharma, S.: An evaluation of multipurpose oil seed crop for industrial uses (Jatropha curcas L.): A review. Ind. Crops Prod. **28**, 1–10 (2008)
12. Kumar, M.S., Ramesh, A., Nagalingam, B.: An experimental comparison of methods to use methanol and Jatropha oil in a compression ignition engine. Biomass Bioenergy. **25**, 309–318 (2003)
13. Selvan, V.A.M., Anand, R.B., Udayakumar, M.: Effect of Cerium Oxide nanoparticles and Carbon Nanotubes as fuel-borne additives in Diesterol blends on the performance, combustion and emission characteristics of a variable compression ratio engine. Fuel. **130**, 160–167 (2014)
14. Bhattacharyya, S., Reddy, C.S.: Vegetable oils as fuels for Internal Combustion engines: A review. J. Agric. Eng. Res. **57**, 157–166 (1994)
15. Altın, R., Çetinkaya, S., Yücesu, H.S.: The potential of using vegetable oil fuels as fuel for diesel engines. Energy Convers. Manag. **42**, 529–538 (2001)
16. Pramanik, K.: Properties and use of jatropha curcas oil and diesel fuel blends in compression ignition engine. Renew. Energy. **28**, 239–248 (2003)
17. Basha, J.S., Anand, R.B.: An experimental investigation in a diesel engine using carbon nanotubes blended water-diesel emulsion fuel. Proc. Inst. Mech. Eng. A: J. Power Energy. **225**, 279–288 (2011)
18. Nwafor, O.M.I.: Emission characteristics of diesel engine running on vegetable oil with elevated fuel inlet temperature. Biomass Bioenergy. **27**, 507–511 (2004)
19. Shaheed, A., Swain, E.: Combustion analysis of coconut oil and its methyl esters in a diesel engine. Proc. Inst. Mech. Eng. A: J. Power Energy. **213**, 417–425 (1999)
20. Kayisoglu, B., Ulger, P., Akdemir, B., Aytac, S.: A research on determining some performance values by using proportional mixture of vegetable oil and diesel fuel at a diesel engine. J. Tekirdag Agric. Fac. **3**, 16–24 (2006)
21. Niemi, S.A., Hätönen, T.T., Laiho, V.O.K.: Results from a durability test of a mustard seed oil Driven Tractor Engine. SAE Tech. Paper **982528** (1998)

Publisher's Note Springer Nature remains neutral with regard to jurisdictional claims in published maps and institutional affiliations.

Springer Nature or its licensor (e.g. a society or other partner) holds exclusive rights to this article under a publishing agreement with the author(s) or other rightsholder(s); author self-archiving of the accepted manuscript version of this article is solely governed by the terms of such publishing agreement and applicable law.

Authors and Affiliations

G. Hima Bindu[1] · M. Ganesh[2] · S. Sathees Kumar[1] · Pravat Ranjan Pati[3] · Jayant Giri[4] · T. Sathish[5] · Emad Makki[6,7]

✉ S. Sathees Kumar
shrutishyami@gmail.com

✉ Pravat Ranjan Pati
pravatpati87@gmail.com

✉ Jayant Giri
jayantpgiri@gmail.com

Emad Makki
eamakki@uqu.edu.sa; emakki@hawaii.edu

[1] Department of Mechanical Engineering, Institute of Aeronautical Engineering, Hyderabad, Telangana 500043, India

[2] MLR Institute of Technology, Hyderabad, Telangana 500043, India

[3] Department of Mechanical Engineering, Graphic Era (Deemed to be University), Dehradun, Uttarakhand 248002, India

[4] Department of Mechanical Engineering, Yeshwantrao Chavan College of Engineering, Nagpur, Maharashtra 441110, India

[5] Saveetha School of Engineering, SIMATS, Chennai, Tamil Nadu 602 105, India

[6] Department of Mechanical Engineering, College of Engineering and Architecture, Umm Al-Qura University, Makkah 24382, Saudi Arabia

[7] Department of Ocean and Resources Engineering, School of Ocean and Earth Science and Technology, University of Hawaii at Manoa, Honolulu, HI 96822, USA